CRUSTAL STRUCTURE AND FORMATION OF THE SOUTHEAST NEWFOUNDLAND CONTINENTAL MARGIN

KRISTA L.M. SOLVASON

CRUSTAL STRUCTURE AND FORMATION OF THE SOUTHEAST NEWFOUNDLAND CONTINENTAL MARGIN

by

© Krista L.M. Solvason

A thesis submitted to the

School of Graduate Studies

in partial fulfilment of the

requirements for the degree of

Doctor of Philosophy

Department of Earth Science/Faculty of Science

Memorial University of Newfoundland

January 2006

St. John's Newfoundland

Abstract

The non-volcanic continental passive margin of southeast Newfoundland offers an ideal place to study rifting, because of the modest amount of sediment cover through which basement structure can be determined. Another advantage is that the Iberia margin has a wide range of data collected over it and offers an intensively studied conjugate margin that can be compared with the Newfoundland margin.

This doctoral thesis is a detailed study of the structures on the southeast Newfoundland margin. It focuses on multi-channel seismic reflection (MCS) data collected during the summer of 2000 with SCREECH (Study of Continental Rifting and Extension on the Eastern Canadian sHelf). The reflection data is processed using standard methods such as filtering, deconvolution, stacking and migration. This data set is supplemented by multi-channel seismic data provided by WesternGeco and GSI, and other industry data that has been released to the Canada Newfoundland and Labrador Offshore Petroleum Board (CNLOPB). Gravity, magnetic and wide angle data were used to enhance and constrain interpretations.

The thesis examines the structural variation and degree of segmentation in the upper crust along the slope area of the margin. The two shelf edge basins (Carson and Bonnition) exhibit a change in half graben polarity and three transfer faults are shown to segment the margin. A major basement ridge extending ~170 km near the present day shelf break separates the shelf basins from the Salar slope basin. The Moho is found to be relatively

flat along the continental shelf and shallows towards the shelf break. Extension values extracted from normal fault restoration and crustal thickness are different, with values based on crustal thickness appearing much larger. It is hypothesized that the unextended crustal thickness was less than the estimated 35 km to account for the discrepancies. To account for the differences in features observed on the Newfoundland and Iberia margins, a wide rift stretching model is favoured with break up occurring at the Iberia end of the rift. The petroleum potential of the area is assessed and the Bonnition and Salar basins are found to be the most prospective, while the Carson Basin is the least prospective.

Acknowledgments

There are many people that need to be thanked for helping make this thesis possible. First is my supervisor Dr. Jeremy Hall for providing a fantastic project to work on, and for all his help along the way. Dr. Sharon Deemer provided much needed seismic processing assistance, and Tony Kocurko helped solve any computer problems that appeared. Michael Enachescu added his vast knowledge of the Grand Banks and provided many ideas. I also need to thank my parents and sisters for all their support.

I would like to thank all of the graduate students at Memorial that made my time here so much more enjoyable. Thanks go to Jonathan Winsor, Rich Wright, and Craig Rowe for their insights into seismic processing and crustal evolution. Steve Kearsey for his love of data loading, gravity and magnetics. Stacey Mansfield for being around to procrastinate with so that I wasn't the only one. Brad Bonnell for making fantastic coffee. Glen Penney for making lunchtime entertaining. Ron Voordouw and Danny Mulrooney for providing a hard rock perspective. Kate Souders and Pete Valley for showing all of us the American way, and Victoria Hardy for making sure we were all informed of the current events.

Last but not least, I have to thank Steve Coulter for all of his support and help to make my thesis less stressful.

I also greatly appreciate data donations from GSI and proprietary data from WesternGeco. Funding from the Pan-Atlantic Petroleum Systems Consortium (PPSC), the School of Graduate Studies, the Department of Earth Sciences, and J. Hall was much appreciated. Software donations from Landmark Graphics, Geo-Logic Systems and Northwest Geophysical Associates aided in the interpretation of the data. Examiners Dr. Phil Bording, Dr. Rick Hiscott, and Dr. Grant Wach are also thanked for suggestions and comments on this thesis.

Table of Contents

List of Figures

List of Tables

List of Plates

List of Abbreviations and Symbols

β - Crustal stretching factor

δ - Lithospheric stretching factor

AGC – Automatic gain control

CDP – Common depth point

CNLOPB – Canada Newfoundland and Labrador Offshore Petroleum Board

e – Crustal extension value

GSC – Geologic Survey of Canada

GSI – Geophysical Service Incorporated

IAP – Iberia Abyssal Plain

Ma – Millions of years before present

MCS – Multichannel seismic reflection data

My – Millions of years

NMO – Normal moveout

NE - Northeast

NW - Northwest

OBH – Ocean bottom hydrophone

OBS – Ocean bottom seismograms

OCT – Ocean continent transition zone

ODP – Ocean Drilling Program

ORB – Ocean RefTek in a ball

RMS – Root mean square

SCREECH – Study of rifting and extension of the eastern Canadian Shelf

SDRS – Seaward dipping reflector sequences

SE - Southeast

Si – Initial subsidence

SW - Southwest

TOC – Total Organic Content

TVS – Time variant scaling

Twt – Two way travel time

WHOI – Woods Hole Oceanographic Institute

CHAPTER 1 Introduction

The Earth's tectonic plates split apart through continental rifting, which may eventually lead to seafloor spreading and the creation of new ocean basins. During rifting, thinning and extension of continental crust occurs along with volcanic activity to create many of the features that are found on present day rifted continental margins. A consequence of the rifting process is the formation of sedimentary basins, which in some cases may contain hydrocarbons. Hence rifted margins are studied to understand the tectonic processes that form them, and also for the petroleum resources that they may contain.

Once seafloor spreading is initiated, continental margins form on either side of the new ocean basin. Such margins are described as conjugate to one another. The Newfoundland and Iberian conjugate margins of the North Atlantic shown in Figure 1.1, are an excellent natural laboratory for the study of continental rifting. Both margins are 'non-volcanic,' - formed with little or no associated volcanic activity taking place, which is important because syn- or post -rift volcanism can interfere with and/or destroy crustal structures and extensional fabrics that relate to processes of continental rifting (Louden and Chian, 1999). Non-volcanic margins tend to preserve clearer evidence of crustal thinning, faulting, and uplift, than volcanic margins, though they do tend to be buried under considerably more sediment, which poses problems for imaging the crust. The Newfoundland and Iberian conjugate margins offer a non-volcanic setting with only a modest amount of sediment cover, making them an ideal place to study rifting (Louden and Chian, 1999).

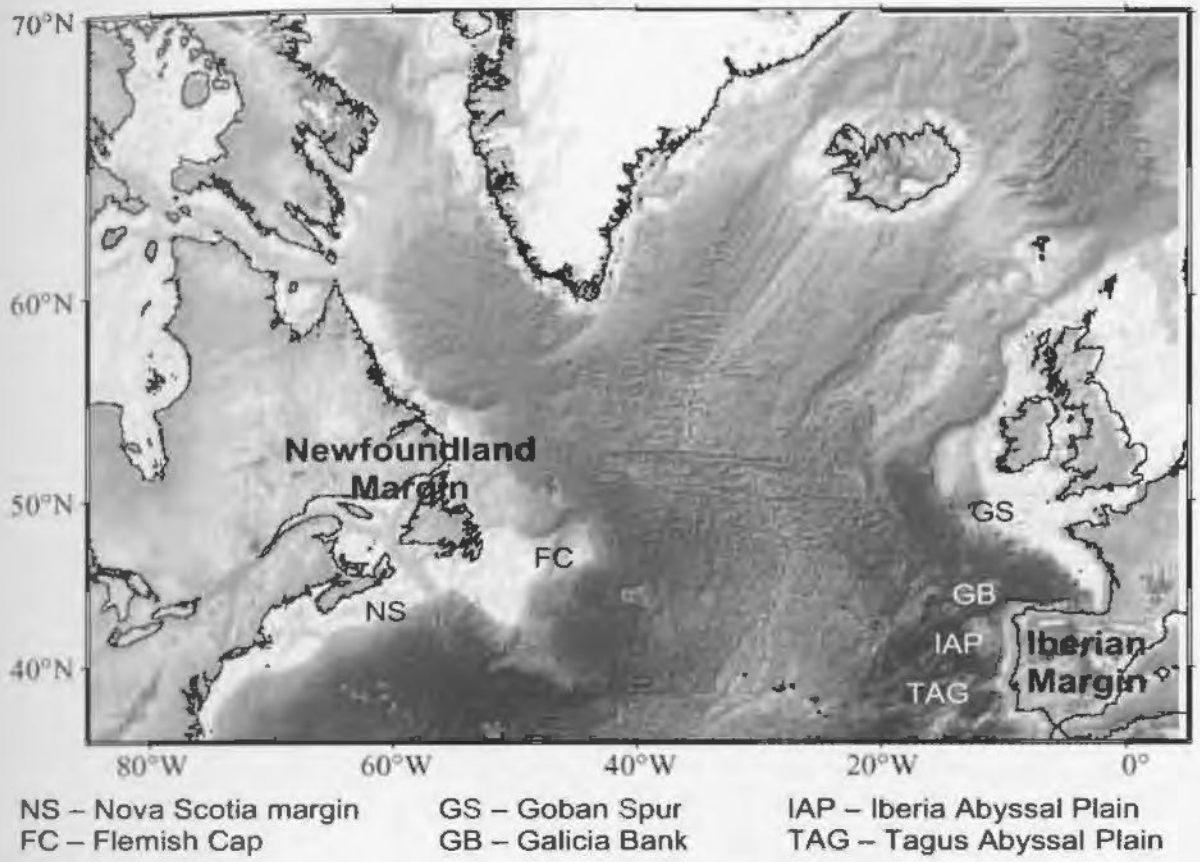

Figure 1.1. Newfoundland and Iberia conjugate margins (*modified from*: Louden and Chian, 1999).

The Iberia margin is one of the most extensively studied non-volcanic margins in the world, having detailed seismic reflection and refraction profiles, gravity and magnetic data and drill samples available across it (Whitmarsh et al. 2001). The extensive data coverage has allowed many lithospheric extension models for the Iberia margin to be proposed. Data sets recently collected on the Newfoundland margin can be compared to data that is already available on the Iberian margin. The Newfoundland margin has reflection seismic, wide angle seismic, gravity and magnetic data sets and drill samples that allow for detailed studies and comparisons across the margin conjugates.

1.1 Passive Continental Margins

"Passive" continental margins are formed by the separation of tectonic plates, and are distinct from "active" margins, which are formed by the collision or subduction of tectonic plates, and are associated with earthquakes, volcanoes and other mountain building processes. A passive margin is formed through continental rifting, which thins the lithosphere and allows continental break up to occur. Seafloor spreading is then able to commence, creating new ocean basins (Boillot and Froitzheim, 2001). Once seafloor spreading has opened up a substantial ocean basin, plate separation occurs at the mid-ocean ridge with minimal tectonic activity on the now passive continental margins. Weathering, erosional and depositional processes tend to dominate these margins in their later history.

1.2 Diagnostic Characteristics of Passive Continental Margins

Passive continental margins have characteristic geophysical signatures that allow them to be easily identified. Geophysical data from magnetics, bathymetry, gravity and seismology (both normal incidence and wide angle) can be used to understand how these margins formed. Linear strip magnetic anomalies are a common feature found on many passive margins. As seafloor spreading occurs, basaltic material rises to the seafloor and preserves a record of the local direction of the Earth's magnetic field as it solidifies. Magnetic reversals tend to occur every 500 000 years, and so give rise to alternating magnetization patterns in the basaltic crust. Figure 1.2 illustrates the magnetic stripe anomalies on the seafloor of the North Atlantic.

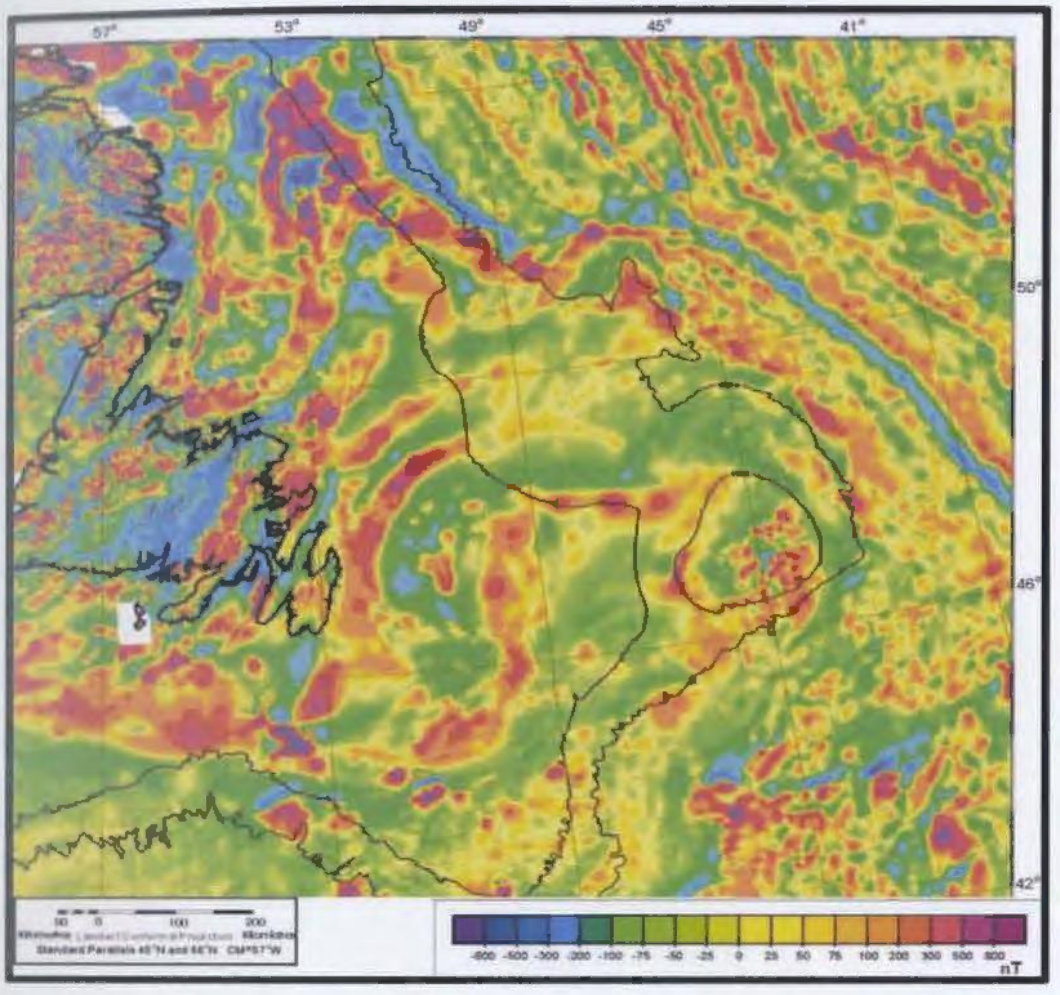

Figure 1.2. Magnetic stripe anomalies on the sea floor of the North Atlantic; most of the map is over continental crust, with sea floor spreading anomalies most obvious in the upper right corner (*modified from:* Oakey and Dehler, 2004).

Gravity anomalies also occur on passive margins. A free air gravity anomaly will be positive on the continental side and negative on the oceanic side, produced by the "edge effect" of thick continental crust abutting deepwater and thin oceanic crust (Keen et al. 1990). Oceanic crust is slightly denser than continental crust, and older oceanic crust is usually slightly thicker than younger oceanic crust. Figure 1.3 shows the free air gravity anomaly effect.

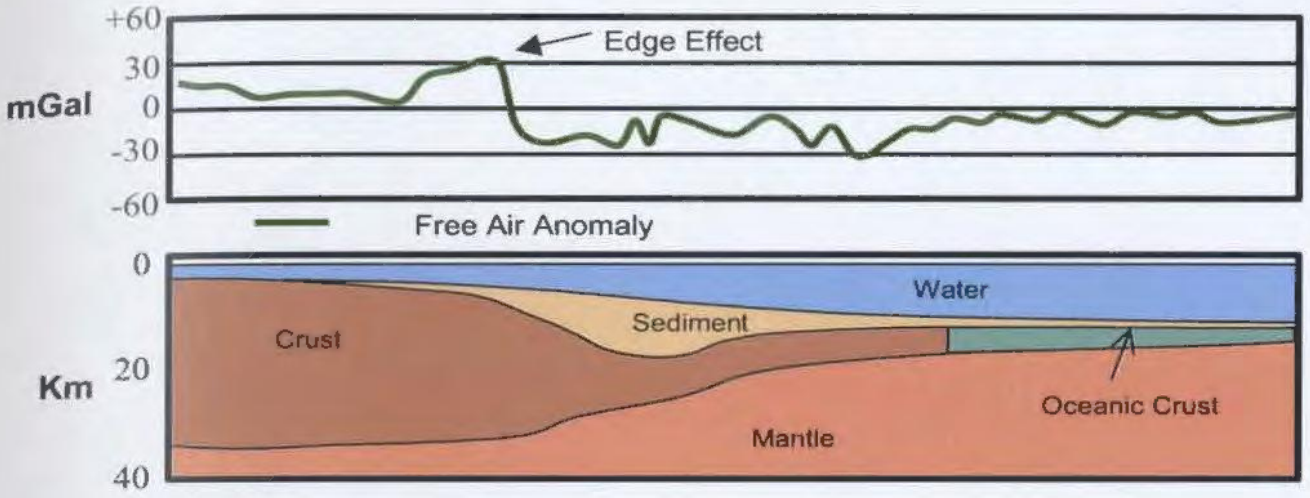

Figure 1.3. Free Air gravity anomaly over passive continental margins (*modified from*: Keen and Dehler, 1997).

1.3 Typical Morphology and Structure

The structure and morphology of continental margins can vary considerably from one margin to another and from one section of a margin to the next. The large variety of passive continental margins can be explained by the amount of sediment present on the margin, the amount of magmatic material that is present and the nature of the rifting structures. Some margins contain relatively thin sediment cover such as on the Goban Spur margin (Peddy et al. 1989) and the Bay of Biscay, whereas others may contain a vast amount of sediment as found on the Nova Scotia margin in the Scotian Basin (Keen and Potter, 1995). Some passive margins may exhibit seaward dipping reflector sequences (SDRS) and/or high P-wave velocities (>7.3 km/s), which provide evidence for mafic extrusive and intrusive rocks (Ruppel, 1995).

Features present on typical passive continental margins can been found in Figure 1.4. The continental shelf is a gently sloping submerged surface that includes continental crust

often with a cover of sedimentary rock. The width of the continental shelf can range from a few tens of kilometres to hundreds, and its usual water depth range is from 0 m to 300 m. The continental slope occurs beyond the edge of the continental shelf and is relatively steep (3-5°). The continental rise is located seaward of the continental slope and is differentiated from the continental slope by its much gentler dip. The abyssal plains of the ocean basins are found in water up to ~5 km deep, but are transected by mid-ocean ridges rising one to three kilometres above the surrounding ocean floor.

The Newfoundland margin in general has a wide continental shelf (~300 km), and contains a large amount of sediment in numerous rift basins, such as the Jeanne d'Arc, Horseshoe and Carson basins. These basins formed at the same time as the shelf-edge basin, but for them rifting did not continue to seafloor spreading.

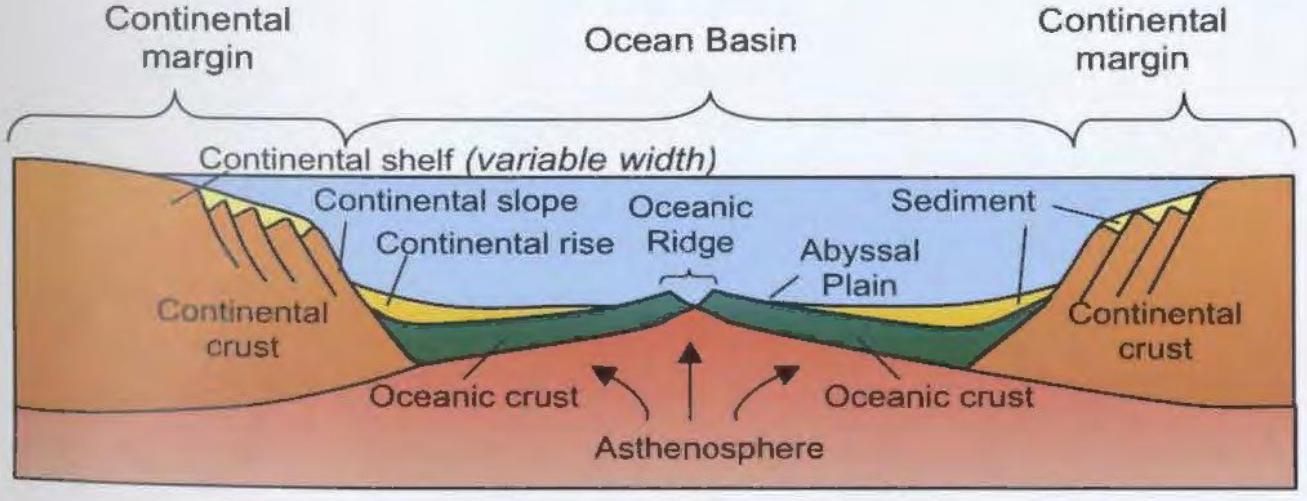

Figure 1.4. Diagram of features found on passive continental margins.

1.4 Models

Models describing the genesis of passive margins by lithospheric extension can be divided into categories based on the style of extension and the resulting geometry and composition of the margin. Conjugate margin pairs may look very similar – symmetrical about the ocean basin, or may exhibit vastly different characteristics – asymmetrical. Many models have been proposed to account for the differences, and listed below is a brief differentiation among some of the more prominent models.

1.4.1 Volcanic and Non Volcanic Margins

"Volcanic" margins show evidence of magmatic activity which can be in the form of extrusive basalts that form seaward dipping reflector sequences (SDRS) (Ruppel, 1995), high velocity underplated layers beneath stretched crust, radially oriented dykes, continental flood basalts, or serpentinite layers in the lower crust. The presence of extruded basalts forming seaward dipping reflectors (SDRS) and underplating lead to volcanic passive margins having a higher elevation than non-volcanic margins because of crustal thickening caused by the addition of high density basalt (Ruppel, 1995).
"Non-volcanic" margins may show some evidence of magmatic activity, but the amount of magmatism is relatively small when compared to volcanic margins. Figure 1.5 illustrates the volcanic and non-volcanic segments of the North Atlantic margin.
The East Greenland passive margin is a good example of a volcanic passive margin. The margin contains seaward dipping reflectors and high velocity underplated layers (Ruppel, 1995). An example of a non-volcanic passive margin would be the Northern Nova Scotia margin. This margin shows little evidence of volcanic processes or SDRS.

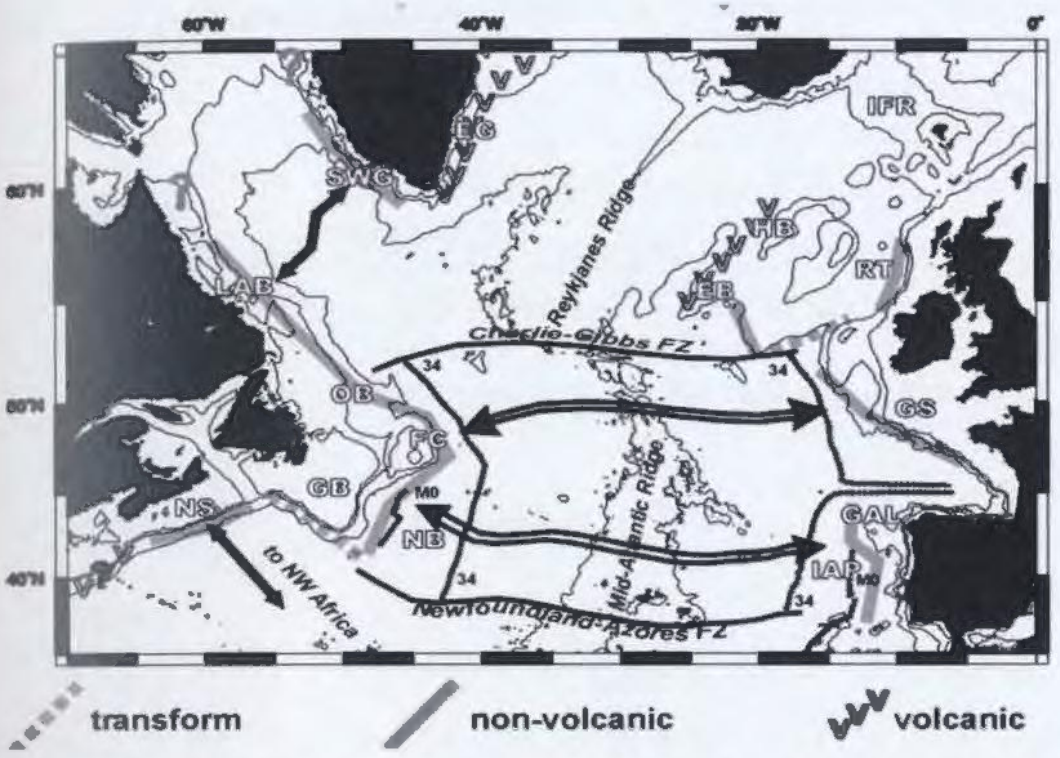

Figure 1.5. Map of the North Atlantic showing volcanic and non-volcanic margins (*from:* Louden and Chian, 1999).

1.4.2 Pure Shear - McKenzie Model

The McKenzie (1978) stretching model incorporates instantaneous pure shear lithospheric extension, which produces a symmetric pattern of thinning between conjugate margin pairs. In its simplest form, the model assumes that the lithosphere responds by deforming as a ductile continuum (Ruppel, 1995). The model assumes that homogeneous thinning of an entire block instantly occurs by a stretching factor of β. β is the ratio of the initial thickness to the final thickness (for extensional thinning $\beta>1$) (Ruppel, 1995). In this model it is assumed that the extending lithosphere is isostatically compensated before and after stretching (McKenzie, 1978). This concept produces initial subsidence (Si) and high heat flow values for various values of β (Neugebauer, 1987), which allow predictions of heat flow as a function of time to be made.

The pure shear model is relatively simple to implement in modelling; but it does have its drawbacks. The model oversimplifies the extension process and does not account for the heterogeneous rheological nature of the lithosphere, which results in faulting as one example of the localization of rifting in narrow zones (Ruppel, 1995). The pure shear model predicts that the lithosphere should thin uniformly and symmetrically. However on many passive margins relatively unextended and highly extended zones of lithosphere are often located adjacent to one another (Ruppel, 1995).

1.4.2.1 Variants – Pure Shear

Variations on the pure shear model proposed by McKenzie have been made by various authors. Jarvis and McKenzie (1980) modified the pure shear model to incorporate finite rifting (Collier and Watts, 1997). From their work they concluded that the previous assumption of instantaneous stretching gives reasonable results when stretching periods are less than 20 My. Royden and Keen, (1980) and Sclater and Christie (1980) proposed a non-uniform pure shear model, where the lithosphere is stretched by different stretching factors above (β) and below (δ) a detachment boundary (Dehler and Keen, 1993), which in most cases is taken to be the base of the crust – the Moho (Ruppel, 1995). The introduction of lithospheric stretching (δ) helps account for the observed variations in syn- and postrift subsidence ratios. In non-uniform stretching models the upper crustal layer shows brittle deformation and extension in the form of faults but may still approximate pure shear on the megascale, while the lower crustal layer exhibits ductile deformation.

Figure 1.6 from Einsele (2000) depicts the predicted structures associated with the pure shear model. The pure shear model with its modifications is able to explain many of the features associated with continental margins, the most common being rotated fault blocks that show a series of symmetric seaward dipping reflectors (Louden and Chian, 1999). The width of the rift zone can be accounted for in pure shear models, as well as the subsidence and uplift history of the margin. The free air gravity edge effect anomaly that is observed at margins can also be explained through pure shear models (Collier and Watts, 1997).

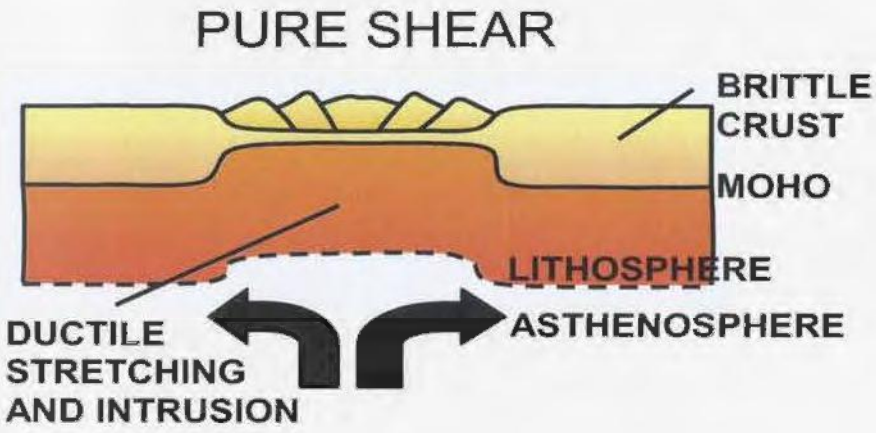

Figure 1.6. Pure shear stretching model *(modified from:* Einsele, 2000*)*.

As noted above the pure shear model does however have its drawbacks. The asymmetry in conjugate margin pairs cannot be readily explained; neither can some basement highs that have been found beneath shelf breaks (Lister et al. 1986). Pure shear models fail to explain the observed differences in the amount of post and syn-rift sediments that are noticed across many margins (Ruppel, 1995), unless there are lateral variations in β and δ in two layer stretching models (Keen and Dehler, 1997). To explain some of these features, other authors prefer to use a simple shear model for extension.

1.4.3 Simple Shear – Wernicke Model

In the simple shear model (Wernicke, 1985), extension occurs along low angle detachment faults that penetrate the crust and possibly the whole lithosphere (Wernicke and Burchfiel, 1982). Extension along the detachment fault results in the thinning between the upper and lower layers to be offset from each other, which produces asymmetric margins (Louden and Chian, 1999). In simple shear models the upper plate is generally composed of rocks that were originally above the detachment while the lower plate is composed of deeper crystalline rocks (Lister et al. 1991). The basement of lower plate margins is generally highly structured with rotational normal faults, tilted blocks and half grabens. The upper plate margin is characterized by normal faulting and is generally only weakly rotational (Lister et al. 1986) and tends to be structurally simple (Manatschal and Bernoulli, 1998). As with the pure shear model proposed by McKenzie, there have been many variants proposed for the simple shear model.

1.4.3.1 Variants – Simple Shear

Lister et al. (1991) have proposed numerous variations on the Wernicke model. These variations are used to explain the formation of structures such as continental ribbons, marginal plateaus, submerged continental fragments and outer highs. Figure 1.7 shows the predicted structures for a simple shear model. The distinguishing feature of simple shear extension would be landward dipping or flat lying reflectors delineating the major detachment fault (Louden and Chian, 1999). There are many seismic profiles covering rifted margins and few show evidence of detachment faults. The "S" reflector on the

Galicia Bank and the "H" reflector on the Iberian margin are presently the best candidates for detachment faults (Collier and Watts, 1997).

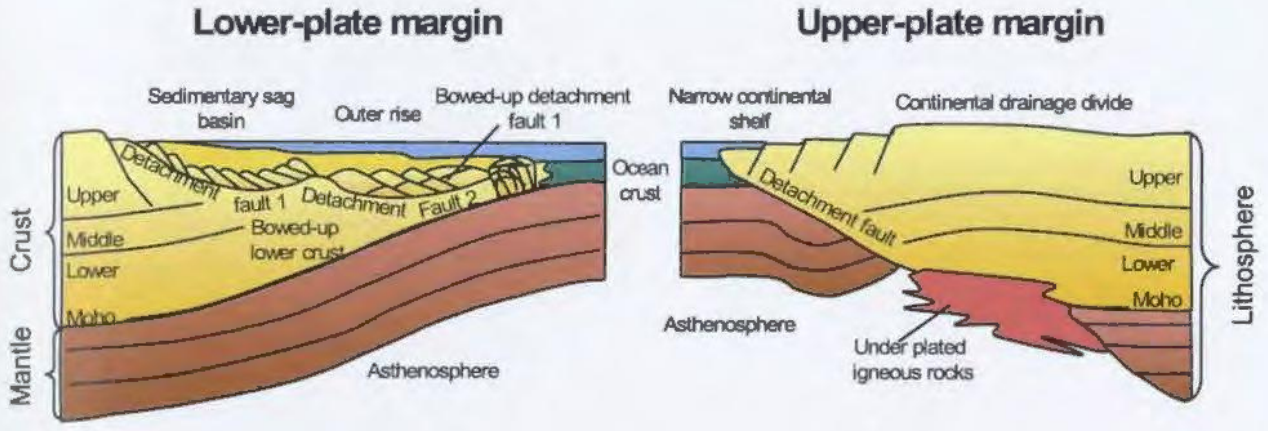

Figure 1.7. Simple shear stretching model and features (*modified from:* Louden and Chian, 1999).

Both pure shear and simple shear models alone are unable to predict and describe all features that are present on passive continental margins. Other models have combined both pure and simple shear ideas to create hybrid models (Ruppel, 1995). Seismic and structural data tend to indicate that a combination of pure shear (ductile stretching) and simple shear (brittle faulting) is the most accurate way to describe rifting on passive margins (Ruppel, 1995). In hybrid models, low angle detachment faults or listric faults dominantly occur in the brittle crust (Ruppel, 1995), with pure shear stretching occurring in the deeper lithosphere (Keen and Dehler, 1993).

Work on the Iberian margin has produced many rifting models, attempting to explain the tectonic evolution of passive margins. Holker et al. 2003 have shown that top basement detachment faults (TBDF) may be an important feature on non-volcanic passive margins

during the later stages of rifting, just before seafloor spreading. These faults initially develop as listric downward convex detachment faults exhibiting a small amount of extension, which change to downward concave faults accommodating a high amount of extension. This higher amount of extension can lead to exhumation of crustal and mantle rocks (Holker et al. 2003), which is a characteristic of the Iberian margin.

1.5 Newfoundland and Iberian Conjugate Margin Pairs

The opening of the North Atlantic took place in discrete stages with the commencement of opening occurring in the Jurassic strata off the east coast of the United States and continuing northward. Major transfer faults segment the margin into discrete sections and separate zones which show different geometries and amounts of extension (Tankard et al. 1989). Figure 1.8 shows the major segments of the Newfoundland Atlantic margin and the major transforms that separate each segment.

Figure 1.8. Transforms separating segments of the Atlantic margin (*modified from:* Tankard et al. 1989).

1.5.1 North Atlantic Spreading/Tectonic History

Rifting and plate tectonic motion resulted in continental break up between Africa and North America in the Triassic to Jurassic periods (de Voogd et al. 1990). Rifting then progressed northward to the Grand Banks and Iberia which broke up during the Early to Middle Cretaceous. The northeast continental margin of Newfoundland (Orphan Basin and Flemish Cap) and Europe then separated during the mid-Cretaceous (Keen et al. 1987b). Labrador and Greenland later broke up in the Late Cretaceous. Figure 1.9 summarizes the major events that occurred on the northeast Atlantic margin.

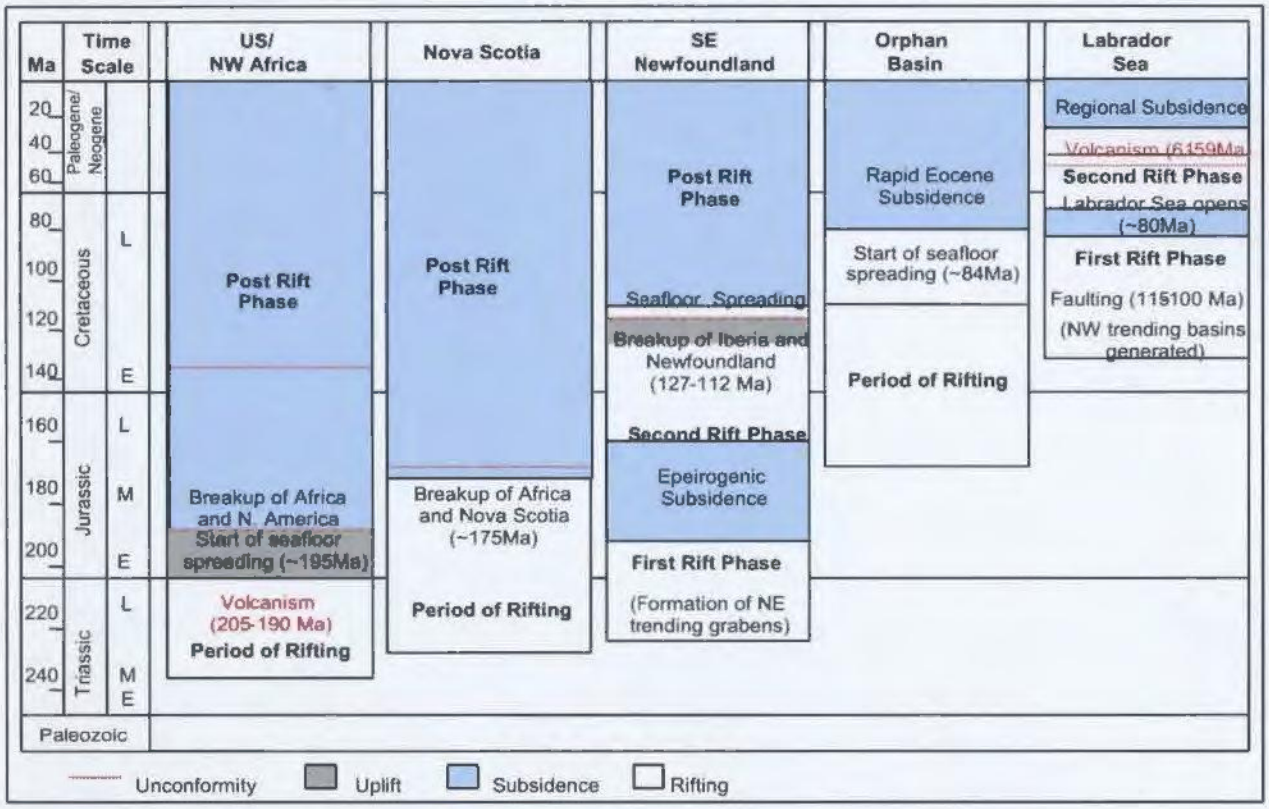

Figure 1.9. Major tectonic events on the west Atlantic margin (*compiled from:* Driscoll et al. 1995, Enachescu, 1988, Grant et al. 1988, Keen et al. 1987a, Sinclair, 1995a and Tucholke et al. 1989).

In the Mesozoic, rifting between the Grand Banks and Iberia took place during two main phases. During rifting, extension of the continental basement occurred, which produced numerous faults and major subsidence across the margin.

This first stage of rifting between the Grand Banks and Iberia lasted for approximately 20 My in the Late Triassic (Tucholke et al. 1989). Others have proposed that rifting may have only lasted 5-10 My based on the lack of syn-rift sequences on reflection profiles (Louden and Chian, 1999). This episode of rifting is associated with the break-up between the African and North American plates (Tucholke et al. 1989) and created a system of Mesozoic rift basins on both the Grand Banks and Iberian platforms, which trend mainly north-east (Tucholke et al. 1989). After this rifting phase that ended during the late Early Jurassic (Grant et al. 1988), a period of widespread subsidence occurred across the margin (Tucholke et al. 1989).

Subsidence was interrupted by a second rifting phase that commenced in Late Jurassic. Grant et al. (1988) interpreted the onset of rifting to begin in Tithonian time (154 Ma) while Tankard and Welsink (1987) have interpreted the rifting onset to be in Callovian time (164 Ma). Faulting around the rift basins and uplift and erosion of highs deposited sandstone and mudstones across many of the basins. Continental break up is interpreted to occur in the mid-Cretaceous no later than Barremian to Aptian time (127-112 Ma) (Driscoll et al. 1995) and is generally thought to have produced widespread local and regional unconformities (Tucholke et al. 1989).

From plate reconstruction models, the spreading of the Atlantic from Newfoundland - Iberia northward took place from approximately 130 Ma (Louden and Chian, 1999) and generally propagated from the south to the north, which is shown by the magnetic anomaly pattern on the seafloor. Figure 1.10 (after Srivastava and Verhoef, 1992) illustrates the position of the Newfoundland and Iberia margins when reconstructed back to M0 (118 Ma, Early Aptian). Determining the onset of seafloor spreading is difficult due to limited sampling (drilling) and the Cretaceous magnetic quiet zone (Driscoll et al. 1995). The magnetic quiet zone ranged from 121 to 84 Ma and is interpreted to be the result of no reversals being produced for 37 My. The large amplitude J anomaly is present west of the ocean continent transistion (OCT) on the Iberia Abyssal Plain, and is located southwest of the SE Newfoundland ridge on the Newfoundland margin. This anomaly is thought by Louden and Chian (1999) to be the first unequivocal indication of seafloor spreading. The J anomaly lies between chron M0 and M2, which would indicate that seafloor spreading commenced at 121 Ma (Louden and Chian, 1999). North of the Newfoundland seamounts Anomaly M0 is not well developed (Driscoll et al. 1995). Along the Iberian margin M0 is not observed north of the Figueiro fracture zone (Driscoll et al. 1995). This suggests that north of the seamounts seafloor spreading occurred after Early Aptian. Seafloor spreading between the Flemish Cap and Goban Spur is thought to have initiated in the Late Albian (110 Ma) (Louden and Chian, 1999).

A third period of rifting occurred during Late Cretaceous time. This period of rifting opened the Labrador Sea and separated the Orphan Knoll and Flemish Cap from Northwest Europe around Santonian time (Tucholke et al. 1989).

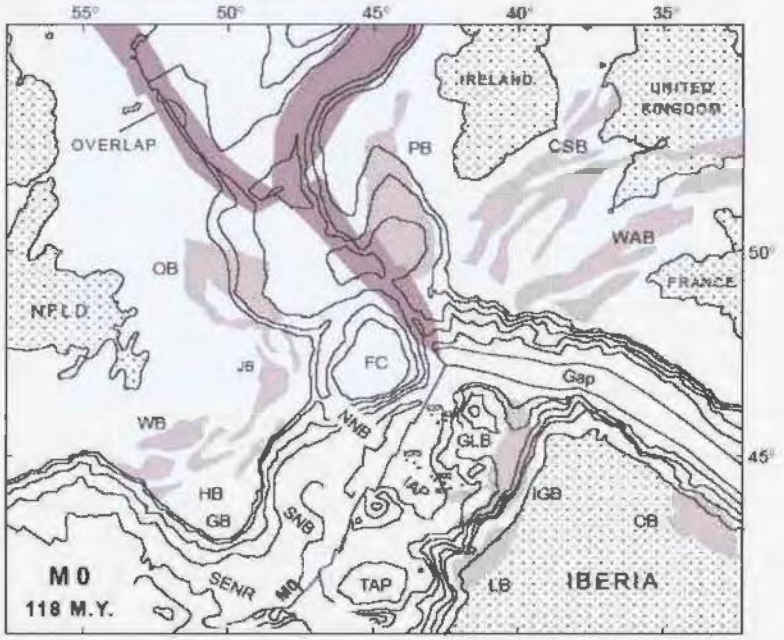

Figure 1.10. Newfoundland Iberia Margins reconstructed back to M0 time approximately 118 Ma, Early Aptian time (*from:* Srivastava and Verhoef, 1992).

1.5.2 Contrasts between Newfoundland and Iberian margins

The Newfoundland and Iberian margins exhibit many differences both structurally and compositionally, which leads to this conjugate margin pair being classified as asymmetric, by many authors (Tankard and Welsink, 1987, Sibuet, 1992 and Enachescu, 1992b). The Iberian margin has a narrow continental shelf as opposed to the very broad platform exhibited on the Newfoundland margin. Iberia has limited rift basin development with the Lusitanian Basin being in shallow water and the Galicia Interior Basin in the deep water to the north. In contrast, the Newfoundland margin has extensive rift basin development in its thick continental crust, with the creation of the Jeanne d'Arc, Flemish Pass, Whale, Carson, Bonnition and Horseshoe basins being most notable (Tankard and Welsink, 1987). The deep basement structure is also quite different below the two margins. In the transition zone between continental and oceanic crust the depth to basement is generally 1 to 2 seconds (two way travel time) longer on the Iberia side

than on the Newfoundland margin (Lau et al. 2005 *in press*). The basement roughness is also different below the two margins in the transition zone. The Newfoundland margin generally has basement with low relief whereas on the Iberia margin relief is much higher (Shipboard Scientific Party, 2004a).

The Newfoundland margin is quite different from most of the North American continental margins. The narrow elongate basins present on the Newfoundland margin are in stark contrast to the wide and broad Orphan Basin to the north and the Scotian Basin (combining the Mohican, Abenaki, and Sable basins) to the south. These two basins are shown in Figure 1.11 and occupy most of their respective continental margins. According to Keen et al. (1987a), it is thought that these regions were subject to greater crustal extension than in the Grand Banks area which resulted in the formation of larger and broader basins as opposed to the narrow ones found offshore Newfoundland.

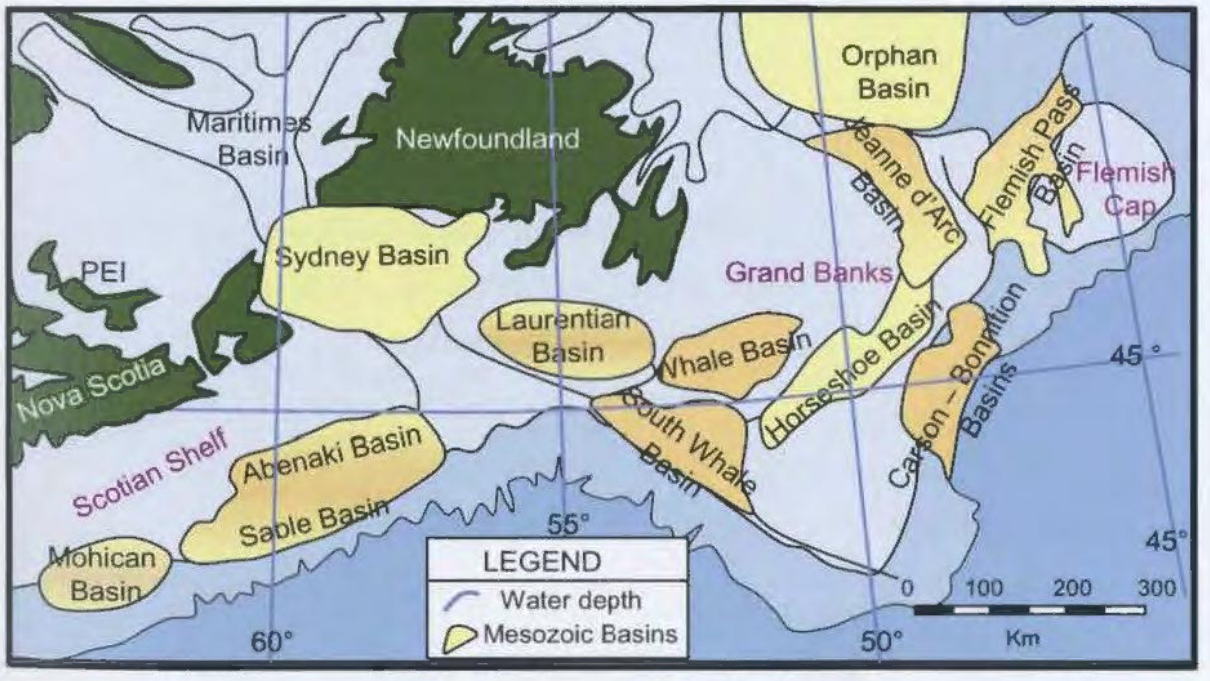

Figure 1.11. Position of basins along the Newfoundland margin (*modified from: Enachescu, 2000*).

On the Iberian margin Galicia Bank is located north of the Iberia Abyssal Plain, while the Tagus Abyssal Plain is located to the south (see Figure 1.12 for locations).

The Iberian margin is generally composed of wide continental blocks which are separated by submarine canyons that relate to major fault lineaments (Alves et al. 2003a). The Porto margin contains a narrow continental shelf (15 -30km) and a narrow, steep (~5°) continental slope. The Lisbon margin located south of the Porto margin has a wider continental shelf (~30 km) and a thick sequence of sediments. In this area the continental slope is also steep (4.5°). The Alentejo margin, further to the south has a gentle continental slope (~0.5°) which is difficult to distinguish from the continental shelf (Alves et al. 2003a).

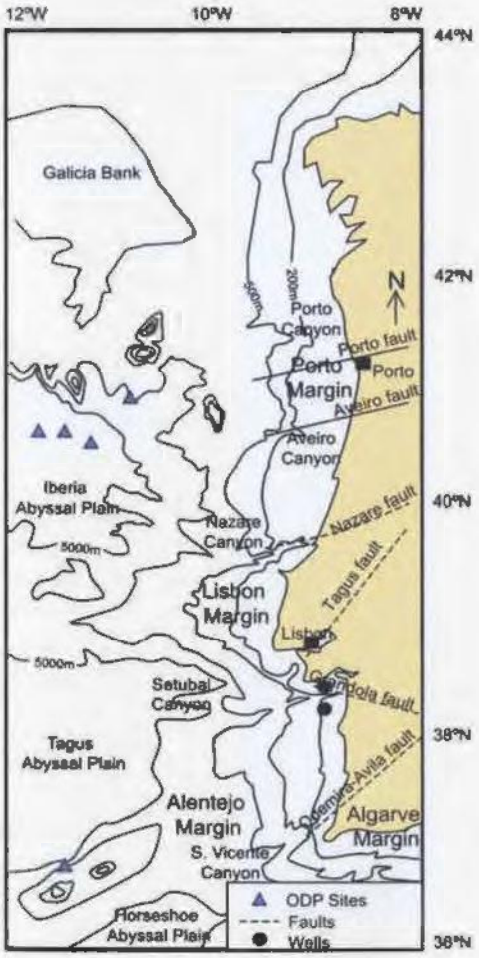

Figure 1.12. Iberian Margin and associated features (*modified from*: Alves et al. 2003a).

1.5.3 S.E. Newfoundland Margin and related basins

The Newfoundland margin contains numerous rift related basins that have developed in thick continental crust. The thickness of continental crust adjacent to the Newfoundland margin is generally between 27 and 35 km, and much of the platform is in shallow water with depths less than 100m. Many of the basins, such as the Jeanne d'Arc, Whale, Horseshoe Bonnition and Carson, formed in the Late Triassic during the first significant episode of rifting. It was also during this time that the Lusitanian Basin on the Iberian margin formed (Alves et al. 2002). These narrow basins were formed by extension and were accommodated by major faults that extend into the deep crust and flatten along or just above the Moho (Keen et al. 1987a) or, arguably, in the mid-crust (Dentith and Hall, 1990). Because of the similarity among many of the Newfoundland basins, it is suggested by Keen et al. (1987a) that the basins formed by the same mechanisms. The basement on the Grand Banks is interpreted to be Hadrynian and possibly older crystalline rock and Paleozoic metasedimentary and sedimentary rock (Enachescu, 1988). Figure 1.13 shows a simplified lithostratigraphic chart of the Grand Banks based mainly on the Jeanne d'Arc Basin.

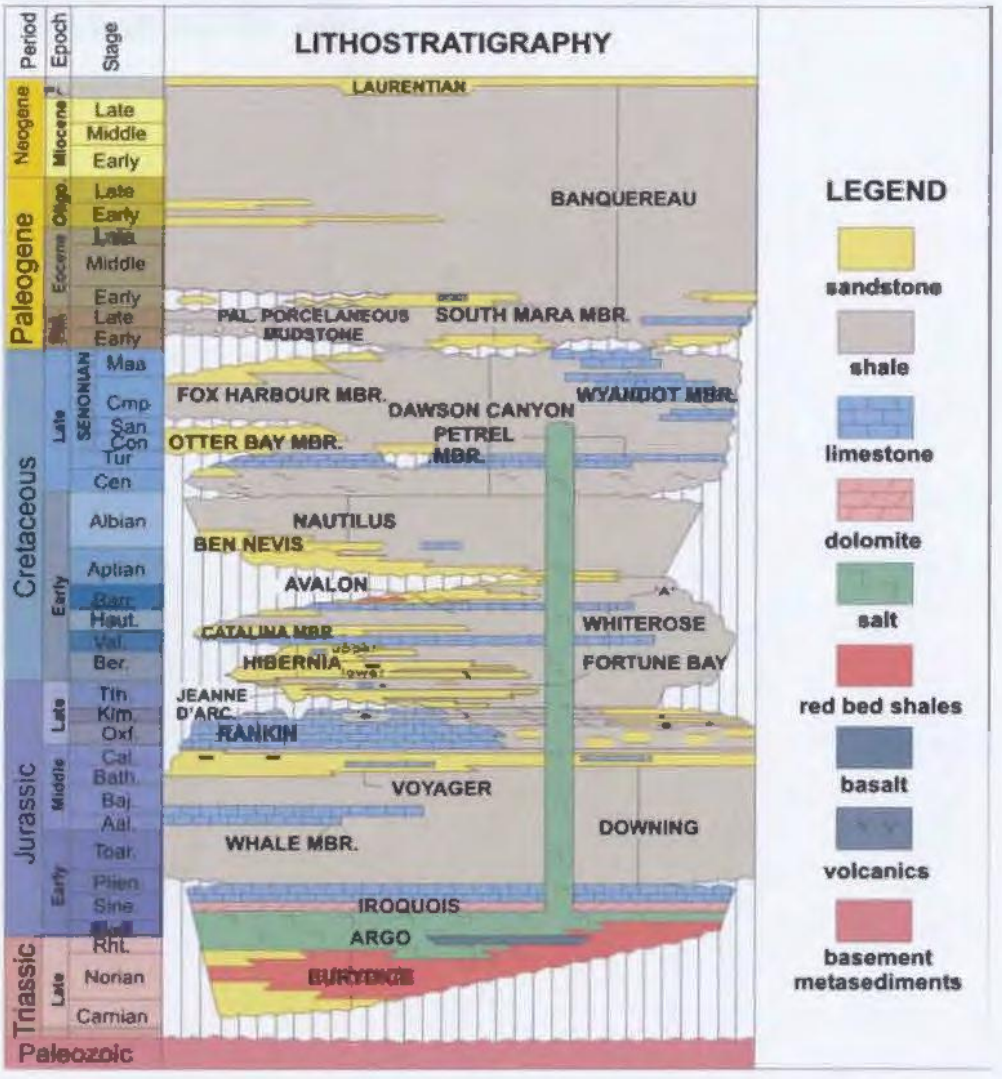

Figure 1.13. Generalized stratigraphic chart for the Grand Banks (*modified from:* Newfoundland Energy Branch, 2000).

1.5.3.1 Generalized Carson and Bonnition basin stratigraphy

The basins on the Newfoundland margin generally accumulated much of the same sediments that filled the Jeanne d'Arc Basin. The Bonnition and Carson basins are located near the shelf break on the southeast Newfoundland margin and occupy a craton-margin setting (Grant et al. 1988). The basins are composed of Mesozoic and Cenozoic sediments and four wells have been drilled in these two basins with none of them reaching basement (Grant et al. 1988). Sediments in the Carson and Bonnition basins

have been variably preserved due to the structure of the basins and the many erosional unconformities that occur. Upper Triassic and Lower Jurassic sediments tend to be preserved in the southern Carson Basin, while the central and northern portions of the Bonnition Basin preserve more of the Upper Jurassic and Lower Cretaceous section (Grant et al. 1988).

The Kettle and Eurydice formations are 'red beds' from Carnian to Norian time containing interbedded conglomerates, subarkosic sandstones and shales, which were most likely produced from the erosion of basement highs and then deposited under arid conditions (Austin et al. 1989). During the Late Triassic to Early Jurassic (Hettangian-Sinemurain) the Osprey and Argo evaporites were deposited in basins on both the Newfoundland and Iberian margins. The evaporites were deposited in a northeast to southwest trending elongated basin and the contact between the evaporites and the Kettle/Eurydice 'red beds' is conformable and sharp (Jansa et al. 1980). The Osprey H-84 well shows that the evaporites are dominated by halite with zones of reddish shale, dolomite, mudstone and siltstone. Subaerial basalt flows are found between the Argo and Osprey formations and provide a strong seismic marker.

In the Early Jurassic (Sinemurian time), carbonates from the Iroquois Formation were then deposited over the evaporites during a period of subsidence across the Grand Banks and Iberia. Carbonate deposition resulted from an Early Jurassic transgression and the contact between the carbonates and the evaporites (Argo and Osprey Formation) is sharp (Jansa et al. 1980). Marine shales were deposited during Late Pliensbachian time (Grant

et al. 1988) and are overlain by a monotonous shale and interbedded limestone succession during Toarcian to Callovian time (Tankard et al. 1989). A variety of lithofacies consisting of sandstone, shale, and limestones were deposited from Oxfordian to Tithonian time in the Rankin Formation. Shale deposited in Middle Kimmeridgian time is the principal source rock for all the oil discovered in the Jeanne d'Arc Basin (Grant et al. 1988). An unconformity is present in the Middle Tithonian above which continental and shallow marine clastics were deposited in the Jeanne d'Arc Formation. The clastic sediments of the Hibernia, Whiterose and Avalon formations overlie the Jeanne d'Arc. The Logan Canyon unit was deposited during Barremian to Cenomanian time, with major unconformities occurring in the Late Aptian and Late Albian. Transgressive marine sediments of the Dawson Canyon Formation were deposited during Cenomanian to Turonian time, and from Coniacian to Maestrichtian time an influx of clastics produced prograding clinoforms. A major unconformity occurs in the Late Cretaceous to Paleocene, with delta front sands and turbidites overlying the unconformity. The Banquereau Formation was deposited in Eocene time to the present and represents mainly deep shales, minor chalks and mudstones.

1.6 Objectives of MARIPROBE

In the summer of 2000 the MARIPROBE project acquired multi-channel seismic (MCS) reflection and wide-angle data (using ocean bottom seismographs, OBS) across three transects of offshore Newfoundland. MARIPROBE is the Canadian component of the international collaboration with the SCREECH (**S**tudy of Continental **R**ifting and **E**xtension on the **E**astern **C**anadian s**H**elf) project. Heat flow measurements were also

taken in locations where data coverage from existing studies was sparse. The overall goals of the MARIPROBE project were to analyze the collected seismic data to create depth sections of the margins and use the heat flow data to constrain models of the lithosphere's thermal structure. Final models created of the margin conjugates would then be interpreted in terms of the style and timing of continental rifting.

Objectives relating to the Newfoundland - Iberian transect include the characterization of regional crustal structure on the Newfoundland margin, which would include the unextended continental crust in the back-shelf regions, the thinned continental crust in the slope and rise, the transitional crust in the deep basin, and the oceanic crust. It is hoped that the new data will define the nature of the crustal boundaries and show how they vary both along the Newfoundland margin and across the margin to the Iberian side. The new data will also provide information to constrain the gross amount of melt produced during rifting. Crustal structure of the Newfoundland margin will be compared with structures on the Iberian margin to determine extensional mechanics. The seismic data also fulfill site survey requirements for ocean drilling program (ODP) sites. Figure 1.14 illustrates the locations of the three transects and the relation of these lines to the ODP Sites that were completed in the summer of 2003.

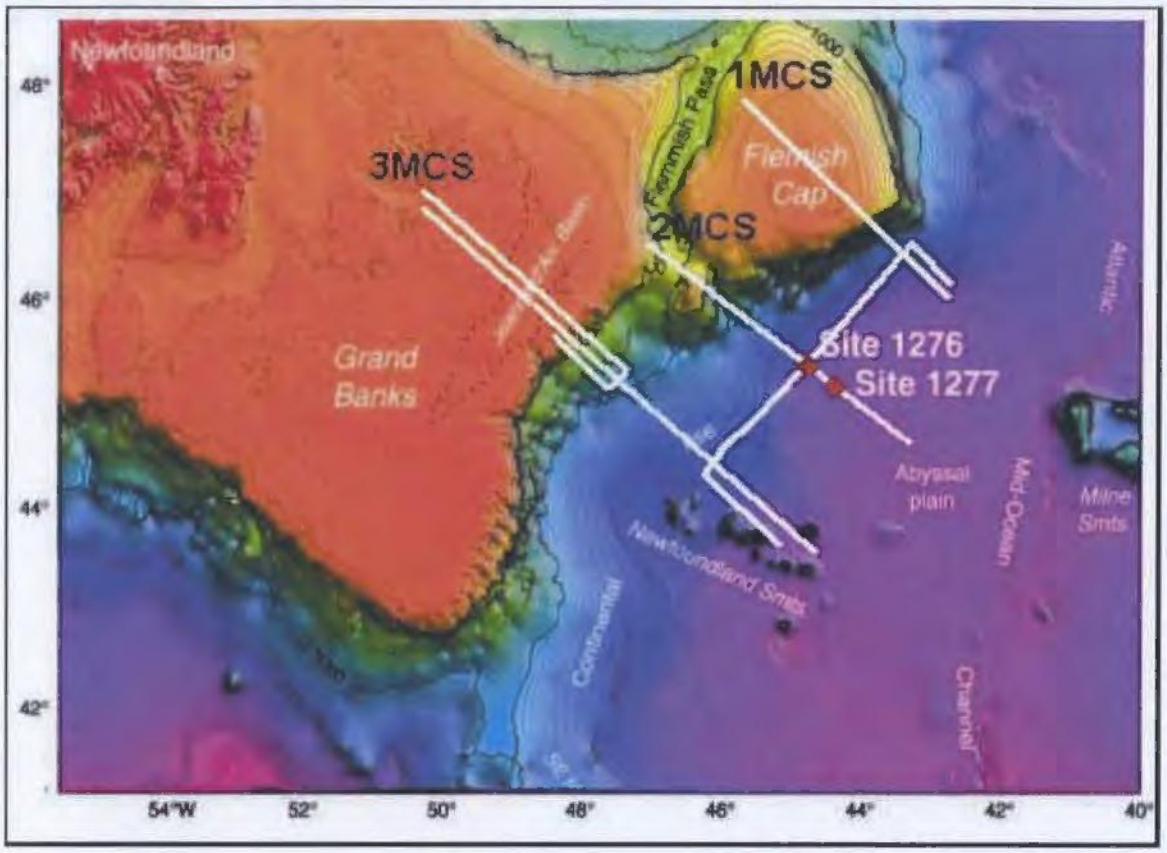

Figure 1.14. Location map of the 3 MARIPROBE transects on the Newfoundland margin, and the ODP Sites 1276 and 1277 (*modified from*: Enachescu et al. 2005).

1.7 Thesis Objectives

This thesis focuses on seismic lines in the area around the southern most SCREECH/MARIPROBE transect. The main seismic lines studied are SCREECH 3MCS, 401,402 and 403. Other seismic data from industry (proprietary data from WesternGeco and data from GSI) and the Canada Newfoundland and Labrador Offshore Petroleum Board (CNLOPB) are also used to study this part of the margin. The main area of interest is on the slope portion of the margin studying the unextended crust out to the extended crust. This thesis has seven main objectives in its examination of the evolution of the basins and crust in the slope area.

1.7.1 Objective 1 – Processing of SCREECH seismic reflection data

The first objective of this thesis is to process the deep seismic reflection data that was acquired in 2000 by the SCREECH project. SCREECH lines 401, 402 and 403 will be processed with the aim to image basins on the shelf and slope area of the margin, as well as image deep crustal structures and the Moho. All seismic processing will be done with the software package ProMAX, which is provided by Landmark Graphics.

1.7.2 Objective 2 – Margin variation along strike

The second objective of this thesis is to examine the structural variation in the upper crust along the Newfoundland margin (slope area) and determine the degree of segmentation along the margin. This will be related to the evolution of rifting and the spreading history of the margin. Previous investigations have focused on variation in crustal structure across margin conjugates, however little work has been done on the variation of margins along strike. Considerable crustal variation along strike can be found on the Newfoundland margin and this variation may play an important role in determining the rifting history. This first objective is achieved by mapping the major structures, sediment packages, faults, basement and any transfer zones on the southeast Newfoundland margin. Mapping is done in Seisworks, a Landmark Graphics software package, using seismic reflection data from the SCREECH project and industry seismic lines tied to well data (including ODP). Gravity and magnetic data also aids in interpretation.

1.7.3 Objective 3 – Structure and composition of the inter-basin ridge

The third objective of this thesis is to determine the significance of the large high located under the continental slope in relation to rifting; and to identify the main composition of the fault block and determine if transfer faults dissect it. Transfer faults segment margins into discrete sections and separate areas where different styles of extension occurred. This objective is achieved via detailed mapping of the major basement block to determine its lateral extent and nature. Seismic reflection lines from SCREECH, WesternGeco, GSI, and CNLOPB along with gravity data have been used in determining the extent of the high, its composition and its influence on the surrounding area.

1.7.4 Objective 4 – Nature and variation of the lower crust and Moho

The fourth objective of this thesis examines the nature and variation of the lower crust and Moho along the margin; and to determine the variability of the lower crust along the margin. Lower crustal reflections along the margin are imaged on many seismic lines that are available. Determining the position of the lower crust and Moho helps gain insight into the evolution of rifting on the margin. This objective is achieved by mapping deep crustal reflections on SCREECH seismic lines and deep industry seismic lines which image lower crustal features. Wide-angle seismic models are compared to the seismic reflection data to aid in constraining interpretations where reflection data is ambiguous.

1.7.5 Objective 5 – Extension and evolution of the Newfoundland margin

The fifth objective of this thesis is to examine the amount of extension that occurred on the Newfoundland margin, and infer the type of stretching model that will best describe the extension. This objective is achieved by restoring various profiles along the Newfoundland margin. Extension (e) from the restoration of normal extensional faults will be calculated as well as crustal stretching values (β) based on crustal thinning.

None of the stretching models currently used to describe extension between Newfoundland and Iberia are able to account for all features that are observed on the conjugate margins. Figure 1.15 illustrates a model from Tankard and Welsink (1987) in which they envision the Murre Fault to be antithetic and converging with a master detachment from the Iberian margin. Figure 1.16 illustrates a model by Sibuet (1992), who proposes the master detachment originates from the Newfoundland side and the "S" reflector on the Iberian margin would represent an extension of this detachment. The results from the Newfoundland margin are compared with those on the conjugate Iberian margin, in order to test the existing stretching models and assess the potential significance of segmentation of the margins.

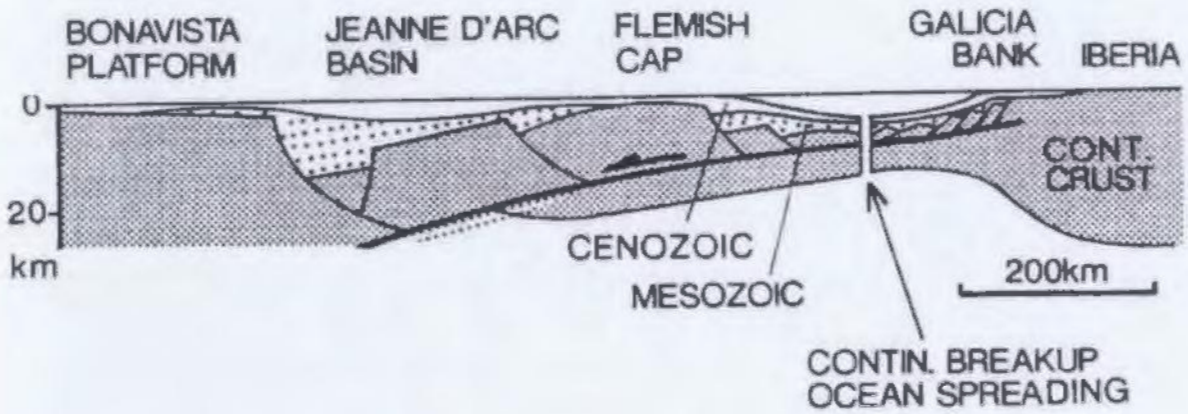

Figure 1.15. Tankard and Welsink's proposed model for the formation of the Newfoundland and Iberian continental margins *(from: Tankard and Welsink, 1987).*

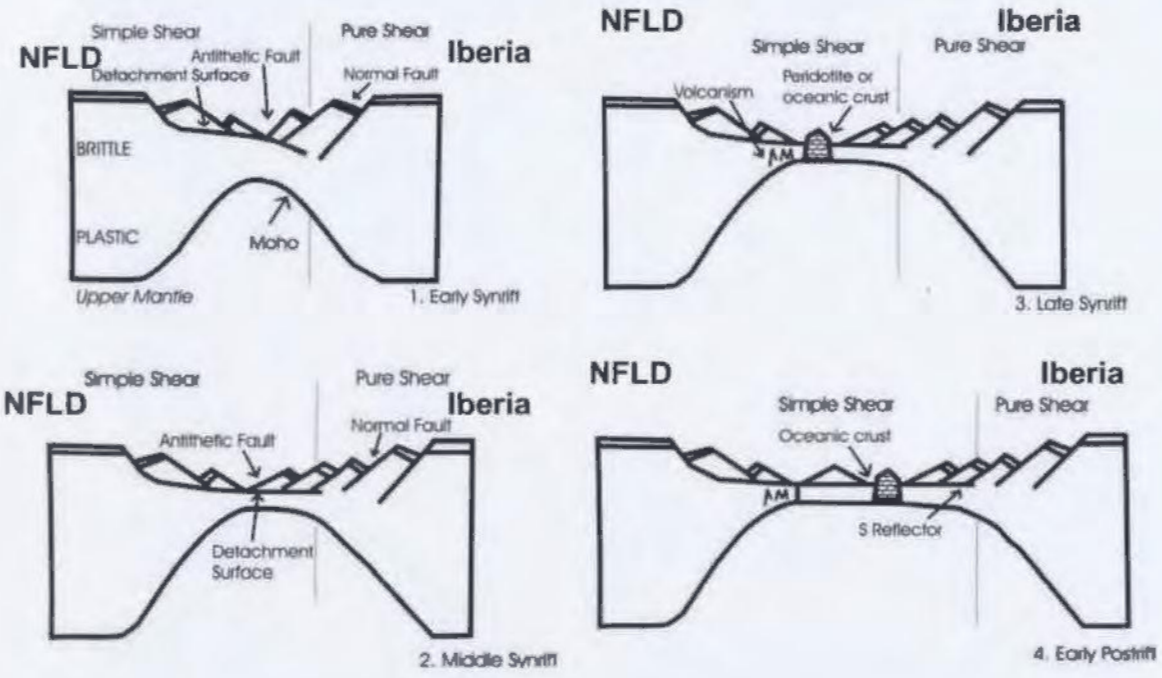

Figure 1.16. Sibuet's proposed models for the formation of the Newfoundland and Iberian continental margins *(modified from: Sibuet, 1992).*

1.7.6 Objective 6 – Comparison of structures on other margins

The sixth objective of this thesis is to relate the structures observed on the Newfoundland margin to those found on other non-volcanic passive margins. Interpretation of major structures on the Newfoundland margin allows comparisons to be made with other non-volcanic passive margins (e.g. Iberia). By comparing structures found on the Newfoundland margin to those present on other margins, structures unique to the Newfoundland margin can be identified.

1.7.7 Objective 7 – Petroleum prospectivity

The seventh objective of this thesis is to assess the petroleum prospectivity of the basins on the southeast Newfoundland margin. Mapping major sequences and structures and relating them to those found in the Jeanne d'Arc Basin will allow potentially prospective areas to be outlined.

CHAPTER 2 Seismic Reflection Acquisition and Data Processing

2.1 Seismic Reflection - Data Acquisition

Multi-channel seismic reflection data (MCS) for the MARIPROBE project was acquired from July 15 to August 17, 2000 as part of the Study of Continental Rifting and Extension on the Eastern Canadian sHelf project (SCREECH). In this project the R/V Maurice Ewing acquired MCS data along three major transects across the Grand Banks of Newfoundland. Figure 2.1 shows the location of the MCS data acquired and the positions of the wide-angle ocean bottom seismographs (OBS) which also recorded during the project. The reflection seismic data were recorded on a Syntrack 480 acquisition system, sampled at 0.004 s and recorded for approximately 16.3 seconds. A 6000m, 480 channel Syntron streamer with a group spacing of 12.5m was used to record the data. A 20 gun 8540 cu in. air gun array was used to shoot every 50m, creating a CDP fold of 60. The air guns and streamer were generally towed at a depth of 7.5m and moved down to 10m in bad weather. Figure 2.2 shows the CDP locations for SCREECH lines 401, 402, 403, and 3MCS which correspond to the CDP locations given in upcoming processed sections. In total approximately 2000 km of MCS data were shot and recorded. The data quality of the SCREECH lines (401, 402 and 403) was generally very good and no major problems were encountered when the data were recorded or processed.

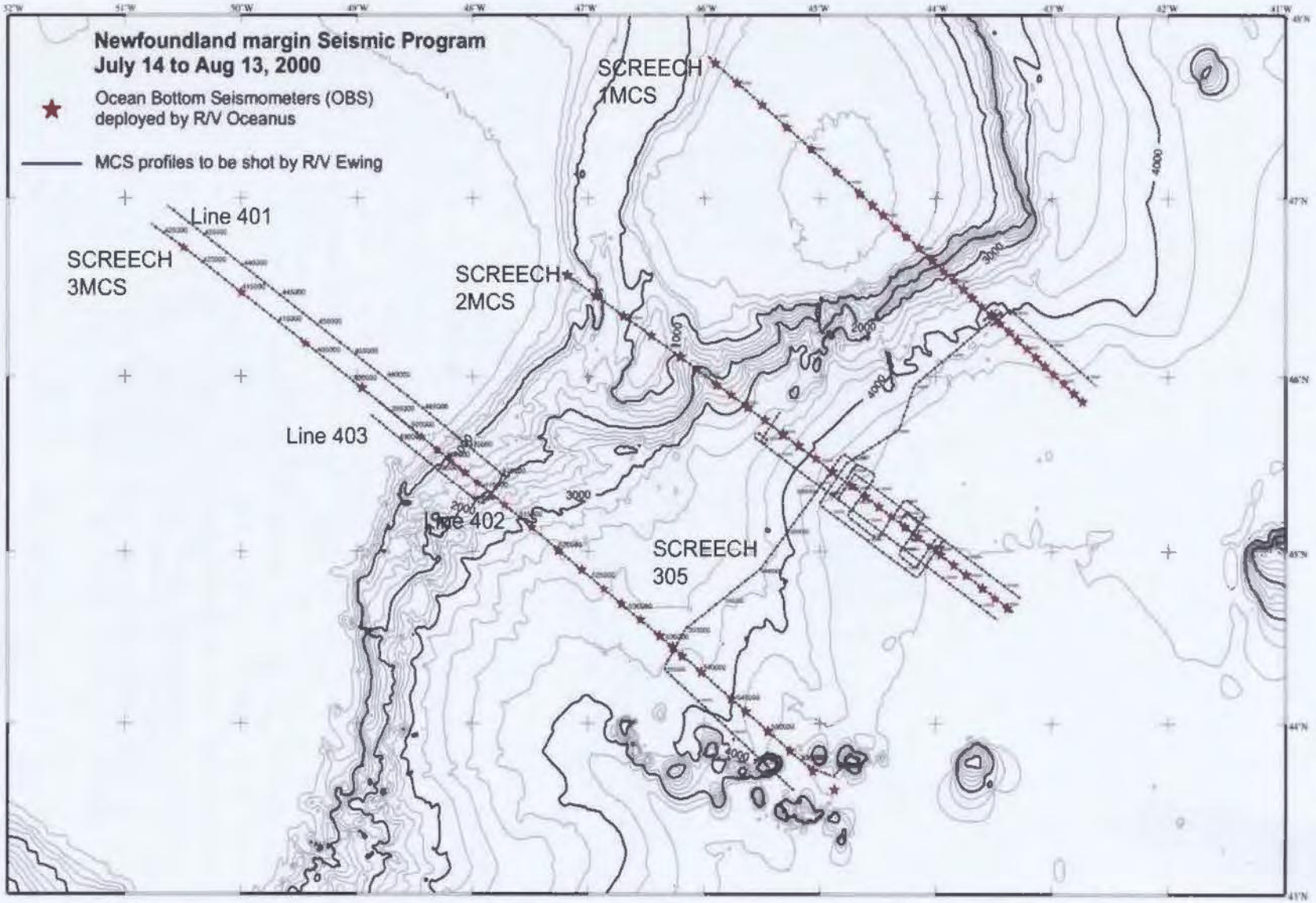

Figure 2.1. Location of MCS and OBS data along the 3 major SCREECH transects. CDP locations are annotated for transect 3 and line 305.

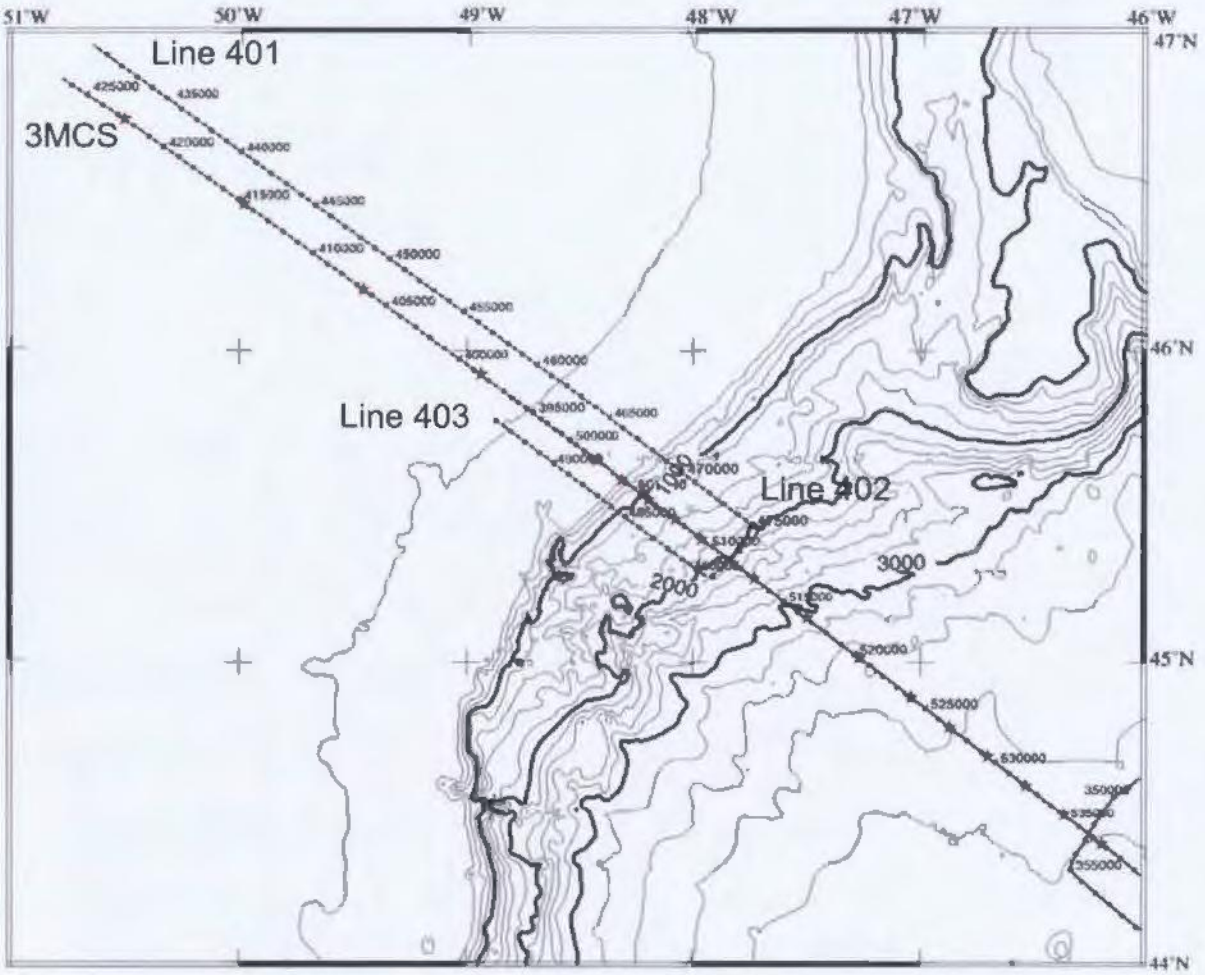

Figure 2.2. CDP values for the lines contained in transect 3. Lines 3MCS 401, 402 and 403.

2.2 Seismic Reflection - Data Processing

The processing portion of this thesis will concentrate on SCREECH lines 401, 402 and 403, which are reflection seismic lines located in the southeast portion of offshore Newfoundland. Seismic line 401 is approximately 300 km long and is mainly located on the continental shelf with its SE end descending the continental slope a few kilometres. Line 402 connects to the slope end of line 401 and runs perpendicular to line 401 for

approximately 25 km. Line 403 connects to the end of line 402 and then runs back up the slope to the shelf, parallel with line 401 for approximately 90 km. Processing the SCREECH lines started from the raw field data tapes and was done in ProMAX, a Landmark Graphics processing application. Along with the three SCREECH lines, 8 proprietary seismic lines made available as post-stack data by WesternGeco were reprocessed to remove noise and enhance the image of the deeper sections (basement and deeper). The reprocessing of the proprietary WesternGeco data only entailed post-stack multiple and noise removal techniques and then migration.

2.3 Processing SCREECH Lines 401 and 403

The processing objective for SCREECH lines 401 and 403 was to produce both stacked and migrated sections from the raw field data. The shelf portion of each line involves a very shallow water bottom (~100 m), with a thin sediment layer (~500 m) overlying basement. The water bottom reaches depths of approximately 2000 m near the slope end of the lines. Sediment cover in the slope area is much thicker than on the shelf. Due to the difference in structure between the shelf and slope area, different processing techniques were applied to these areas to enhance the final image. Extensive testing was done both pre- and post-stack to determine the optimum processing parameters. The following sections detail the final processing techniques applied to the line as well as some of the techniques that were tested but deemed unacceptable. The pre-stack processing will first be explained in detail, with explanations of what parameters were used and their effect on the data, and after this the post-stack processing sequence will be

detailed. Figures 2.3 and 2.4 are condensed overviews of the processing techniques that were applied to lines 401 and 403 to produce the final migrated sections. The complete processing flow for both lines can be found in Appendix 1.

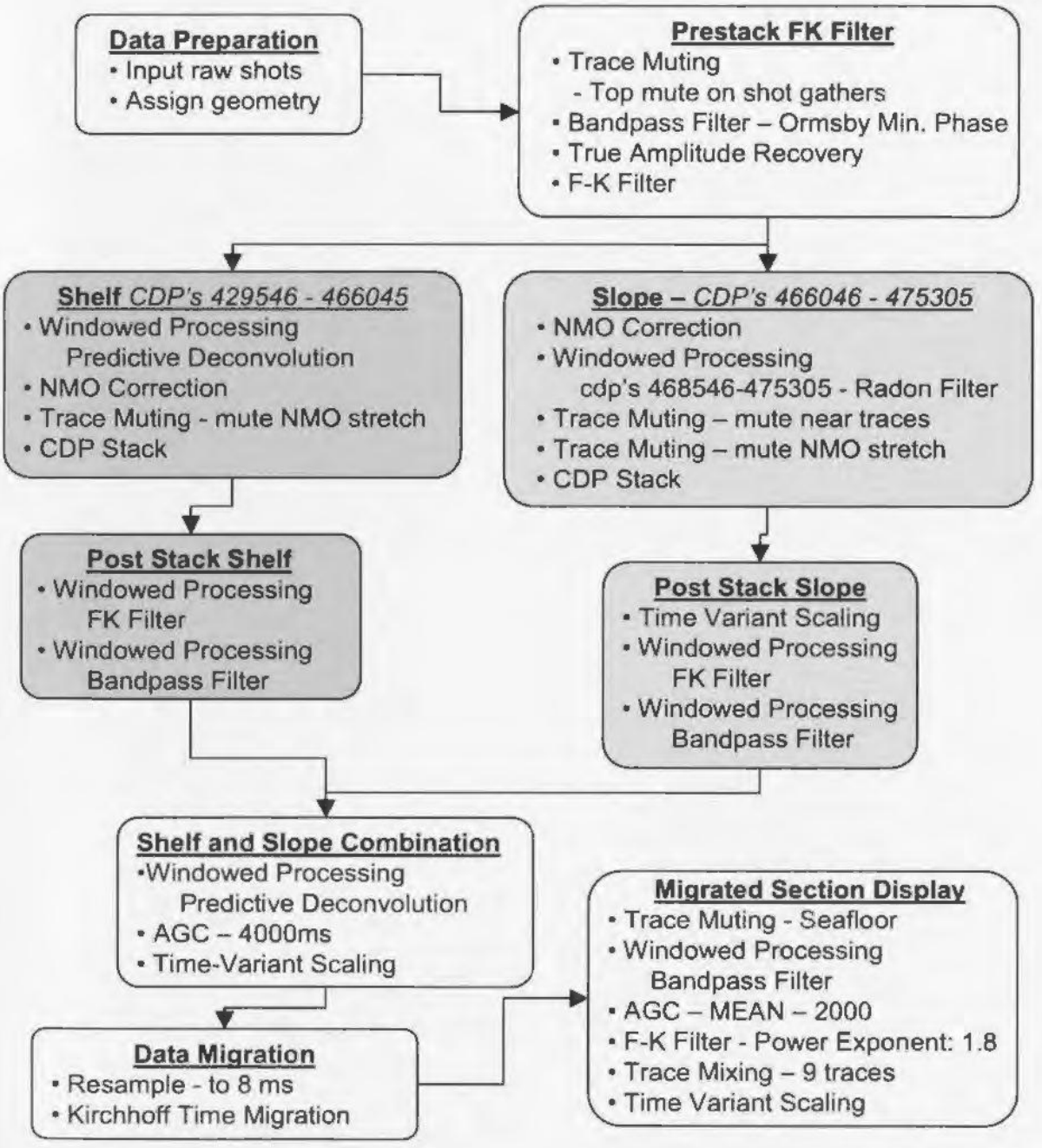

Figure 2.3. Processing flow for Line 401.

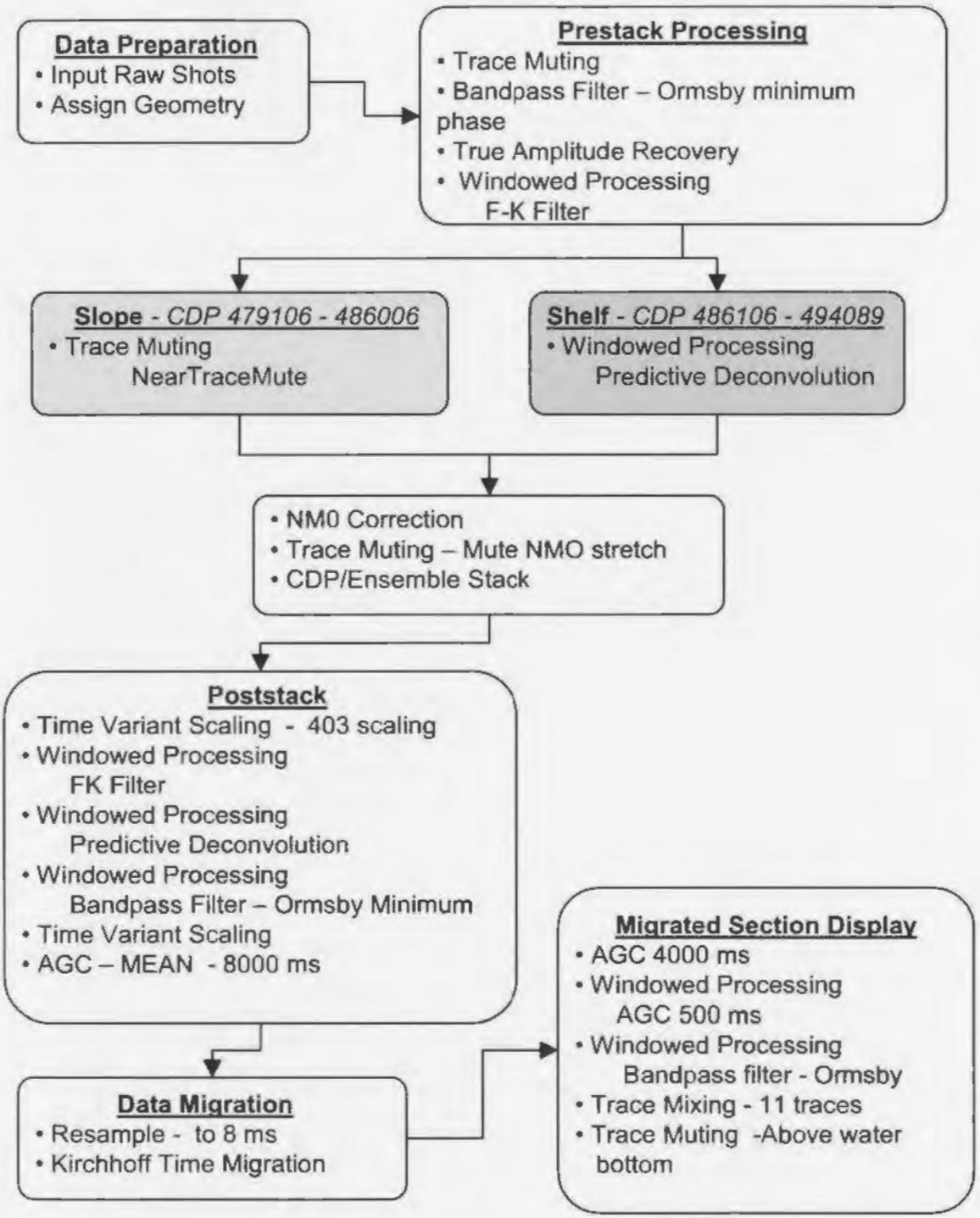

Figure 2.4. Processing flow for Line 403.

2.3.1 Pre-stack Processing

Line 401 contains 5661 shot gathers and line 403 is composed of 1814 shot gathers. Each of the shot gathers is comprised of 480 traces and these gathers were checked for bad traces. Line 403 contained no bad traces whereas noisy traces were found on line 401 on some shot gathers ranging from shot 1072 to 1285. The noise on these traces generally only occurred below 10 000 ms. A bottom mute, which is illustrated in Figure 2.5, was picked on the traces to remove this noise. The noise was only contained in approximately 12 shot gathers. The specific shot gathers affected were as follows; 1072, 1129, 1154, 1164, 1168, 1169, 1175, 1186, 1199, 1223, 1269, 1285. After determining that the rest of the shots were good, a top mute was applied in the shot domain to both line 401 and 403 to remove the direct wave and refracted arrivals. Figure 2.6 shows a typical top mute that was applied to the shot gathers on the shelf portion of the lines, as well as one that was applied to the slope portion of the lines.

2.3.1.1 Bandpass Filter

Shot gathers were analyzed to determine the dominant frequencies of the data. Figure 2.7A shows a typical shelf shot gather (1501 of line 403) and its corresponding frequency spectrum. In these images the shot gathers do not have a top mute applied, however in the processing flow the top mute was applied before the bandpass filter is applied. The shot gather contains both low and high frequency noise and the dominant signal frequencies tend to range between 8 and 70 Hz.

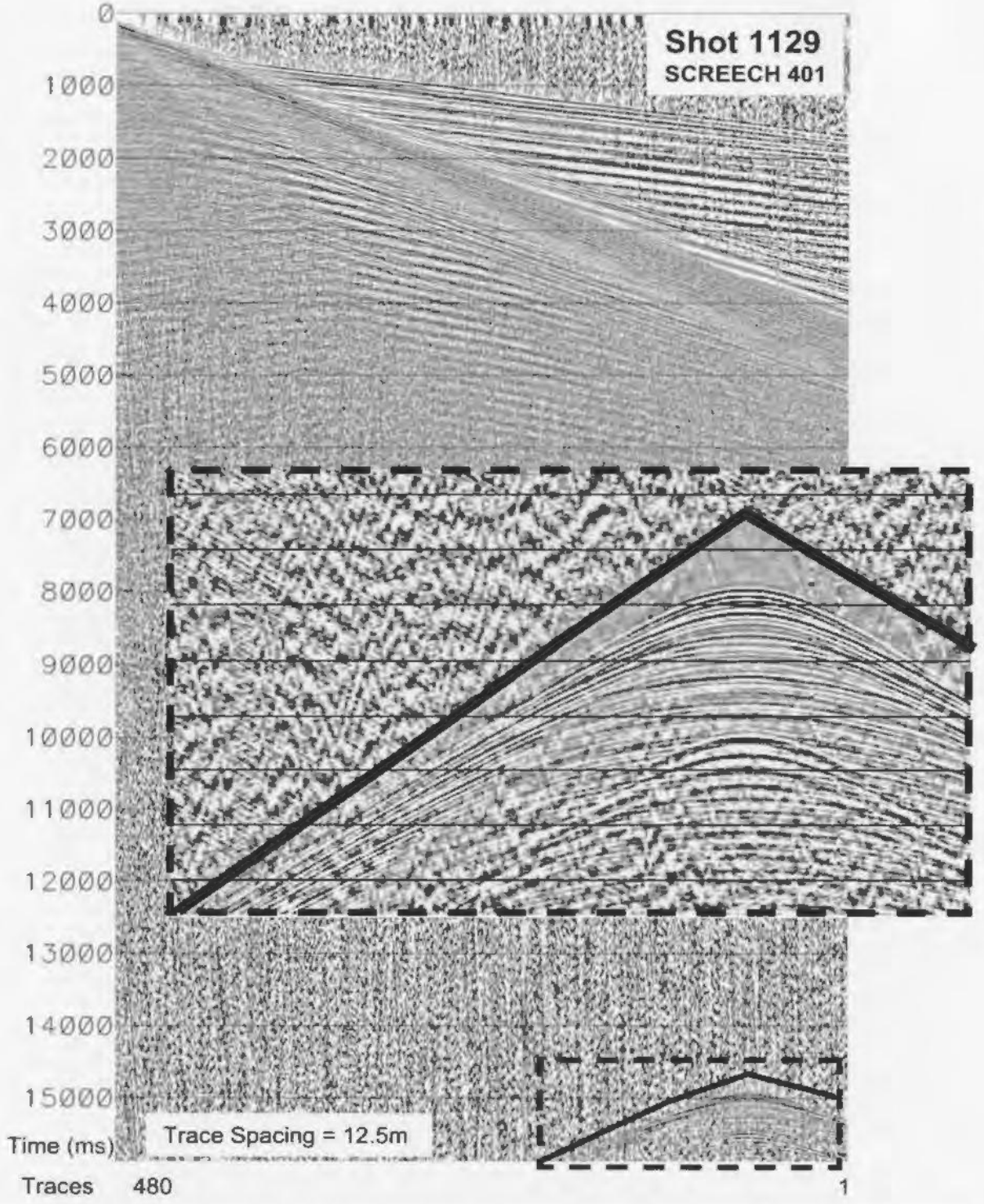

Figure 2.5. Shot gather 1129 on line 401 showing noisy traces and the bottom mute applied to remove the noise. The area surrounded by the dashed box near the bottom of the shot gather is enlarged and shown in the center of the figure. Data below tbe mute (solid black line) is removed.

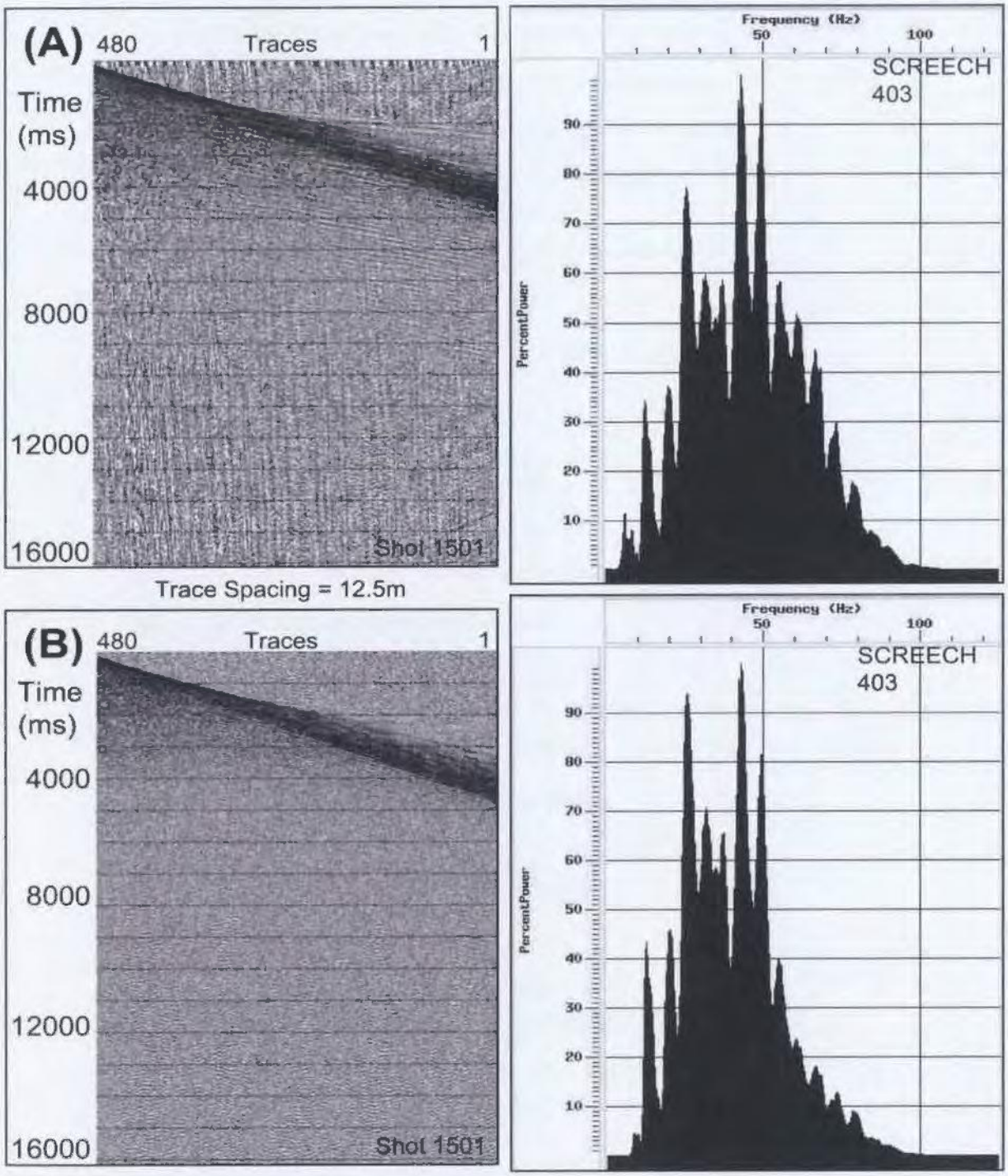

Figure 2.7. Frequency spectrum analysis on shot gather 1501from line 403. (A) Shot gather and frequency spectrum before bandpass filter. (B) Shot gather and frequency spectrum after application of an Ormsby minimum phase bandpass filter. Filter parameters were: 7-10-90-110 Hz applied from 0-1500 ms, 7-10-50-60 Hz applied from 3000-6000 ms, and 5-8-40-50 Hz applied from 9000 -16000 ms.

A minimum phase time-variant Ormsby bandpass filter was applied to all shot gathers on both lines to remove the unwanted high and low frequency noise. Figure 2.7B illustrates the effect of the bandpass filter on the shot gather 1501. The filter was designed to be time variant so that higher frequencies could be kept in the shallower portions of the data, and lower frequencies kept at deeper times. The frequency parameters used are listed below and correspond to the [100% low cut frequency] - [0% low cut frequency] – [0% high cut frequency] - [100% high cut frequency].

- 7-10-90-110 Hz applied from 0-1500 ms
- 7-10-50-60 Hz applied from 3000-6000 ms
- 5-8-40-50 Hz applied from 9000-16000 ms

Between the time gates, the corner frequency values were interpolated. Figure 2.8 shows the effect of applying the bandpass filter to shot gather 1501. It is evident in this figure that a large amount of noise has been removed from the shot gather by the bandpass filter.

2.3.1.2 Spherical Divergence

After the application of a top mute and a bandpass filter, a spherical divergence correction (time x vel^2) was made, where vel the estimated RMS velocity. Testing was done on shot gathers, both in the shelf and slope area of the line and the final values chosen produced the most uniform amplitude across the shot gathers. Table 2.1 below

shows the values used to correct for spherical divergence for both the shelf and slope portions on line 401.

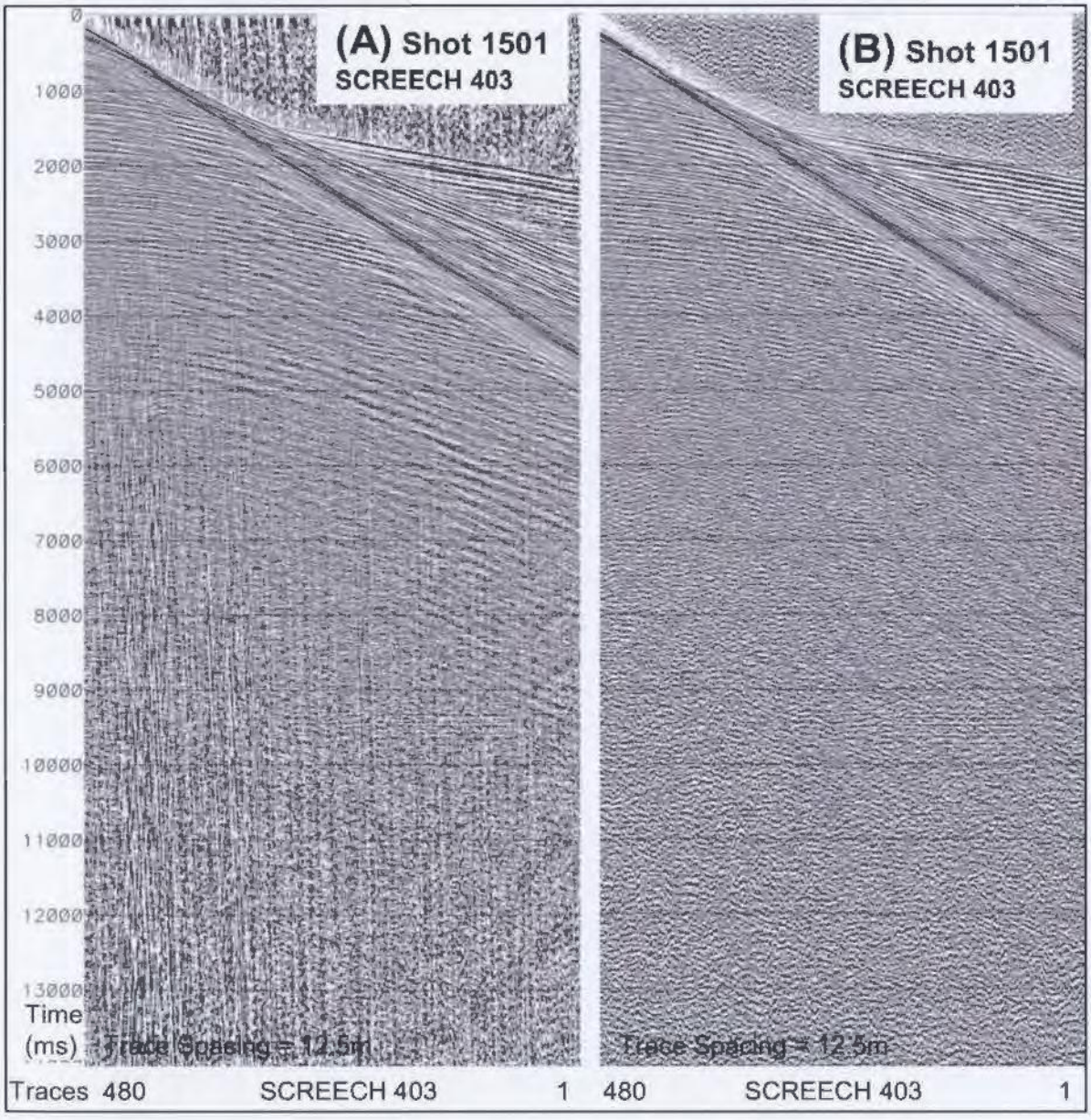

Figure 2.8. (A) Raw shot gather 1501 from line 403 on the shelf displayed with AGC. (B) The same shot gather with a time variant minimum phase Ormsby bandpass filter applied. 7-10-90-110 Hz applied from 0-1500 ms, 7-10-50-60 Hz applied from 3000-6000 ms, and 5-8-40-50 Hz applied from 9000-16000 ms. AGC (500 ms window) was also applied to the shot gather for display.

Table 2.1. Spherical divergence corrections for line 401.

SHELF – (Shots 1-4680)		SLOPE – (Shots 4681-5661)	
Time (ms)	**Velocity (m/s)**	**Time (ms)**	**Velocity (m/s)**
0 ms	1480 m/s	0 ms	1480 m/s
2000 ms	2500 m/s	1000 ms	2500 m/s
5000 ms	4500 m/s	5000 ms	3000 m/s
8000 ms	4500 m/s	8000 ms	4500 m/s
16000 ms	3500 m/s	16000 ms	4800 m/s

Table 2.2 shows the values used to correct for spherical divergence on line 403. On this line it was determined that one spherical divergence correction adequately corrected the shot gathers and a separate correction for the shot gathers on the shelf was not required.

Table 2.2. Spherical divergence corrections for line 403.

Time (ms)	RMS Velocity (m/s)
0 ms	1480 m/s
2000 ms	2200 m/s
4000 ms	3200 m/s
8000 ms	4500 m/s
16000 ms	4700 m/s

Figure 2.9 shows a shot gather on the shelf of line 403 before and after spherical divergence was applied. Note the fairly uniform amplitudes in the shot gather after the correction. The same spherical divergence correction was applied to both the shelf and slope sections of the line. For line 401 a slightly different correction was used for the shelf portion of the line with similar results to those depicted in Figure 2.9. Testing was also done using constant velocities and exponential (dB/s) gain to correct for spherical divergence. Tests showed that amplitudes are too strong near the bottom of the gather and too weak in the middle. Based on these results, this technique was not pursued and spherical divergence was corrected on both lines by using the previously explained user-defined function.

2.3.1.3 F-K Filter

Coherent dipping noise deeper in the crust (8000 ms – 16000 ms) was a major problem in this data set. In a brute stack shown in Figure 2.10, linearly dipping noise is shown to dominate the lower portion of the data set. This noise was also evident in shot gathers, but not as noticeable in CDP gathers because it was coherent only in the shot domain. The major source of this noise was thought to be side scatter energy bouncing off rough basement or seabed irregularities. Larner et al. (1983), have shown that while this type of noise is dominant in the shot domain, it is undistinguishable in the CDP domain, and then reappears when the CDPs are stacked. The coherent linearly dipping noise in the stacked section makes interpretation extremely difficult. To reduce this noise, a pre-stack F-K filter in the shot domain must be applied.

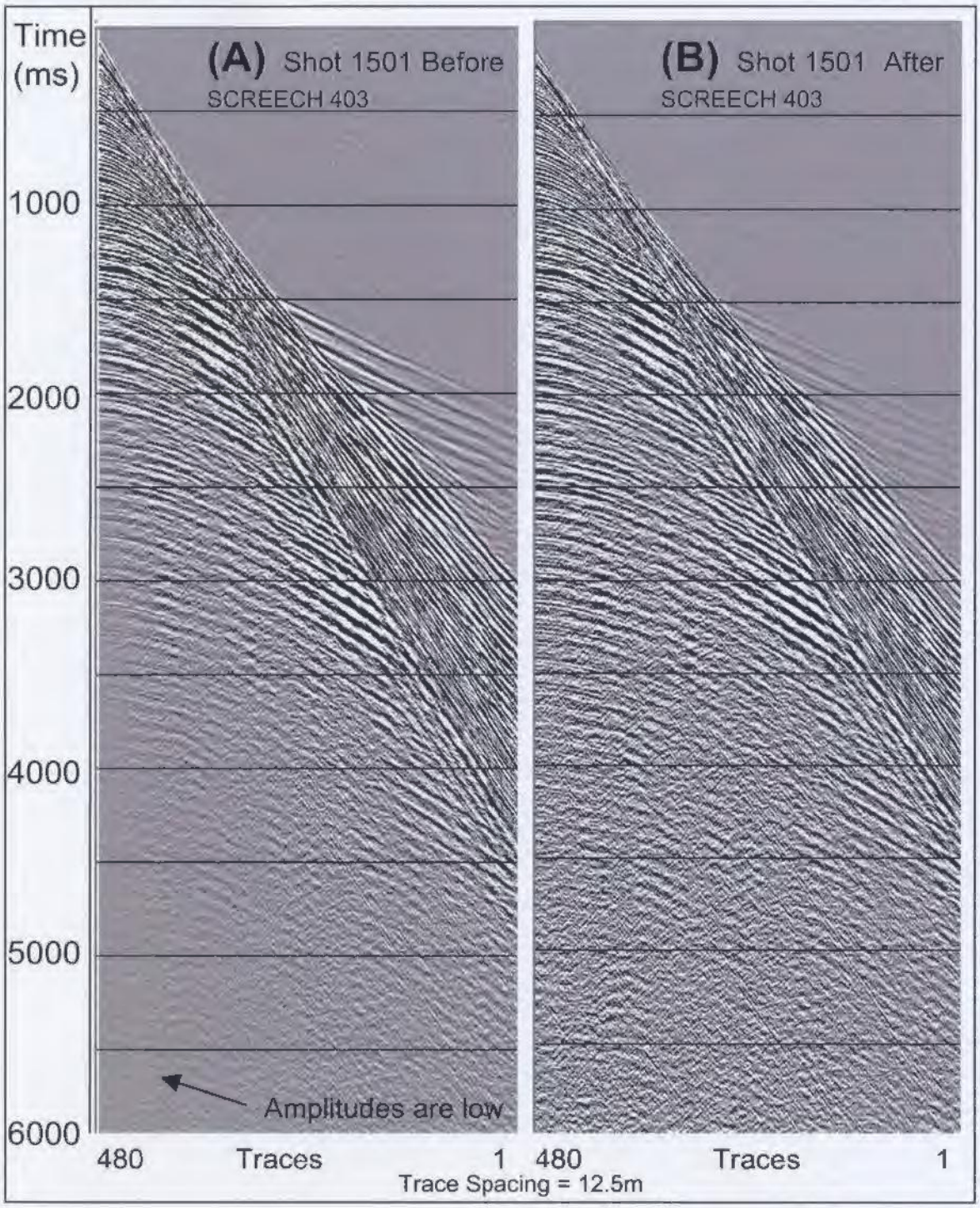

Figure 2.9. Shot gather 1501 from line 403 on the shelf before (A) and after (B) the application of a spherical divergence correction 1/(time x vel^2). In Part B the amplitudes at times greater then 3000ms in the near trace region are more consistent with the rest of the shot gather.

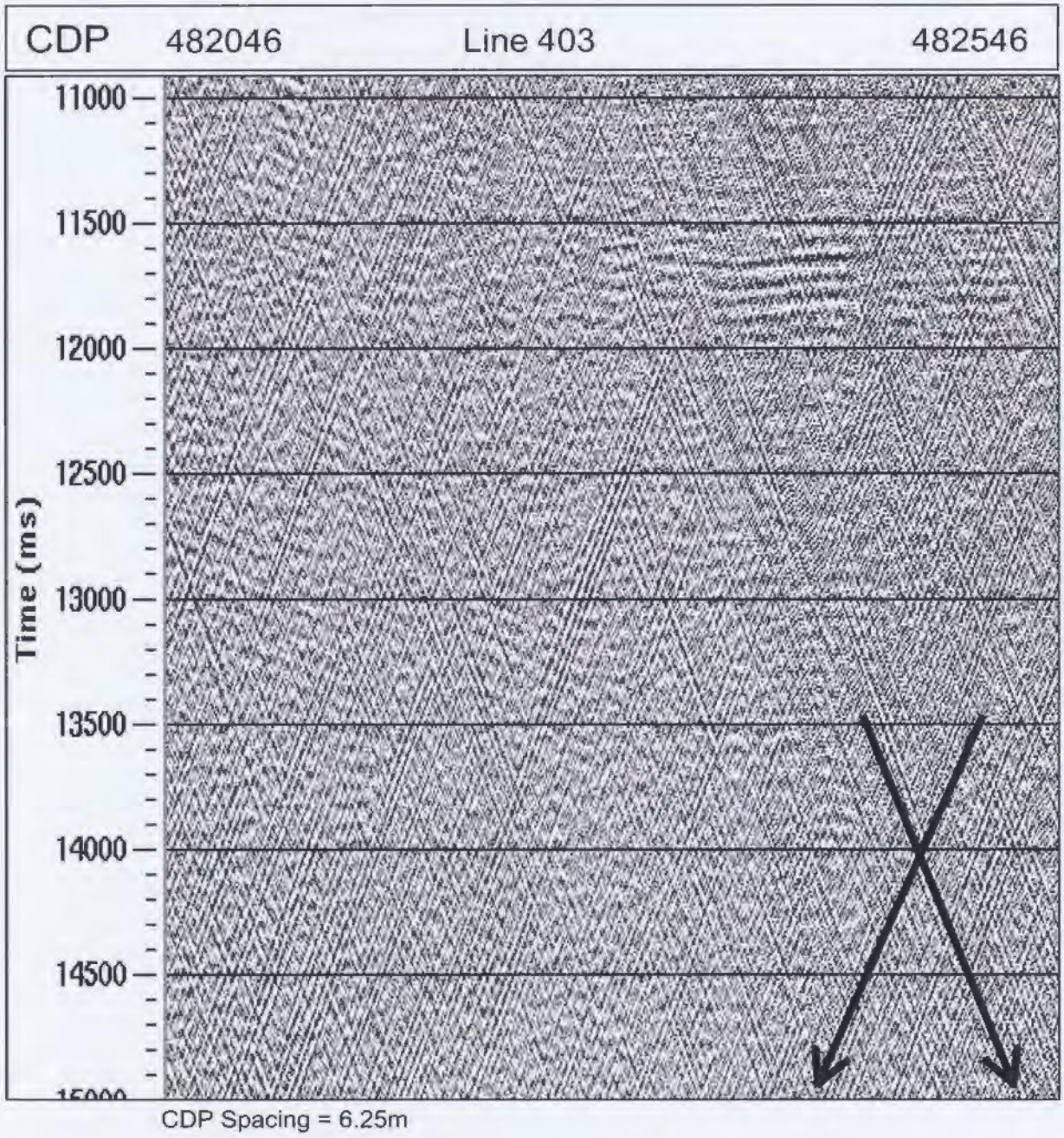

Figure 2.10. Rough stacked section of line 403. Showing linearly dipping coherent noise. The source of this noise is thought to be side-scattered energy.

Figure 2.11 shows typical filter polygons (retain data inside; reject outside) that were picked in the F-K domain, and the before and after results of applying the F-K filter to the shot gathers. The pre-stack F-K filter does a very good job at removing most of the dipping noise in the shot gathers, and once the CDP gathers are stacked the dipping noise is shown to be diminished.

2.3.2 Shelf Pre-stack Processing

2.3.2.1 Predictive Deconvolution

On the shelf portion of line 401 from CDP# 429546 to 466045, and on line 403 from CDP# 486106 to 494089 reverberatory noise is present in the CDP gathers down to about 7000 ms. To remove this noise a predictive deconvolution was applied to the CDP gathers. An autocorrelation was done on the CDP gathers to aid in picking the parameters for deconvolution. A sample of the autocorrelation from line 403 is shown in Figure 2.12. The window in which the deconvolution would be applied to the CDPs is also depicted in Figure 2.12. Many operator lengths and gaps were tested, and in the end the operator length used was 300 ms and the gap was 90 ms. The design window was picked from 0 ms to 5000 ms for near traces (channel 480) and from 5000 ms to 8000 ms for the far traces. The design window was interpolated between the near and far offsets. Figure 2.13 shows CDP gathers from line 403 before and after the application of the predictive deconvolution. Note the removal of most of the reverberatory noise on both the near and far traces. While the CDP gathers may show that the reverberatory noise has been diminished, this may not be the case when the CDPs are stacked.

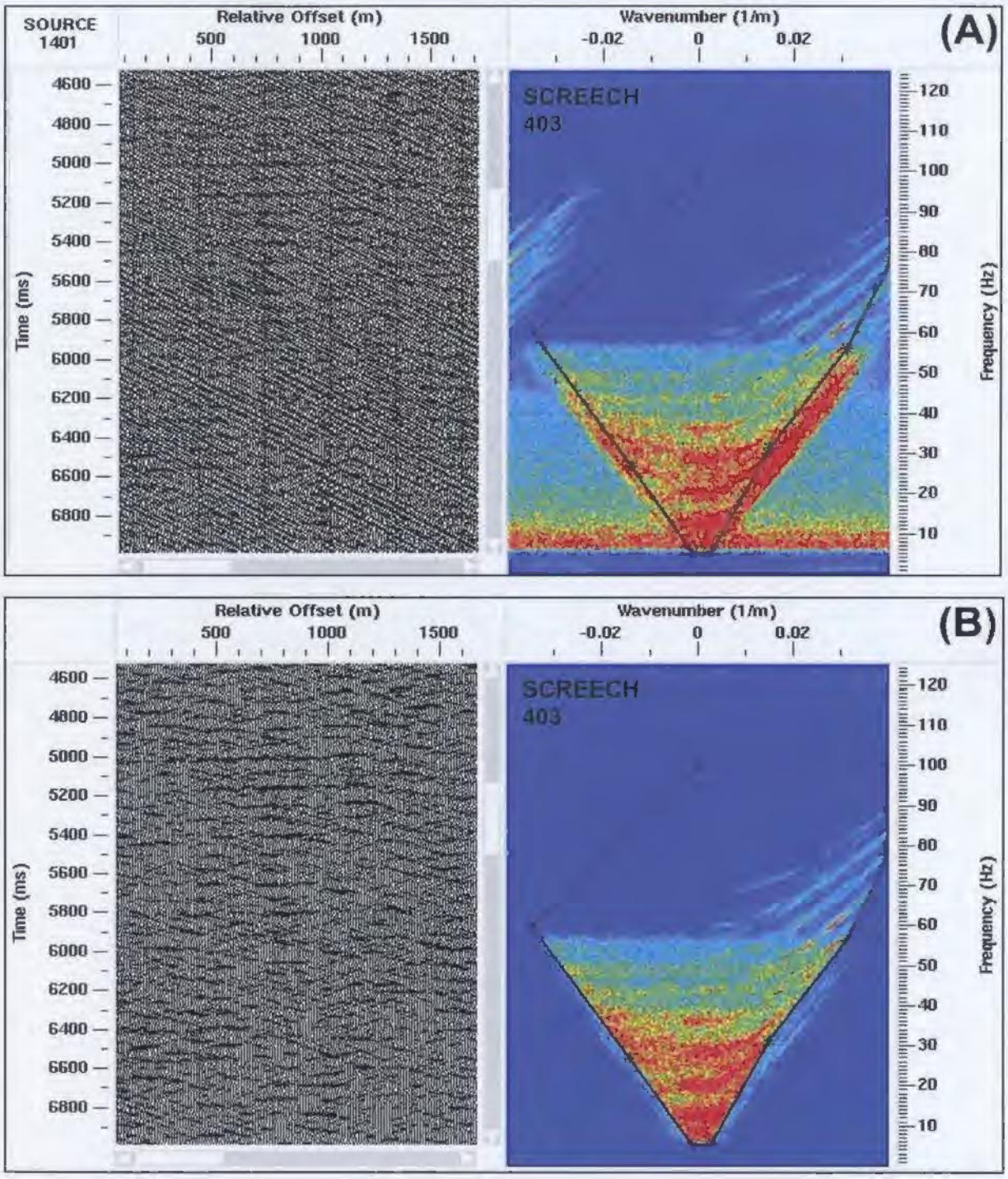

Figure 2.11. (A) Shot gather 1401 on line 403 and FK spectrum before the application of an FK Filter. (B) Shot gather and FK spectrum after the application of an FK Filter. The filter polygon is designed to keep the signal which is inside in the polygon. Note the reduction of linearly dipping noise in the shot gather after the filter is applied.

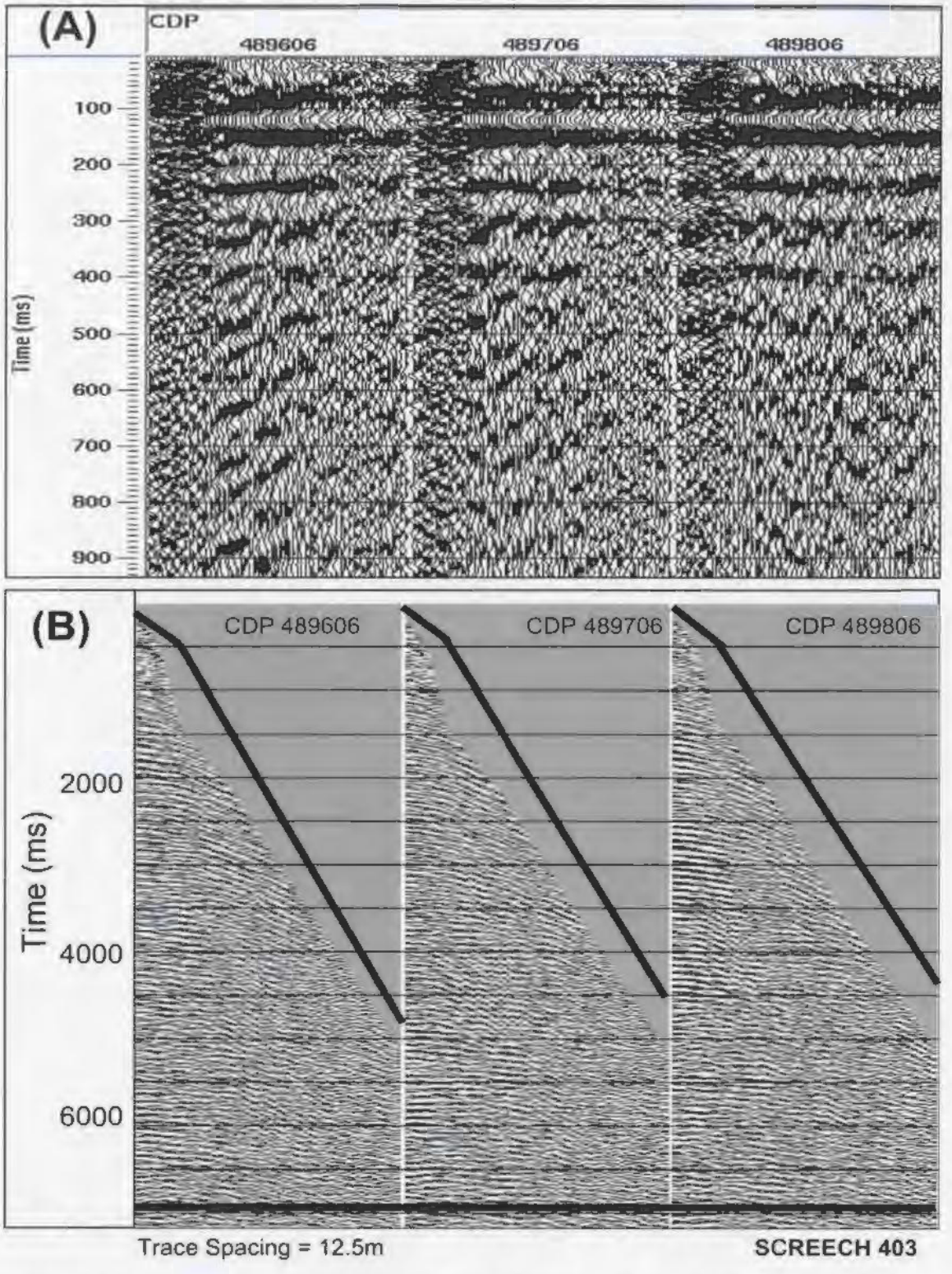

Figure 2.12. (A) shows the autocorrelation of CDP gathers on line 403. (B) shows the area of the CDP's in which deconvolution will be applied (between the black lines).

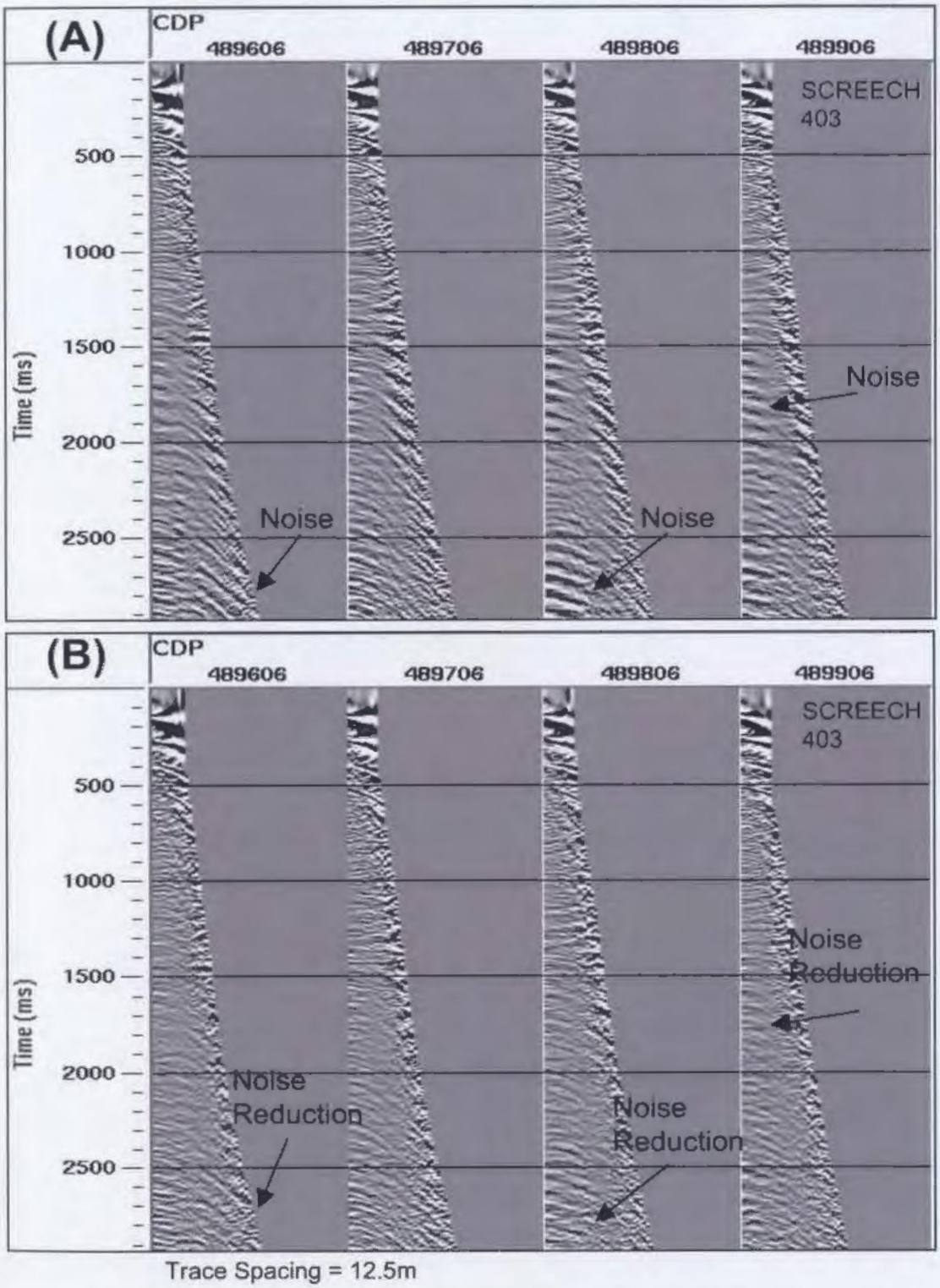

Figure 2.13. (A) shows CDP gathers on line 403 which have been corrected for NMO. (B) shows the same CDP gathers with a predictive deconvolution applied. Operator length of 300 ms and gap of 90 ms. The gathers were then corrected for NMO, as in (A). Note the reduction of reverberatory noise as highlighted by the black arrows.

When the CDPs are stacked and compared it is easy to see which pre-stack predictive deconvolution parameters are effective at removing the reverberatory noise. Figure 2.14 shows a stacked section on line 401 from CDP 434546 to 436546 both with and without the pre-stack deconvolution applied to the CDP gathers. Note how the reverberatory noise in the stacked section is diminished with the application of the deconvolution. Alternative deconvolution gaps were tested (eg. 60, 120ms) but found to be less effective.

Unfortunately not all portions of the line reacted the same way to the pre-stack predictive deconvolution. Testing done on line 401 between CDPs 443546 to 445546 showed that pre-stack deconvolution was ineffective at removing reverberatory noise. Figure 2.15 shows the stacked CDPs with and without pre-stack predictive deconvolution applied. It is noticeable in this figure that there is little to no improvement in removing the reverberatory noise when pre-stack predictive deconvolution is applied. This was also the case when different deconvolution gap parameters (60 and 120 ms) were tested on this portion of the line. Based on testing on both lines 401 and 403, pre-stack deconvolution was applied to the shelf CDPs of both lines using an operator length of 300ms and a gap of 90ms. The design window depicted in Figure 2.12 was also used.

2.3.3 Slope Pre-stack Processing

One of the largest processing challenges for both SCREECH lines 401 and 403 was the removal of multiple energy in the slope area.

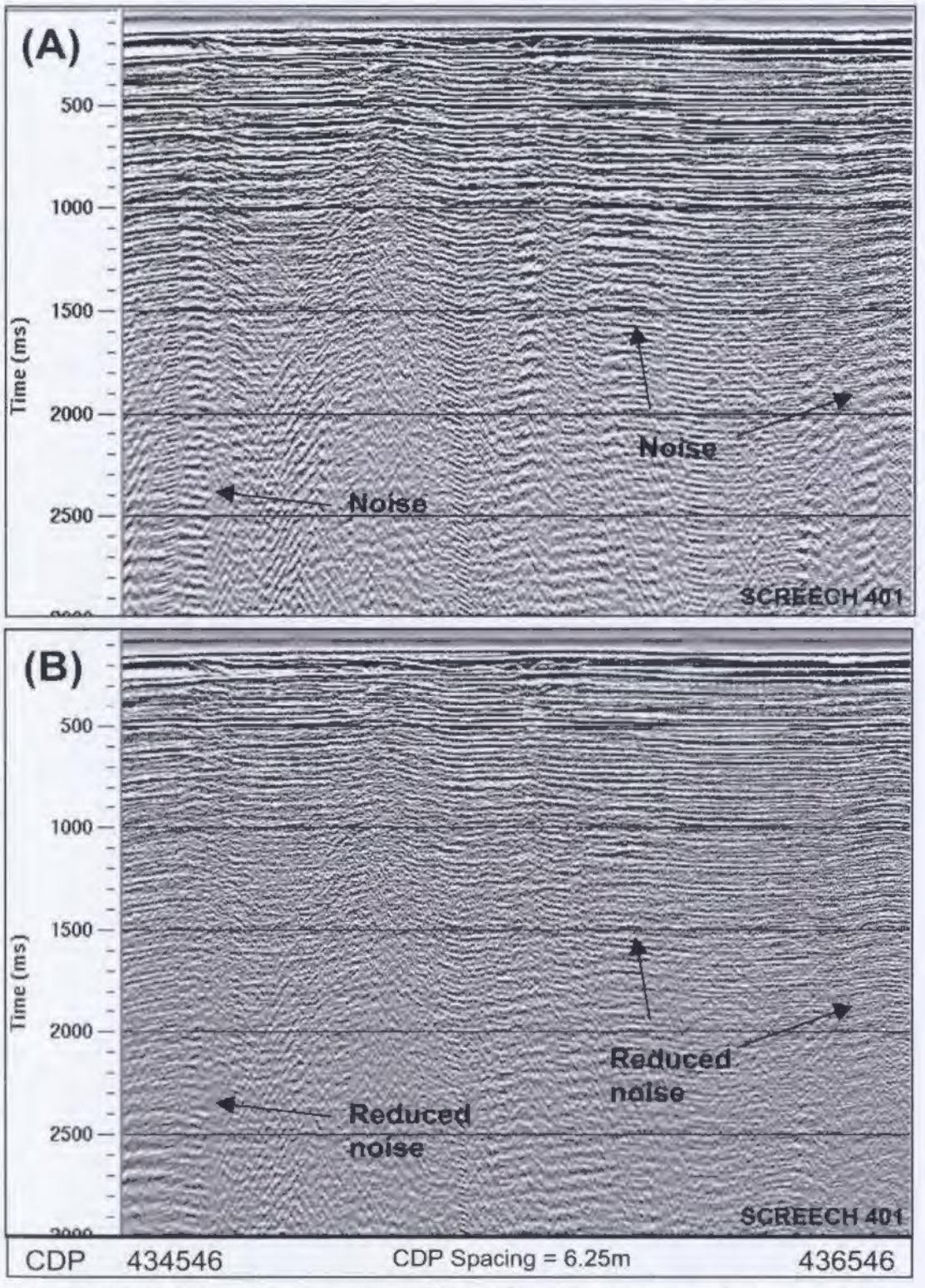

Figure 2.14. (A) Stacked section of line 401without pre-stack deconvolution applied. (B) Stacked section with pre-stack deconvolution applied. Operator length = 300 ms, gap = 90 ms. A large portion of the reverberatory noise has been removed.

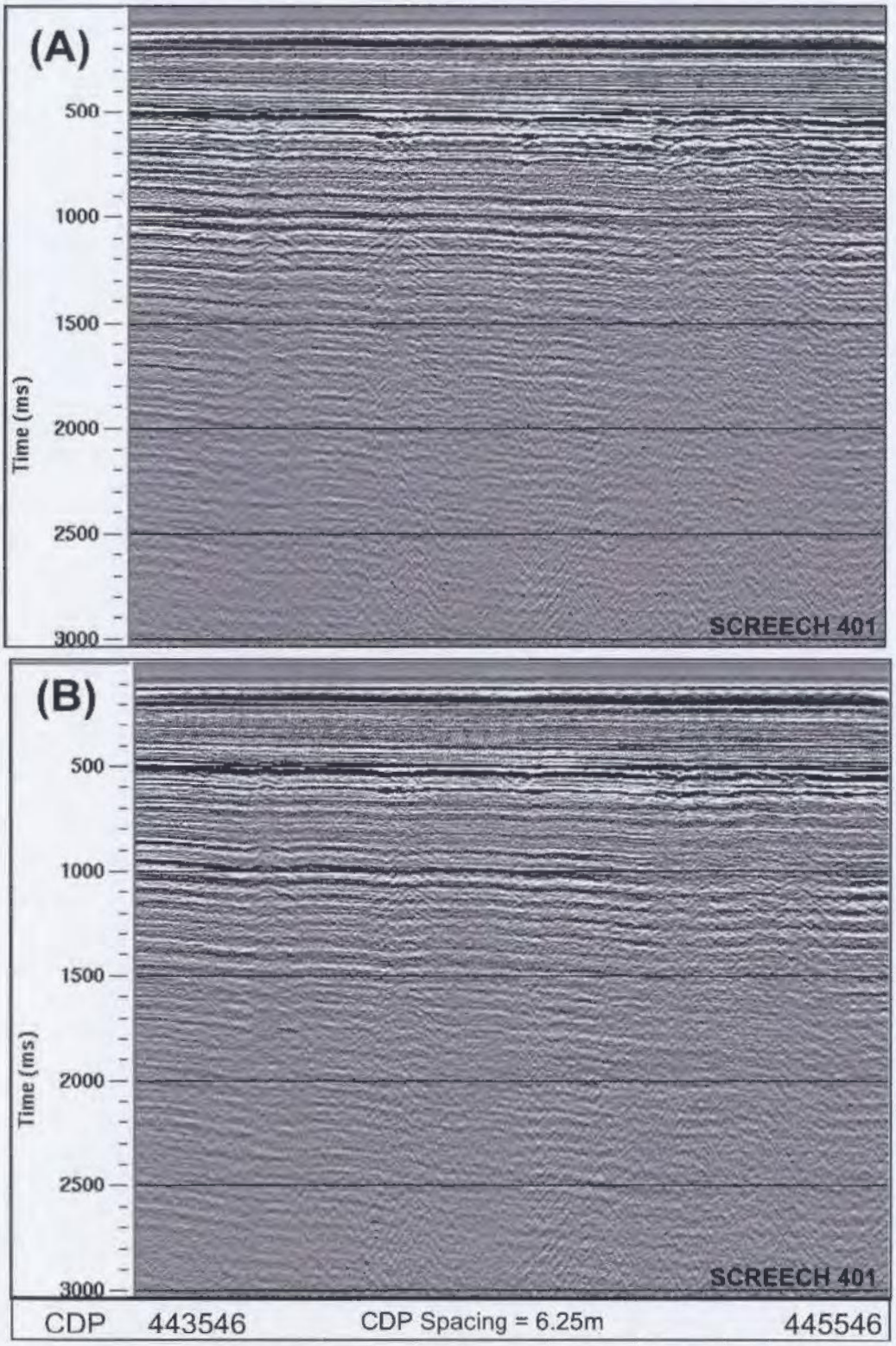

Figure 2.15. (A) Stacked section on line 401 with no pre-stack deconvolution. (B) Stacked section after application of pre-stack deconvolution: Operator length = 300 ms, gap = 90 ms. Little to no improvement is noticeable in the section with deconvolution applied.

Strong reflections from the water bottom, sediments and a basement high produced simple and peg leg multiples in the slope area when the CDPs were stacked. Figures 2.16 and 2.17 show brute stacks of the slope area for both line 401 and line 403. The water bottom, sediment and basement surface multiples are illustrated in each figure. Multiples tend to be more prevalent and also more difficult to remove in line 401 than in line 403. Radon filtering, radon velocity filtering and near trace muting were all tested for their effectiveness at removing these multiples.

2.3.3.1 Radon Filtering

In viewing semblance plots from velocity analysis and time-moveout transforms of data from the slope area, it was thought that a radon filter might provide favourable results at removing water bottom multiples. The radon filter used transforms NMO corrected CDPs into the time vs. move-out domain. A mute is applied in this domain to remove the primary energy (ProMAX Reference Guide, 1998), and then the inverse transform is subtracted from the original gather. The distinction between primary and multiple energy is based on the residual move-out from near to far offsets. Primary energy should appear to have very little move-out since NMO corrections have been applied and multiple energy after NMO should appear to have a parabolic form of residual move-out in the CDP gathers (ProMAX Reference Guide, 1998). On a time vs. move-out plot, the primary energy will tend to plot towards the time axis in move-out space, where as multiple energy will plot towards the positive move-out space.

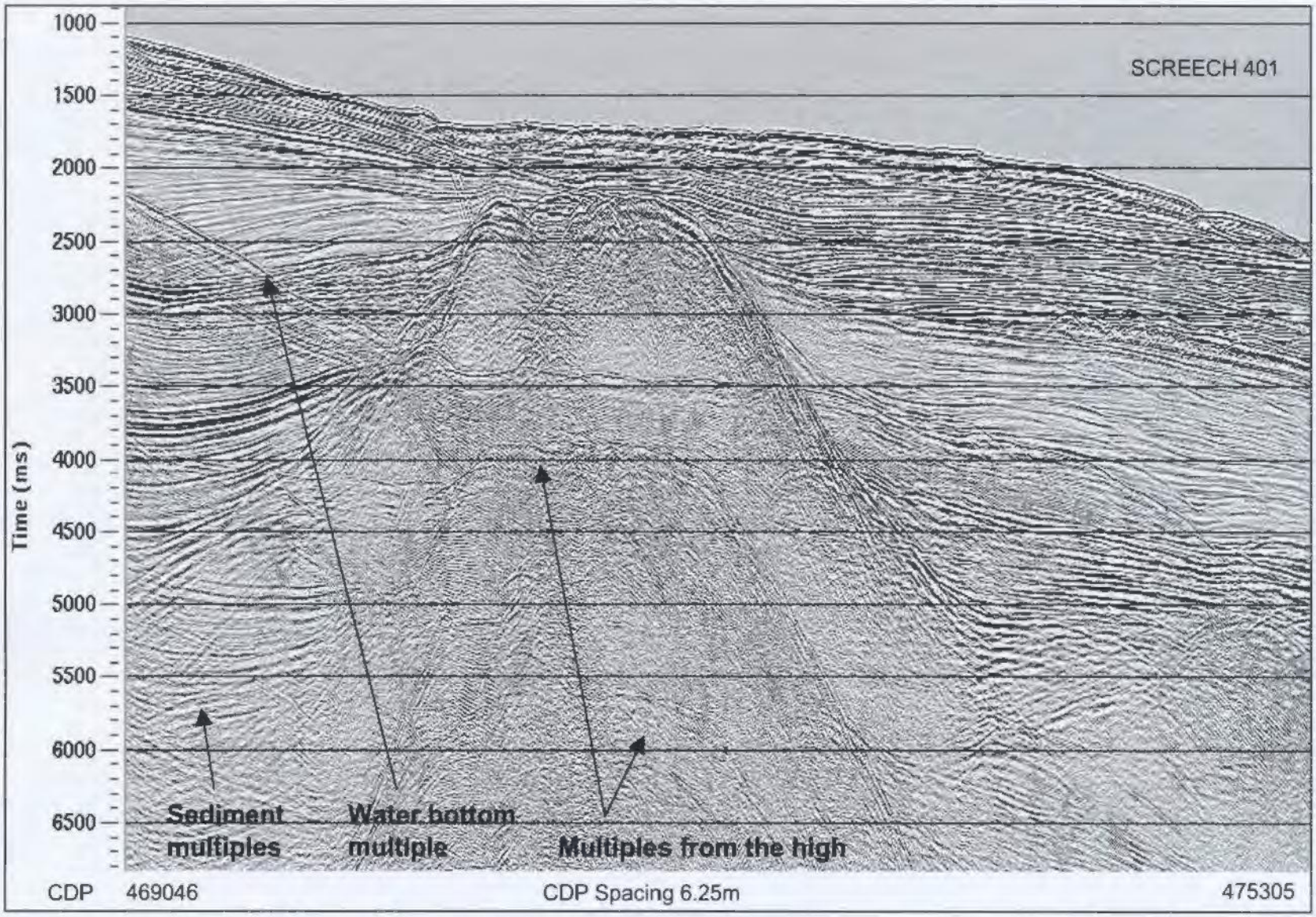

Figure 2.16. Brute stack of the slope section for line 401 showing multiples of the water bottom and the basement high.

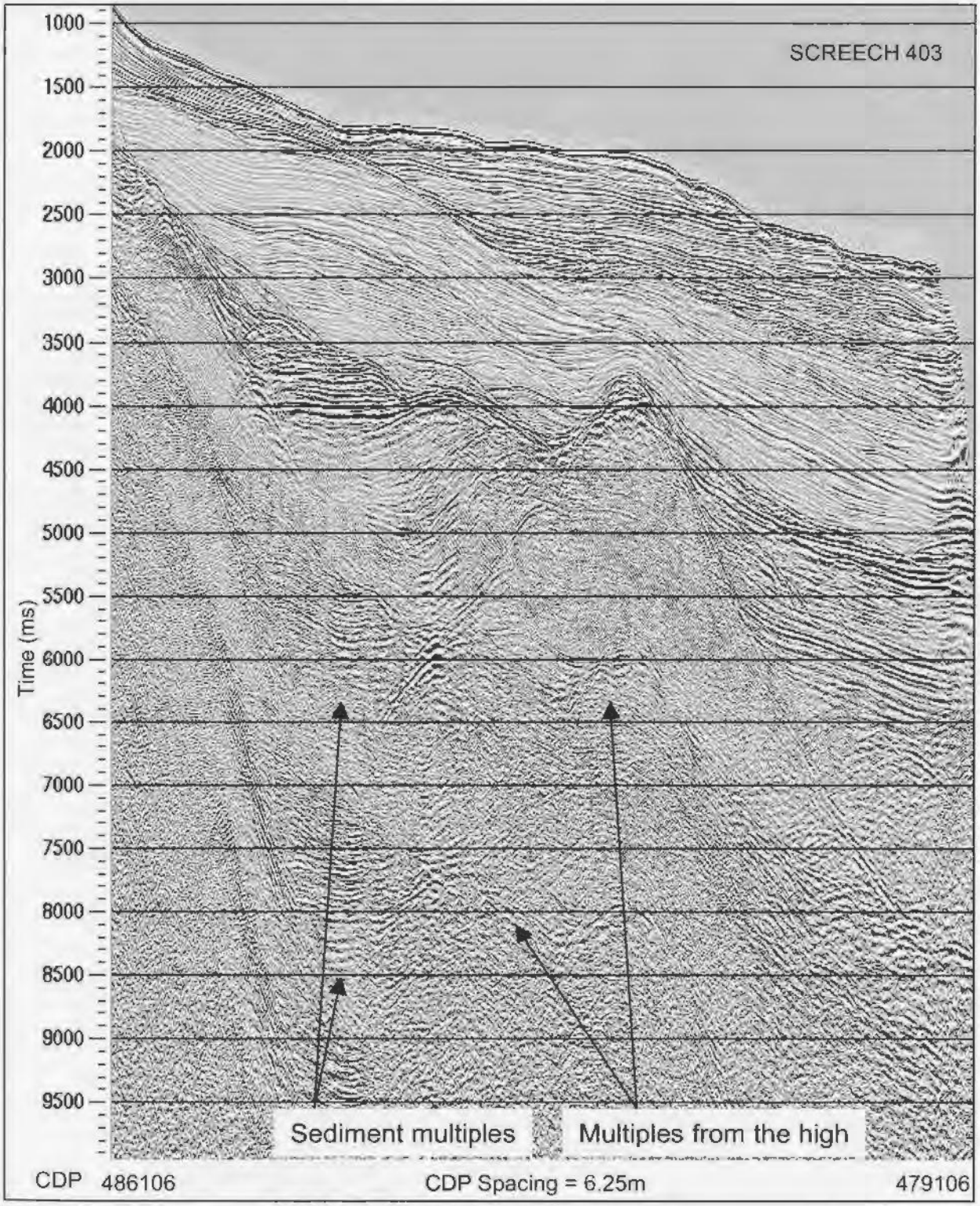

Figure 2.17. Brute stack of the slope section for line 403 showing multiples from the water bottom and basement high. The multiples in this section are not as severe as the multiples found in the slope portion of Figure 2.16.

Figure 2.18 illustrates the results of applying the radon filter to a CDP gather on line 403. CDP 479600 was selected and is shown in part A of the Figure. In the time vs. move-out domain, primary energy is muted (shown in part B) leaving only the multiple energy. The result of inverting the transform back to the time-offset domain is a gather which should only contain multiple energy as depicted in part C. This gather with multiple energy is then subtracted from the original gather. The result of subtracting the multiple energy is then shown in part D. Tests on both lines 401 and 403 show that the radon filter is effective in removing multiple energy at the far offsets, but multiple energy still remains in the nearer offsets.

A stacked slope section of line 401 is shown in Figure 2.19 with the radon filter applied before stacking. It is clear from this figure that multiple energy has been diminished, when compared to Figure 2.16. The first water bottom multiple has almost completely been removed in the shelf break area, however much multiple energy still remains in the stacked section especially under the high. The small amount of multiple energy present in the near traces after the radon filter was applied becomes enhanced when the gather is stacked, resulting in little multiple removal in the slope area. Figure 2.20 shows the stacked slope section of line 403 with the radon filter applied. As with Figure 2.19, some multiple energy has been diminished, but some still remains especially under the high. The radon filter in general performed only modestly, except on line 401 where it was effective at diminishing the first water bottom multiple near the shelf break.

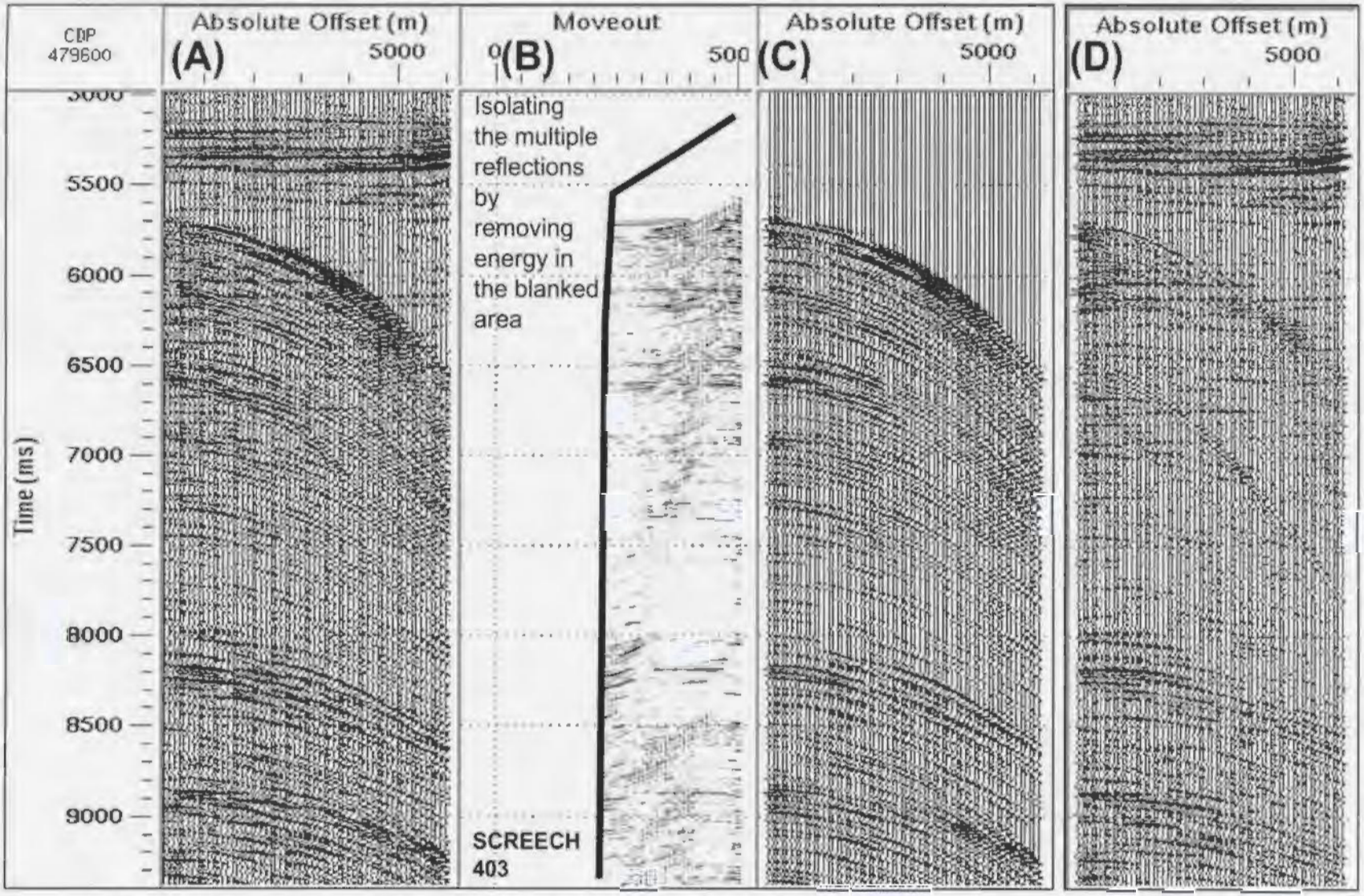

Figure 2.18. (A) NMO corrected CDP gather 479600 from line 403. (B) Mute picked in time vs. residual moveout space to remove primary energy. (C) Gather with the mute from (B) applied, leaving multiples. (D) Result of subtracting the multiple gather (C) from the original gather (A).

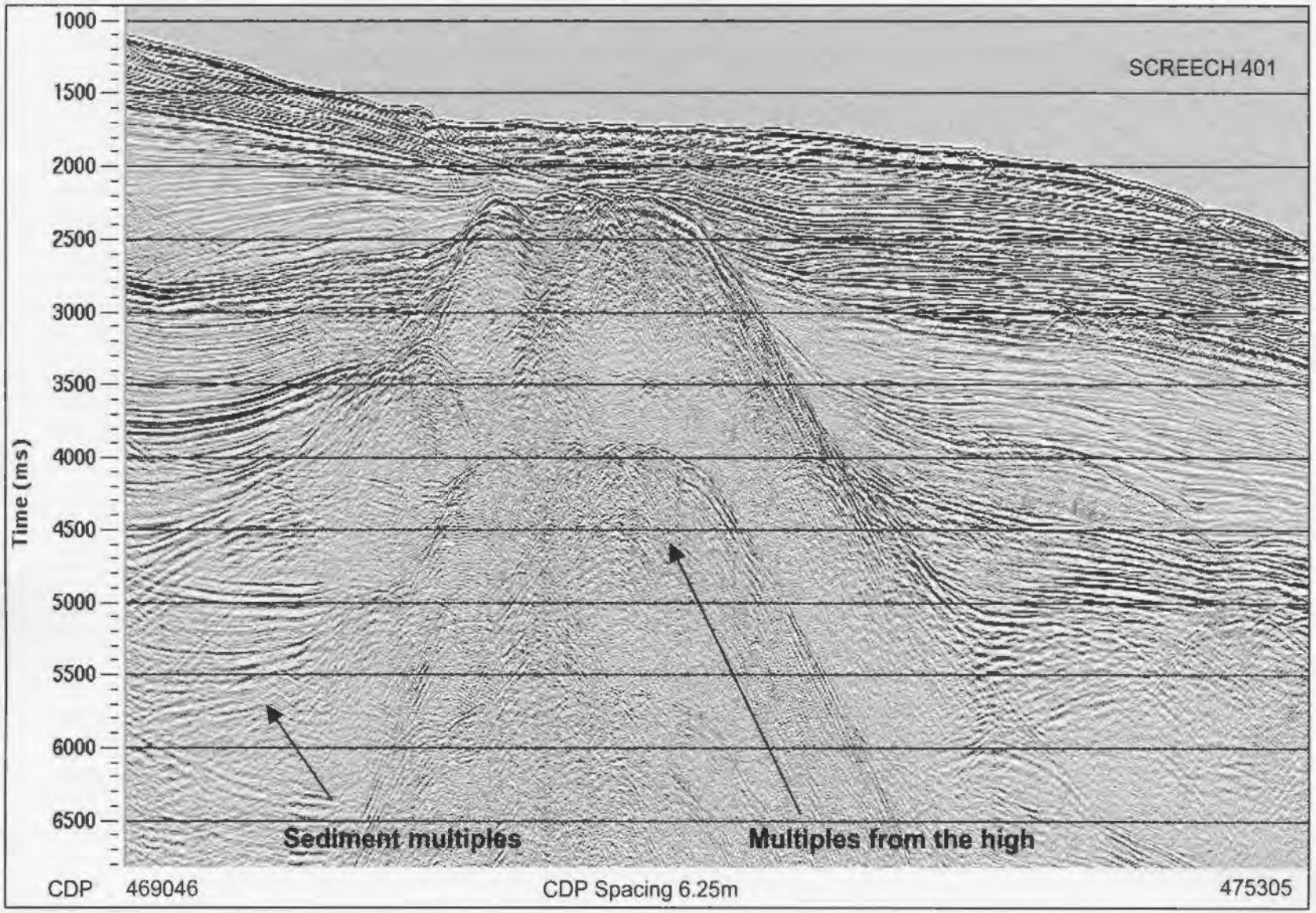

Figure 2.19. Radon filtered stacked section of the slope for Line 401.

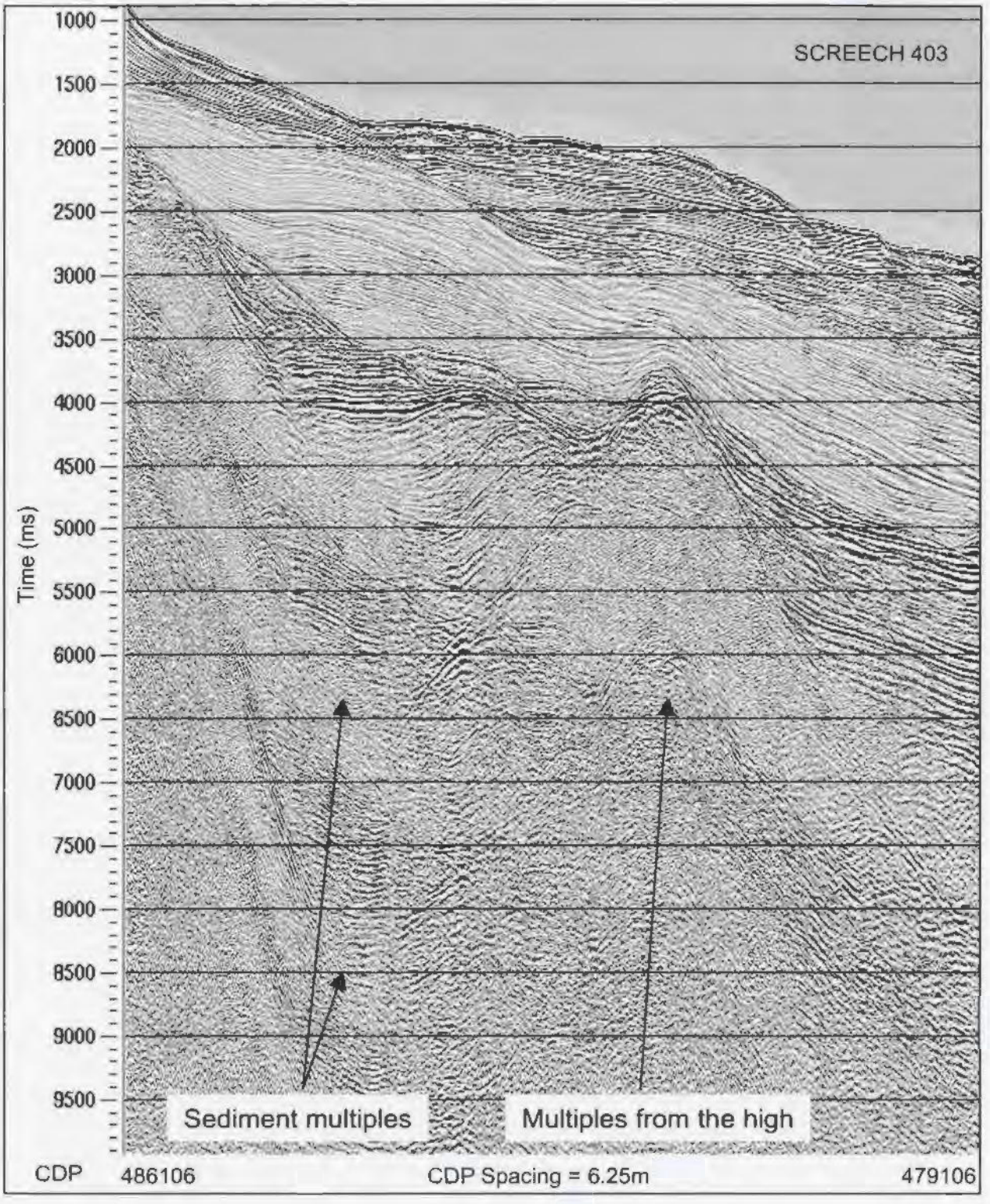

Figure 2.20. Radon filtered stacked section of the slope for Line 403.

2.3.3.2 Radon Velocity Filter

A radon velocity filter was also investigated in the slope area for both lines 401 and 403. This type of filter is a more refined version of the radon filter mentioned above. The mutes to remove primary energy are determined by choosing low and high percentages of velocities to keep (ProMAX Reference Guide, 1998). The low velocity percentage will keep a specified percentage less than the picked NMO velocity and the high velocity percentage will keep a percentage higher than the NMO velocity. Figure 2.21 shows a typical CDP gather in the slope region and the velocities that were picked for NMO correction. In this area there is a large velocity separation between the primaries and the multiples. The multiples appear to be confined to velocities between 1500 m/s to 2500 m/s which are quite distinct from the primary energy. Many radon velocity filter trials were done using different low and high velocity percentages, examples of kept ranges of velocities for an NMO velocity of 4000 m/s are detailed below in Table 2.3.

Table 2.3. Example of NMO velocity ranges kept for a velocity of 4000 m/s.

Percentage of NMO velocity to keep	Resulting range in velocity kept
30	2800 m/s – 5200 m/s
20	3200 m/s – 4800 m/s
10	3600 m/s – 4400 m/s

Figure 2.22 shows a stacked section of line 403 with the radon velocity filter applied. Velocity percentages were set to keep 20% above and below the picked NMO velocity.

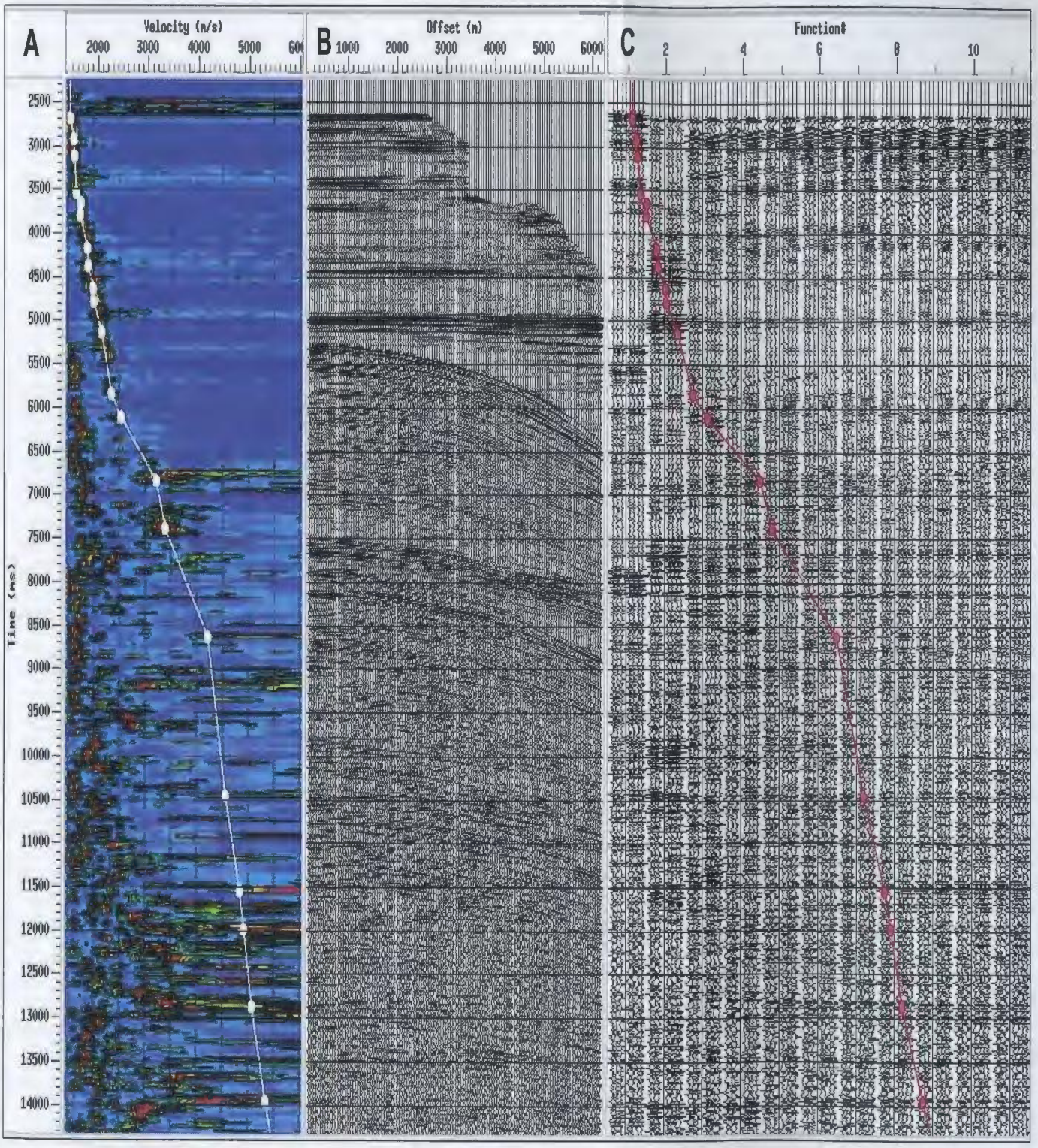

Figure 2.21. (A) Semblance plot, (B) NMO corrected gather and (C) Constant velocity stacks for CDP 480500 on line 403. Note in the semblance plot that multiple energy tends to plot in the velocity range from 1500 – 2500 m/s. The white line in the semblance plot and the red line on the constant velocity stacks depict the velocities picked for NMO correction.

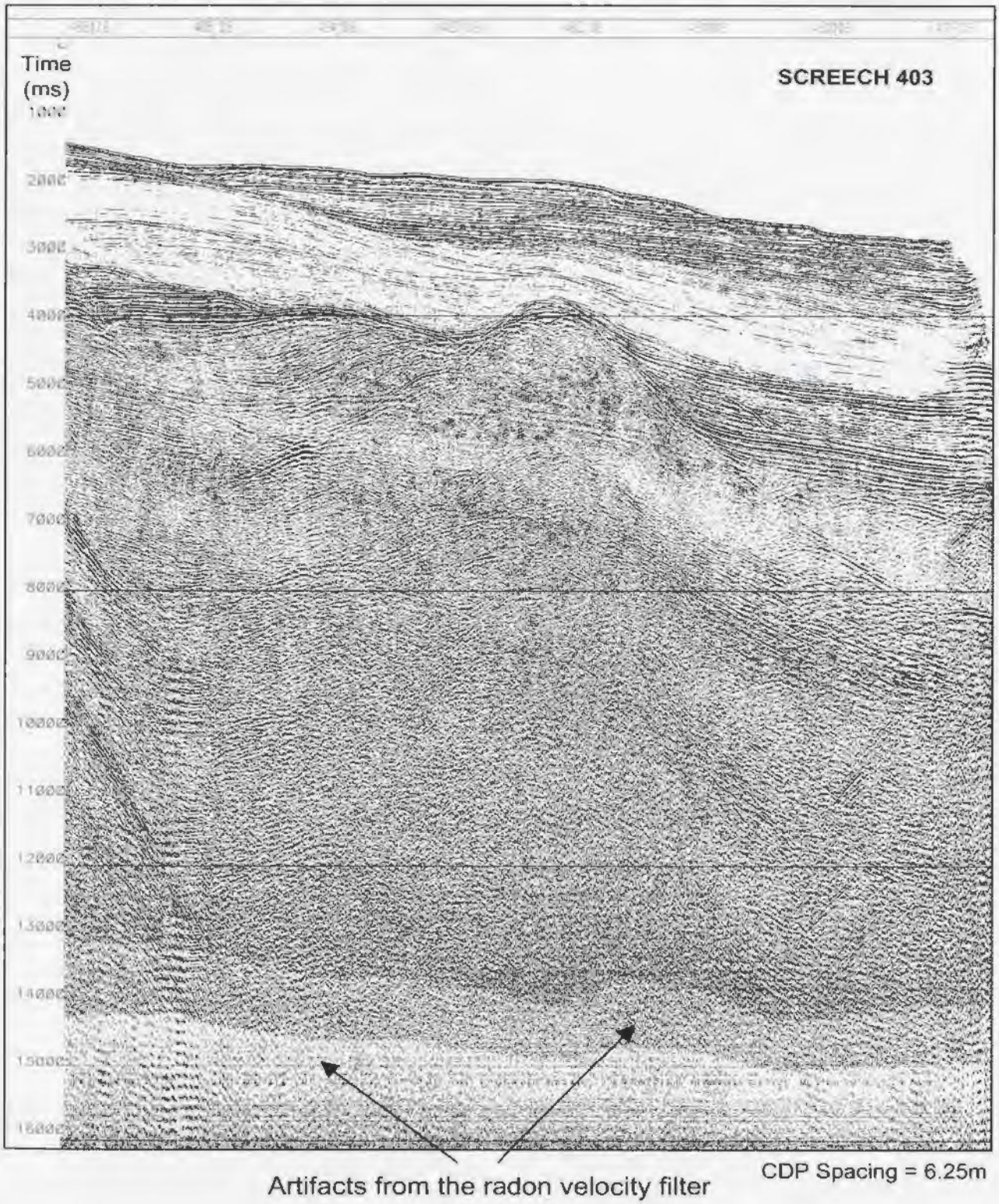

Figure 2.22. Artifacts created by the radon velocity filter on line 403.

Examination of Figure 2.22 found that artifacts were introduced into the data with the application of the radon velocity filter and are evident deeper in the data at times greater than 14000 ms. This presumably results from an error in the way the ProMAX algorithm deals with ends of data, and varies with the percentage above and below the NMO velocity that is kept. Testing was done varying the percentages kept from 10-30%. Artifacts were much stronger when only 10% above and below the NMO velocity were kept, especially in the deeper sections of the data. In the shallow sections where it was thought a narrower range would prove to be effective at removing multiples, however no improvement was noticed. Keeping 30% above and below the NMO velocity also produced artifacts deeper in the section, but these were not as severe as in the 10% and 20% kept instances. By keeping 30% above and below the NMO velocity, velocities around 2500 m/s which are typical in the shallow portion of the data will keep a range between 1750 -3250 m/s which is much too large to remove any of the multiples. Based on these results the radon velocity filter was not applied to the slope area.

2.3.3.3 Near Trace Mute

It was shown above in discussion of the radon filter that one of the main difficulties in multiple removal is the lack of differential move-out between primaries and multiples at near offsets. A near trace mute was tested on the slope portions of both lines to determine its effectiveness to removing multiple energy. Figure 2.23 shows the extent of the near trace mute on CDP gathers on line 403. For most CDPs generally only the first 15 to 20 traces were muted. These traces correspond to the area where multiples tend to

appear the flattest in NMO corrected CDP gathers. Figure 2.24 illustrates the stacked slope section of line 401 with the near trace mute applied. Examination of this section shows that most of the energy from the multiples is reduced. When compared to the radon filtered section in Figure 2.19, the water bottom multiple is stronger, however the sediment multiples have been greatly reduced along with the multiples from the high. Figure 2.25 illustrates the near trace stack applied to the slope portion of line 403. When compared to Figure 2.20, it is noticeable that the multiples from the basement high and the sediment have been diminished to a much greater extent by the near trace mute.

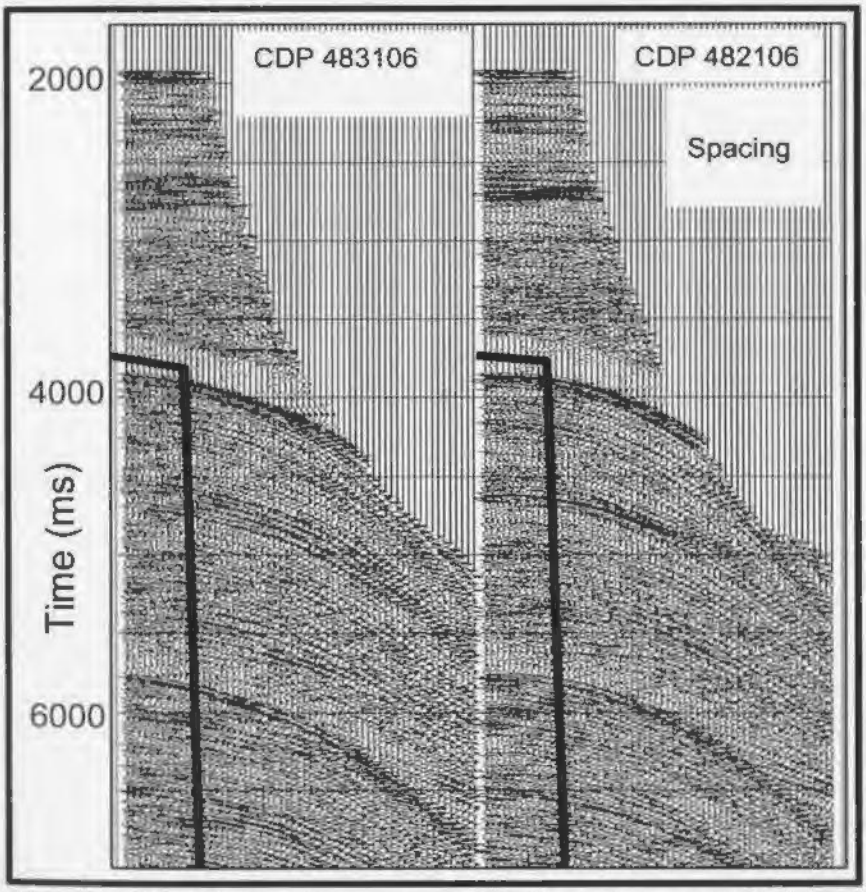

Figure 2.23. Shows the near trace mute that was applied to CDP gathers in the slope region of line 403. Each CDP contains 60 traces and is shown with an NMO correction applied. Note how at near traces multiple energy appears to be flattened along with the primary energy. Since the multiple energy is strong and flat at the near traces it appears in the stack.

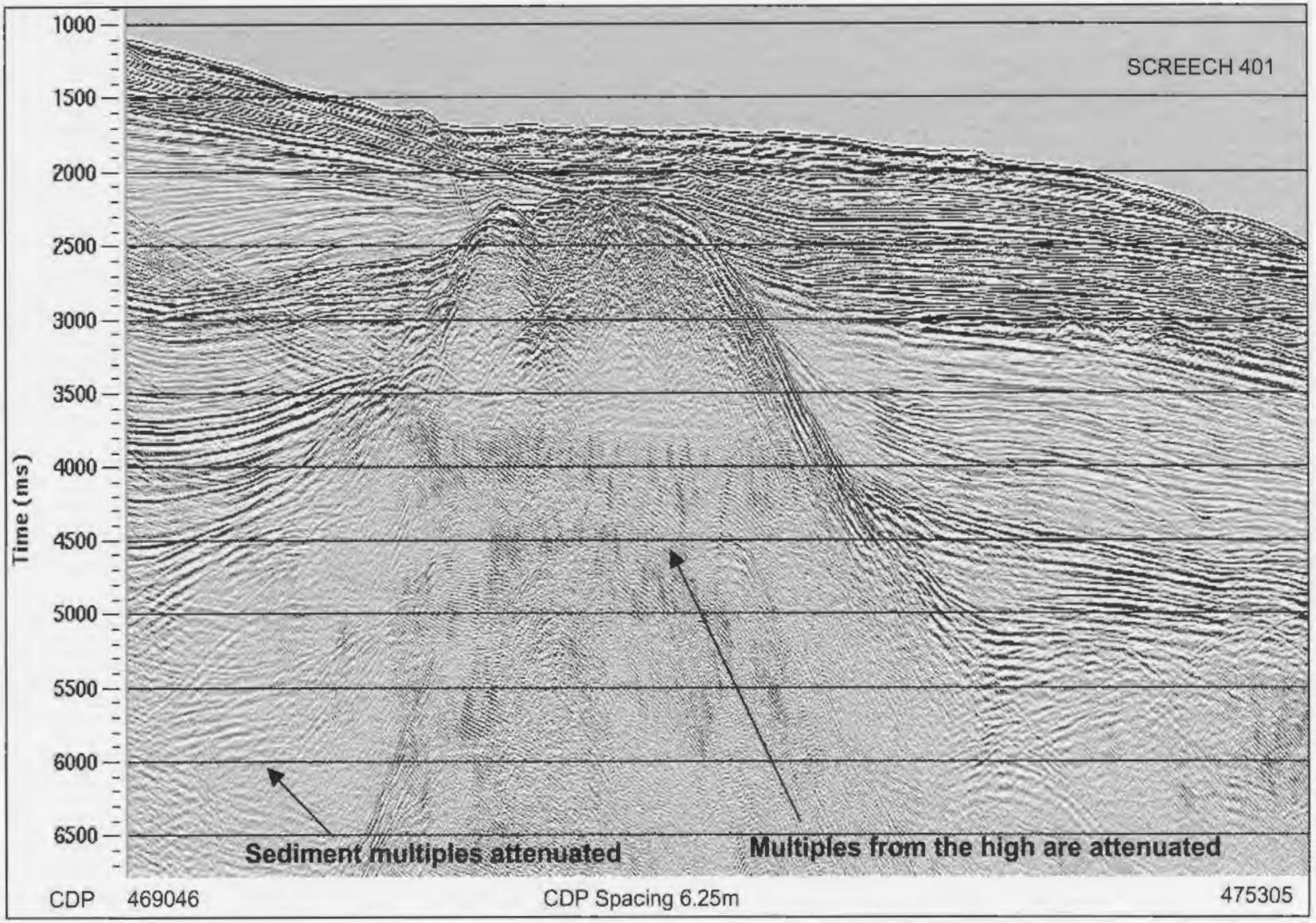

Figure 2.24. Near trace mute stack of the slope area of Line 401. This stacked section shows the most multiple removal of any of the techniques tried.

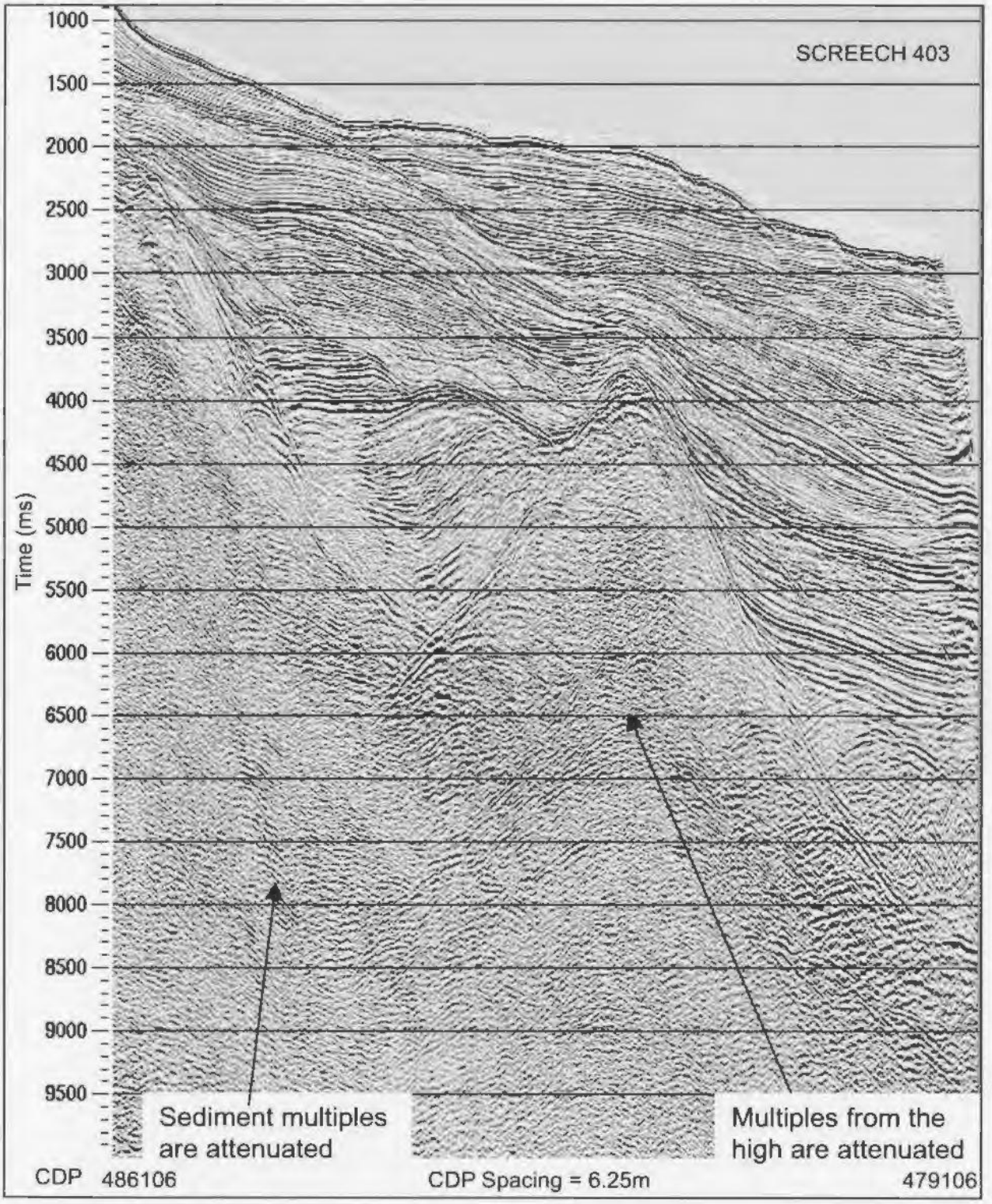

Figure 2.25. Near trace mute stack of the slope area of Line 403. This stacked section shows the most multiple removal of any of the techniques tried.

Based on all the pre-stack testing on the slope area for both SCREECH lines 401 and 403, a near trace mute was applied to all the slope CDPs of both lines to attenuate the multiples. A radon filter was also applied to line 401 on CDPs 468546 to 475305 to remove the first water bottom multiple. These two processes were found to be the only methods that effectively removed most of the multiples created by the water bottom, the sediment and the basement high.

2.3.4 Stacking Lines 401 and 403

Stacking velocities were picked based on semblance plots, constant velocity stacks and CDP gathers on every 500th CDP, which corresponds to every 3125 m. Figures 2.26 and 2.27 show examples of stacking velocities that were picked for various CDPs. Once the velocities were picked they were applied to the CDPs and Figure 2.28 shows move-out corrected gathers in the slope area of line 403. Above the first multiple the primary energy is flattened and will stack well but below this, primary velocities are difficult to pick since the multiple energy is so strong. The entire stacking velocity field that was picked is shown in Figure 2.29 for line 401 and 2.30 for line 403. These figures illustrate how the stacking velocities vary from CDP to CDP across the line.

The automatic 30% NMO stretch mute in ProMAX that is applied to the CDPs after NMO and before they are stacked, was found to cut out the water bottom reflections mainly in the shelf area, so it could not be used.

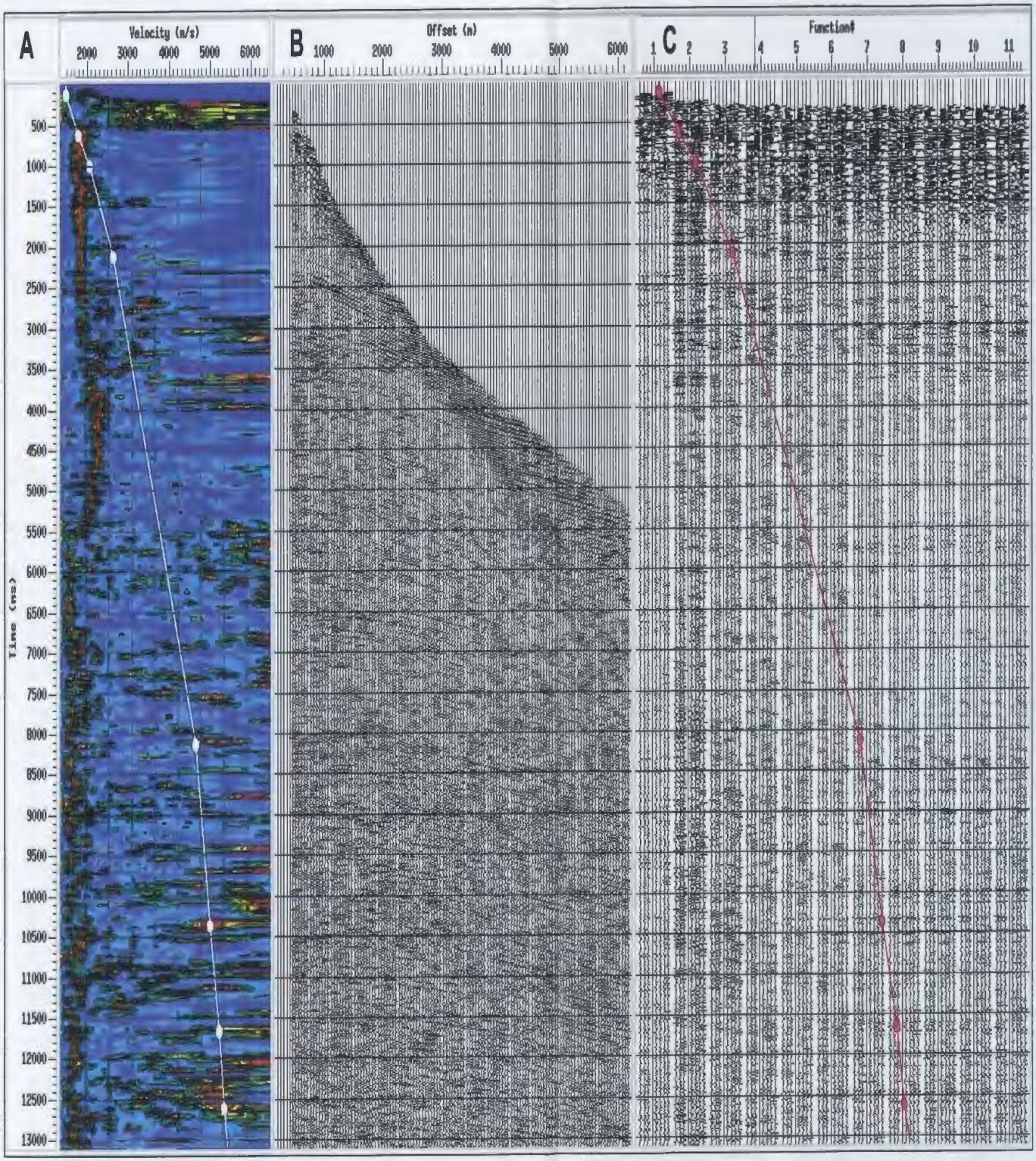

Figure 2.26. (A) Semblance plot, (B) NMO corrected gather and (C) Constant velocity stacks of CDP 446000 on line 401. The white and red lines represent the picked NMO velocities.

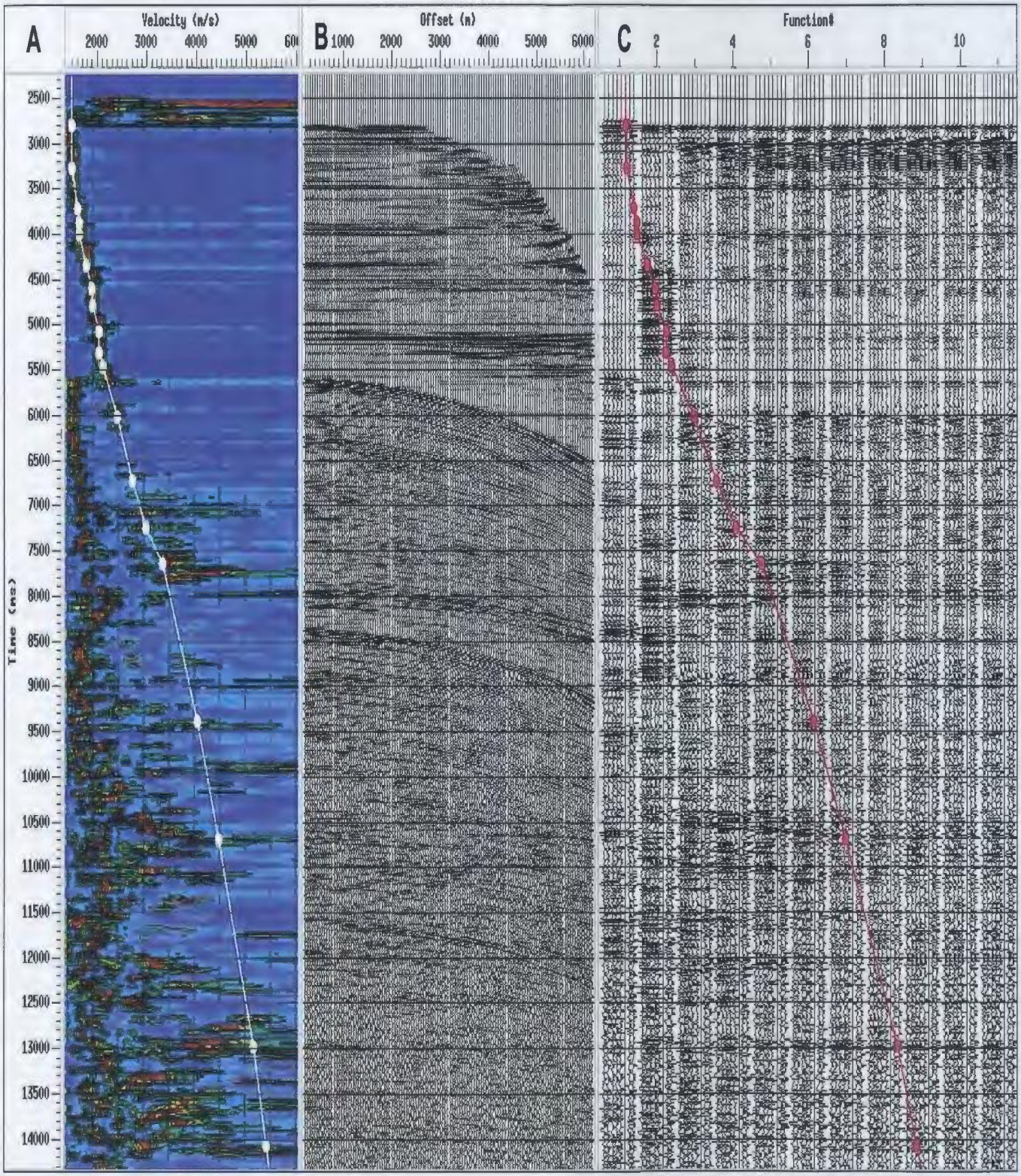

Figure 2.27. (A) Semblance plot, (B) NMO corrected gather and (C) Constant velocity stacks of CDP 480000 on line 403. The white and red lines represent the picked NMO velocities.

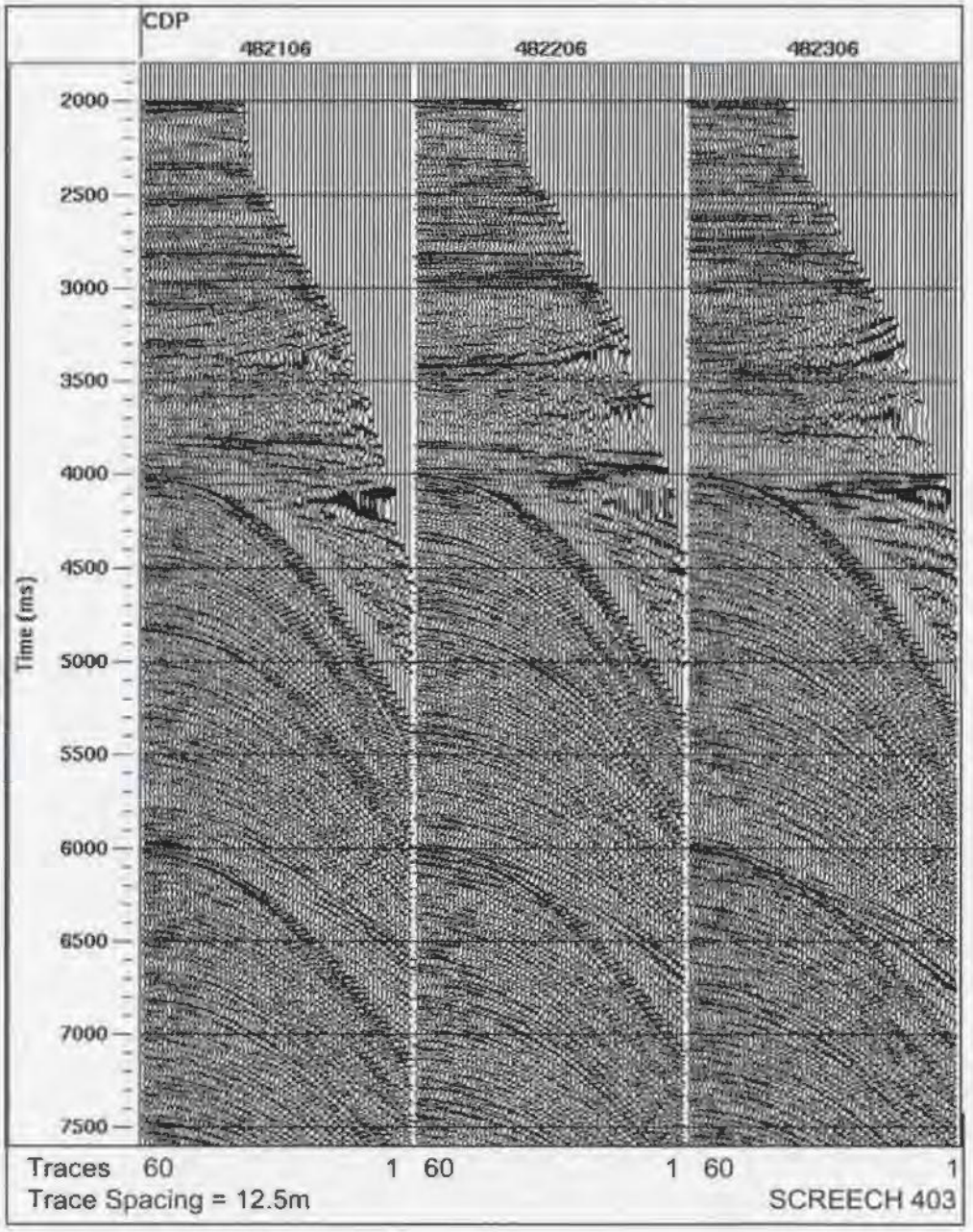

Figure 2.28. CDP gathers from line 403 with NMO corrections applied. Note how well reflections above the first multiple are flattened. Below the first multiple, primary energy is difficult to identify because of the amplitude of multiple energy.

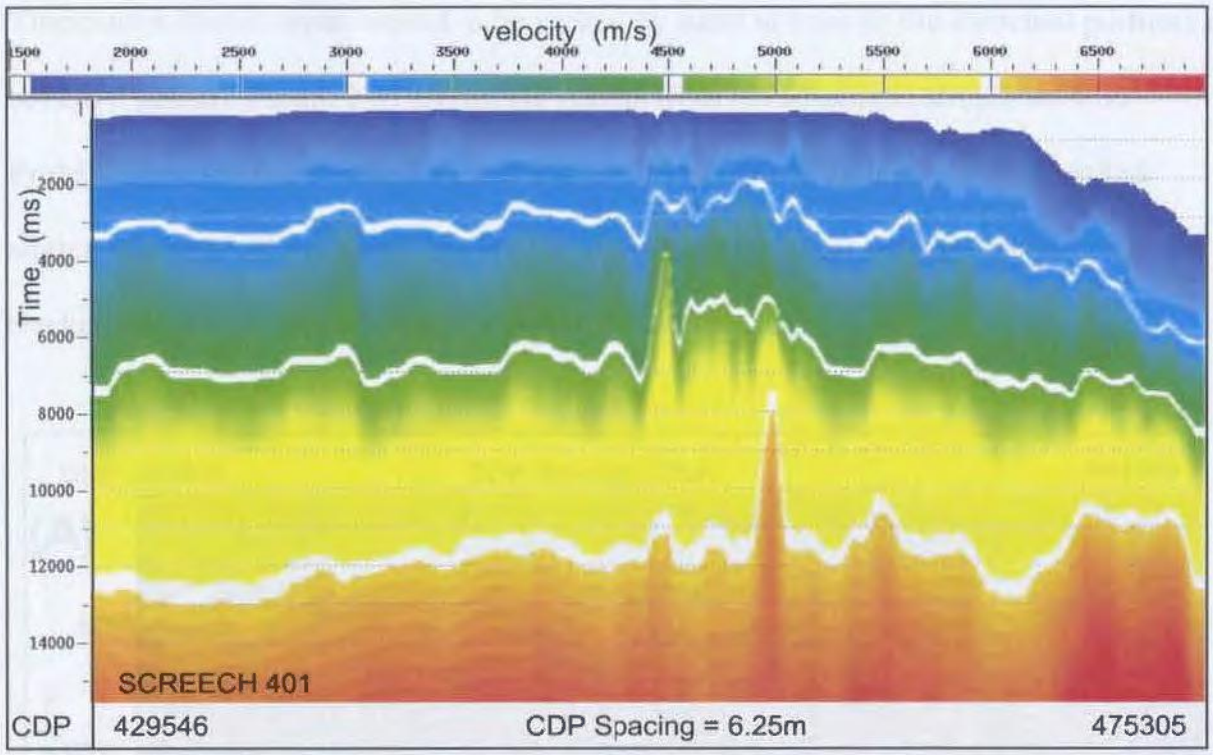

Figure 2.29. NMO velocities picked through velocity analysis for Line 401

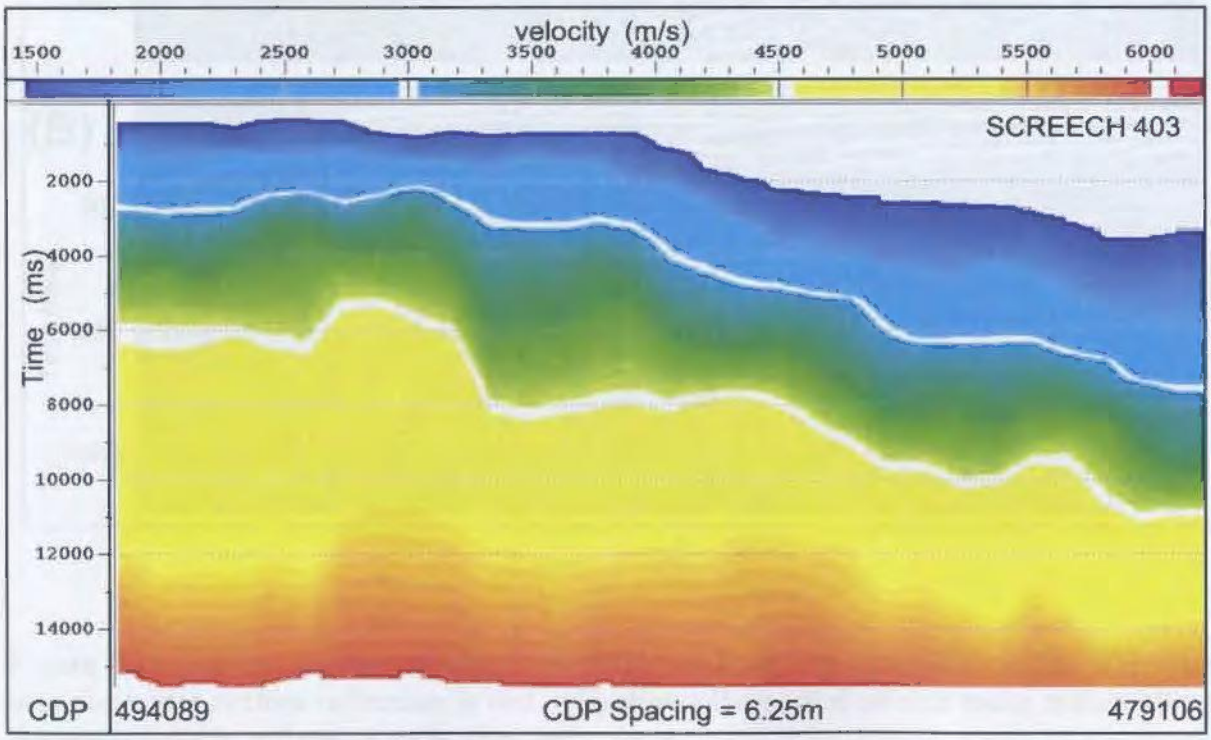

Figure 2.30. NMO velocities picked through velocity analysis for Line 403.

Therefore a stretch mute needed to be picked by hand to remove the stretched portions of the CDP gather. Figure 2.31 shows the results from the automatic stretch mute in ProMAX and the hand picked stretch mute, while Figure 2.32 illustrates the picked stretch mute on CDP gathers. Each CDP containing 60 traces was stacked to create the stacked sections for both line 401 and 403.

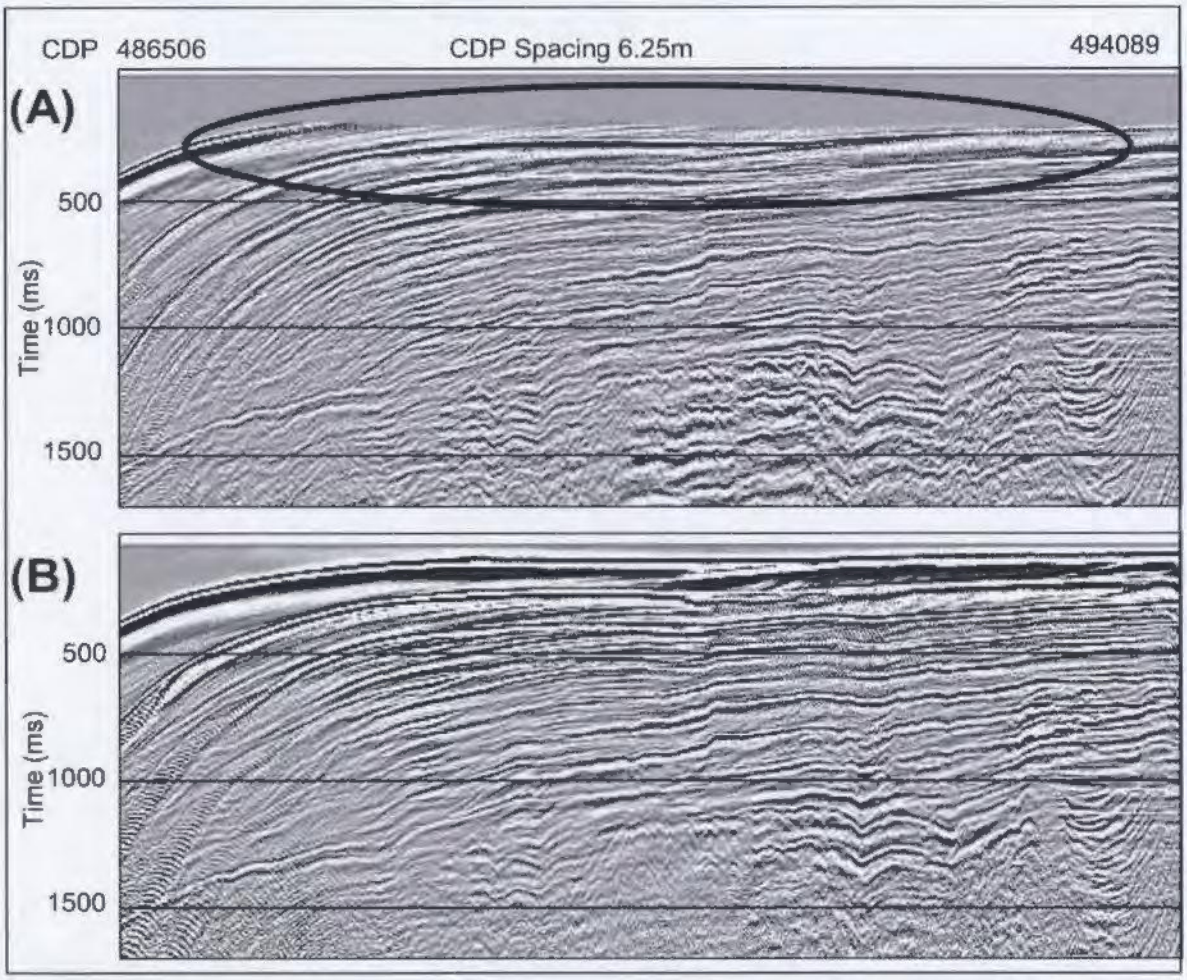

Figure 2.31. (A) Shows the automatic stretch mute built into ProMAX on line 403. Note how the water bottom reflection is lost. (B) shows the picked stretch mute, which allows the water bottom reflection to be retained.

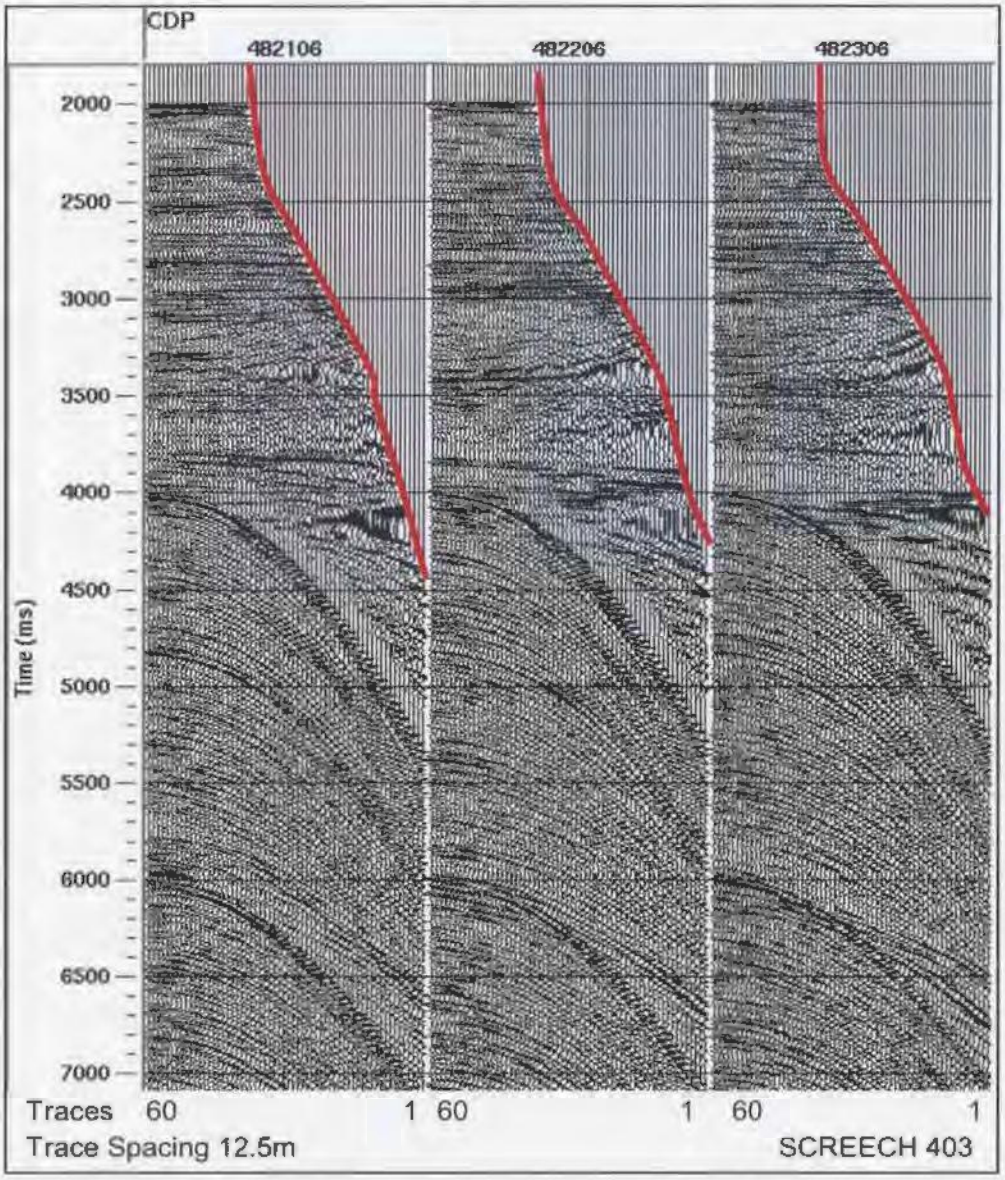

Figure 2.32. NMO corrected CDPs on line 403, showing the NMO stretch mute that was picked. This mute allows the water bottom reflection to be retained when stacked and also removed badly stretched portions of the CDP gather.

2.3.5 Poststack Processing

The stacked sections still contain many areas of noise and multiple energy despite efforts to remove them pre-stack. The shelf break portion of the line contains the largest amount of noise that must be removed before the section can be migrated. Time variant scaling

(TVS) was applied to both lines to balance the sediment and basement reflections and create a more uniform section before any post-stack processing is done. TVS allows sections of the line to be multiplied by a user specified scalar value (ProMAX Reference Guide, 1998). By applying a scalar, the gain on a specific area of the line can either be increased or decreased in order to create a more uniform section. After this balancing was completed, a post-stack F-K filter was applied to the entire section.

2.3.5.1 F-K Filter

The stacked sections show areas of steeply-dipping coherent noise (Figure 2.33 part A) that probably arises from shallow scattering. The post-stack F-K filter was applied as a windowed process to both lines 401 and 403 to reduce such noise. The filter window was picked to target the areas affected by the steeply-dipping coherent noise. It was generally picked just above the first multiple in the slope area and just below basement on the shelf and extends down until the bottom of the stacked section at 16000ms. The design of the F-K filter changed along both lines, to target different types of noise: an example is shown in Figure 2.33. 2000 traces are input into each F-K filter across the stacked section. As with the pre-stack F-K filters, the filter polygons accept the data inside and reject the data outside of the polygon. It is evident from the figure that most of the remaining coherently dipping noise in the stack is removed from the stacked section by the F-K filter.

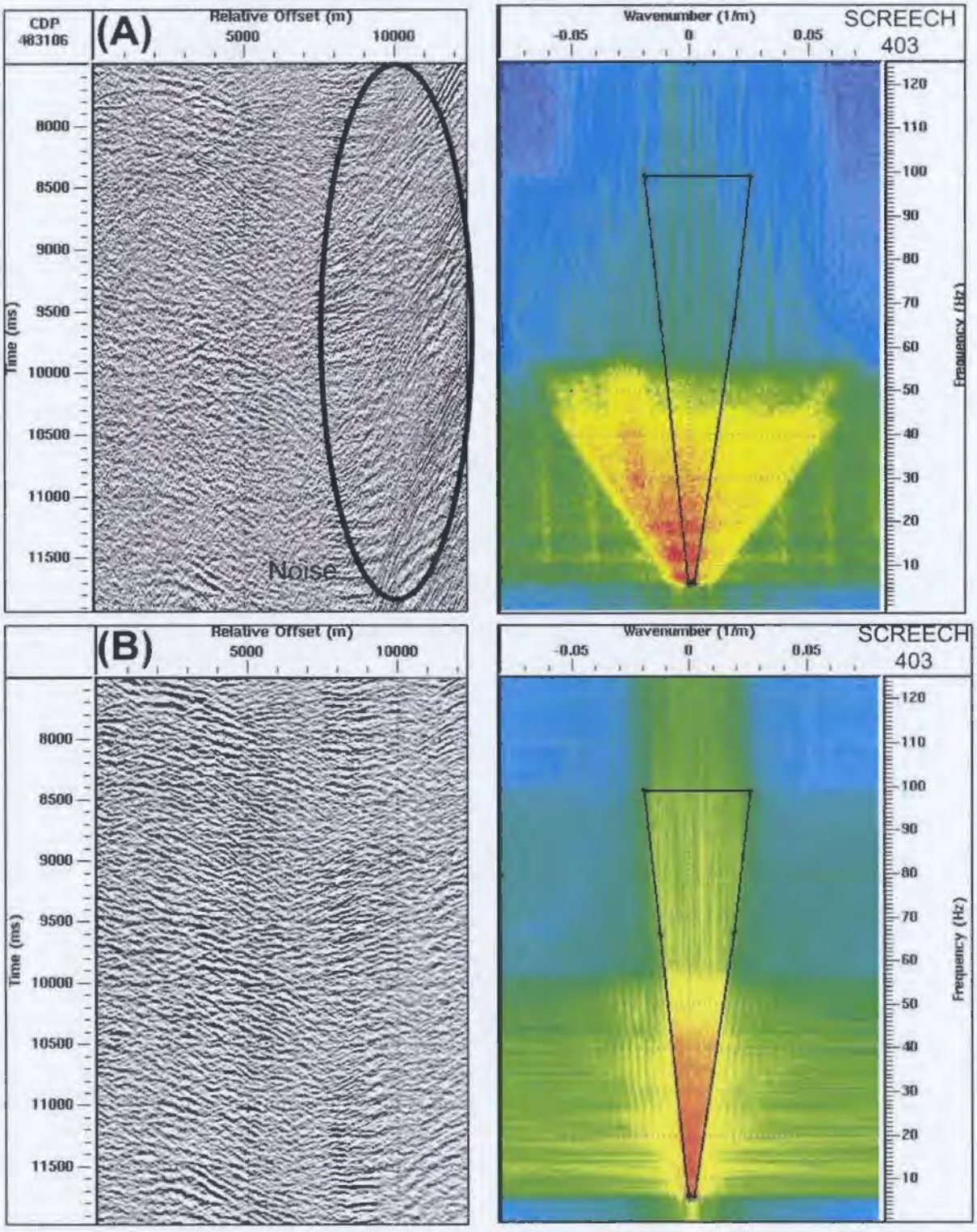

Figure 2.33. Post-stack F-K filter on line 403. (A) Stack and F-K plot before the application of filter. (B) After the application of the F-K filter. This F-K filter was applied to the slope break portion of the line. Notice how dipping noise is removed.

2.3.5.2 Deconvolution

After the stacked sections are F-K filtered, a predictive deconvolution is applied to the line as a windowed process. The deconvolution window picked for lines 401 and 403 is similar to the window picked for the F-K filter. The window starts just before the first multiple on the slope and just below basement on the shelf and extends all the way down to the end of the section (16000 ms). The deconvolution was applied as a windowed process to preserve sediment reflections in the shelf break area that are distorted when a window is not used.

In applying the deconvolution, two design windows were picked on both lines 401 and 403. On line 401 starting at CDP 429546 on the shelf: the first design window ranged from 0 to 7000 ms, the second design window ranged from 5000 to 16000 ms. For line 403, at CDP 479106 on the slope: the first window ranged from 6000-12000ms, and the second window ranged from 10000-16000ms. At CDP 486106: the first window ranged from 1500-7000ms, and the second window ranged from 5000-16000ms. In each design window, the operator length was 300 ms and the gap was 90 ms. The design windows were picked on each line to correspond to the areas that contain most of the reverberatory noise. Figure 2.34 shows that reverberatory noise on line 403 is attenuated. Other post-stack deconvolution parameters were also tested but were not found to be as effective as using a gap of 90 ms and an operator length of 300ms.

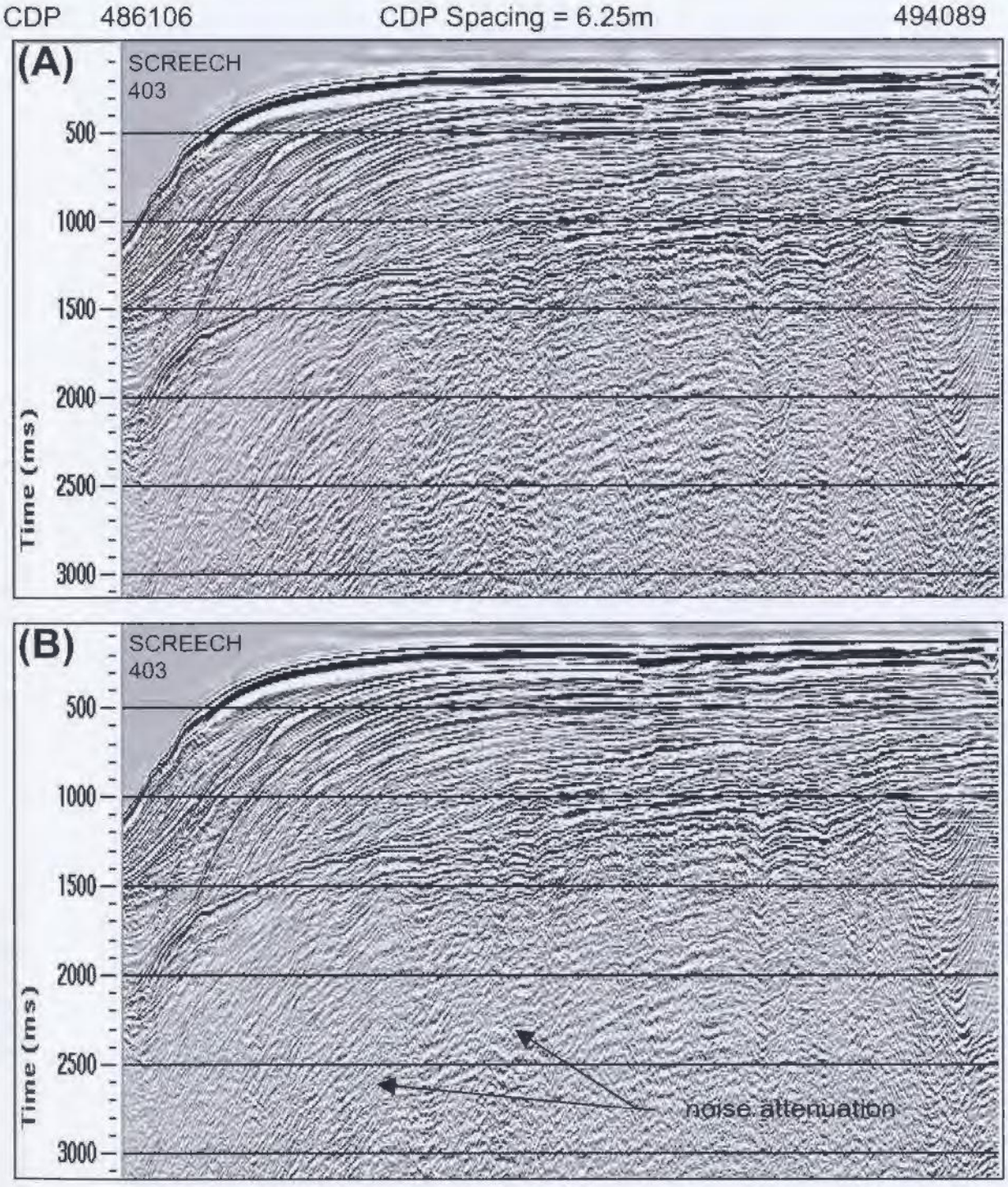

Figure 2.34. (A) Stacked section of line 403 without post stack predictive deconvolution applied. (B) Same as the section from (A) with a post stack deconvolution applied as a windowed process. Operator length = 300 ms, gap = 90 ms, and design windows at CDP 479106: 6000-12000ms (not illustrated), 10000-16000ms, and CDP 486106: 1500-7000ms, 5000-16000ms. Note attenuation of reverberatory noise.

2.3.5.3 Bandpass Filter

A minimum phase Ormsby bandpass filter was then applied to the section as a windowed process. The bandpass filter was applied to remove any remaining high frequency noise that is still present in the section. The high frequency noise is generally associated with the linearly dipping noise, as well as with some of the noise around the shelf break. The bandpass filter needed to be applied in a windowed process below the water bottom and in some places the basement to avoid the creation of reverberation tails on the strong water bottom and basement reflections. Figure 2.35 illustrates the reverberatory noise that is created on the slope portion of line 401 and Figure 2.36 illustrates the noise on the shelf portion of line 403. The window picked for the bandpass filter is similar to the window for the post-stack F-K filter and deconvolution filter. The bandpass filter parameters for the windowed bandpass filter for line 401 are shown in Table 2.4.

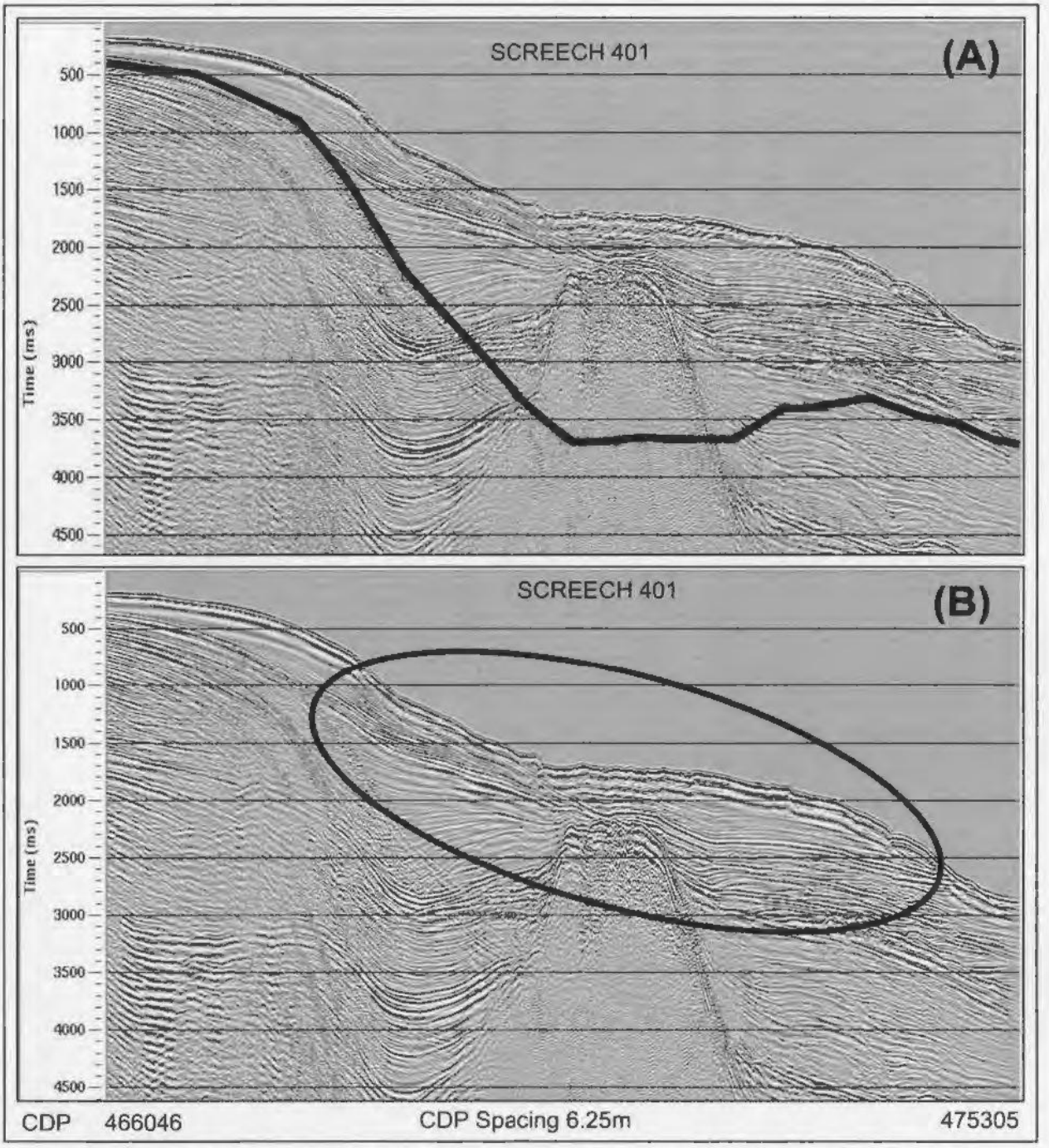

Figure 2.35. (A) Post stack bandpass filter applied to the slope portion of line 401. The bandpass filter is applied below the black line to the bottom of the section (16000 ms). (B) Shows noise caused by not applying the bandpass filter as a windowed process ie. applying the filter to the whole profile. The water bottom reflection is extremely reverberatory as is the reflection from the high. Filter parameters are listed in text.

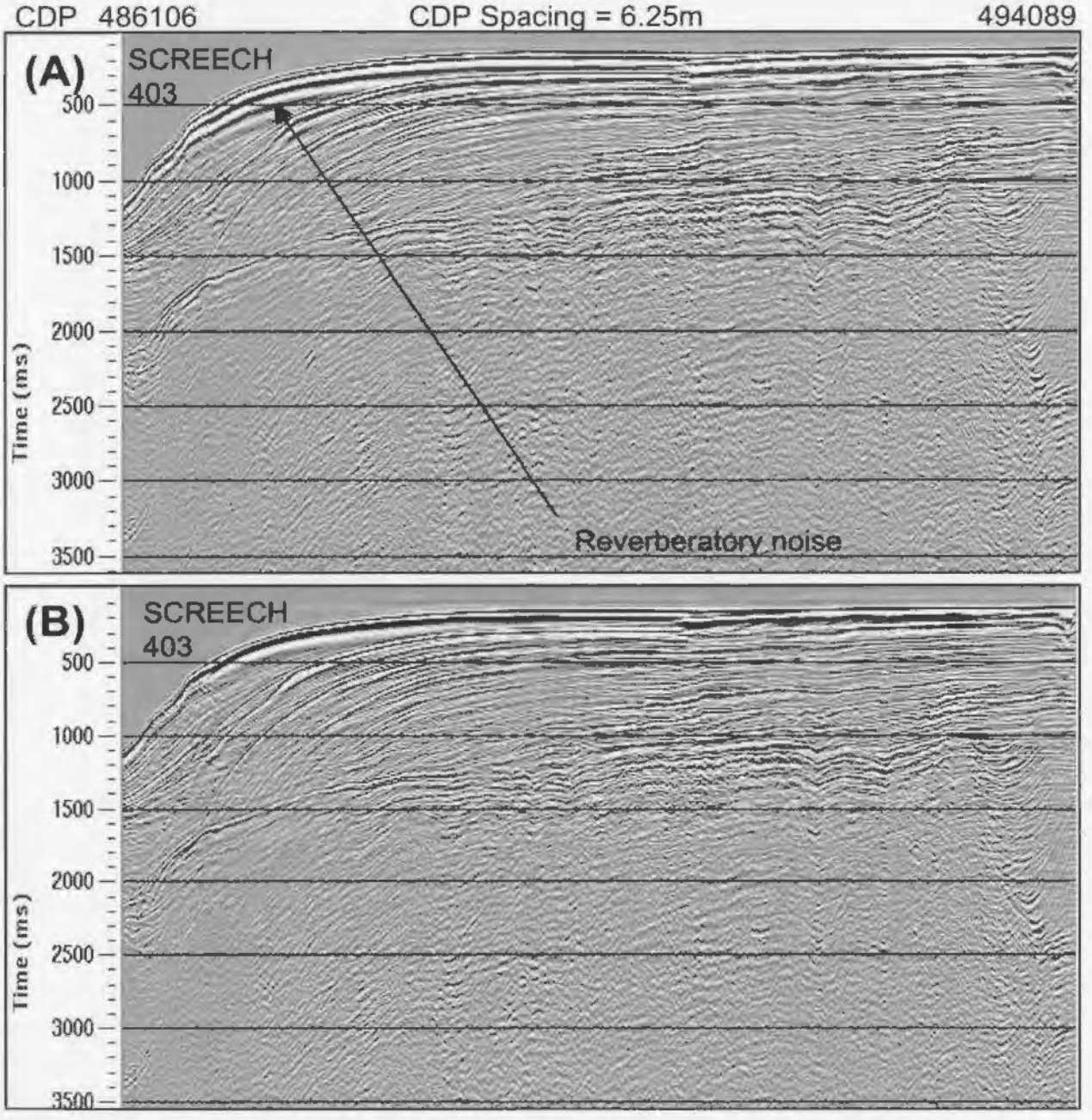

Figure 2.36. (A) Stacked shelf section of line 403 with a bandpass filter applied as follows: CDP 479106: 8-10-60-80Hz from 2-8 s, 5-8-35-50 Hz from 10-16 s. CDP 485506: 8-15-60-80 Hz from 0.5-8 s, 5-8-35-50 Hz from 10-16 s. CDP 487606: 7-10-80-100 Hz from 0.2-8 s, 5-8-35-50 Hz from 10-16 s. Note the reverberation tails created at the water bottom.
(B) Same as (A), bandpass is applied as a windowed process as follows: CDP 479106: 8-10-60-80Hz from 6-10 s, 5-8-35-50 Hz from 12-16 s. CDP 485506: 8-15-60-80 Hz from 2-8 s, 5-8-35-50 Hz from 10-16 s. CDP 487606: 7-10-80-100 Hz from 1-8 s, 5-8-35-50 Hz from 10-16 s.

Table 2.4. Bandpass filter parameters for line 401.

CDP Span	Ormsby Bandpass Filter	Time Window (ms)
429546 to 466045	7-10-70-90	0 - 1500 ms
	7-10-45-60	3000 - 6000 ms
	5-8-30-45	9000 - 16000 ms
466046 to 469046	7-10-65-80 Hz	0 - 1500 ms
	7-10-35-45 Hz	3000 - 6000 ms
	5-8-30-45 Hz	9000 - 16000 ms
469047 to 471046	7-10-50-65 Hz	0 - 2000 ms
	7-10-35-50 Hz	9000 - 16000 ms
	5-8-30-45 Hz	3000 - 6000 ms
471047 to 475305	7-10-40-60 Hz	0 - 2000 ms
	7-10-35-45 Hz	3000 - 6000 ms
	5-8-30-40 Hz	9000 - 14000 ms

For line 403 the bandpass filter parameters are shown in Table 2.5.

Table 2.5. Bandpass filter parameters for line 403.

CDP Span	Ormsby Bandpass Filter	Time Window (ms)
479106 to 485505	8-10-60-80 Hz	6000 - 10000 ms
	5-8-35-50 Hz	12000 - 16000 ms
485506 to 487605	8-15-60-80 Hz	2000 - 8000 ms
	5-8-35-50 Hz	10000 - 16000 ms
487606 to 494089	7-10-80-100 Hz	1000 - 8000 ms
	5-8-35-50 Hz	10000 - 16000 ms

2.3.5.4 Post-stack Scaling

To create reasonably uniform signal level across the section after post-stack processing has been applied, time variant scaling and automatic gain control (AGC) were applied. Since amplitude variations are much stronger through the sediment layers than through the basement, AGC alone could not create a uniform signal level across the seismic lines which made the application of a time variant scalar necessary. AGC was applied to line 401 using a 4000 ms operator length and applying the scalar by computing the mean value from the window. After the AGC, time variant scaling was done using user defined values. A summary of the values and the time gates can be found in Appendix 1. For line 403, time variant scaling using user defined values was first applied to the line. A summary of the values and time gates can also be found in Appendix 1. AGC was then applied using an 8000 ms operator length and computing the scalar by determining the mean value from the window. Most of the multiples on the shelf area have been removed, as well as many of the multiples associated with the shelf break. The linear coherently dipping noise has mainly been removed and so has most of the reverberatory noise.

2.3.6 Migrating Lines 401 and 403

After the pre- and post-stack processing is complete, the lines must be migrated. Figures 2.37 and 2.38 show the final migration velocities (RMS) that were picked and used to migrate both line 401 and 403. In order to avoid the creation of migration smiles at the bottom of the data set, velocities were reduced to approximately 3600 m/s at 16000 ms.

Generally the migration velocity values tended to be slightly less than the NMO velocities. A Kirchhoff post-stack time migration was used to migrate these lines. The RMS velocities relate the time down each trace to a locus of points in the subsurface (ProMAX Reference Guide, 1998). In this migration the RMS velocity field is allowed to vary both vertically and laterally in time. The main advantage of this migration is that it can handle steep dips, lateral and vertical velocity variations and it is moderately fast (ProMAX Reference Guide, 1998).

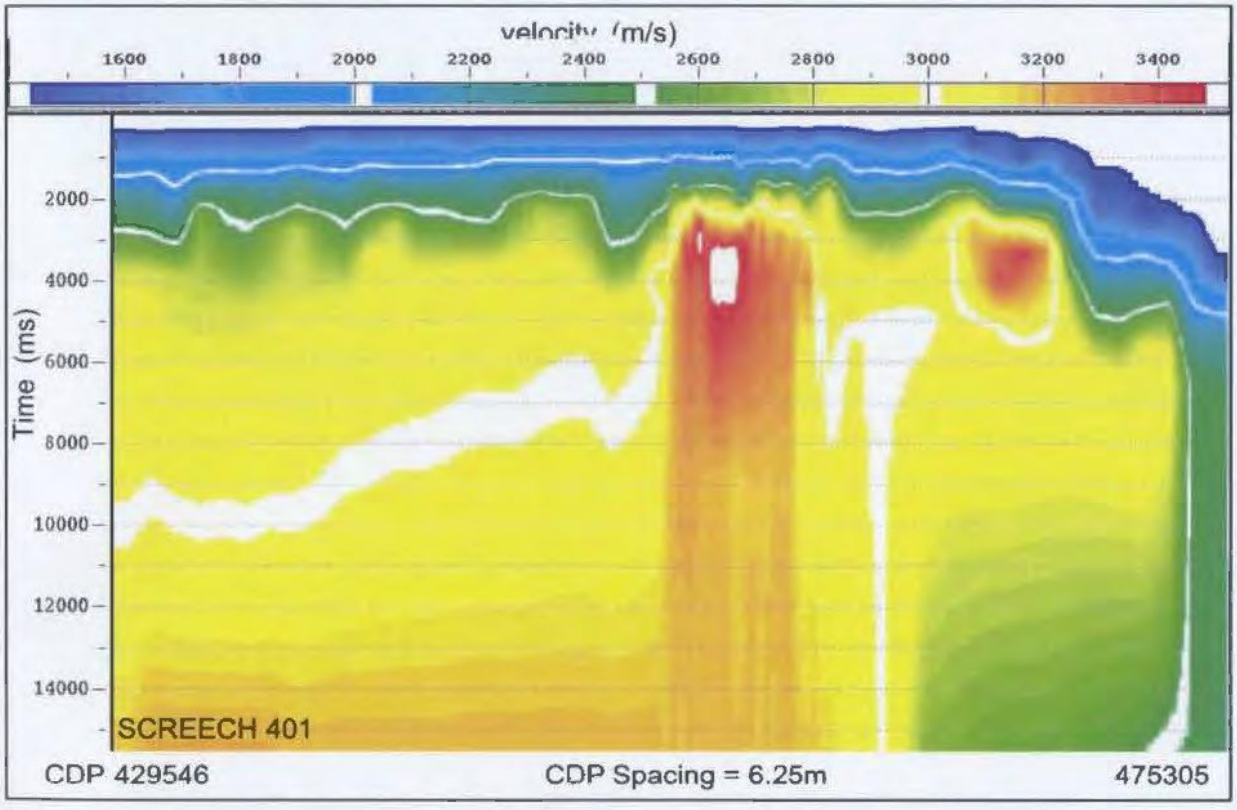

Figure 2.37. RMS Migration velocities for line 401.

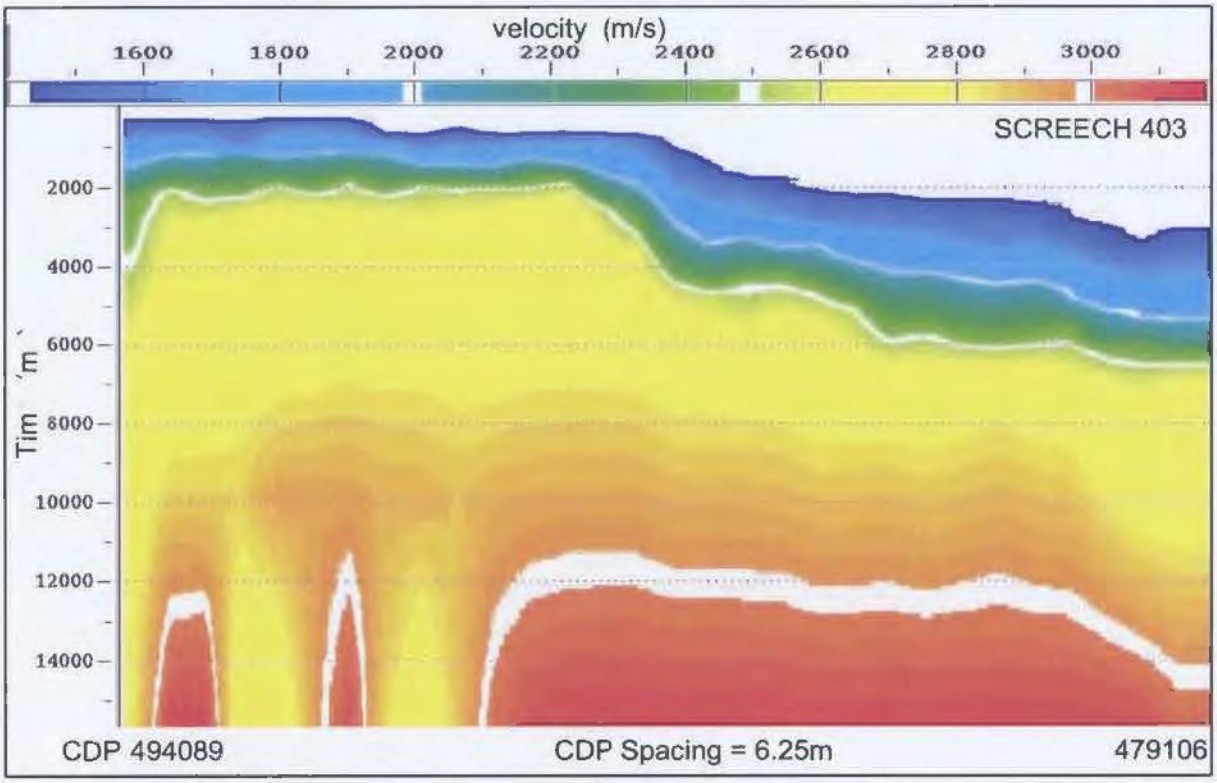

Figure 2.38. RMS Migration velocities for line 403.

2.3.7 Displaying the migrated sections for lines 401 and 403

To display all 16 seconds of these two lines a few processes are applied for cosmetic purposes to present a uniformly scaled line. For line 401 a trace mute to remove any noise above the water bottom was applied as was an Ormsby minimum phase bandpass filter which was applied as a windowed process. The filter parameters for the bandpass filter were 5-9-75-100 Hz. An AGC with an operator length of 2000 ms was applied using the mean value from the window as the scalar. A F-K power exponent filter was applied with the power being 1.2. The F-K power exponent filter transforms the data into the F-K domain and raises all the values to a power (1.2 in this case) (ProMAX Reference Guide, 1998). The data is then transformed back into the T-X domain. This

filter was used to help enhance the continuity of the data. A nine trace weighted mix was then applied to the section to enhance coherency of the deeper crustal reflections. Lastly time variant scaling was applied to the section. For line 403 an AGC with an operator length of 4000 ms was applied using the mean value from the window as the scalar. Another AGC with a 500 ms operator length and mean value as the scalar was also applied but only as a windowed process and only applied to the sediments above basement because amplitude variations are larger and more rapid in this part of the section. A final bandpass filter was applied as a windowed process using the same window that was used when applying the post-stack bandpass filter. The parameters for this minimum phase Ormsby filter were 5-10-70-100 Hz and this was applied to the entire windowed section. An eleven trace weighted mix was then applied to the section to enhance coherency of the deeper crustal reflections, and finally a top mute which removed any noise above the water bottom was applied for plotting purposes. The final migrated and scaled versions of SCREECH lines 401 and 403 can be found on Plates 1 and 2 respectively.

2.4 Processing SCREECH Line 402

The processing objective for Line 402 was to produce both stacked and migrated sections from the raw field data. Line 402 is a slope parallel line that connects line 401 to line 403. This line also intersects Line 3MCS as shown in Figure 2.2. The water bottom depth is approximately 2000 m along the length of the line. Extensive testing was done both pre- and post-stack to determine the optimum processing parameters. The following

sections detail the final processing techniques applied to the line as well as the techniques that were tested, but deemed unacceptable. The pre-stack processing will first be explained in detail, with explanations of what parameters were used and their effect on the data, and after this the post-stack processing sequence will be detailed. Figure 2.39 is a condensed overview of the processing techniques that were applied to this line to produce the final migrated section. The complete processing flow can be found in Appendix 1.

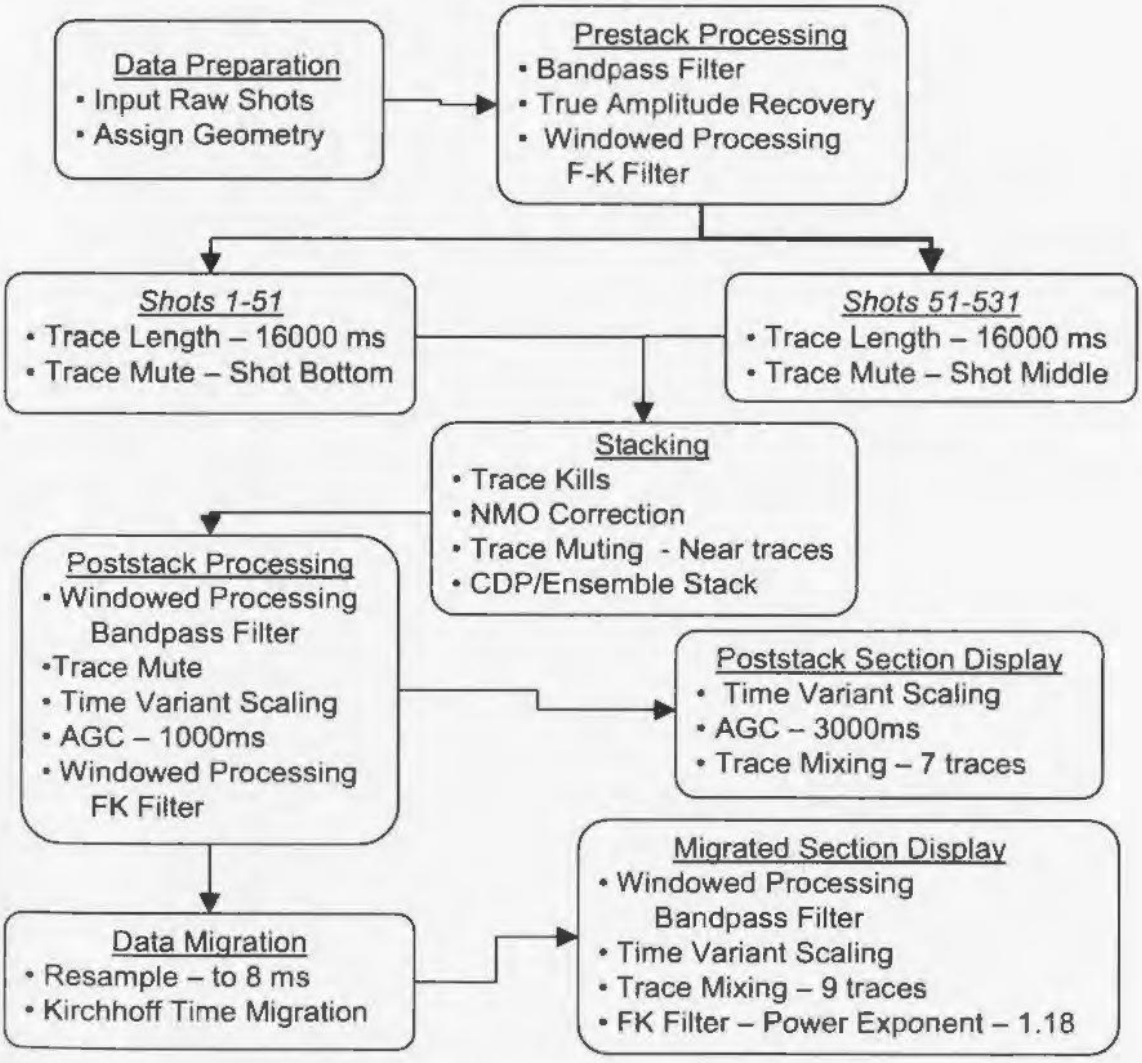

Figure 2.39. Processing flow for Line 402.

2.4.1 Pre-stack Processing

SCREECH line 402 contains 531 shot gathers each consisting of 480 traces. The shot gathers were analyzed to determine the dominant frequencies of the data and Figure 2.40 shows the dominant frequencies in the top and bottom portions of shot gather 1. The gather contains low frequency noise and the dominant signal frequencies tend to range between 8 and 60Hz.

2.4.1.1 Bandpass Filter

A minimum phase time-variant Ormsby bandpass filter was applied to the shot gathers to remove the unwanted low frequency noise. The filter was designed to be time variant, so that higher frequencies could be kept in the shallower portions of the data, but filtered out at deeper times. It is also designed to allow lower frequencies to be removed at shallow times, but kept at deeper times. The frequency parameters used are listed below and correspond to the [100% low cut frequency] - [0% low cut frequency] – [0% high cut frequency] - [100% high cut frequency].

- 7-10-80-100 Hz applied from 2000-3000 ms
- 7-10-40-60 Hz applied from 5000-7000 ms
- 5-8-35-45 Hz applied from 9000-14000 ms

Between the time gates, the frequency values are interpolated. Figure 2.41 shows the frequency response of the filtered shot gather.

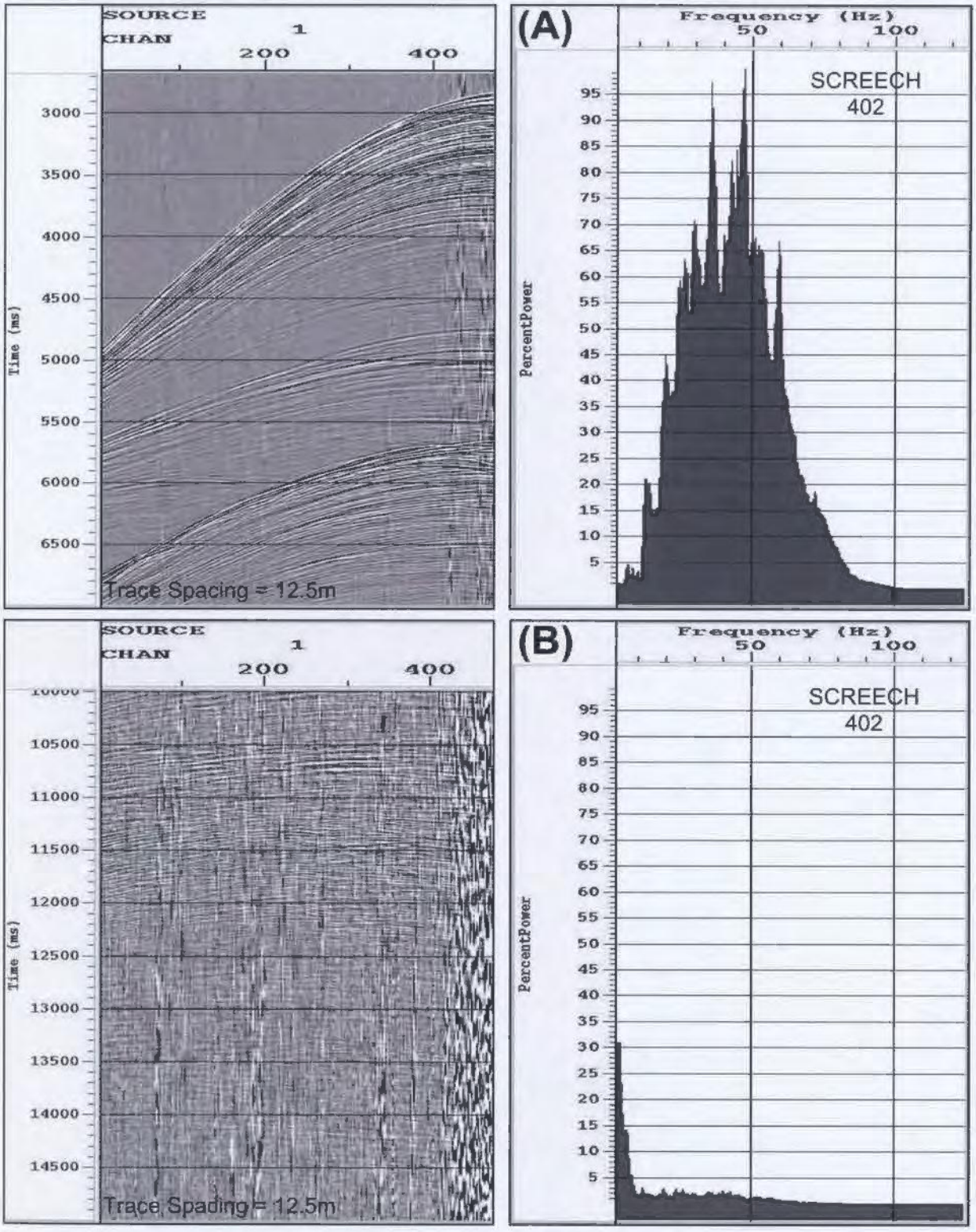

Figure 2.40 . Frequency spectrum for the upper section (A) and lower section (B) of shot 1 on line 402 before a bandpass filter is applied.

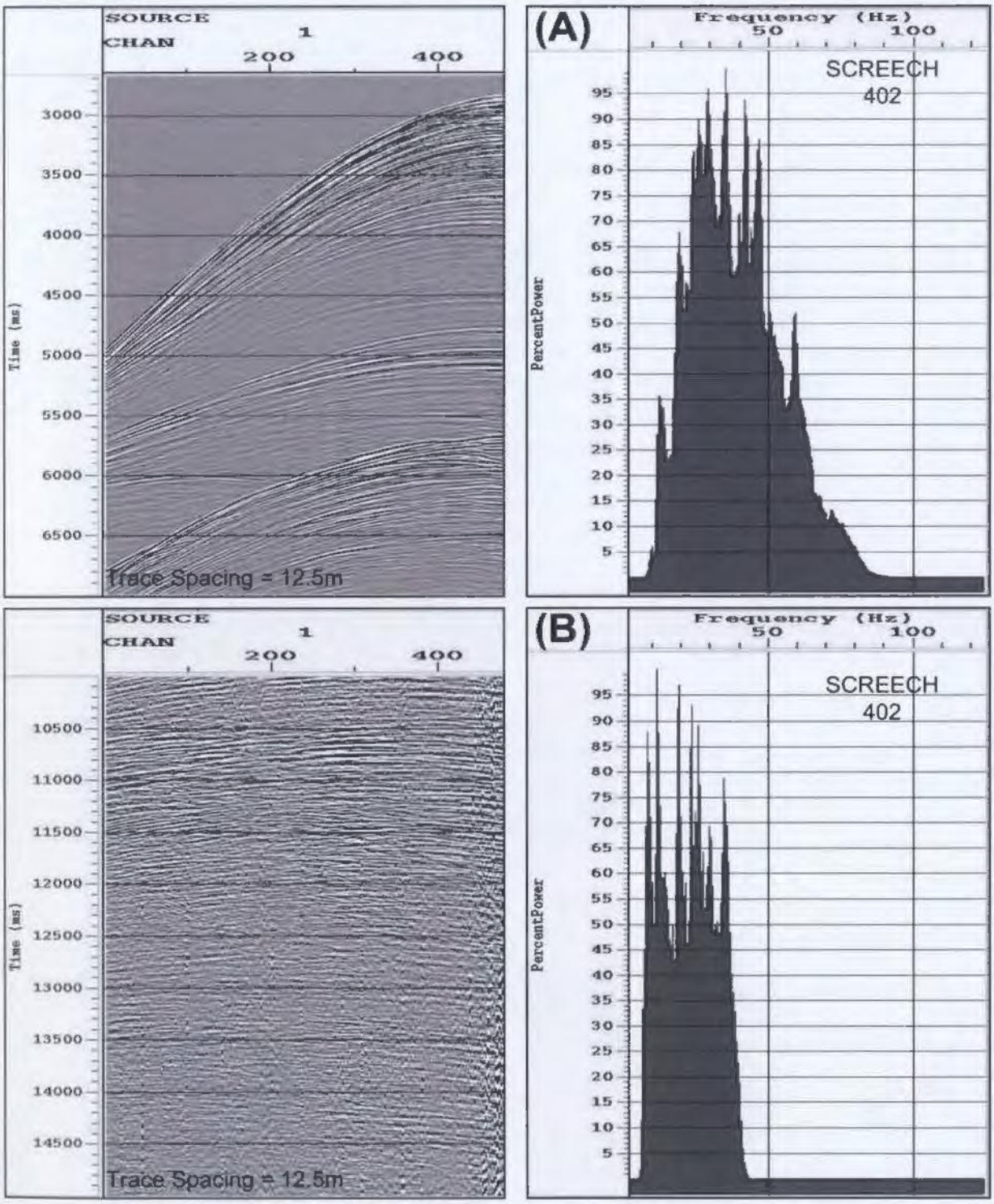

Figure 2.41. (A) Frequency spectrum for the upper section of shot 1 on line 402 with a bandpass filter applied. (B) Frequency spectrum of the lower section of shot 1 with a bandpass filter applied. Ormsby minimum phase bandpass filter parameters were: 7-10-80-100 Hz applied from 2000-3000 ms, 7-10-40-60 Hz applied from 5000-7000 ms, and 5-8-35-45 Hz applied from 9000-14000 ms. Note noise reduction on the near traces.

In this figure (compared with Figure 2.40) notice how the low frequency noise found mainly in the near traces is almost removed and primary reflections are more noticeable. Figure 2.42 shows a near trace gather along the line before and after the bandpass filter. From this figure it is noticeable that not all the noise is removed with the bandpass filter. From Shot 1 to Shot 50 there is still considerable noise present in the traces.

2.4.1.2 Spherical Divergence

After the application of a bandpass filter, a spherical divergence correction (time x vel^2) was made where vel = the estimated rms velocity. Table 2.6 below shows the values used to correct for spherical divergence.

Table 2.6. Values used to correct for spherical divergence on line 402.

Time (ms)	RMS Velocity (m/s)
0 ms	1480 m/s
2000 ms	1480 m/s
3000 ms	1900 m/s
8000 ms	2500 m/s
12000 ms	3000 m/s

Testing was done on shot gathers and the final values chosen produced the most uniform gain across them. Figure 2.43 shows a shot gather before spherical divergence has been applied. At times greater than ~8000 ms the signal in the shot gather is quite faint.

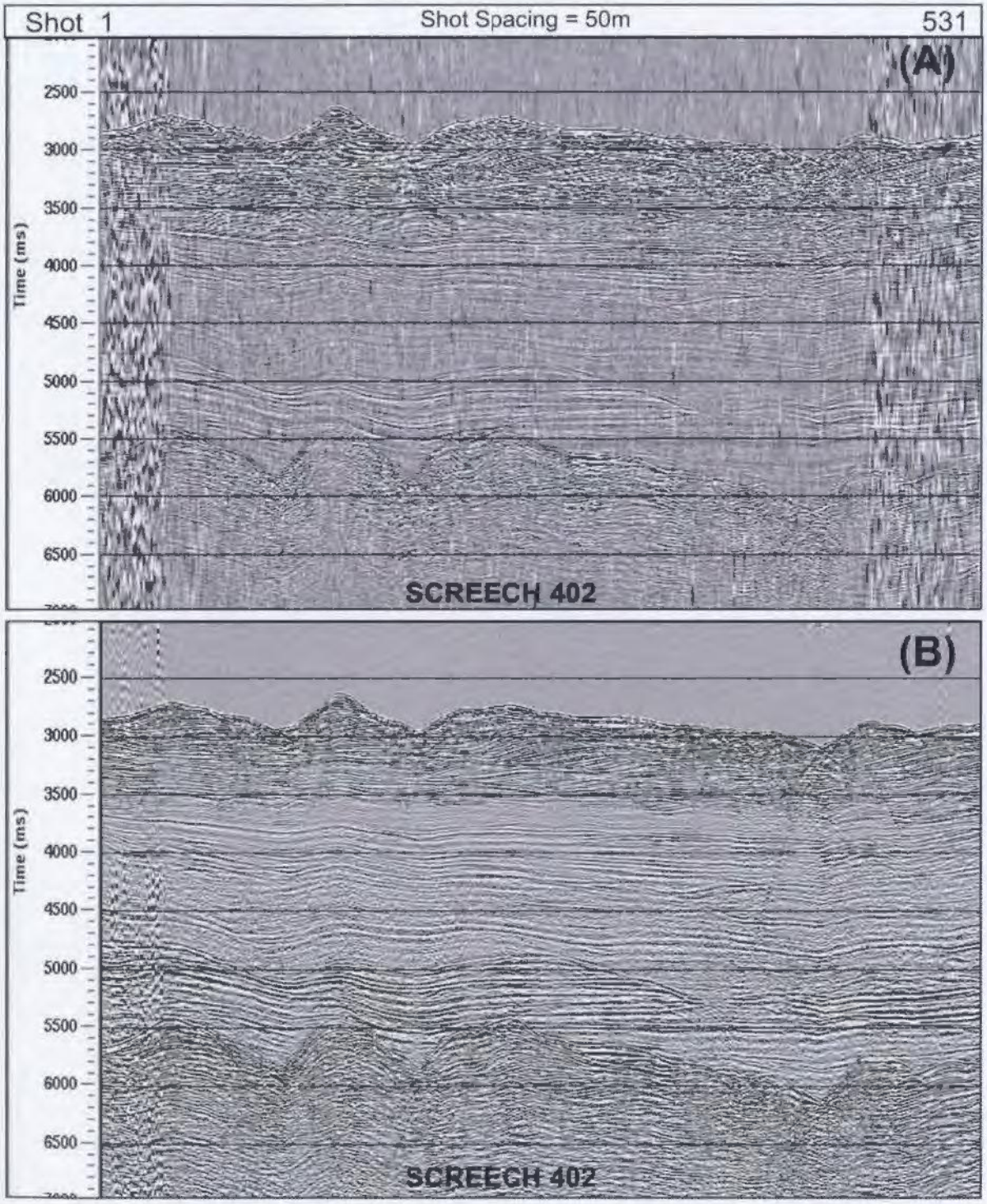

Figure 2.42. Near trace gather on Line 402 before (A) and after (B) a bandpass filter is applied. Filter parameters are: 7-10-80-100 Hz applied from 2000-3000 ms, 7-10-40-60 Hz applied from 5000-7000 ms, and 5-8-35-45 Hz applied from 9000-14000 ms. Note how around Shot 1 noise is still present after the filter.

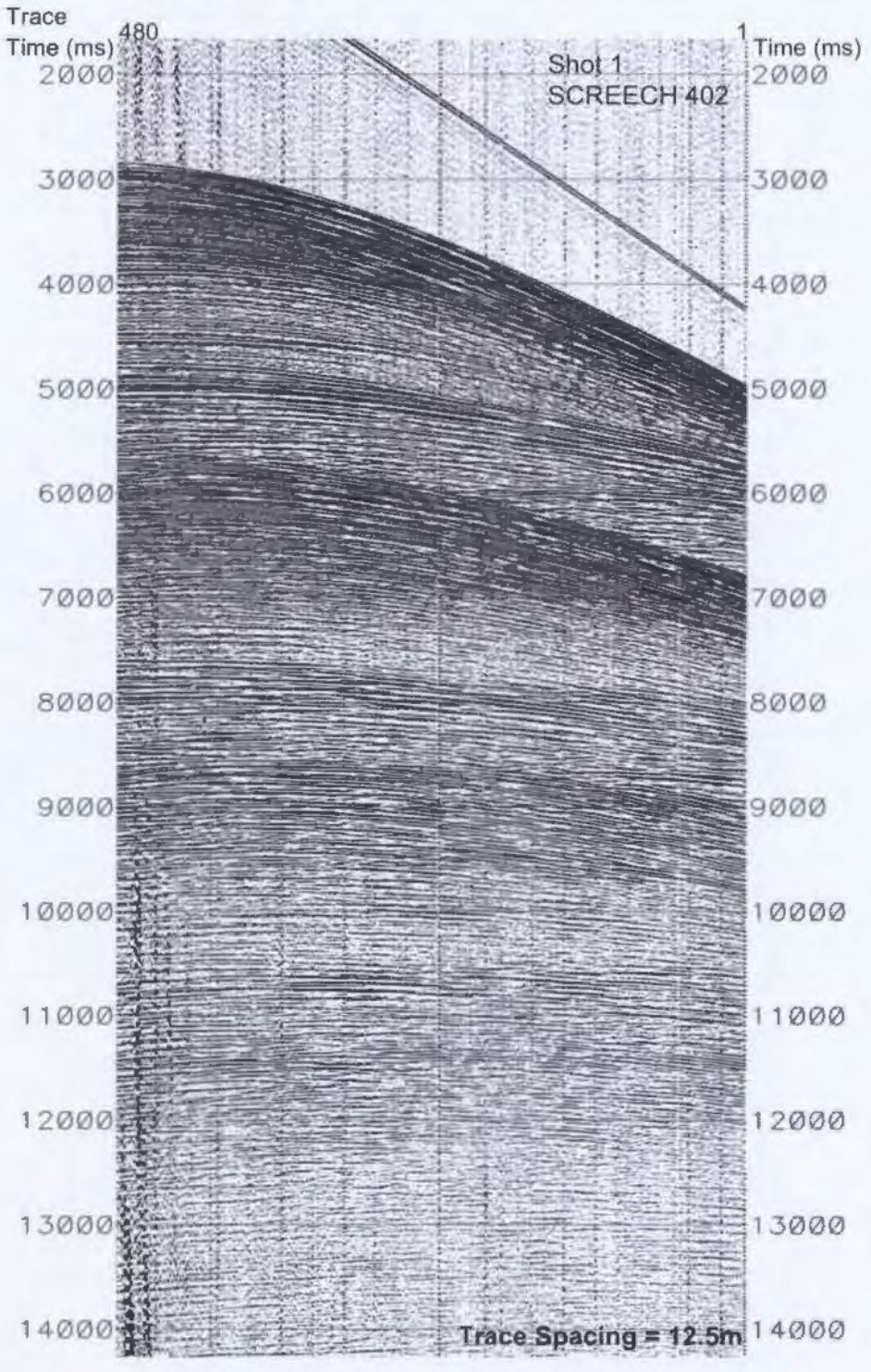

Figure 2.43. Shot gather 1 on line 402 without a spherical divergence correction applied. At times greater then ~8000 ms the shot gather shows amplitudes that are much lower when compared to the upper section of the gather.

Figure 2.44 shows the shot gather with the spherical divergence correction shown above applied. Note the fairly uniform amplitudes in the shot gather, even at times greater than 8000 ms. Testing on shot gathers was also done using a constant velocity and an exponential (dB/s) gain, however the results from some of these tests were undesirable and thus not used.

2.4.1.3 F-K Filter

Coherent linearly dipping noise deeper in the crust (8000 ms – 16000 ms) is a slight problem in this data set. As with lines 401 and 403 this type of noise is dominant in the shot domain, undistinguishable in the CDP domain, and then reappears when the CDPs are stacked. Side scatter noise located at the far offsets is illustrated in Figure 2.45. This side scatter noise starts at ~4000 ms and carries on down the shot gathers. To remove this noise, a pre-stack F-K filter in the shot domain must be applied. Figure 2.46 shows a typical polygon that was picked in the F-K domain, and the before and after results of applying the F-K filter to the shot gathers. The entire shot gather - 0 to 16000 ms and all 480 traces - is input to the filter. The polygon was chosen to accept the data inside the area and filter data outside the polygon. The pre-stack F-K filter does a good job at removing most of the steeply-dipping noise in the shot gathers, and once the CDP gathers are stacked the dipping noise is diminished.

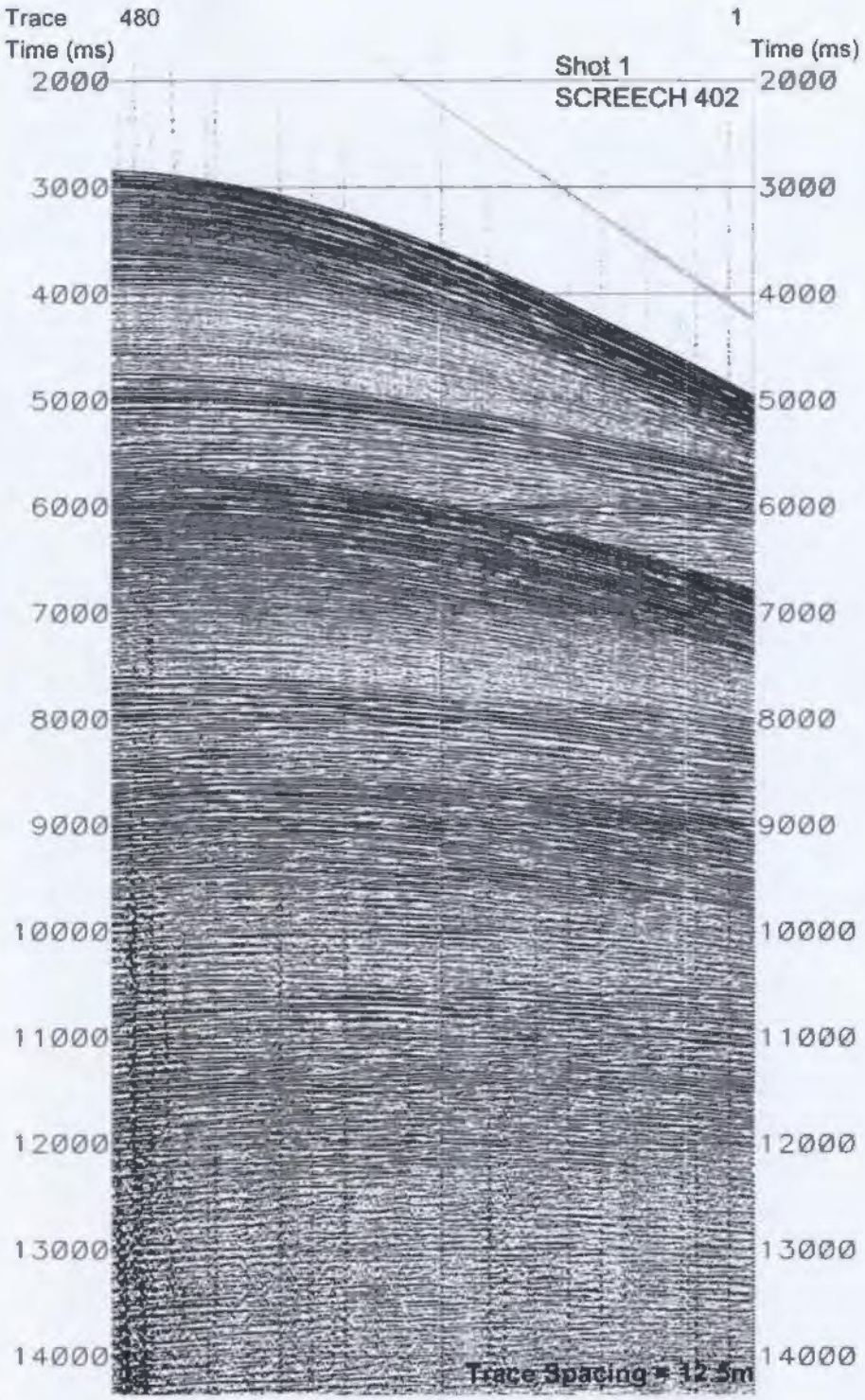

Figure 2.44. Shot gather 1 on line 402 with a spherical divergence correction applied. Vel – Time corrections are: 1480m/s – 0 ms, 1480 m/s – 2000 ms, 1900 m/s – 3000 ms, 2500 m/s – 8000ms, 3000 m/s – 12000 ms. The amplitudes in the entire gather are now more uniform.

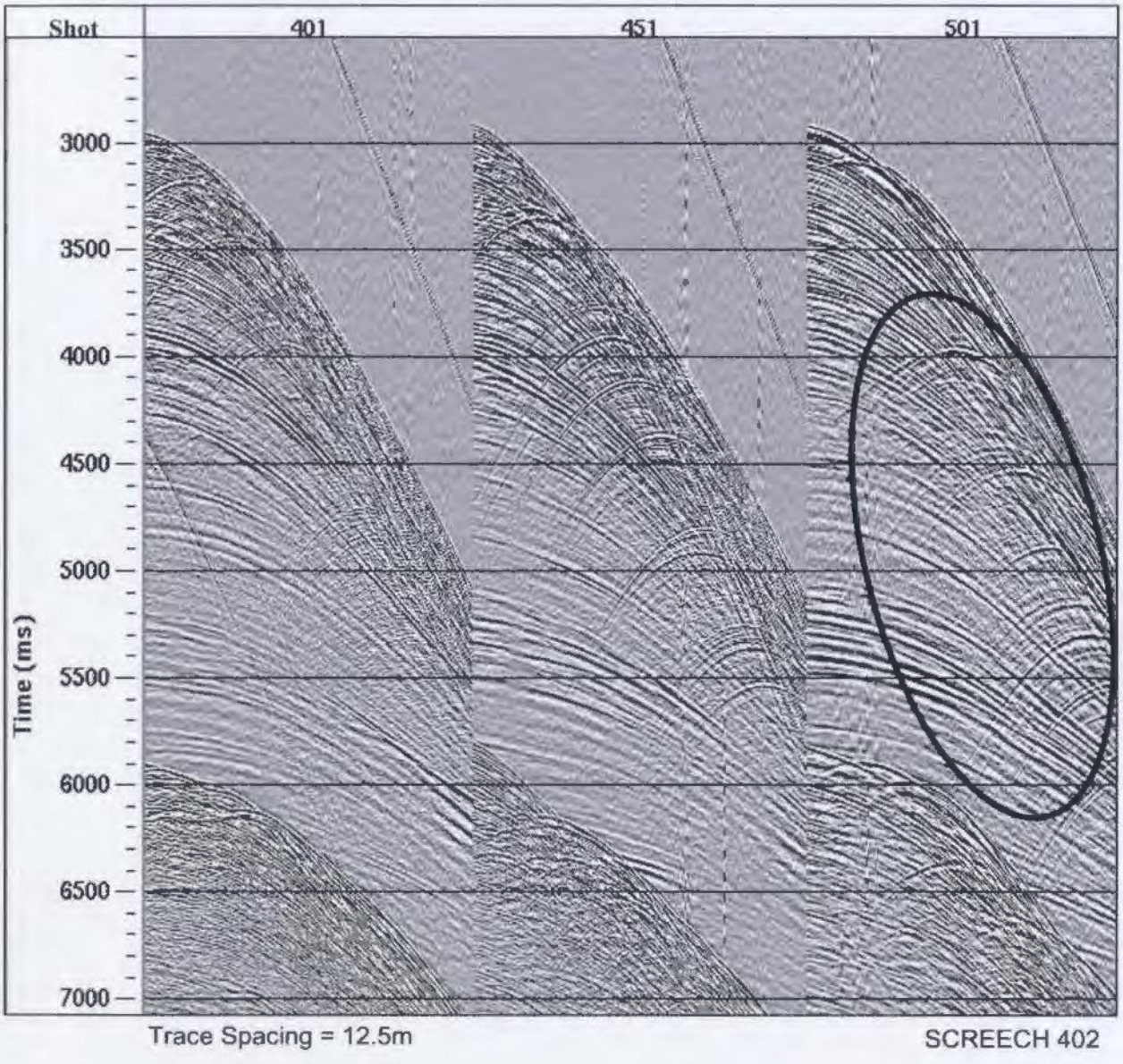

Figure 2.45. Shot gathers on line 402 showing side scatter noise, most likely due to irregularities in the water bottom or sediment layers. Side scatter in these gathers is found at the far offsets and at shallow times.

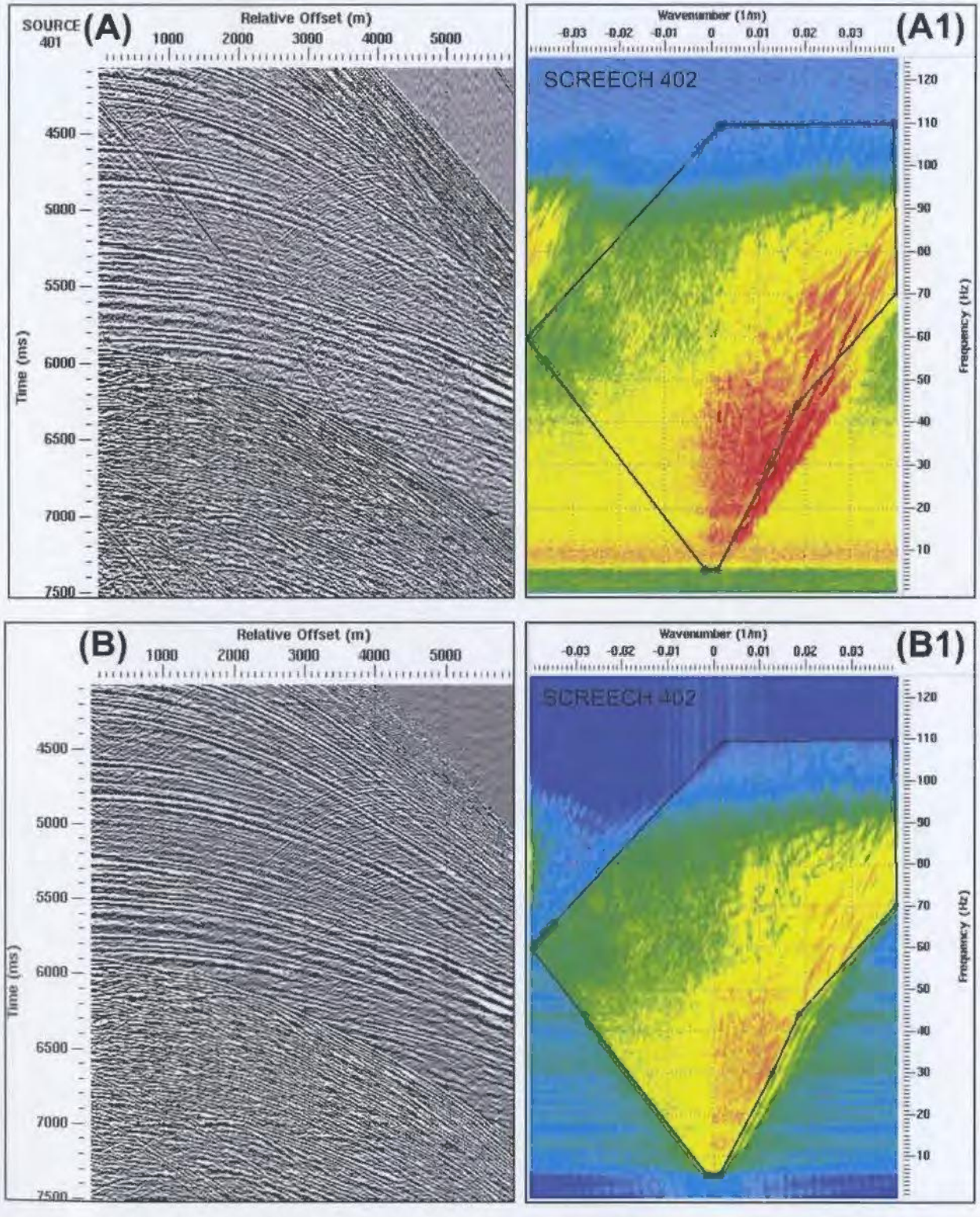

Figure 2.46. (A) A portion of shot gather 401 on line 402 before filtering in the F-K domain. Note the coherently dipping noise. (A1) illustrates the accept F-K polygon to be applied to the shot gather. (B) and (B1) Display the resulting shot gather and F-K spectrum after the application of the F-K filter.

2.4.1.4 Muting and Trace kills – Shot domain

When this line is stacked noise tends to dominate certain areas in the lower part of the section (8000 – 16000 ms). Three different bottom mutes were used to target the noise in the lower portions of the CDP gathers. Figure 2.47 shows one of the bottom mutes applied to shot gathers to remove this unwanted noise. The first mute was applied to all shots ranging from 1 to 51 and removed noise that was found at the near traces of the shot gathers. The second mute was applied to shot gathers 51 to 91 to remove noise found in the middle of the shot gathers, and the third mute was applied to shots 501 to 531 to also remove noise found in the middle of the shot gathers. The origin of the noise in these shots is unknown. The noise is not constrained to any specific channels, it moves throughout the shot gathers from near to mid offsets along the length of the line. Upon checking the log book, no problems were noted that may explain the origin of the noise. Along with noisy sections in the gathers, channels one and two in all gathers across the line contain a large amount of noise, and because of this channels one and two were both killed. As well as channels 1 and 2 being noisy, there is also some random noise present throughout the shot gathers, most of these traces are identified and killed.

2.4.1.5 Velocity Analysis

Velocity analysis is performed on the CDP gathers to pick the NMO velocities that will be used to correct for NMO. Stacking velocities were picked based on semblance plots, constant velocity stacks and CDP gathers on every 500th CDP, which corresponds to every 3125 m.

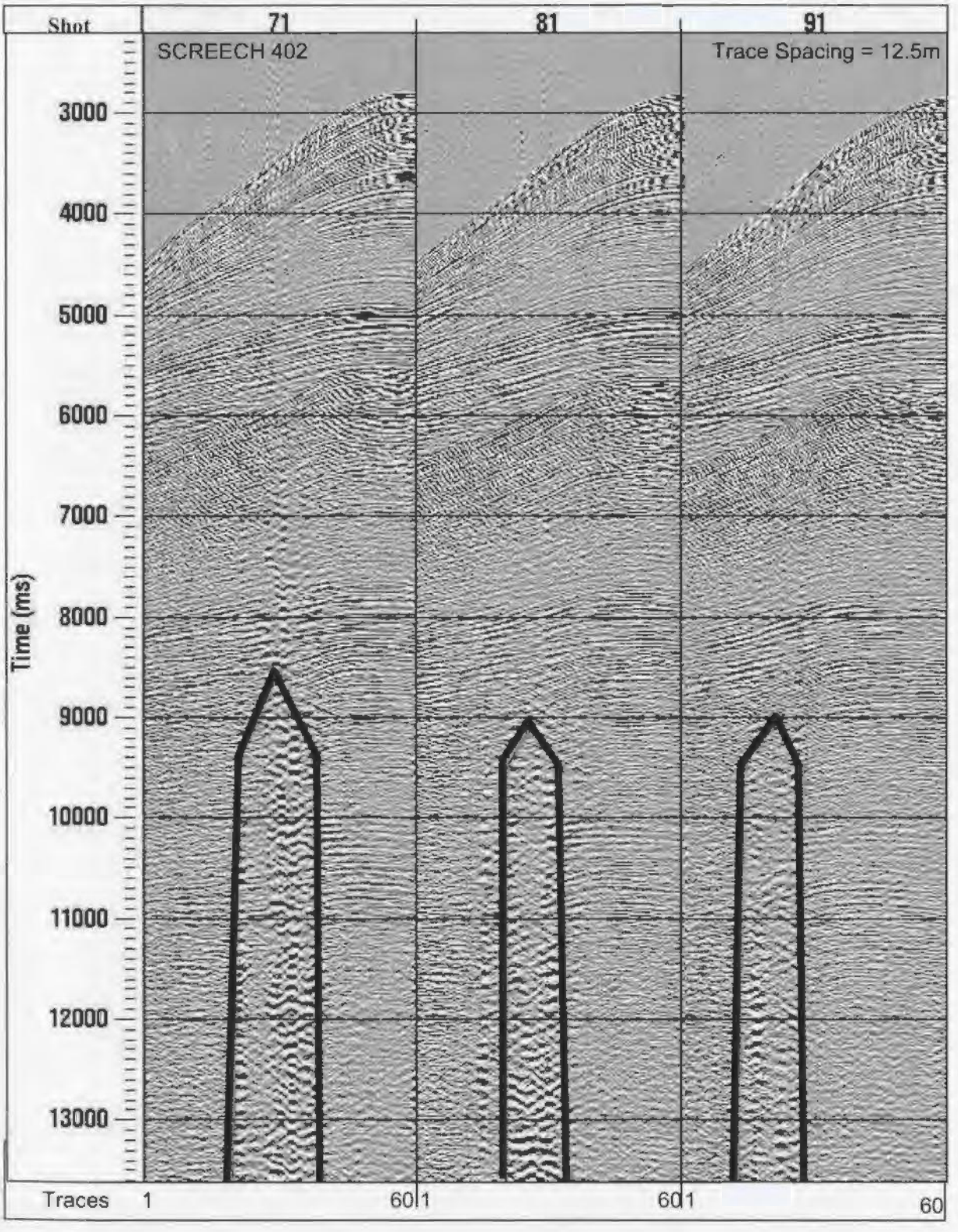

Figure 2.47. Bottom mute on shot gathers to mute out noise near the mid traces. This mute was applied to shots 51 to 91 on SCREECH line 402.

Figure 2.48 shows an example of stacking velocities that were picked for various CDPs. Above the first multiple the primary energy is flattened and will stack well but below the multiple primary velocities are difficult to pick since the multiple energy is so strong. The entire stacking velocity field that was picked is shown in Figure 2.49. Using these picked velocities, a stack of line 402 was created. To create this stack the minimum phase bandpass filter, the spherical divergence correction, the F-K filter, trace mutes and NMO corrections were applied before the CDPs were stacked. The resulting stack is shown in Figure 2.50 and the water bottom multiple is very much evident in this stacked section around 6000ms. In viewing the semblance plot and constant velocity stacks shown in Figure 2.48, it was thought that a radon filter may provide favourable results at removing the water bottom multiple since there is a fairly good separation between move-out of multiple and primary energy in this area which would lend well to radon methods.

2.4.1.6 Pre-stack multiple removal

Many processes were tested on this line to remove the multiples caused by the water bottom. Radon filtering, radon velocity filtering, wave equation multiple removal, and near trace muting were all tested for their effectiveness in removing the multiples.

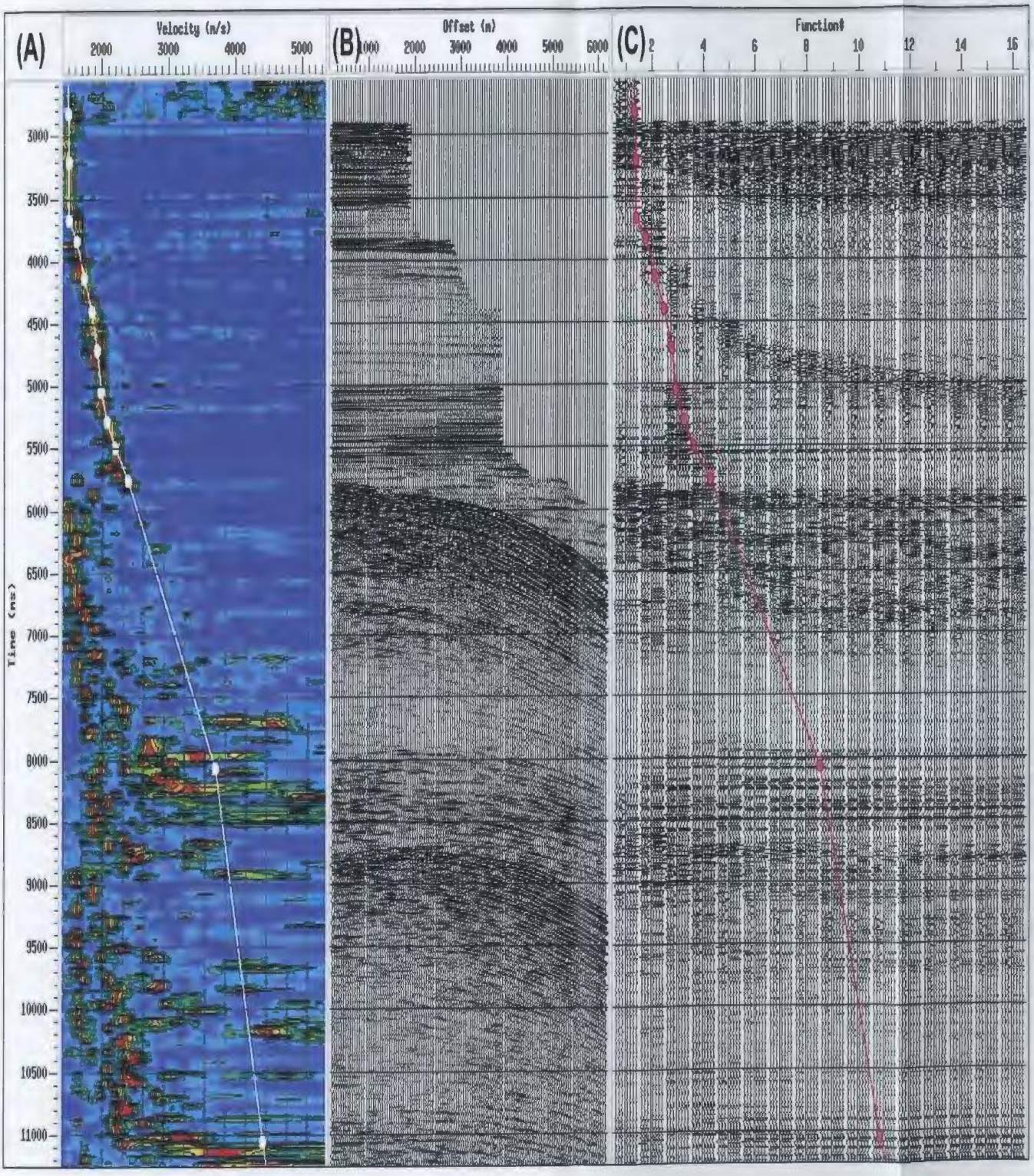

Figure 2.48. Velocity Analysis of CDP 476800 on line 402. (A) Shows the semblance plot (B) the NMO corrected gather, and (C) shows the constant velocity stacks. In the semblance plot multiple energy is visible (ranging from ~1600 m/s to 3000 m/s), which makes identifying the primary events from the multiple events is difficult past 6000 ms.

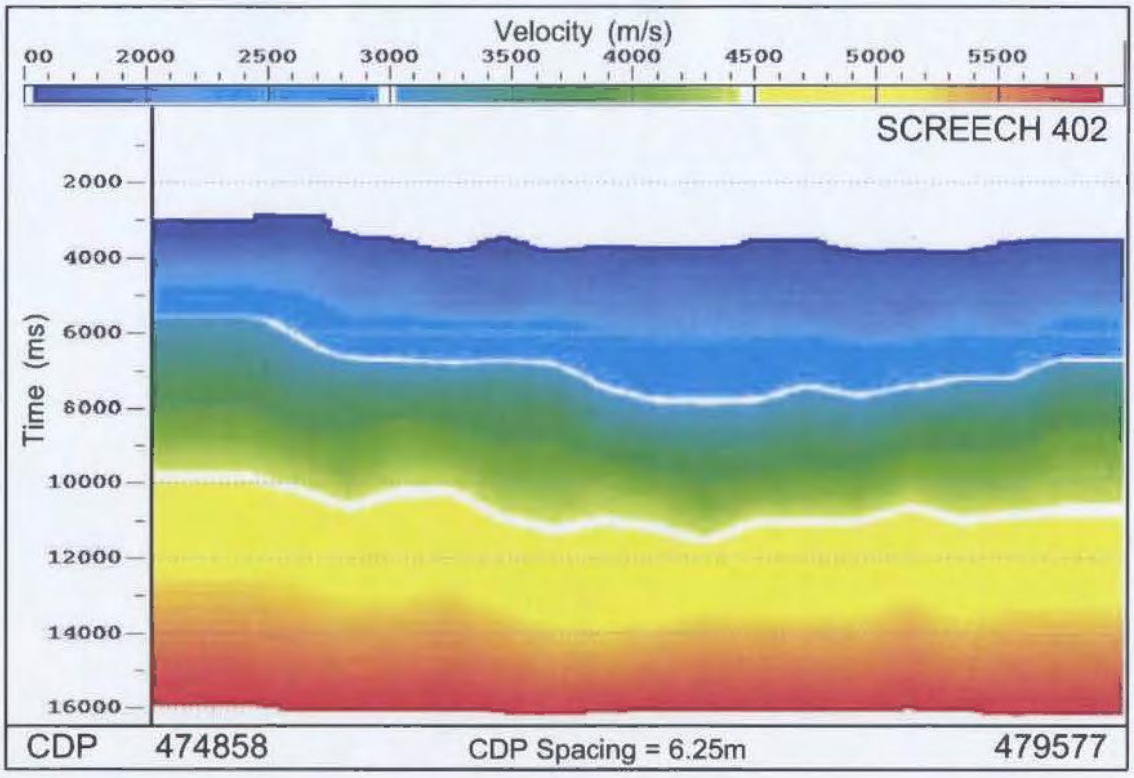

Figure 2.49. NMO velocities on line 402 for all CDPs as picked using the semblance plots, CDP gathers and constant velocity stacks.

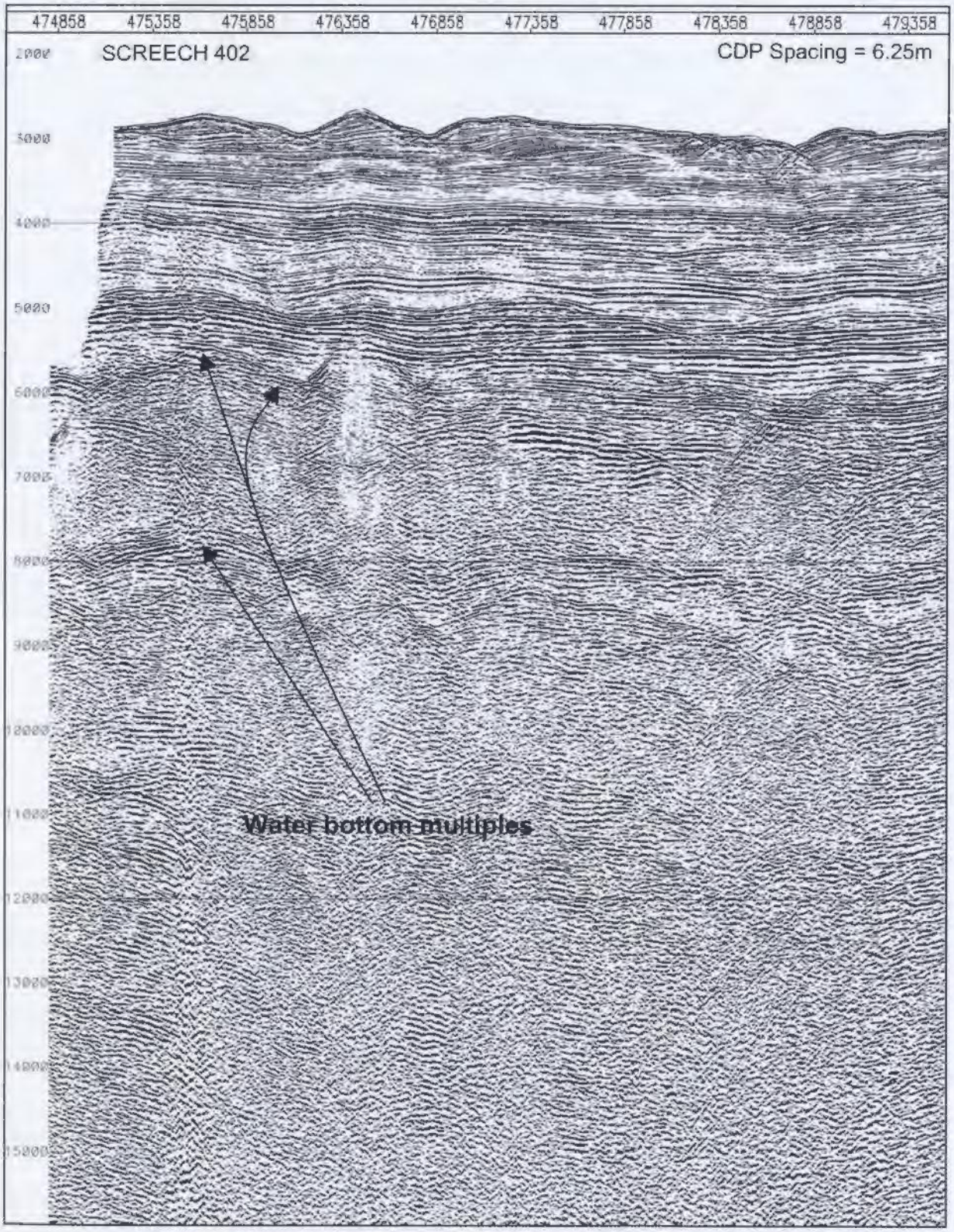

Figure 2.50. Stack of Line 402 with bandpass filter, spherical divergence, F-K filter, bottom mutes and trace kills applied. Note water bottom multiple around 6000 ms.

2.4.1.7 Radon Filtering

Radon filtering was applied (see Section 2.3.3.1). Figure 2.51 illustrates a typical radon mute that was picked for Line 402. Figure 2.52 illustrates a stack of line 402 with the radon filter applied. The radon filter removed portions of the first multiple, and a small amount of the second water bottom multiple, hut also produced some undesirable streaks in the data. Due to the streaks and the relative ineffectiveness of the radon filter at removing multiples, the radon filter was not applied to the line.

2.4.1.8 Radon Velocity Filtering

A radon velocity filter was also investigated on this line. This filter was explained earlier in Section 2.3.3.2. Figure 2.53 shows the results of a radon velocity filter. In this Figure the mutes were picked by keeping 20% above and below the NMO velocity, while the rest is excluded. Many trials were done using different low and bigh velocity percentages, however it was found that artifacts were introduced into the data and this method was abandoned.

2.4.1.9 Wave Equation Multiple Removal

Wave equation multiple removal (WEMR) was also tested on this line to determine its effectiveness at removing water bottom multiples. According to the ProMax Reference Guide, (1998), this process will be most effective when the water bottom is flat. Simple water bottom multiples should be eliminated, whereas more complex peg-legs will only be modestly reduced. Since Line 402 has a rather rough and irregular water bottom, it is hoped that this technique will at least reduce some of the multiples found on this line.

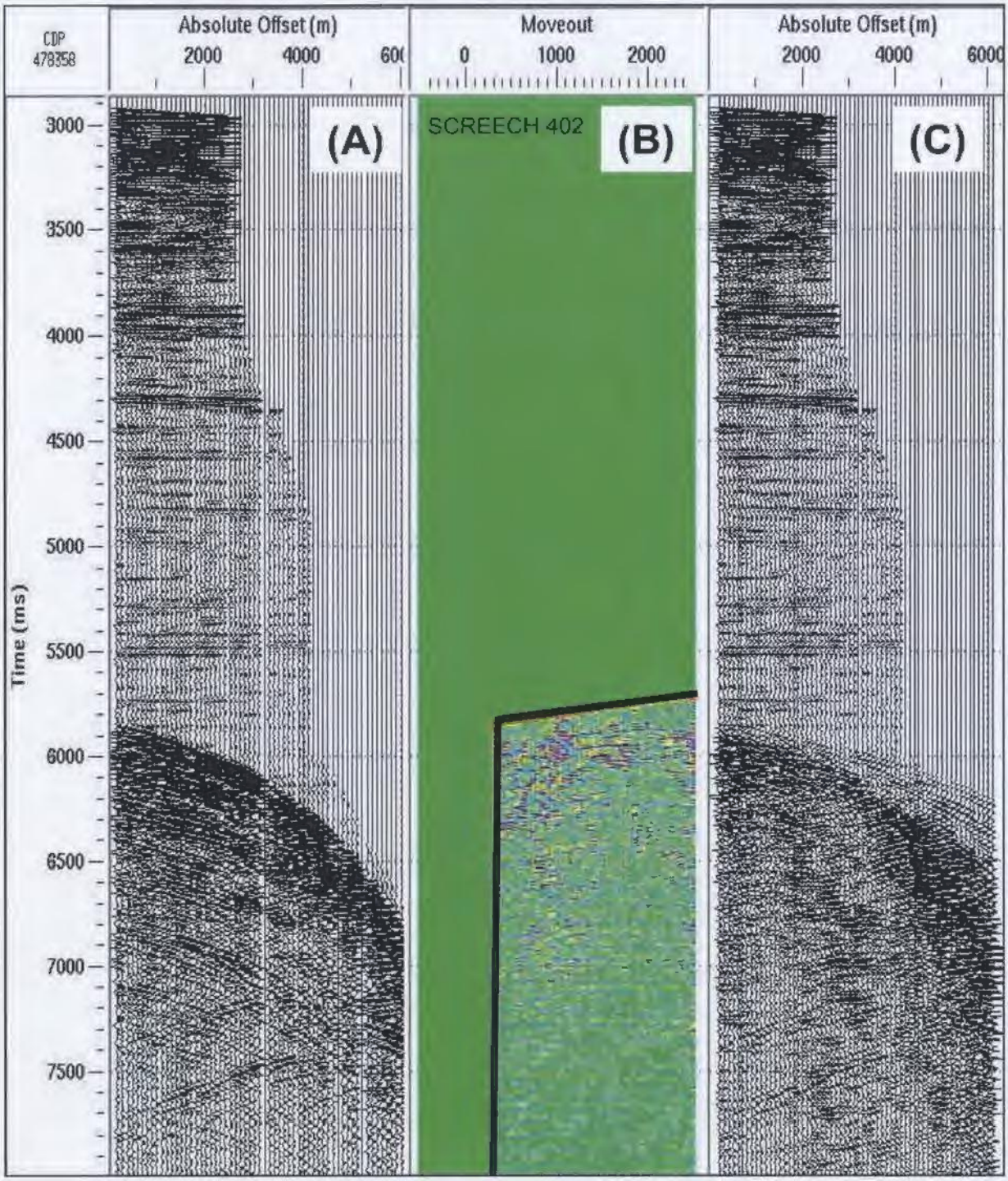

Figure 2.51. CDP 478358 on line 402 (A) shows the NMO-corrected gather before a radon filter is applied. (B) shows the radon mute that was picked in time vs. moveout domain. Primary energy is excluded in the mute so that multiple energy remains. This multiple energy is then subtracted from the original gather giving rise to the gather depicted in (C).

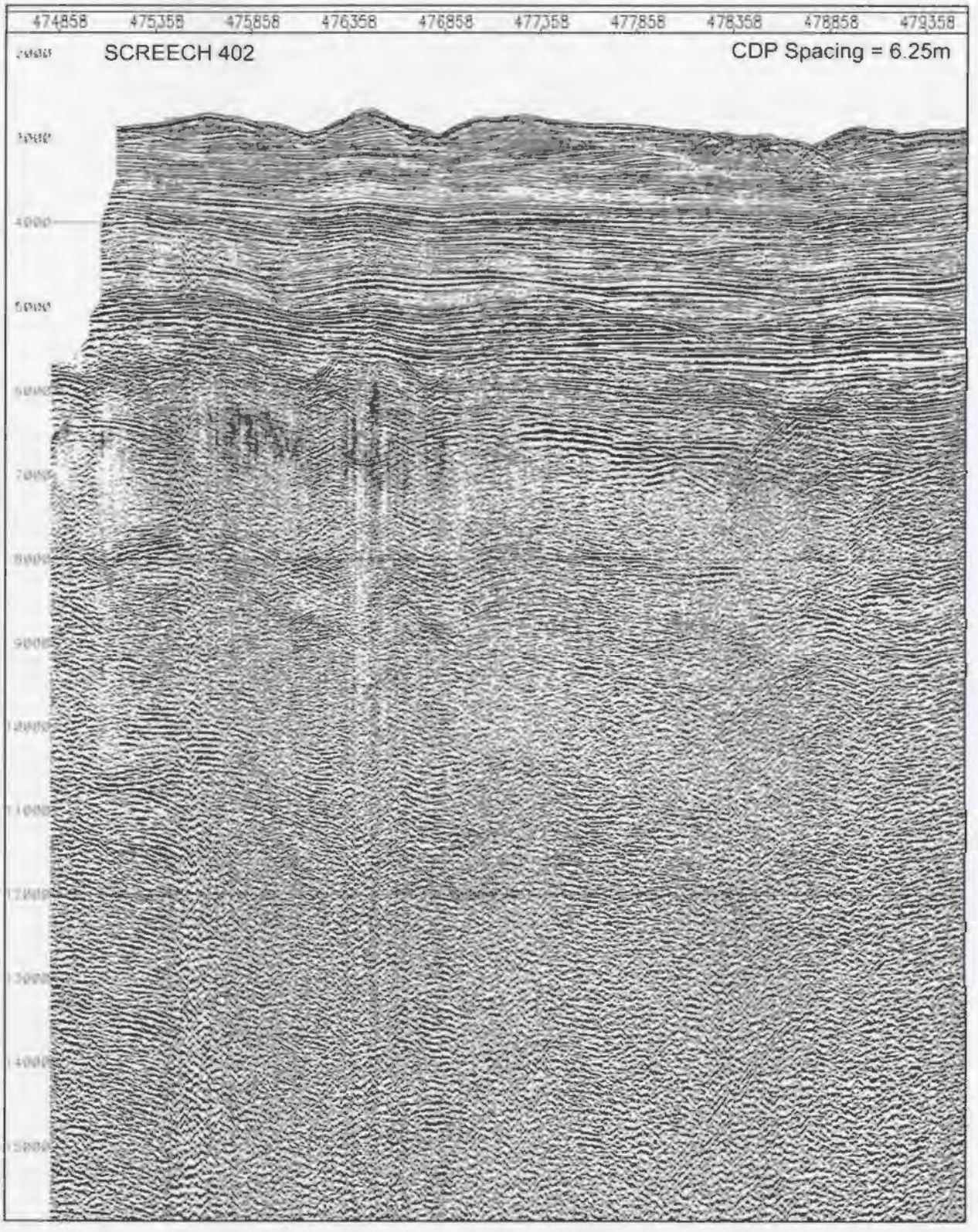

Figure 2.52. Radon filtered stacked section of line 402. Note artifacts created near the middle of the stack due to aliassing.

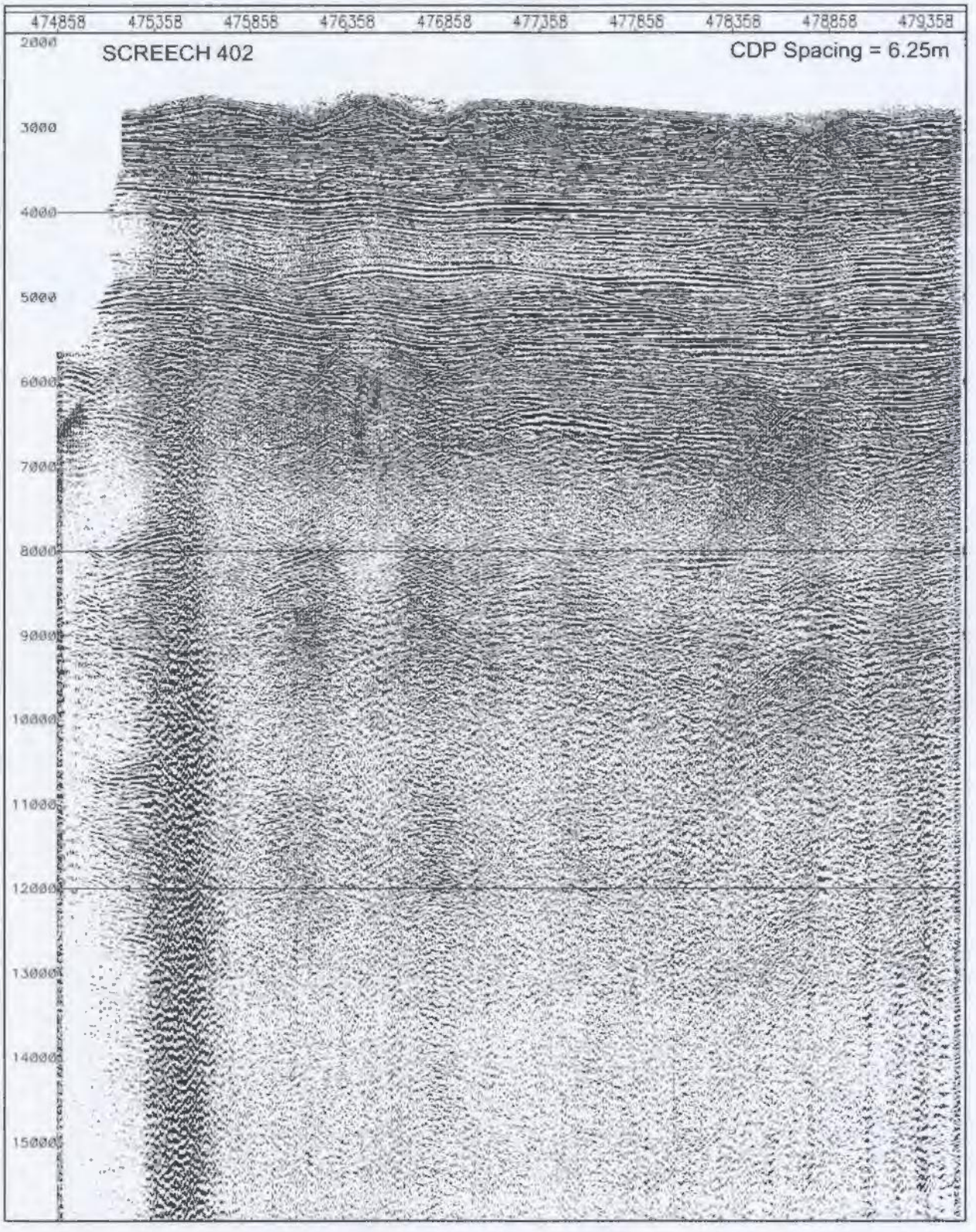

Figure 2.53. Radon velocity filtered stacked section of line 402.

The wave equation multiple rejection program in ProMAX estimates multiples with F-K extrapolation from shot records and subtracts them from the records (ProMAX Reference Guide, 1998). The average water depth under all receivers in the source ensemble is used to extrapolate the water layer. Removal of the estimated multiples is done by a 3 component method on a trace by trace basis (ProMAX Reference Guide, 1998). Traces are analyzed for the optimum time shift, amplitude factor and phase angle before the multiple trace is subtracted from the original trace (ProMAX Reference Guide, 1998). The results from applying the WEMR are shown in Figure 2.54. Both the first and second water bottom multiples are still visible and no significant amount of attenuation is noticeable.

2.4.1.10 Near Trace Mute

A near trace mute was applied to all CDPs in an attempt to remove the water bottom multiples. Figure 2.55 shows the extent of the near trace mute that is picked on all CDPs. This mute was found to be reasonably effective in attenuating the water bottom multiples when the section is stacked. Figure 2.56 illustrates the results of applying the near trace mute before stacking. In this figure the water bottom multiples are still present, however when compared to Figure 2.50 they are noticeably attenuated. As well when compared to Figures 2.52, 2.53, and 2.54, the section with the near trace mute is shown to be the most effective at attenuating multiples and does not introduce unwanted noise into the section.

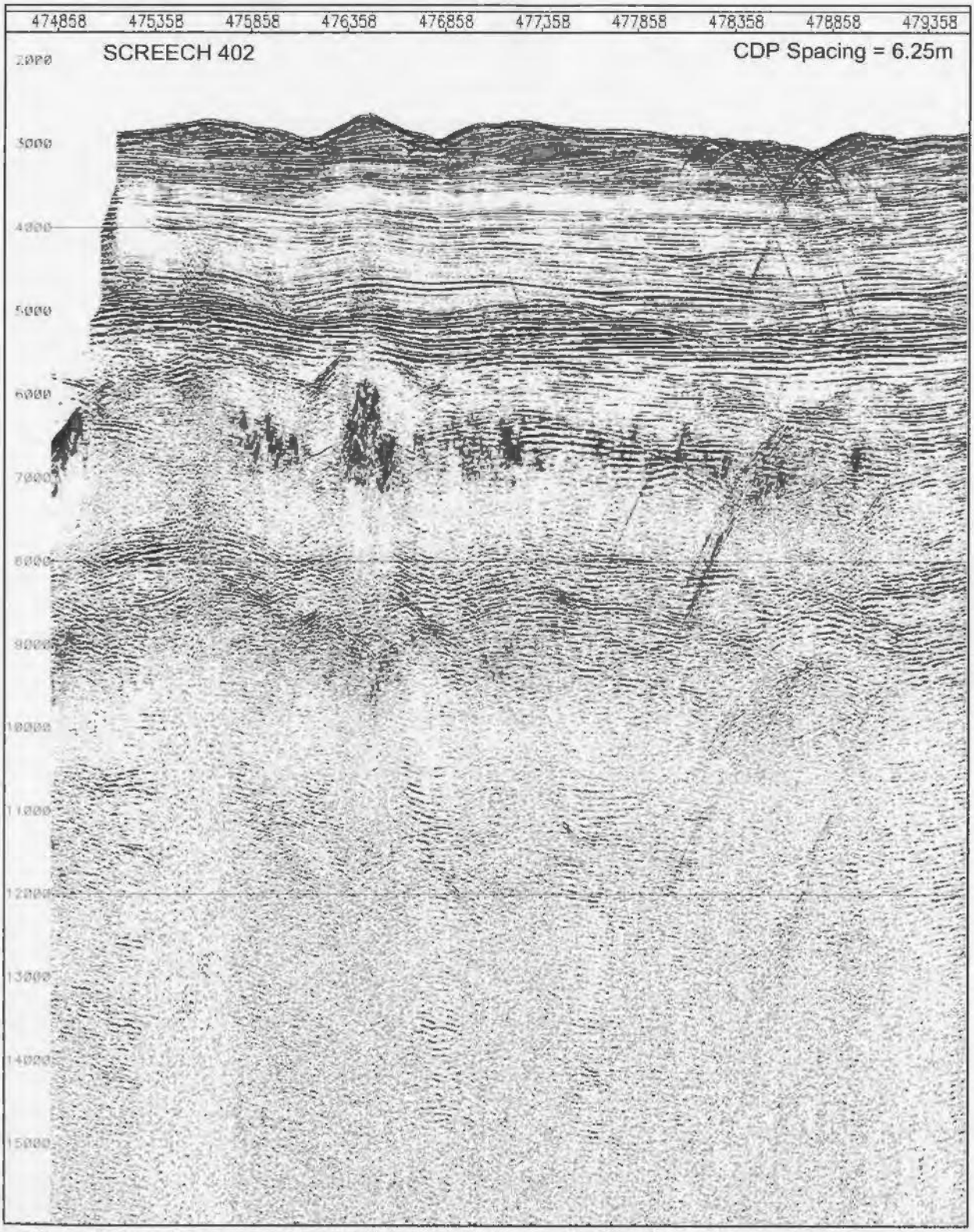

Figure 2.54. Wave equation multiple rejection stacked section of line 402. The first and second water bottom multiples are still present in the stacked section. This method of multiple removal offers little improvement over the original stacked section.

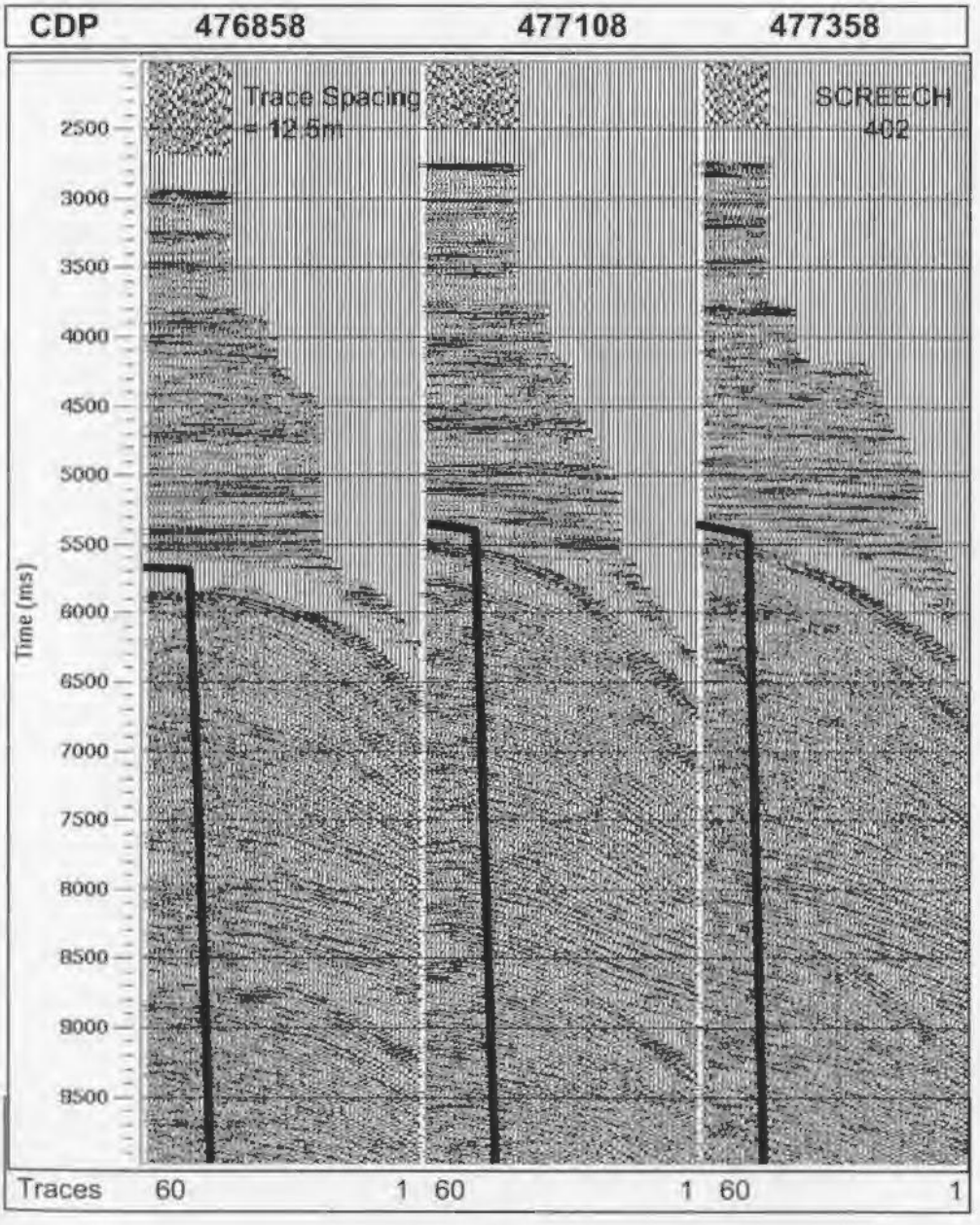

Figure 2.55. Near trace mute applied to all CDP's on line 402 to remove the water bottom multiples and peg-leg multiples. These CDP's are displayed with NMO corrections applied.

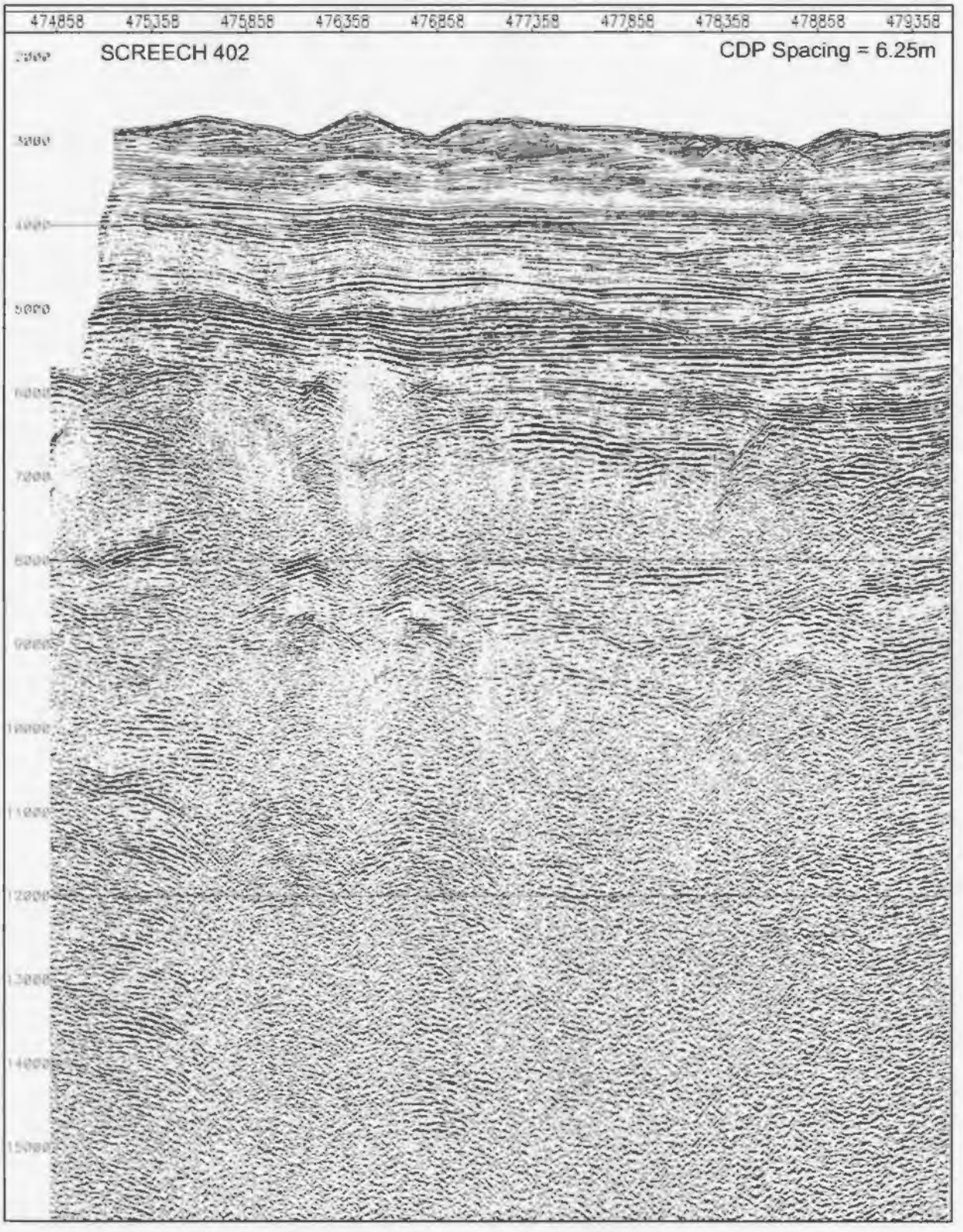

Figure 2.56. Stacked section of Line 402 with the near trace mute applied. When compared to Figure 2.50 the water bottom multiple is better attenuated.

2.4.2 Stacking Line 402

After the above pre-stack processing was performed on the shot and CDP gathers, each CDP containing 60 traces was then stacked to create the final stacked section. Figure 2.56 illustrates the stacked section with all the pre-stack processing applied.

2.4.3 Post-stack Processing

The stacked section shown in Figure 2.56 still contains some areas of noise and multiple energy despite efforts to remove the noise pre-stack.

2.4.3.1 Post-stack Bandpass Filter

A minimum phase Ormsby bandpass filter was applied to the section as a windowed process. The bandpass filter was applied to remove any remaining high and low frequency noise that is still present in the section. The bandpass filter needed to be applied as a windowed process below the water bottom to avoid the creation of reverberations at the strong water bottom reflection. Figure 2.57 illustrates the results of applying the bandpass filter with and without windowed processing. The window depicted in Figure 2.57 extends all the way down to the end of the section (16000 ms). The bandpass filter parameters are as follows: 7-10-65-75Hz from 3500-5000ms, and 7-10-35-45 Hz from 6000-9000 ms, and 5-10-35-45Hz from 10000-16000ms. If the bandpass filter is not applied as a windowed process, the resulting section exhibits a large amount of ringing, especially around the water bottom, as shown in Figure 2.57 (part A).

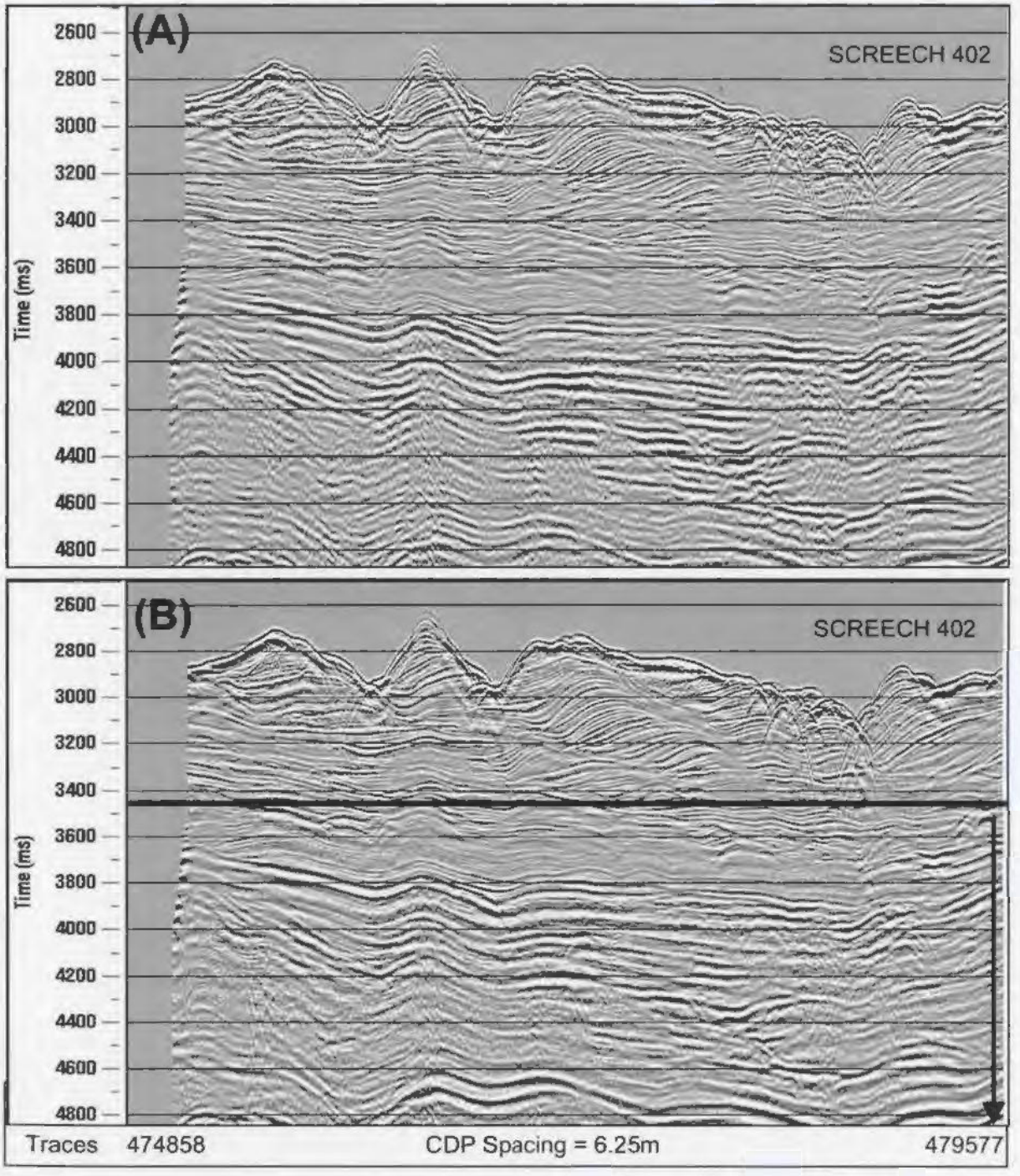

Figure 2.57. (A) Bandpass filter applied to entire section of line 402. (B) Bandpass filter applied as a windowed process. The top of the window is shown as a black line and extends all the way down to the bottom of the section (16000 ms). The bandpass filter is only applied within the window and the filter parameters were: 7-10-65-75Hz from 3500-5000ms, 7-10-35-45 Hz from 6000-9000 ms, and 5-10-35-45Hz from 10000-16000ms. Comparing the two sections shows that (A) is more ringy than (B).

When the bandpass filter was applied as a windowed process (Figure 2.57 part B) the ringy character is eliminated.

2.4.3.2 Trace Muting

A trace mute is applied to the top of the stacked section to remove noise present above the water bottom.

2.4.3.3 Time Variant Scaling

Time variant scaling (TVS) was applied to balance the sediment and basement reflections and create a more uniform section before a post-stack F-K filter is performed. TVS allows sections of the line to be multiplied by a user specified scalar value. By applying a scalar, the gain on a specific area of the line can either be increased or decreased in order to create a more uniform section. After this balancing was completed an automatic gain control (AGC) with a length of 1000 ms was applied to the section to aid in creating a uniformly gained section. After the AGC was added, a post-stack F-K filter was applied to the entire section.

2.4.3.4 Post-stack F-K Filter

The F-K filter was applied as a windowed process, with the window starting just above the first multiple ~5500 ms and continuing down until 16000 ms. The design of the F-K filter changed only slightly along the line. 2000 traces are input into each F-K filter across the stacked section. As with the pre-stack F-K filters, these polygons accept the

data on the inside and filter or reject the data on the outside of the polygon. Figure 2.58 shows the stacked section and F-K spectrum before and after the application of the post-stack F-K filter. It is evident from the figures that most of the remaining noise is removed from the stacked section by the F-K filter. The final post-stack processed version of line 402 is shown in Figure 2.59. Most of the noise has been removed and the water bottom multiples have been attenuated.

2.4.4 Migrating line 402

After the pre- and post-stack processing is complete, the line must be migrated. Figure 2.60 shows the final migration velocities (rms) that were picked and used to migrate the line. In order to avoid the creation of migration smiles at the bottom of the data set, velocities were reduced to approximately 3500 m/s at 16000 ms. A Kirchhoff post-stack time migration was used to migrate this line, described in Section 2.3.6.

2.4.5 Displaying the migrated section for line 402

To display all 16 seconds of this line a few processes are applied for cosmetic purposes. A final bandpass filter was applied as a windowed process using the same window (shown in Figure 2.57) as in the post-stack bandpass. The parameters for this minimum phase Ormsby filter were 7-10-65-75 from 3500 to 5000 ms, 7-10-35-45 from 6000 to 9000 ms, and 5-10-40-50 from 10000 to 16000 ms.

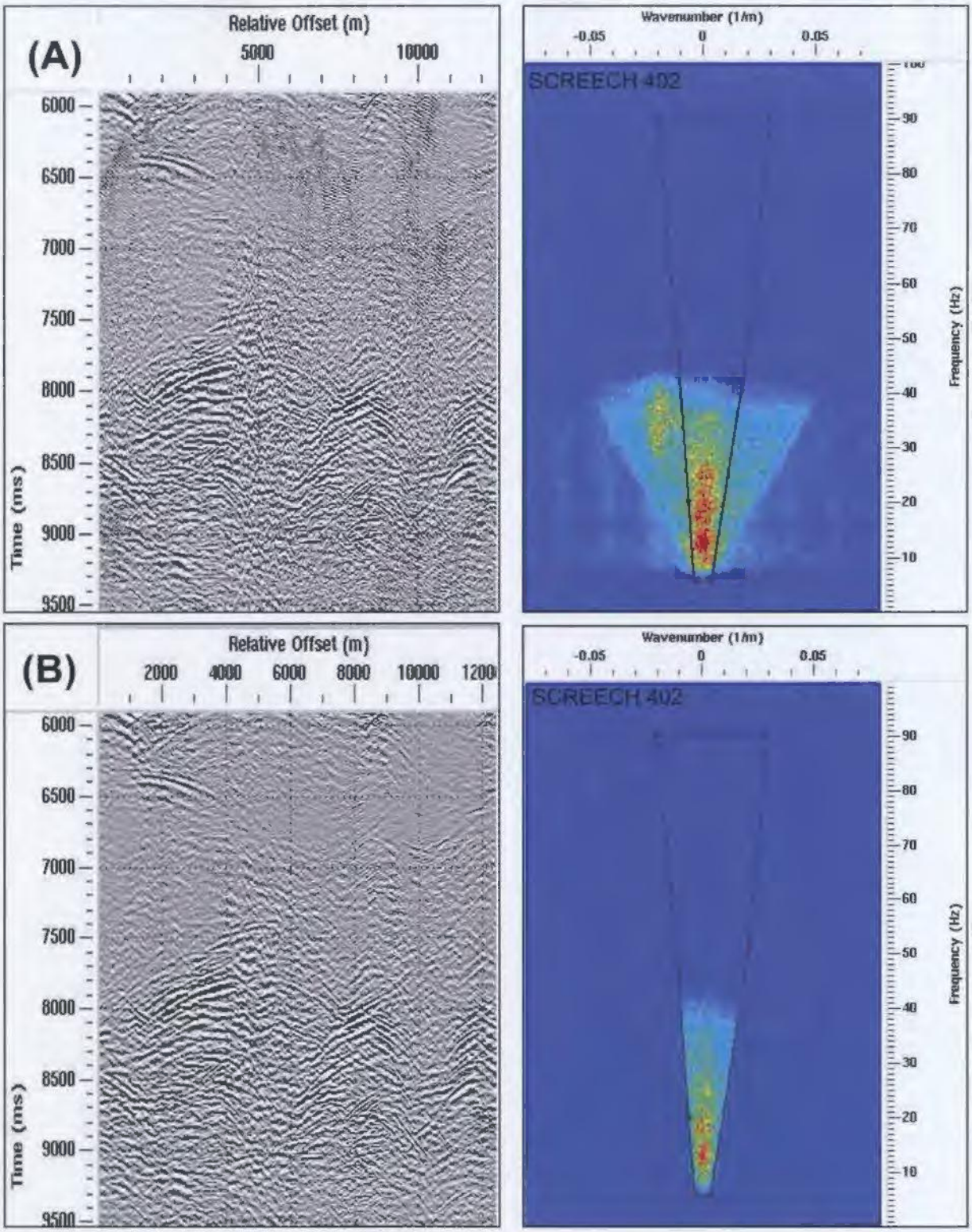

Figure 2.58. (A) First 2000 stacked CDPs on line 402 and F-K spectrum before application of the F-K filter. (B) First 2000 stacked CDPs on line 402 and F-K spectrum after the application of the F-K filter.

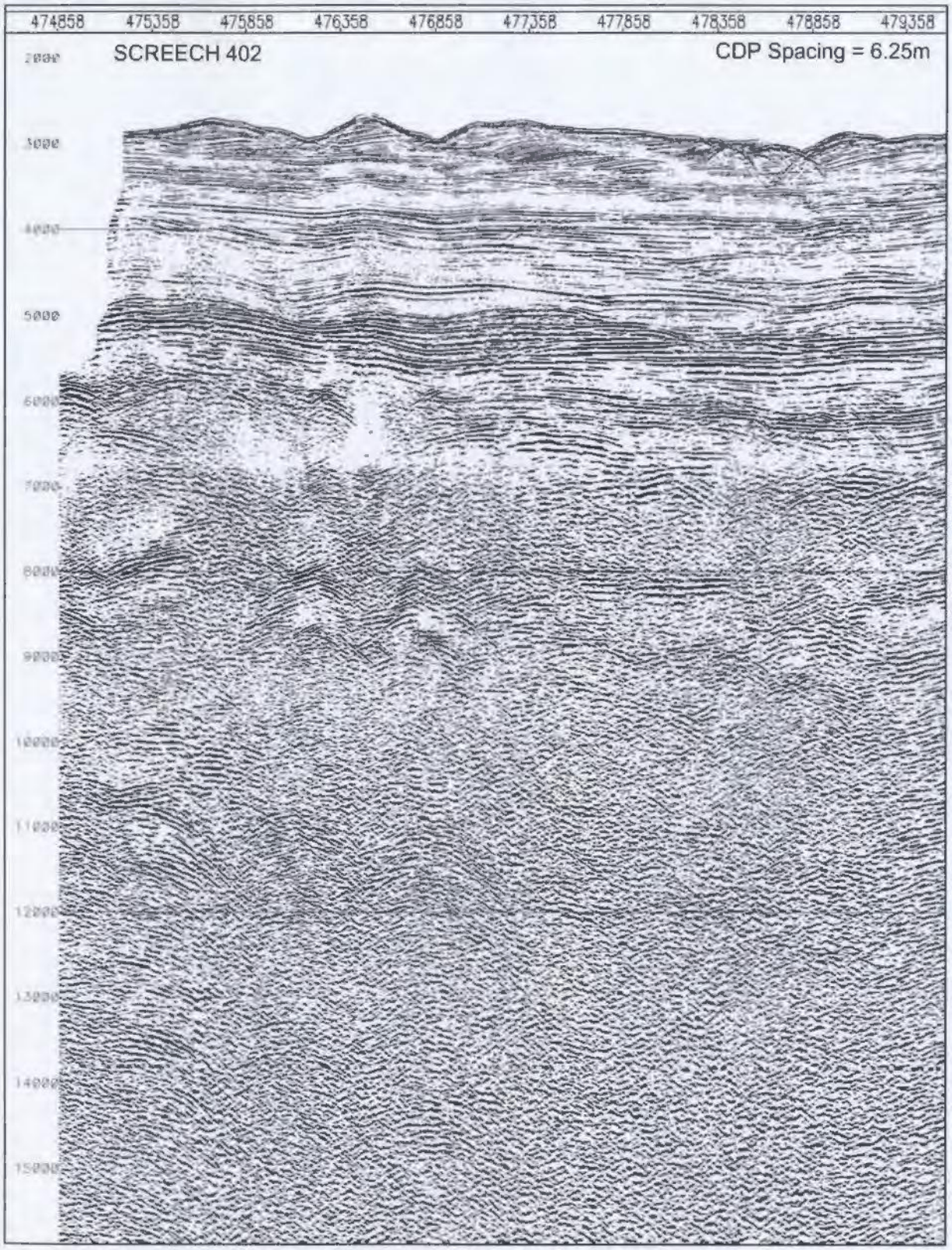

Figure 2.59. Post stack version of Line 402.

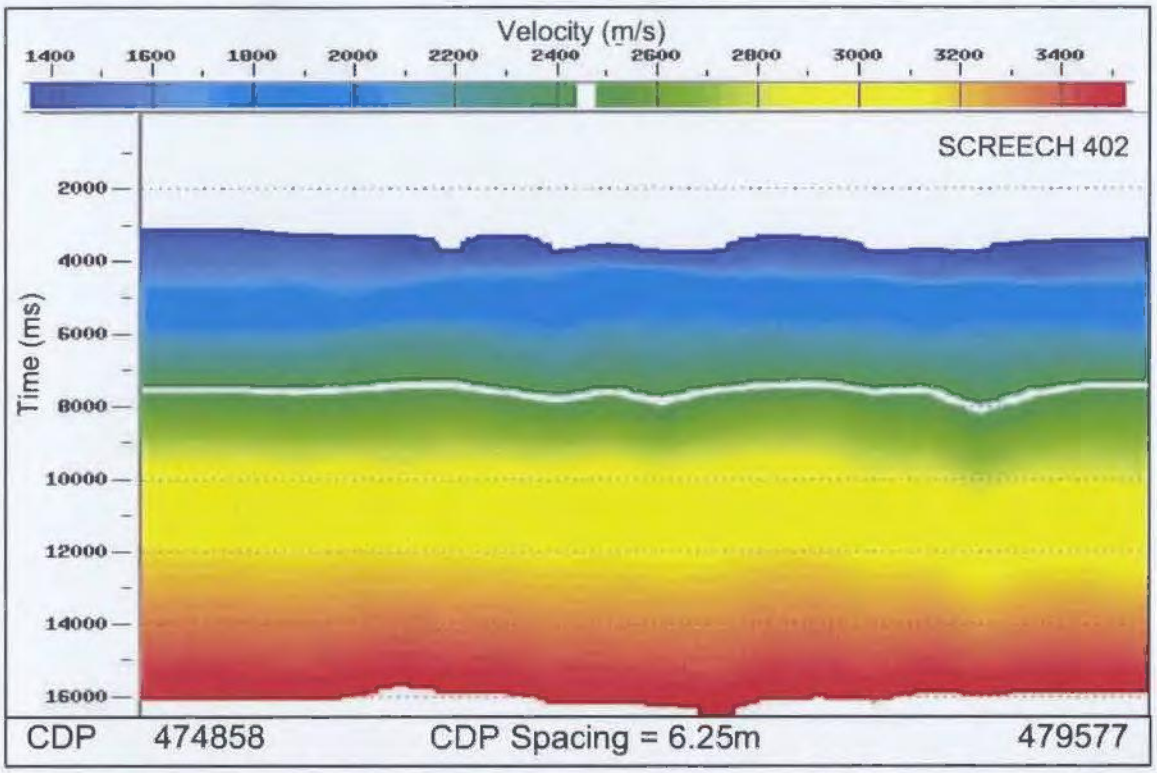

Figure 2.60. Final RMS velocities used to migrate Line 402.

Time variant scaling was then done to produce a uniformly scaled section. A nine trace weighted mix was applied to the section along with an F-K power exponent filter. These last two processes were performed to increase coherency in the displayed section. Figure 2.61 shows the final migrated and scaled section for Line 402.

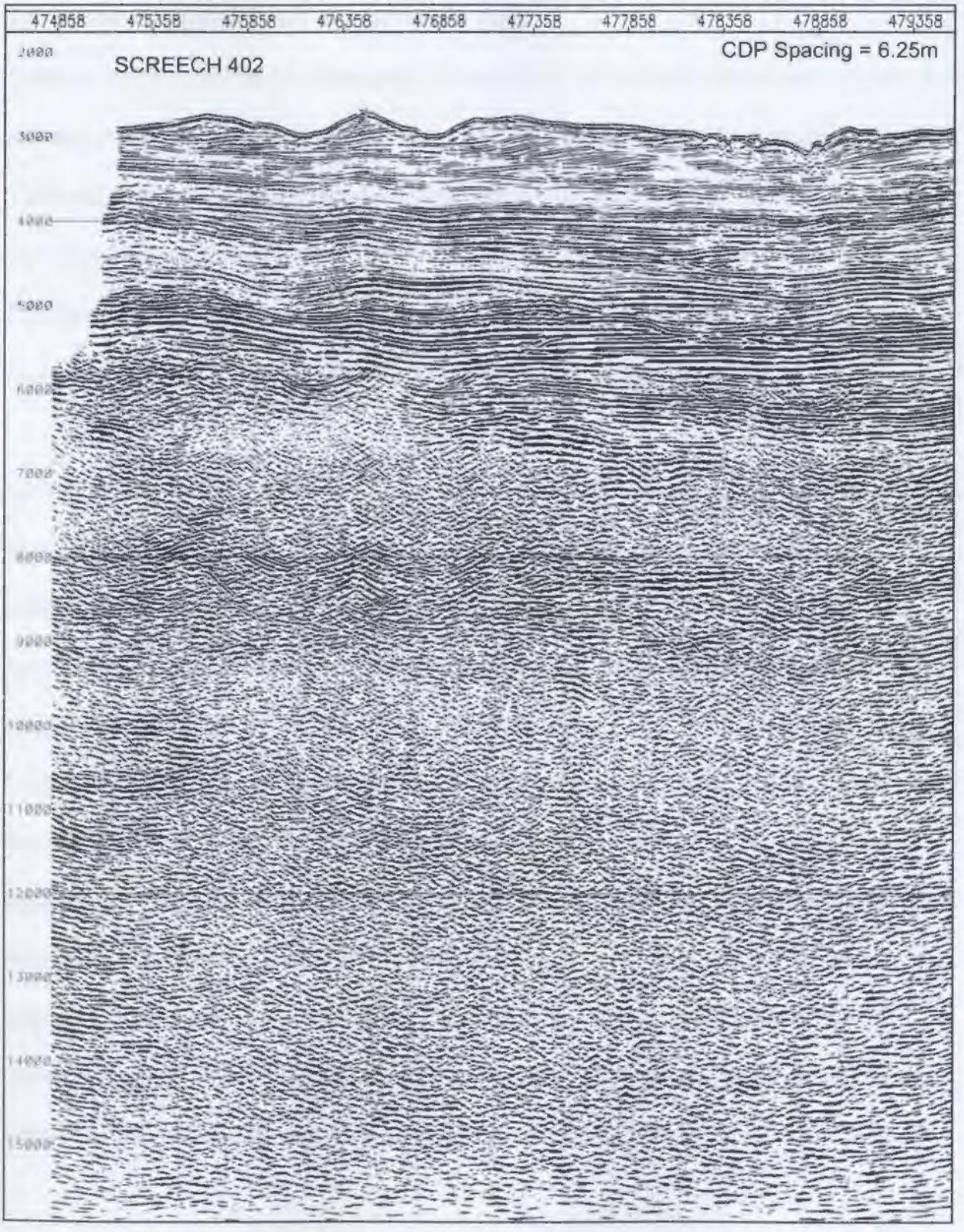

Figure 2.61. Line 402 migrated using the RMS velocities from Figure 2.60.

2.5 Processing proprietary WesternGeco lines

Eight regional proprietary multichannel seismic lines from WesternGeco were obtained and reprocessed to improve image quality below basement. These lines were acquired in 1999 and they recorded 12 seconds of data with a CDP spacing of 12.5m. When the lines were initially processed the main focus was on imaging sedimentary layers above basement and little attention was paid to deep crustal reflections. The goal of reprocessing these lines is to obtain better images of the deep sub-surface.

WesternGeco provided digital stacked sections of each line and migrated sections to allow for comparison. Since only stacked seismic sections were available, noise or multiple removal processes could only be applied post-stack. The deeper portions of the seismic lines contained linear coherently dipping noise similar to the SCREECH profiles and this was removed from the stacked sections before the lines were remigrated. Figure 2.62 shows the position of the WesternGeco lines in relation to the SCREECH lines. All the WesternGeco seismic lines were processed in a fairly similar manner with broad equivalence to the post-stack processing of the SCREECH lines. The processing sequence is summarized below for lines labelled A, B, C, D, E, F, G, and H. This sequence is generalized and some lines have some processes applied in a slightly different manner. Since the processing is rather similar in intent and approach to that applied to the SCREECH line, only a general description is offered here.

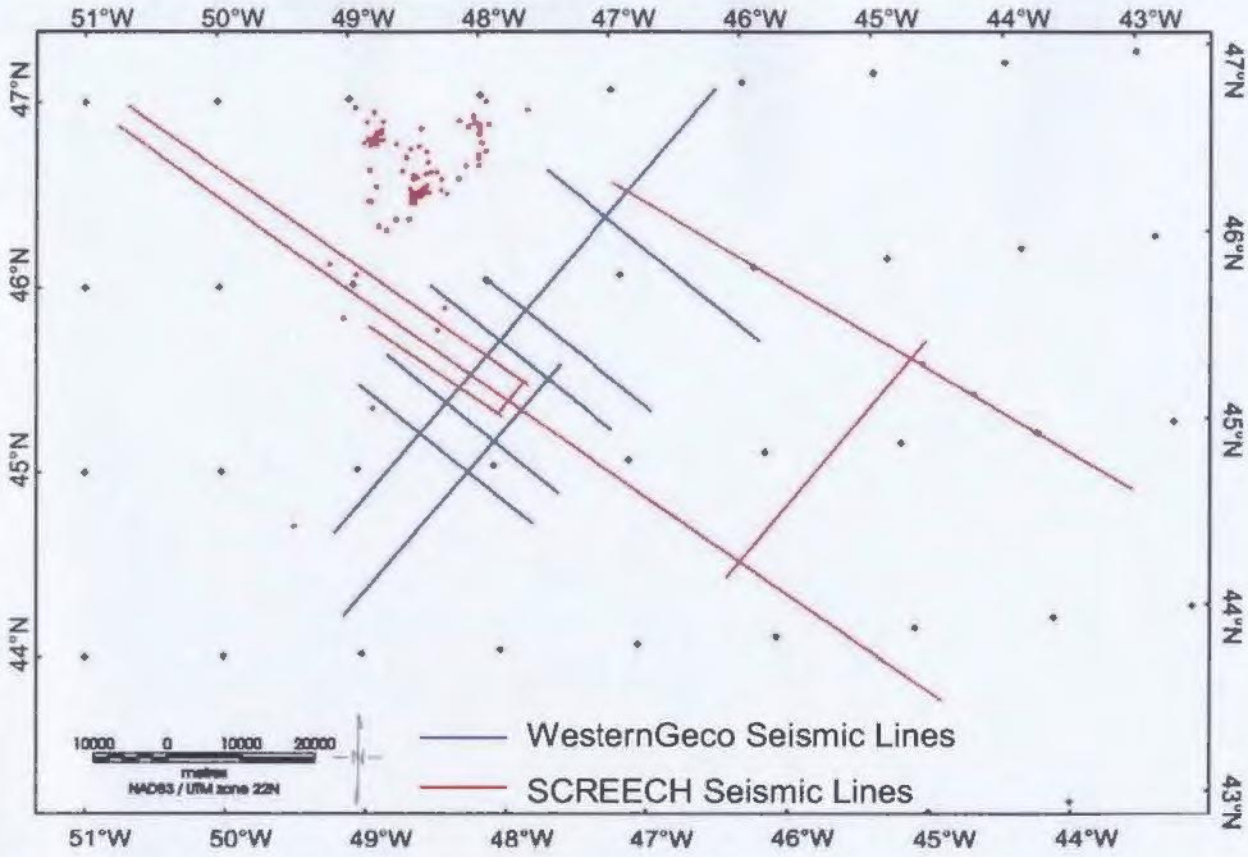

Figure 2.62. Position of proprietary WesternGeco seismic lines in relation to the SCREECH lines.

2.5.1 Post-stack F-K Filter

A post-stack F-K filter was applied to all seismic lines to remove any coherently dipping noise that is present in deeper parts of the sections. In most cases the filter is only applied to sections of the line where dipping noise is especially bad. For all lines the F-K filter was applied as a windowed process. The window was generally picked below basement and continues to the bottom of the section as in SCREECH lines.

2.5.2 Time Variant Scaling and AGC

Time variant scaling and/or an AGC was applied to the seismic sections after F-K filtering was applied. The scaling and AGC was applied so that the section appears more uniform and continuous.

2.5.3 Post-stack Deconvolution

Post-stack predictive deconvolution was applied to lines A, B, C, E, and H to remove reverberatory noise created by the sediment layers and basement. For line C only the shelf portion of the line had predictive deconvolution applied and it was applied as a windowed process. For the five lines the operator length used on all lines was 300 ms and the gap was 90 ms.

2.5.4 Migrating proprietary WesternGeco lines

The WesternGeco lines were also migrated using a Kirchhoff time migration as mentioned in Section 2.3.6. Migration velocities (RMS) were created for each seismic line. Velocity values were created at every 500th CDP (6250m), and in more complex areas at every 250th or 125th CDP (3150m to 1575m). Figures 2.63 to 2.70 show the migration velocities that were picked for each of the WesternGeco lines.

2.5.5 Bandpass filter

A minimum phase Ormsby bandpass filter was applied to all the WesternGeco seismic lines to remove unwanted frequencies. The bandpass filter was applied to all lines as a

2.5.2 Time Variant Scaling and AGC

Time variant scaling and/or an AGC was applied to the seismic sections after F-K filtering was applied. The scaling and AGC was applied so that the section appears more uniform and continuous.

2.5.3 Post-stack Deconvolution

Post-stack predictive deconvolution was applied to lines A, B, C, E, and H to remove reverberatory noise created by the sediment layers and basement. For line C only the shelf portion of the line had predictive deconvolution applied and it was applied as a windowed process. For the five lines the operator length used on all lines was 300 ms and the gap was 90 ms.

2.5.4 Migrating proprietary WesternGeco lines

The WesternGeco lines were also migrated using a Kirchhoff time migration as mentioned in Section 2.3.6. Migration velocities (RMS) were created for each seismic line. Velocity values were created at every 500th CDP (6250m), and in more complex areas at every 250th or 125th CDP (3150m to 1575m). Figures 2.63 to 2.70 show the migration velocities that were picked for each of the WesternGeco lines.

2.5.5 Bandpass filter

A minimum phase Ormsby bandpass filter was applied to all the WesternGeco seismic lines to remove unwanted frequencies. The bandpass filter was applied to all lines as a

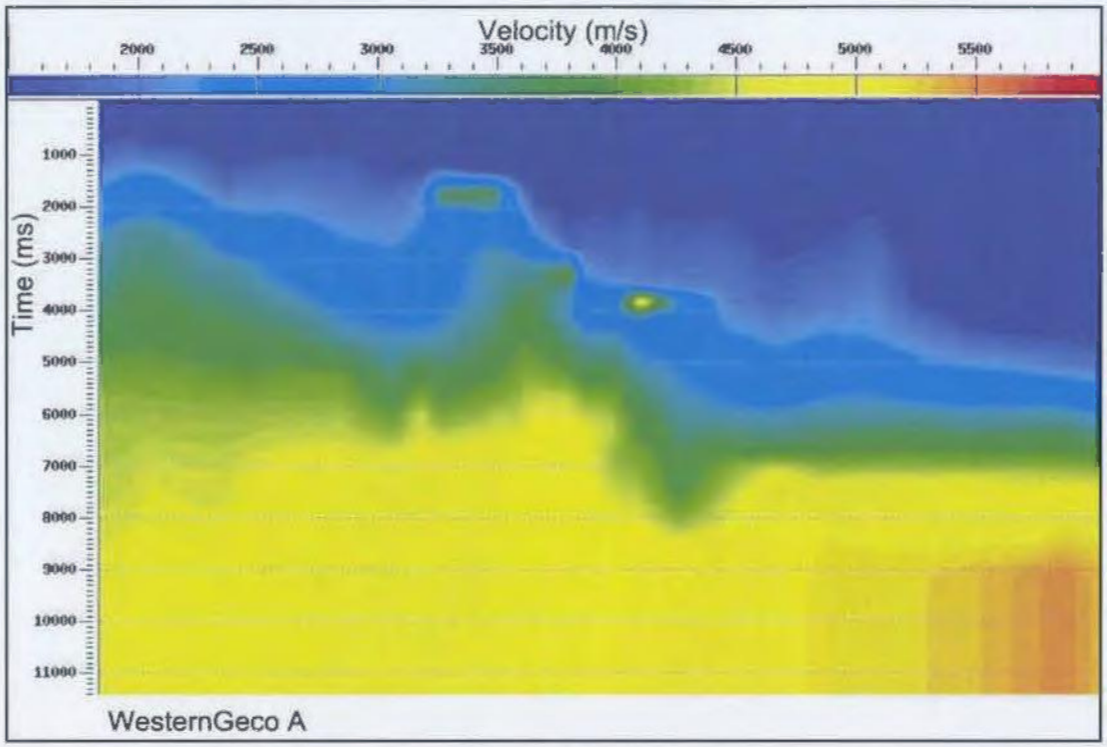

Figure 2.63. RMS Velocity model for proprietary WesternGeco seismic line A.

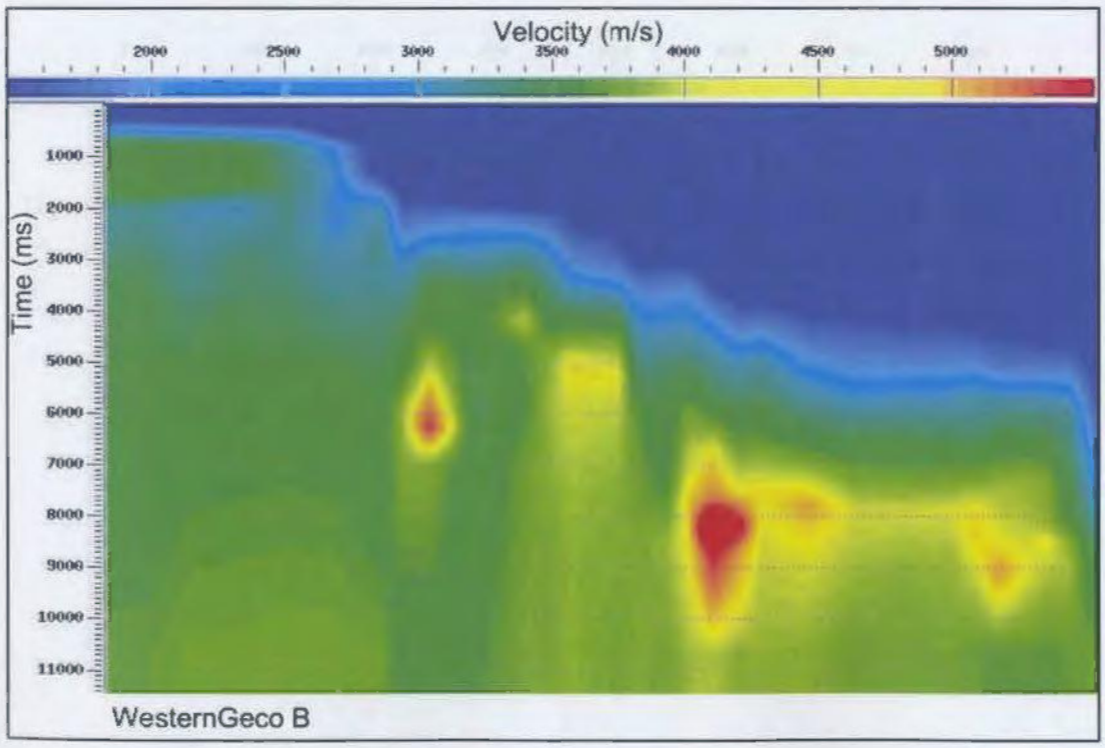

Figure 2.64. RMS Velocity model for proprietary WesternGeco seismic line B.

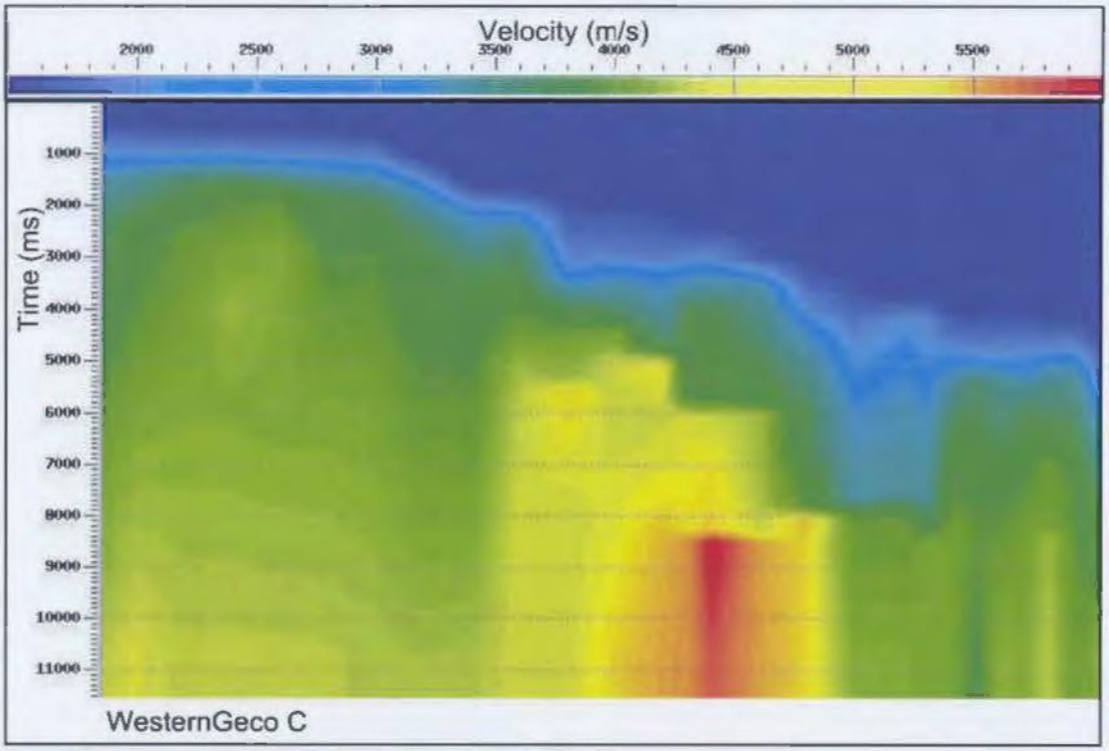

Figure 2.65. RMS Velocity model for proprietary WesternGeco seismic line C.

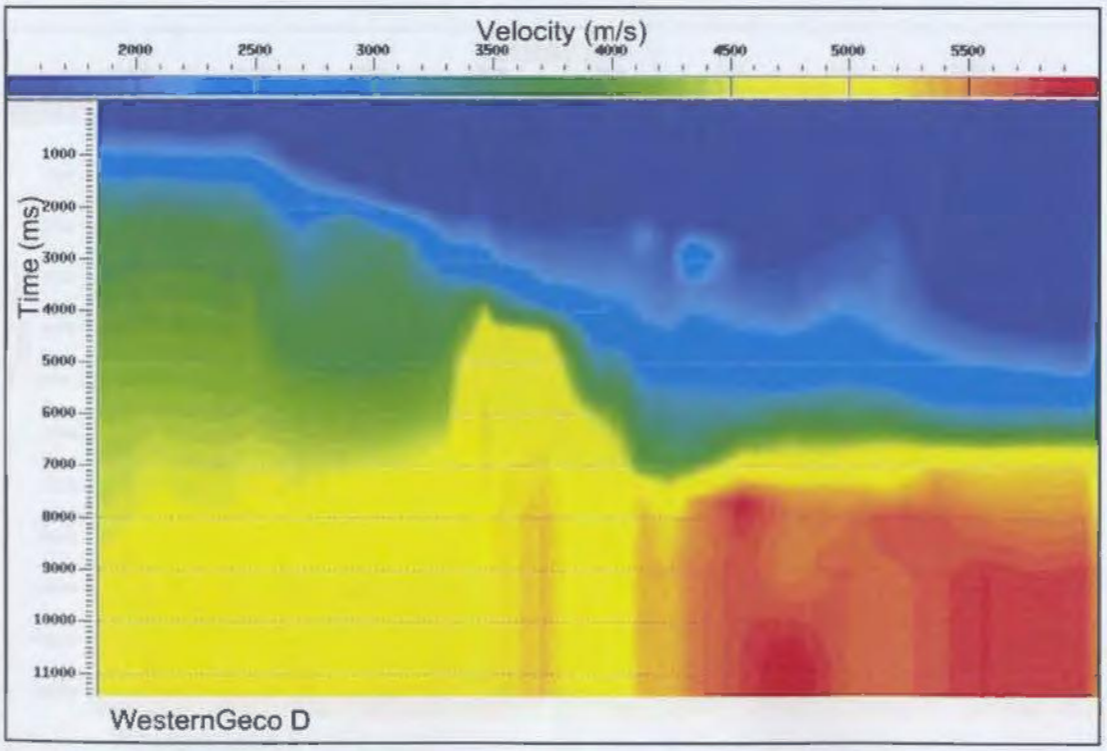

Figure 2.66. RMS Velocity model for proprietary WesternGeco seismic line D.

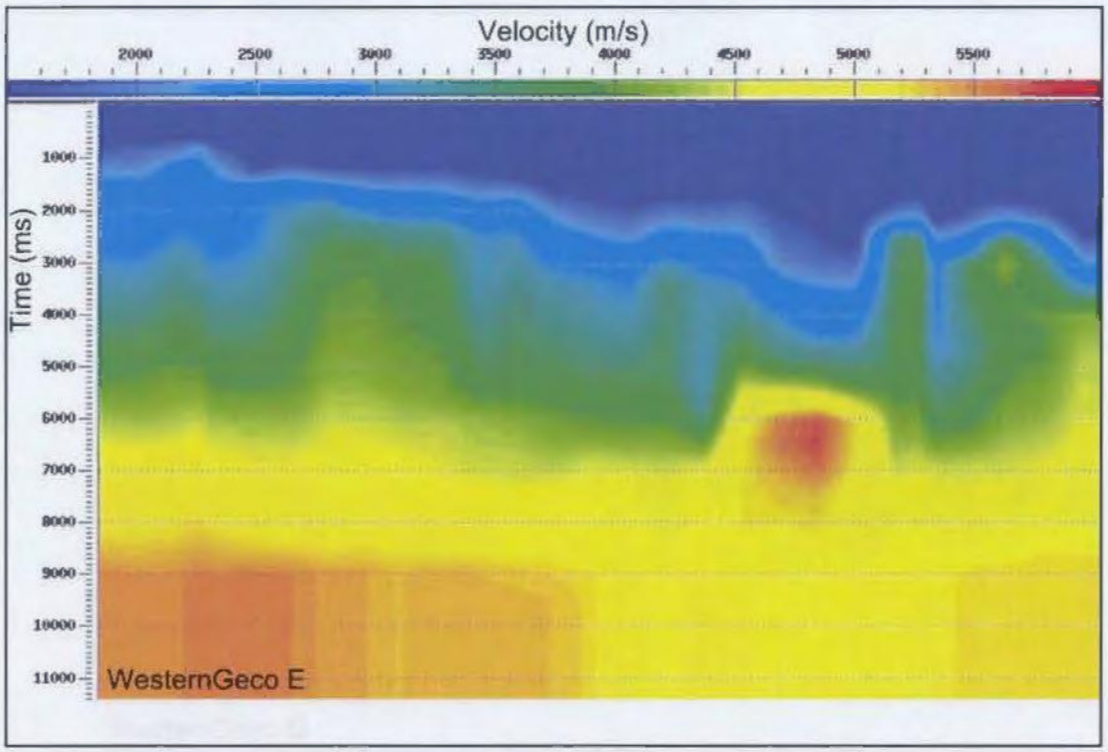

Figure 2.67. RMS Velocity model for proprietary WesternGeco seismic line E.

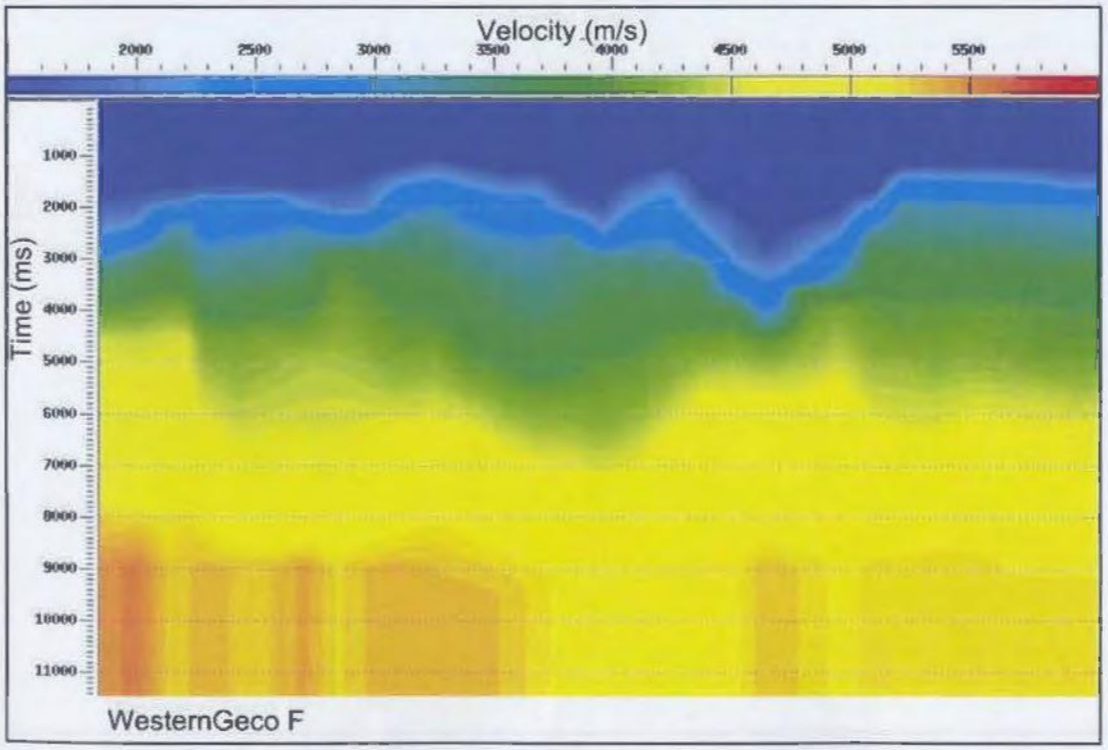

Figure 2.68. RMS Velocity model for proprietary WesternGeco seismic line F.

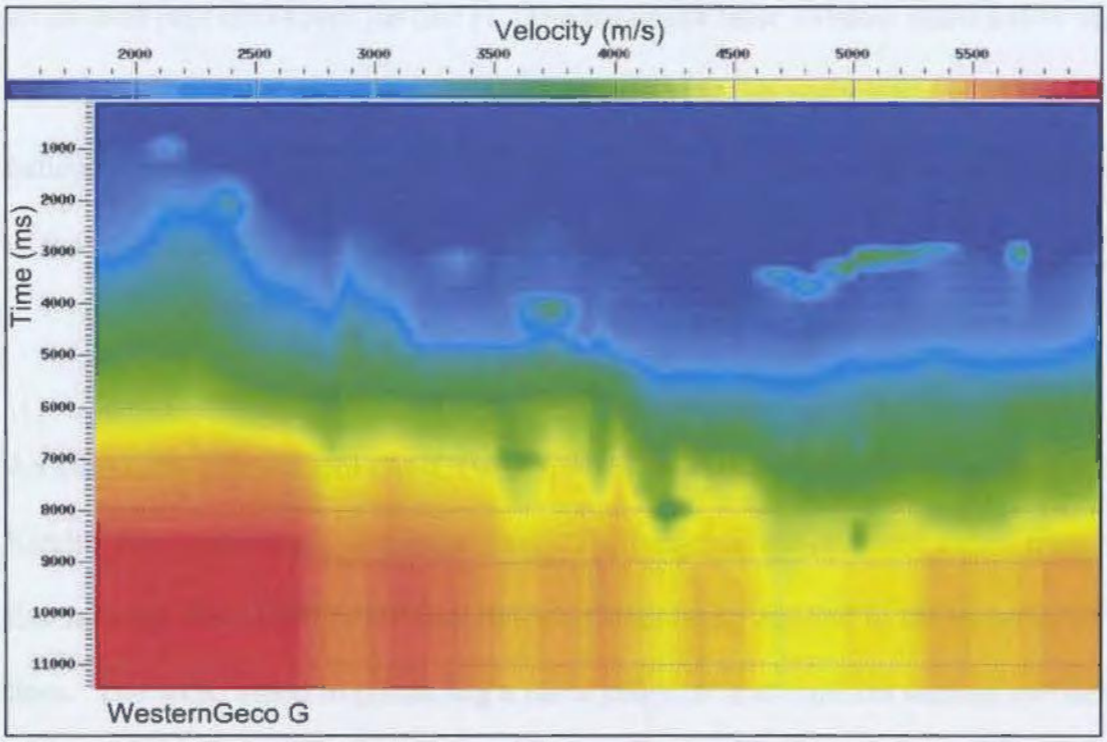

Figure 2.69. RMS Velocity model for proprietary WesternGeco seismic line G.

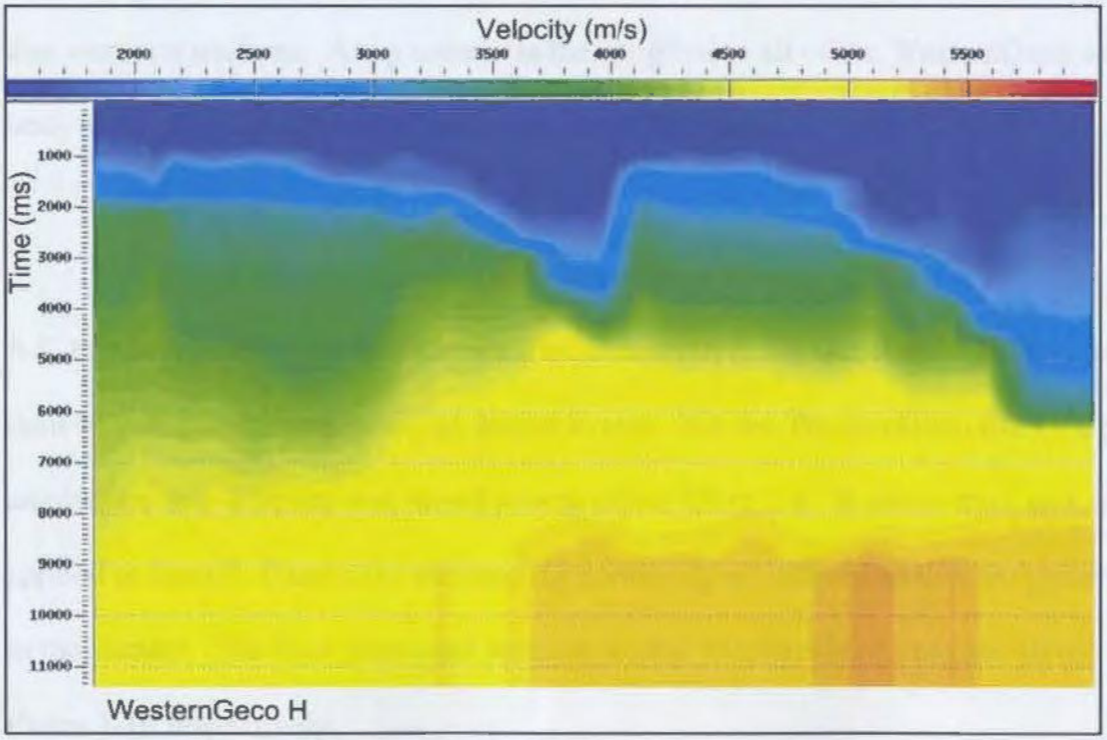

Figure 2.70. RMS Velocity model for proprietary WesternGeco seismic line H.

windowed process except for line H. The bandpass filter window starts below the water bottom so that reverberatory noise was not created at the water bottom. A time variant bandpass filter was used to allow higher frequencies to be kept in the shallower portions of the seismic line, but filtered out at deeper times.

2.5.6 AGC and Time Variant Scaling

An automatic gain control (AGC) was applied to all the seismic sections after the Kirchhoff migration and bandpass filter. The length of the operator varies from line to line ranging from 1000 to 4000ms, with 1000ms being applied to the majority of the lines. The AGC aided in producing a more coherent and uniform section and helped remove the noticeable window effects created by windowed processing. Time variant scaling was applied to seismic lines A, B, C, and H after the AGC to enhance any spots that were not uniform. A top mute was then applied to all of the WesternGeco seismic lines to remove any noise present above the water bottom reflection.

2.5.7 F-K Power Exponent Filter and Trace Mixing

A F-K power exponent filter is applied to lines A, B, C, D, and H after all processing is done to enhance the coherency of deeper events. For the WesternGeco lines the power of amplitudes in F-K space was raised to was either 1.3 or 1.4. A seven trace mix was applied to lines E, F and G to increase the continuity of reflections that are present deeper in the dataset. The final processed sections for the WesternGeco lines are shown on Plates 3-10 respectively.

CHAPTER 3 Interpretation

3.1 Datasets Available

3.1.1 Reflection Seismic Data

The area of investigation for this thesis extends from ~ 44°N and 46.5°W to 47°N and 49.5°W. Along with the SCREECH and proprietary WesternGeco seismic lines which are of excellent quality, there are other digital seismic lines available in the study area. Seismic lines donated by GSI covering the Carson, Bonnition, Salar and Flemish Pass basins were used to aid in the interpretation (green and purple lines, Figure 3.1). Most of these lines were collected in 1982 and 1983 and are recorded down to 8 seconds. The data quality of these lines is fairly good down to basement but the quality degrades to poor below basement. Other seismic lines shot between 1979 and 1985 were also available in paper format from the Canadian Newfoundland and Labrador Offshore Petroleum Board (CNLOPB) (black lines, Figure 3.1). Most of these lines are generally recorded to only 6 or 8 seconds limiting their usefulness for imaging deep crustal structures. These seismic lines are generally of poor quality (low signal to noise ratio), and have multiple and other imaging problems. Some of the CNLOPB lines were also only available as stacked sections without migration, which makes interpretation difficult. The GSI and CNLOPB seismic lines provide reasonable ties to the SCREECH and WesternGeco datasets and aid in the interpretation of horizons around the study area, especially where the better quality SCREECH and WesternGeco datasets have sparse data coverage.

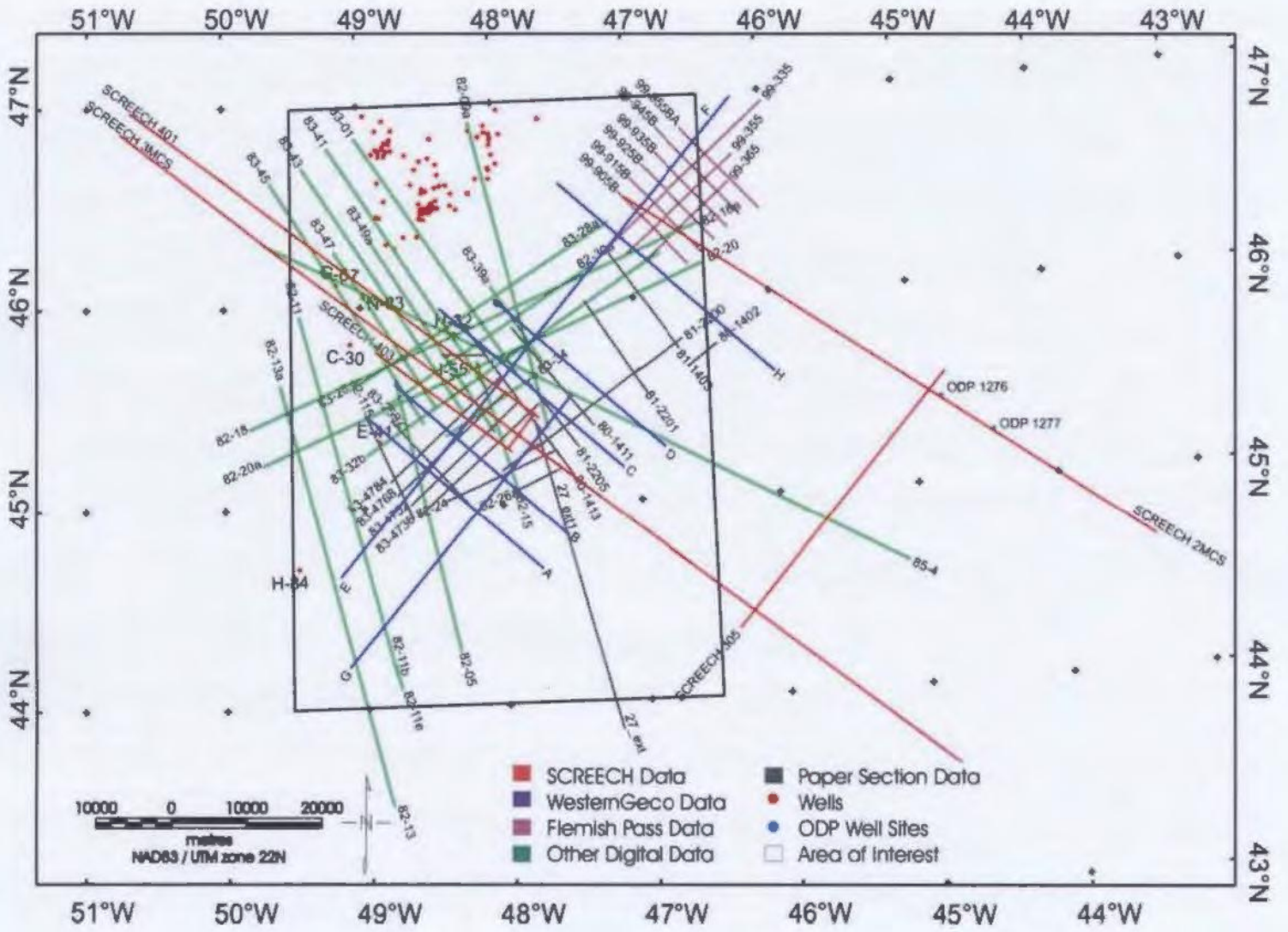

Figure 3.1. Location map of seismic lines used for interpretation in this thesis. Seismic lines are colour coded to separate the different vintages. Well locations are also illustrated as is the main area of interest for this thesis. Well identities: G-67 = Murre, N-83 = Cormoramt, C-30 = Spoonbill, H-32 = Bonnition, J-55 = St. George, E-41 = Skua, H-84 = Osprey.

All seismic lines shown in Figure 3.1 were used for interpretation. The SCREECH and WesternGeco seismic lines were the main datasets used, and provided the best resolution. The GSI data were used as a secondary data set and the paper section data from CNLOPB were used as a tertiary data set where data quality allowed. The CNLOPB lines provide valuable information along the slope portion of the margin and allow interpretations in this area to be more confidently made. The WesternGeco and GSI seismic lines had bulk time shifts applied and their amplitudes balanced to match the SCREECH lines to create a consistent dataset. The locations of all seismic images used in figures can be found in Appendix 2 and all intersecting seismic lines are annotated on the figures.

3.1.2 Wide Angle Seismic Data

Wide angle ocean bottom seismograph (OBS) data were also collected during the SCREECH project. The OBS transects shown previously in Figure 2.1, were collected with the use of 29 ocean bottom instruments, consisting of ocean RefTek's in a ball (ORB's), ocean bottom hydrophones (OBH's) and ocean bottom seismographs (OBS's) (15 from the Woods Hole Oceanographic Institute (WHOI), 8 from the Geological Survey of Canada, and 6 from Dalhousie University). A 20 gun, 8540 cubic inch airgun array was used to fire shots at a 200 m spacing for the ocean bottom instruments. The wide angle data over Transect 3 is of most use for this thesis. The data were used to create a velocity model (shown in Figure 3.2, from Lau et al. 2005b) that can be used to constrain corresponding densities and thicknesses in gravity modelling and when performing structural and stratigraphic reconstructions of the margin evolution.

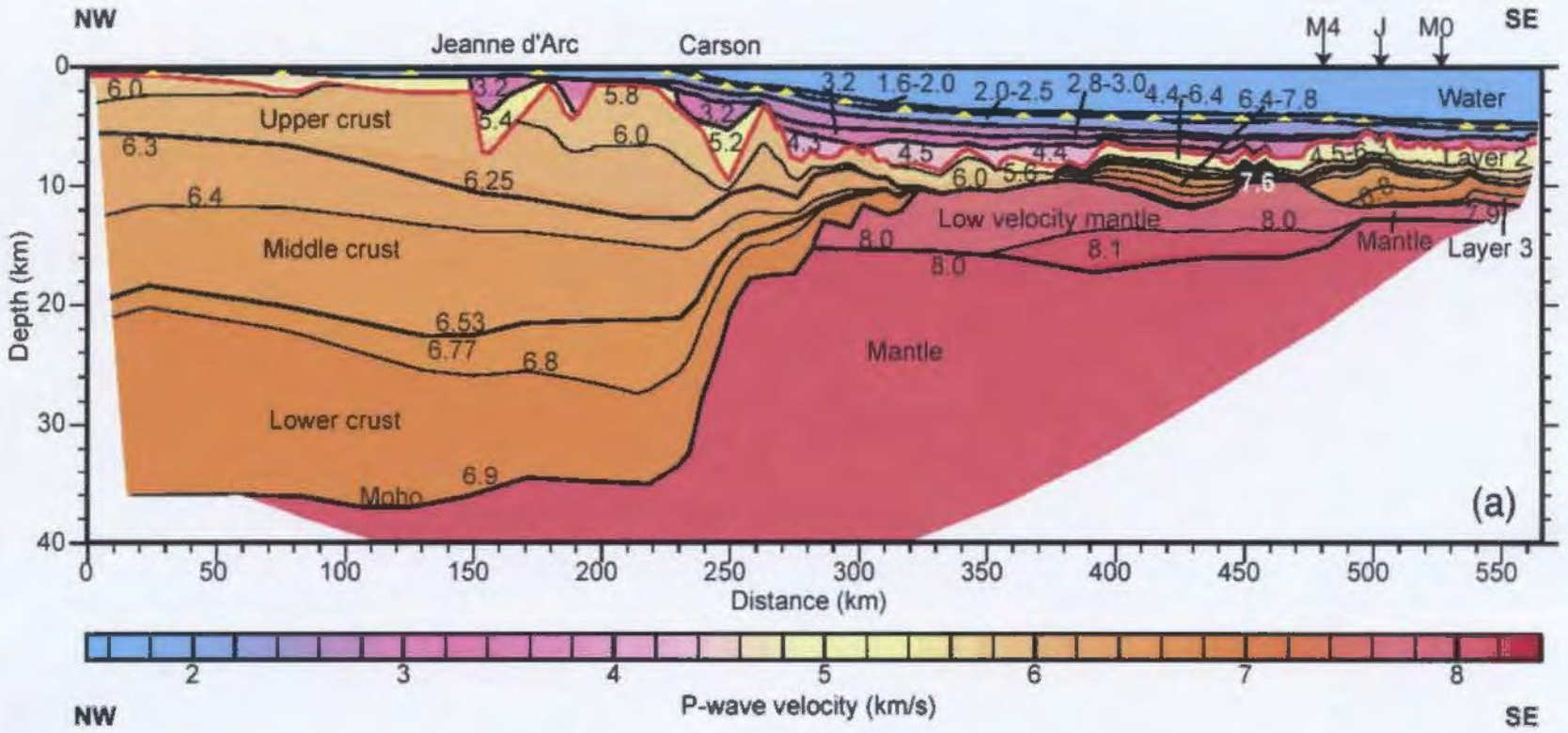

Figure 3.2. Velocity model for SCREECH 3MCS from wide angle data. (From Lau, et al., 2005b).

3.1.3 Potential Fields Data – Gravity and Magnetics

Along with the seismic data, gravity and magnetic data were also gathered on the SCREECH cruise along the transects. Both the gravity and magnetic data were recorded at 1 minute intervals along the lines which provided detailed data for modelling. Gridded regional free-air gravity and total field magnetic maps are also available for the Grand Banks from the Geological Survey of Canada (GSC). These maps were most useful for interpreting large structures along the margin. Figure 3.3 illustrates the gridded gravity and magnetic data available over the study area. The gravity lows give a rough outline of the major basins that are present on this portion of the margin.

3.2 Introduction to Geological and Geophysical Interpretation

The shelf portion of the SE Newfoundland margin contains the Carson Basin (Tucholke et al. 1989) or the Inner Carson Basin as referred to by Grant et al. (1988). Other authors have also termed this basin as the Carson-Bonnition Basin (Enachescu, 1992b, Keen and de Voogd, 1988). In this thesis the Carson Basin will refer to the southern-most shelf edge basin in the study area while the Bonnition Basin will refer to the more northern shelf edge basin. The extent and position of these basins will be illustrated in greater detail in the following sections. The slope portion of the SE Newfoundland margin in the thesis study area was termed the Outer Carson Basin by Grant et al. (1988), where as Tucholke et al. (1989) named the basin on this portion of the margin the Salar Subbasin. In this thesis the terminology of Tucholke et al. (1989) is used to describe the extent and position of the Salar Basin.

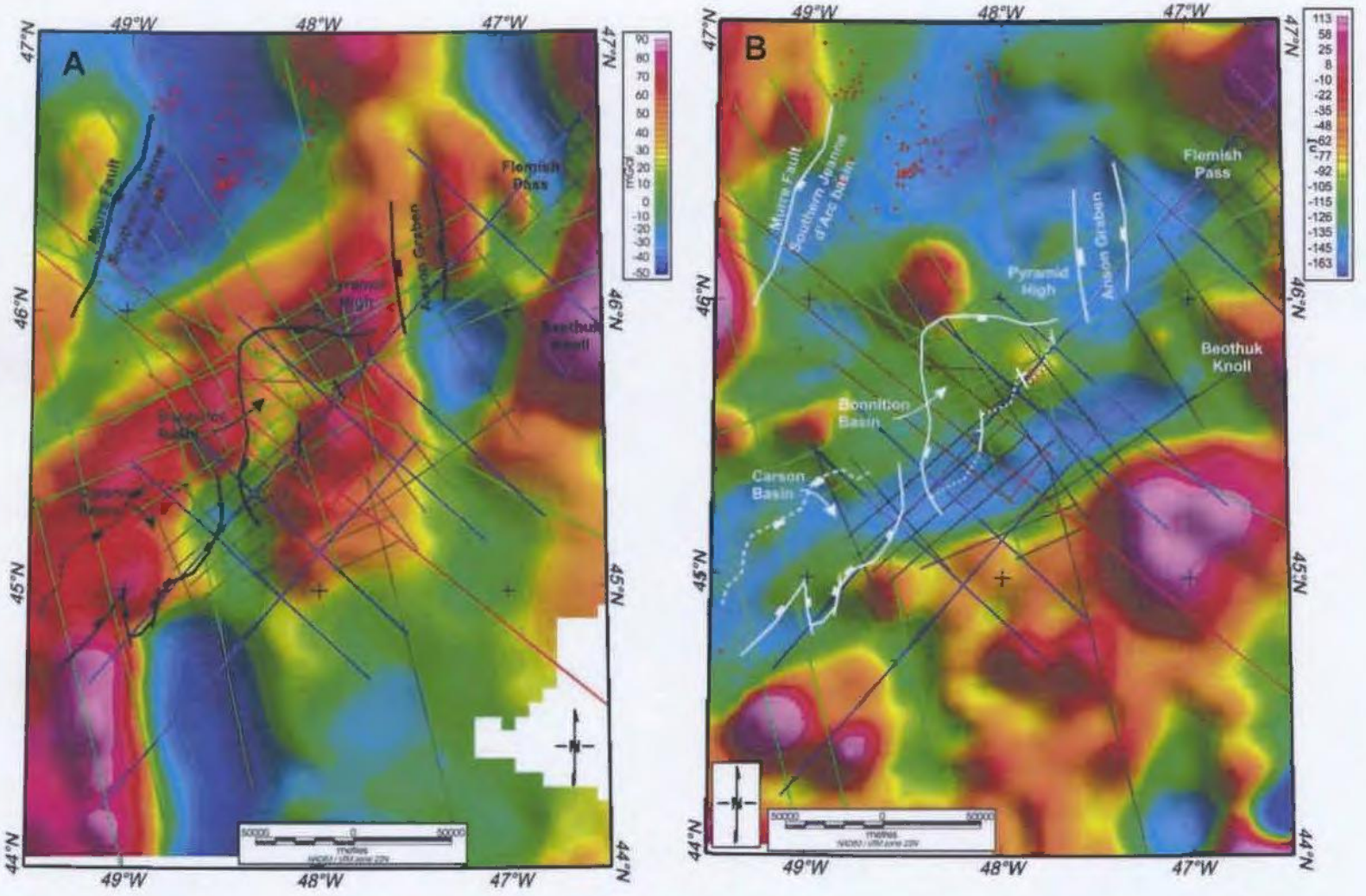

Figure 3.3. Gravity (A) and Magnetic (B) maps of the study area. Gravity field is Free-Air taken from data provided by the Geological Survey of Canada. The Magnetic field is total, and these data are also from the Geological Survey of Canada. Note that the outline of the Southern Jeanne d'Arc, Carson and Bonnition basins is evident on the gravity map.

3.2.1 Available Well Data

Four wells are located in or near the Carson and Bonnition basins and are used to provide stratigraphic ties to prominent seismic markers. The four wells are: St. George J-55, Skua E-41, Osprey H-84, and Bonnition H-32. An additional three wells (Spoonbill C-30, Cormorant N-83 and Murre G-67) are located in or near the Southern Jeanne d'Arc Basin and these give a detailed picture of the stratigraphic record in that closely adjacent basin. Figure 3.1 illustrates the location of all these wells in relation to the seismic data that are available for interpretation. All of these wells in the Carson, Bonnition and Southern Jeanne d'Arc basins, are located on the shelf area of the margin. Figures 3.4 and 3.5 illustrate time stratigraphic sections for wells in the Carson and Bonnition basins and wells in the Southern Jeanne d'Arc Basin. Because of the well locations, few ties can be confidently extended into the slope area of the margin and down into the Salar Basin. In the summer of 2003, Leg 210 of the Ocean Drilling Program (ODP) drilled two sites on the Newfoundland margin. These two drill sites were located in deep water to the northeast of the study area in the Newfoundland Basin. Site 1276 recovered a large portion of the sedimentary section and bottomed in a sill, while Site 1277 drilled a basement high. Although these wells are approximately 60 km to the northeast of the study area (illustrated in Figure 3.1), they contain valuable information on the slope sediments that no other wells can provide and they aid in the correlation of sediments in the slope region. Figure 3.6 illustrates the results from the ODP Site 1276, showing the age and rock types that were encountered.

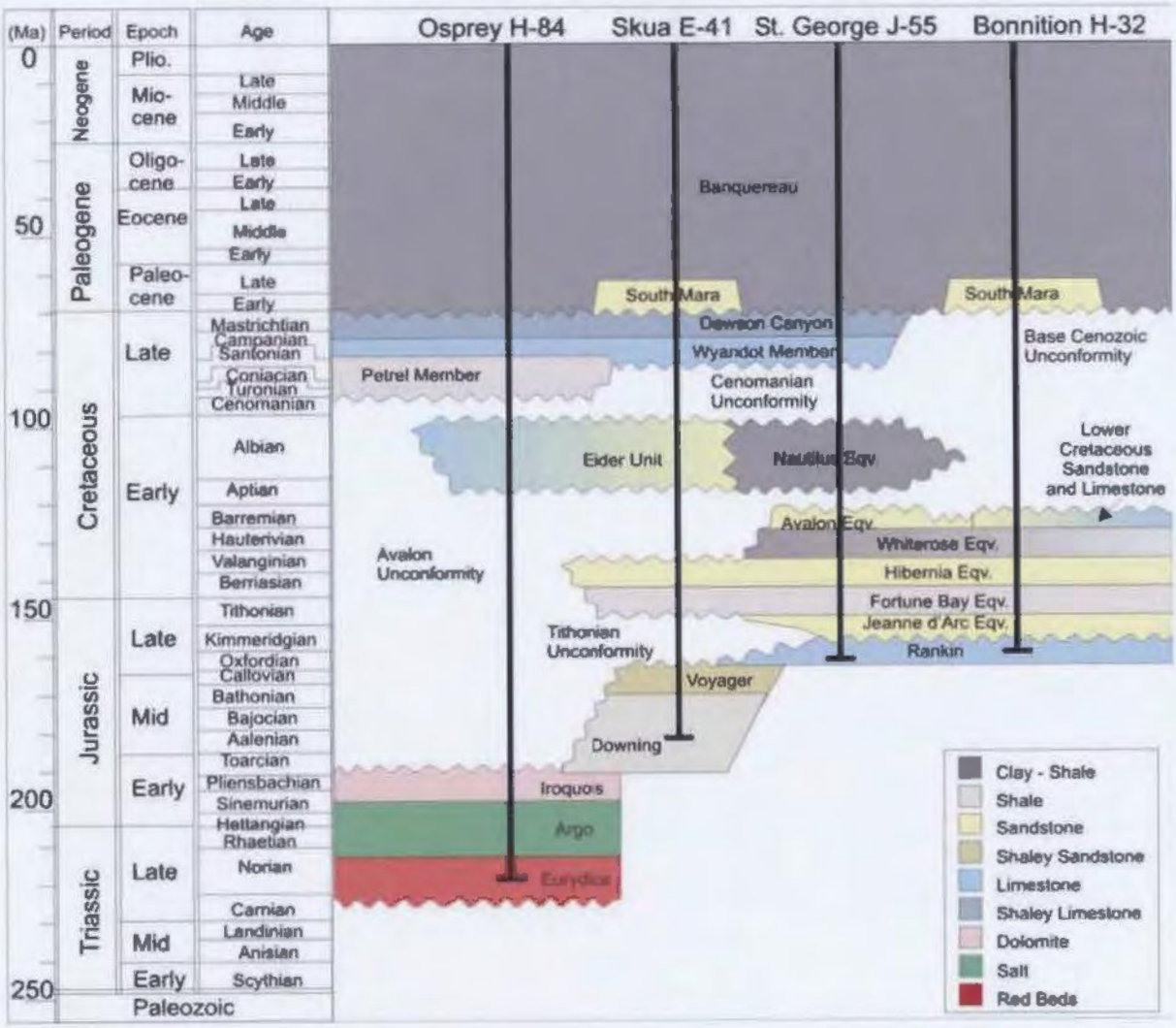

Figure 3.4. Time-stratigraphic section of the Carson and Bonnition basins. The Osprey and Skua wells are located in the Carson Basin, while the St. George and Bonnition wells were drilled in the Bonnition Basin. *Modified from:* Grant et al. (1988).

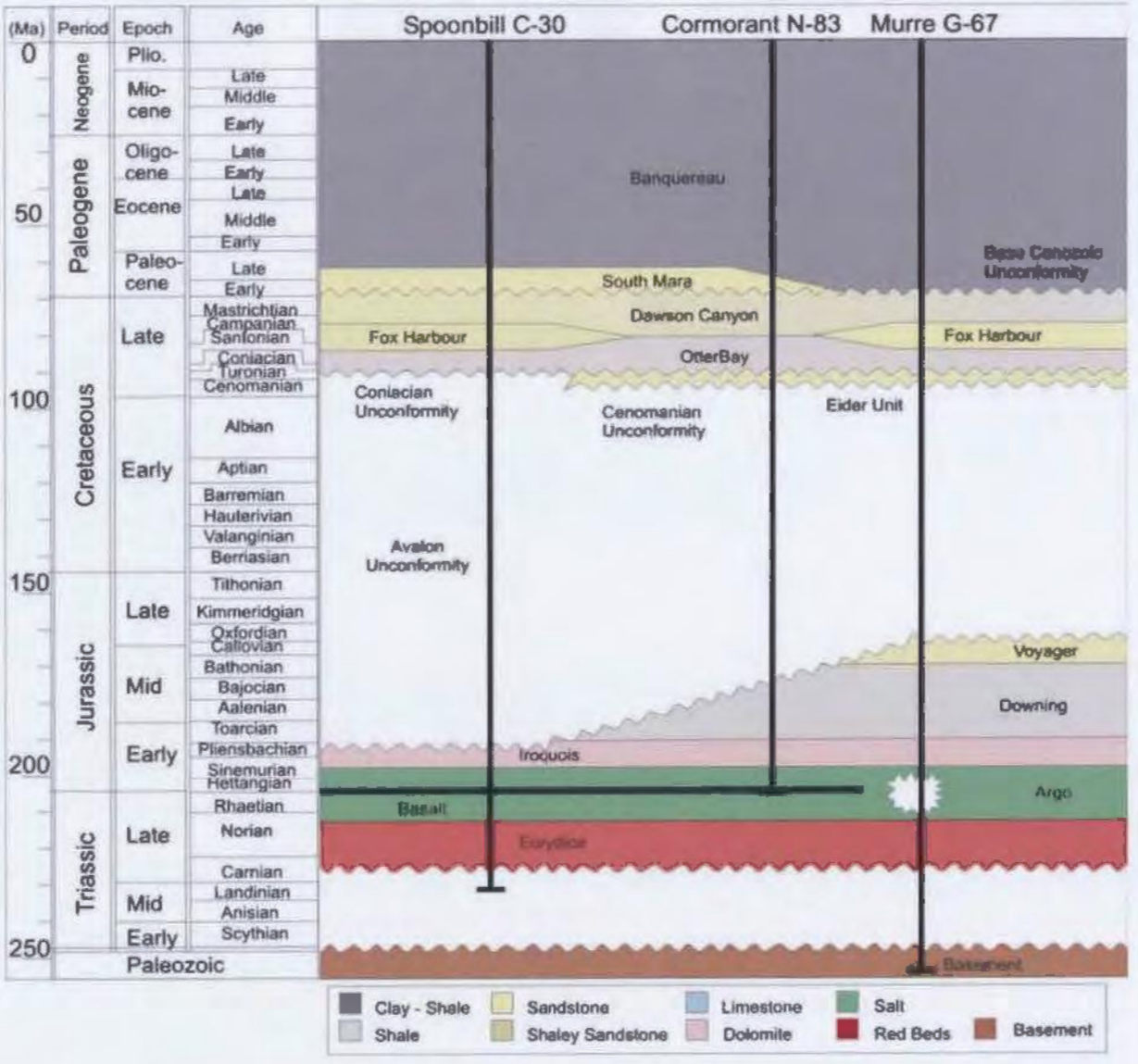

Figure 3.5. Time-stratigraphic section of the Southern Jeanne d'Arc Basin showing three wells near the study area. *Modified from*: Grant et al. (1988).

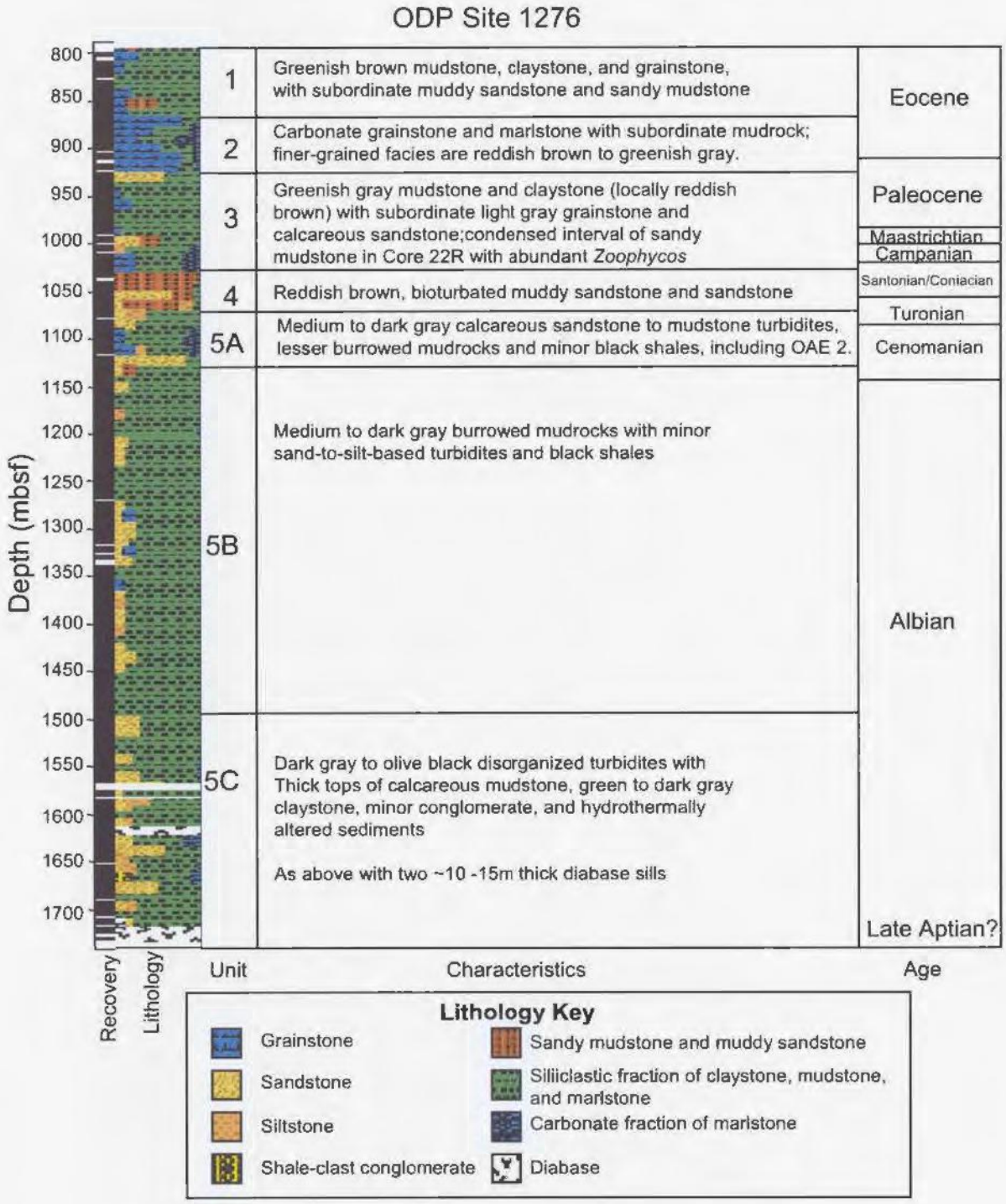

Figure 3.6. ODP Site 1276. Description of units. *Modified from:* Shipboard Scientific Party, (2004b). The location of the well is found in Figure 3.1.

Time-depth data from six wells on the shelf (Murre, Comorant, Spoonbill, Bonnition, St. George, and Skua) and velocity information gathered from ODP Site 1276 cores were used to correlate the wells to nearby seismic data. The time-depth well data was also used to create an interval velocity model to convert the seismic data from the time domain to the depth domain. Table 3.1 below summarizes the time-depth values for the three wells in the Carson and Bonnition basins, and Table 3.2 shows the time-depth values for the other four wells.

Table 3.1. Time-depth curve values for wells in the Carson and Bonnition basins. Data provided from CNLOPB.

Skua Well		**Bonnition Well** Two Way		**St. George Well** Two Way	
Time (s)	Depth (m)	Time (s)	Depth (m)	Time (s)	Depth (m)
0.00	1.52	0.00	0.00	0.00	0.00
0.10	76.20	0.13	131.67	0.02	17.52
0.40	362.41	0.33	304.80	0.14	110.36
0.50	461.77	0.43	396.24	0.17	131.02
0.90	876.30	0.63	579.12	0.48	412.09
1.00	988.16	0.80	762.00	0.50	432.74
1.40	1540.15	0.95	914.40	0.74	657.41
1.50	1689.51	1.12	1097.28	0.77	681.24
1.90	2435.05	1.28	1267.97	0.98	911.17
2.00	2614.57	1.36	1371.60	1.01	936.18
2.30	3181.50	1.48	1554.48	1.49	1534.39
2.32	3208.63	1.62	1737.36	1.51	1568.16
		1.75	1920.24	2.50	3194.63
		1.88	2103.12	2.52	3232.46
		2.00	2286.00	2.99	4021.89
		2.11	2468.88	3.00	4039.75
		2.23	2651.76	3.00	4041.64
		2.33	2834.64	3.01	4051.08
		2.42	3017.52		

Table 3.2. Time-depth curve values for wells outside the Carson and Bonnition basins and time-depth values from core at the ODP Site 1276. Data provided from CNLOPB and Shipboard Scientific Party, (2004b).

Spoonbill Well Two Way	
Time (s)	Depth (m)
0.08	95.10
0.26	259.08
0.46	432.21
0.58	579.12
0.74	746.76
0.86	914.40
0.92	1042.42
1.01	1234.44
1.08	1371.60
1.18	1584.96
1.31	1828.80
1.41	2005.58
1.48	2133.60
1.55	2286.00
1.62	2438.40
1.69	2567.64

Cormorant Well Two way	
Time (s)	Depth (m)
0.00	0.00
0.02	15.20
0.14	110.00
0.20	164.70
0.32	274.40
0.38	329.90
0.50	440.10
0.56	500.00
0.72	683.50
0.80	787.20
0.96	979.40
1.04	1074.90
1.20	1292.20
1.36	1544.00
1.44	1662.10
1.62	1955.80
1.82	2414.60
2.02	2834.70
2.08	2962.50

Murre Well Two Way	
Time (s)	Depth (m)
0.00	0.00
0.02	20.00
0.14	140.00
0.20	200.00
0.32	320.00
0.38	380.00
0.50	500.00
0.56	560.00
0.72	720.00
0.80	800.00
0.96	960.00
1.04	1040.00
1.20	1200.00
1.36	1360.00
1.44	1440.00
1.62	1620.00
1.82	1820.00
2.00	2000.00
2.06	2060.00
2.16	2160.00

ODP Site 1276 Two Way	
Time (s)	Depth (m)
0.00	0.00
0.08	86.00
0.20	236.00
0.25	286.00
0.40	461.00
0.43	486.00
0.57	686.00
0.60	711.00
*Values from Cored Section	

Appendix 3 contains the final interval velocity values that were used to create the velocity model for the study area to perform the depth conversion. The interval velocity model was created using Landmarks OpenWorks software package. The program TDQ was used to create the interval velocity model. The time-depth values from the wells were input into TDQ and converted to interval velocities. Interval velocities (computed from RMS stacking velocities) from 20 locations picked along the SCREECH and WesternGeco seismic lines in deeper water were then added to the well interval velocity data to provide additional constraints for the deep water areas.

3.2.2 Well ties to seismic marker horizons

Five of the seven wells on the shelf portion of the margin are located near seismic data that is used in this thesis. Two of these wells are located in the Southern Jeanne d'Arc Basin, while the other three are located in the Carson and Bonnition basins. The two ODP Sites (1276 and 1277) in the deep water are located near the SCREECH 2MCS seismic line. Figure 3.7 shows the Murre and Cormorant wells in the Southern Jeanne d'Arc Basin and their tie to seismic lines 83-45 and 83-47. The two wells (Murre and Cormorant) in the Southern Jeanne d'Arc Basin provide good ties to the surrounding seismic data, sampling into the Triassic and in the case of the Murre well bottoming in basement metasediments.

The Bonnition well is located near seismic line 83-41 and Figure 3.8 illustrates the tie between the well and seismic data. This well is drilled near the edge of the basin and ties fairly well to the seismic data. As shown in Figure 3.4, the well drilled through Cenozoic and some Lower Cretaceous sediment before ending in the Upper Jurassic Rankin Formation. Similar to the Bonnition well, the St. George well is also located near the basin margin and penetrates Cenozoic and Cretaceous sediments before ending in the Rankin Formation. Seismic line 83-49a is the closest to this well and is shown in Figure 3.9. Seismic lines 83-32 and 83-32a are strike seismic lines that are closest to the Skua well (as shown in Figure 3.10). These lines are not coincident with the well, and as such the seismic data is not expected to tie exactly to the well. Most of the Skua well picks tie to the seismic data except for the Tithonian Unconformity which is slightly off. The

Skua well drilled through Cenozoic, thin Cretaceous sediments, the Upper Jurassic Voyager Formation and bottomed in the Middle Jurassic Downing Formation. In the deep water Newfoundland Basin, ODP Hole 1276 provides a good tie to the SCREECH 2MCS seismic line (shown in Figure 3.11). This Hole sampled Eocene to Late Albian sediments, and seismic horizons tied to this well can be traced into the Salar Basin.

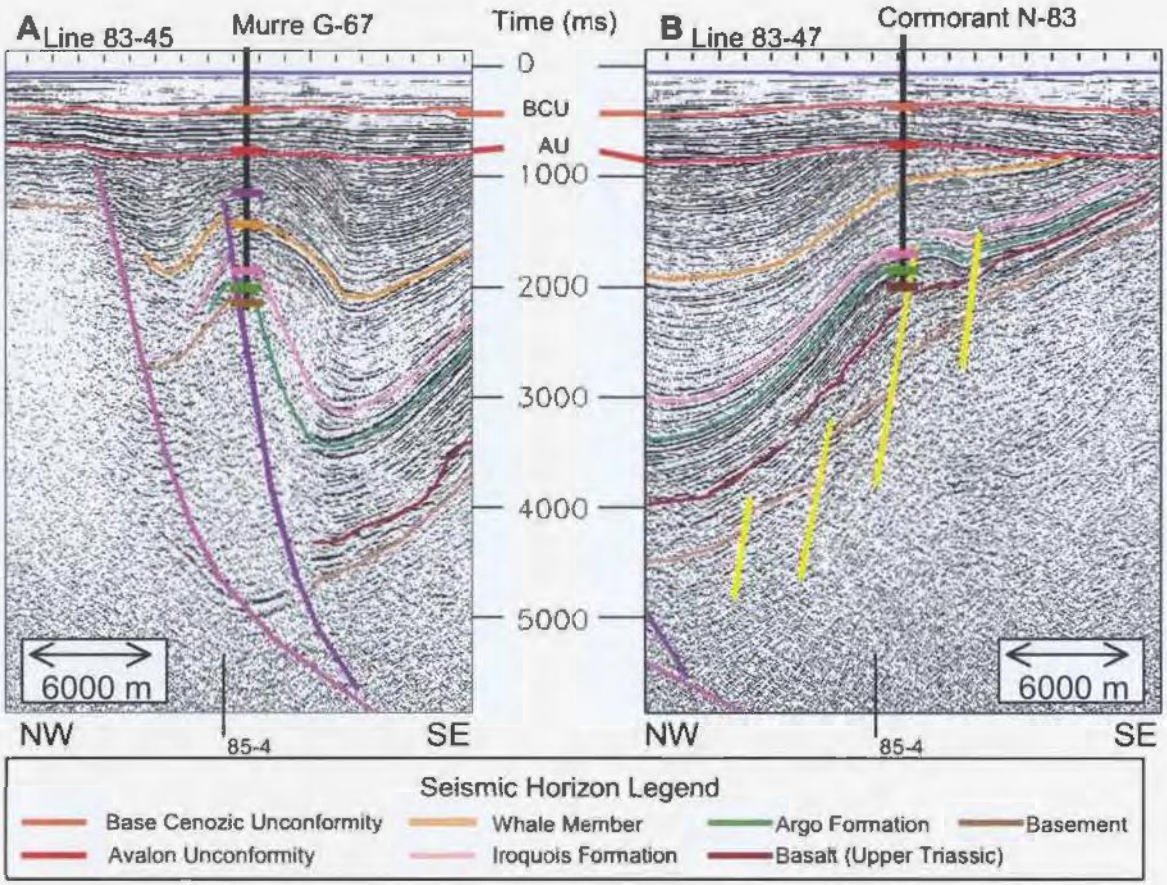

Figure 3.7. A) Seismic line 83-45 adjacent to the Murre G-67 well. B) Seismic line 83-47 adjacent to the Cormorant N-83 well. These sections show the seismic and well log ties for major formations and unconformities. The Base Cenozoic Unconformity (BCU) is in orange, and the Avalon Unconformity (AU) is in red. The Whale Member (Mid Jurassic) provided a strong tie (orange-yellow). In both sections the top of the Iroquois Formation (Lower Jurassic) is shown in pink, the top of the Argo/Osprey Formation (Upper Triassic) is shown in green and Basement is shown in brown. A basalt layer in the Southern Jeanne d'Arc Basin separating the overlying Argo Formation from the Osprey Formation is shown in reddish-brown.

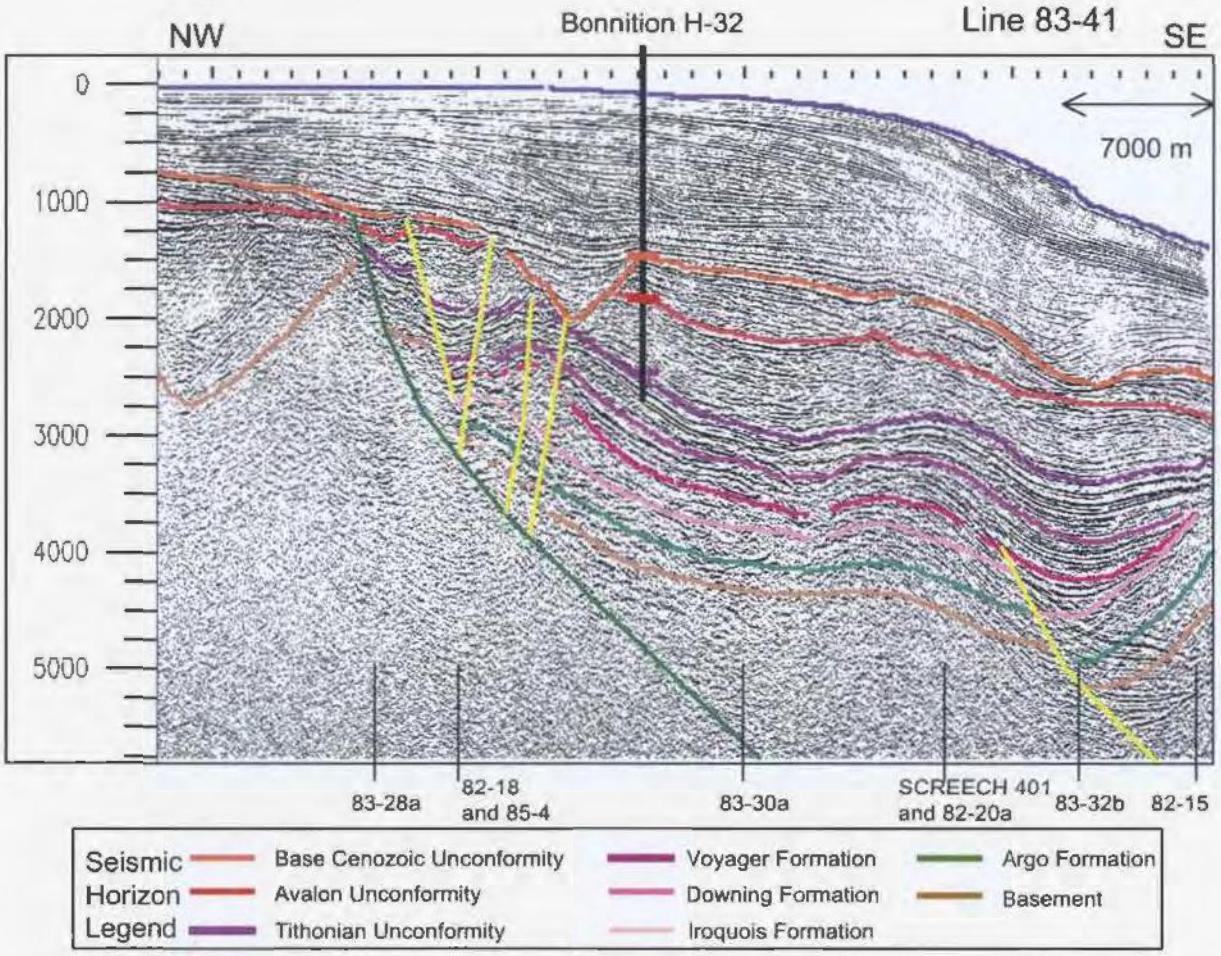

Figure 3.8. The Bonnition H-32 well ties to seismic line 83-41. This section shows the seismic and well log ties for major formations and unconformities in the well. The Base Cenozoic Unconformity is shown in orange, and the Avalon Unconformity shown in red. The Tithonian Unconformity is shown in dark purple. The well bottoms in the Upper Jurassic Rankin Formation.

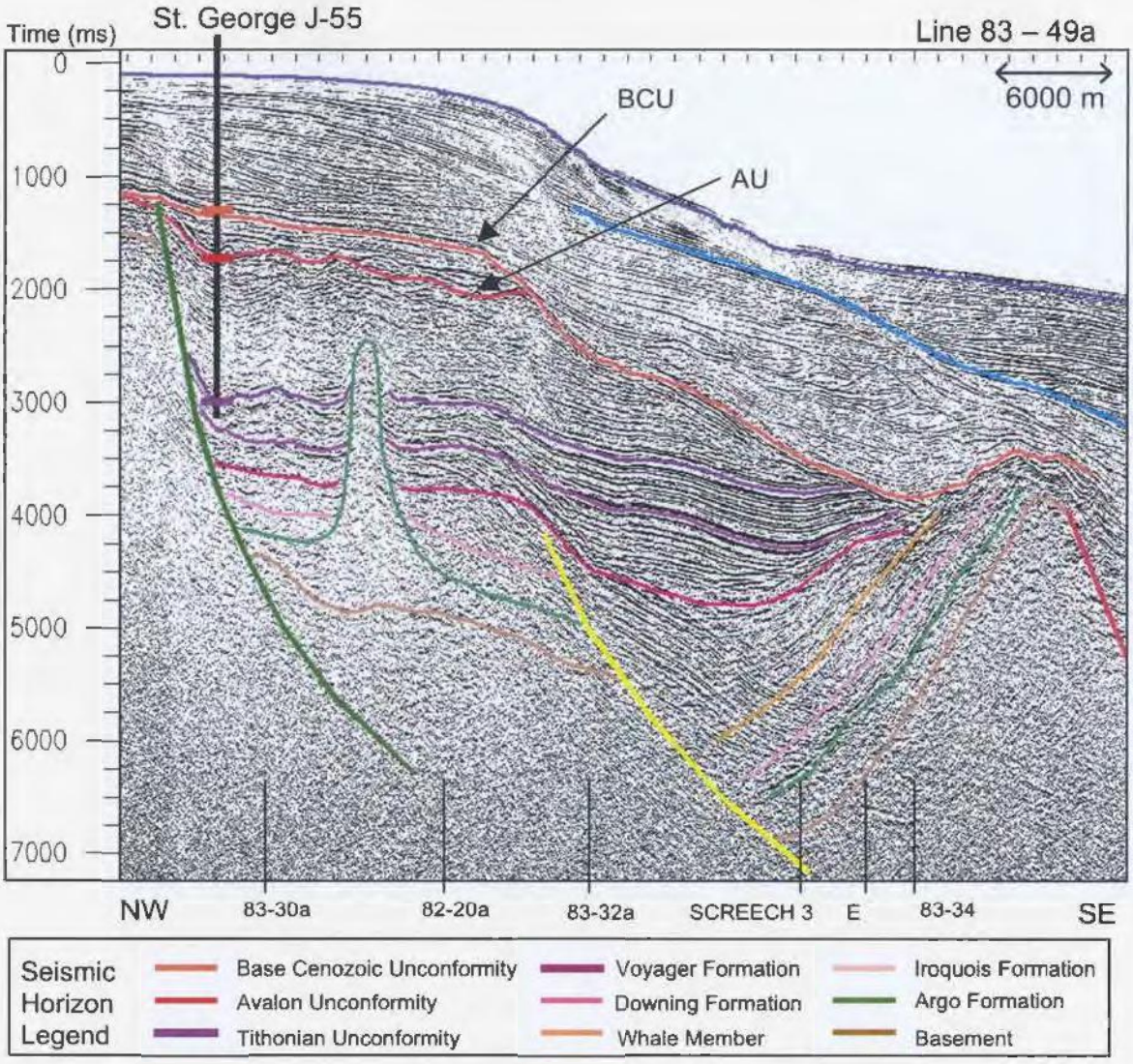

Figure 3.9. The St. George J-55 well ties to seismic line 83-49a. This section shows the seismic and well log ties for major formations and unconformities in the well. The Base Cenozoic Unconformity (BCU) is shown in orange, and the Avalon Unconformity (AU) shown in red. The Tithonian Unconformity ties well to the seismic data. This well bottoms in the Rankin Formation.

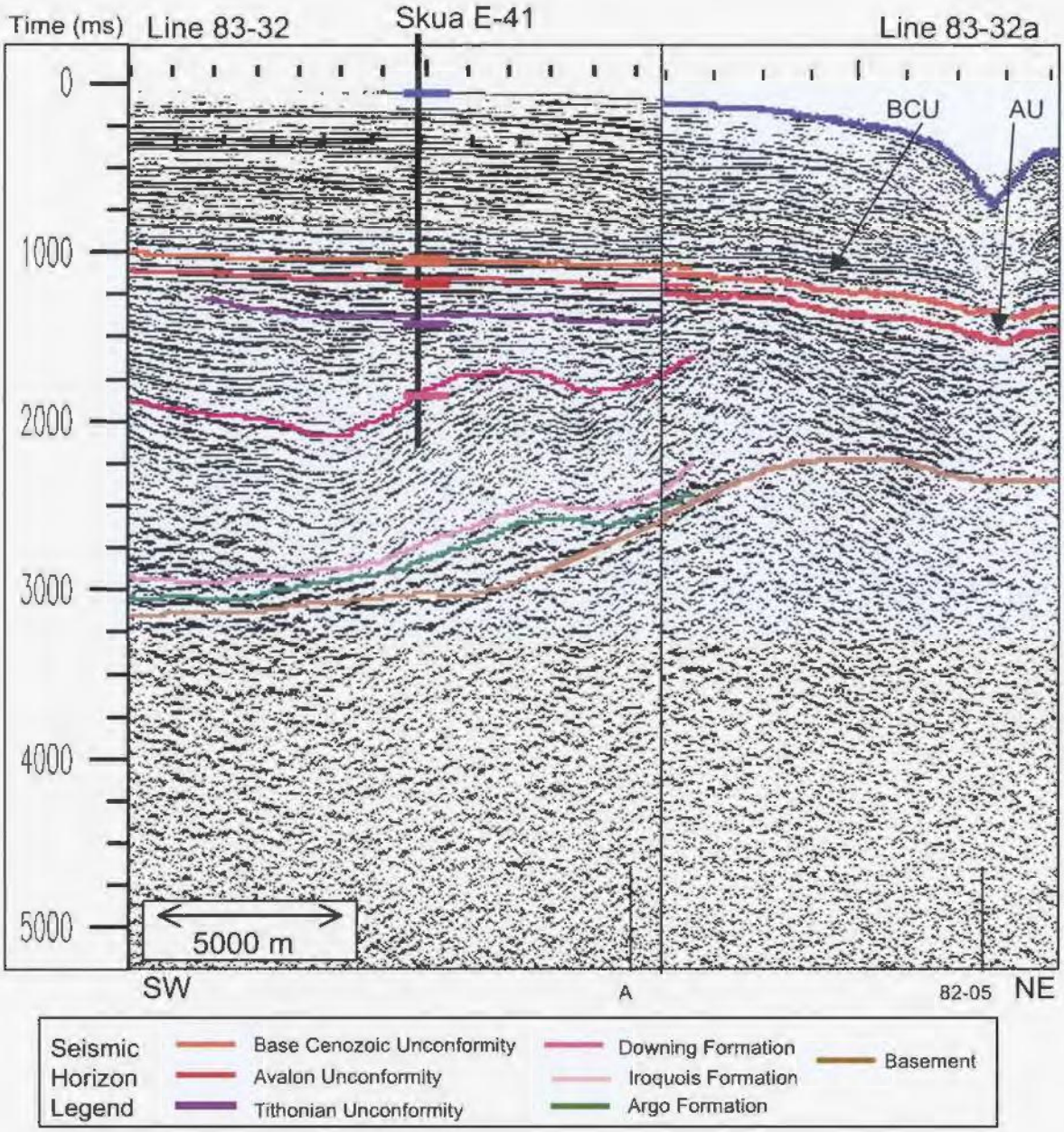

Figure 3.10. The Skua E-41 well ties to seismic lines 83-32 and 83-32a. This section shows the seismic and well log ties for major formations and unconformities in the well. The Base Cenozoic Unconformity (BCU) is shown in orange, and the Avalon Unconformity (AU) shown in red. The well tie to the Tithonian Unconformity (dark purple) is slightly off, while the tie to the Downing Formation (fushia) is reasonable.

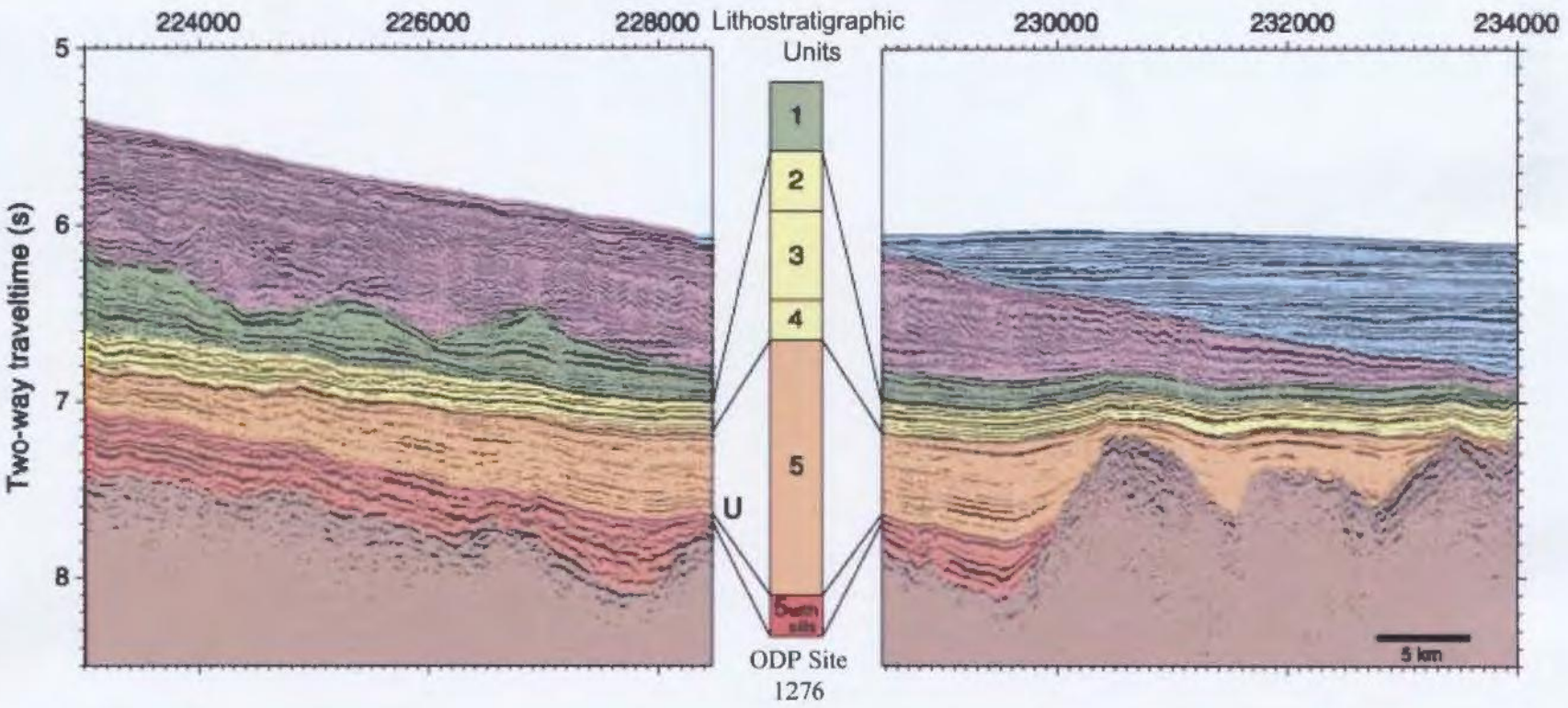

Figure 3.11. ODP Site 1276 correlations to seismic data. The seismic section is a portion of SCREECH Line 2MCS. The lithostatigraphic units correspond to the units described in Figure 3.6. *Modified from:* Shipboard Scientific Party, (2004b).

3.2.3 Sequences

Previous work by McAlpine (1990) and Grant et al. (1988) has divided the Jeanne d'Arc, Carson, Bonnition and Salar basins into depositional and seismic sequences. Depositional sequences are defined as conformable successions of strata bound at the top and base by unconformities or their correlative conformities (Vail et al. 1977, Vail et al. 1984), that represent intervals of geologic time. Seismic sequences are depositional sequences that are identifiable by their seismic character. The depositional and seismic sequences that have previously been interpreted in the Carson, Bonnition and Salar basins are outlined below in the following sections. In the Southern Jeanne d'Arc Basin sediments younger than Cenomanian overlie tilted Upper Jurassic to Upper Triassic sediments (Sinclair, 1995a). This observation also holds true for the Carson and Bonnition basins so the divisions of the Upper Triassic to Upper Jurassic by McAlpine (1990) in the Southern Jeannne d'Arc will be used for correlation wherever possible. For the Cretaceous and younger sections in the Carson and Bonnition basins the divisions by Grant et al. (1988) will be followed. For the Salar Basin, Grant et al. (1988) have divided the area into 6 seismic sequences and these will be followed for interpretation. Shipboard Scientific Party (2004b) have divided the deepwater Newfoundland Basin into 5 sequences (illustrated in Figure 3.11) based on the two deepwater wells drilled in 2003. Figure 3.12 illustrates the divisions of the depositional and seismic sequences used previously in the Carson, Bonnition and Salar basins, and the overlying colour coded seismic surfaces are the surfaces that will be mapped in this study. The seismic reflection surfaces that were chosen for mapping have a widespread presence across the margin.

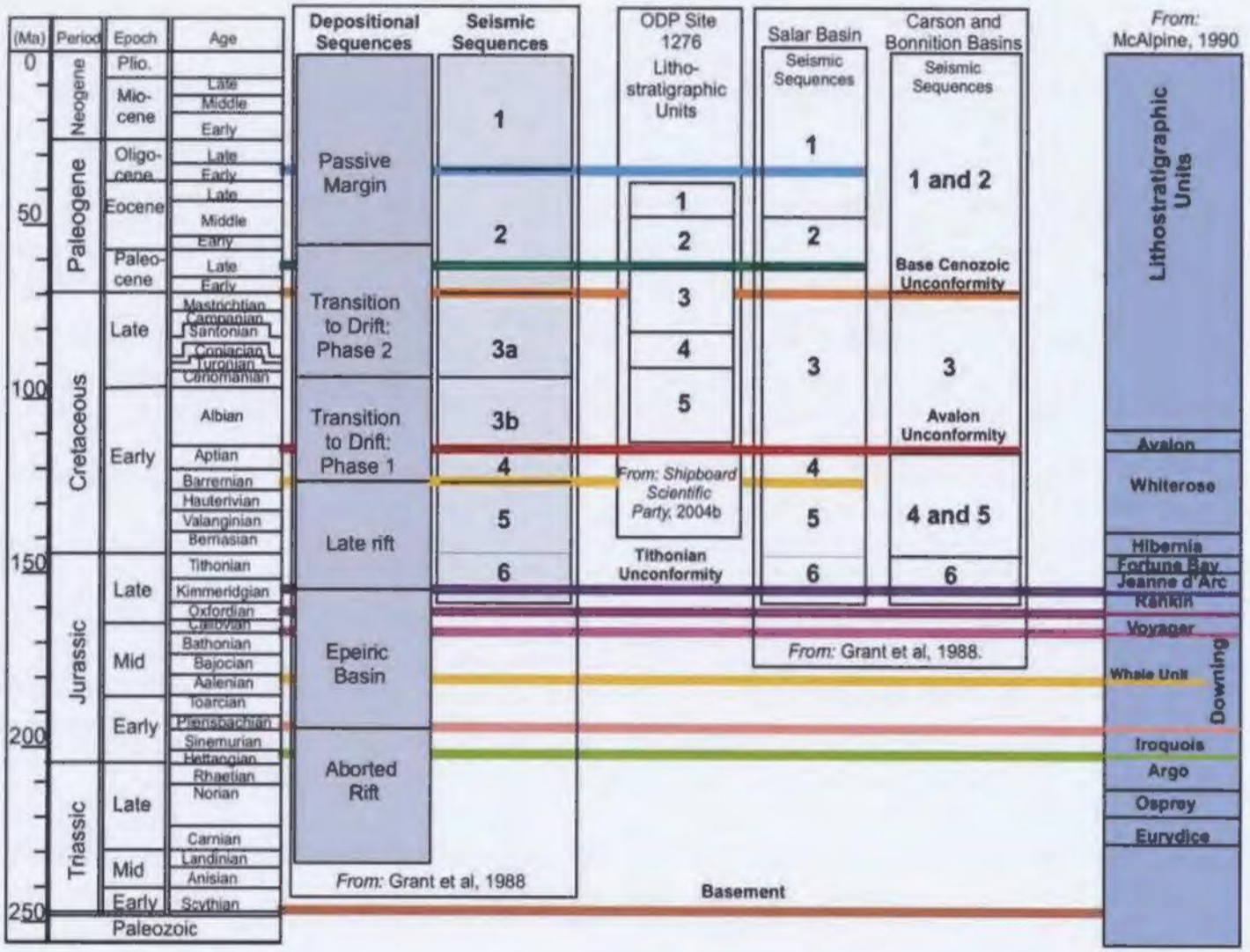

Figure 3.12. Naming conventions used by authors McAlpine, 1990, Grant et al. 1988, and Shipboard Scientific Party, 2004b, in the Carson, Bonnition and Salar basins. Sequences and formations that were interpreted in this thesis are divided by colour coded reflector surfaces shown in the columns for the Salar, Carson and Bonnition basins.

3.2.3.1 Formations in the Carson and Bonnition basins

McAlpine (1990) defined several lithostratigraphic formations ranging from Triassic to Jurassic in age in the Jeanne d'Arc Basin. The first is the Eurydice Formation which is Carnian-Norian to Rhaetian in age and deposited in generally arid conditions. The Osprey Formation which overlies the Eurydice is Carnian – Norian to Rhaetian – Early Hettangian in age and consists of halite interbedded with shale. This formation is unconformably overlain by the Argo Formation which is another evaporite formation of coarse crystalline halite of Late Hettangian to Early Sinemurian age. Its base in the Jeanne d'Arc Basin is generally correlated with an igneous unit, while the top of the formation is overlain conformably by the Iroquois Formation. The Iroquois Formation is an evaporite and dolomitic limestone unit that ranges in age from Pliensbachian to Toarcian. This formation is conformably overlain (unconformably in localized areas) by the Downing Formation which is Pliensbachian to Oxfordian-Early Tithonian in age. This formation consists of a lower thick silty shale, a middle limestone and an upper shale. The middle limestone unit is defined as the Whale Member and its age is constrained to the Toarcian to Bajocian. The Downing Formation is generally conformably overlain by the Voyager Formation which is an interbedded sandstone, shale limestone unit ranging in age from Late Bathonian to Early Oxfordian. This formation is overlain by the Early Oxfordian to Early Tithonian massive limestones of the Rankin Formation. The Rankin Formation generally consists of limestones and sandstones and is bounded on top by the Tithonian Unconformity, which is either angular or represented by its correlative conformity in the centre of the basin.

3.2.3.2 Depositional Sequences in the Salar Basin

Grant et al. (1988) proposed that the stratigraphic record around the Salar Basin can be divided into six depositional sequences that have a large aerial extent. The first depositional sequence is termed the Aborted Rift System and spans the Late Triassic to the Early Jurrassic. This sequence contains the Kettle red beds, the Eurydice shale-siltstone, the Osprey and Argo evaporites (halite) and the Iroquois dolomite and limestones. This depositional sequence shows a progression from deposition in a continental environment to deposition in a marine environment. The second sequence is the Epeiric Basin Sequence, which spanned Early to Late Jurassic. The shale and limestone Whale Member is deposited at the base of this sequence, the Voyager shale and Rankin limestone are then deposited with the top of this sequence being defined as the Middle Tithonian Unconformity. The third depositional sequence is termed the Late Rift. This sequence spans from Late Jurassic to Barremian time and sandstones from the Jeanne d'Arc, Hibernia and Avalon formations are separated by shale units that were deposited during this period. The fourth sequence is the Transition to Drift: Phase 1. This sequence spanned from Barremian to Cenomanian time with siliciclastics forming the Logan Canyon Formation. The fifth sequence is the Transition to Drift Phase 2, and covers Late Cretaceous to Paleocene time. Transgressive marine sediments of the Dawson Canyon Formation were deposited. The breakup of Labrador and Greenland and Greenland and Northern Europe is inferred to be represented by the Late Cretaceous and Early Cenozoic Unconformities. The sixth is the Passive Margin sequence which spans

from Eocene to present. The margin was tilted seaward during this time allowing shales, chalks and mudstones of the Banquereau Formation to be deposited.

3.2.3.3 Seismic Sequences in the Carson and Bonnition basins

The Carson and Bonnition basins contain sediments ranging from the Late Triassic to the present. Figure 3.13 illustrates two seismic profiles, a strike line (part A) and a dip line (part B). This figure shows the general seismic characteristics of the seismic units that were interpreted on the margin. Basement on both seismic profiles is shown to be fairly unreflective and difficult to pick. Overlying basement is the Eurydice red-beds, the Osprey and the Argo Formations. These formations compose the next seismic unit (between the green and brown horizons). The top of this sequence is generally a high amplitude low frequency reflection, representing the top of the Argo Formation. Below this reflection the unit can be unreflective and slightly chaotic. The Iroquois Formation overlies the Argo Formation and it is characterized as a medium amplitude reflection in most areas with a weaker reflective package below it. In Figure 3.13 the top of this formation is coloured light pink. The Downing Formation overlies the Iroquois Formation and the reflections in this unit exhibit large variations in amplitude. In areas where the Whale Member is well developed, a strong reflection sequence is present as shown in Figure 3.13 part A. In the absence of the Whale Member, weak internal reflections are present. The Voyager Formation overlies the Downing Formation and is weakly reflective when compared to the overlying and underlying formations. The Upper Jurassic Rankin Formation below the Tithonian Unconformity in Figure 3.13 part

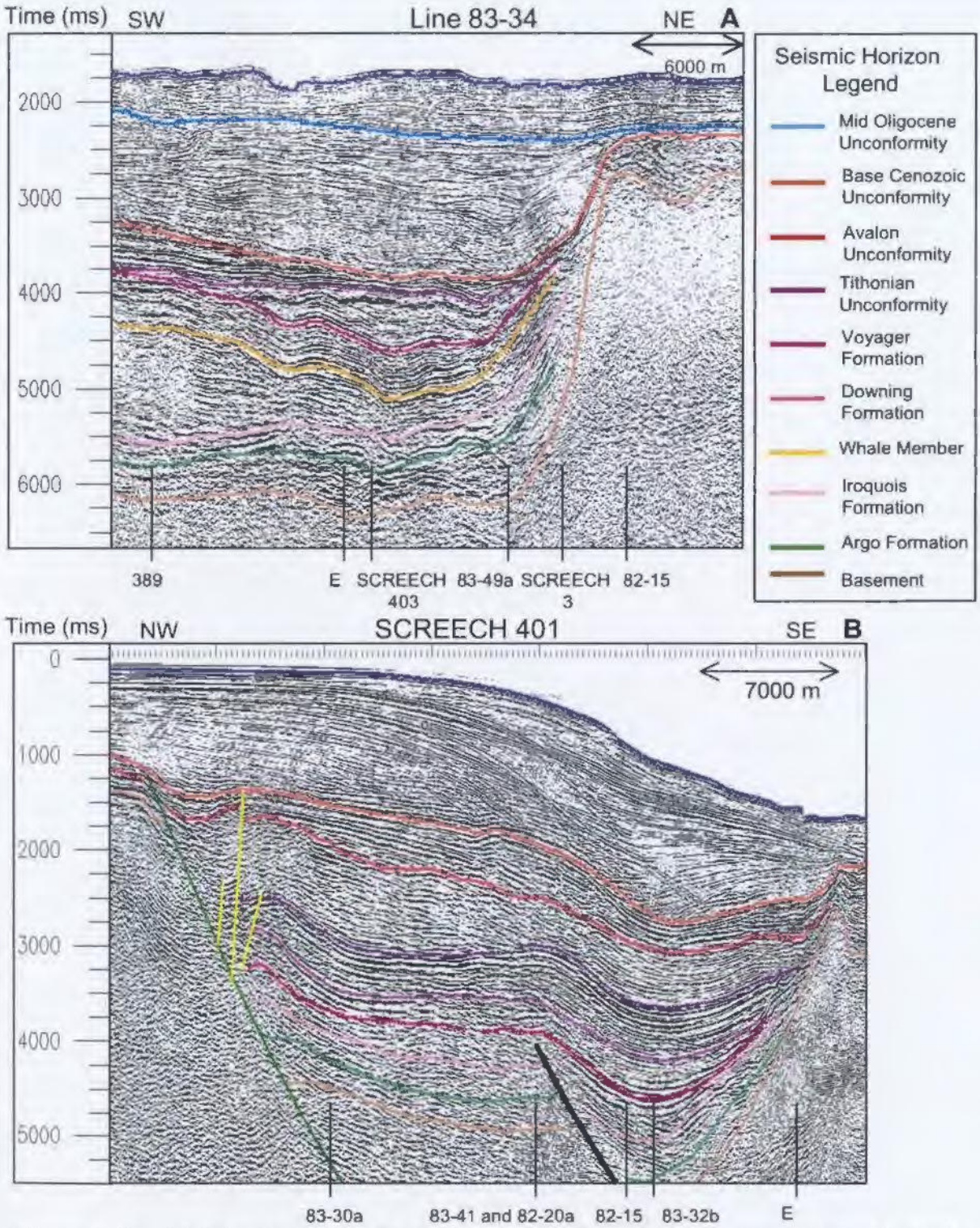

Figure 3.13. A) Seismic section 83-34 illustrating the major sequences picked in both the Carson and Bonnition basins and their general seismic character. In this section the Tithonian Unconformity has been eroded by the Base Cenozoic Unconformity. B) SCREECH line 401 also showing the major sequences. In this line the Base Cenozoic, Avalon and Tithonian unconformities are all present.

B, and below the Base Cenozoic Unconformity in Figure 3.13 part A is a high amplitude reflection sequence which is easily distinguishable from the overlying and underlying sediments. Cretaceous sediments are bound on top by the Base Cenozoic Unconformity and at their base by the base of the Hibernia Formation. The amplitude of the Cretaceous reflections appear to be fairly uniform. When comparing the reflections from the Cenozoic sediments to the reflections from the Cretaceous sediments, the Cretaceous reflections appear to be slightly higher in amplitude. Upper Cretaceous sediments (shown in Figure 3.13 part B) are roughly separated from Lower Cretaceous sediments by the Avalon Unconformity. While the seismic amplitude of the Cretaceous sediments for the most part appears to be seismically uniform, it is noticeable that the Upper Cretaceous sequence is slightly higher in amplitude than the Lower Cretaceous. In Figure 3.13 the Base Cenozoic Unconformity is clearly evident and is shown to erode units below.

3.2.3.4 Seismic Sequences in the Salar Basin

Grant et al. (1988) delineated six seismic sequences that were mapped around the SE Newfoundland margin. These sequences which are shown in Figure 3.12 will be mapped in the Salar Basin, along with a few additional seismic horizons. Figure 3.13 illustrates the seismic characteristics of the sequences that were interpreted in the Salar Basin. Basement in the Salar Basin is difficult to map as it appears to generally be non-reflective (mapped as the brown horizon in Figure 3.14). The Upper Triassic Osprey or the Lower Jurassic Argo evaporate Formations are found in the Salar Basin (top is shown in green on Figure 3.14). The top of this sequence is marked by a high amplitude reflection, with

weak reflectivity below. Grant et al.'s (1988) seismic sequence 6 is interpreted to contain Upper Jurassic carbonates (Rankin Formation) and possibly other earlier formations. The sequence is bound at the top by the Tithonian Unconformity (purple in Figure 3.14) and the sequence contains a few high amplitude events that are separated by thick intervals of low reflectivity. Sequence 5 from Grant et al. (1988) is interpreted to represent Cretaceous sediments that are of Barremian age and older. The sequence generally shows weak reflectivity across most of the basin and the top of the sequence is a major unconformity, shown in yellow on Figure 3.14. Sequence 4 from Grant et al. (1988) is fairly thin and is generally only clearly found in the basin axial zone. The sequence is bound at the top by the Avalon Unconformity and Grant et al. (1988) interpret the base of sequence 4 to represent the transition to drift. The interval is weakly reflective and interpreted by Grant et al. (1988) to be composed of alternating marls, pelagic carbonates and turbidites and ranges from Barremian to Aptian in age. The top of Sequence 3 is bound by the Base Cenozoic Unconformity, while the base is the Avalon Unconformity which is Aptian in age. This sequence is generally reflective across the basin, showing strong well developed internal reflections. The Middle Oligocene Unconformity separates Grant et al's (1988) Sequence 2 from Sequence 1, and reflections above and below this unconformity are shown to be quite variable in seismic character.

3.3 General structure of the study area

The Newfoundland continental margin developed during several phases of northward propagating rifting and spreading (Hubbard et al. 1985). Rifting commenced during the

Late Triassic in the SE portion of the margin and continued until the Early Jurassic. Prior to describing the various components of the margin, a broad description of the overall structure is given to provide a context for the detail that follows. Figure 3.15 is a map of the major structural features and trends. The margin is dominated by the NE-SW trending Carson, Bonnition and Salar basins. The major basement faults on the margin also trend NE-SW and terminate towards the north of the study area, where the generally N-S trending faults of the Flemish Pass take over. To the south the basement faults continue trending NE-SW to the South Bank High where they terminate.

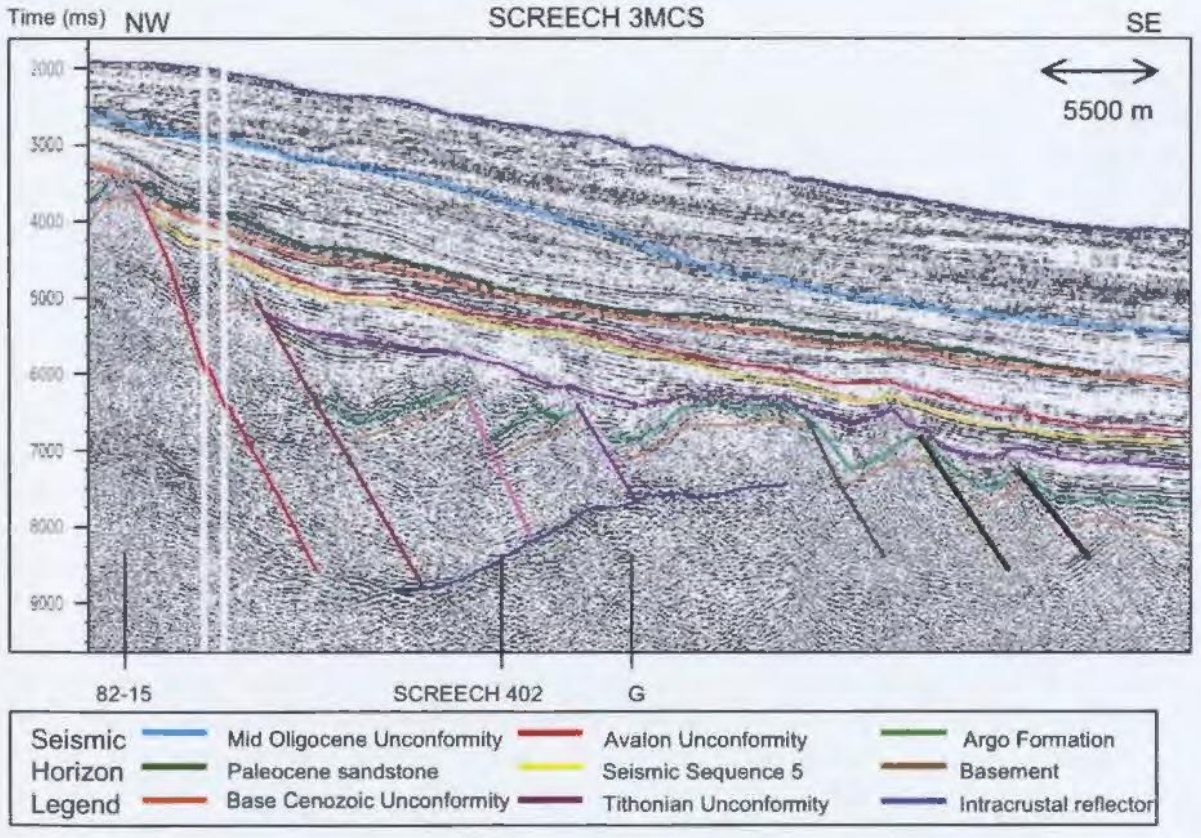

Figure 3.14. Seismic section from SCREECH 3 MCS illustrating the major sequences in the Salar Basin.

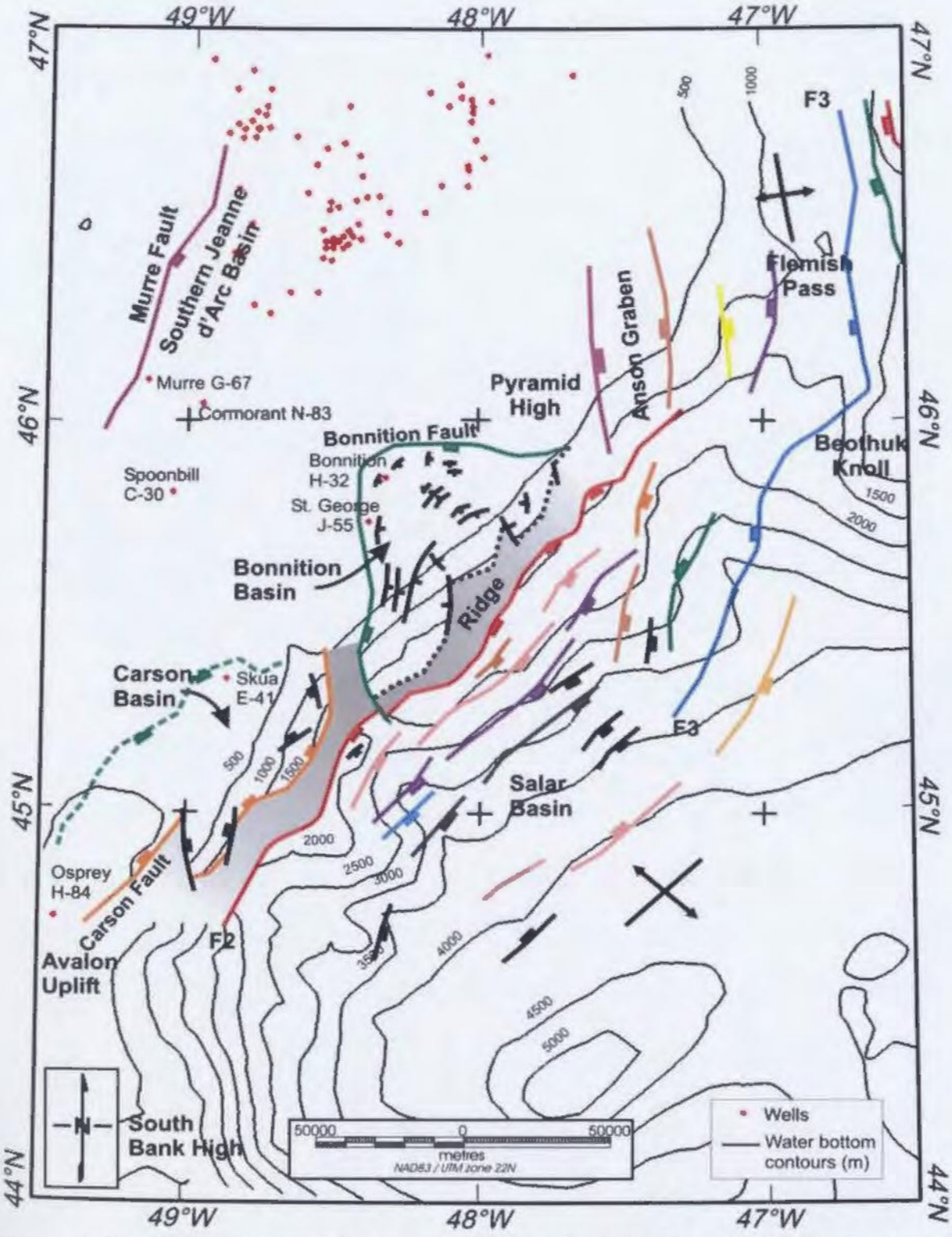

Figure 3.15. Major structural features on the Newfoundland margin in the thesis study area. Note the two distinct directions of rift faults: the generally N-S trend in the Flemish Pass area and the NE-SW trend in the Carson, Bonnition, and Salar basin areas.

The Carson and Bonnition basins both occupy the shelf slope margin but vary significantly in their structure. The Bonnition Basin is bounded to the west by a major listric fault (here named the Bonnition Fault) with down throw to the east. The Carson Basin to the south is bounded to the east by a major basin bounding fault (here named the Carson Fault) which down throws to the west. The area between the basins represents a change along strike in the fault polarity. It is in this area that an accommodation zone has formed. An accommodation zone in this thesis is defined as a region separating oppositely dipping rift-border and intra-basin fault systems (Younes and McClay, 2002).

The Bonnition Basin (shown in Figure 3.15) is slightly wider and more irregularly shaped than the Carson Basin and internally it is complexly faulted. Salt movement plays a significant role in its deformation and structure. The northern boundary of the Bonnition Basin is provided by a combination of the Bonnition Fault, which curves to the east, and the N- to NE- trending faults of Flemish Pass. The eastern boundary of the basin is a large ridge that trends NE –SW. This ridge extends from south of the study area to the north into the Flemish Pass where it eventually dies out. It is generally wider towards the north and south and more deeply buried where it crosses the area forming the accommodation zone. A large portion of this ridge can be clearly identified on the gravity map of the area (Figure 3.3).

The Carson Basin (depicted in Figure 3.15) is separated from the Bonnition Basin to the north by an accommodation zone. It is bounded to the east by the Carson Fault which is

shown to be offset along the margin. The western boundary of the Carson Basin is provided by a fault antithetic to the Carson Fault, which throws to the east. The Carson Basin extends to the southwest and eventually terminates against the South Bank High (Grant et al. 1988). This basin is less complexly faulted than the Bonnition Basin, but salt movement causes sedimentary layers to fold, changing their dip and creating structure in the basin.

The Salar Basin, as defined by the sub-basin of Tucholke et al. (1989), extends from the Flemish Pass Basins in the north through the study area continuing to the South Bank High. The basin is located east of the major ridge. The fault associated with the eastern edge of the ridge was termed 'F2' by Enachescu (1992a), and it runs in a NE-SW direction along a large portion of the margin. This fault throws down to the east and its throw tends to be greater in the northern and southern portions of the Salar Basin when compared with the central area. The F2 Fault tends to show the least throw in the area adjacent to the accommodation zone. To the east, the Salar Basin is generally bounded by the continuation of the Beothuk Knoll which runs NNE-SSW from the Flemish Pass Basins. The western side of the Beothuk Knoll is bounded by a western dipping fault. This fault represents the continuation of the western side of the Beothuk Knoll in the thesis study area. It was defined as F3 by Enachescu (1992b) and is a major antithetic fault (down to the west) dying as its throw decreases in the central region of the study area. In some areas, the F3 Fault bounds salt structures that form the eastern edge of the basin. The Salar Basin is highly faulted, consisting of many rotated basement fault

blocks that have moved down to the east and salt structures that have formed in localized areas.

3.3.1 Faulting

Major basement faults in the Carson, Bonnition and Salar basins follow a NE-SW trend as sbown in Figure 3.15. Most of the major faults are normal faults with movement down to the east, except for the basin bounding Carson Fault, which moves down to the west. Figure 3.16 illustrates a typical seismic section and the faulting that occurs in both the Bonnition and Salar basins. Faults in the Bonnition Basin that are synthetic to the basin-bounding Bonnition Fault generally offset basement. In the Salar Basin many faults synthetic to the F2 Fault are present. For these faults the intervening rotated fault blocks have widths of between 5 and 10 km and the bounding faults exhibit throws from 1 to 2 seconds of two way travel time (equivalent to ~ 1500 to 3000 m, assuming a velocity of 3000 m/s) as illustrated in Figure 3.16.

In the Carson Basin a major fault antithetic to the Carson Fault defines the western limit of the basin and forms along the same trend as the Bonnition Fault. Figure 3.17 illustrates the typical faulting that occurs in the Carson Basin. In this figure it is evident that the Carson Fault moves down to west. The figure also shows movement on the antithetic fault. In this section the Carson Fault tends to be steep and exhibits a large amount of throw when compared to other faults in both the Bonnition and Salar basins.

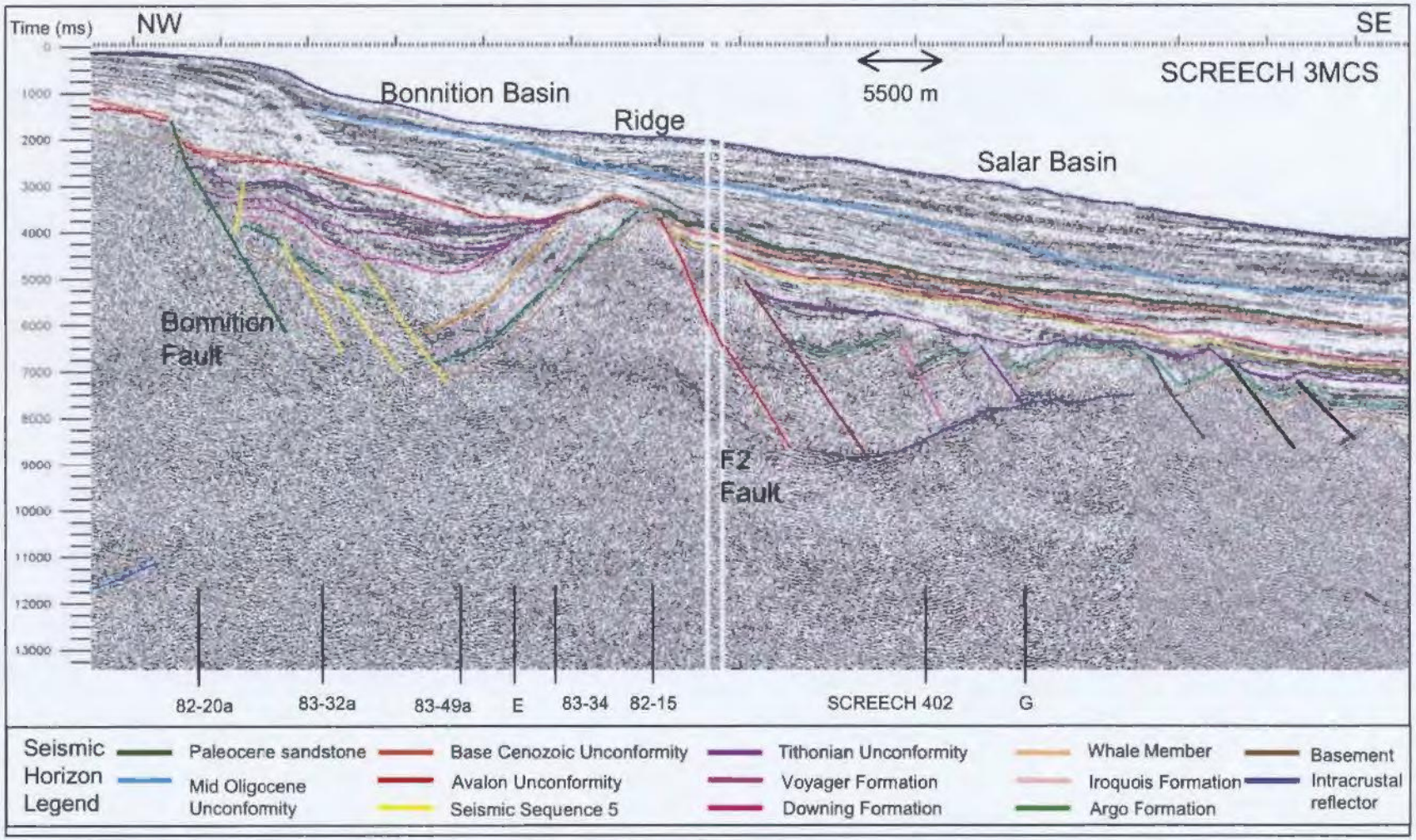

Figure 3.16. Seismic section from SCREECH 3 MCS. This transects passes through the Bonnition and Salar basins and illustrates the typical faulting and structure that occurs in both basins. The seismic horizons that were interpreted are also indicated on the seismic line.

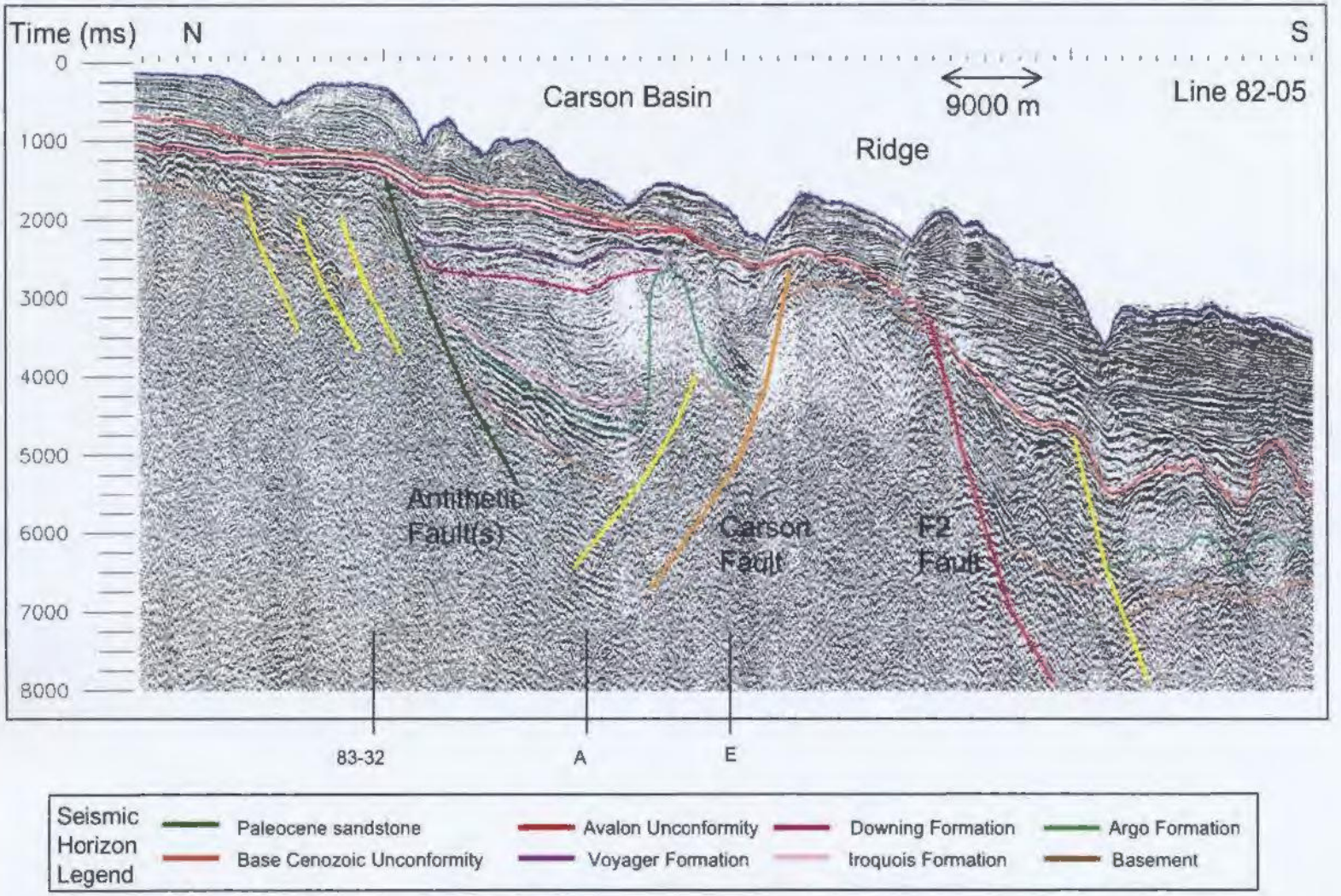

Figure 3.17. Seismic section 82-05 through the Carson Basin illustrating the typical faulting that occurs in this basin. Note the basin-bounding Carson Fault and the major antithetic fault.

The faults in the Salar Basin offset basement and the fault tips tend to lie at or around major angular unconformities in the sediment record (for ages, see below). In the Salar Basin antithetic faults tend to be associated with salt structures. A major transfer zone cuts through the Salar Basin, separating zones where rifting has occurred at different orientations. This transfer zone occurs between the N-S trending grabens of the Flemish Pass and the NE- SW faulting of the Salar Basin.

3.4 Development of Seismic Sequences in Study Area

The seismic sequences and horizons that were used to interpret the thesis area were shown previously in Figure 3.12, and the seismic characteristics of the units were explained in Section 3.2.3. The seismic sequences interpreted were different between the two basins on the shelf (Carson and Bonnition) and the Salar basin because the shelf and slope portions of the margin record different periods of the stratigraphic record. Jurassic and older strata are more readily preserved in the shelf areas in the Carson Basin, while a more extensive Cretaceous and Cenozoic section is generally found under the slope.

Landmark's SeisWorks software package was used to map the horizons and faults in the study area. All horizons were loop correlated around the study area, and tied to well data where available. The seismic horizons and faults were all interpreted in the time domain, and formation picks represent the top of the various formation. The horizons were then converted to depth using the interval velocity model previously explained in Section 3.2.1, and found in Appendix 3.

3.4.1 Shelf - Carson and Bonnition basins

3.4.1.1 Basement

Basement in this area of the margin is most likely composed of Paleozoic or Precambrian rocks (Enachescu, 1992a). Basement depth is fairly uniform on the shelf around 1500m (1500 ms two-way travel time), while in the Carson and Bonnition basins the depth varies considerably along the margin. In the Carson Basin the deepest section is found in the north-eastern area of the basin at approximate depths of 8000m (5200 ms – two way travel time and assuming a velocity of 3000 m/s). In the Bonnition Basin the deepest section is generally found in the south-west area of the basin at a depth of approximately 10000m (7000 ms – two way travel time and assuming a velocity of 3000 m/s). No wells penetrate basement in the Carson or Bonnition basins and as in the southern Jeanne d'Arc Basin, top basement is difficult to image due to the thickness of the overlying sediments and multiples that can mask the reflection. Therefore the interpreted top basement picks in the Carson and Bonnition basins represent "acoustic" basement and real basement may be deeper. On all seismic sections this unit is annotated brown and represents the deepest reflections (or lack thereof) imaged on the seismic lines. Figure 3.18 is a depth structure contour map illustrating the depth (m) to basement. The major basins (Carson, Bonnition, Southern Jeanne d'Arc, Flemish Pass and Salar) are evident on this map.

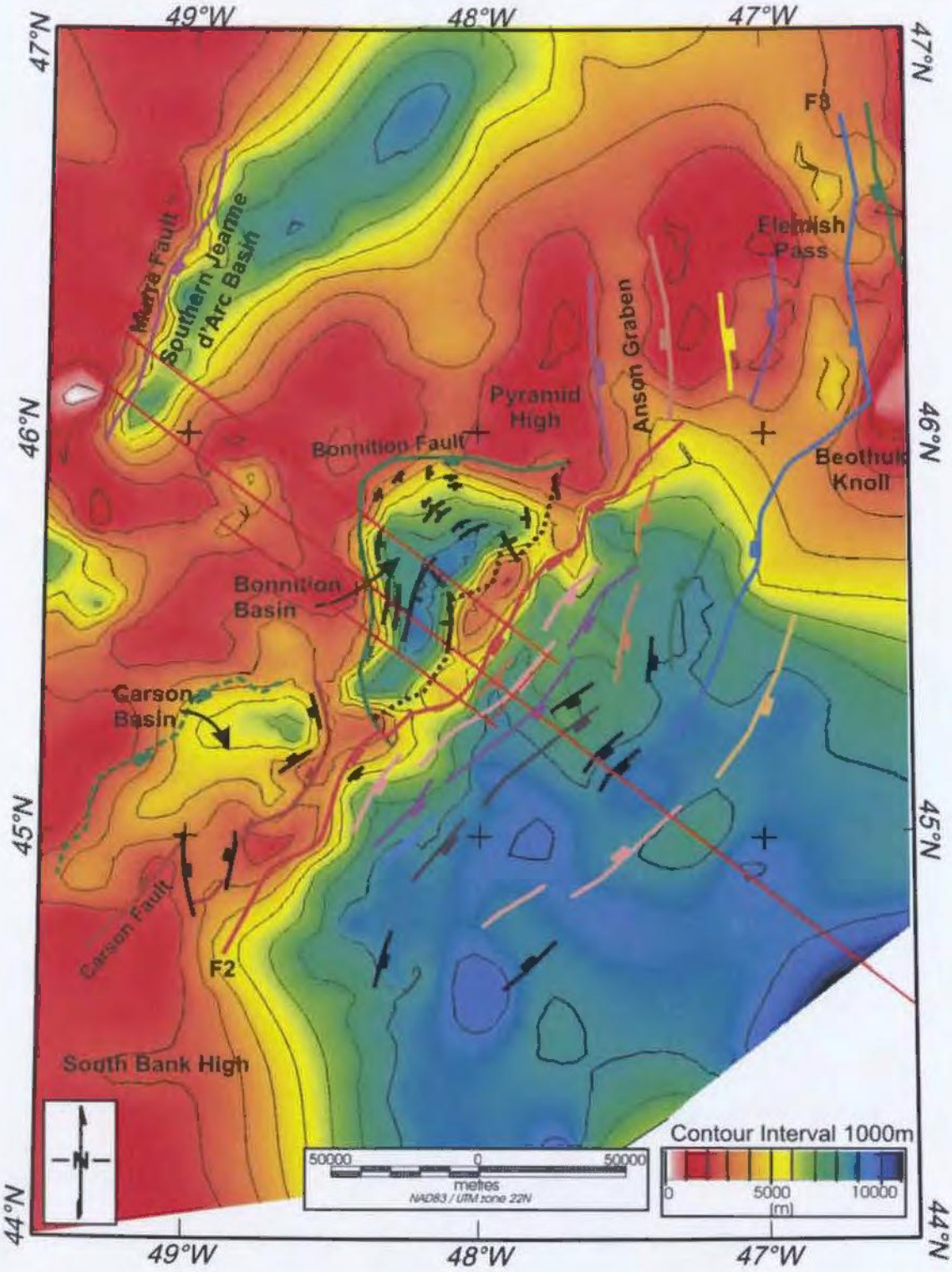

Figure 3.18. Depth structure contour map to basement in the thesis study area. Note the locations of the Carson, Bonnition and Southern Jeanne d'Arc basins.

3.4.1.2 Eurydice, Osprey and Argo Formations

The Eurydice Formation is the oldest preserved formation in the Carson and Bonnition basins, and in the Jeanne d'Arc Basin it directly overlies basement. In the Carson and Bonnition basins this formation was not mapped separately due to difficulty in distinctly differentiating it from the overlying formations. The Osprey Formation overlies the Eurydice and in the Southern Jeanne d'Arc Basin its top is generally defined by an igneous (basalt) unit. In the southern Jeanne d'Arc Basin, this reflector is widely mappable and can be used to separate the Osprey and the overlying Argo Formation.

Figure 3.19 shows an interpreted seismic section adjacent to the Cormorant well in the Southern Jeanne d'Arc Basin and a typical seismic section in the Bonnition Basin. In this figure it is evident that the basalt reflector which is noticeable in the Jeanne d'Arc Basin is not readily distinguished in the Bonnition or Carson basins.

In the Bonnition and Carson basins a widely mappable and relatively strong reflector represents the top of the Argo evaporites that overlie the Osprey and Eurydice Formations. This reflector was mapped throughout the basins and on all seismic sections it is coloured green. Figure 3.20A, a depth structure contour map of the Top Argo illustrates its extent and structure across the basins. In the Carson Basin the Argo Formation is bounded to the NW by the major antithetic fault and to the NE by the accommodation zone and the Carson Fault. The extent of the Argo Formation to the SE is limited by the ridge. The thickness of this formation in the Carson Basin is variable

with thicker sections tending to be found towards the south. Small amounts of diapirism are visible which is generally concentrated near the bounding faults as shown in Figure 3.21. In this basin the general dip direction of this unit is to the northeast.

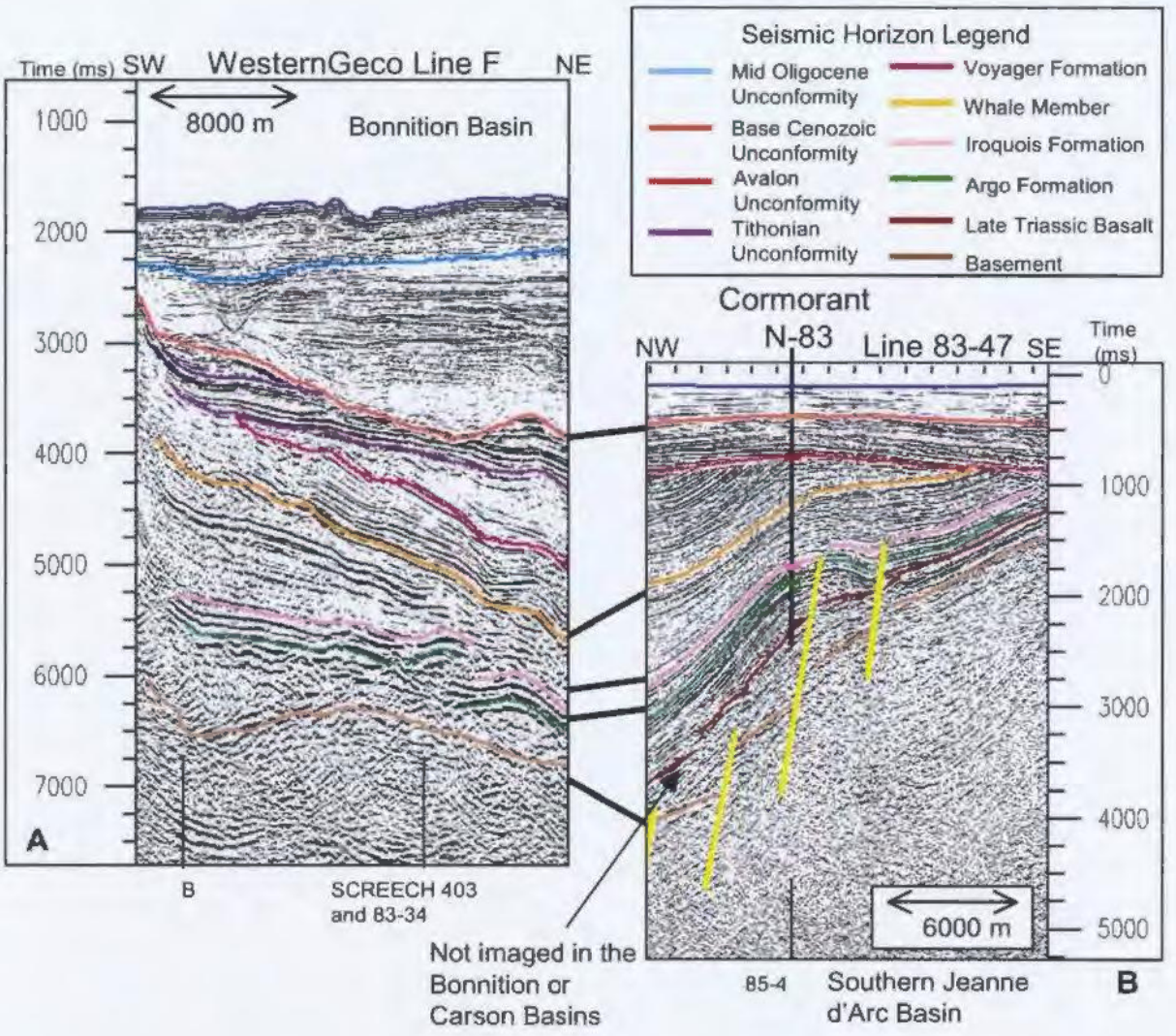

Figure 3.19. Interpreted seismic sections comparing seismic characteristics of reflections in the Southern Jeanne d'Arc and Bonnition basins. Part A shows proprietary line WesternGeco F in the Bonnition Basin. Part B shows the Cormorant N-83 well on line 83-47 in the southern Jeanne d'Arc Basin. The strong basalt reflection (dark red) in the Southern Jeanne d'Arc Basin is not imaged in the Bonnition Basin.

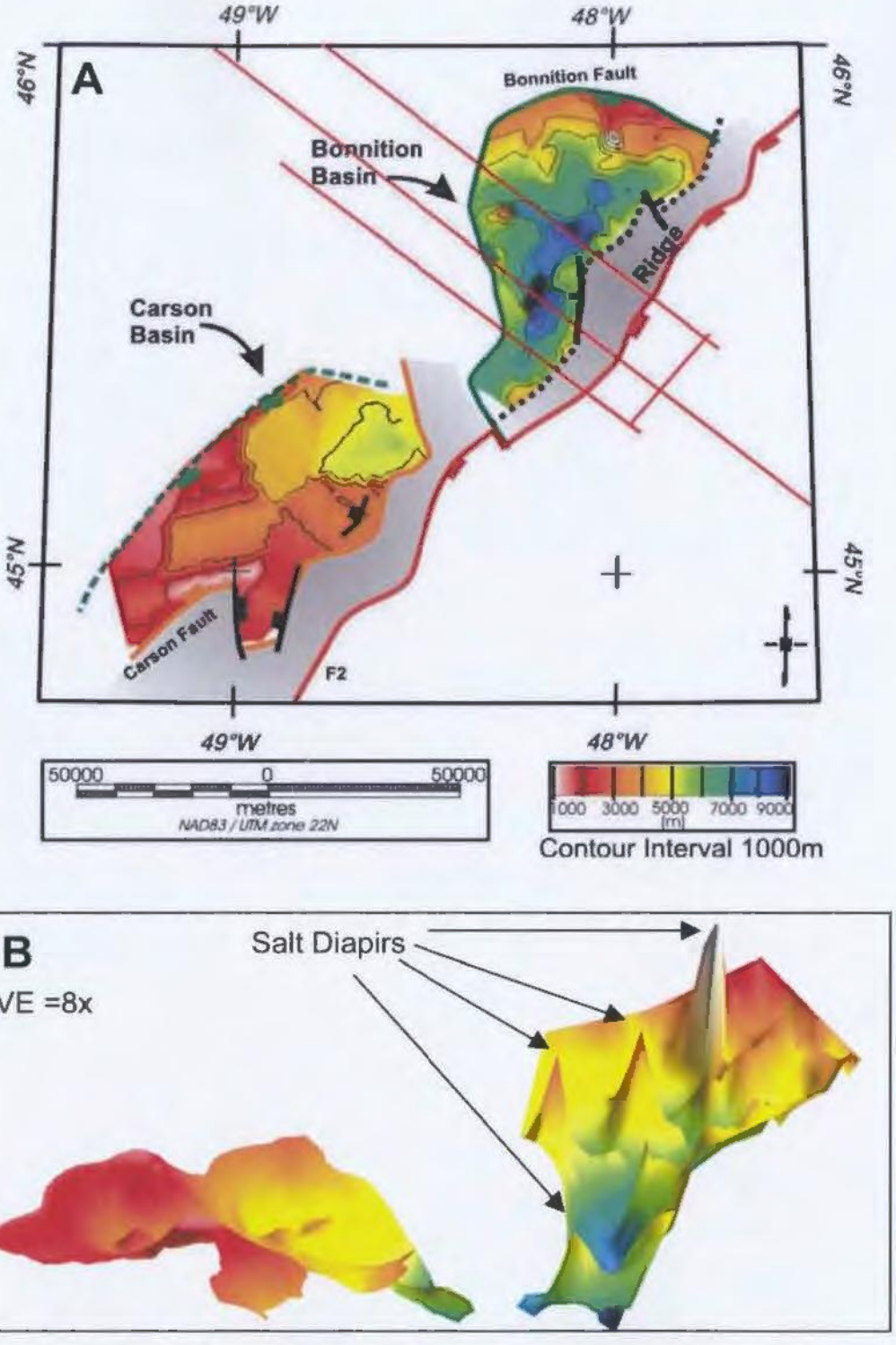

Figure 3.20. A) Depth structure contour map of the top of the Argo and Osprey Evaporites in the Carson and Bonnition basins. B) A 3-dimensional view the top of the formation at 8x vertical exaggeration. The reflector is tilted near the basin margins and many salt diapirs appear near the basin edges.

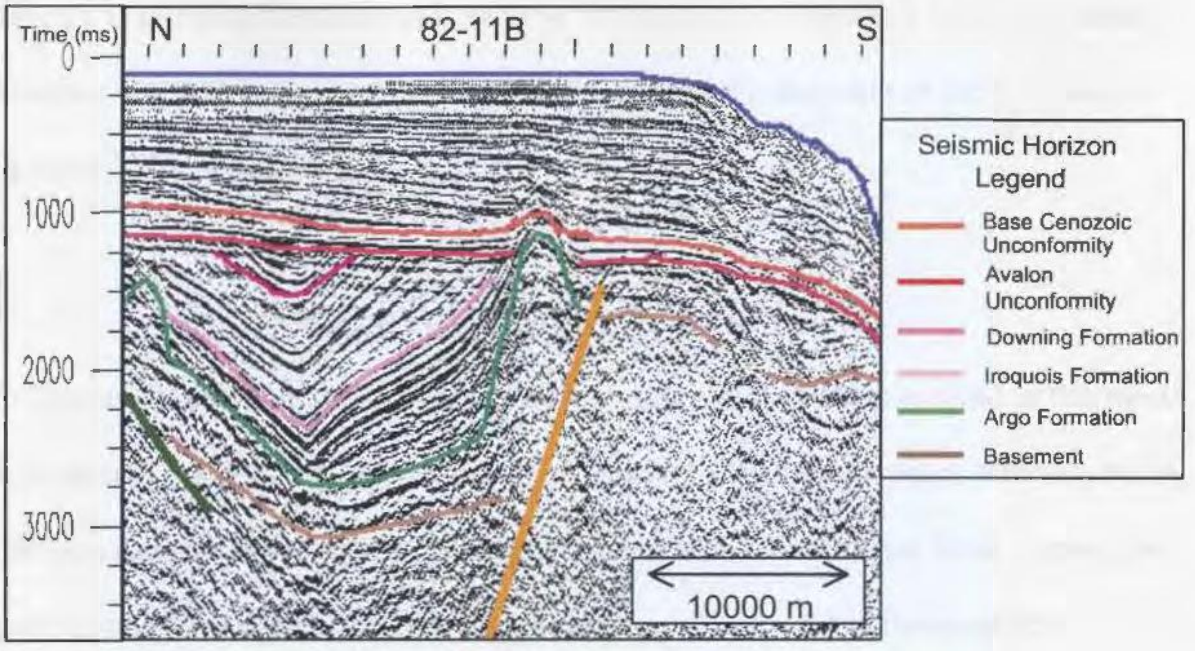

Figure 3.21. Seismic Line NF 82-11B illustrating salt diapirism in the Carson Basin. This diapirism is generally located near major faults in the basin.

In the Bonnition Basin the Argo Formation is bounded to the north and west by the Bonnition Fault, and in the south the formation is truncated or eroded by the Base Cenozoic Unconformity as it reaches the ridge. To the east the formation is limited by the ridge. On the depth structure contour map (Figure 3.20) local salt diapirs are present, and the top of the formation is structurally complex. The formation top is tilted in areas near the basin boundaries and plunges deep into the centre of the basin, especially in the southern area. Salt diapir formation tends to be constrained to the edges of the basin.

A large domal salt feature is interpreted towards the NE portion of the basin. Figure 3.20B highlights areas where salt diapirism occurs. The thickness of this unit (the Argo,

Osprey and Eurydice formations) is variable throughout the Bonnition Basin, but tends to be thicker towards the centre of the basin. The general dip direction of the formation in this basin is to the south-west.

3.4.1.3 Iroquois Formation

The Iroquois Formation overlies the Argo Formation, on all seismic sections in this thesis the formation top is coloured light pink. In Figure 3.19 the seismic characteristics of this formation can also be compared to those in the Southern Jeanne d'Arc Basin. From this figure a reasonable correlation between the Southern Jeanne d'Arc Basin and the Bonnition and Carson basins can be made. Figure 3.22 illustrates a depth structure contour map of the Iroquois Formation. In the Bonnition Basin the formation is bounded to the south and southeast by the ridge, or eroded by the Base Cenozoic Unconformity in areas where the formation top is highly tilted on the basin margins. In the north and west it is bounded by the Bonnition Fault and in the east it is generally tilted and eroded by the Base Cenozoic or it onlaps onto the Argo Formation. Similar to the Argo Formation, the Iroquois also generally dips toward the southwest.

In the Carson Basin, the Iroquois Formation is bounded to the west and the north by an antithetic fault and to the east by the accommodation zone and the Carson Fault. To the south the ridge and the Carson Fault bound the formation. The formation in the Carson Basin generally dips to the northeast. The thickness of this unit seems to remain relatively uniform throughout the basin.

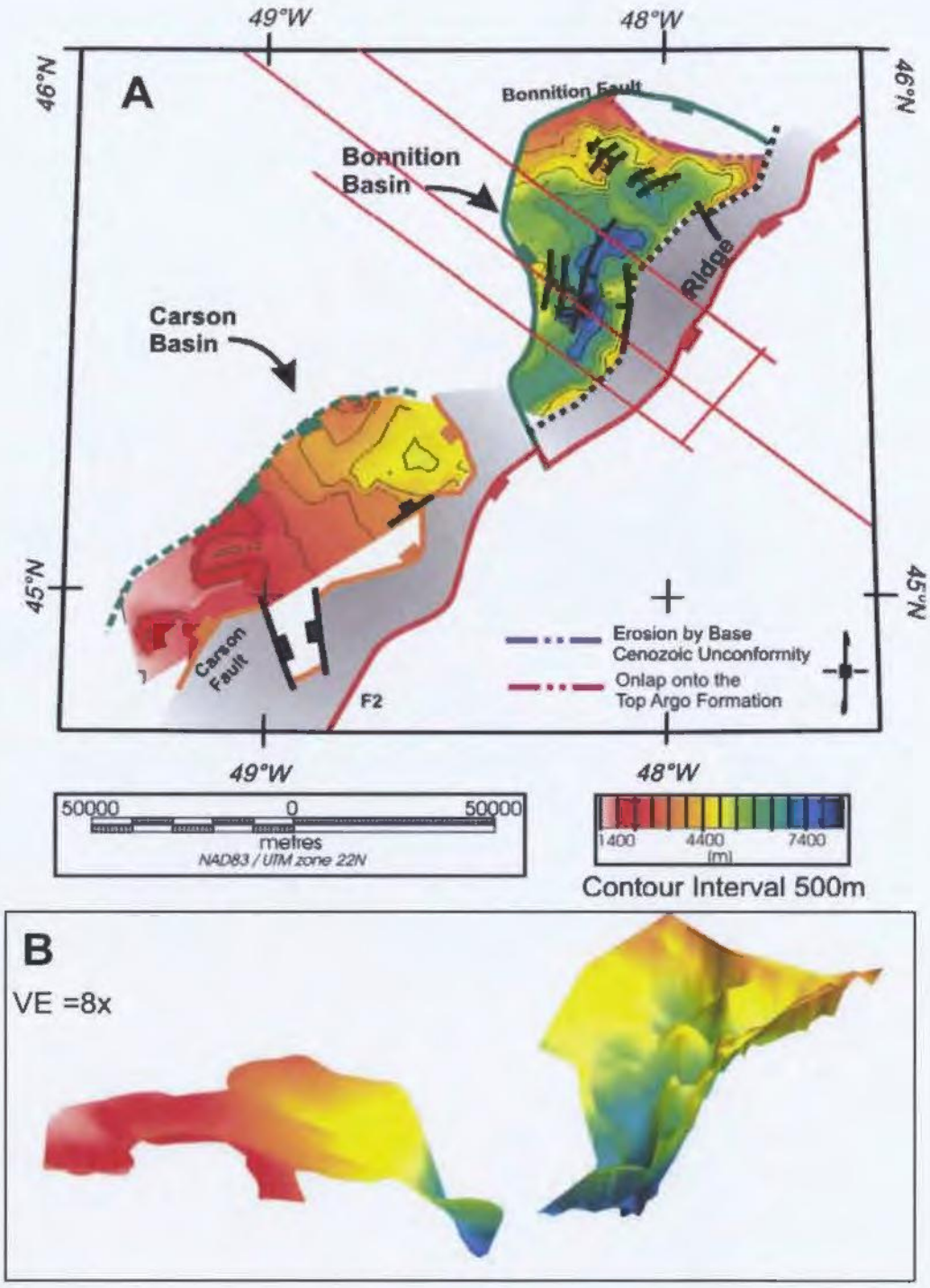

Figure 3.22. A) Depth structure contour map of the top of the Iroquois Formation. The formation closely follows the structure of the Top of the Argo Formation. B) A 3-dimensional view of the top of the formation at 8x vertical exaggeration. This reflector is also tilted near the basin margins.

3.4.1.4 Downing Formation

The Downing Formation overlies the Iroquois Formation and the contact between the two formations tends to be conformable although in localized areas it can be unconformable with the Downing downlapping onto the Iroquois Formation as shown in Figure 3.23. On all seismic sections this contact is coloured fuschia. The Downing Formation shows strong internal reflections in some areas, especially where the Whale Member is well developed. In other areas, weak internal reflections are present.

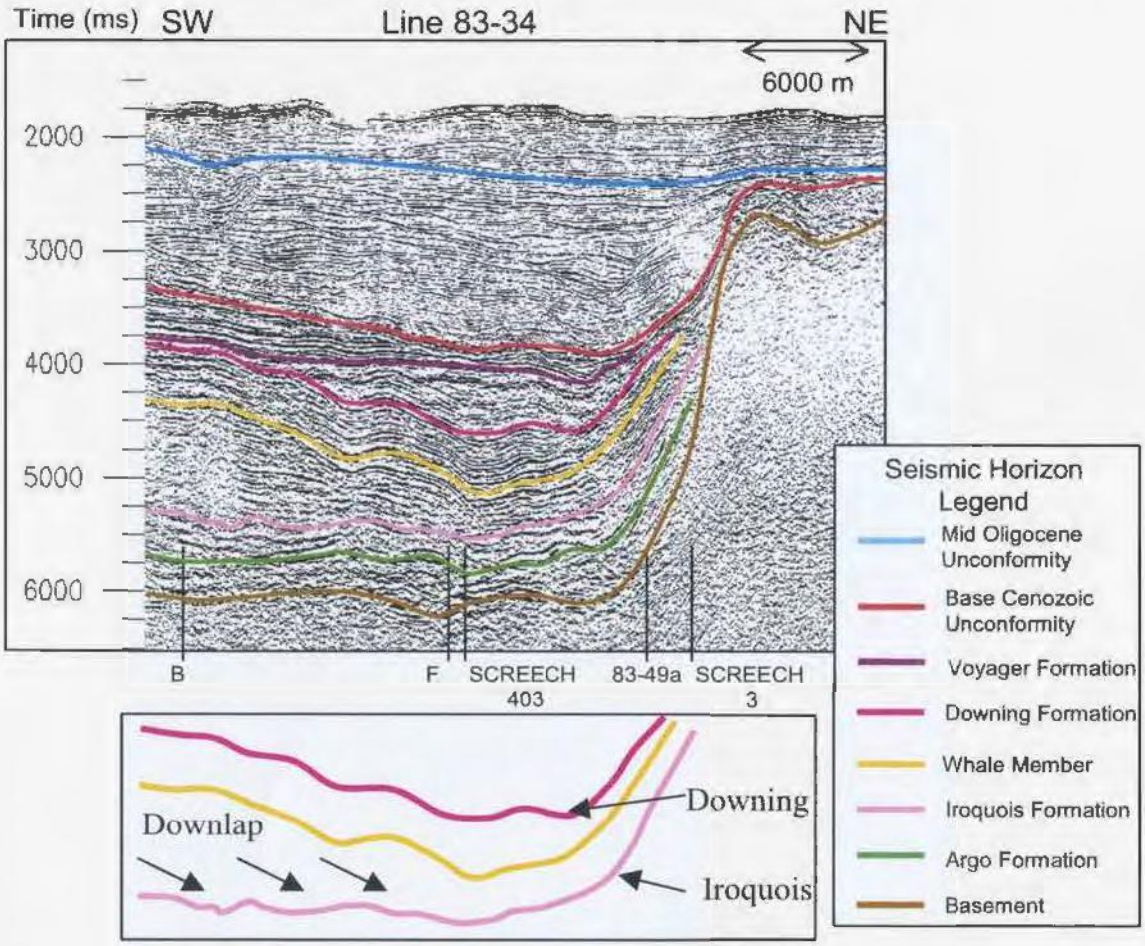

Figure 3.23. Seismic Line 83-34 showing the unconformable contact between the Iroquois Formation and the Downing Formation (refer to Figure 3.12) at the top of the Lower Jurassic. On this strike section the Downing Formation is downlapping onto the Iroquois Formation.

Figure 3.24 illustrates the depth structure contour map of the top of the Downing Formation. In the Carson Basin the formation is bounded towards the north by an antithetic fault and to the east by the accommodation zone. To the south the formation is bounded by the Carson Fault or eroded by the Avalon Unconformity, and to the west it becomes eroded by the Avalon unconformity. The general dip direction for the Downing Formation in the Carson Basin is toward the north-east. In the Bonnition Basin, the Downing Formation is bounded to the south and east by the ridge and to the west by the Bonnition Fault. In the northern areas of the basin the Downing Formation onlaps onto the Iroquois Formation. In this basin the formation generally tends to dip toward the south-west and is shown to be tilted at the edges of the hasin. This thick formation is folded and in the Carson Basin it is thickest in the centre of the basin especially towards the eastern side. In the Bonnition Basin this formation thickens towards the centre of the basin in the south and south-west areas. It is in these thick areas where the Whale Member is well developed.

The Whale Member is a strong seismic marker across the southern portion of the Bonnition Basin and the north-eastern section of the Carson Basin. On seismic sections the Whale Member is coloured orange-yellow. Figure 3.25 illustrates a depth structure contour map of this unit. It has a limited extent, confined to areas where the Downing Formation is relatively thick. In the Carson Basin it is eroded to the south-west by the Avalon Unconformity and to the east it is bounded by the Carson Fault.

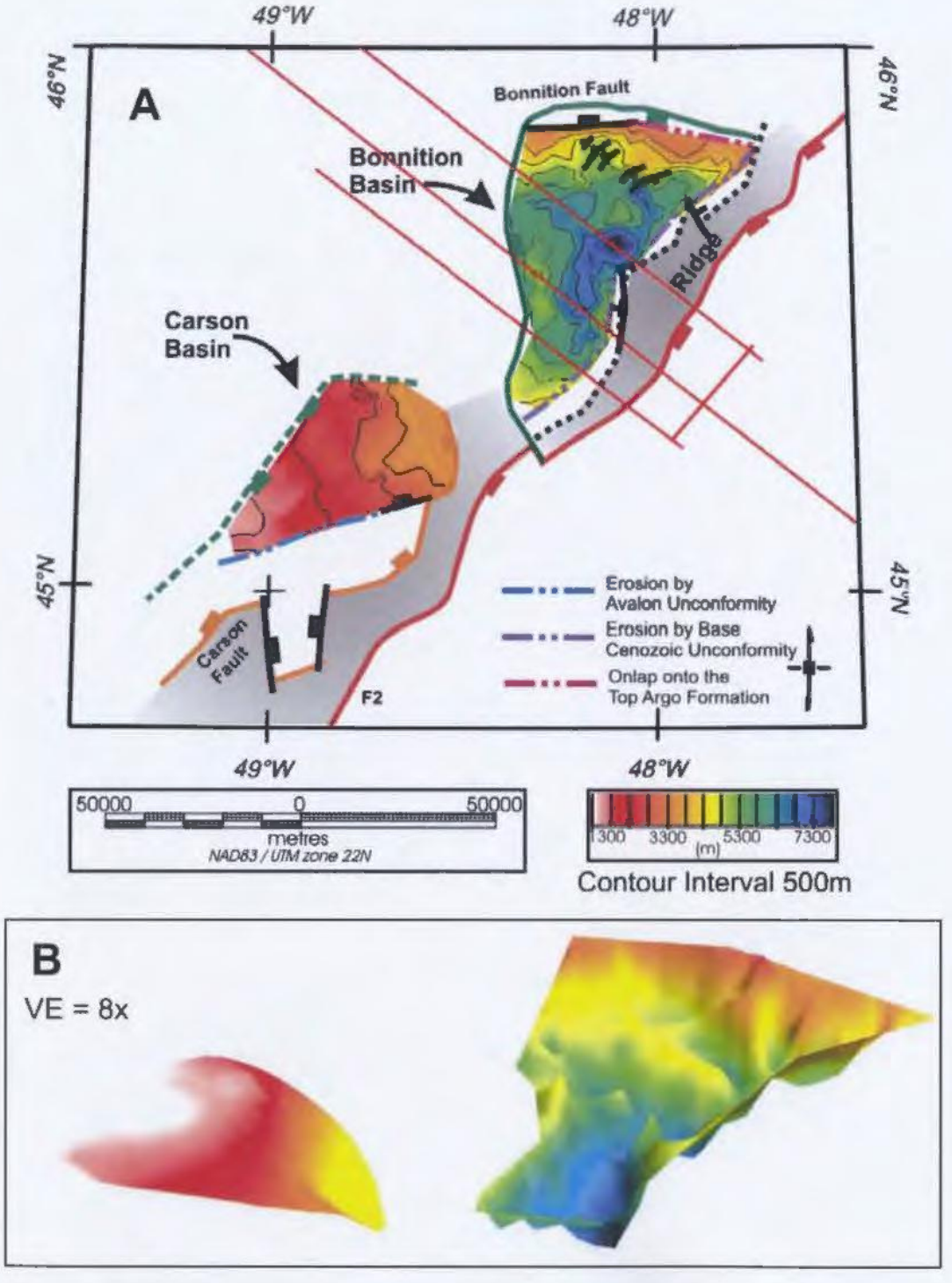

Figure 3.24. A) Depth structure contour map of the top of the Downing Formation. B) a 3-dimensional view of the top of the formation at 8x vertical exaggeration.

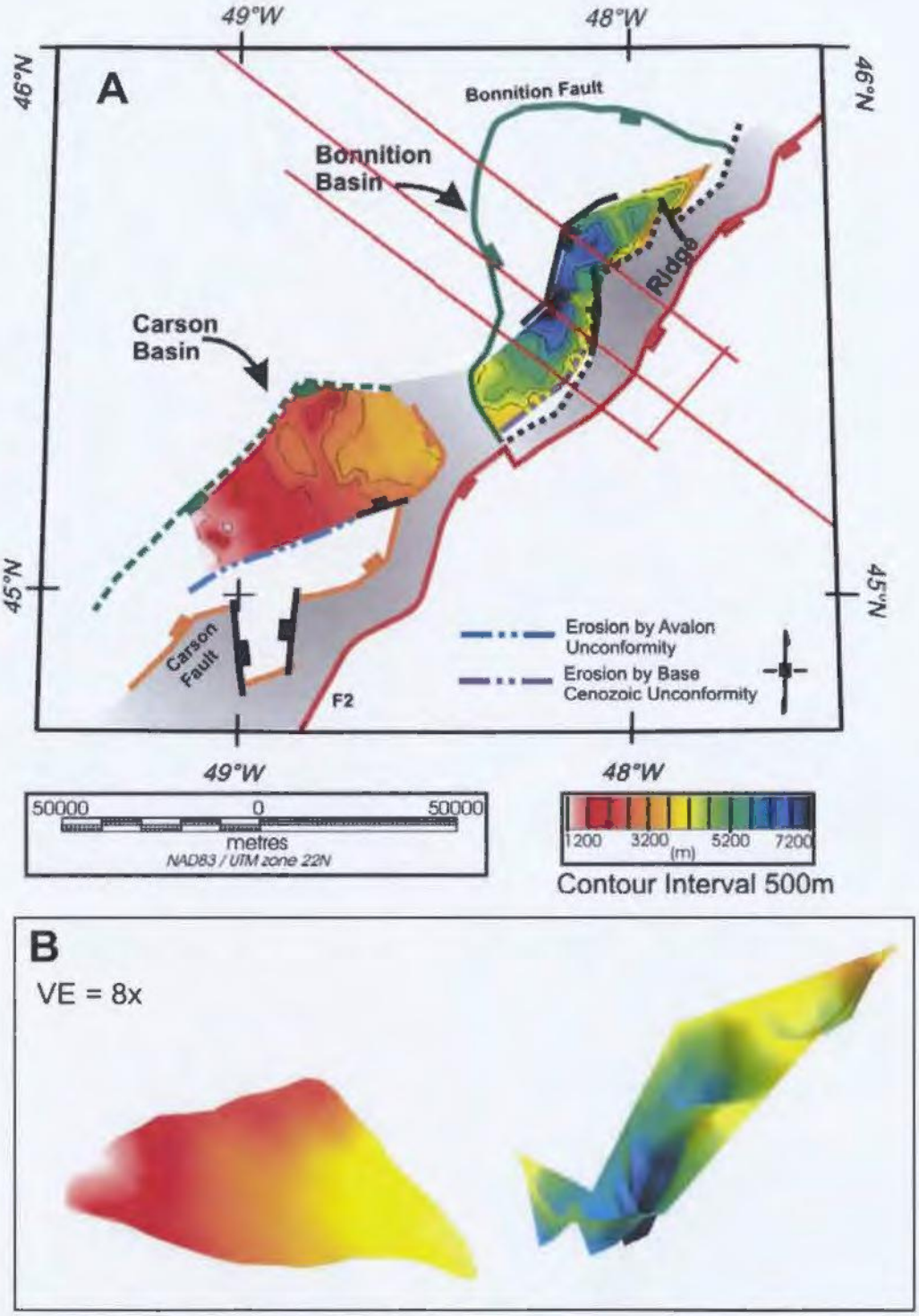

Figure 3.25. A) Depth structure contour map to the Whale Member in the Downing Formation. This unit is less extensive then the previous formations that have been mapped and tends to be present in the thickest sections of the Downing Formation. B) A 3-dimensional view of the top of the member at 8x vertical exaggeration.

In the north the member is generally bounded by an antithetic fault or it onlaps onto the Iroquois Formation. The general dip direction of this unit in the Carson Basin is the same as the Downing Formation, dipping towards the northeast. In the Bonnition Basin the Whale Member either terminates at the accommodation zone in the south or it is eroded by the Base Cenozoic Unconformity. To the north it either onlaps onto the Argo Formation or terminates against a northeast - southwest trending fault. In this basin the unit generally dips towards the south-west and is folded and tilted at the basin margins.

3.4.1.5 Voyager Formation

The contact between the overlying Voyager Formation sandstones and the Downing Formation is mainly conformable in both the Carson and Bonnition basins. The Voyager Formation tends to have a weakly reflective seismic character and is less extensive in the basins than the Downing and is also less folded. The thickness of the Voyager Formation varies across the margin with the thickest portions being confined to the centers of the basins. This formation is generally overlain by the Rankin Formation, except in the Carson Basin and southern parts of the Bonnition Basin where the Tithonian, Avalon and Base Cenozoic Unconformities have eroded down into the Voyager Formation.

The contact between the Voyager Formation and the Rankin Formation in the Bonnition Basin is an angular unconformity throughout most areas. In many areas the base of the Rankin Formation has eroded the underlying Voyager Formation as shown in Figure 3.26 where the base of the Rankin (near top of Voyager) is illustrated in purple.

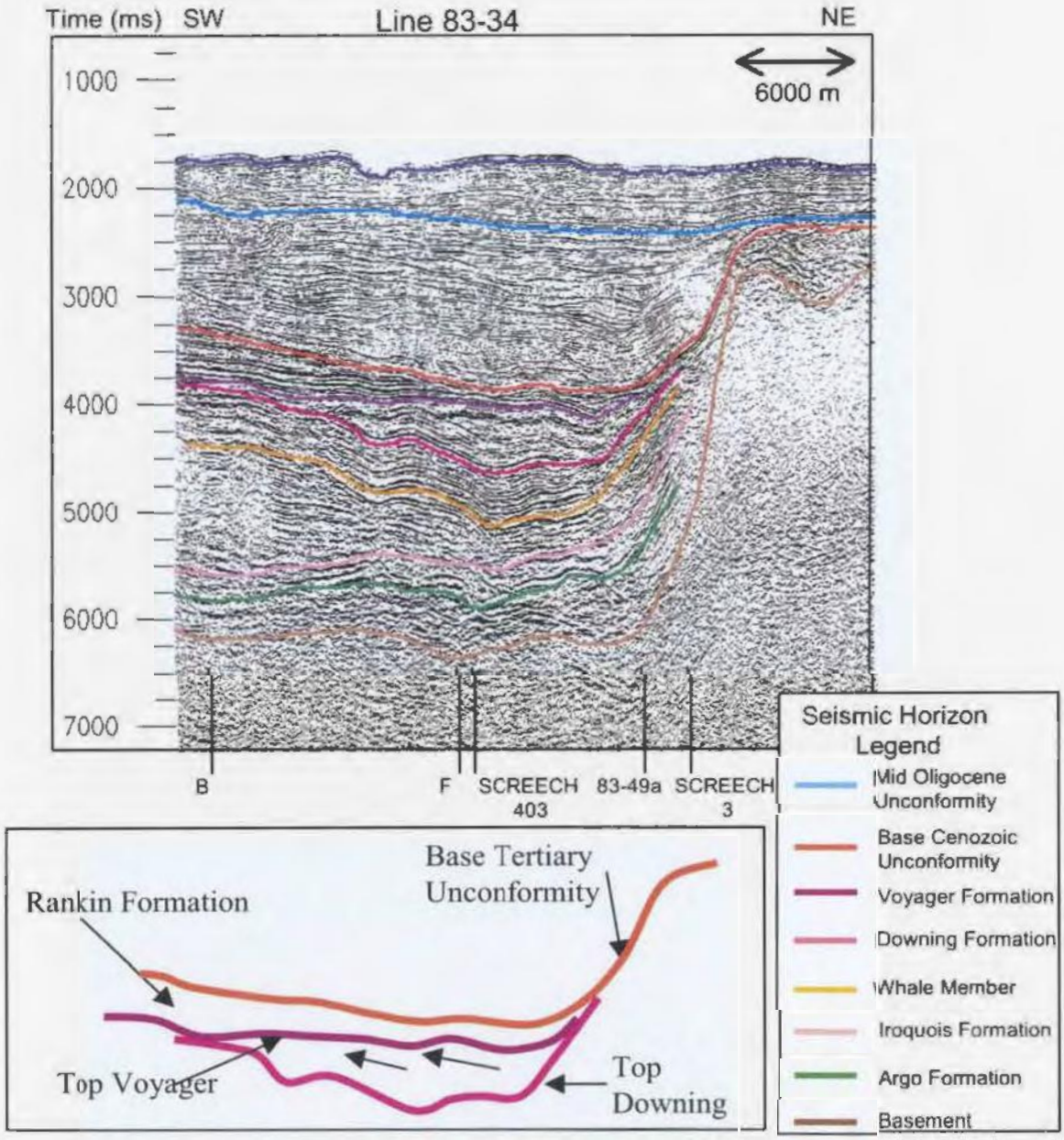

Figure 3.26. Seismic section 83-34 detailing the angular unconformity between the Rankin and Voyager Formations.

Figure 3.27 illustrates a depth structure contour map of the base of the Rankin Formation (in some places the top of the Voyager Formation).

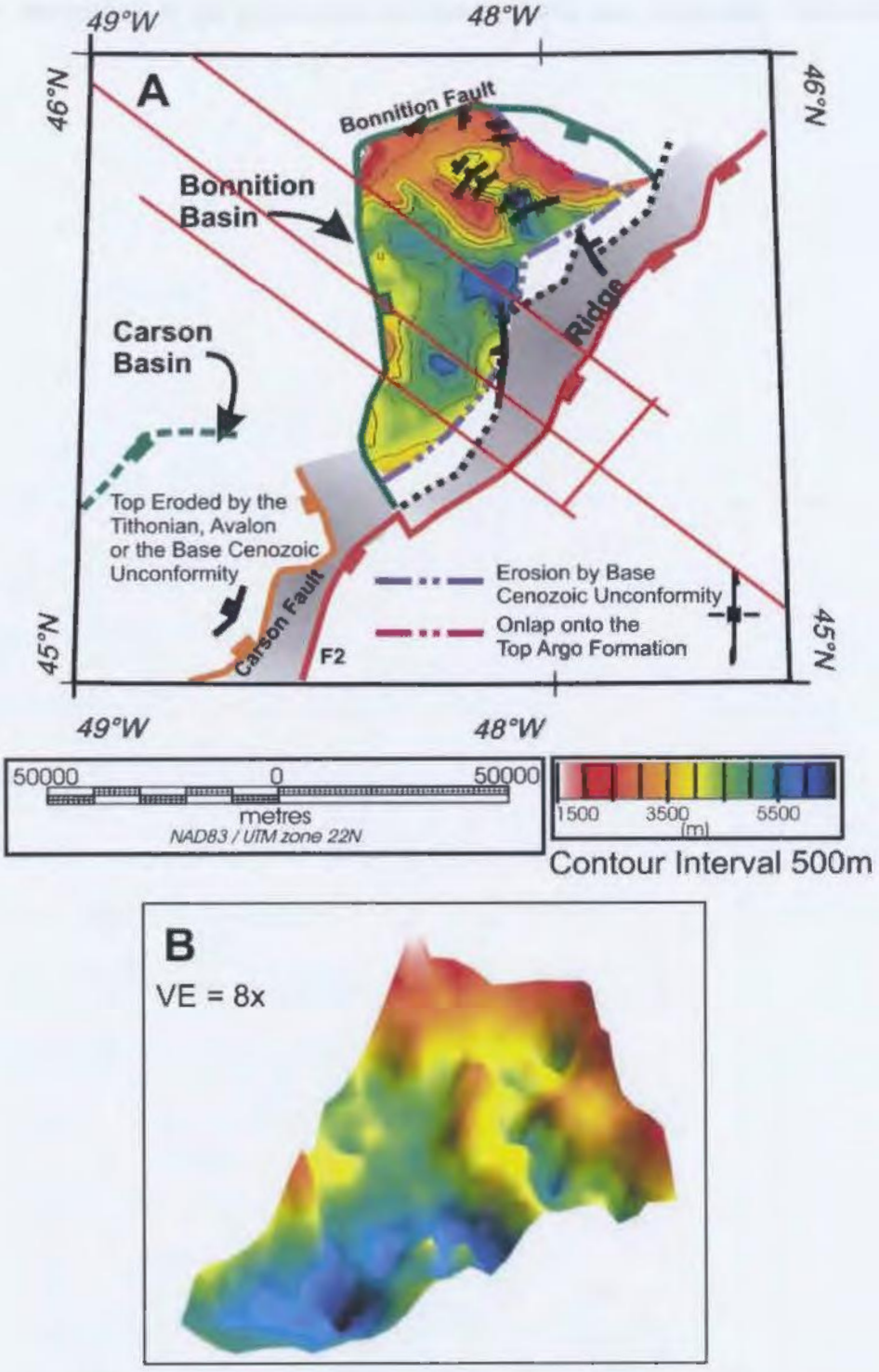

Figure 3.27. A) Depth structure contour map of the top of the Voyager Formation. The top of this formation shows less structure than the previous formations. B) A 3-dimensional view of the top of the Voyager Formation at 8x vertical exaggeration.

Note how the contact is not present in the Carson Basin due to erosion. Towards the north, east and south in the Bonnition Basin the Voyager Formation is generally eroded by the Base Cenozoic Unconformity, except in a localized area to the north where it onlaps onto the Argo Formation. To the west the formation is bounded by the Bonnition Fault, and the general dip direction of the formation is to the south-west.

3.4.1.6 Rankin Formation – Tithonian Unconformity

The top of the Rankin Formation is generally marked by the Kimmeridgian - Tithonian Unconformity. This unconformity has in many areas of the basin eroded the top portion of the Rankin Formation. On seismic sections throughout this thesis, this unconformity is marked a dark purple colour. The unconformity as described by Grant et al. (1988) is highly faulted especially near the Bonnition well, but than becomes paraconformable moving further seaward in the Bonnition Basin. The unconformity is present throughout the basins except towards the north and east where the Tithonian Unconformity becomes cut by the Base Cenozoic Unconformity in the Bonnition Basin (Figure 3.28) or by the Avalon Unconformity towards the south in the Carson Basin. The Tithonian Unconformity tends to be overlain by either low amplitude reflections from the Upper Jurassic to Lower Cretaceous in the northern areas of the Bonnition Basin, or by reflections from the Upper Cretaceous to Cenozoic in the southern areas of the Carson Basin. Figure 3.29 is a depth structure contour map of this unconformity.

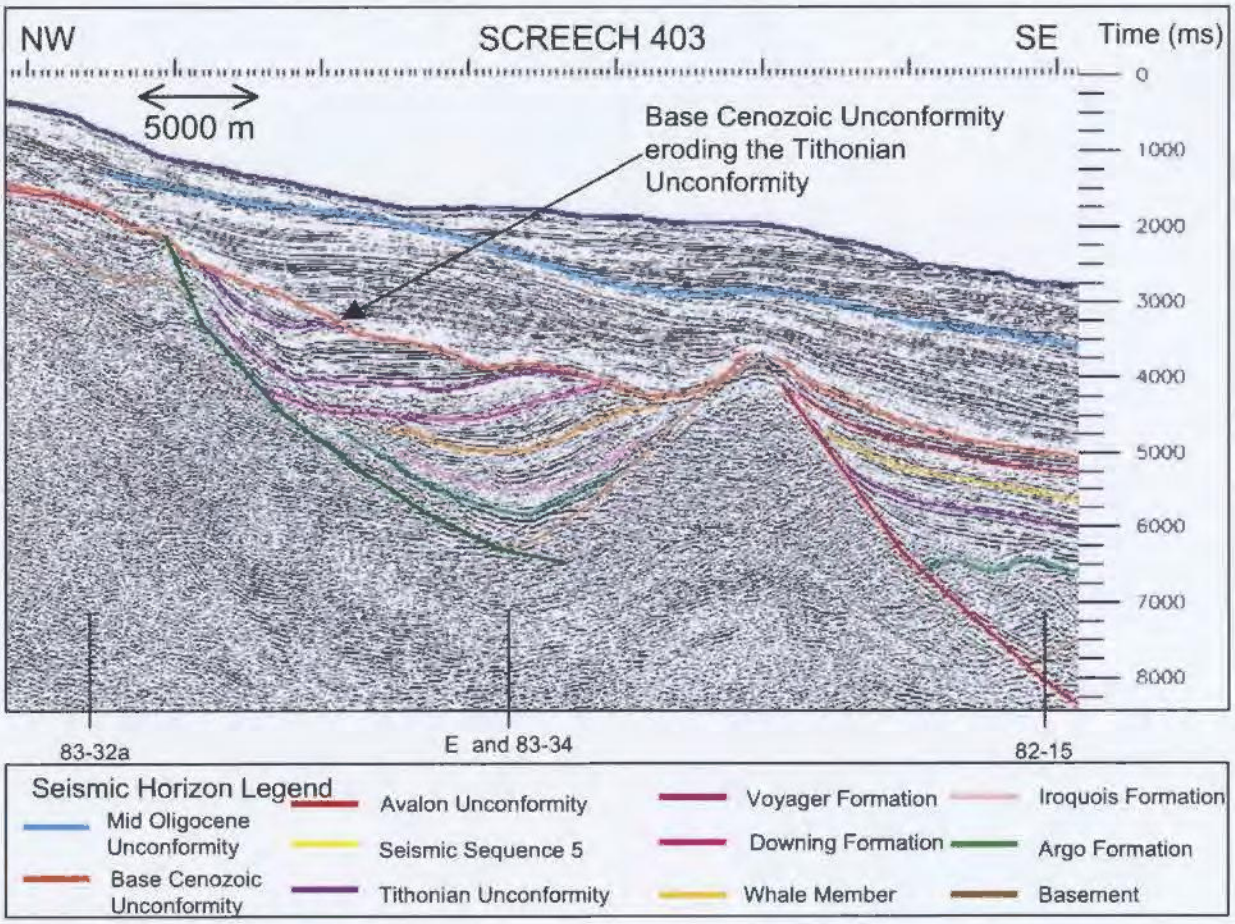

Figure 3.28. Seismic line SCREECH 403 illustrates the Base Cenozoic Unconformity shown in orange which has eroded the Tithonian Unconformity shown in dark purple.

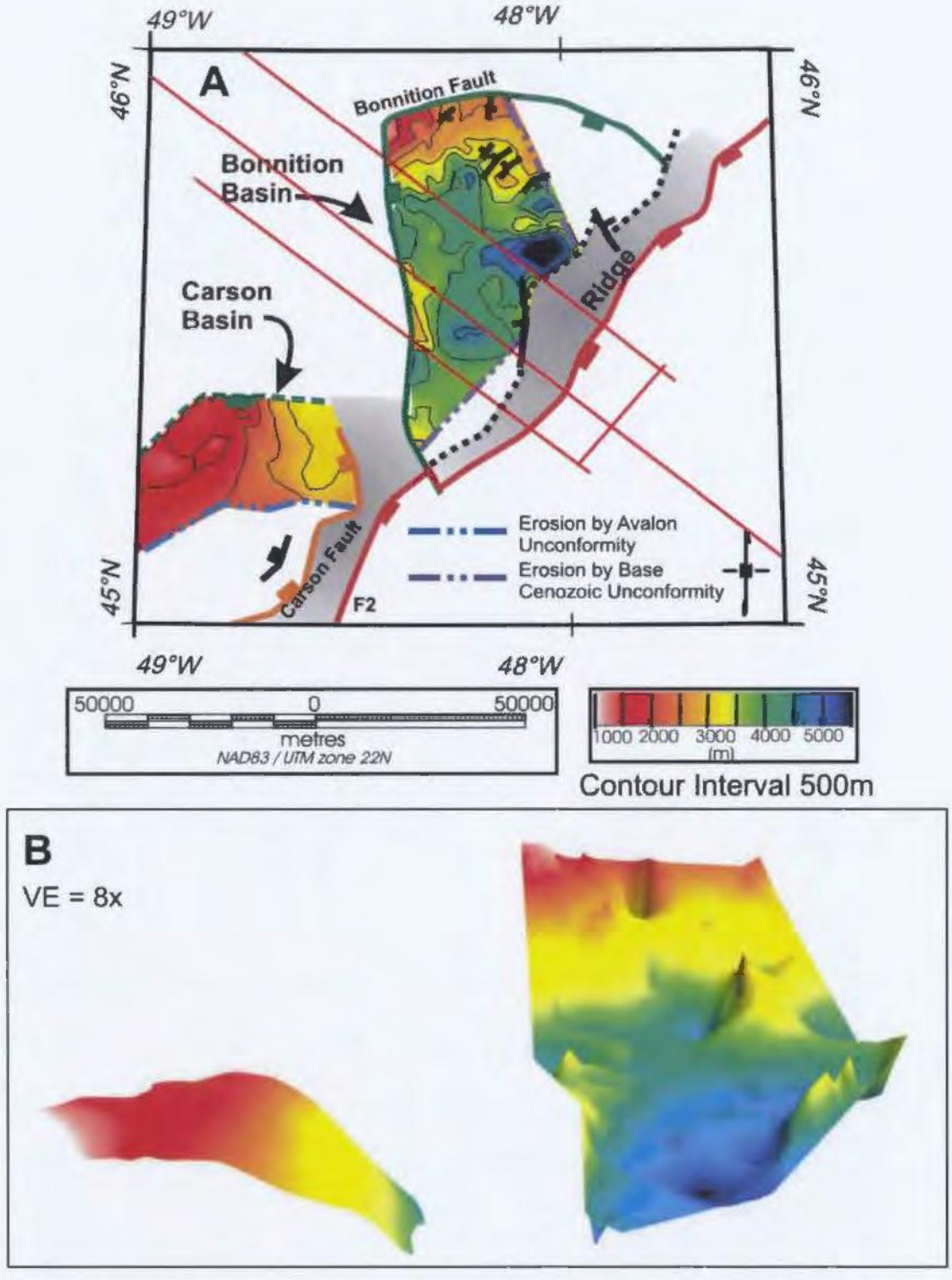

Figure 3.29. A) Tithonian Unconformity (~Top Rankin Formation) depth structure contour map. Notice the areas that have been eroded by either the Base Cenozoic Unconformity or the Avalon Unconformity. B) A 3-dimensional view of the top of the Rankin Formation at 8x vertical exaggeration.

3.4.1.7 Avalon Unconformity

This unconformity is defined as being Aptian to Albian in age. It corresponds to the sequence boundary between sequences 3 and 4 (refer to Figure 3.12) of Grant et al. (1988). It is present on the shelf portion of the margin, however it is cut and eroded over parts of the Bonnition Basin (especially towards the south and east) by the Base Cenozoic Unconformity. On all interpreted seismic sections this unconformity is coloured red. The contact between the two sequences tends to be disconformable in many areas on the shelf. Figure 3.30 is a depth structure contour map of this unconformity which is interpreted to represent the transition from the rifting stage to the drifting stage (Grant et al. 1988).

3.4.1.8 Cretaceous Deposits

The thickest Cretaceous deposits in the Bonnition and Carson basins are of Early Cretaceous age, as most Upper Cretaceous strata have been eroded away at the Base Cenozoic Unconformity, or just not deposited. Lower Cretaceous strata are thickest in the central portion of the Bonnition Basin and the north-eastern section of the Carson Basin. Figure 3.31A is an isopach map of the interval between the Tithonian Unconformity and the Avalon Unconformity, while Figure 3.31B is an isopach map of the interval between the Avalon Unconformity and the Base Cenozoic. Based on these divisions the isopach map in Figure 3.31A roughly represents Lower Cretaceous strata, while the isopach map in Figure 3.31B generally represents Upper Cretaceous strata.

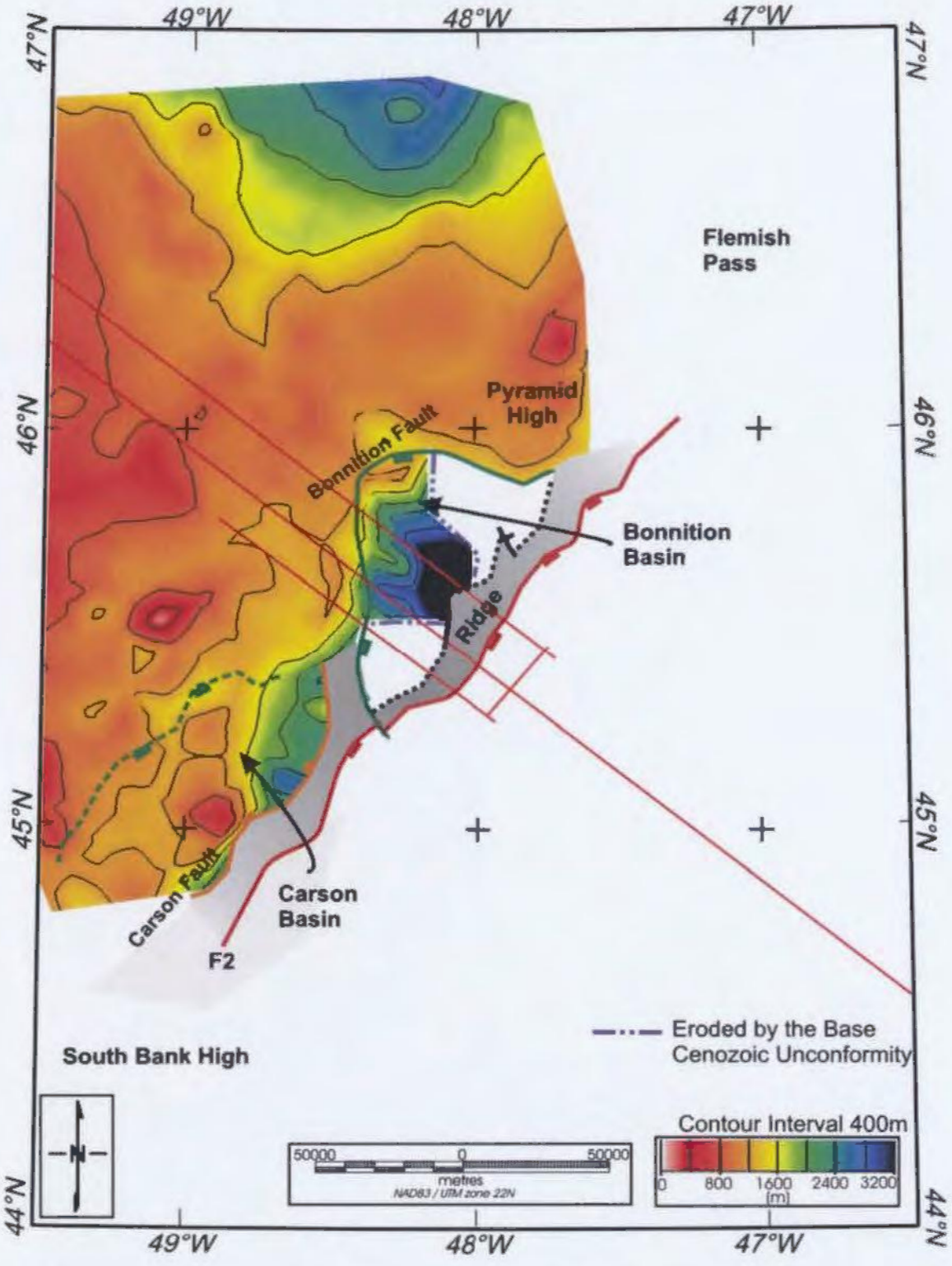

Figure 3.30. Depth structure contour map of the Avalon Unconformity on the shelf portion of the margin.

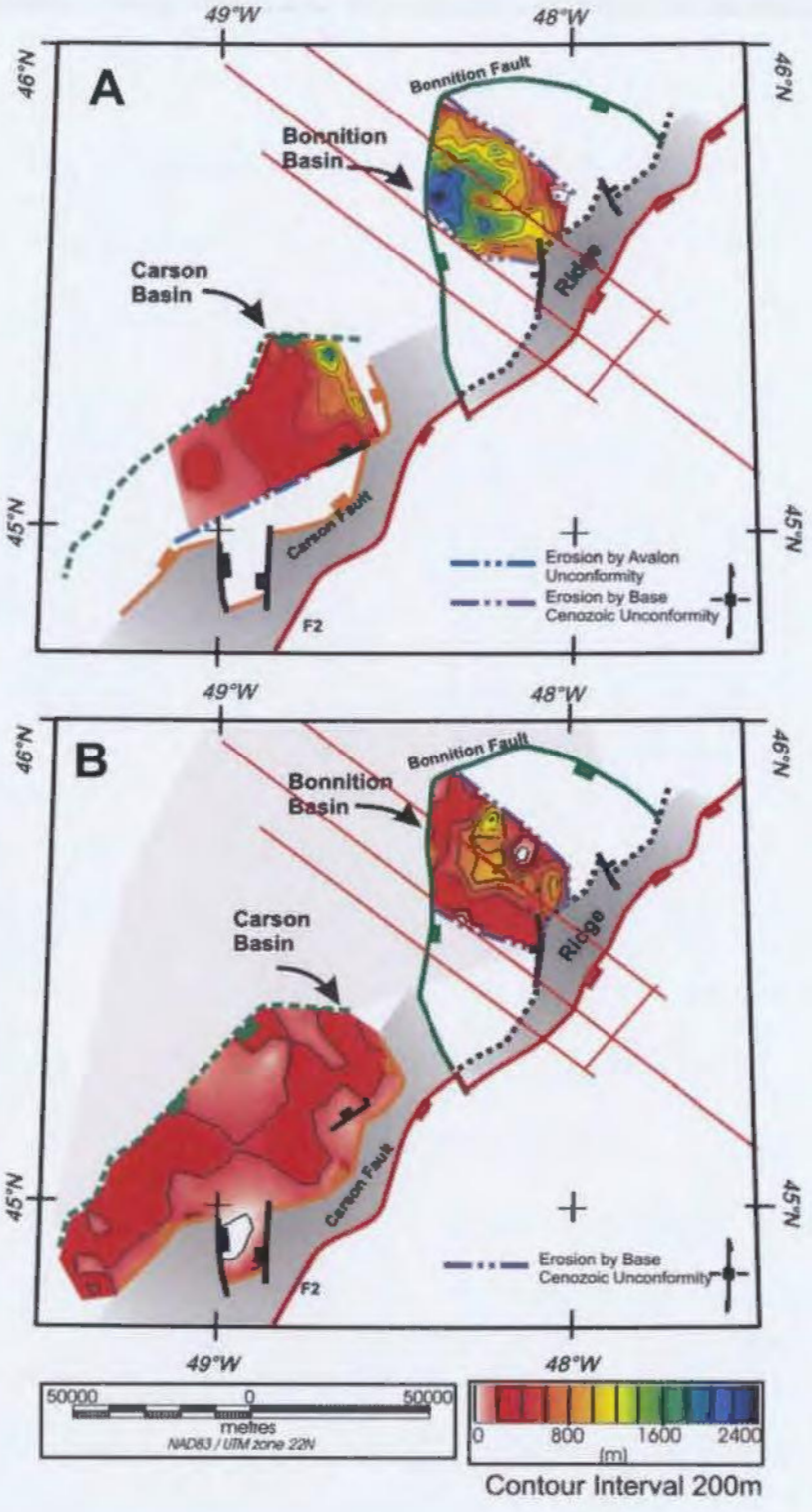

Figure 3.31. A) Isopach map of Lower Cretaceous formations. B) Isopach map of Upper Cretaceous formations.

The extent of the Lower Cretaceous deposits (Figure 3.31A) in the Bonnition Basin is controlled by the Base Cenozoic Unconformity. The northern, eastern and southern boundaries are all formed by the Base Cenozoic Unconformity eroding the Lower Cretaceous. In the Carson Basin the southern portion of the Lower Cretaceous strata has been eroded by the Avalon Unconformity.

The Upper Cretaceous strata are relatively thin and show only a small variability in thickness throughout both of the basins. In the Bonnition Basin the extent of these strata is controlled by the Base Cenozoic Unconformity, while in the Carson Basin the Upper Cretaceous strata cover the entire basin and are relatively uniform in thickness.

3.4.1.9 Base Cenozoic Unconformity

On the shelf portion of the margin, the Base Cenozoic Unconformity is a strong, mainly continuous reflector. This marker represents the base of sequence 2 and the top of sequence 3, defined by Grant et al. (1988). The contact is mainly disconformable (represents a period of erosion or non-deposition) on the shelf with some angularity in regions. In the south-west portion of the Bonnition Basin the unconformity overlies Jurassic rocks while towards the north-east section of the basin it overlies Upper Cretaceous sequences. Near the slope break in the Bonnition Basin the overlying Banquereau Formation may onlap or downlap onto the unconformity surface in localized areas. Figure 3.32 is a depth structure contour map of the horizon across the margin.

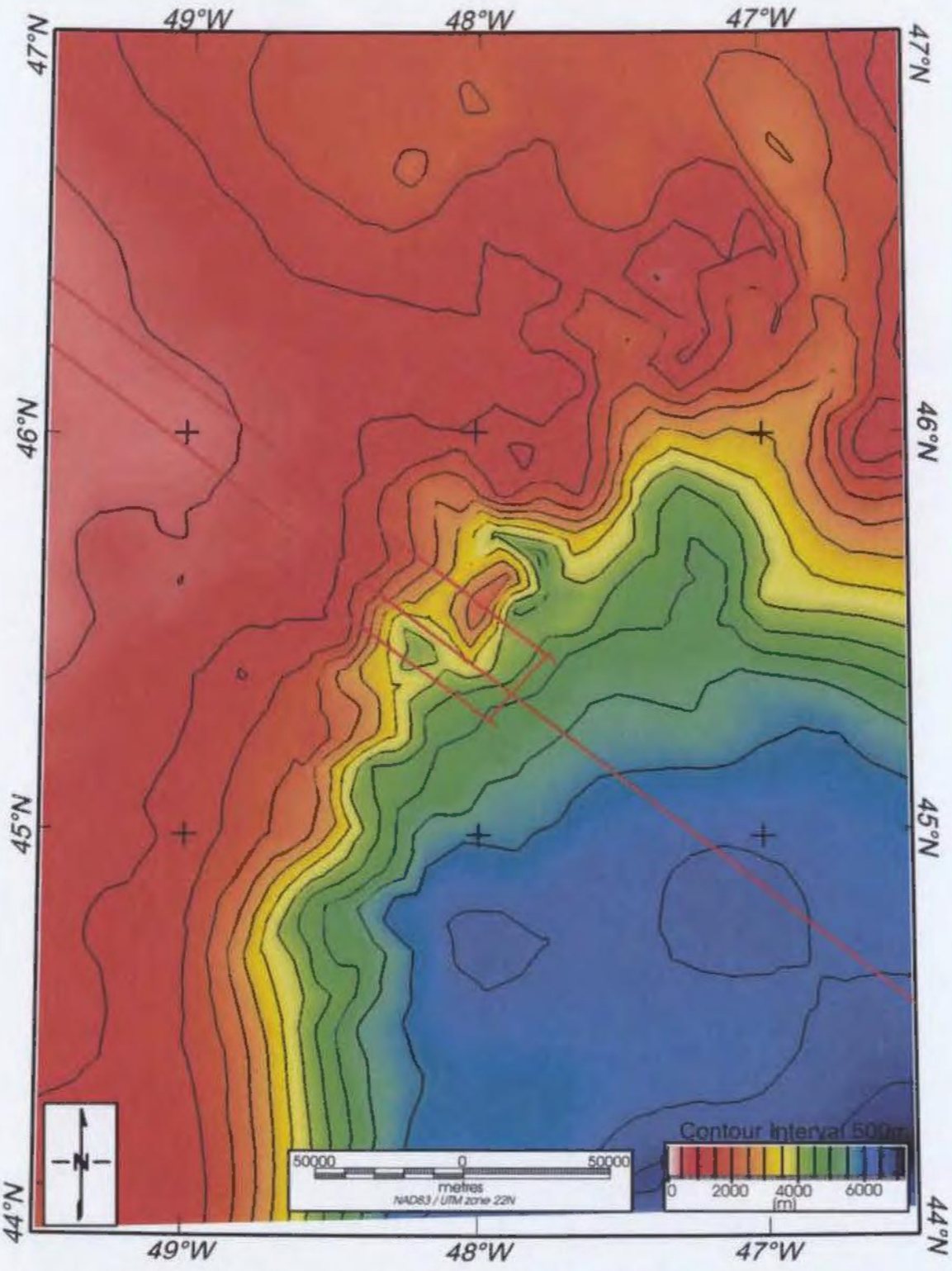

Figure 3.32. Depth structure contour map of the Base Cenozoic Unconformity.

3.4.2 Slope - Salar Basin

3.4.2.1 Basement

Basement in the Salar basin is poorly imaged due to interference from the first water bottom multiple and salt which is present in the overlying stratigraphic sequence. For these reasons basement in the Salar Basin is difficult to accurately constrain and the interpreted picks represent "acoustic" basement in many areas. Figure 3.14 previously shown in Section 3.3 illustrated the seismic sequences that were interpreted in the Salar Basin. Basement in the Salar Basin tends to be highly faulted, with normal faults creating rotated half grabens in the basin. As in the Carson and Bonnition basins, top of basement in this basin is coloured brown and the structure contour map was shown previously in Figure 3.18.

3.4.2.2 Lower Jurassic Salt

In the Salar Basin, the next identifiable seismic sequence above basement is the salt, either of Late Triassic (Osprey Formation) or Early Jurassic (Argo Formation) origin. Salt in the Salar Basin is difficult to image due to its depth. Given the limited ability to correlate the salt, its age here (ie., Osprey vs. Argo) cannot be ascertained. In the interpreted seismic sections the top of the salt is coloured green and is correlated with the Top of the Argo Formation. Salt related structures are found in many areas of tbe Salar Basin, especially near the southern extent of the Beothuk Knoll. Salt diapirs can be found at the base of the slope and towards the north of the Salar Basin. The salt seems to be most active around the area where the direction of faulting changes from NE-SW to a

more N-S direction. The salt tends to be the thickest in the northern portion of the Salar Basin and thins to the central area. Moving to the southern portion of the study area the salt again thickens and diapirism is present and noted on Figure 3.33, which is a depth structure contour map of the interpreted top salt horizon. The true extent of the salt to the north and south is limited by the seismic line locations. The sparse data coverage in these areas makes it difficult to confidently extend the top of the salt surface any further.

3.4.2.3 Rankin Formation – Tithonian Unconformity

Above the top of the Argo Formation, the next mappable formation that is present is the Rankin Formation, and its top is shown in purple on all seismic sections. The top of the Rankin Formation tends to correlate with the Tithonian Unconformity in the Carson and Bonnition basins (Grant et al. 1988). In the Salar Basin, the interval between the top of the Argo Formation and the top of the Ranking Formation is relatively thin, when compared to the same interval in the Carson and Bonnition basins. In the Salar Basin either most of the Jurassic section (Iroquois, Downing and Voyager formations) is missing or it is extremely thin. Seismic reflections in the Rankin Formation are generally high in amplitude. Figure 3.34 illustrates a depth structure contour map of the top of this formation in the Salar Basin. This unit shows variable thickness across the basin and tends to be thin towards the north, thicker and more extensive in the central portions of the basin and thins considerably towards the southern areas. In the north the eastern extent of this sequence is bounded by the Beothuk Knoll extension. In the central area of the basin the sequence is deposited eastward of the Beothuk Knoll extension

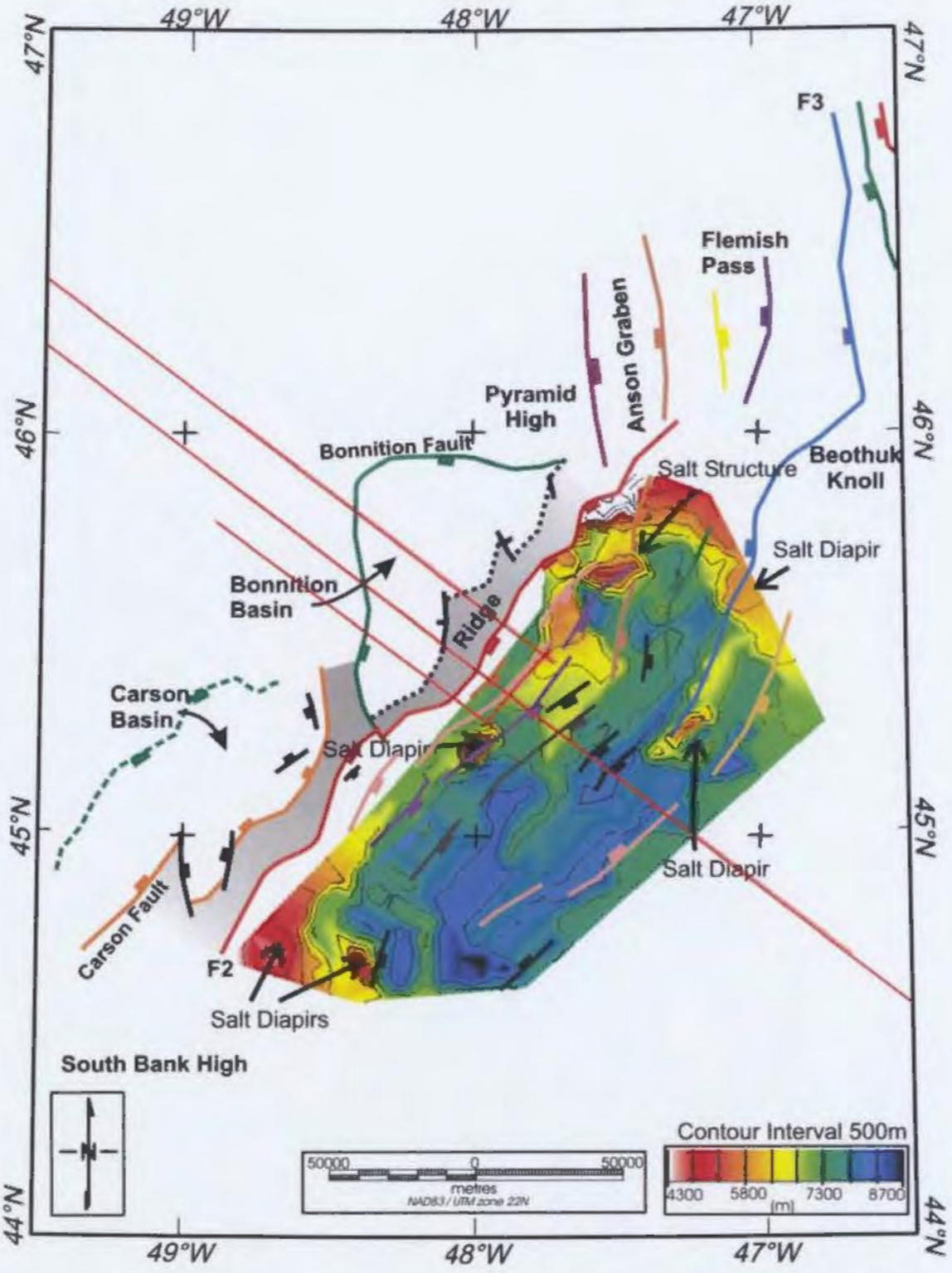

Figure 3.33. Depth structure contour map of the top of salt (Argo Formation) in the Salar Basin. Areas where diapirism is present are noted on the map.

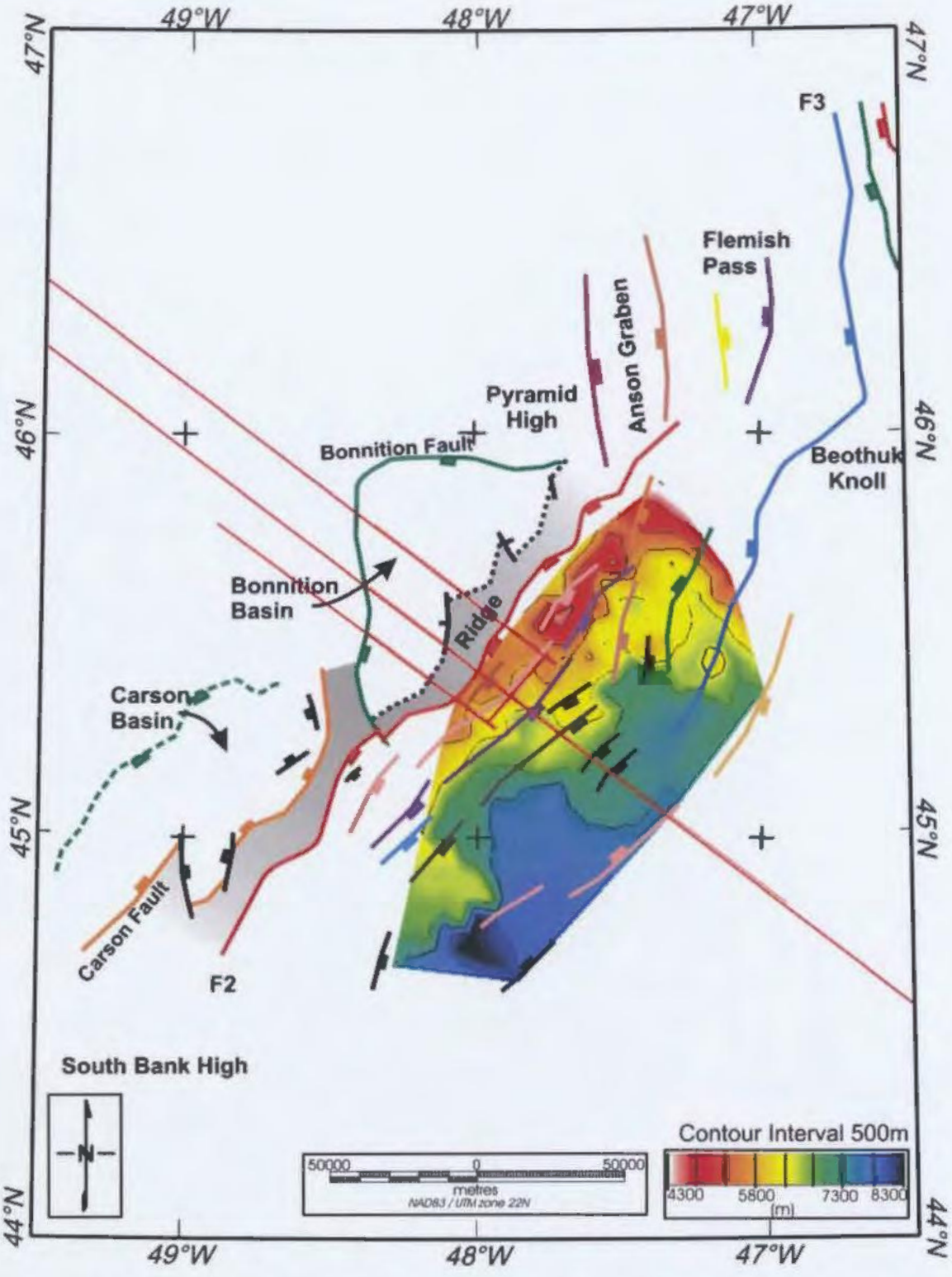

Figure 3.34. Depth structure contour map of the top the Rankin Formation. This boundary generally corresponds to the Tithonian Unconformity in the Carson and Bonnition basins.

downlapping onto basement or salt. In the southern portion of the Salar Basin this unit downlaps on to the underlying salt sequence westward of the Beothuk knoll extension, as shown in Figure 3.35. The northern and southern extent of this sequence is undetermined due the sparse data coverage.

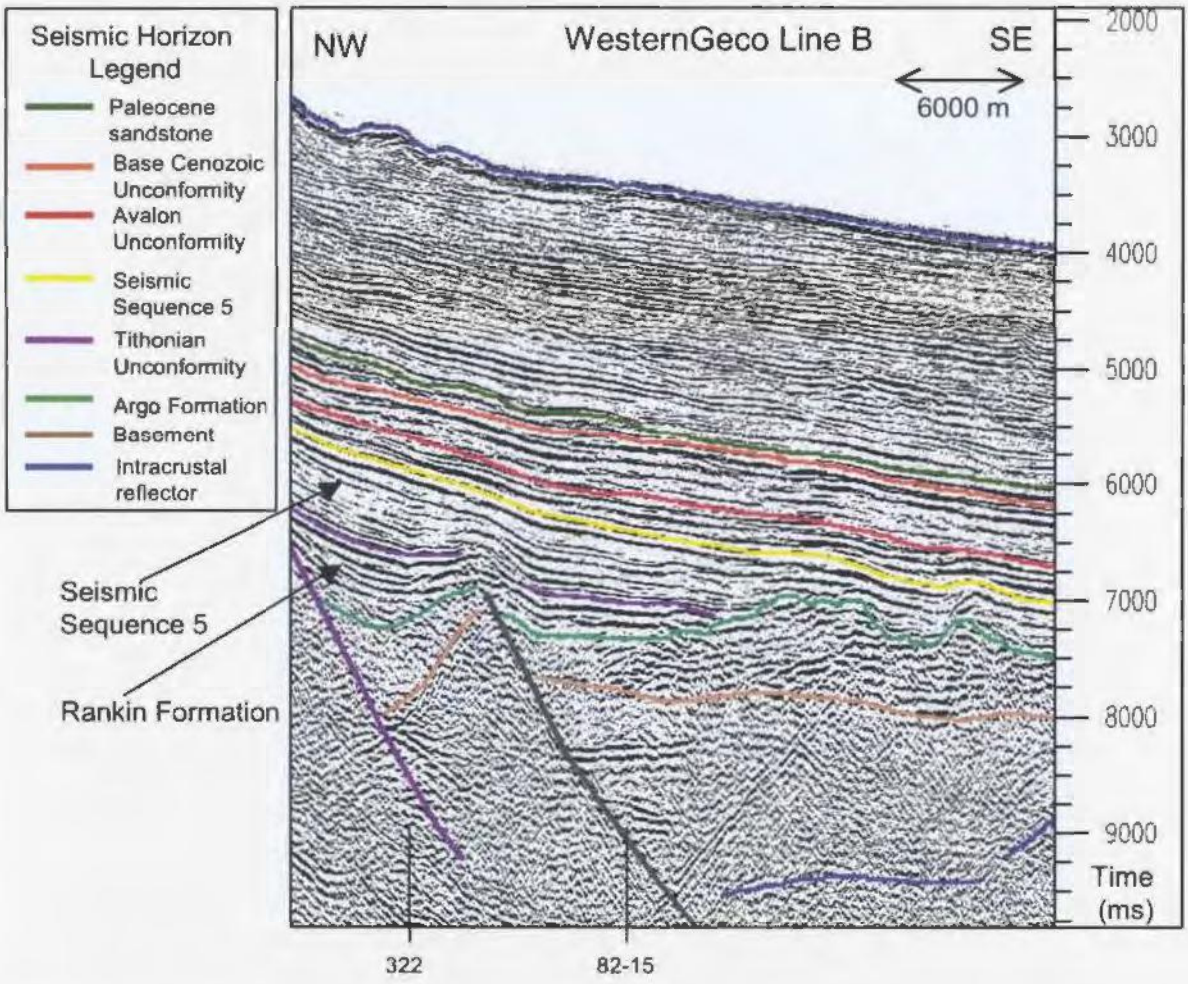

Figure 3.35. Proprietary WesternGeco line B, showing downlap of the top of the Rankin Formation onto the top of the Argo salt in the Salar Basin. The Rankin Formation is defined by a high amplitude reflection sequence in the Salar Basin. Seismic Sequence 5 has a well defined seismic reflection indicating the top of this sequence and then weak reflectivity below. As shown in the figure the thickness of the Rankin Formation varies, thickening across faults.

3.4.2.4 Seismic Sequence 5

The top of seismic sequence 5 of Grant et al. (1988) is shown in yellow in all interpreted seismic sections. This surface represents the beginning of the transition to drift phase (depositional sequence 4) from Grant et al. (1988). The sequence top is marked by a strong seismic marker over most of the Salar Basin, with weak reflectivity below. In some areas well defined parallel seismic events are visible in the sequence (Grant et al. 1988). This sequence has a large areal extent, shows growth across faults (Grant et al. 1988), and thickens towards the east in the central area of the basin as shown in Figure 3.35. Figure 3.36 is a depth structure contour map of the top of this sequence. This map illustrates the extent of the sequence where to the north and south it is not well constrained due to lack of data. To the east it has an extent similar to the Rankin Formation.

3.4.2.5 Seismic Sequence 4 – Avalon Unconformity

Seismic Sequence 4 overlies Sequence 5 mainly in the axial portions of the Salar Basin (Grant et al. 1988). The sequence is variable in thickness and tends to be eroded in many areas by the overlying Avalon Unconformity. The reflection character of this sequence tends to show weak reflectivity internally, except at the base which is the well developed unconformity mentioned in Section 3.4.2.4 (Grant et al. 1988). Figure 3.37 illustrates two seismic lines that show the variability of the sequence across the margin. In Figure 3.37A the sequence is thicker and the overlying sequence onlaps onto Sequence 4. In Figure 3.37B sequence 4 is shown to be very thin. The top of Sequence 4 is defined by

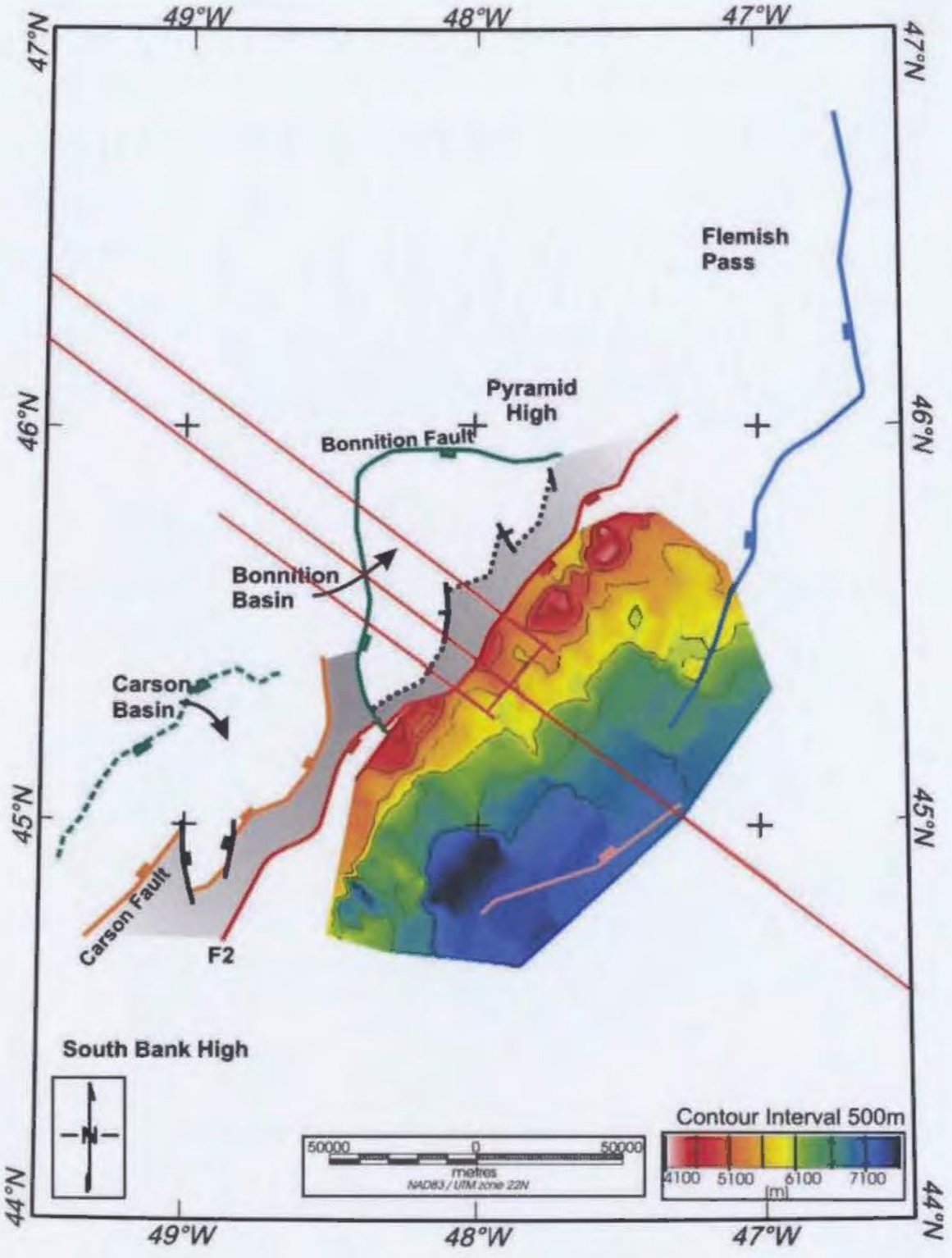

Figure 3.36. Depth structure contour map of the top of Sequence 5.

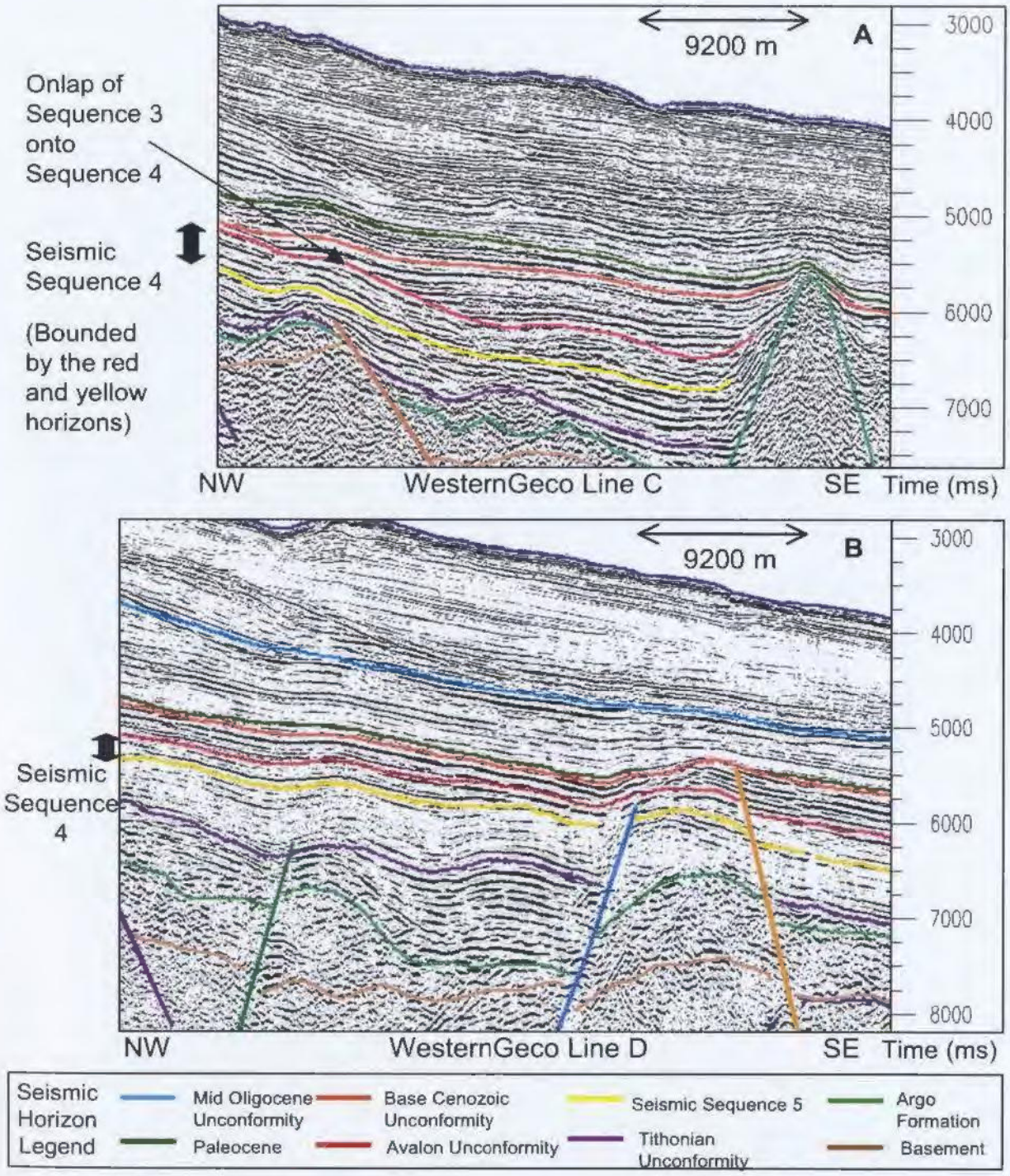

Figure 3.37. Part A and B) Proprietary WesternGeco seismic lines showing the character of seismic Sequence 4. Both lines show that the base (yellow) is a well developed reflector and the internal reflectivity is generally weak. In both lines the sequence is also thin. The Base Cenozoic Unconformity is shown in orange and the Avalon Unconformity is shown in red. Part A shows that Sequence 3 (orange to red) onlaps onto Sequence 4 in some areas of the basin.

the Avalon Unconformity and a depth structure contour map of the top of this sequence is shown in Figure 3.38 illustrating its structure across the Salar Basin.

3.4.2.6 Seismic Sequence 3 – Base Cenozoic Unconformity

Seismic Sequence 3 is bounded by the Avalon Unconformity at its base (red in seismic sections), and the Base Cenozoic Unconformity at the top (orange in seismic sections). The Avalon Unconformity separates Sequence 4 from Sequence 3 and is marked by a continuous reflector throughout the Salar Basin. Reflections in Sequence 3 tend to show onlap onto the top of Sequence 4 as shown in Figure 3.37. The Base Cenozoic Unconformity represents the boundary between Grant et al.'s (1988) Sequence 2 and Sequence 3. The unconformity is a high amplitude seismic reflection and is continuous throughout the basin. In the slope area the unconformity is generally conformable with the underlying sediment. Figure 3.32 shown previously also illustrates the time structure contour map of the Base Cenozoic Unconformity over the Salar Basin.

3.4.2.7 Paleocene Sandstone Unit

Paleocene sandstones are found above the Base Cenozoic Unconformity. Their extent and thickness vary along the margin, although they are generally found in the axial areas of the basin, and are interpreted as the product of shelf-edge erosion (Grant et al. 1988). In the Jeanne d'Arc Basin during Paleocene time, many basin floor and submarine fans are noted by Deptuck et al. (2003). In the Salar Basin the top of the Paleocene sandstone seismic sequence is defined by a moderately continuous undulating reflection, while the

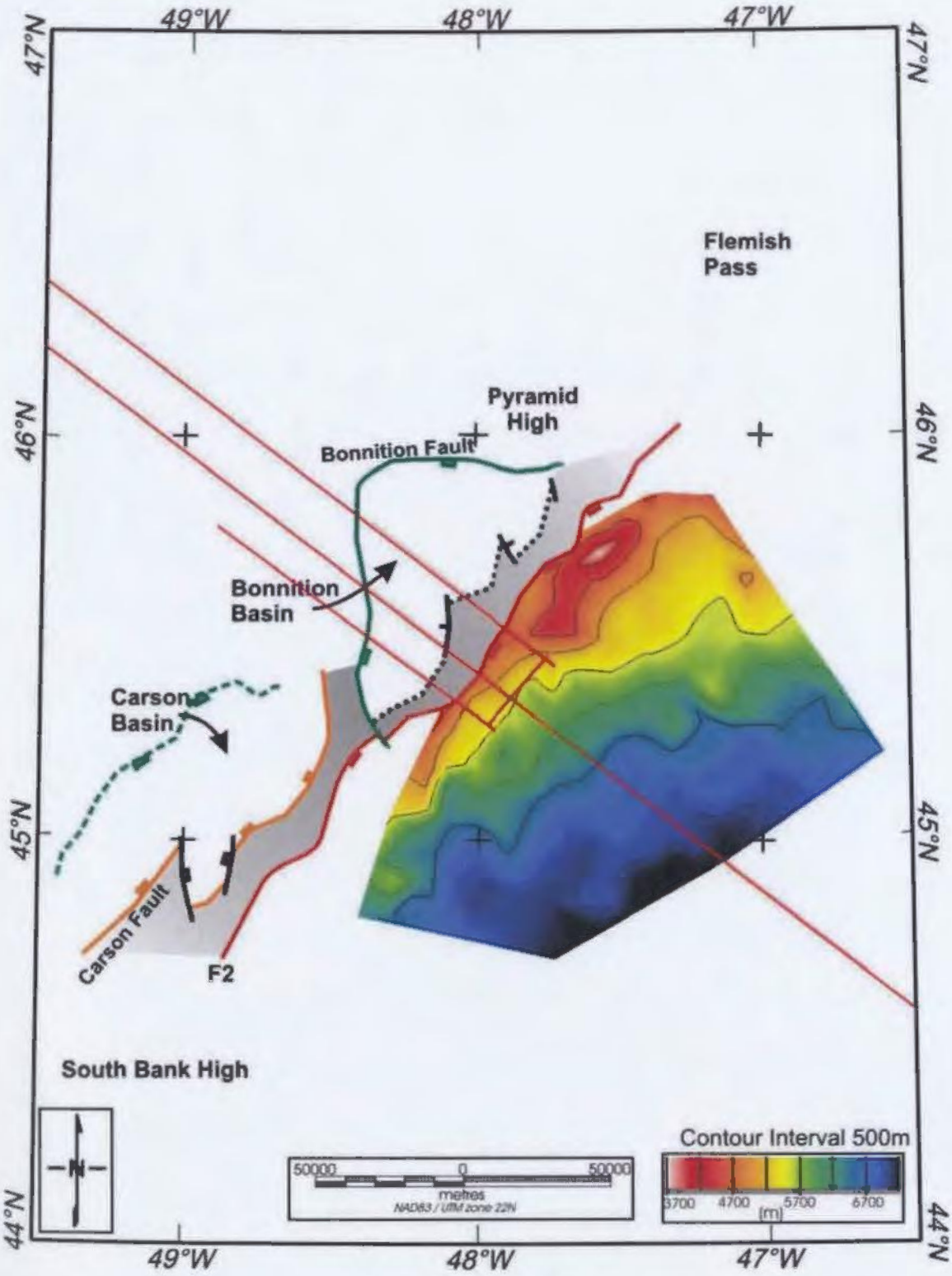

Figure 3.38. Depth structure contour map of the top of Sequence 4 (the Avalon Unconformity).

internal reflections tend to be hummocky as shown in Figure 3.39. The reflection character of this sequence indicates that it is composed of turbidites and gravity flow deposits. The thickness of the unit is variable across the margin. A depth structure contour map of the top of this seismic unit is shown in Figure 3.40. Drilling ODP Site 1276 drilled through an almost complete Paleocene to Eocene section. Core recovered at ODP Site 1276 shows that many of the debris flows in the Paleocene contain many calcareous benthic foraminifers and holococcoliths. Siliciclastic turbidites tend to dominate this sequence, and they are interpreted to be a succession of deposits from repeated pulses of high density turbidity currents.

3.4.2.8 Seismic Sequence 2

The top of Seismic Sequence 2 is defined by the Mid-Oligocene unconformity and represents the sequence boundary between Sequences 1 and 2 of Grant et al, (1988). This unconformity is thought by Vail et al. (1977) to represent a sea level lowstand. This unconformity is widespread over the slope section of the margin is an angular unconformity near the slope break becoming conformable as the water depth increases. Seismic Sequence 2 is bounded at its base by the Base Cenozoic Unconformity. The sequence is composed of the Paleocene sandstone unit and sediments up to Mid-Oligocene in age. The sequence is dominated by turbidites, submarine canyons, channels and fans developed by shelf edge erosion (Parker, 1999 and Grant et al. 1988).

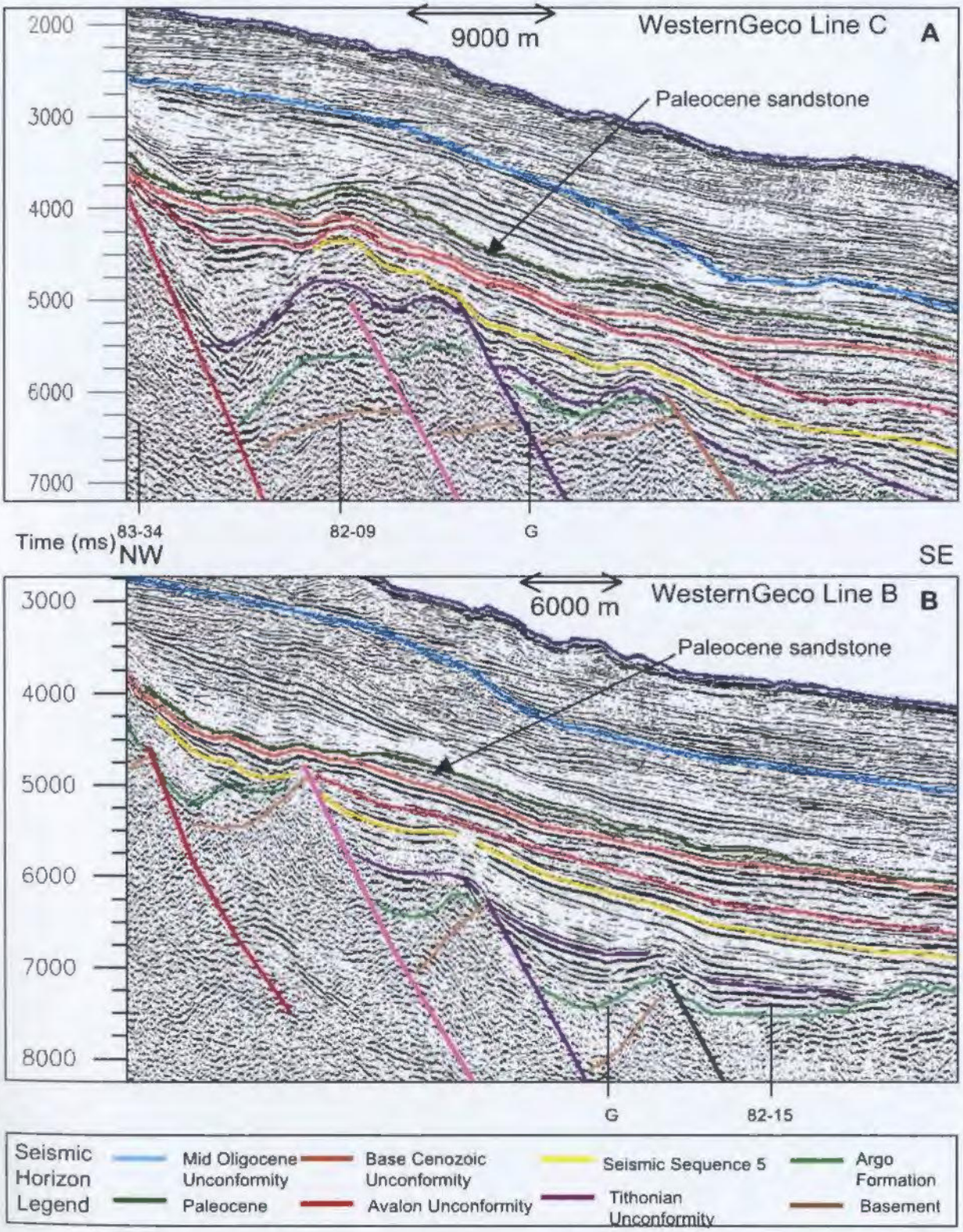

Figure 3.39. Proprietary WesternGeco seismic sections illustrating the seismic character of the Paleocene sandstones in the Salar Basin. In both sections the top of the Paleocene sandstone is coloured dark green.

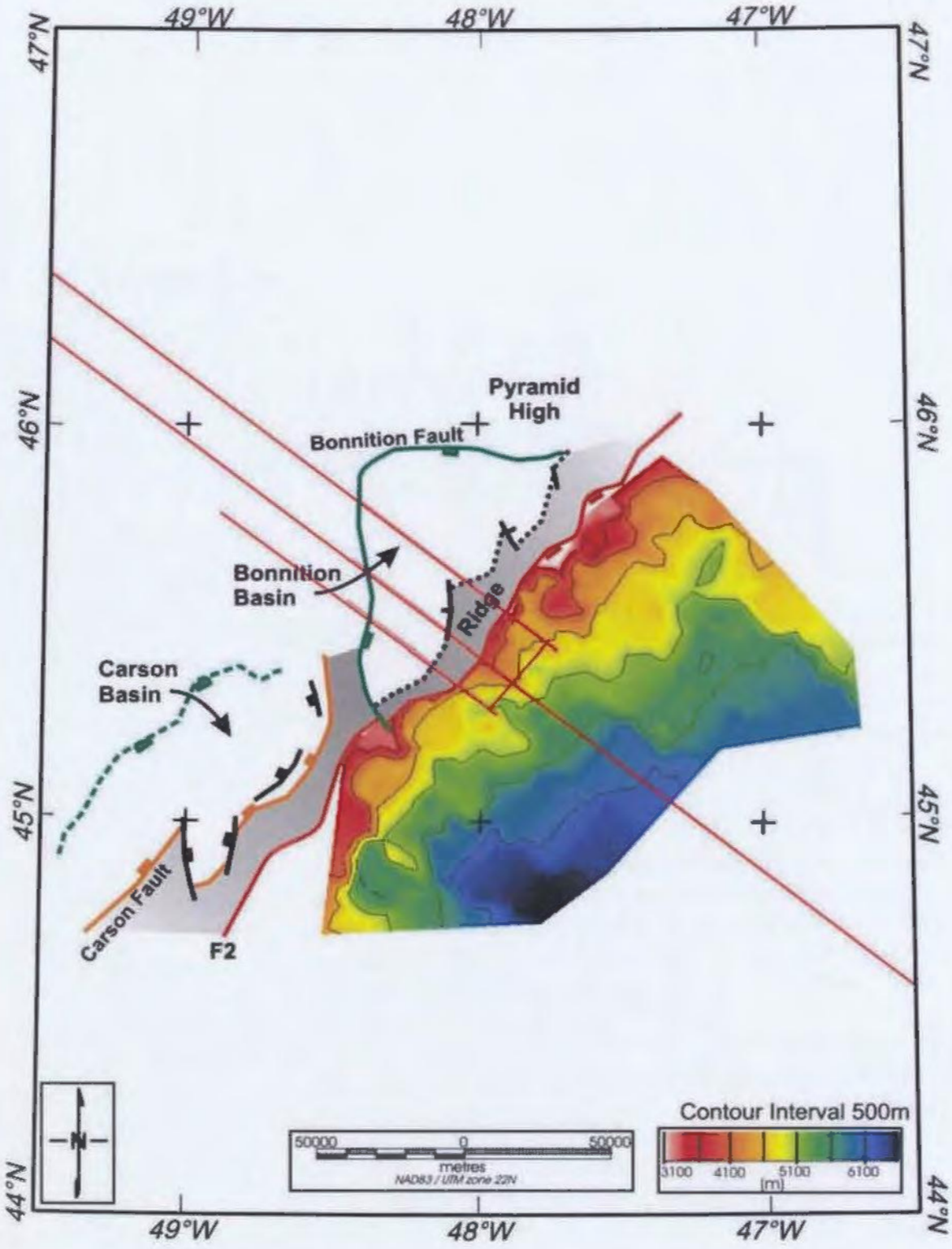

Figure 3.40. Depth structure contour map of the top of the Paleocene sandstone.

3.4.3 Intracrustal reflections

Intracrustal reflections are found below the Salar Basin. These reflections are mainly present on the proprietary WesternGeco seismic lines. One intracrustal reflection series is located near the Beothuk Knoll extension and generally dips landward over the study area. This reflection series tends to terminate seaward of the fault F2 which is associated with the major high bounding the western extent of the Salar Basin. Figure 3.41A shows the landward dipping intracrustal reflection on a WesternGeco seismic line that runs in the central portion of the Salar Basin. The overlying faults in the Salar Basin tend to terminate at/or above this reflection when it is present. A second intracrustal reflection series is found closer to the north of the study area. These reflections tend to dip seaward and are located near the fault F2, which bounds the ridge (Figure 3.41B). This reflection is not as extensive as the first intracrustal reflection series that was detailed. Figure 3.42 maps the extent of these dipping reflections across the margin.

3.4.4 Crustal and Moho reflections

Reflections from the mid and lower crust and the Moho are found on the shelf on SCREECH lines 401, 403 and 3MCS. Moho reflections are less confidently identified on WesternGeco lines A, B, E and G. The Moho is interpreted as the base of the strong lower crustal reflections. Wide angle modeling from SCREECH 3MCS line is also used to constrain the position of the Moho. These reflections indicate that the Moho and lower crust appear to be shallowing towards the southeast, in the direction of the South Bank High. SCREECH line 403 (Figure 3.43) shows the best example of the lower crustal and

Moho reflections near the shelf break and on the continental shelf. The reflections on this line are shown to shallow towards the shelf break (west to east) as well. Figure 3.44 is a time structure contour map to the top of the Moho. The time structure map shows the Moho shallowing to the south and east. The unextended continental shelf of the Newfoundland margin is composed of Precambrian and Paleozoic rocks belonging to the Avalon Zone (Williams, 1984), as well as rocks from the Meguma zone. SCREECH line 401 in Figure 3.45 shows mid and lower crustal reflections in the unextended crust on the continental shelf. The lower crustal reflections are shown to be relatively flat along the continental shelf and the Moho is picked at the base of the strong reflections. Westward dipping reflections shown in Figure 3.45 are found near the horizontal lower crustal reflections and may in some places cut Moho. Numerous westward and eastward dipping mid-crustal reflections are found under the continental shelf and are highlighted on Figure 3.45. These mid-crustal reflections are interpreted to represent older neoproterozoic crustal fabrics.

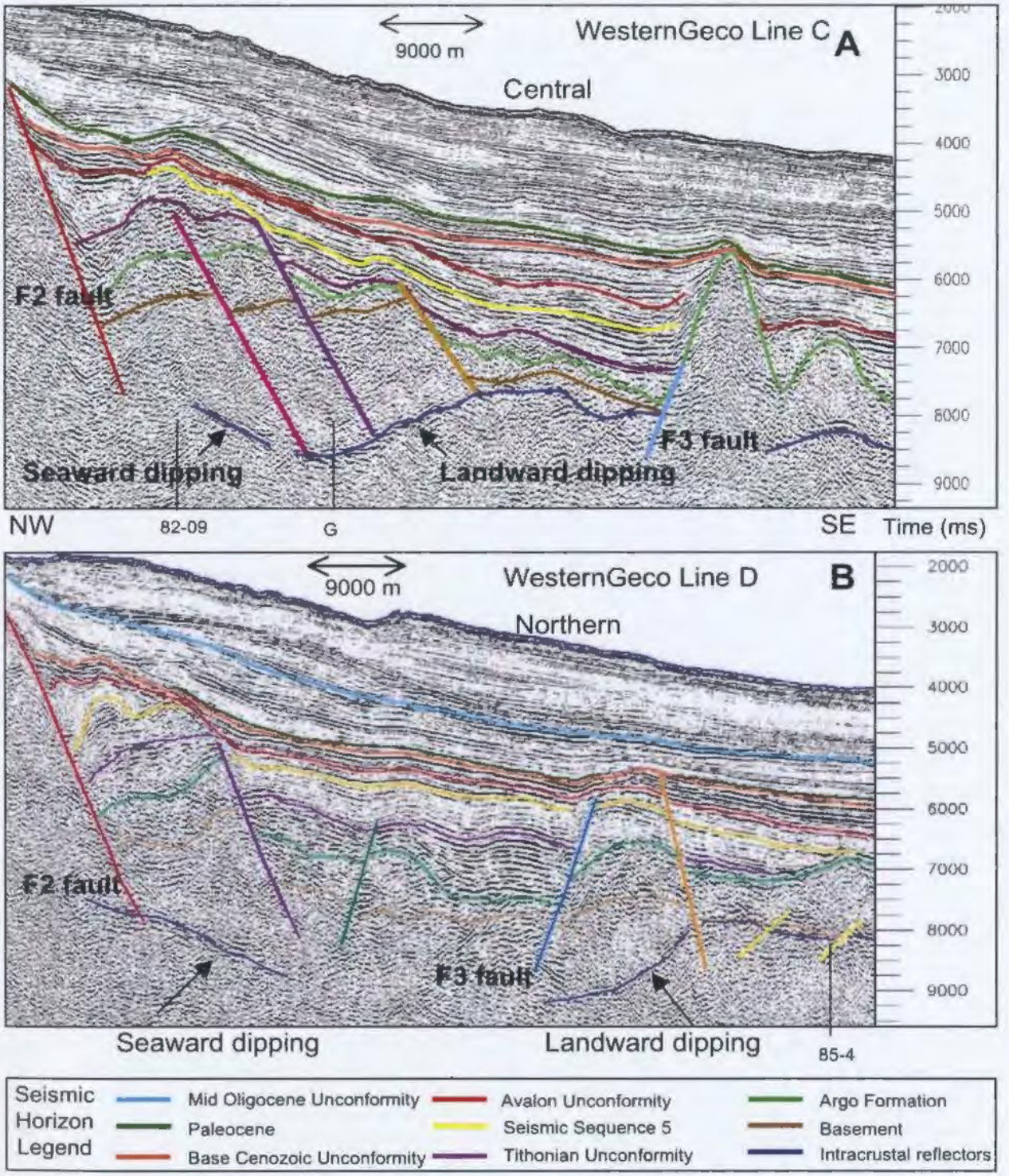

Figure 3.41. Interpreted proprietary WesternGeco seismic sections showing the intracrustal reflections in dark blue. Part A) This section runs across the central portions of the Salar Basin. Part B) This section runs across the northern part of the Salar Basin. These sections show how the intracrustal reflectors change shape across the margin.

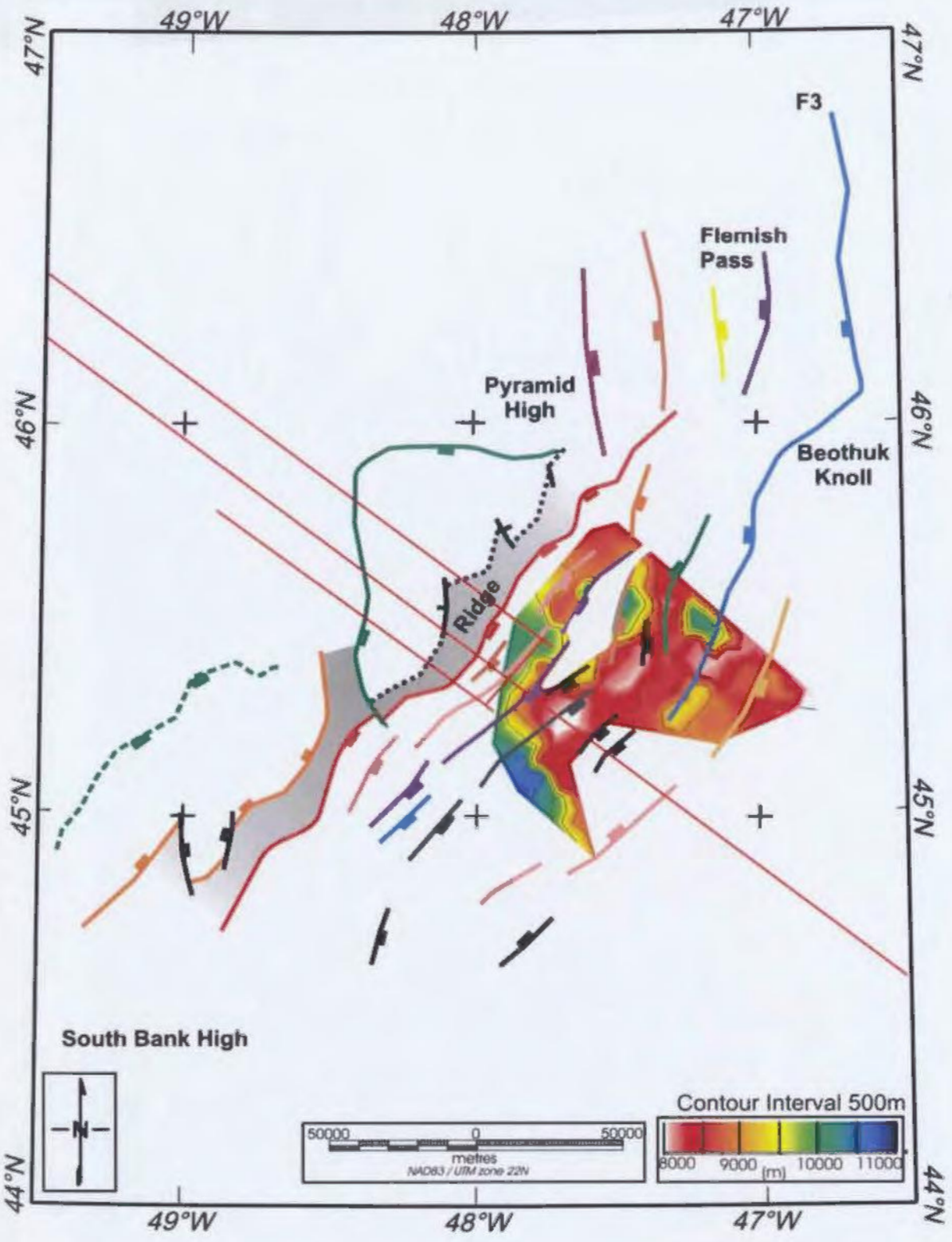

Figure 3.42. Depth structure contour map of the intracrustal reflections.

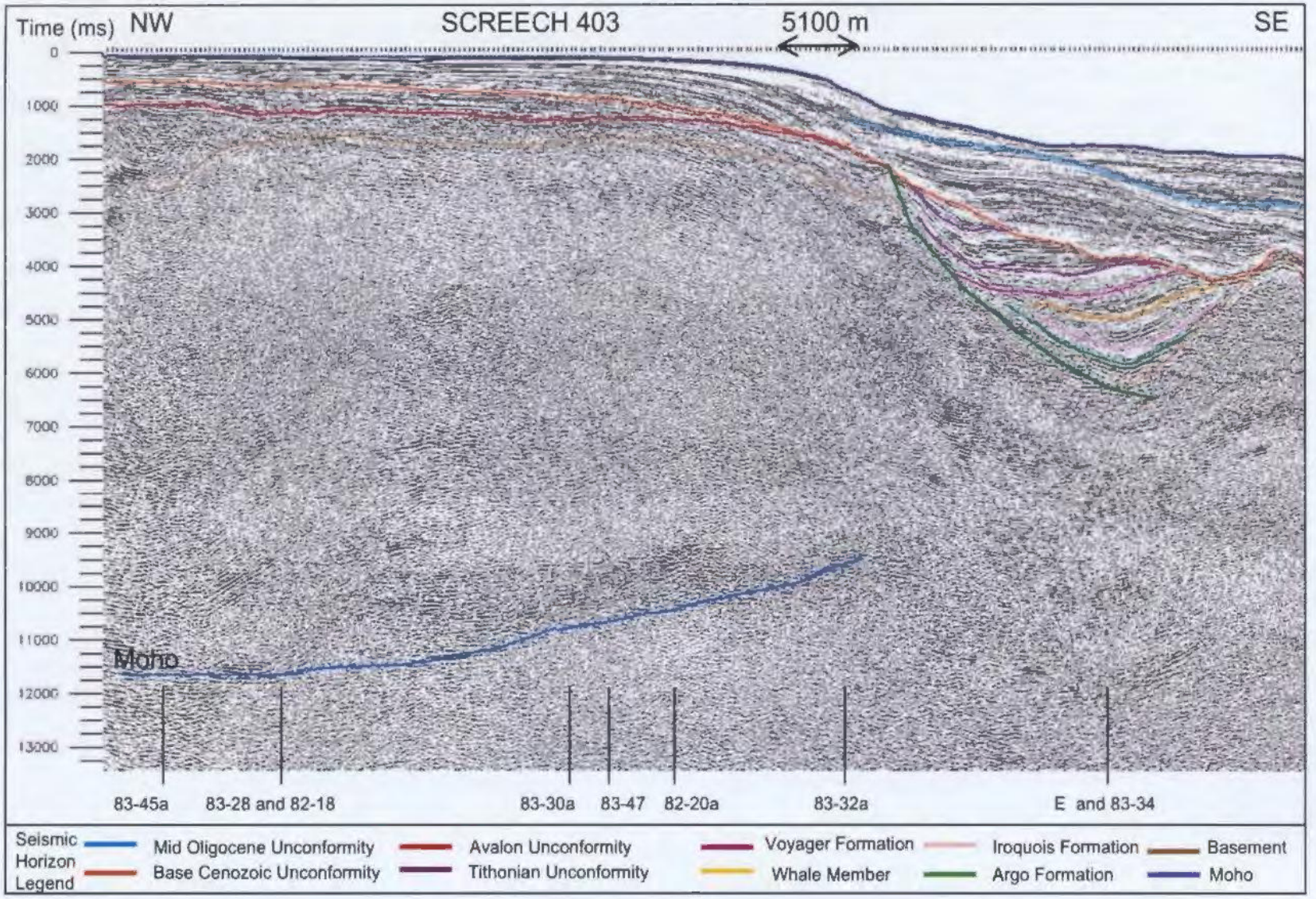

Figure 3.43. Seismic line SCREECH 403. This line shows the reflections from the lower crust and the position of the interpreted Moho.

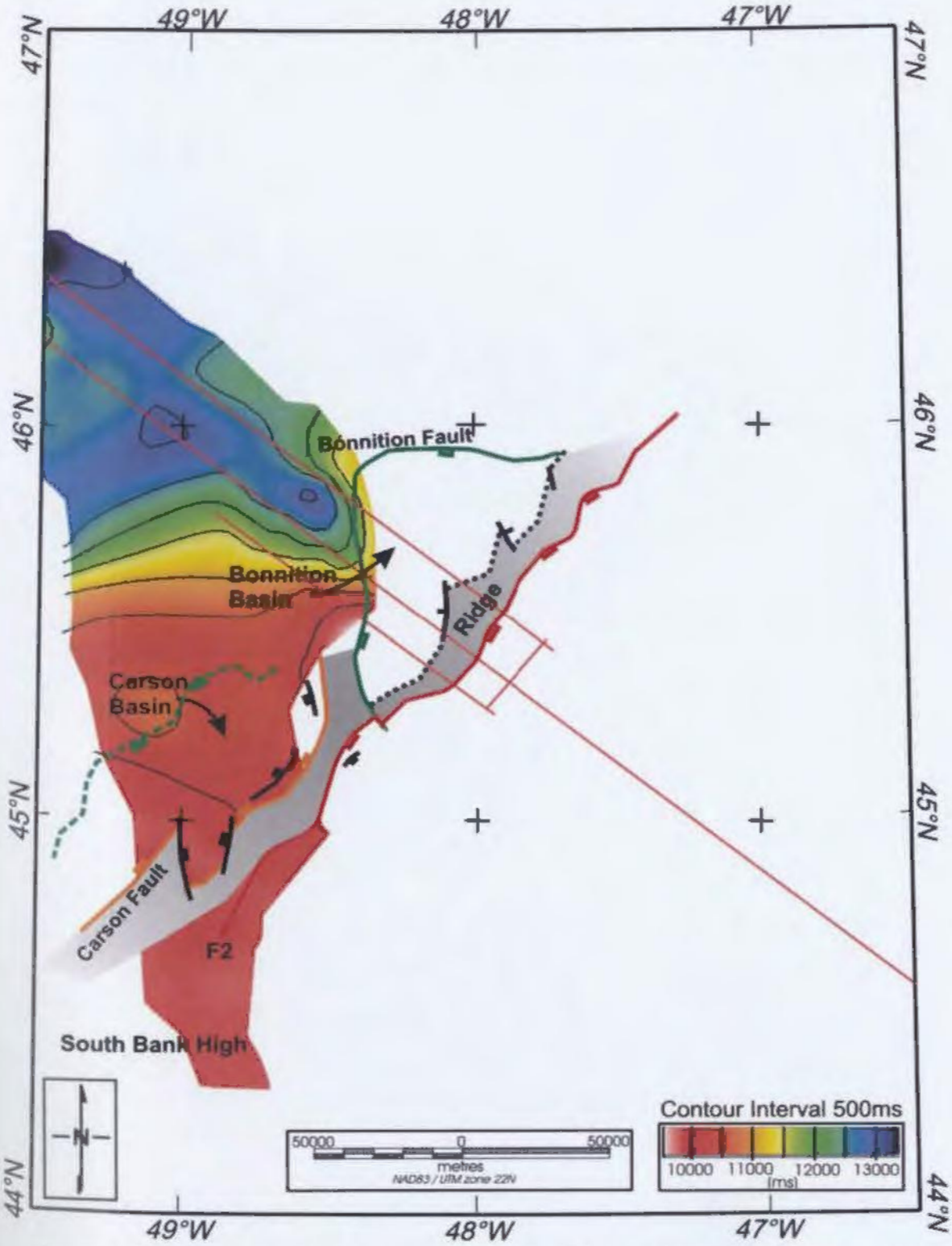

Figure 3.44. Time structure contour map of the Moho, shown to shallow to the south towards the South Bank High as well as to the east.

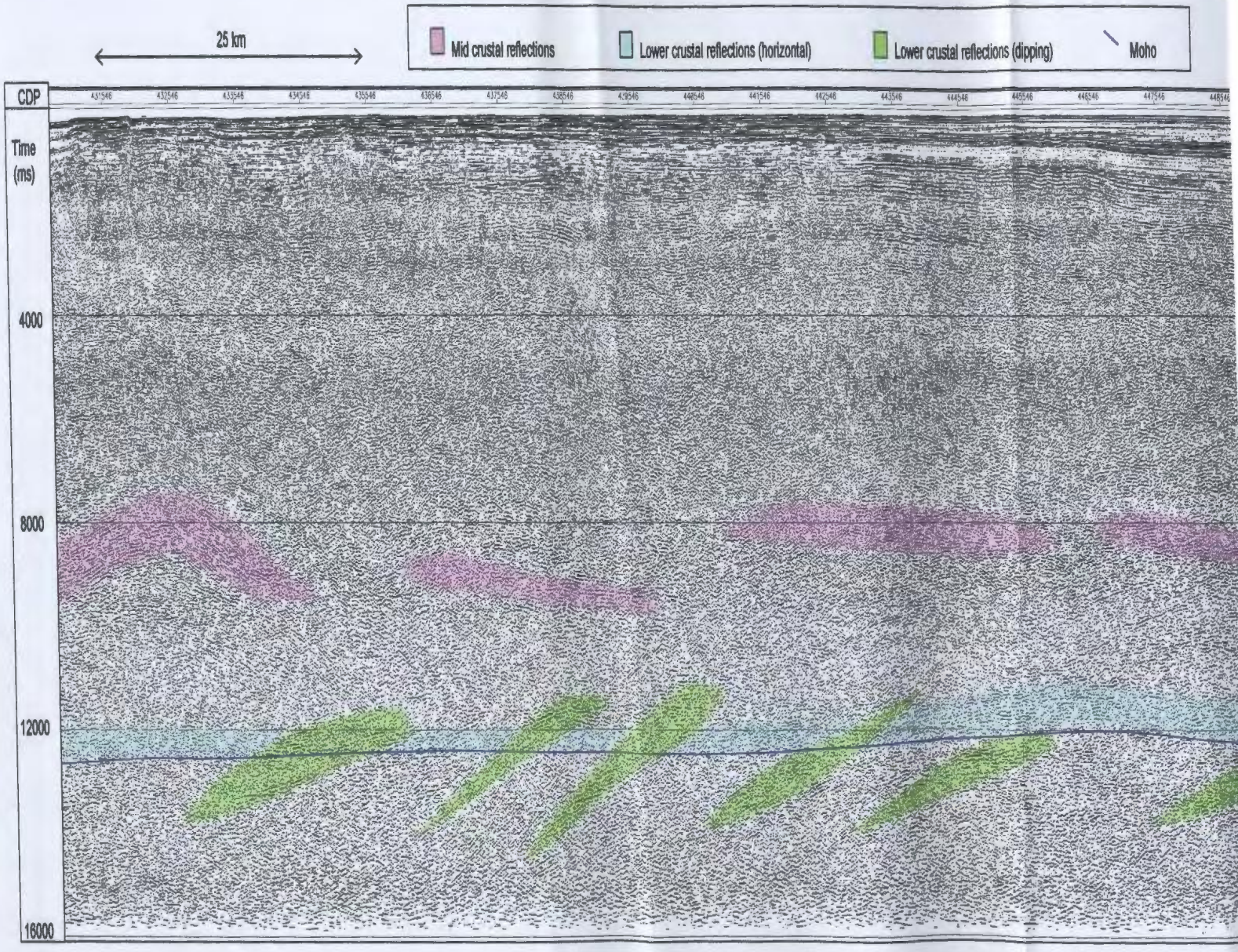

Figure 3.45. Shelf portion of seismic line SCREECH 401. This line shows reflections from the mid crust (pink) and horizontal lower crustal reflections (blue). Dipping lower crustal reflections are shown in green and the position of the i

Moho

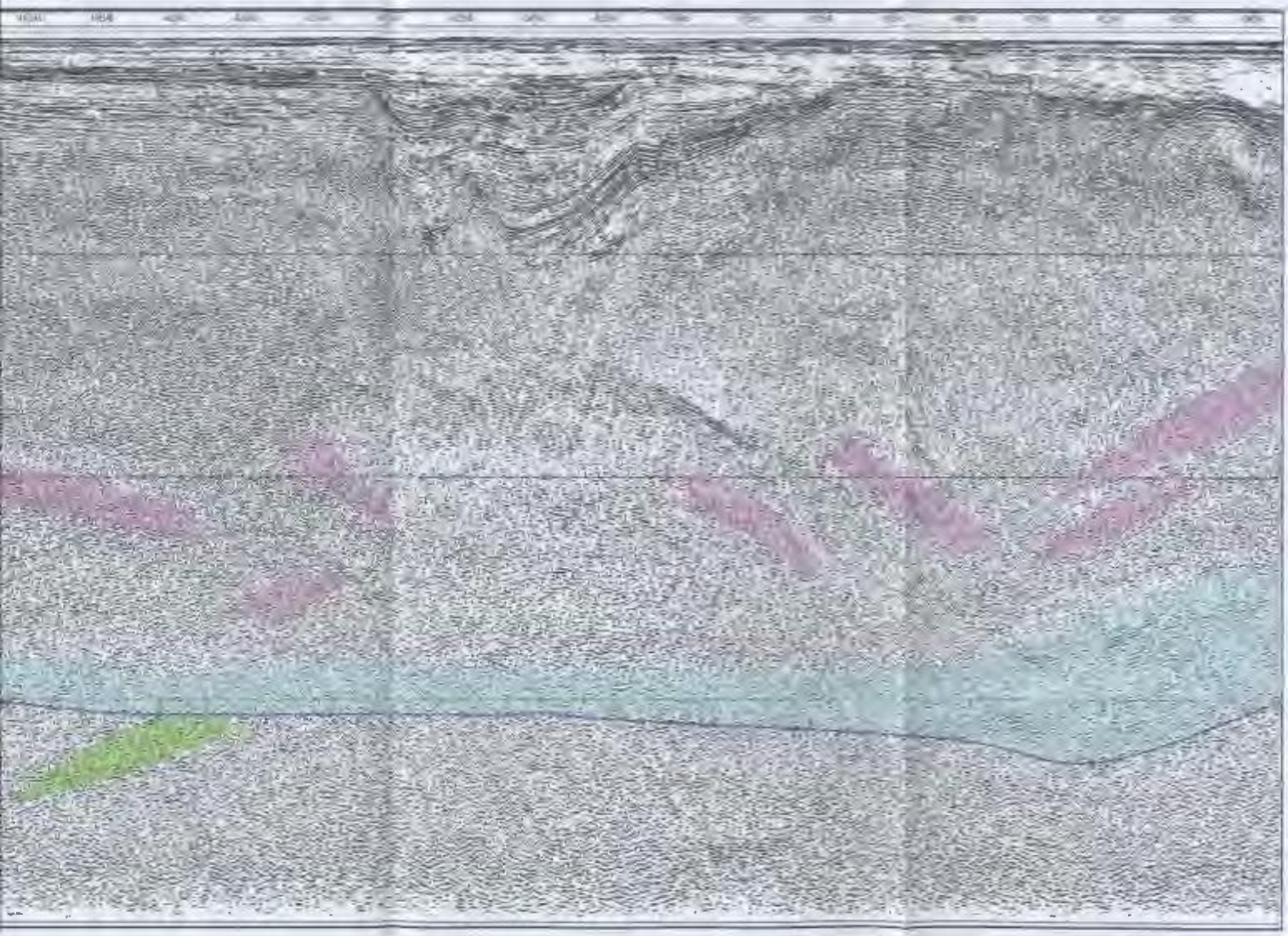

e position of the interpreted Moho is shown in blue.

3.5 Gravity Modeling

Gravity modelling was used to aid in constraining the composition of features that were considered ambiguous. The software package GM-SYS by Northwest Geophysical Associates (NGA) was used to model different geological scenarios. The software allows you to create different geological models and test their accuracy by comparing the modeled gravity response to the observed measurements. Gravity modelling was performed on the slope section of SCREECH lines 401, 3MCS and 403. The main objective of the modeling was to determine the composition of a prominent high in the slope region of the study area. Reflection seismic data (plotted in depth) for the three SCREECH lines were input into the GM-SYS software and were used to help determine the different layer boundaries in the model.

The depth to the seafloor was picked for each line and the water layer was given a density value of 1.0 g/ cm^3. For each model three layers were picked. The first layer corresponds to Cenozoic and younger strata and this layer was given a density of 2.35 g/cm^3. The second layer corresponds to the sediments in the Carson Basin. These strata are mainly Cretaceous, Jurassic and in some places Triassic deposits. These strata were given an average density value of 2.5 g/cm^3. The third layer corresponds to the strata below the Cenozoic in the slope region. These strata are Cretaceous and Jurassic and were given an average density of 2.55 g/cm^3, due to the thickness of Cenozoic strata over laying them. The crust was divided into two sections; an upper and lower section with the upper section having a density value of 2.65 g/cm^3. The lower crust was given a

density value of 2.9 g/cm^3. Below the lower crust and Moho the mantle is assigned a density value of 3.3 g/cm^3.

The composition of the high in the slope area is thought to either be basement material or salt so two different densities were assigned to the high and tested for each line. Assuming that the high was composed of salt, a density of 2.25 g/cm^3 was assigned. When the high was assumed to be composed of basement material the density was 2.7 g/cm^3. Figures 3.45 to 3.47 show the results of modelling for each line. In figures 3.46 to 3.487 an arbitrary position was chosen across the profile to tie the results of the modeled gravity values to the observed gravity values. In the figures the tie point is indicated by a red star joining the observed and calculated gravity values. Upon examination of the models it is evident that the model which interprets the high as basement material matches the observed gravity measurements extremely well. The models interpreting the high as salt do not produce results that match the observed data. Based on these models it is determined that the high is mainly composed of basement material, though some small amount of salt may be present.

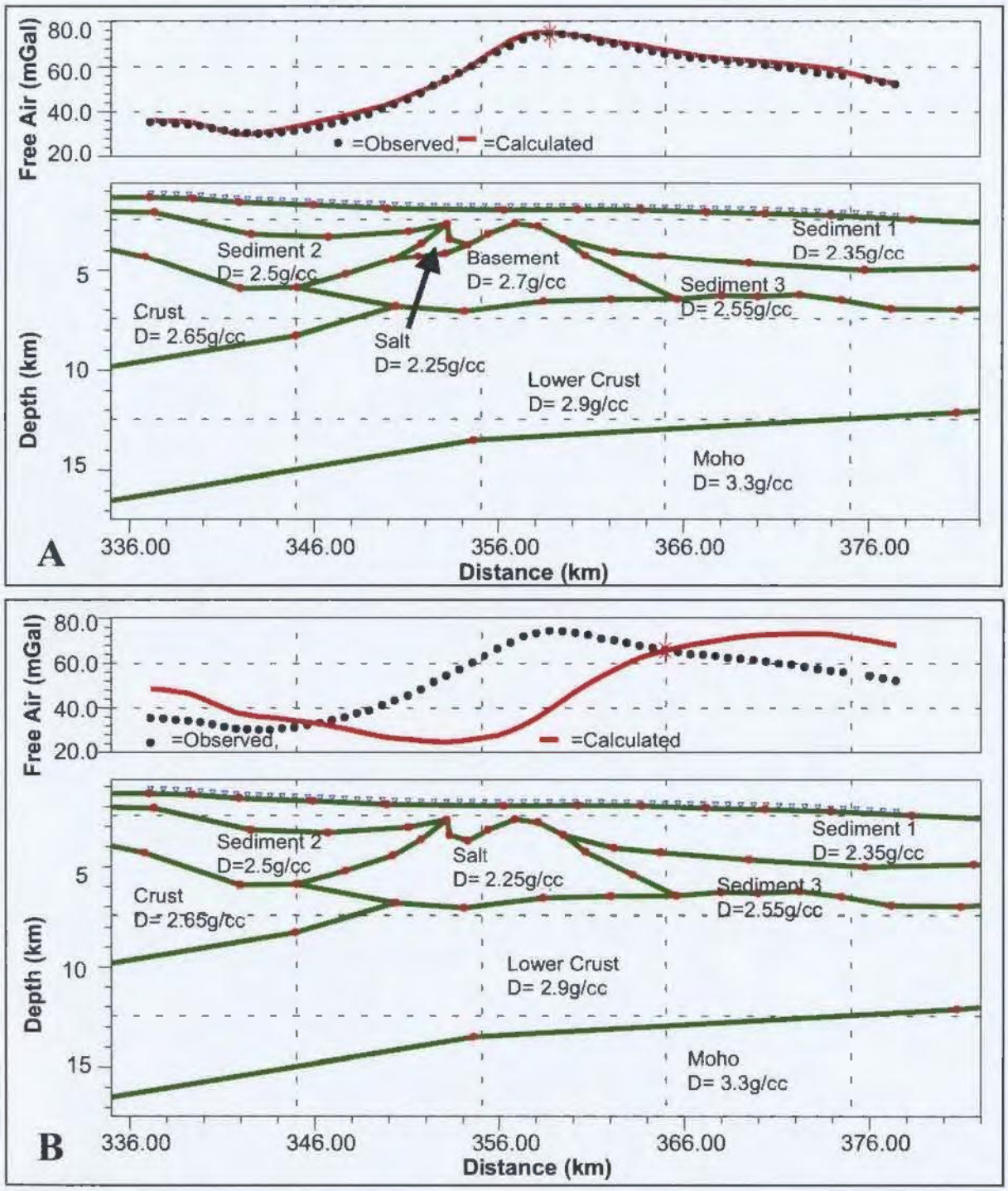

Figure 3.46. Gravity modeling performed on line 401. Figure A illustrates the model when the high is composed of basement material, while Figure B models the high as salt. The modeled gravity response in Figure A closely matches the observed gravity data, while the model in Figure B does not.

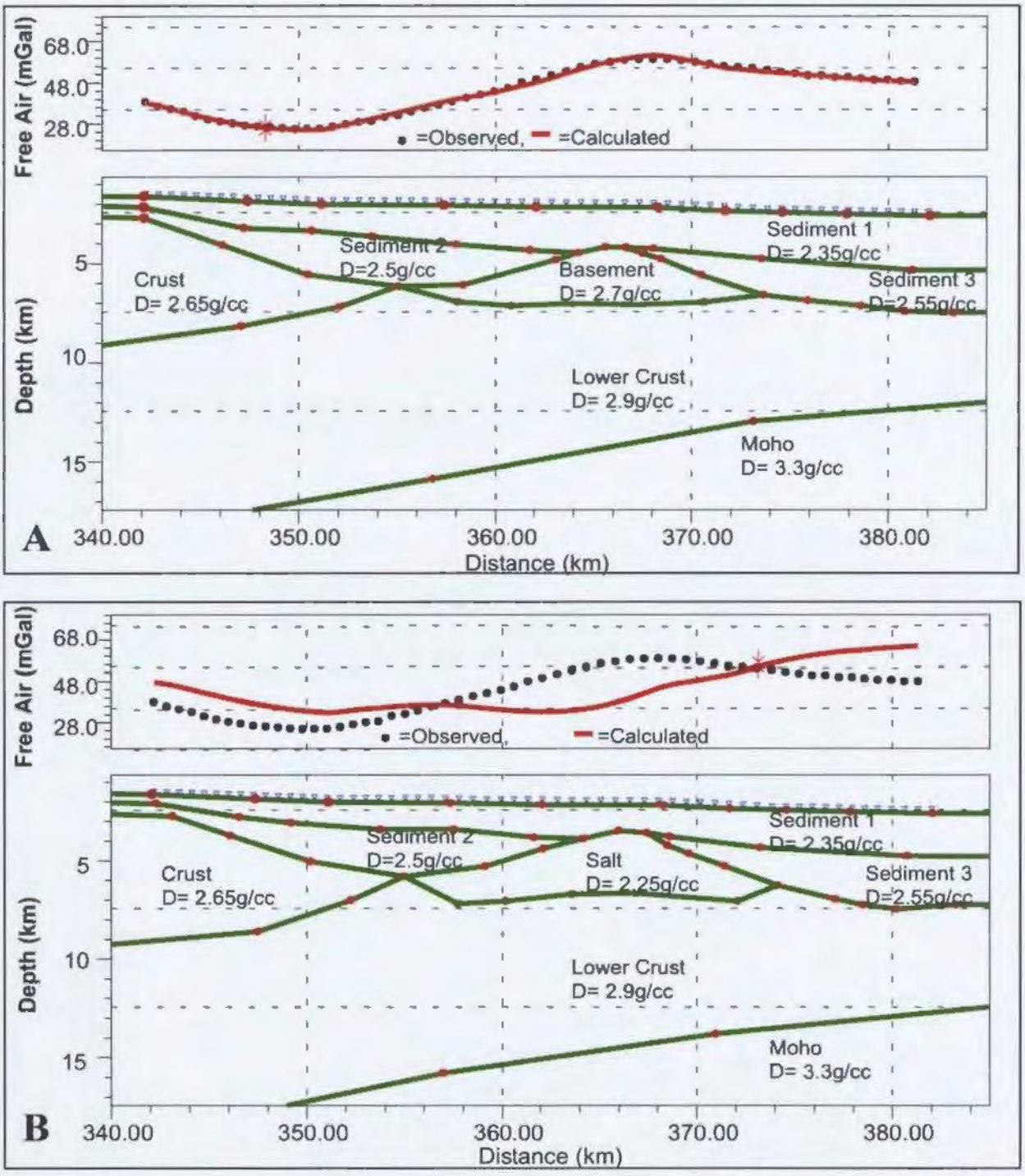

Figure 3.47. Gravity modeling performed on line 403. Figure A illustrates the model when the high is composed of basement material, while Figure B models the high as salt. The modeled gravity response in Figure A closely matches the observed gravity data, while the model in Figure B does not.

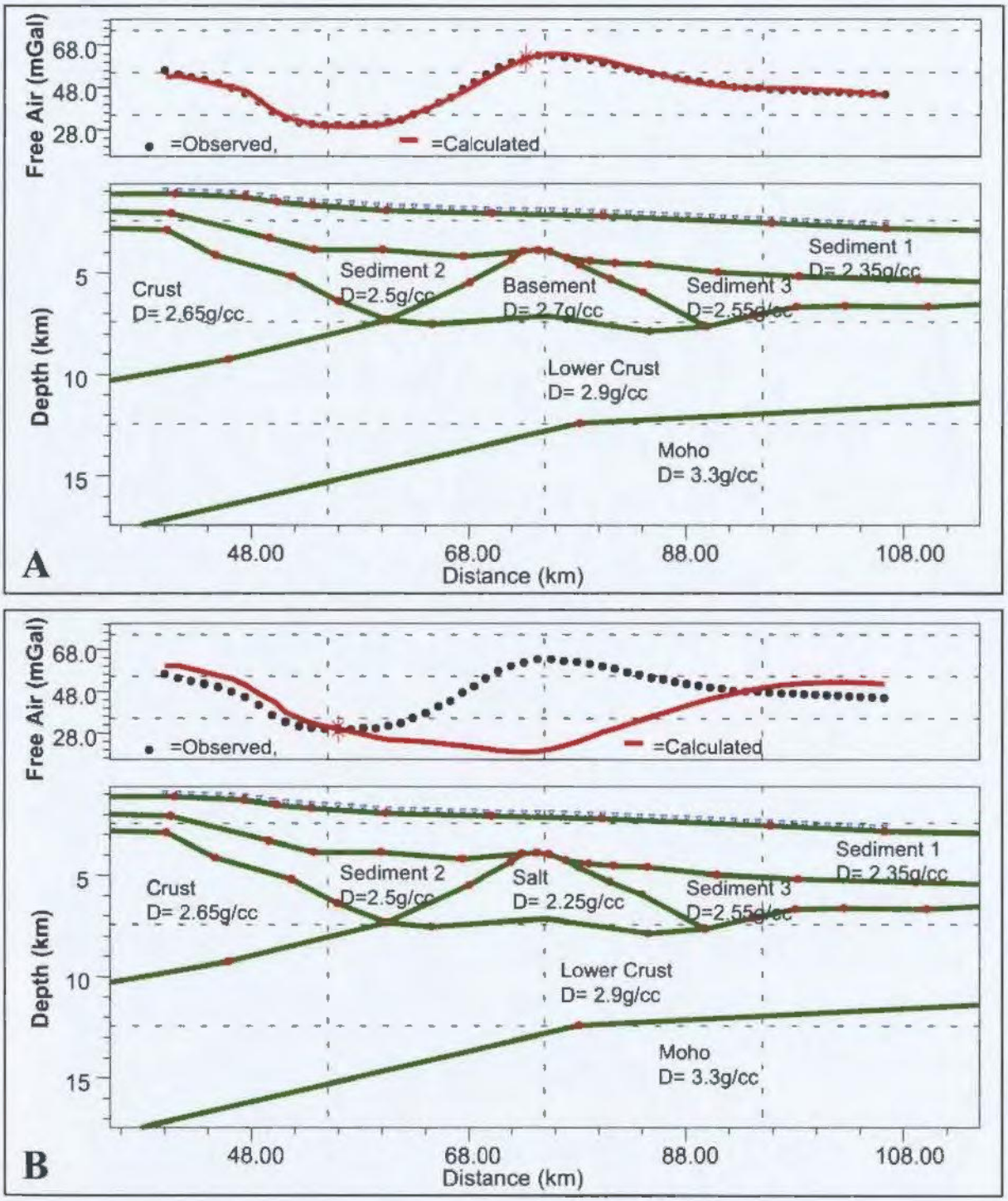

Figure 3.48. Gravity modeling performed on line 3MCS. Figure A illustrates the model when the high is composed of basement material, while Figure B models the high as salt. The modeled gravity response in Figure A closely matches the observed gravity data, while the model in Figure B does not.

CHAPTER 4 Structural formation of the south-east Newfoundland margin

4.1 Rift Basin Structures

The southeast Newfoundland margin has a complex evolutionary history with the Carson, Bonnition, Salar and other basins forming on the margin. Tectonic control on rift basin architecture depends on fault propagation, linkage and growth (McLeod et al. 2002). Rosendahl (1987) illustrates the numerous different structural configurations that can arise when rift basins are formed. Rift basins are typically formed through a series of narrow half grabens, which may show alternating polarity along strike (Younes and McClay, 2002 and Rosendahl, 1987). The zones of alternating polarity along strike are separated by accommodation zones, following the terminology of Younes and McClay, 2002. The term 'transfer zone' will refer to a fault or fault zones connecting individual rifts, without the need for a reversal in polarity of their dip directions (Younes and McClay, 2002). Accommodation zones are generally higher in elevation than the surrounding area, 15 to 30 km wide, and cut by many steeply dipping synthetic and antithetic faults. Figure 4.1 illustrates a conceptual model of an accommodation zone showing an along-strike change in the polarity of a half-graben.

Studies of active normal faults in the Basin and Range and East Africa areas, indicate that many of these normal faults are segmented along strike (Gawthorpe and Leeder, 2000). The boundaries of fault segments are marked by highs and lows in the hangingwall and footwall elevations. Boundaries can also be marked by an increase in density of small

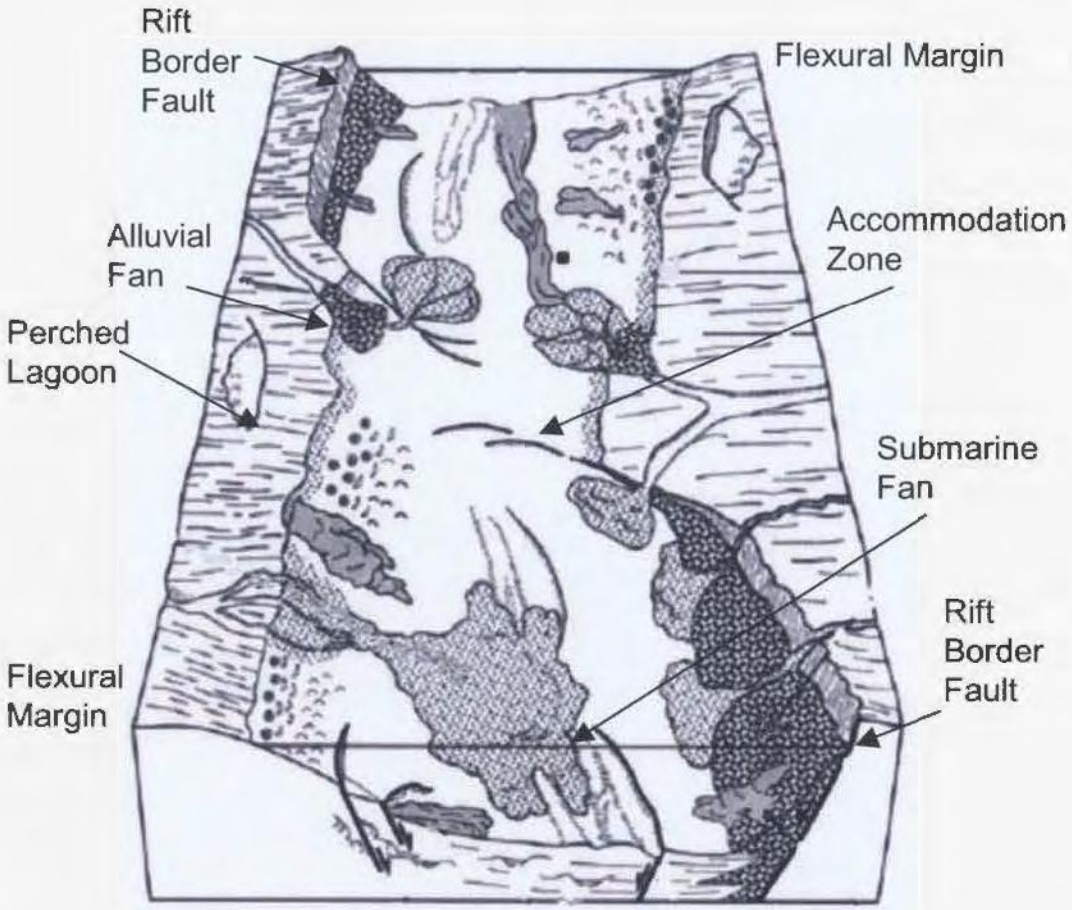

Figure 4.1. Model of an accommodation zone showing a change in the half-graben polarity along strike. The model also illustrates various sedimentary features that may be found in the half-graben. *Modified from:* Younes and McClay, (2002)

displacement faults. Folding contributes to the development of normal fault zones. In the hangingwall of normal faults, transverse anticlines and synclines develop and define the displacement maxima (synclines) and minima (anticlines) (Gawthorpe and Leeder, 2000). At fault segment boundaries, anticlines form. Figure 4.2, from Gawthorpe and Leeder (2000), illustrates some of the features associated with normal faults in extensional environments, and their evolution through time.

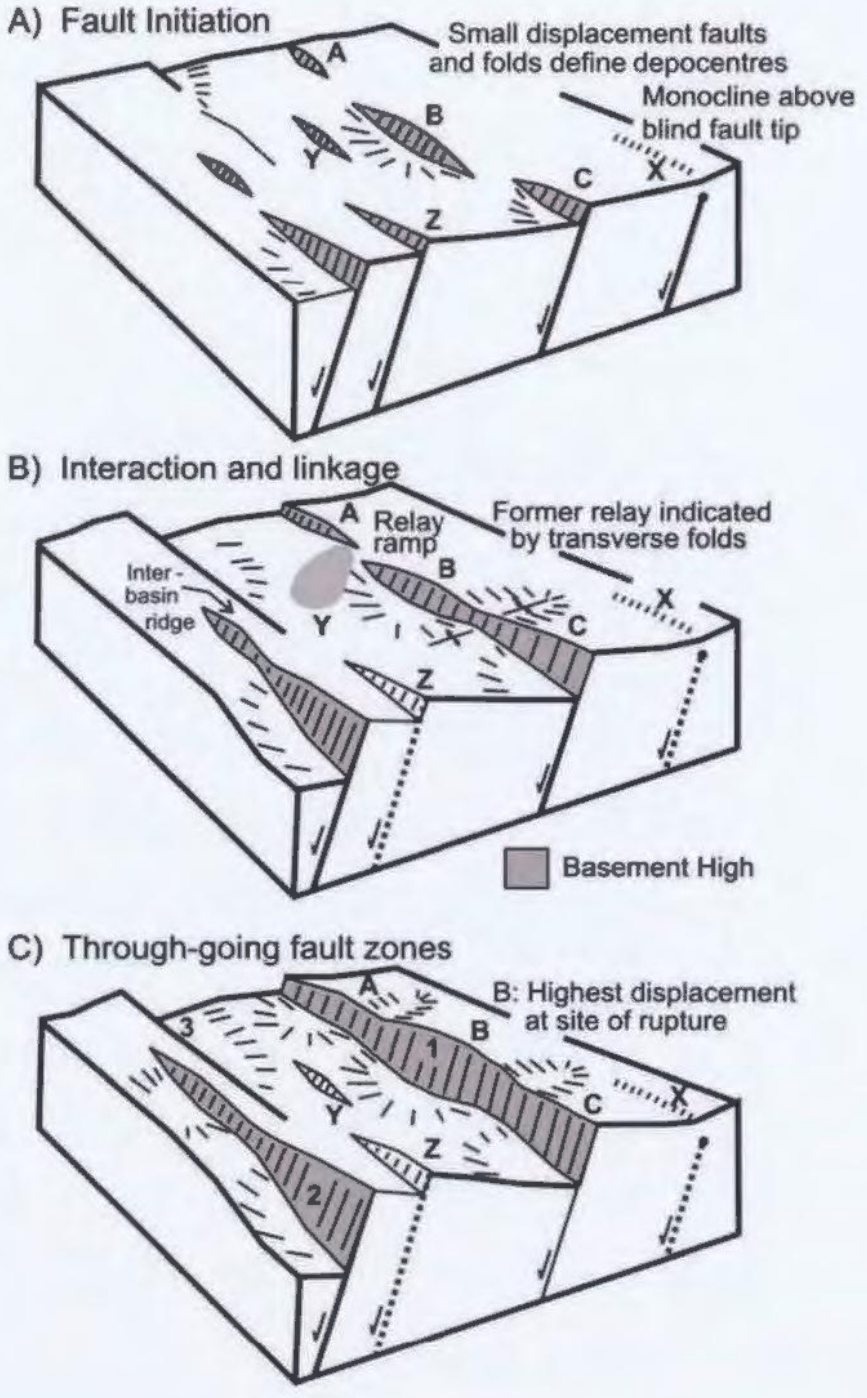

Figure 4.2. Illustrations of normal fault evolution. A) Fault initiation with numerous small fault segments. B) Fault interaction and linkage stage where deformation becomes localized along major fault zones. C) Deformation is localized along major border fault zones, creating half graben depocentres. *Modified from:* Gawthorpe and Leeder (2000).

4.2 Basin Formation

In the Jeanne d'Arc Basin the Murre Fault, which forms the western boundary of the half graben, exhibits numerous bends along strike suggesting that the fault formed initially as a series of en echelon faults which later became linked (Sinclair, 1995b). The major basin bounding faults in the thesis study area most likely formed in a similar manner. The faults would have originated initially as fault segments, which through their evolution eventually link to produce major fault zones. Figure 4.3 illustrates the major features present on the margin and their orientation. The structural evolution of each basin is discussed in depth in the succeeding sections, but some generalisations may provide a useful context at this stage. The Carson Basin initially formed by normal fault segments with throw down to the west, while the Bonnition Basin was formed by normal fault segments with throw down to the east. Figures 3.15 and 3.16 in Chapter 3 illustrate the general structure of each of the basins, and show the change in the polarity of the major basin bounding faults. The bounding faults for the Carson Basin generally trend northeast– southwest. In the Bonnition Basin the bounding fault trends north-south in the southern portion of the basin and east-west in the north. In the southern portion of the basin, the fault is interpreted to have formed as a series of left stepping normal fault segments, which later became linked. In the Salar Basin, the southern and central portion formed through a series of northeast– southwest trending normal fault segments, while the northern portion of the basin formed through north-south trending normal antithetic and synthetic fault segments.

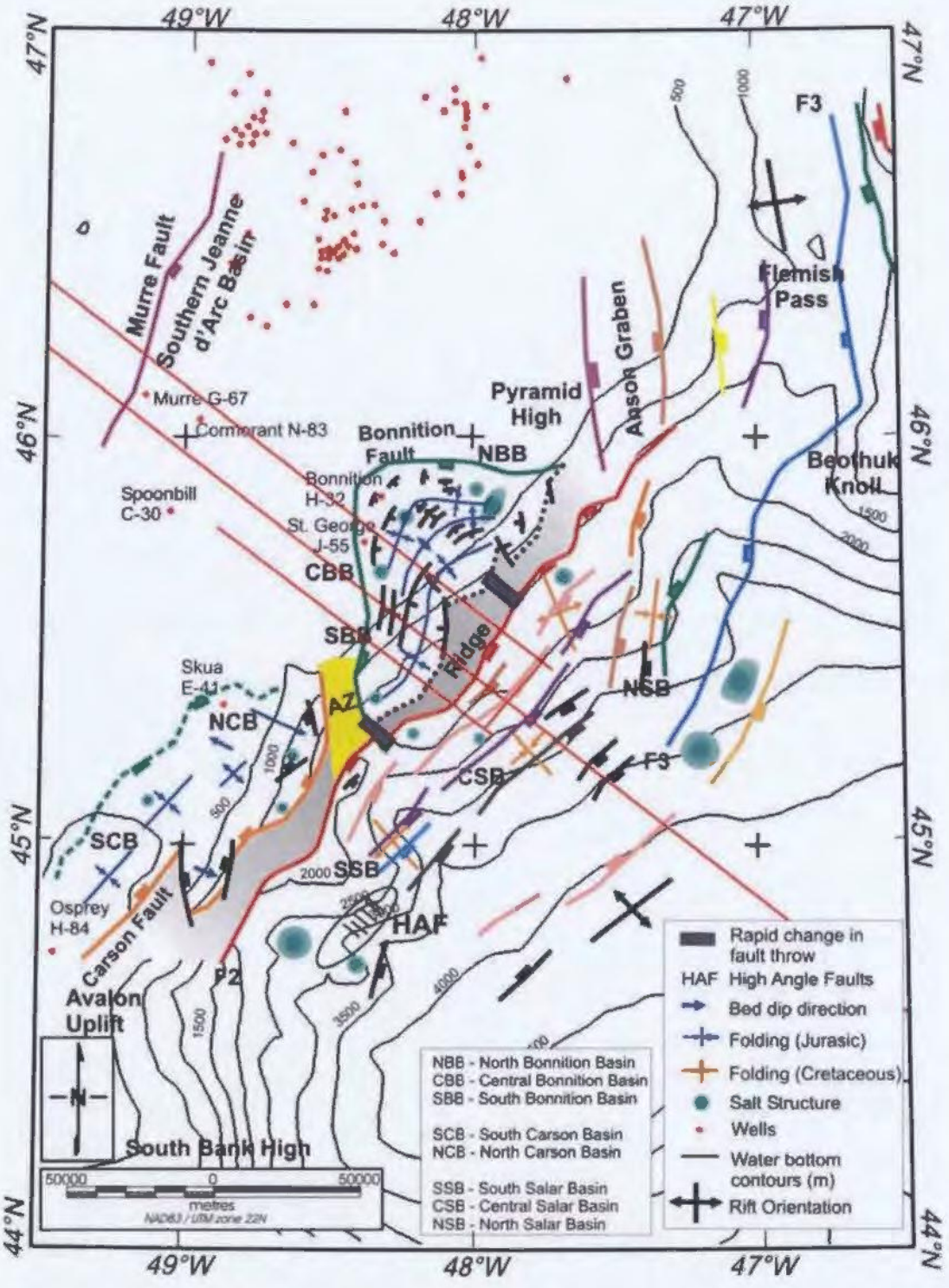

Figure 4.3. Structural map of the Carson, Bonnition and Salar basins. A change in the half-graben polarity is shown by the formation of an accommodation zone (AZ). NNB=North Bonnition Basin, CBB=Central Bonnition Basin, SBB= South Bonnition Basin, SCB=South Carson Basin, NCB=North Carson Basin, SSB=South Salar Basin, CSB=Central Salar Basin, NSB=Northern Salar Basin, HAF= High Angle Faults.

The Bonnition and Carson basins exhibit a contrast in half-graben polarity along strike, with an accommodation zone between them as illustrated in Figure 4.3. This accommodation zone appears as a structurally higher area separating zones of oppositely dipping faults and sediments. A general tectono-stratigraphic outline for the Bonnition and Northern Salar basins is given in Figure 4.4, and for the Carson and Southern Salar basins in Figure 4.5. These figures show the general timing of the major faults and the deposition of sedimentary sequences in the basins. As previously shown in Chapter 3, Figures 3.8, 3.9, and 3.10 illustrate the well ties (Bonnition, St. George and Skua) to nearby seismic lines. These wells aid in constraining the interpretation of the seismic horizons in the thesis area. Table 3.3 in Chapter 3 gives an overview of the seismic horizons that are interpreted and their ages. The structure of the two shelf edge basins (Carson and Bonnition) shows that they both underwent a markedly different evolution despite being adjacent to one another. Extensional faulting tends to dominate in the basins on the margin, however there are indications of strike-slip movements occurring in the region. On the margin, it is generally thought that strike-slip deformation is caused by changes in the extensional stress regime from different episodes of rifting (Sinclair, 1995b; and Enachescu, 1987), which causes structural distortion and changes in the trend of pre-existing faults (Sinclair, 1995b). The presence of an accommodation zone also indicates that strike-slip motion may be present as they usually have a strike-slip component.

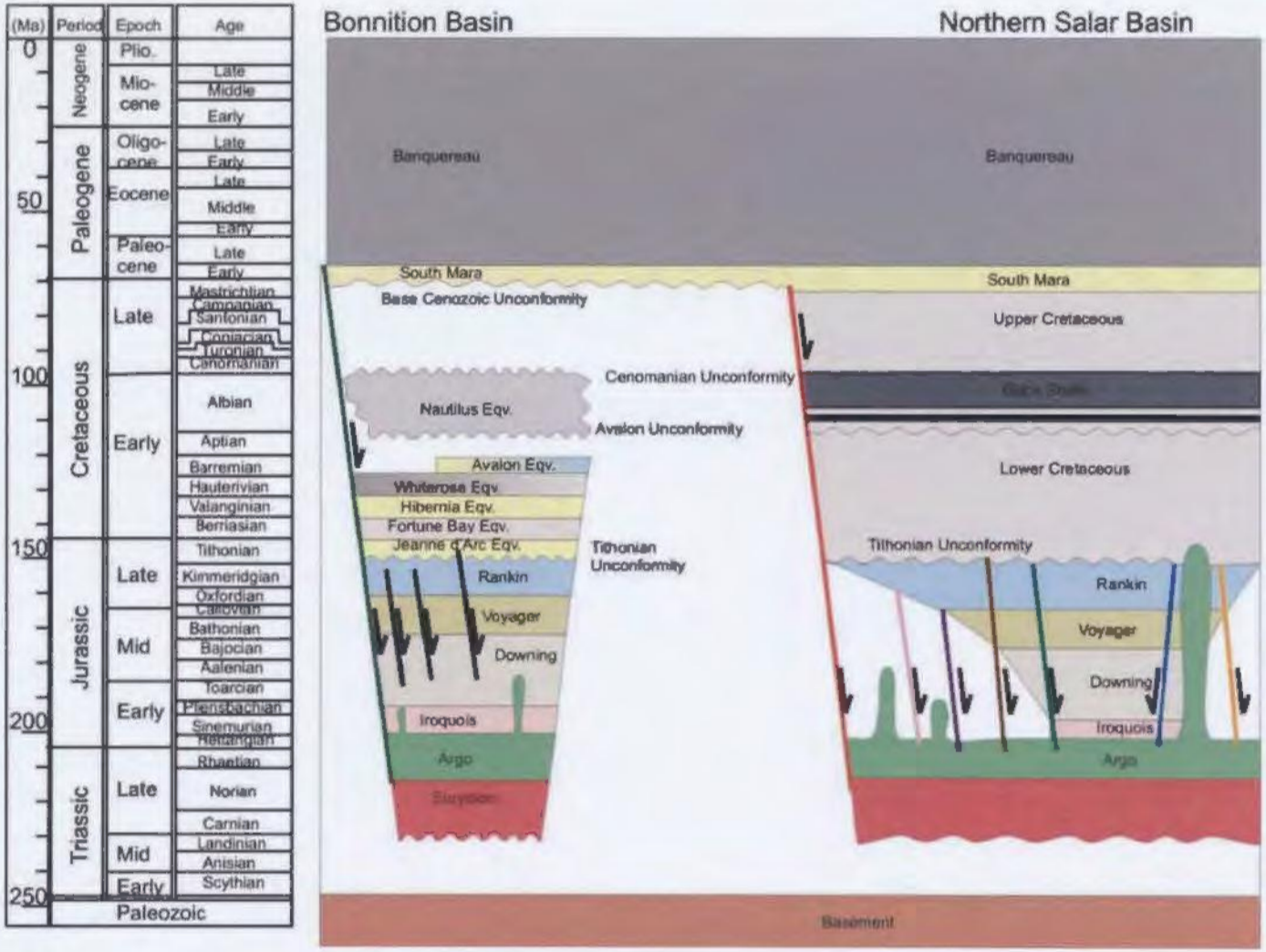

Figure 4.4. Tectono-stratigraphic illustration of the Bonnition and Northern Salar basins. Timing of fault activity and sediment deposition is indicated. Lengtb of the fault arm indicates the total period the fault displayed motion. During this time the fault may have moved intermittently. Fault colours correspond to the mapped locations shown in Figure 4.3.

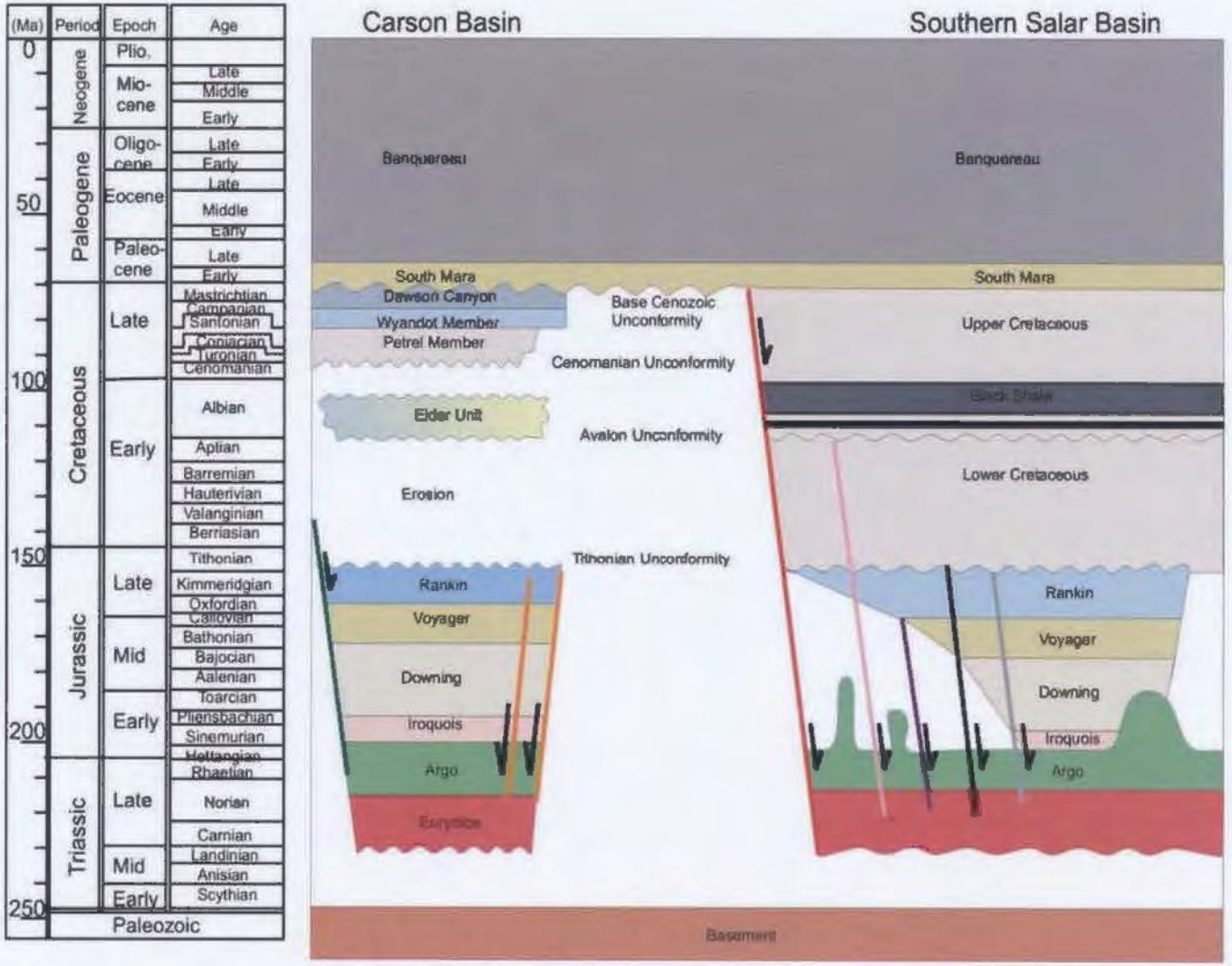

Figure 4.5. Tectono-stratigraphic illustrations of the Carson and Southern Salar basins. Timing of fault activity and sediment deposition is indicated. Length of the fault arm indicates the total period the fault displayed motion. During this time the fault may have moved intermittently. Fault colours correspond to the mapped locations shown in Figure 4.3.

4.2.1 Southern Carson Basin

The Carson Basin was mainly formed by the down-to-the-west Carson Fault. The southern portion of the Carson Basin is relatively shallow and narrow when compared to the northern section and the amount of sediment accumulation is considerably less, as shown in Figure 4.6 (A) and (B). The formation of the Avalon Uplift (shown in Figure 4.3) in the southeast portion of the margin has a large influence on the structure and composition of the Carson Basin. This large basement arch was formed by two distinct periods of uplift, erosion and non-deposition during the Tithonian to Valanginian and the Barremian to Albian (Sinclair, 1995b). In the southern Jeanne d'Arc Basin Sinclair (1995b) noted that the formation of the uplift caused Triassic and Jurassic layers to become tilted, which were then overlain by Cenomanian and younger sediments. In the Carson Basin the formation of the uplift also produces tilting and truncation of Upper Triassic and Lower Jurassic sediments as well as a period of non-deposition or erosion in this basin. Mid to Upper Jurassic sequences were eroded or not deposited in the south and preserved towards the northern portion of the basin. These sequences are then overlain by thin Upper Cretaceous sediments as shown in Figure 4.6(B). Movement of the Lower Jurassic salt sequences disrupts some of the overlying syn- and post-rift sequences. The salt tectonism in the southern portion of the basin aids in the creation of a syncline in the basin centre. This syncline affects the Iroquois and Downing formations and because of their unchanging thickness across it, appears to have formed after these layers were deposited. Salt movement appears to persist until shortly after the beginning of the Cenozoic.

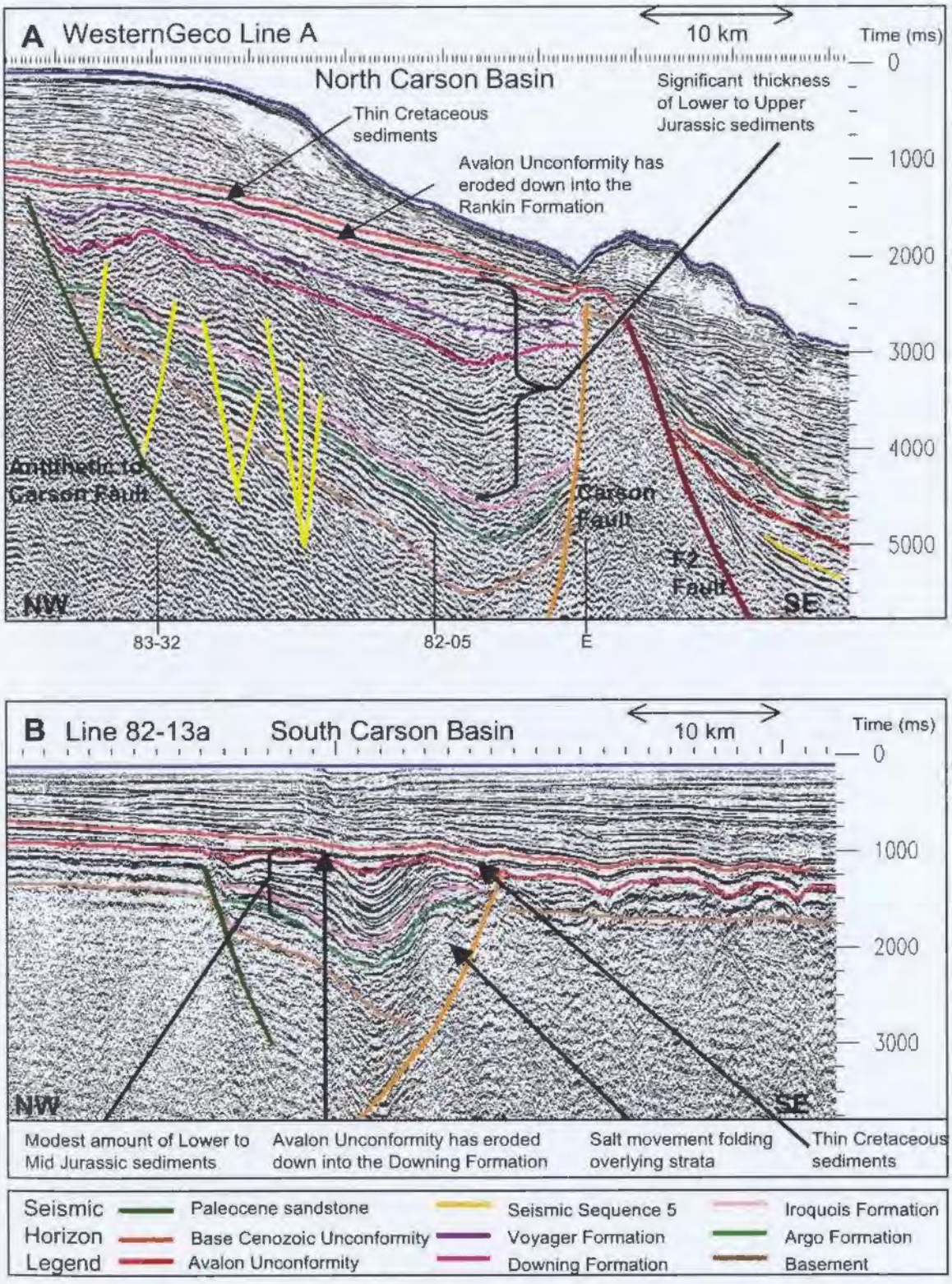

Figure 4.6. Comparison of sediment fill and structure between the northern (A) and southern (B) Carson Basin. In the south, the basin appears shallower and narrow, whereas towards the north the basin is wider and deeper.

4.2.2 Northern Carson Basin

The northern Carson Basin is wider than the southern portion and the Carson Fault offsets basement material and appears active until approximately the Mid to Late Jurassic, with much of its movement occurring during the Late Triassic to the Early Jurassic creating the deepest portion of the basin towards the north-east. The fault antithetic to the Carson Fault is active during the same time period; however the displacement across the fault is much less than that of the more dominant Carson Fault as illustrated in Figure 4.6A. As in the southern portion of the basin, salt movement disrupts the overlying sediment in localized areas. The salt mainly disrupts the synrift sequences as shown in Figure 4.7.

The sparse seismic coverage over the Carson Basin makes correlation difficult and creates uncertainty in the final interpretation. Few salt diapirs are imaged in the basin and little internal faulting has been imaged. It is difficult to say for certain whether these are characteristics of the entire basin or if the sparse data coverage has a strong influence on the interpretation.

4.2.3 Southern Bonnition Basin

The Bonnition Basin is largely influenced by the major down-to-the-east Bonnition Fault. In the southern portion of the basin, this fault offsets basement and largely controls the structure of the basin, creating a depocentre in which sediments accumulate. In this area the Bonnition Fault is active from Late Triassic and persists until the Early Cenozoic. The southern portion of the basin tends to be the deepest however there is a relatively

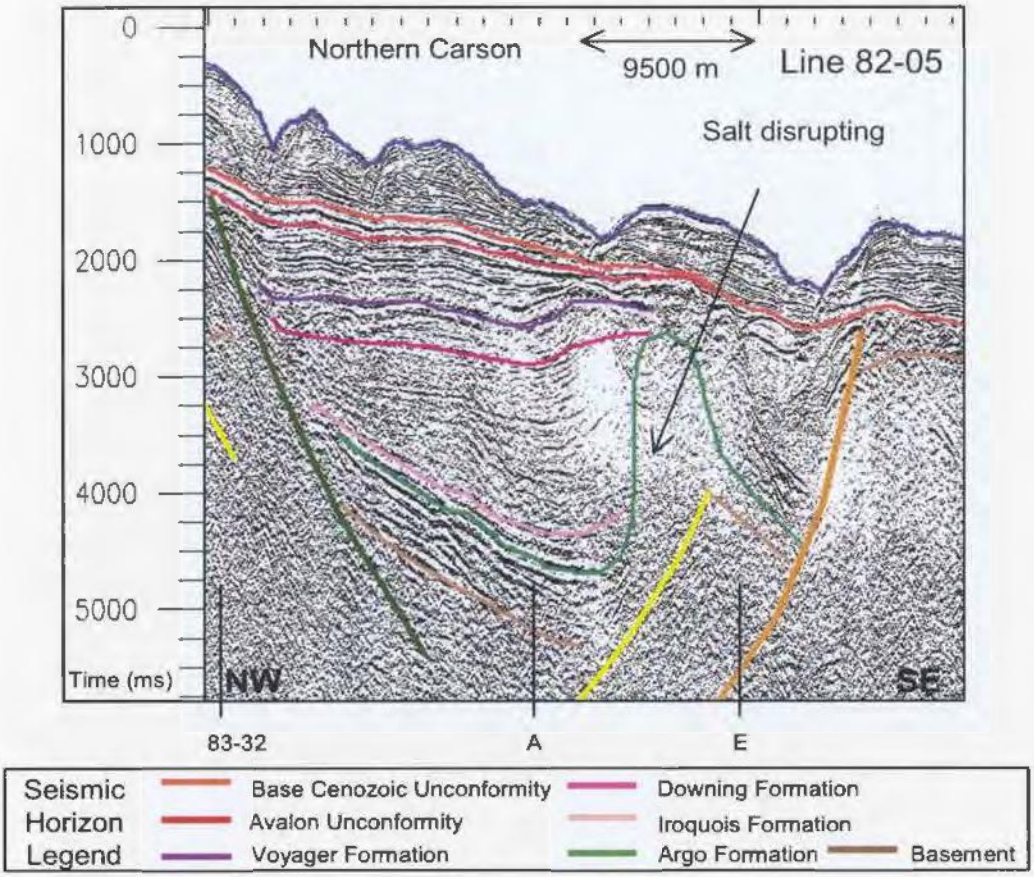

Figure 4.7. Line 82-05 in the northern Carson Basin showing Early Jurassic salt (Argo Formation) disrupting the overlying synrift sequences.

small amount of syn-rift sediment accumulated in the basin when compared to the central and northern sections. The sequences found in this portion of the basin (Lower Jurassic to Upper Jurassic) are all thin and total ~2000 ms twt (2500m thick, assuming a velocity of 2500 m/s) as shown in Figure 4.8. In this area the basement ridge has the least relief and is buried underneath the most post-rift sediment cover. The structure of the southern portion of the Bonnition Basin is relatively simple and the basin becomes more complex towards the north. The southern section shows Lower Jurassic to Mid Jurassic sequences which are slightly tilted and folded and overlain by less tilted and deformed Upper

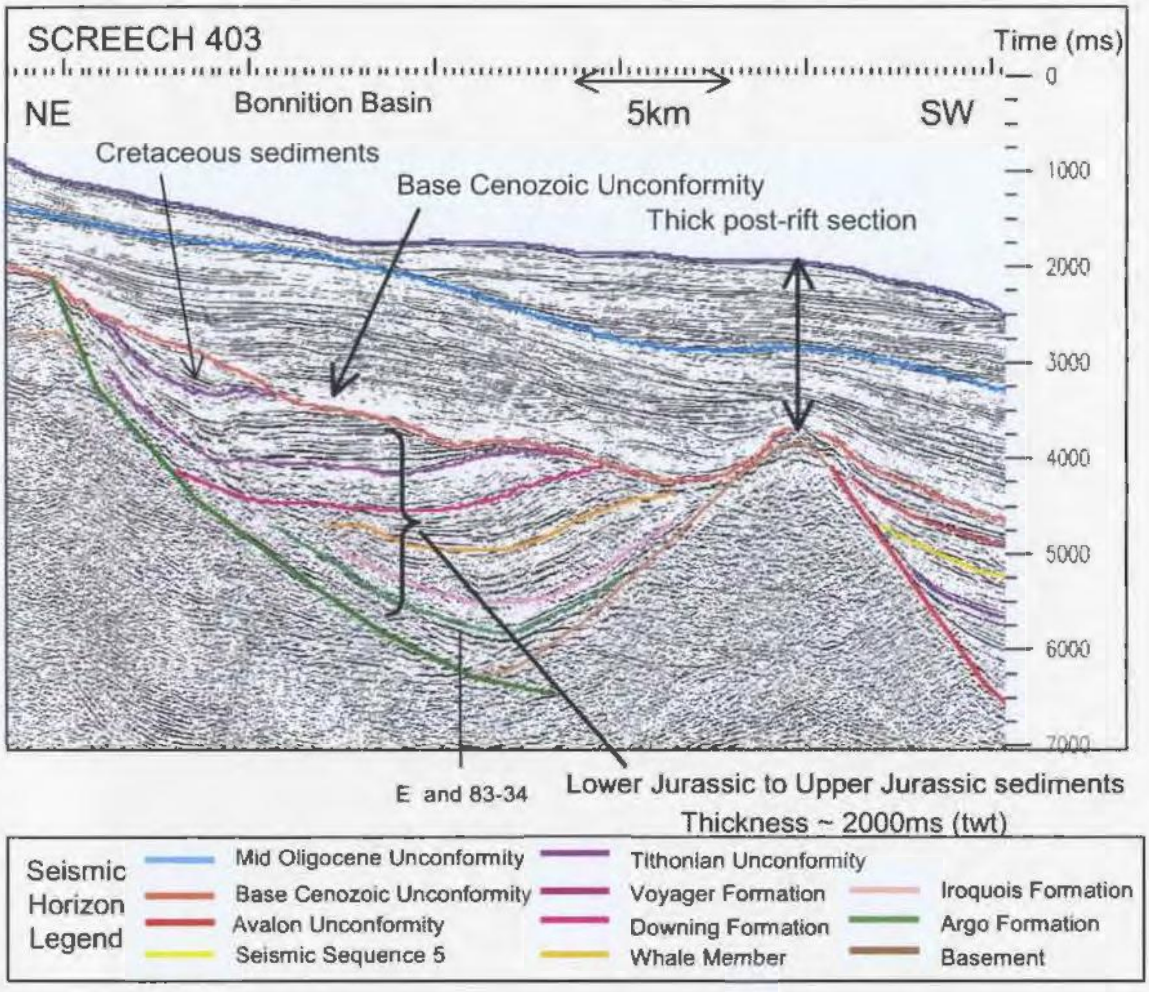

Figure 4.8. SCREECH 403 seismic line in the southern Bonnition Basin showing the basement ridge buried under a large amount of sediment cover and the Bonnition Basin filled with thin sequences of sediment.

Jurassic sediments (Figure 4.9). The Base Cenozoic Unconformity as shown in Figure 4.8 has eroded the Cretaceous sediments. The southern portion of the basin shows little internal fault activity when compared to the other sections. Salt tectonism is minimal in this section of the basin, with only a small diapir developing adjacent to the basement ridge in the southern corner of the basin.

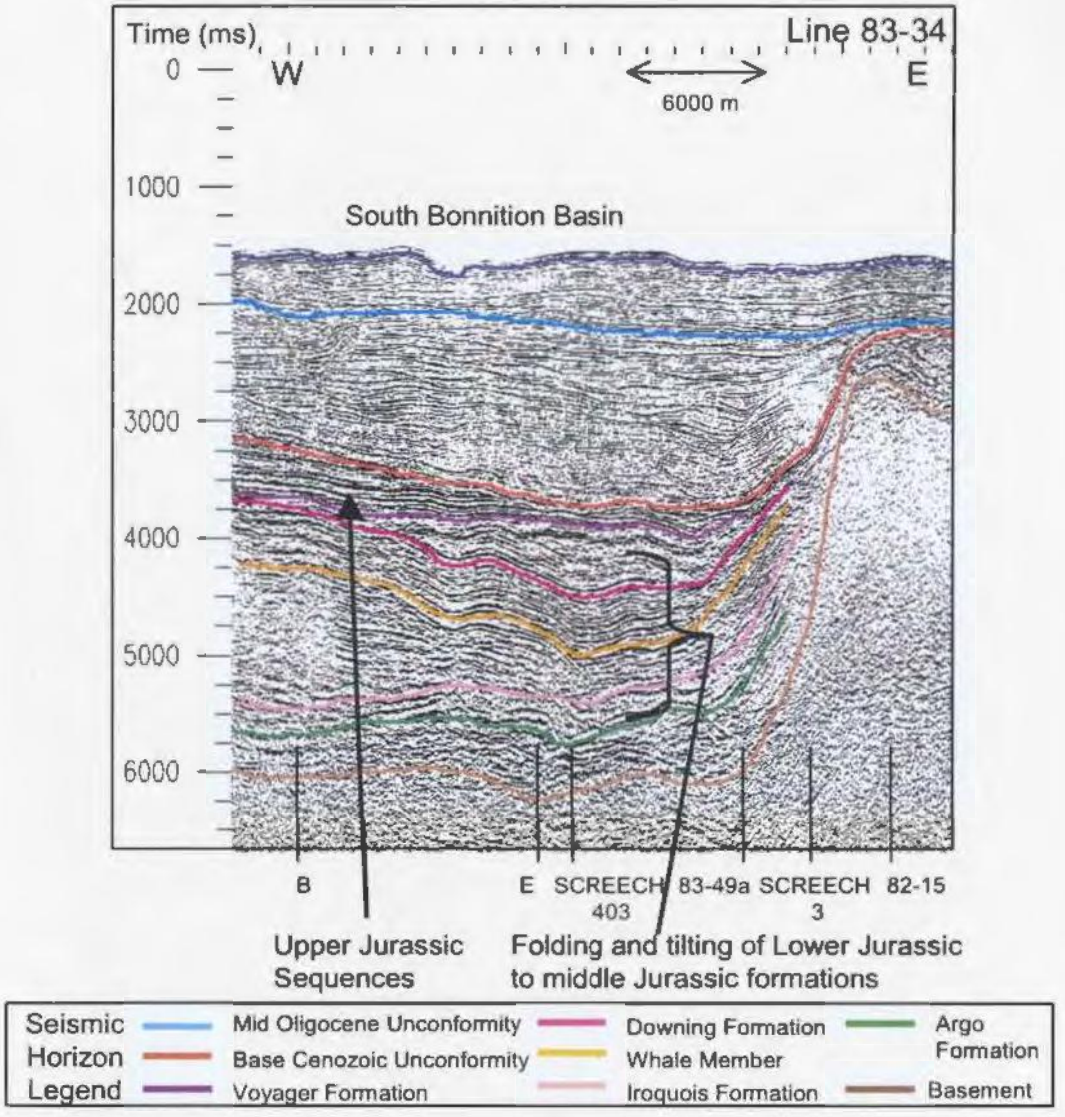

Figure 4.9. Seismic line 83-34 through the southern Bonnition Basin showing tilting and folding of the Lower to Middle Jurassic sediments.

4.2.4 Central Bonnition Basin

The central portion of the Bonnition Basin is strongly influenced by the Bonnition Fault, however a set of north-south trending synthetic faults greatly influence the internal structure of the basin. This group of faults has the largest amount of movement and

activity during the Mid Jurassic and these faults show growth into the Late Jurassic/Early Cretaceous. The faults offset basement and Lower to Middle Jurassic sediment (i.e. Argo, Iroquois and Downing Formations) as shown in Figure 4.10. The thickness of the Lower to Upper Jurassic sediments is approximately ~3000ms (twt), which is ~3750m, assuming a velocity of 2500m/s. The Lower to Mid Jurassic sediments are tilted west of the basement ridge. The overlying Cretaceous section has a moderate thickness in the central area of the basin and appears to thicken towards the Carson Fault, where less erosion from the overlying Base Cenozoic Unconformity has occurred (Figure 4.11). The basement ridge is found to be buried under less post-rift sediment and is structurally higher than in the southern section of the basin. Limited salt movement occurs in the central portion of the basin. One small diapir developed near the Bonnition Fault and rises into Lower Cretaceous sediment as shown in Figure 4.11.

4.2.5 Northern Bonnition Basin

The northern portion of the Bonnition Basin has a complex evolutionary history. The three north-south trending faults in the central portion of the basin die out towards the north. Antiforms and synforms develop in the transition from the central to northern portions of the basin, and other fault groups develop as shown in Figures 4.3 and 4.12 (A) and (B). Faulting in the northern portion of the basin is much more complex than in the central and southern areas. Most faults appear to form around Mid to Late Jurassic time with some offsetting basement and most offsetting Lower to Middle Jurassic sequences. The faults develop as northeast-southwest trending normal synthetic and antithetic faults

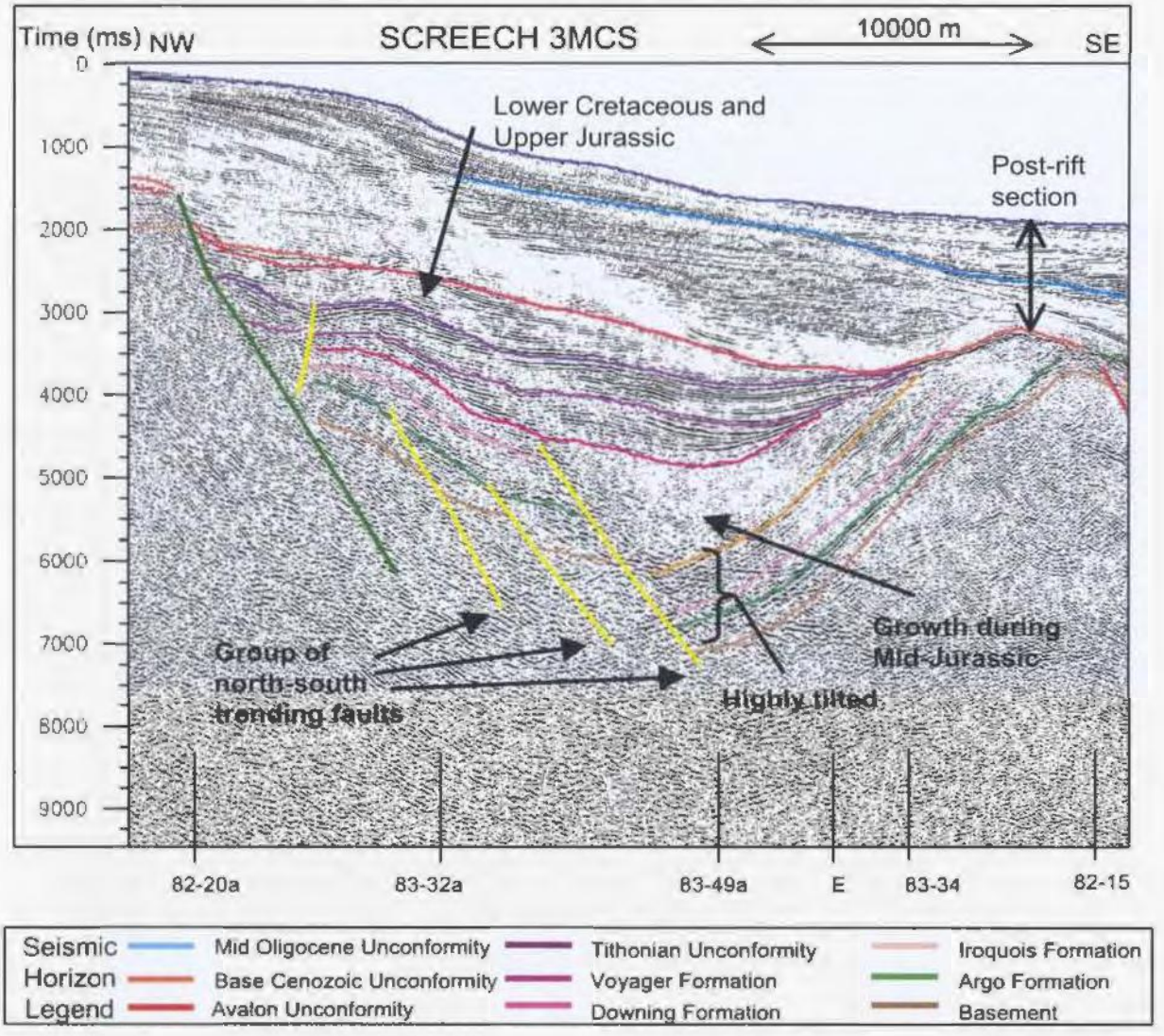

Figure 4.10. Seismic line SCREECH 3MCS in the Bonnition Basin showing the north-south trending group of faults (shown in yellow). These three faults in the Bonnition Basin offset basement as well as the Argo, and Iroquois formations. The faults show growth into the Downing, Voyager, and Rankin formations.

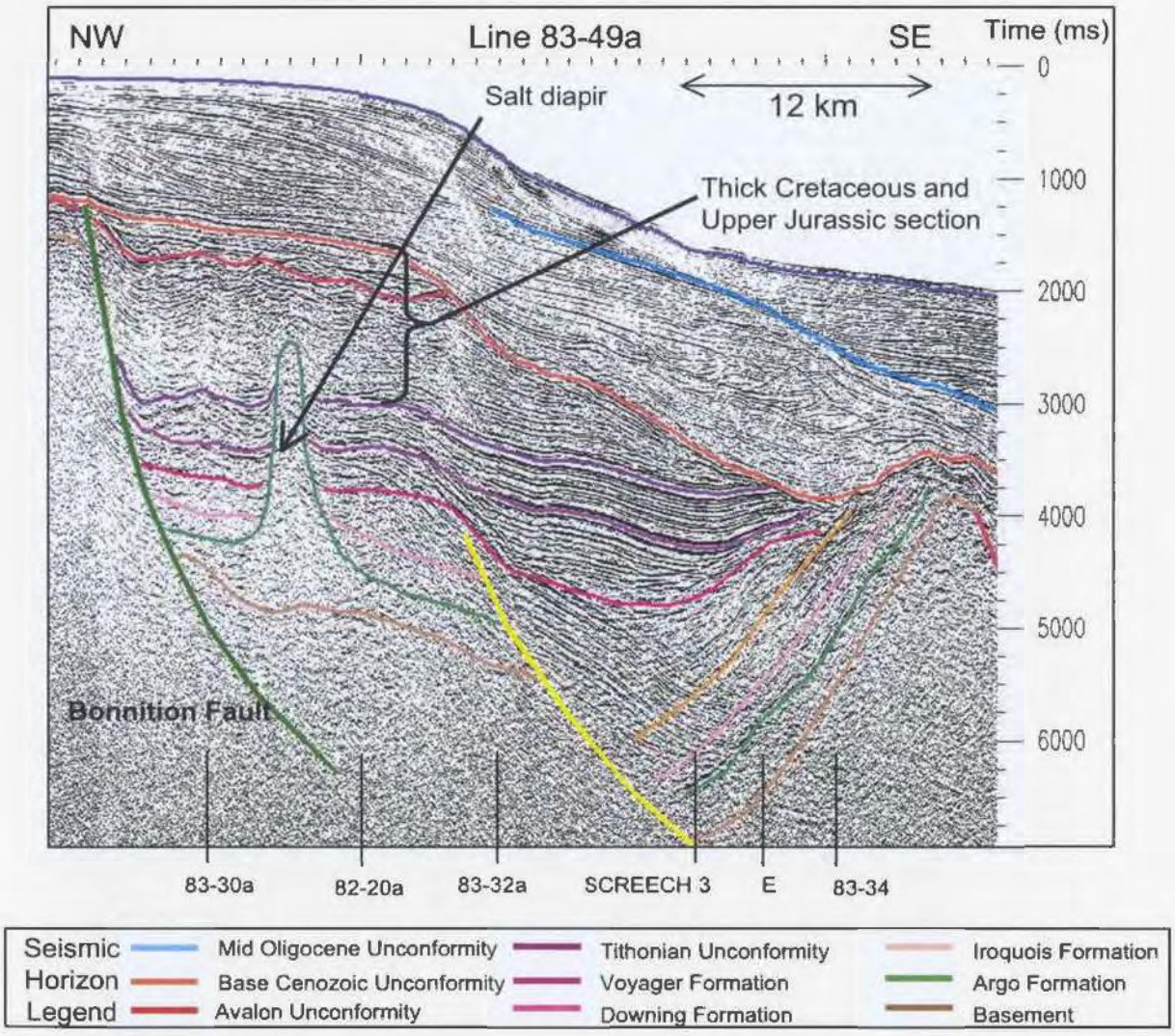

Figure 4.11. Seismic line 83-49a in the Bonnition Basin showing diapirism near the Bonnition Fault.

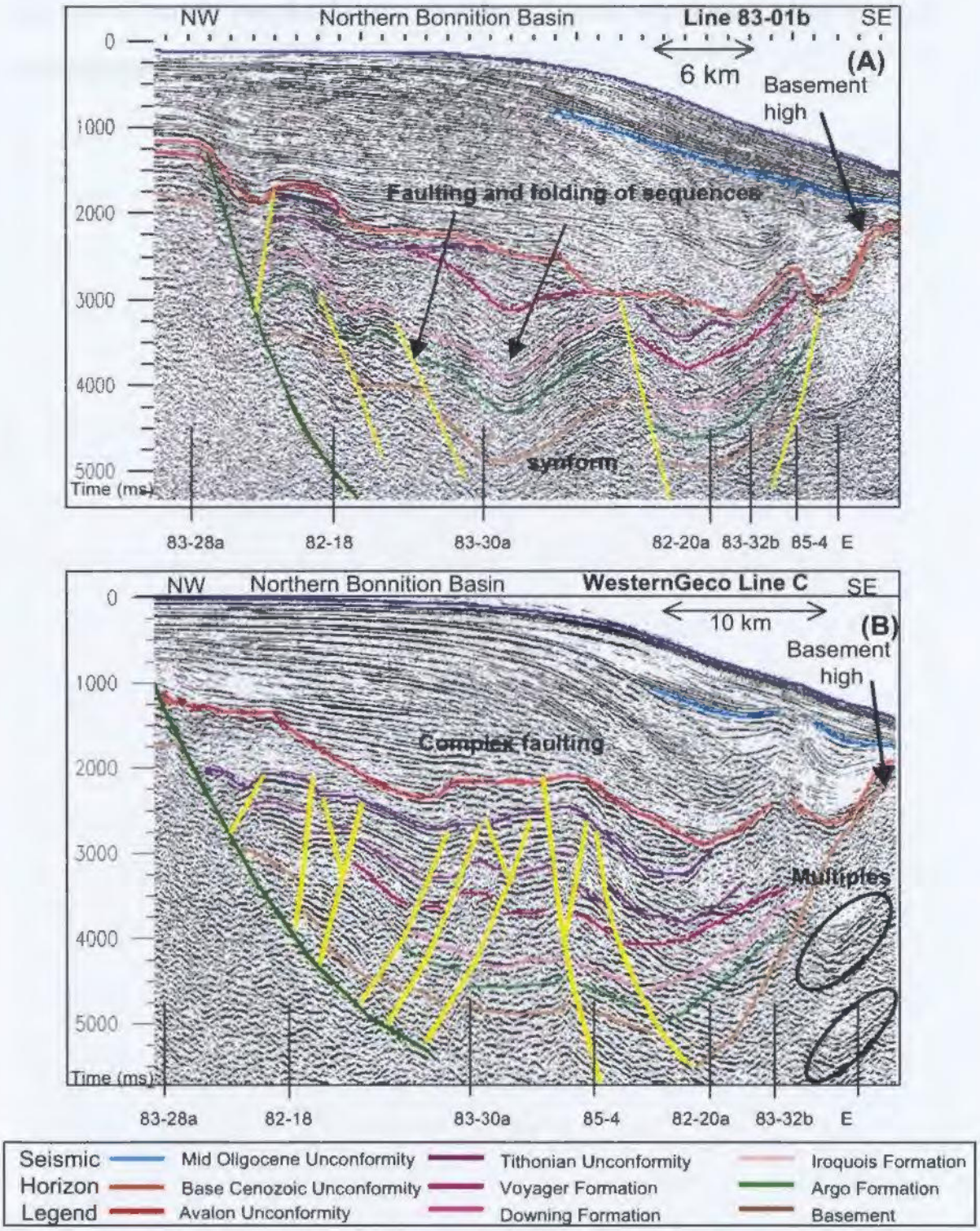

Figure 4.12. (A) Seismic line 83-01b in the northern Bonnition Basin showing faulting of Lower Jurassic sequences, and synforms developed around Mid-Jurassic time. (B) Proprietary WesternGeco seismic line C showing faulting of Lower to Upper Jurassic sequences.

with growth mainly found in Middle and Upper Jurassic sequences. Antiforms and synforms appear to develop around Mid Jurassic time as well and deform the Argo, Iroquois and Downing formations, as shown in Figure 4.12 (A). The thickness of the Lower to Upper Jurassic sediments is ~2000ms (twt), which is 2500m, assuming a velocity of 2500m/s. Cretaceous sediments are eroded in a large portion of the northern Bonnition Basin. The Lower Jurassic salt shows movement in the northeast corner of the basin, forming diapirs and domal features as illustrated on Figure 4.3. The northeast corner of the basin is strongly influenced by the salt movement and is strongly folded and deformed. Interpretation in this area is not possible on 2D seismic lines as the structure changes too rapidly for easy correlation between lines. In this section of the basin, the basement high appears very shallow and is covered by little post-rift sediment when compared to the other areas of the basin.

4.2.6 Salar Basin

Faults in the Salar Basin generally trend northeast-southwest, with some normal faults showing changes in their orientation along strike as illustrated on Figure 4.3. The major F2 Fault located to the east of the basement ridge and bounding the Salar Basin to the west shows numerous changes in direction along strike and exhibits changes in throw along the margin. The sinuous nature of this fault indicates that it possibly formed initially as fault segments that became linked as the fault evolved. The major F2 Fault is shown to be active from the Late Triassic, offsetting basement in the Salar Basin and generally ceasing around Cenozoic time. The fault exhibits the greatest throw in the

northern portion of the basin, which is also where it shows the most relief. In the central portion of the basin, north of the accommodation zone the fault shows the least relief and penetrates the deepest. In the south the fault shows the least amount of throw. Figure 4.13 illustrates the changes in the throw of the F2 Fault across the margin. The figure was constructed by measuring the throw of the fault, as it offsets basement material. The most rapid changes in the throw of the F2 Fault across the margin correspond to areas in the Salar Basin where there is a distinct structural change as noted in Figure 4.13 and on Figure 4.3.

4.2.6.1 Southern Salar Basin

In the Southern Salar Basin, syn-rift and post-rift sequences thin towards the South Bank High (Figure 4.3). The major normal faults in this area offset basement and some Lower Jurassic sequences. They appear active from Early Triassic time and some show growth into the Early Cretaceous. The faults in this area are generally spaced about 10 km apart and most faults show throws of about 200 ms -twt (~250 m, assuming a velocity of 2500 m/s). In this area it is difficult to determine if Mid – Upper Jurassic sediments are extremely thin or not deposited. Lower Jurassic salt is shown to be mobile in the south, creating diapirs as illustrated in Figure 4.3. Near the area where salt diapirs are evident there is also an area where high density, high angle faulting occurs as denoted in Figure 4.3 as 'HAF' and shown in cross-section in Figure 4.14. Salt appears to have moved and migrated along the high angle faults in this area, causing some deformation in Lower and Upper Cretaceous sequences.

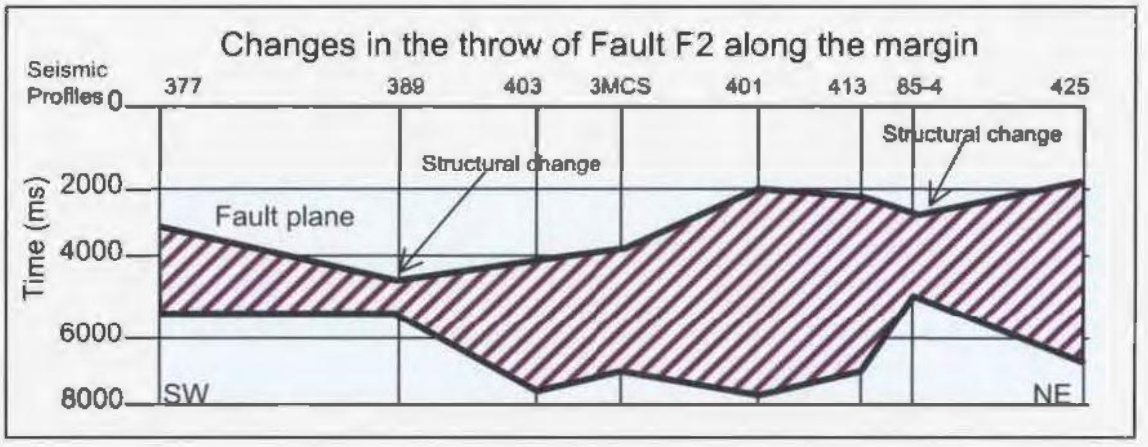

Figure 4.13. Changes in the throw of the major basin bounding F2 fault in the Salar Basin. Fault is shown in red on Figure 4.3. The throw is calculated between basement. Areas where major structural changes across the margin occur are indicated.

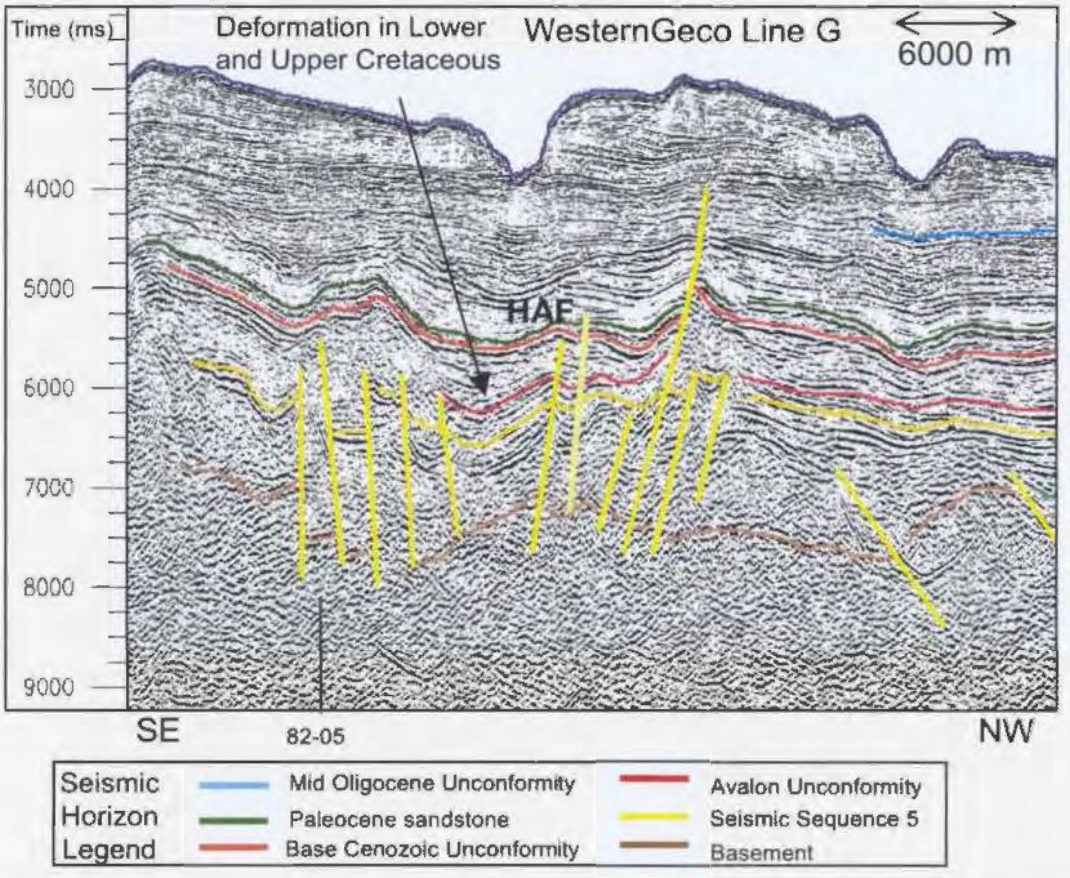

Figure 4.14. Proprietary WesternGeco line G illustrating a zone where high angle faults occur in Jurassic and Cretaceous sediments. Area of high angle faulting is denoted by "HAF". Deformation of the Lower and Upper Cretaceous sediments is evident.

4.2.6.2 Central Salar Basin

In the central portion of the Salar Basin, syn-rift sediments (Lower Jurassic to Lower Cretaceous) and the post-rift sequences tend to be the thickest when compared to the southern and northern areas of the basin. Normal faults in the central portion of the basin trend northeast-southwest and offset basement to Lower Jurassic sequences. The normal faults appear to be active during the Early Jurassic and persist until Early Cretaceous time. The faults closest to the major F2 Fault (illustrated on Figure 4.3 as the pink and purple faults) show growth into the Early Cenozoic. The faults in this area are spaced between 5 and 10 km apart, with a greater frequency of faulting occurring towards the north. The two faults near the F2 Fault show throws of ~600 ms -twt (750 m, assuming a velocity of 2500 m/s). Faults further to the east show less throw (~300 ms - twt, ~375 m). Figure 4.15 illustrates the change in throw of faults in the Salar Basin from west to east. An antithetic fault is found further to the east (coloured pink on Figure 4.3). This fault exhibits a small throw, and may possibly be a southward extension of the F3 fault illustrated on Figure 4.3 in blue. Upper Jurassic sequences thicken toward the central portion of the basin and show growth across the normal faults, as do the Lower Cretaceous sequences. Very little salt movement is evident in the central portion of the basin, with only a few small diapirs present.

4.2.6.3 Northern Salar Basin

In the northern Salar Basin the major normal faults are spaced about 5 km apart and compared to the southern and central portion of the basin, there are more antithetic

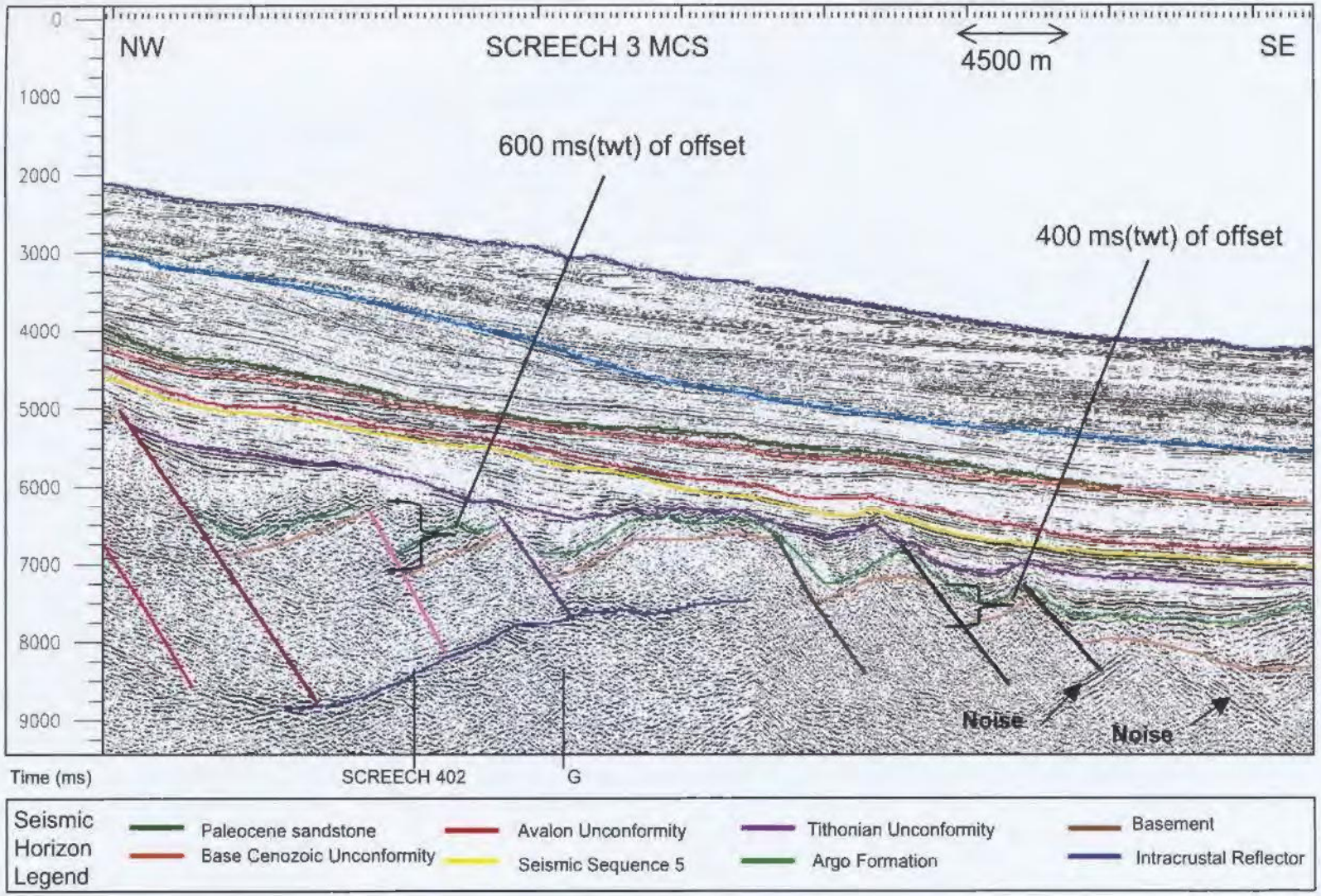

Figure 4.15. Seismic line SCREECH 3MCS showing faulting in the Central Salar Basin. The throw of the faults decreases towards the southeast. Jurassic sequences show growth across faults and little salt movement is evident.

normal faults present. In this section of the basin the faults change their orientation from northeast-southwest to trend in a more north-south direction and begin to align with the dominant fault direction in the Flemish Pass area (Figure 4.3). The faults in this area mainly offset basement to Upper Jurassic sequences. The faults appear active from the Early Triassic to the Late Jurassic and some show growth into the Early Cretaceous as shown in Figure 4.16. The fault throw in the northern area is generally around 400 ms – twt (~500 m). As the fault orientation changes and more antithetic faults evolve, localized mini-depocentres are created. A major antithetic fault occurs near the eastern limit of the basin. This fault is named F3 on Figures 4.3 and 4.16, and is thought to represent the continuation of the Beothuk Knoll. Throw on this fault increases northward into the Flemish Pass area. Movement of Early Triassic salt is more pronounced in the north than in the central area. Salt structures are found to the east of the Beothuk Knoll extension (F3 Fault), forming diapirs and a domal feature. The salt diapir penetrates into Lower Cenozoic sequences as shown in Figure 4.17. Salt movement mainly deforms the overlying Upper Jurassic and Lower Cretaceous sequences.

4.3 Major Accommodation / Transfer Zones

The southeast portion of the Newfoundland margin exhibits many structural changes along strike in the Carson, Bonnition and Salar basins. Accommodation and transfer zones are present on this area of the margin and separate areas that exhibit differences in structural style. Transfer zones in rift basins generally form parallel or nearly parallel with the principal direction of horizontal extension (Gibbs, 1984).

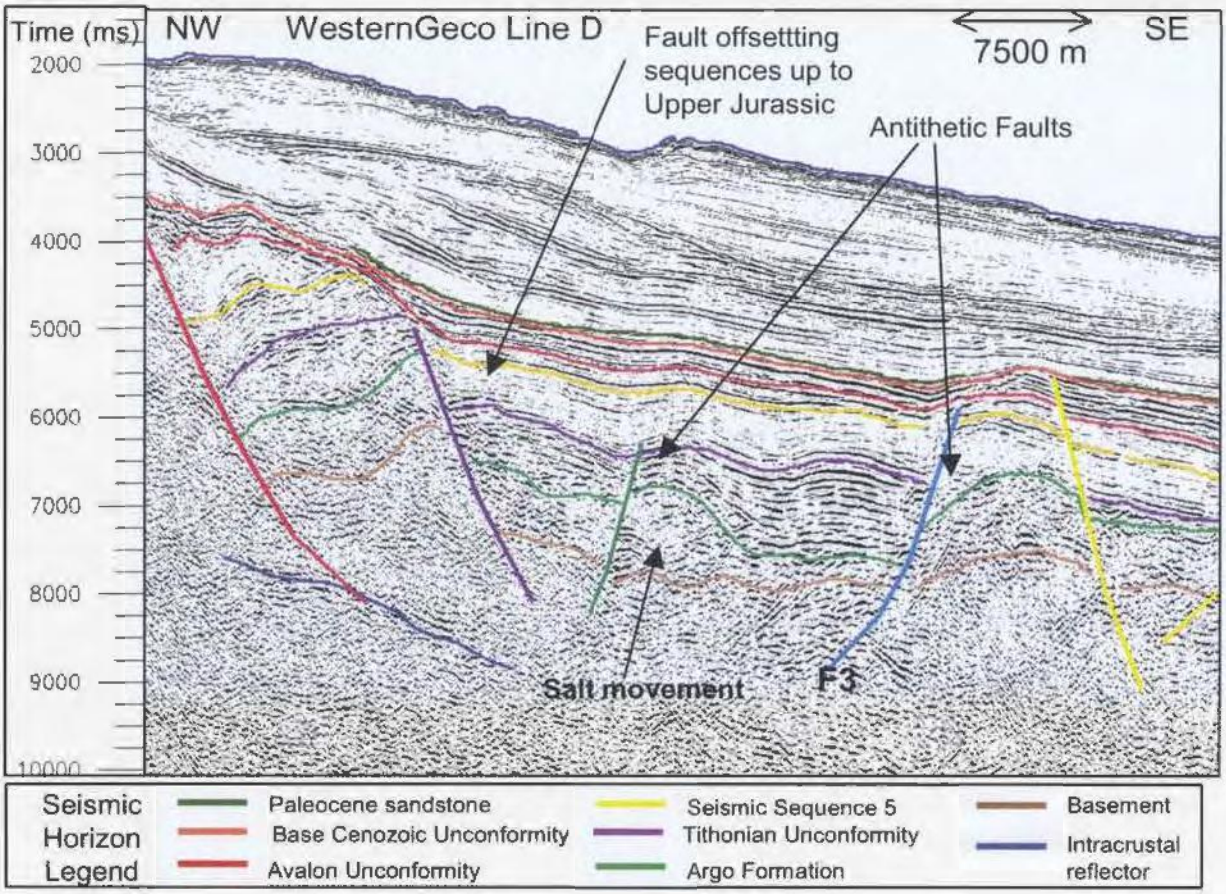

Figure 4.16. Proprietary WesternGeco seismic line D illustrating faulting in the Northern Salar Basin. Note the increased presence of antithetic faults. Faults generally tend to offset basement to Upper Jurassic sediments.

Figure 4.18 depicts the regions where major transfer zones have formed on the margin and are labeled one to three. These three transfer zones separate areas with different structural character. The direction of horizontal-slip movement is also indicated on the transfer zones. Along with movement in the strike direction, dip-slip movement would have occurred as well, giving rise to oblique faulting.

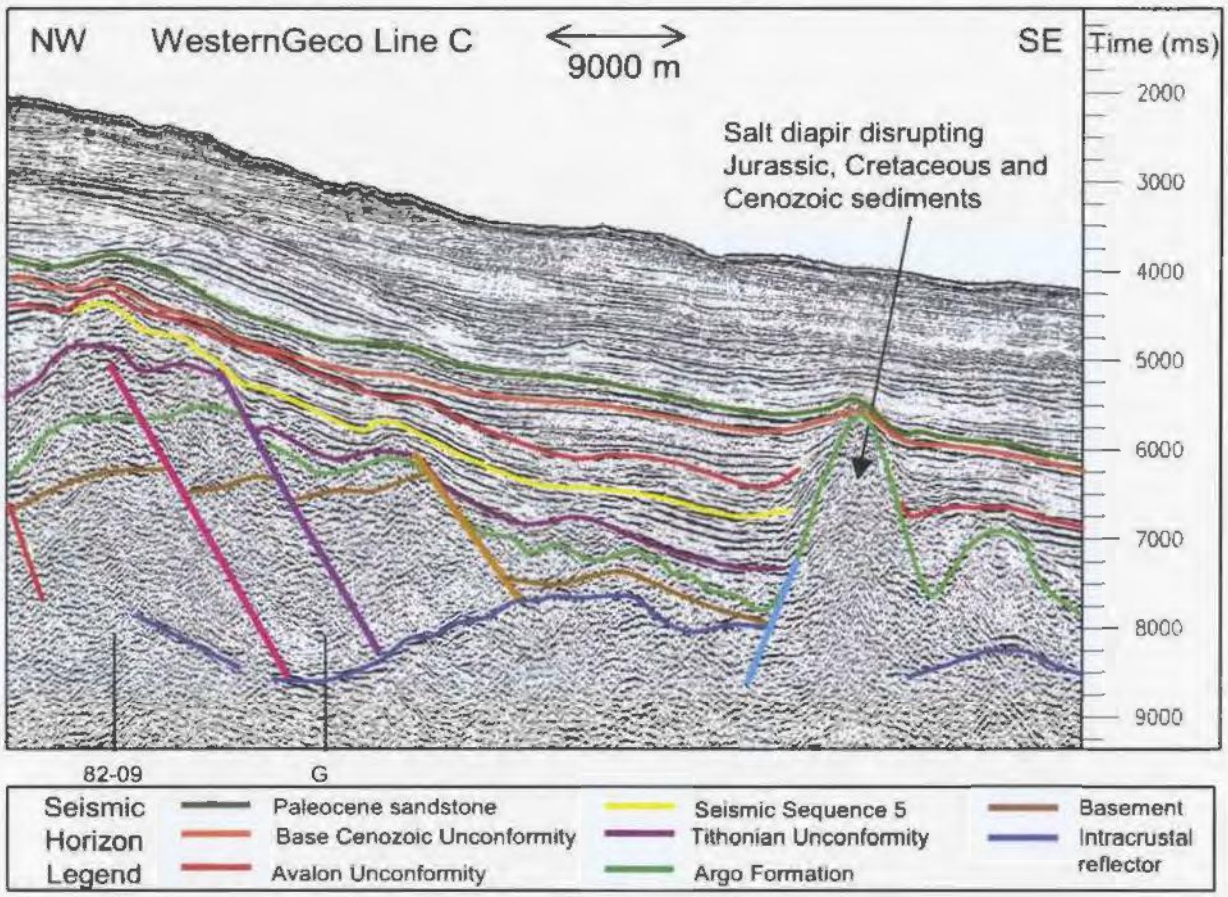

Figure 4.17. Proprietary WesternGeco seismic line C illustrating salt diapir formation in the eastern section of the Salar Basin. The salt diapir disrupts Jurassic, Cretaceous and Early Cenozoic sediments.

The first major transfer zone (1) cuts through the Carson Basin in the area separating the northern Carson Basin from the southern section. The transfer zone interpreted in this area is a left lateral fault. East of the fault is also where the Carson Basin widens. This transfer zone also crosses through the area in the Salar Basin where high density and high angle faulting occurs.

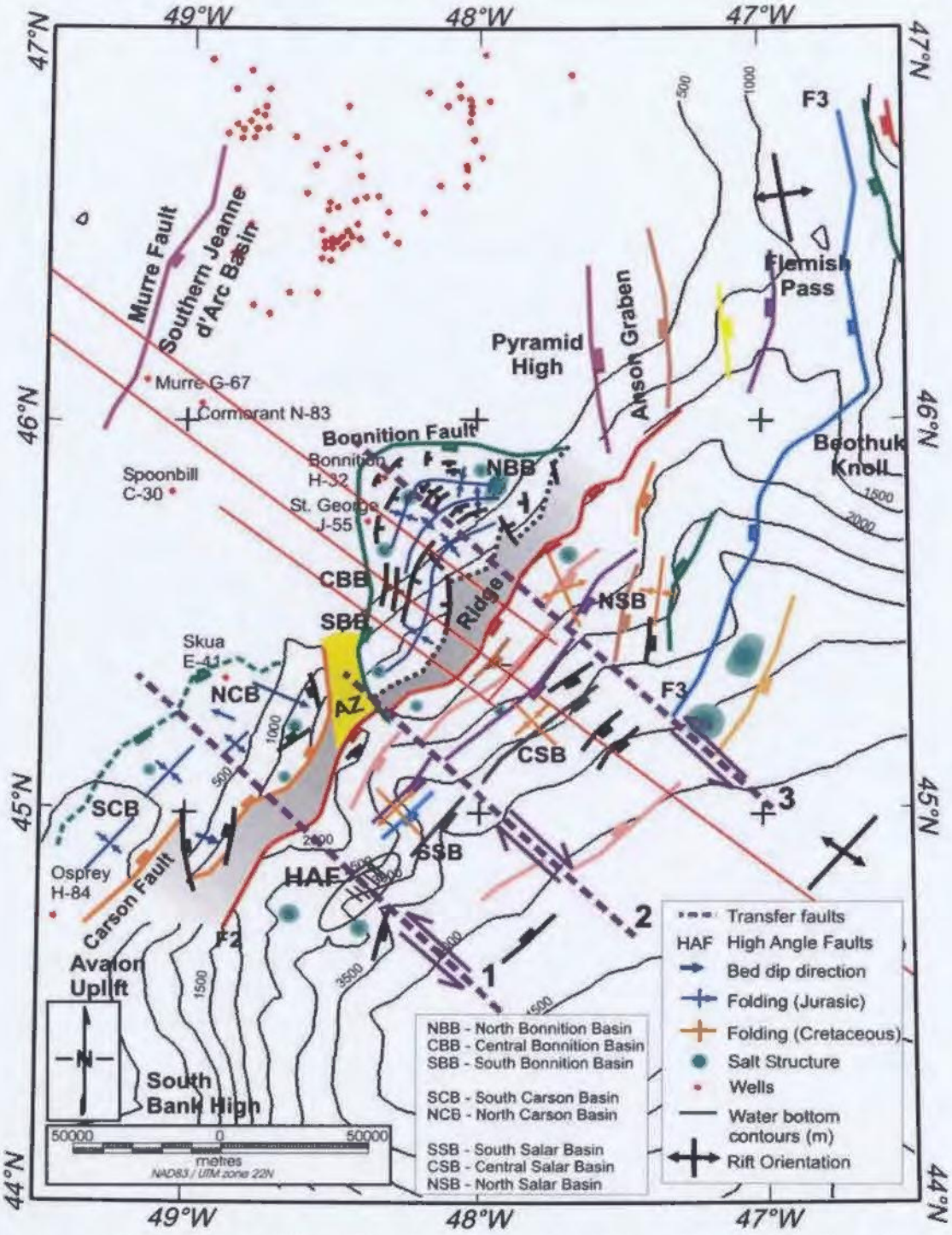

Figure 4.18. Diagram of transfer zones present on the south-east Newfoundland margin and transecting the Carson, Bonnition, and Salar Basins. NNB=North Bonnition Basin, CBB=Central Bonnition Basin, SBB= South Bonnition Basin, SCB=South Carson Basin, NCB=North Carson Basin, SSB=South Salar Basin, CSB=Central Salar Basin, NSB=Northern Salar Basin, HAF= High Angle Faults.

The second major transfer zone (2) forms north at the northern portion of the accommodation zone and is interpreted to act as a right lateral fault. The transfer zone cuts the basement ridge in the area where there is a large change in its height and throw. In the Salar Basin this fault separates the Southern Salar Basin from the Central Salar Basin. The central portion of the basin is generally deeper and less faulted than the southern portion.

The third major transfer zone (3) separates the central Bonnition Basin from the northern Bonnition Basin. The transfer zone is interpreted as a left lateral fault. Figure 4.19 illustrates 2 strike profiles transecting the Bonnition Basin and depicting the location of transfer fault 3. In this figure note the thickness changes in the units across the zone especially in Figure 4.19A. In this area of the Bonnition Basin there is a major change in the structure and width of the basin. The central and southern sections are rather narrow, while the northern section widens. The northern section is also more complexly faulted. In the Salar Basin the transfer zone separates the central and northern sections, where the northeast-southwest trending faults in the central area are replaced by the north-south trending faults in the north. In the Salar Basin this transfer zone separates areas where rifting took place in two distinct directions.

Figure 4.20 illustrates a portion of SCREECH line 305, which is a strike line in deep water (line location found in Figures 2.1, 3.1 and in Appendix 2). This seismic line, processed and illustrated in an honours thesis dissertation by Eustace (2002) shows little

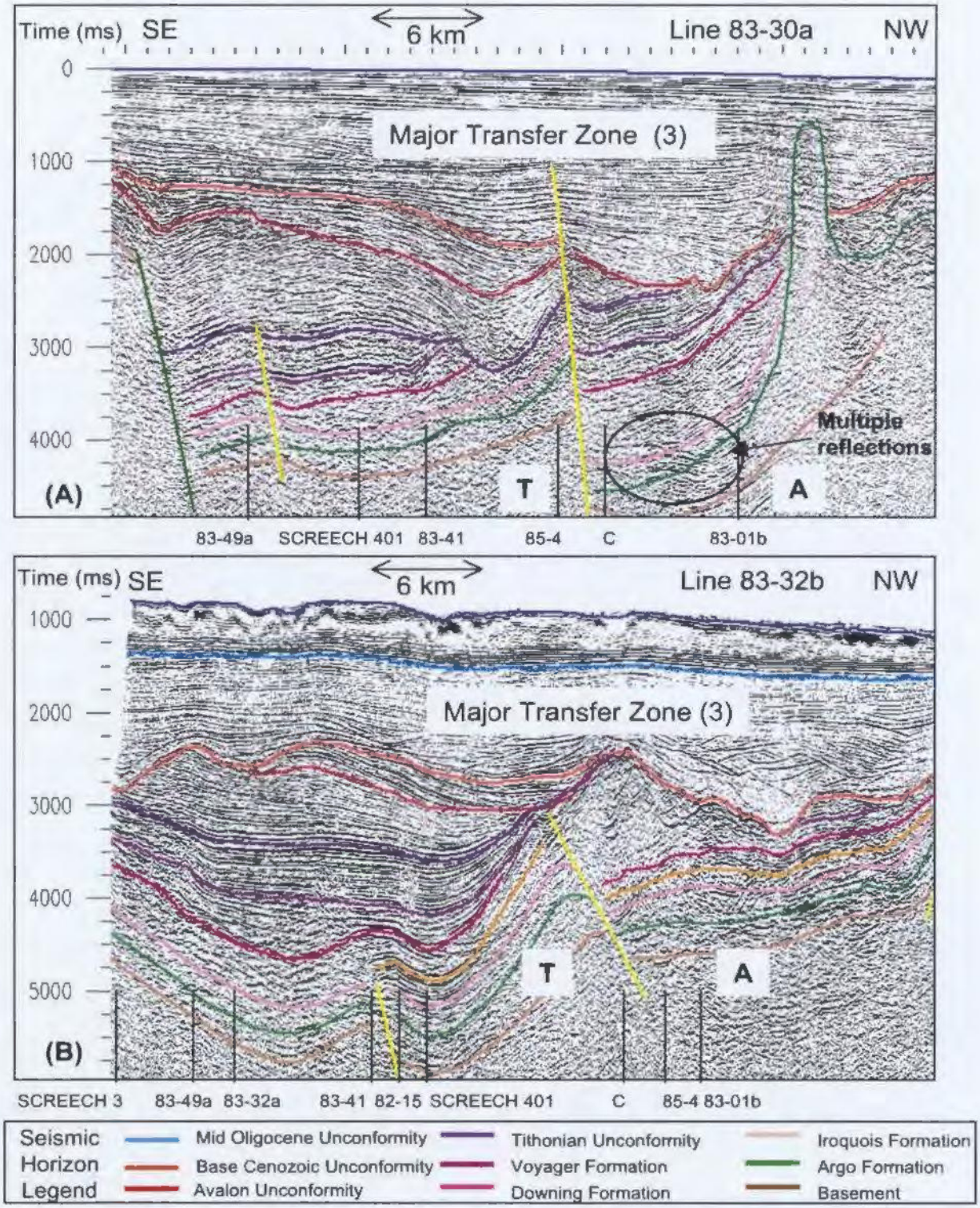

Figure 4.19. Strike profiles 83-30a (A) and 83-32b (B) crossing the Bonnition Basin and imaging the transfer zone. Note the changes in unit thickness across the transfer zone. A – indicates movement away from the viewer and T – indicates movement toward the viewer.

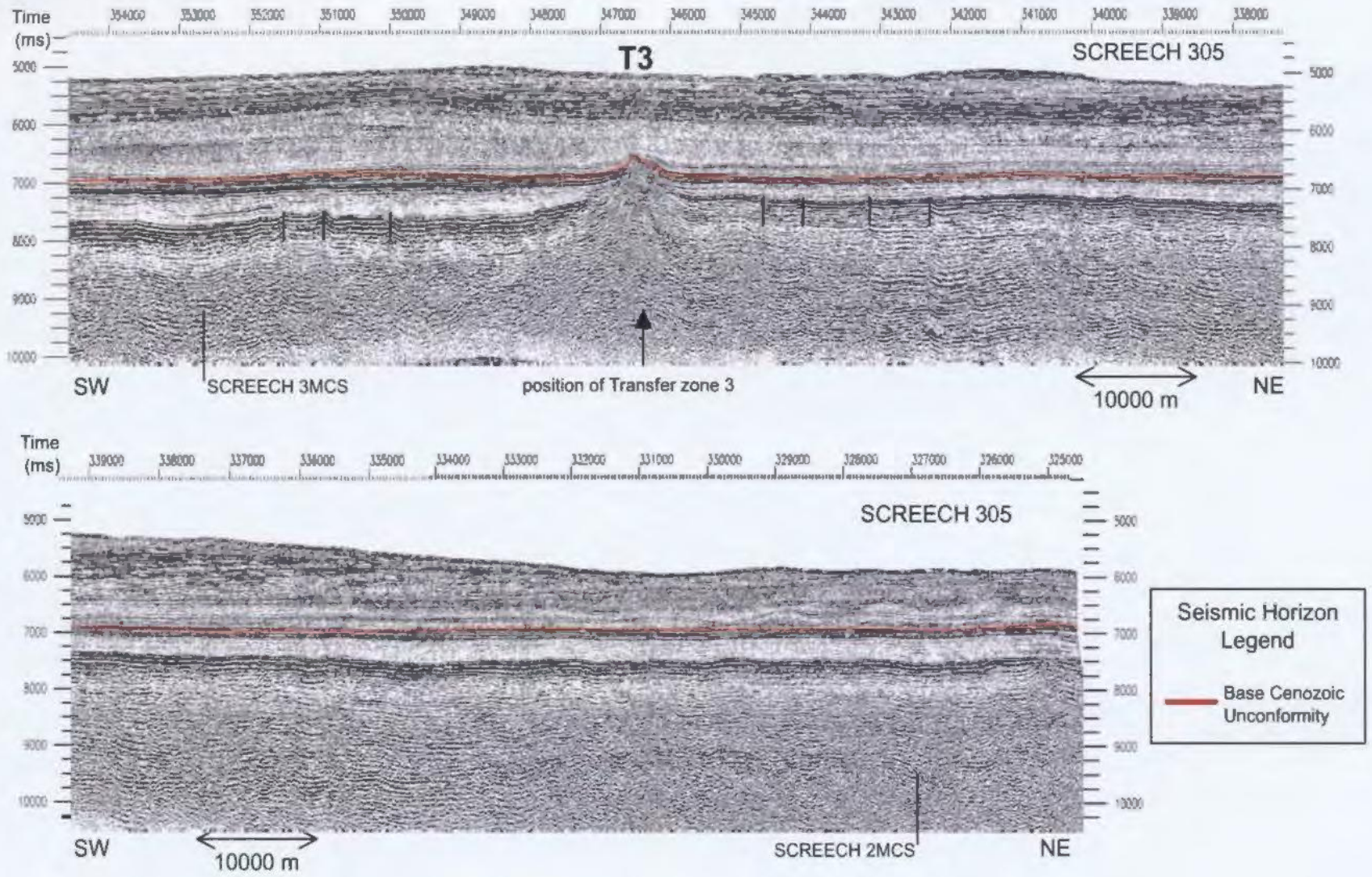

Figure 4.20. SCREECH line 305 strike line processed by Eustace, (2002) across the deep water area of the Newfoundland margin. The only major discontinuity on the line (annotated as T3) corresponds with the interpreted position of the third transfer zone.

structural variability along its length and many small vertical faults, which are interpreted to be strike-slip in origin. The only feature that is present on this line is found near the southwestern portion of the line and it lines up with the interpreted location of transfer zone 3, shown in Figure 4.18.

4.4 Impact of Rifting Events

The two major rifting episodes on the Newfoundland margin and the change in orientation of the extensional direction have an effect on the formation of the shelf-edge and slope basins. As briefly explained in Chapter 1, the first rifting event affecting the Grand Banks initiated in the Late Triassic and formed northeast-southwest trending normal faults on the Newfoundland margin. This rifting event is thought to have lasted for 20 My creating faults in response to the northwest-southeast directed extension. The faulting created two shelf edge basins (Carson and Bonnition) on the southern and central Newfoundland margin. The two half grabens formed adjacent to each other during this time, however they formed with oppositely dipping polarity. The Bonnition Basin Fault most likely formed through a series of left stepping fault segments orientated northwest-southeast and dipping down to the east, while the Carson Basin Fault was formed by fault segments dipping to the west. As these faults evolve and link they form the major faults that bound the basins. An accommodation zone is present between these two basins and the faults bounding the accommodation zone are orientated in a more or less north-south direction. In the Salar Basin during this first major rifting stage, extension created northeast-southwest trending normal faults.

Transfer zones are present on the margin and these were likely initiated during this first rifting event as well. From the sparse grid of seismic data it is difficult to determine the timing of movement on the transfer zones. It is speculated that these zones are important to the development and structure of the basins and probably formed around the same time as the major basin bounding faults on the margin, however there is no direct evidence for this.

The first major rifting phase on the Grand Banks was followed by a period of widespread subsidence across the margin. This period of subsidence initiated at the end of the Early Jurassic and lasted to the Late Jurassic. This allowed evaporites, carbonates and shales to be deposited in the basins along the shelf. Thicker sequences of evaporites and sediments appear to have been deposited in the Carson Basin compared to the Bonnition Basin. In the Salar Basin, the evaporite sequences are shown to be thicker towards the south of the study area. The Early, Middle and Late Jurassic sediments overlying the evaporite unit appear thin when compared to the thickness of the post-rift sediments.

A second rifting phase interrupted subsidence on the margin. Extension for this rifting phase was orientated in an east-west direction and initiated around the Late Jurassic, possibly earlier in southern areas, and likely caused reactivation of the pre-existing Late Triassic faults on the shelf and slope area of the margin. This rifting phase continued until the Early Cretaceous and lead to break-up and seafloor spreading that eventually occurred around Barremian to Aptian time. In the Carson Basin salt appears to have

mobilized at this time in localized areas and caused deformation in the overlying sedimentary units. In the Central Bonnition Basin, the three north-south trending faults in the basin were active during this time, offsetting basement, Lower and Mid Jurassic sediments. In the northern Bonnition Basin, salt appears to have mobilized in localized areas causing overlying sequences to deform. Salt movement in this area continues into the Cenozoic in some cases. The faults bounding the accommodation zone between the shelf basins are orientated in a north-south direction, which when reactivated by the second rifting phase caused the basins to deepen along these faults. In the Salar Basin normal faults offset basement and Lower Jurassic sediments. Upper Jurassic sequences show growth across faults. The Lower Jurassic salt layer in the Salar Basin appears to be active during the second rifting phase in localized areas.

The formation of the Avalon Uplift beginning around Barremian time caused uplift and widespread erosion on the margin removing some of the Early Cretaceous sediments in the Carson and Bonnition basins. This unconformity formed across the margin around the time of break-up between Newfoundland and Iberia. After continental break-up occurred the margin underwent another period of subsidence. Near the beginning of the Cenozoic another prominent widespread unconformity develops. This unconformity, referred to as the Base Cenozoic Unconformity is responsible for eroding a large portion of the Cretaceous and even Late Jurassic sequences in the Carson and southern Bonnition basins. Post-rift sediment thickness varies across the margin, with the largest variations in thickness seeming to occur in Cenozoic sediments.

The southeast Newfoundland margin exhibits a complex rifting history with the different rifting events having a large influence on the final structure of the basins. The basins have an overall northeast-southwest trend due to the first rifting event, but also exhibit many north-south trending features that formed in response to the second rifting event.

4.5 Petroleum Prospectivity

The Carson and Bonnition basins have in the past been explored for their petroleum potential. As mentioned in Chapter 3, four wells have been drilled in the Carson and Bonnition basins. These wells were drilled in the mid-1970's and mid-1980's, with none of the wells encountering hydrocarbons. Since then no other wells have been drilled in either of these basins, and little exploration has occurred. No wells have been drilled in the Salar Basin, and only recently (in 2003) were ODP sites drilled in the nearby Newfoundland Basin (northeast of the Salar Basin) to investigate the nature of the underlying crust. In the process of attempting to drill to basement, these ODP sites collected a large section of the Cenozoic and Cretaceous sedimentary record in the Newfoundland Basin.

4.5.1 Source Rock Extent

The major concern in the shelf edge basins is the presence of source rock. None of the four wells on the shelf drilled into source rock. The main source rock in the region is the Kimmeridgian Egret shales. The Egret Member is an organic rich carbonaceous shale that began generating hydrocarbons in the Late Cretaceous (Enachescu and Fagan, 2004).

Since wells in the Carson, Bonnition and Salar basins do not sample the source rock, the source rock location must be inferred and estimated on the seismic data. Based on well information from the Jeanne d'Arc Basin, the Egret Member is interpreted to be located in the Rankin Formation, and the shale unit is generally found to be widely distributed across the Grand Banks (Williamson, 1992 and Newfoundland Energy Branch, 2000). Based on this information, the seismic horizon that is closest to the inferred position of the source rock is the top of the Rankin formation or the Tithonian Unconformity, which was previously described in Sections 3.4.1.6 and 3.4.2.3. This surface will be used to estimate the expected distribution of the Egret Member.

The Egret Member is stratigraphically located closely below the Tithonian Unconformity. Since the mapped surface is an unconformity, the Egret Member is likely only preserved where there is a relatively thick succession of the underlying Rankin Formation. This makes the definition of its area of current presence difficult to ascertain. But nevertheless it is possible to use the thickness of the Rankin Formation as an indicator of relative probability of existence of the Egret Member.

These uncertainties are of less significance in the Salar Basin, where Tithonian erosion is rather less. Figure 4.21 is an approximate representation of the source rock distribution in the Carson, Bonnition and Salar basins. Based on part A of the figure, only a small area of source rock is present in the northern section of the Carson Basin.

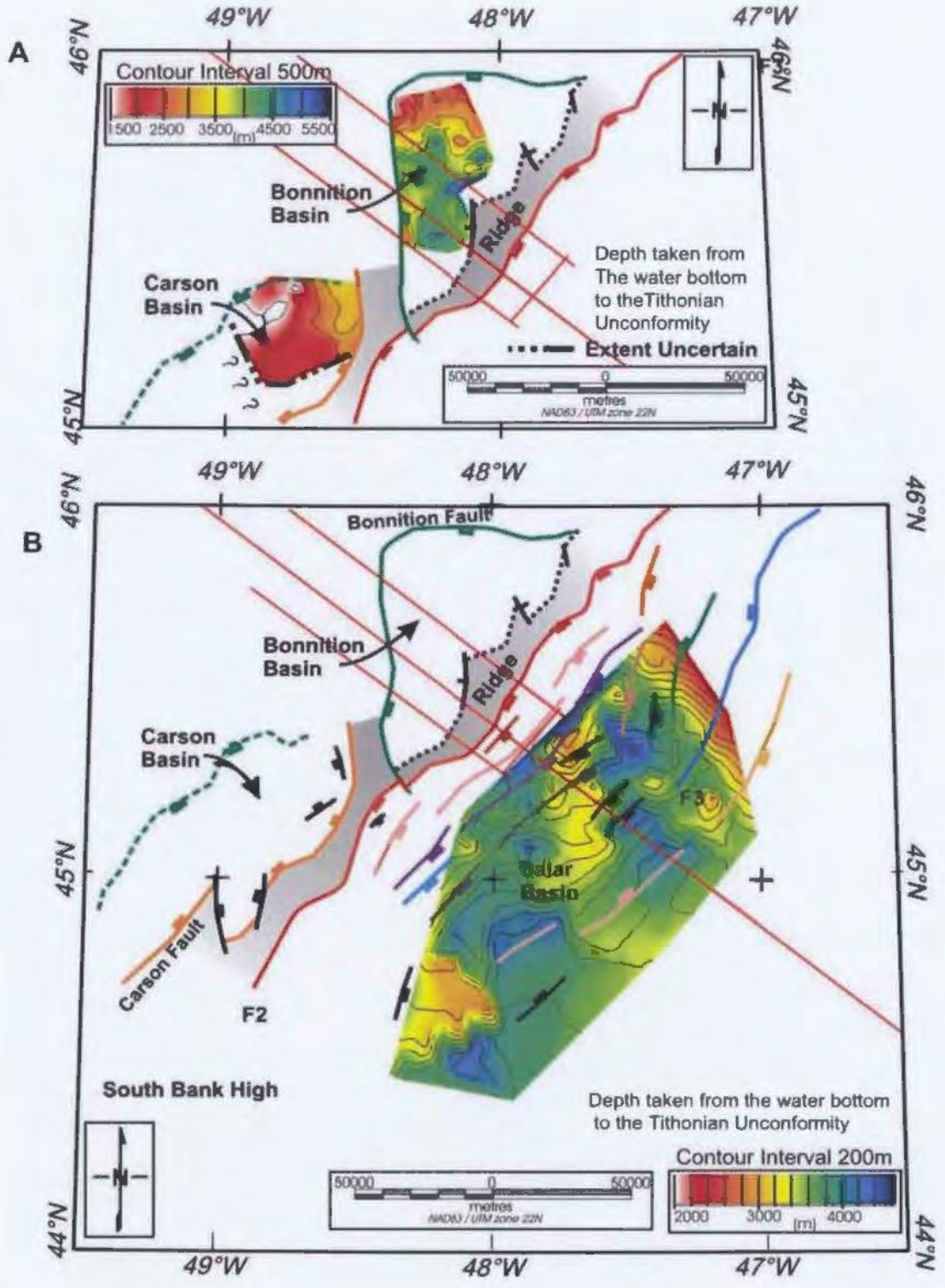

Figure 4.21. Possible extent and present day depth of burial of the Kimmeridgian Egret Member in the Carson, and Bonnition basins (A) and the Salar Basin (B). The Egret Member, the main source rock for the Grand Banks, is shown to have limited extent in the Carson and Bonnition basins, while appearing to be widespread across the Salar Basin.

This interpretation is however questionable as the top of the Rankin Formation is also eroded by the Base Cenozoic Unconformity in this area. In the Bonnition Basin, source rock appears to be concentrated in the central portion of the Basin. In the southern and northern areas, source rock is probably eroded by overlying unconformities and does not exist. Over the Salar Basin, shown in part B, the source rock may be widespread. Only drilling can ultimately confirm the presence or absence of the Egret Member.

Oil or gas generation from organic rocks occurs within a definite temperature range at a certain burial depth. In the Jeanne d'Arc Basin the oil window (depth at which oil will be generated from organic matter) generally occurs at burial depths between 2.5 km and 4 km (MacKay and Tankard, 1990, Williamson, 1992 and Enachescu, 2005 pers. comm.). The gas window (depth at which gas will be generated from organic material) occurs from 4 to 6 km. Figure 4.21 illustrates the depth to the Egret Member below the water bottom. If this figure accurately represents the distribution and position of the Egret Member, then in the shelf basins (Carson and Bonnition) the source is presently buried at depths ranging from ~ 1500 m to 4500 m, which is mainly within the hydrocarbon generation window, indicating that hydrocarbons could have been generated in most areas. In the Carson Basin, the depth to the source rock is shown to be the least, and in some areas the source may be too shallow to have gone into the hydrocarbon generating window. In the Salar Basin, the source rock is buried at depths ranging from ~2000m to 4500 m in the deeper water, indicating that it has generally been buried to great enough depths to permit hydrocarbon generation. Figure 4.22 is a rough estimate of the burial

history of the Egret source rock in the Carson, Bonnition and Salar basins. The plot was created by taking an average burial depth in each of the basins.

The source rock map in Figure 4.21 assumed that the main source was the Egret Member, but it is possible that other sources may be present in the basins. In the Salar Basin, the ODP Site 1276 drilled through Albian black shales with a Total Organic Content (TOC) of >2 % (Shipboard Scientific Party, 2004b). These shales are thin and mostly terrestrial in origin, and have the potential to be a source of gas throughout the basin. The Albian black shales would be located stratigraphically above the Avalon Unconformity. To assess the current burial depth of the Albian section, the Avalon Unconformity will be used as an approximation. Figure 4.23 shows that the depth from the water bottom to the Avalon Unconformity is generally from ~2000 m to ~3500 m over most of the Salar Basin, indicating that this source would be less mature than the Egret source and portions of it may not be within the oil generation window.

4.5.2 Potential Reservoir Rock

Wells in the Bonnition Basin drill through potential reservoir rock, as shown in Figure 3.4. Both the Bonnition (H-32) and St. George (J-55) wells contain Lower Cretaceous and Jurassic sandstone units. These sandstones are interpreted to be equivalent to the Avalon, Hibernia and Jeanne d'Arc formations found in the Jeanne d'Arc Basin (Newfoundland Energy Branch, 2000). These formations in the Jeanne d'Arc Basin are the reservoir rocks for the Hibernia, Terra Nova and White Rose fields and are proven to

be quality reservoir rocks (Enachescu and Fagan, 2004). The Lower Cretaceous sandstones appear fairly widespread throughout the Bonnition Basin, except in the southern area where they have been eroded by the Base Cenozoic Unconformity.

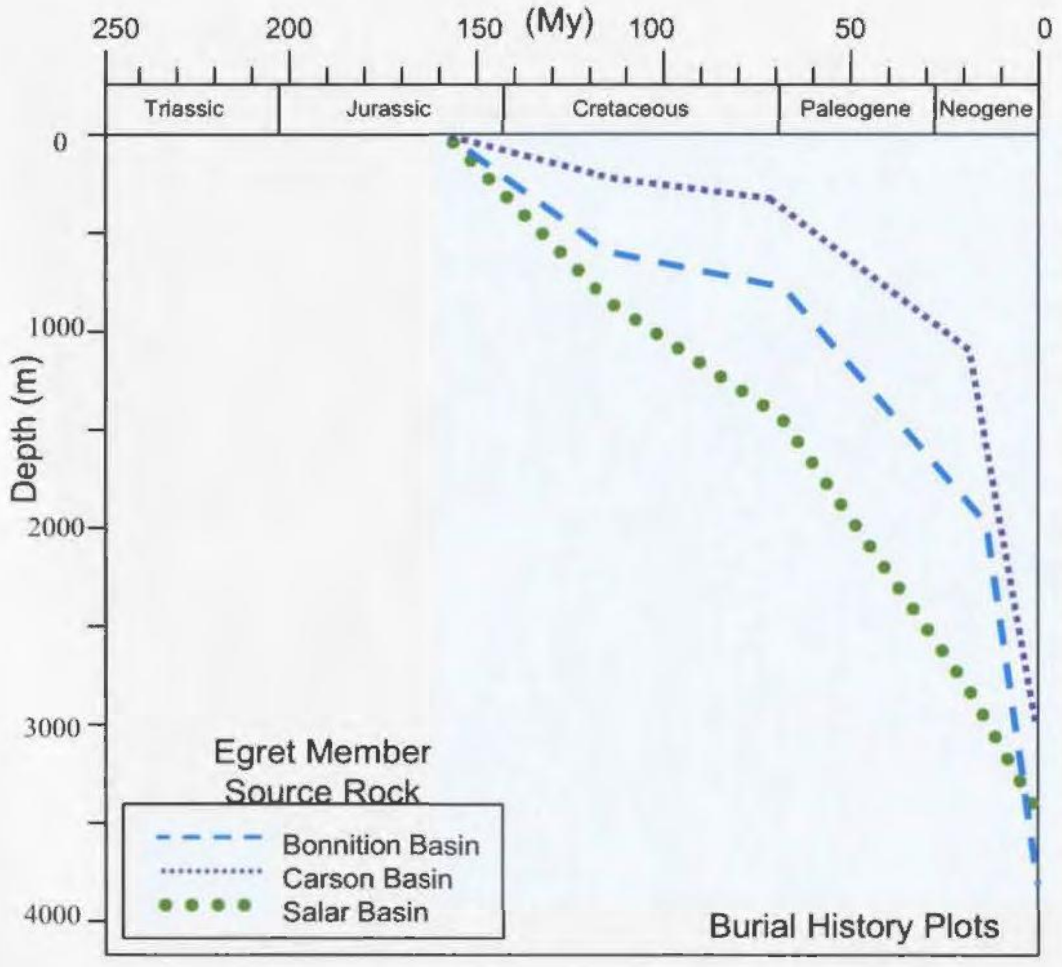

Figure 4.22. A rough estimate of the burial history of the Kimmeridgian Egret Member (potential source rock) in the Carson, Bonnition and Salar basins.

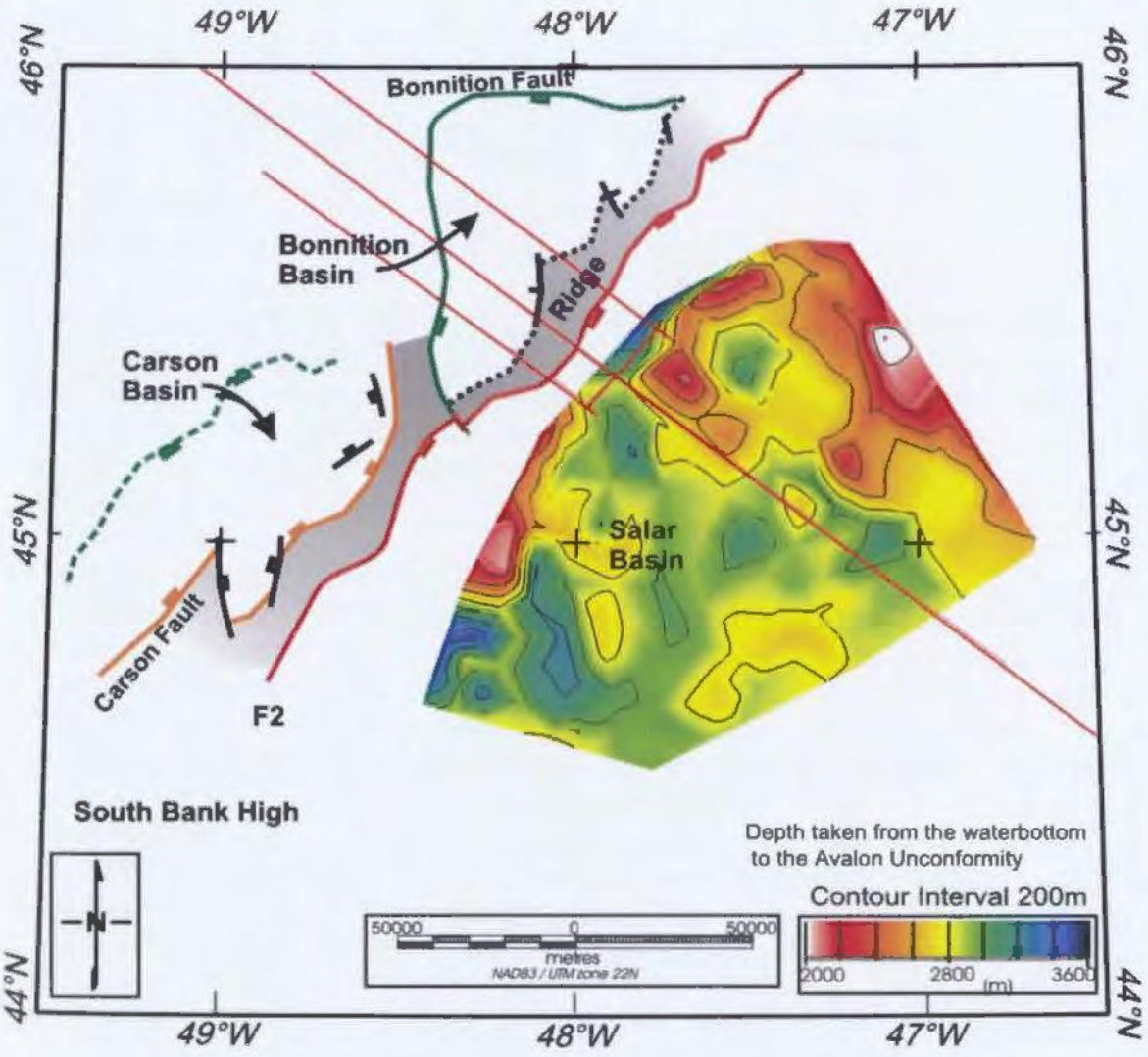

Figure 4.23. Extent and depth of burial of the potential source rock of Albian age in the Salar Basin.

The two wells in the Bonnition Basin also drilled through Upper Cretaceous and Lower Cenozoic sand units that have the potential to be reservoir rocks.

In the Carson Basin, Lower Cretaceous units are less abundant, especially in the southern portion of the basin, where they have been eroded. The Osprey well H-84 contains no record of the Avalon, Hibernia or Jeanne d'Arc Formations, however it does contain a thin Lower Cretaceous sandstone, the Eider Formation (McAlpine, 1990). The Skua well in the northern Carson Basin encounters thin Lower Cretaceous sandstones (Eider Formation). In the Salar Basin, the Cretaceous section varies in thickness across the basin and is found to be widespread.

4.5.3 Traps

Both the Carson and Bonnition basins show structures that are capable of trapping hydrocarbons. The Carson Basin is folded and faulted in many areas and movement of the Lower Jurassic salt layer aids in creating potential hydrocarbon traps. The Bonnition Basin also contains many faulted and folded areas that create structures to trap hydrocarbons and salt movement also allows traps to form. The Bonnition Basin tends to show more structural variation than the Carson Basin and appears to contain a greater number of potential hydrocarbon traps.

The Salar Basin shows little fault activity at the Cretaceous level, with most of the major faults tending to offset Jurassic and older strata. This basin would mainly rely on

stratigraphic traps and turbidite plays to trap hydrocarbons, however structural traps are also present.

In order for hydrocarbons to collect in the traps mentioned above, oil or gas generation needs to occur after the traps have been formed. In the Carson and Bonnition basins, the source rock was probably not buried to deep enough depths until the Late Cretaceous, at which time many of the traps would have already been formed. In the Salar Basin, since only a small amount of erosion is interpreted to have occurred, the Cretaceous and a large portion of the Cenozoic section needs to be present in order for the source to be buried at great enough depths for oil generation to occur. This means that for this area, oil generation most likely did not begin until later in the Cenozoic, when most of the traps would have already formed.

4.5.4 Overall Prospectivity

Based on the above analysis, the Carson Basin is found to have low hydrocarbon prospectivity due to the small amount of source rock, and thin Cretaceous reservoir rock. The Bonnition Basin appears to be more prospective, with a wider extent of source rock and a larger thickness of Lower Cretaceous sand units, which are proven reservoir rocks in the Jeanne d'Arc Basin. The Salar Basin is also considered prospective, with source rock assumed to be widely distributed and Cretaceous sequences present as well as a thick Cenozoic section that potentially contains reservoir rock.

CHAPTER 5 Reconstruction of the geologic evolution of the southeast Newfoundland continental margin.

5.1 Analysis of extension on the Grand Banks

Pure shear models of extension have been used in the past to estimate the amount of stretching that a margin underwent and to explain features that form due to extension. One of the most widely used models is the McKenzie (1978) model for pure shear extension. On continental margins a wide variety of post-rift, syn-rift and crustal thickness are observed. Pure shear extension models have difficulty explaining the differences observed in the relative thicknesses of syn- and post-rift sediment (Keen and Dehler, 1997). Depth-dependent stretching models were created in an attempt to account for the observed differences. The amount of crustal thinning or subsidence that a margin underwent can be used to estimate stretching values assuming 2D conservation of mass (Keen and Dehler, 1993). On continental margins, estimates of stretching can be determined from subsidence histories that are obtained from borehole data. This method however, only provides stretching estimates at a particular borehole location or along a cross-section of boreholes. In the Orphan Basin, Keen et al. (1987b) computed crustal stretching values (β) of ~1.5 to 2.0 and lower lithospheric stretching values (δ) of ~4.2 to 8 from well subsidence curves and a depth-dependent extension model which allowed estimates of δ and β (stretching parameters) to be made. Various quantitative stretching models have been applied to continental margins, ranging between the pure shear to simple shear end members. Keen and Dehler (1993) have used sediment thickness values

to estimate subsidence, and then used a two-layer extension model which allowed the crust (β) and lower lithosphere (δ) to thin by different amounts. Estimates from Dehler and Keen, (1993) show that some basins on the Grand Banks tend to show larger crustal stretching values than lower lithospheric stretching values ($\beta>\delta$), producing narrow half-graben basin architecture. Basins with high δ values in comparison to β values tend to form wider basins (ie. Orphan Basin) (Dehler and Keen, 1993). Average crustal stretching values (β) in the Jeanne d'Arc Basin range from ~1.5 to 2 (Keen and Dehler, 1993) based on subsidence estimates.

Crustal thinning can be used to estimate crustal stretching (β) values. β is determined by the ratio of the unextended crust to the extended crust. Based on crustal thickness estimates, in the Jeanne d'Arc Basin area, β is estimated at ~1.3 (Keen and Dehler, 1993).

Previous studies by Keen et al. (1987a) and Keen et al. (1987b) have used seismic data to restore normal faults to their pre-rift positions to determine the amount of horizontal superficial extension across some of the basins on the Grand Banks. Their studies showed a total extension factor (e) of 1.7 estimated across only the Jeanne d'Arc and Flemish Pass basins and 1.3 to 1.5 (e) estimated across the Orphan Basin. Their estimate for extension across the southern Jeanne d'Arc Basin is 1.17. Estimates from Keen and Dehler (1993) across the northern Grand Banks give rise to average crustal stretching values (e) of ~ 1.3. It is believed that the range in extension values across different portions of the Grand Banks can be accounted for by the presence of transfer faults

separating areas such as the Jeanne d'Arc and southern Jeanne d'Arc basins (Keen et al. 1987a).

Kinematic extension models (both symmetric and asymmetric and detailed in Chapter 1, section 1.4) are able to interpret many of the features that are found on continental margins. While these models are effective at describing observed geometries, they explain little about the dynamic rifting process (Huismans and Beaumont, 2003). Recent studies using numerical models by Huismans and Beaumont (2003) have provided insight into the controls and mechanisms of both asymmetric and symmetric modes of extension. In general, previous numerical models have only considered first order extension weakly dependent on strain, which tends to predict symmetric extension. Huismans and Beaumont (2003) studied frictional plastic and viscous strain softening in cases where the crust is either coupled to, or decoupled, from the mantle. Symmetric, asymmetric and mixed modes of rifting models were all predicted. Their studies suggest that strain softening promotes asymmetry and that asymmetric rifting is strongest when the lithosphere is coupled and rifting velocities are low. Symmetric rifting appears to be favoured when strain softening is absent or if high rifting velocities are present (Huismans and Beaumont, 2002). Their various models are similar to the kinematic models that have been proposed by McKenzie (1978), Wernicke (1985) and Lister (1986).

5.2 Profiles and Software

Structural reconstruction of the development of the SE Newfoundland margin was performed to gain an understanding of how the margin evolved through time and to determine if the extension of the margin varies significantly along strike. The kinematic models created through structural restoration have the ability to animate structures and monitor variations in the extension of the margin. These models only investigate crustal stretching and ignore effects of lower lithosphere thinning. Six longer profiles transecting the margin were used for this investigation (Figure 5.1). These profiles were chosen because they cover the shelf and slope portions of the margin and most are close to the same orientation. The chosen profiles transect the Carson, Bonnition and Salar basins and cross from the shelf to the slope area of the margin. The profiles begin eastward of the Jeanne d'Arc and Southern Jeanne d'Arc basins and therefore extension related to basins inboard of these profiles is not evaluated or included. Extension values from the shelf/slope portion of the margin will however be compared to values from intercontinental basins on the Grand Banks which are landward of the slope.

The computer program LithoTect (from Geo-Logic Systems) was used to create the reconstructions of each profile. This program allows the user to perform reconstructions by assuming that either flexural, vertical/oblique or complex slip occurred. The user has the ability to choose the type of reconstruction to perform and in the case of oblique slip, the angle of the slip system can be defined (LithoTect manual, 2005).

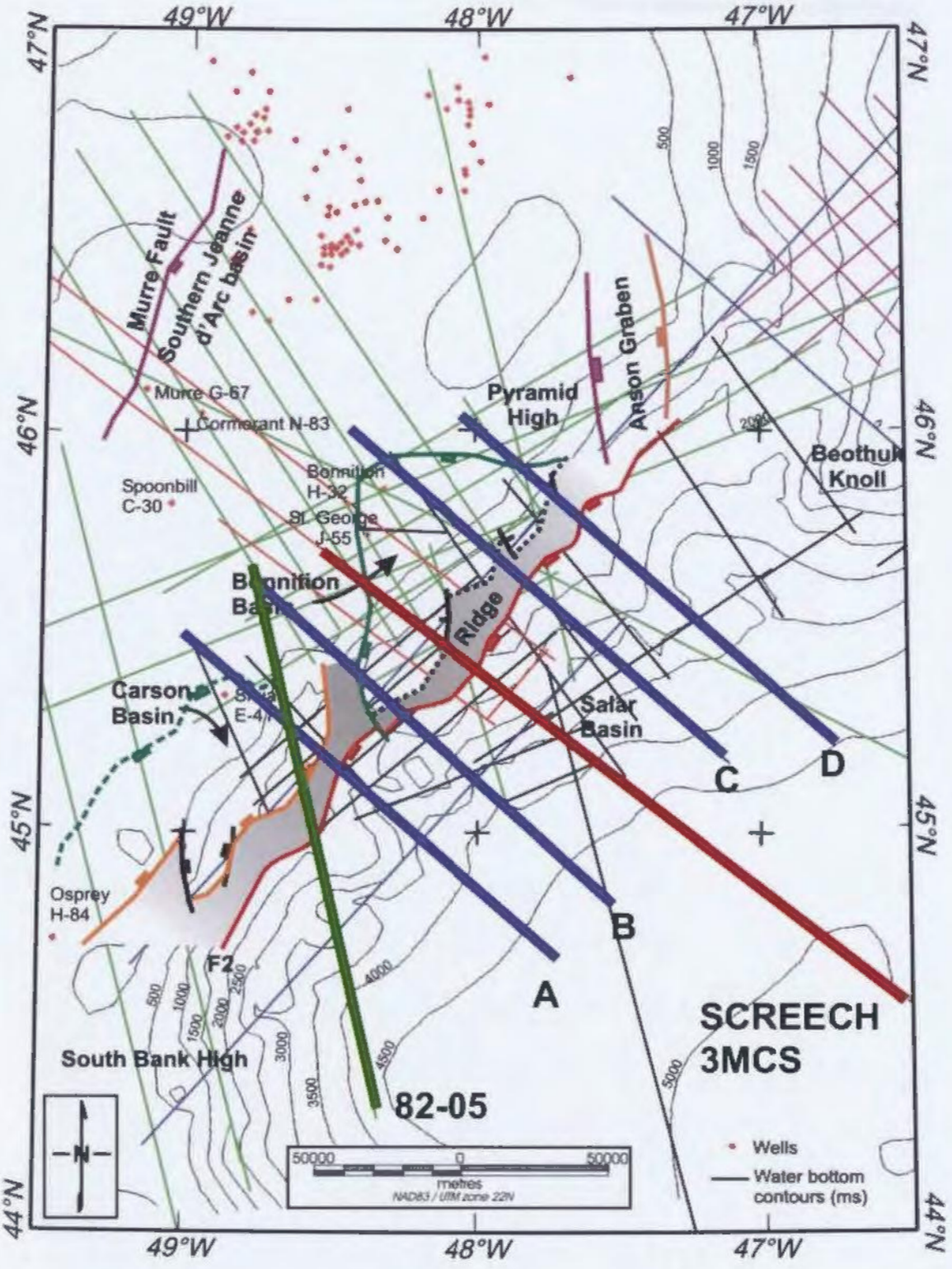

Figure 5.1. Transects selected for restoration of the margin. Lines A to D are WesternGeco proprietary seismic lines.

For reconstruction in extensional environments, the vertical/oblique slip method of restoration is the most appropriate method to use, and was used on all profiles in this thesis. The angle of the slip system orientation was set to vertical for all layers. In this orientation, regions are filled with vertical sample lines as shown in Figure 5.2. Reconstruction is achieved by the vertical sample lines in each region sliding past one another. Restoration techniques are based on area preservation between deformed and restored states, and the vertical slip method maintains horizontal bedlength distances. In reality, slip is likely to occur on extensional minor faults (to small to be imaged) both parallel and in complementary directions to the imaged shear. In the absence of clear indication of the predominant set of minor faults, it is reasonable to use a starting assumption of vertical shear (attributable to equal contributions from synthetic and antithetic faults). The restoration methods are all based on simple shear methodologies and in the case of the vertical and oblique slip methods they are used with a straight slip vector. In areas were salt is present, the salt cannot be treated like other layers during the restoration (LithoTect manual, 2005). The area of salt is rarely ever preserved in 2D and therefore when restoring the profiles, the sections above the salt and below the salt are reconstructed independently. In the Carson Basin the salt layer will not be restored since the salt geometry is rather complex, however on the Bonnition and Salar basin profiles the salt unit appears to be flat lying and an attempt to restore the unit will be made. In the restoration of the salt layer, salt diapirs will be ignored and it will be assumed that the top of the salt layer carries on horizontally through diapirs. Another approach to restore the salt layer would be to spread the area of the salt structure out over length of the salt layer.

This option was not used since there may be a significant amount of salt that could have come from out of the plane of the profile, and would therefore result in an overestimation of the original thickness of the salt layer.

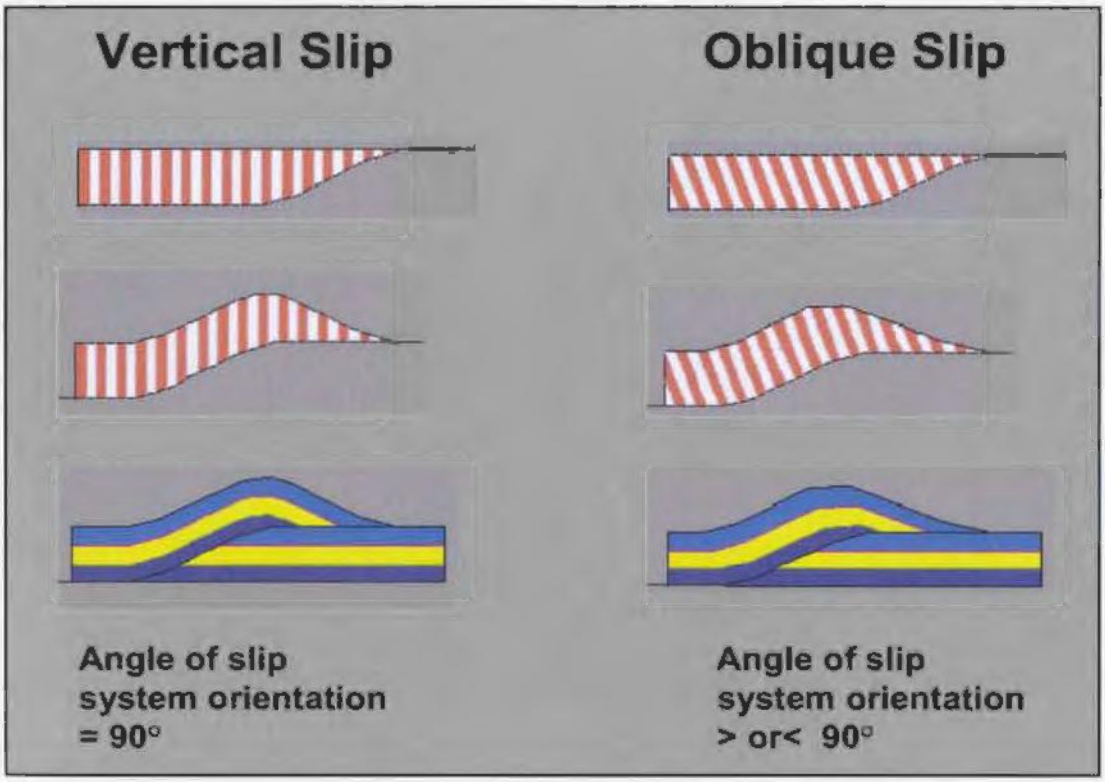

Figure 5.2. Restoration method. Vertical and oblique slip orientation angles are shown. These types of slip systems are most commonly applied in extensional environments. The techniques are based on area preservation between the deformed and restored states. The vertical slip technique maintains horizontal bedlength distances and is based on simple shear methodologies.

Another assumption that is made is that each horizon is restored to a regional datum (in this case sea level), which assumes that all sediment deposition is in shallow water. The presence of deeper water facies in the sedimentary record on the margin indicates that deposition did not always occur in shallow water and therefore this assumption is a

generalization. Restoring horizons to sea level also assumes that no emergence occurred. This is simplistic since the presence of unconformities in the sedimentary record indicates that portions of the margin did emerge and erosion occurred. Erosion across some areas of the margin is significant, resulting in a substantial amount of sediments that were removed, however it is difficult to determine how much sediment was removed at various times and in various locations throughout the evolution of the margin. While these assumptions simplify the restoration process, they should still provide meaningful results relating to the evolution of the Newfoundland margin and allow extension values to be calculated across various profiles along the margin.

5.3. Profile Interpretation

To perform the reconstructions the margin was divided into nine units as illustrated in Figure 5.3. The stratigraphic chart shown in Chapter 1, Figure 1.13, illustrates the geologic formations that would be encompassed in each unit. Interpretations of the profiles were all done in the time domain and all crustal faults were assumed to be listric faults. Alternative methods of analyzing normal faults include the collapsing dominos model of extension but the planar faults involved create volume problems along the basal detachment and adjacent undeformed blocks (Gibbs, 1984) and require large extensions before thinning occurs (as shown in Figure 5.4). In the six profiles, listric faults curving towards a detachment (assumed to be in the mid-crust, eg., Dentith and Hall, 1990) are interpreted and used to alleviate these problems.

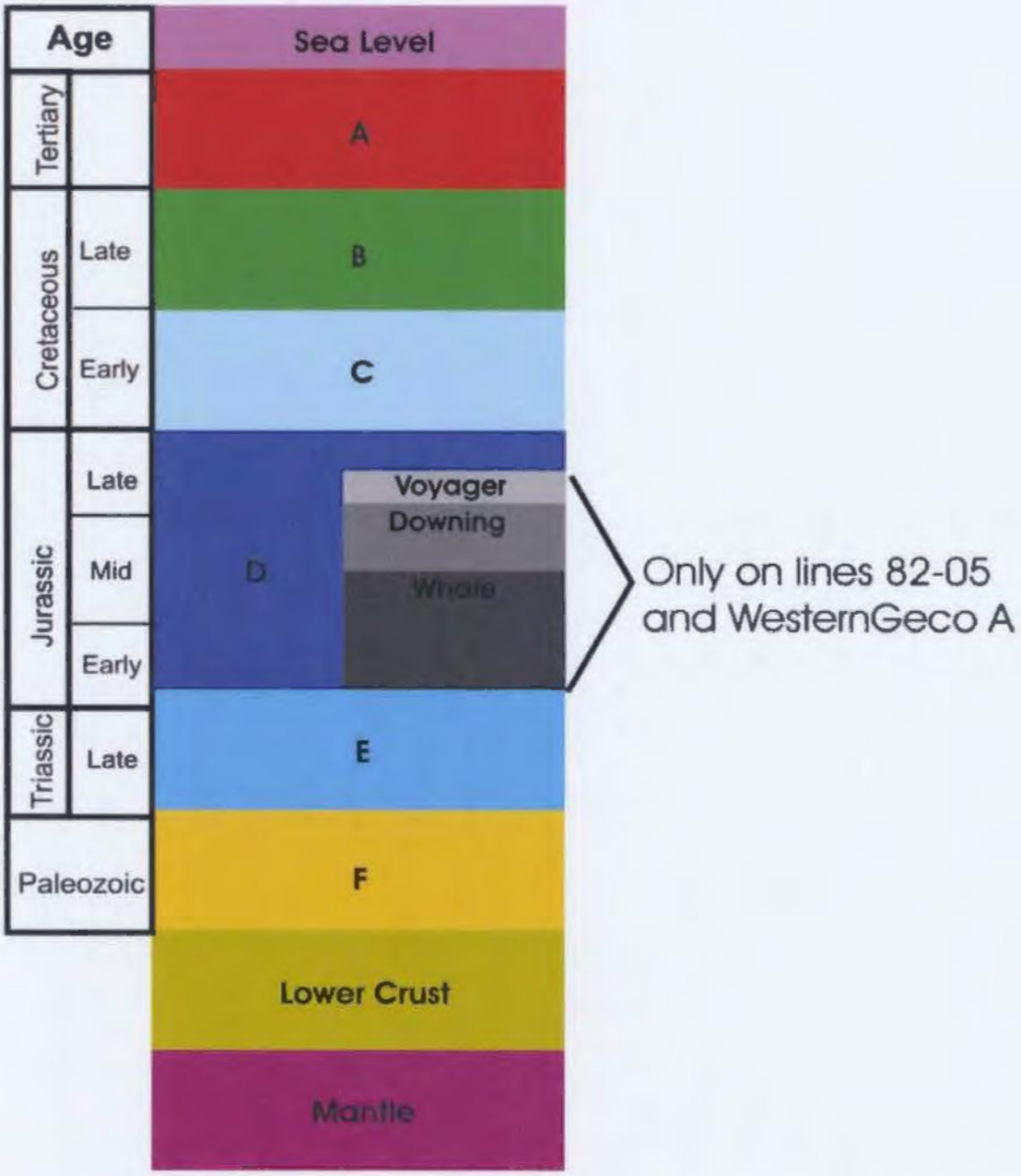

Figure 5.3. Layer boundaries and colours assigned to each layer on the transects. All the layers are used in all profiles, except for the Voyager, Top Downing and the Top Whale Unit, which are only divided in profiles 82-05 and WesternGeco proprietary line A. In the other profiles, these units are just classified as Layer D.

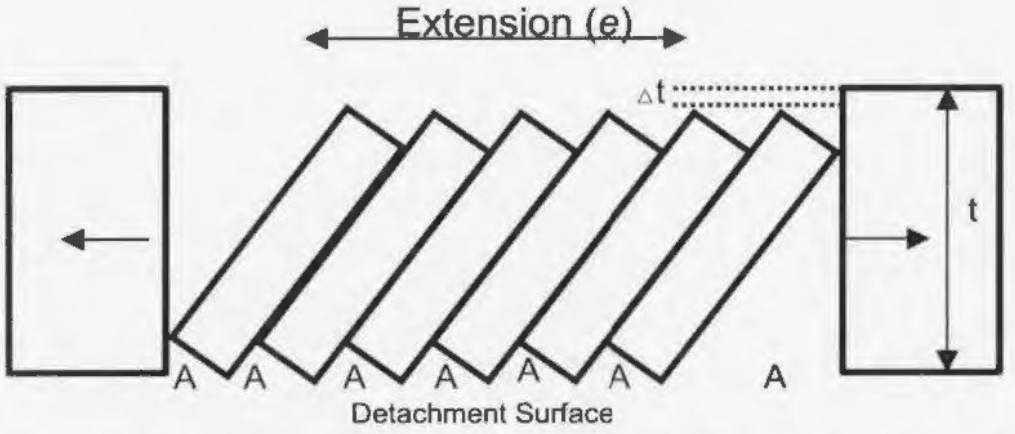

Figure 5.4. Space problems created with extension along planar faults (denoted as A). Also shown is the large amount of extension that is required for a small amount of thinning (Δt) to occur. (*Modified from*: Gibbs, 1984)

The first layer down encompasses the water layer and in all profiles this layer varies in thickness, getting thicker towards the east. The second layer (A) spans from the sea floor to the Base Cenozoic, and it represents all preserved sediment deposition from the Cenozoic to the present. The third layer (B) represents the Upper Cretaceous, spanning from the Base Cenozoic to the Avalon Unconformity. The fourth layer (C) represents the Lower Cretaceous from the Avalon Unconformity to the Upper Jurassic, which is defined by the top of the Rankin Formation or the Tithonian Unconformity. The fifth layer (D) spans from the top of the Tithonian Unconformity to the top of the Argo salt and represents the Lower, Middle and Upper Jurassic deposits. This layer is further subdivided on profiles 82-05, WesternGeco A and SCREECH 3MCS. On these three seismic profiles, the Middle and Upper Jurassic section is extensive and has been divided into the following sections; "Voyager" - which spans from the top of the Voyager Formation to the top of the Downing Formation, the "Downing" - which spans from the top of the Downing Formation to the top of the Whale Member, and the "Whale" - which

spans from the top of the Whale Member to the Base of the Iroquois Formation. The sixth layer ("E") encompasses the salt sequence, bounded at the base by either Triassic sediments or basement material. The seventh layer ("F") very generally represents basement and the upper crust. The base of this layer is arbitrarily chosen. The eighth layer (labelled "Lower Crust") generally represents the mid to lower crust and is added to the model to provide a ductile layer for the basement faults to move on and terminate into. The ninth layer ("Mantle") completes the model and represents the mantle from the top of the Moho to a depth of around 37 km.

All the layers described above except for the eighth (Lower Crust) and ninth (Mantle) layers were interpreted from the seismic reflection profiles in the time domain and then converted to depth. Figure 5.5 shows the six profile interpretations in the time domain. A depth conversion was performed on these profiles by assigning interval velocity values to individual units and then converting from the time domain to the depth domain. The velocity values for the interpreted layers were mainly estimated from well data. Four wells on the shelf; St. George J-55, Bonnition H-32, Spoonbill C-30 and Skua E-41 were used to determine sediment velocities. These wells all had interval velocity values that were available from the CNLOPB. Of the seven layers that were interpreted in the time domain for each profile, only the top five layers have velocity information available from well logs. For layer F (basement), velocity information from wide angle modelling performed on SCREECH 3 MCS was used (Lau et al. 2005b, in press). Figure 5.6 illustrates the velocity values that were obtained from each well for each layer.

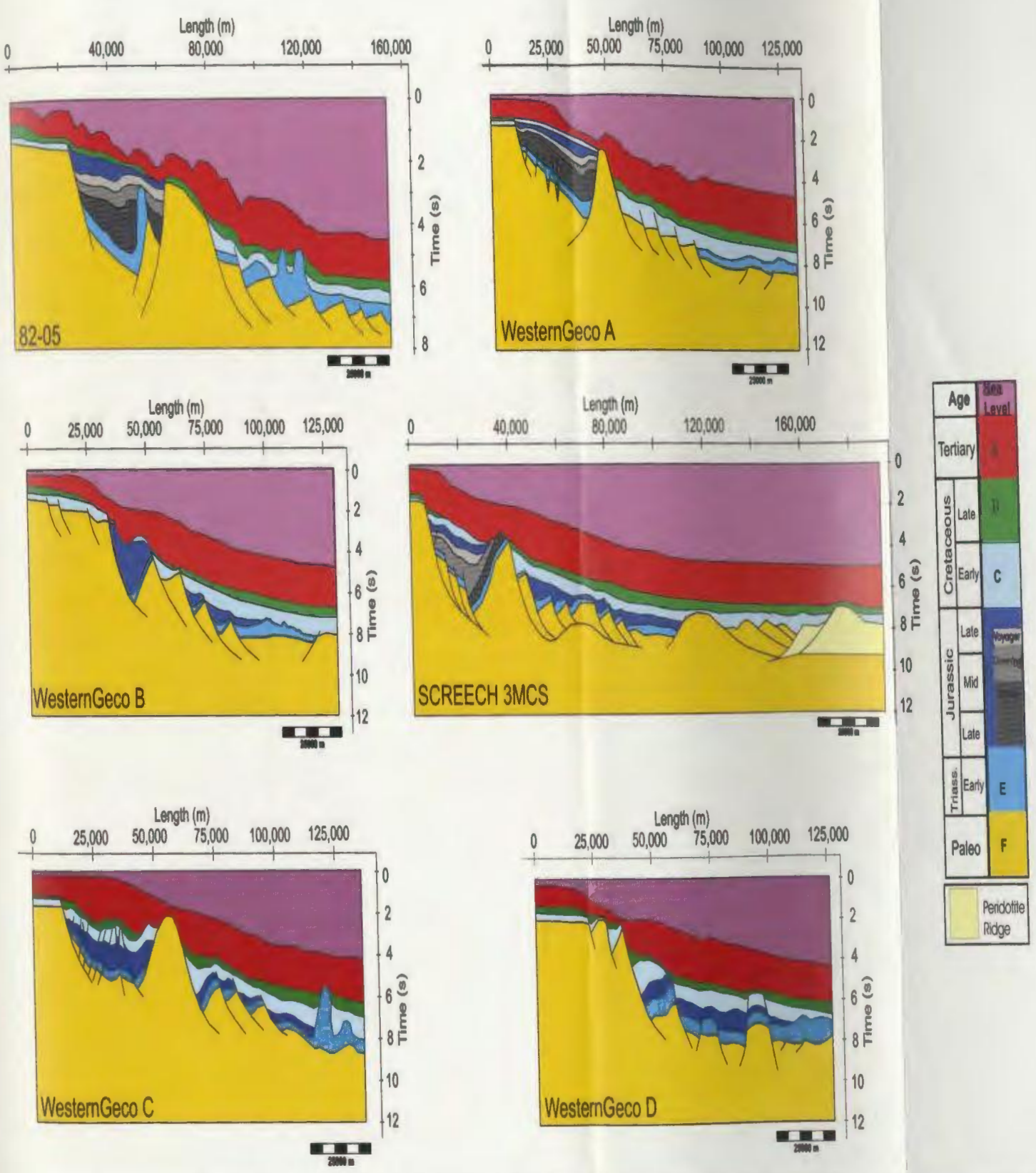

Figure 5.5. Time interpretations of the six profiles (82-05, A, B, SCREECH 3MCS, C and D) along the margin. Lines A, B, C and D are based on proprietary WesternGeco seismic data.

Bonnition

Two-Way Time (ms)	Interval Velocity (m/s)
0.00	1524.00
0.12	1706.88
0.32	1737.36
0.52	1950.72
0.62	2011.68
0.80	2072.64
0.86	2179.32
1.04	2194.56
1.20	2255.52
1.26	3048.00
1.28	3048.00
1.48	2834.64
1.62	2926.08
1.76	3474.72
1.88	2712.72
1.94	2956.56
2.00	3230.88
2.06	4114.80
2.16	3413.76
2.28	3322.32
2.42	4632.96
2.44	3108.96

Spoonbill

Two-Way Time (ms)	Interval Velocity (m/s)
0.00	1524.00
0.08	1645.92
0.26	2316.48
0.46	2316.48
0.58	2316.48
0.74	2865.12
0.86	2865.12
0.94	3108.96
1.00	4389.12
1.08	3962.40
1.18	4206.24
1.32	3779.52
1.40	3535.68
1.48	3992.88
1.54	4267.20
1.62	4267.20
1.68	3901.44

Skua

Two-Way Time (ms)	Interval Velocity (m/s)
0.00	1524.00
0.05	1524.00
0.10	1524.00
0.40	1969.92
0.45	2258.26
0.50	2133.90
0.90	1842.39
0.95	2501.19
1.00	2247.87
1.40	3201.62
1.45	2947.42
1.50	3027.58
1.90	3763.67
1.95	3670.40
2.00	3791.71
2.30	3736.18
2.32	3940.15

St. George

Two-Way Time (ms)	Interval Velocity (m/s)
0.00	1523.00
0.14	1796.00
0.41	1796.00
0.50	1796.00
0.74	2030.00
0.75	2053.00
0.77	2177.00
0.98	2263.00
1.00	2201.00
1.00	2167.00
1.01	2232.00
1.49	2901.00
1.50	2831.00
1.51	2902.00
1.51	2900.00
2.50	3518.00
2.51	3239.00
2.52	3162.00
2.99	3650.00
3.00	3774.00
3.01	3776.00

Layers	Interval Velocity	
Sea Level	1500 m/s	Based on Well Data
A	2000m/s	
B	2500 m/s	
C	3300 m/s	
D	3500 m/s	
E	4100 m/s	From Wide-angle Modelling
F	6000 m/s	
Lower Crust	6200 m/s	
Mantle	8200 m/s	

Figure 5.6. Velocity values estimated for each layer. Well data was provided by CNLOBP for all wells except the ODP well, which came from Shipboard Sceintific Party, 2004. The velocity values are coloured to correspond to the sequences in Figure 5.3. The velocities from wide-angle data came from Lau et al. (2005, in press).

Figure 5.7 illustrates the resulting interval velocity profile for each seismic line that was used to convert the seismic line to depth. Since velocity information is limited, and each layer chosen incorporates many different geologic units, the interval velocities are considered a rough estimate and provide reasonable depth values.

Once the profiles were converted to depth, the eighth and ninth layers were added to each profile. In order for layer F (basement) to be reconstructed, the assumption was made that basement fault displacement was accommodated by the Mid to Lower Crustal layer (eighth layer). When the LithoTect program is used to restore layer F (basement) it assumed that the eighth layer (Lower Crust) acted as "toothpaste" to accommodate fault displacement. The depth to the ninth layer (Mantle) was determined from wide angle modelling that was performed on SCREECH 3MCS. Figure 5.8 illustrates the five profiles in depth with the eighth and ninth layers added.

5.4 Reconstruction Steps

The margin was reconstructed by first removing the water layer in each of the profiles which is shown in Figure 5.9 parts A. After the water layer was removed Layer A (the Cenozoic sediments) were then removed from the profiles (Figure 5.9 parts B). Layer B (Upper Cretaceous sequences) were then removed as well (Figure 5.9 parts C). At this point the restored sections should resemble the end of rifting period and the beginning of drift. In all of these profiles, the amount of extension that occurs during this interval is very small, indicating that the margin has extended little since the end of rifting.

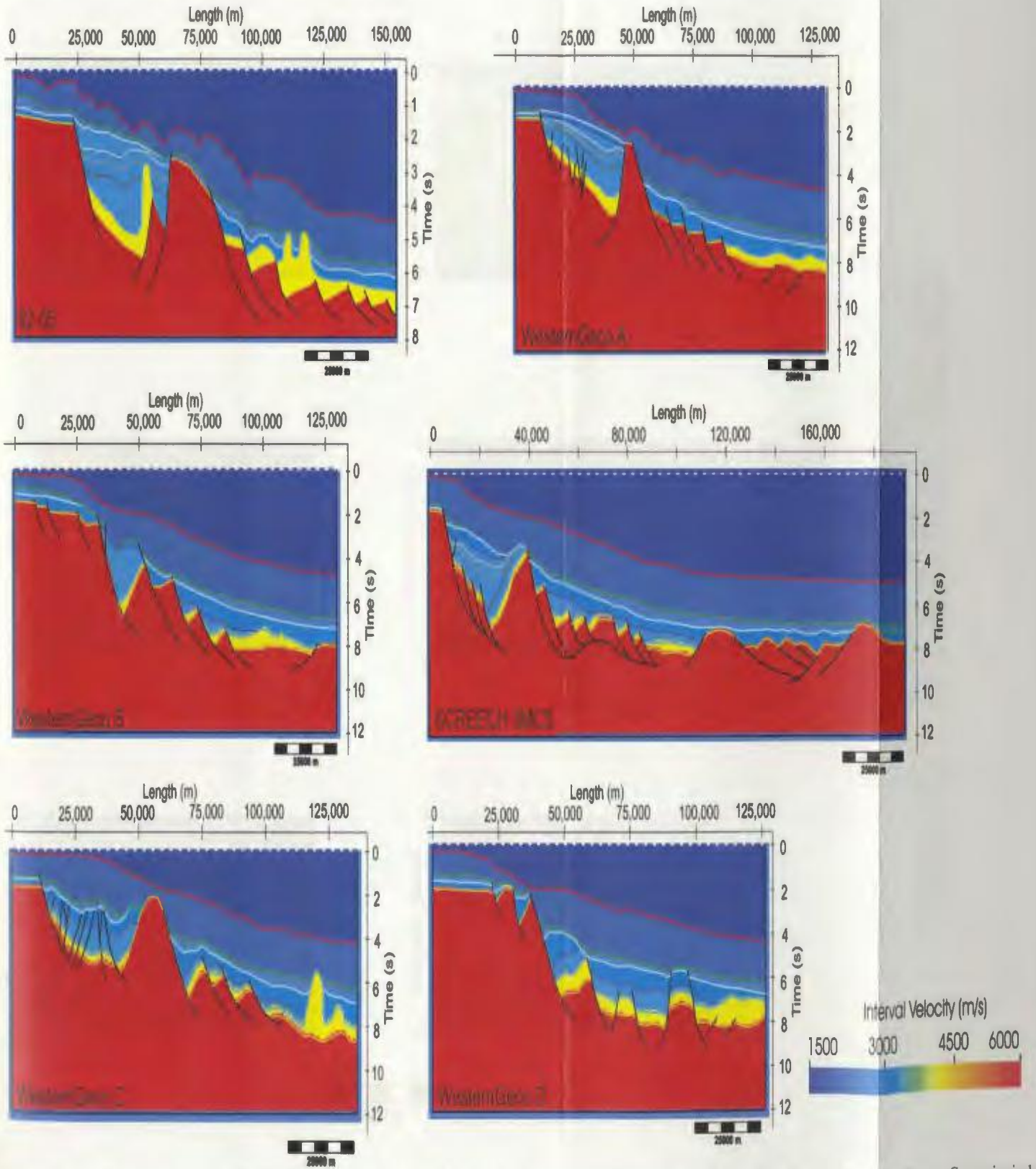

Figure 5.7. Interval velocity profile for each seismic line (82-05, A, B, SCREECH 3MCS, C and D) along the margin. Lines A, B, C and D are based on proprietary WesternGeco seismic data. Velocities were based on available well data.

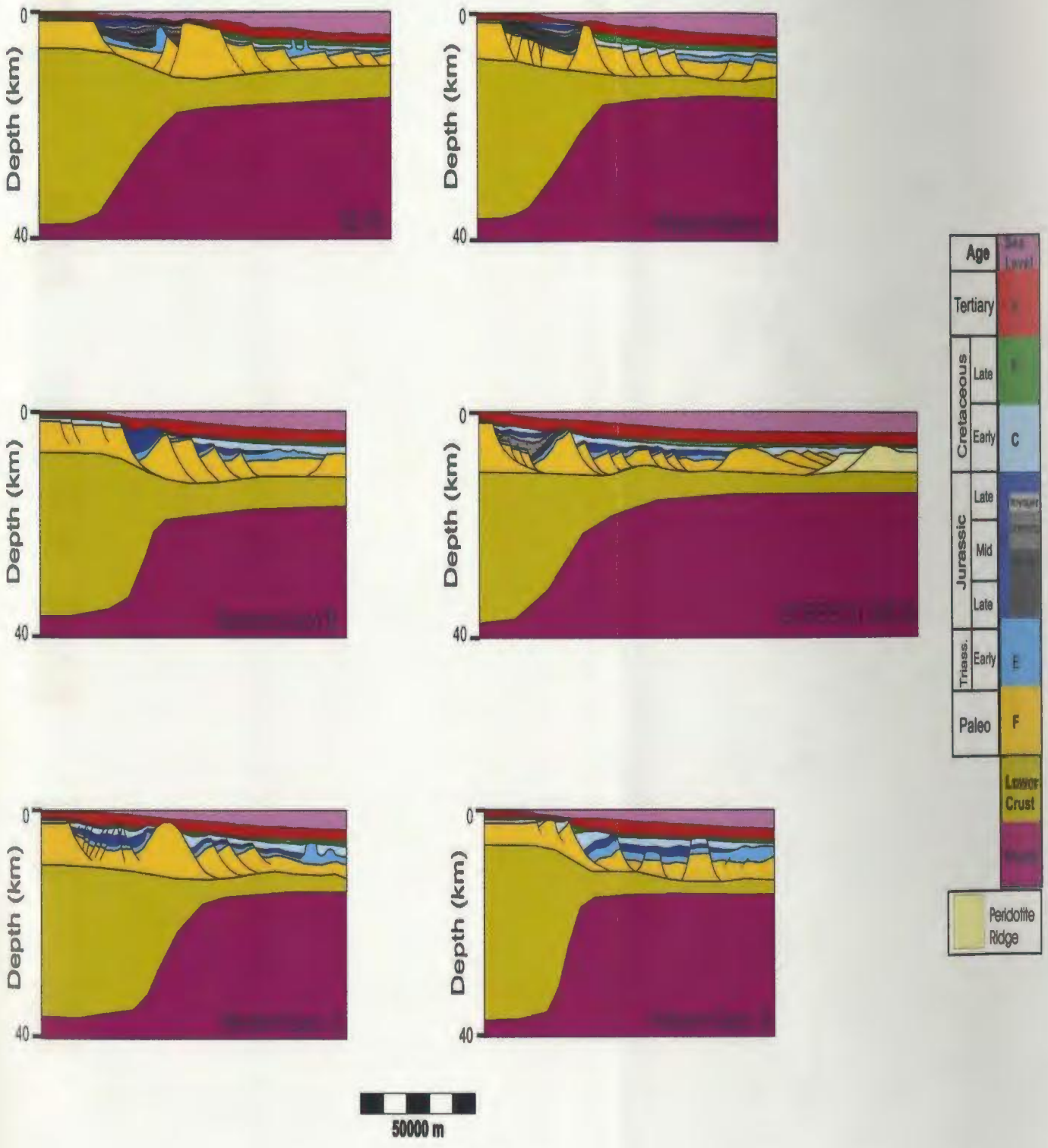

Figure 5.8. Depth converted versions of the six profiles, 82-05, A, B, SCREECH 3MCS, C and D along the margin. Lines A, B, C and D are based on proprietary WesternGeco seismic data.

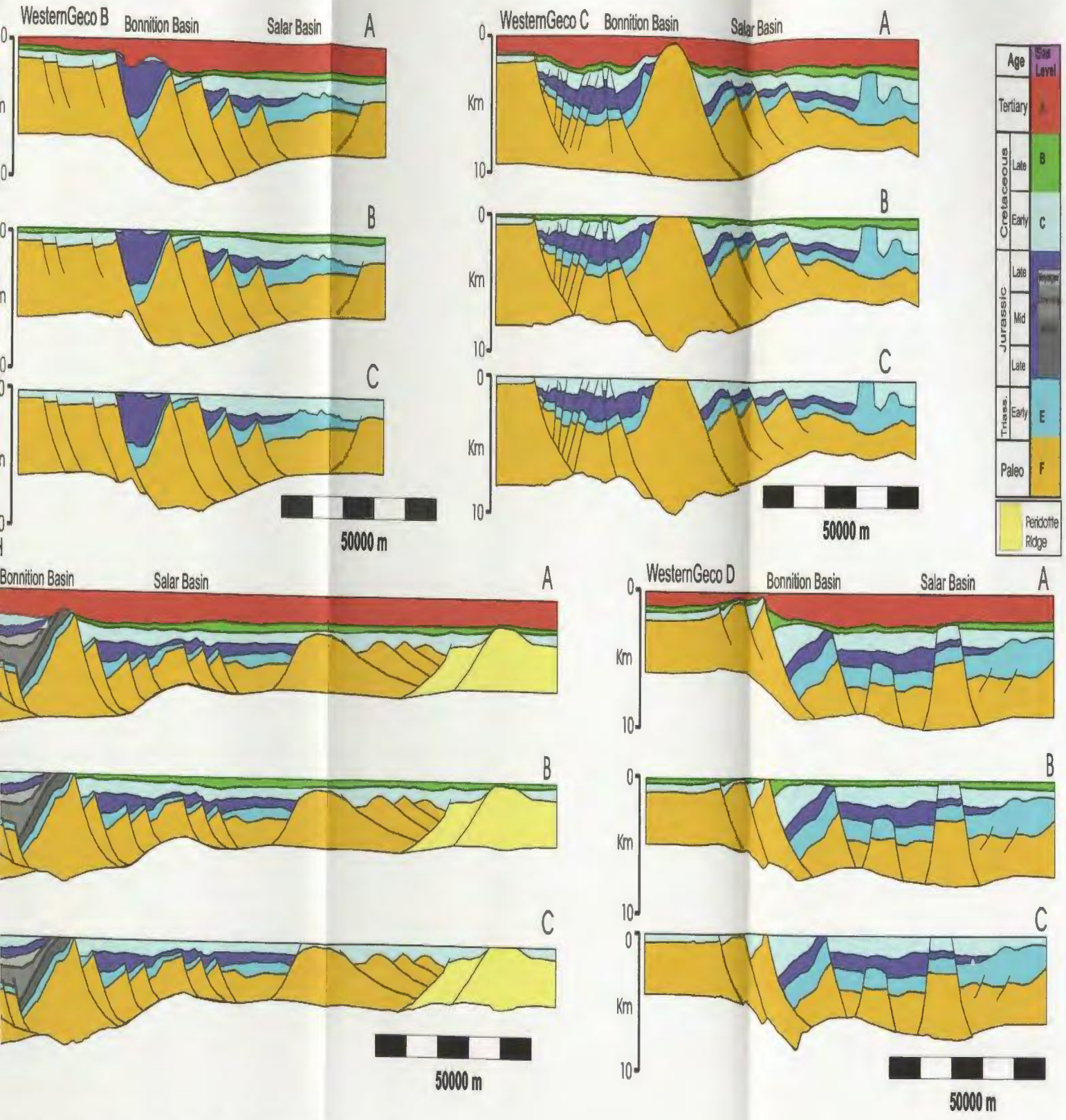

nsition from rifting to drift. Lines A, B, C and D are based on proprietary WesternGeco seismic data.

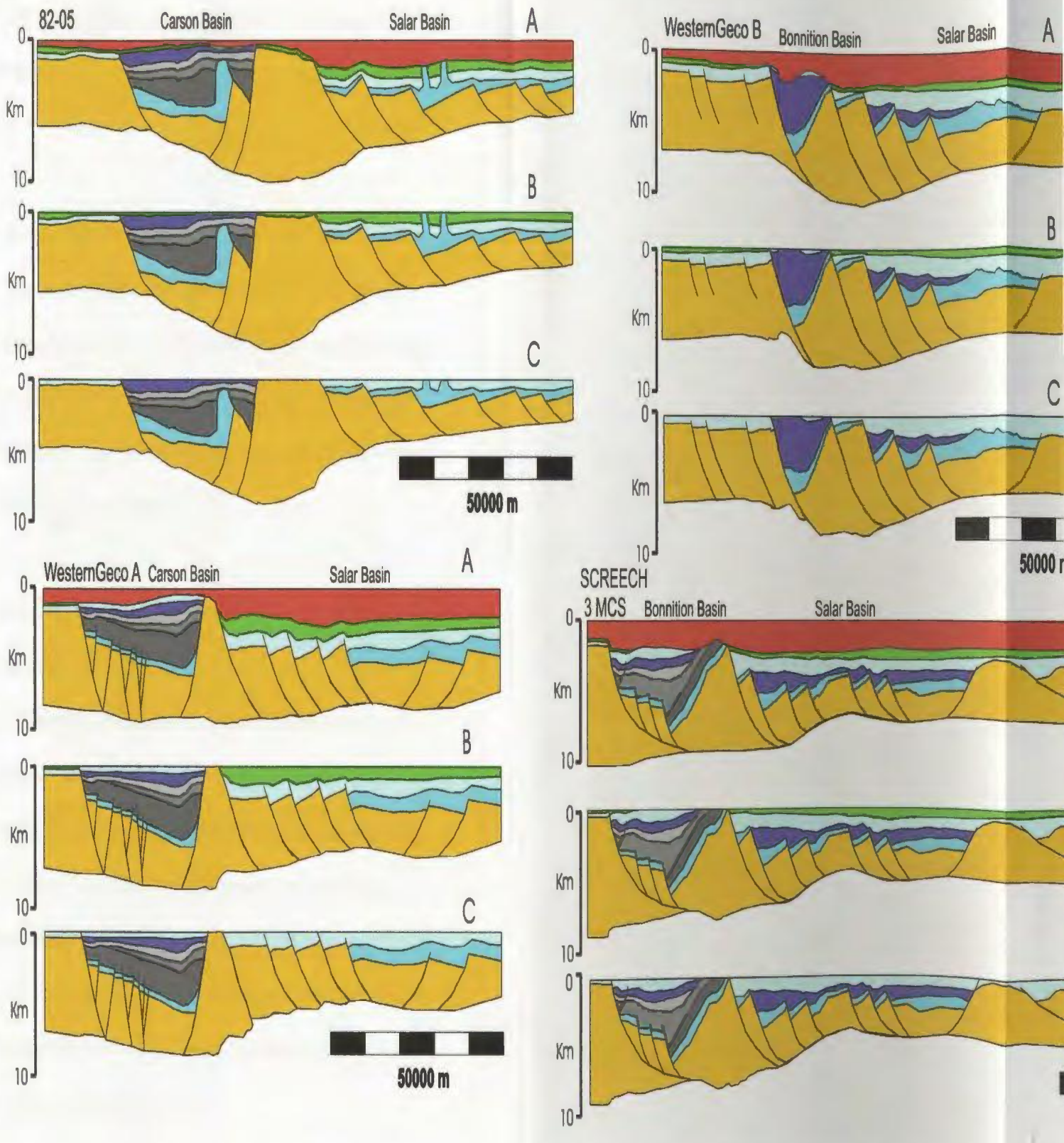

Figure 5.9. Reconstruction of the six profiles to top of Layer 3 (Avalon Unconformity) time. This time roughly represents the transition from rifting to drift. Lines A, B, C and D are based on proprietary Western

The restoration of each layer makes the assumption that no erosion has occurred, which in reality is not the case. The Base Cenozoic Unconformity (base of Layer A) has eroded deeper layers on many of the profiles, as has the Avalon Unconformity (top of Layer C).

At the rift-drift transition (Figure 5.9 part C on all lines), similarities and differences are shown to exist between the profiles. The late stages of syn-rift deposition would have occurred in the Early Cretaceous, which is approximately equivalent to the upper most layer visible in the profiles in Figure 5.9 parts C. The Lower Cretaceous sediments are fairly uniform in thickness on WesternGeco line A, while on line 82-05 they have been eroded by overlying unconformities.

In the Bonnition Basin the four lines (WesternGeco lines B, C, and D and SCREECH 3MCS) appear to indicate a fairly similar pattern of sediment fill and fault activity. In these profiles the Lower Cretaceous (Figure 5.9 parts C) sediment thickness is quite variable. On WesternGeco line B the Lower Cretaceous is eroded in most areas of the Bonnition Basin by the overlying Base Cenozoic Unconformity. SCREECH 3MCS shows that more Lower Cretaceous sediment is present towards the east dipping Bonnition Fault and eroded towards the basement high. On WesternGeco line C, the Lower Cretaceous is generally uniform in thickness across the Bonnition Basin. WesternGeco line D shows a thick Lower Cretaceous sediment sequence that thickens towards the east dipping Bonnition Fault.

In the Salar Basin, the Lower Cretaceous sediments are generally uniform in thickness on each profile, except in faulted areas where the sediment thickens toward the faults. Examination of the reconstructed profiles shows that the Lower Cretaceous appears to increase in thickness toward the north of the study area.

On all profiles, restoration of the post-rift layers through vertical slip causes unnatural effects and geometries to be propagated through the underlying sediment and basement layers. These effects are most readily illustrated in the geometry of the large basement high on all profiles (Figure 5.9), especially on WesternGeco lines A and C. The base of the basement high has an unnatural shape when the overlying layers are restored. The shape of the base of the basement is due to assuming that deformation occurred through vertical slip, meaning that all displacement will occur vertically and not be accommodated in various oblique directions as may be the case in reality. It was also assumed that the boundary between Layer F (basement) and the Lower Crust layer acts as "toothpaste". This assumption means that displacement is accommodated by the Lower Crust layer, thus allowing for irregularities in the shape of Layer F (basement layer) to form. The shape of the base of the basement high can also be attributed to the assumption that no erosion has occurred. The present shape of the basement high and other faults has been modified through erosion, meaning that reconstruction of the margin back to the pre-rift conditions will be a rough estimate since the original size and shape of some features has been destroyed.

5.4.1 Syn-rift Reconstruction

After the post-rift phase was reconstructed, the syn-rift phase of the margin was reconstructed. This involved removing the Layers C, D, and E (Early Cretaceous, Jurassic and Triassic). Figure 5.10 illustrates the reconstruction of Lines 82-05 and WesternGeco A, both of which are in the Carson Basin, and Figure 5.11 shows the reconstruction of lines WesternGeco B, C and D and SCREECH 3MCS, all of which are in the Bonnition Basin.

On line 82-05 Layer D in Figure 5.10A (Late Jurassic) in the Carson Basin appears thicker towards the east-dipping western boundary antithetic fault, whereas on WesternGeco line A, Layer D appears thicker towards the west dipping Carson Fault. The Upper to Mid Jurassic sequences are influenced by movement of the Lower Jurassic salt layer on line 82-05. The movement of the salt into a diapir near the west-dipping Carson Fault appears to cause uplift in the sediment layers near the Carson Fault, creating a depocentre for sediment over near the east-dipping antithetic during Late Jurassic time. This uplift also causes erosion of the Upper Jurassic sequences (Layer D).

Reconstruction of the Carson Basin to the Voyager layer (light grey layer, Mid Jurassic, Figure 5.10 parts B) shows that this layer was deposited fairly uniformly on line 82-05, and on WesternGeco line A it thickens toward the centre of the basin. Reconstruction to the Downing layer (grey layer, Mid Jurassic, Figure 5.10 parts C) shows a thickening of the layer towards the west dipping Carson Fault on both lines 82-05 and WesternGeco A,

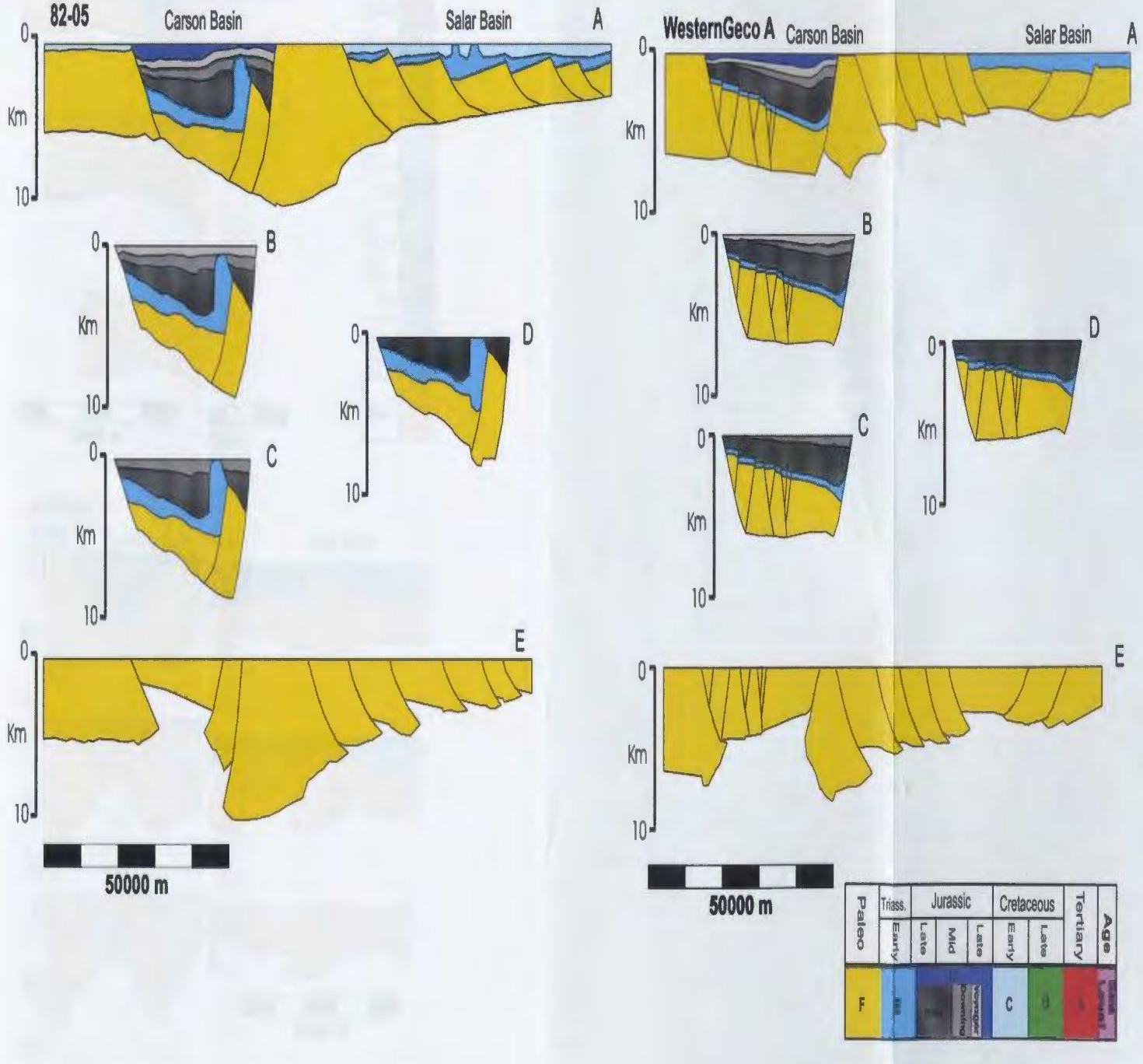

Figure 5.10. Reconstruction of profiles 82-05 and WesternGeco A in the Carson Basin. These reconstructions represent the syn-rift period and the pre-rift state.

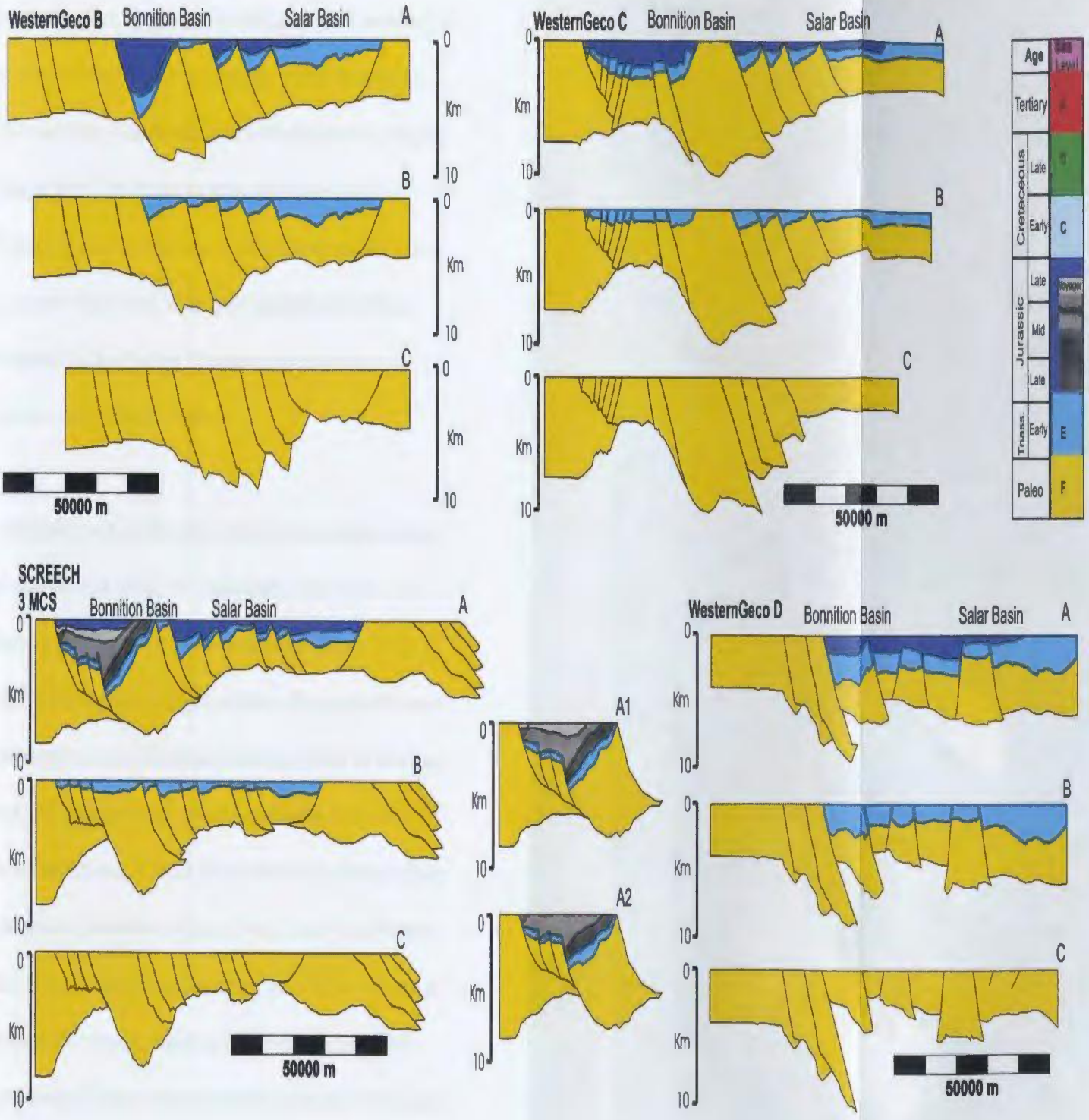

Figure 5.11. Reconstruction of profiles WesternGeco B, SCREECH 3MCS, WesternGeco C and WesternGeco D in the Bonnition Basin. These reconstructions represent the syn-rift period and the pre-rift state.

indicating that the fault was active during the Mid Jurassic. When the Whale layer is restored (dark grey layer, Figure 5.10 parts D) on both lines 82-05 and WesternGeco A, it also shows a thickening towards the Carson Fault, again indicating that the fault was active during this time period. Reconstruction of the Carson Basin to the top of the Early Jurassic salt (layer E, light blue layer) was not performed on either line 82-05 or WesternGeco A since salt movement cannot be restored accurately and line 82-05 shows a large amount of salt movement. Final images of the restored profiles (82-05 and WesternGeco A) to the level of Layer F (basement) which represents the pre-rift geometry are illustrated in Figure 5.10 parts E.

In the Bonnition Basin the profiles in Figure 5.11 parts A show the margin reconstructed to Layer D (Mid to Late Jurassic). The Jurassic sediments on these profiles are not as extensive as the profiles in the Carson Basin and are therefore only subdivided on SCREECH 3MCS where they show significant thickness. The deposition of the Jurassic sediments varies on each of the profiles shown in the Bonnition Basin. On WesternGeco line B, Layer D thickens towards the east dipping Bonnition Fault, but remains thickest near the centre of the basin. SCREECH 3MCS also shows that the sediments are thickest in the centre of the basin as shown in Figure 5.11 parts A, A1 and A2. On WesternGeco line C, the thickest section of this layer is found in the centre of the basin and it thins as the basin margins are reached. WesternGeco line D shows that the layer is slightly thicker towards the Bonnition Fault and also indicates that at this time and in this area the Bonnition Basin and the Salar Basin may have been linked together. Reconstruction of

the profiles to layer E (Early Jurassic, light blue layer) is shown in Figure 5.11 parts B. This layer is composed of carbonates, evaporites and Triassic red beds and only shows minor amounts of salt movement, so reconstruction was attempted. On WesternGeco line B the layer appears to thicken toward the Bonnition Fault, but appears to remain uniform on profiles SCREECH 3MCS and WesternGeco line C, thinning slightly towards the edges of the basin. WesternGeco line D shows that the layer is fairly uniform in the basin and also shows that at this time the Bonnition and Salar basins may have once been linked together. Final images of the restored profiles are shown in Figure 5.11 parts C.

All profiles in Figures 5.10 and 5.11 show the Salar Basin and depict how it evolved during the syn-rift period. In the southern portion of the Salar Basin (Figure 5.10) no Middle to Upper Jurassic sediments (Layer D) are deposited. Layer E (Early Jurassic) is fairly uniformly deposited across the basin, thickening slightly near faults. Areas of salt diapirism are present and are ignored during the reconstruction. In the northern portion of the Salar Basin (Figure 5.11) Layer D (Jurassic) and Layer E (Early Jurassic) thicken towards faults and also appear to thicken toward the north. The most northern profile (WesternGeco line D) shows that during the Jurassic and Late Triassic the Bonnition and Salar basins were most likely connected.

After Layer F (basement) was restored, the underlying layers (Lower Crust and Mantle) were then added to the profiles to image their approximate position and structure with the basement layer restored. Figure 5.12 illustrates the profiles with the additional layers

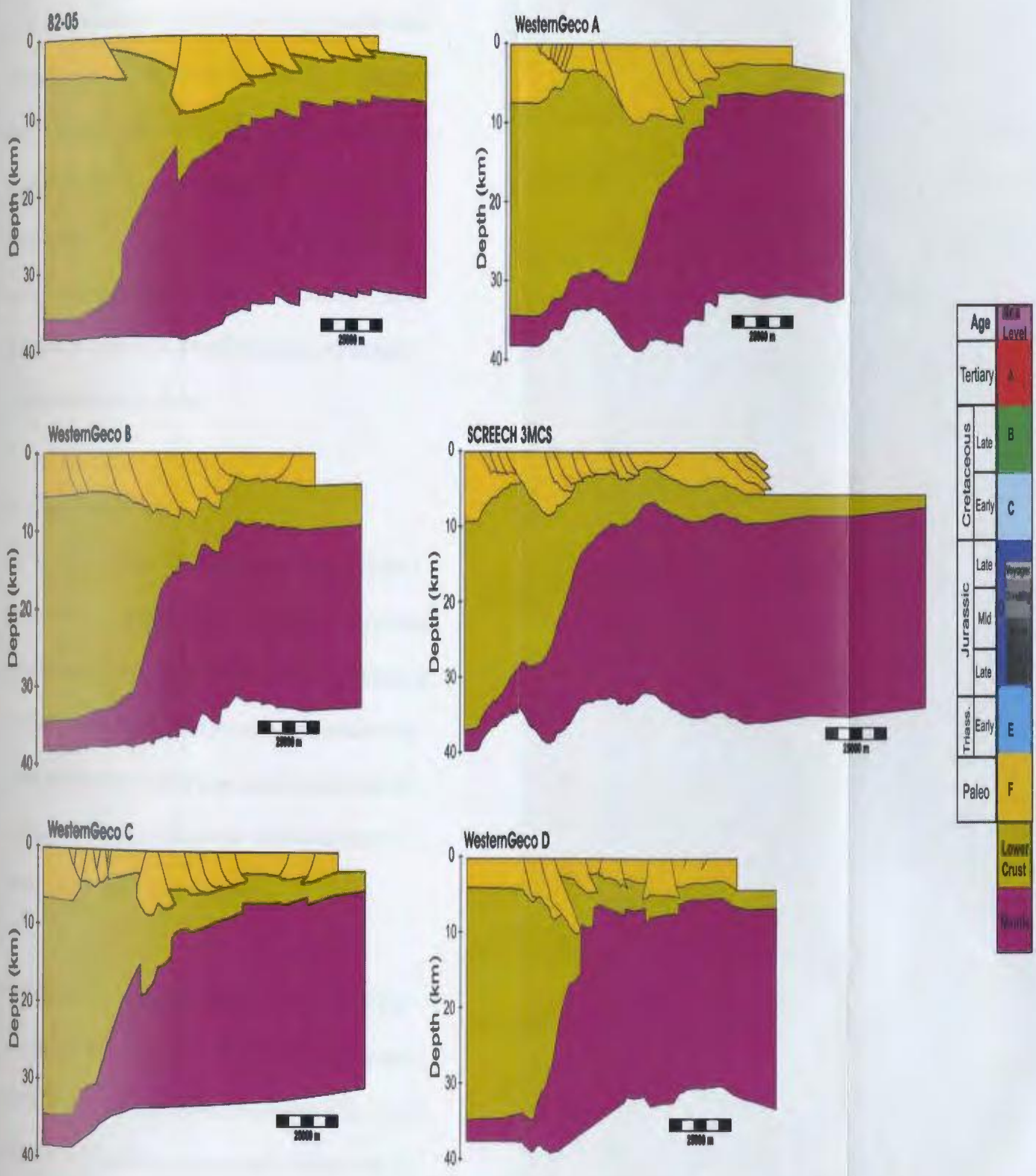

Figure 5.12. Reconstruction of the basement, detachment and Moho layers of profiles 82-05, A, B, SCREECH 3MCS, C and D in the Carson, Bonnition and Salar Basins. Lines A, B, C and D are based on proprietary WesternGeco seismic data.

Table 5.1 Extension amounts on profiles.

Profile	Extended Length (km)	Unextended Length (km)	Actual Extension (km)	Percentage Stretched	Extended/ Unextended
82-05	153.3	132.7	20.6	13.44%	1.16
WesternGeco A	131.6	118.2	13.4	10.18%	1.11
WesternGeco B	130.1	109.8	20.3	15.60%	1.18
3MCS*	157.4	136.7	20.7	13.15%	1.15
WesternGeco C	136.5	115.2	21.3	15.60%	1.18
WesternGeco D	126.2	109.5	16.7	13.23%	1.15

* Calculated from the western edge of the Bonnition Basin to the eastern edge of the peridotite ridge.

than in the Bonnition Basin, ranging from 1.11 to 1.16. The discrepancy in extension values between the profiles in the Carson Basin can most likely be attributed to their orientation. The two profiles cross the Carson Basin are at very different orientations, and it is to be expected that the amount of extension calculated would be different due to the difference in orientation. The extension values obtained for this portion of the margin are similar to the values calculated by Keen, et al. (1987b) for the southern Jeanne d'Arc ($e \sim 1.17$). In general, the amount of extension measured across all profiles is fairly similar, therefore it is interpreted that this portion of the margin under went a fairly uniform amount of extension.

5.6 Crustal stretching values

Stretching values based on crustal thicknesses can be determined across two profiles on the Newfoundland margin (SCREECH 2 and SCREECH 3). Where data was available, the unextended and extended crustal thicknesses were measured across the margin and used to calculate the β values. The unextended crustal thickness is taken on each profile as the thickness of crustal basement where it underlies unextended thin sediment (i.e. the

platform). Figure 5.13 illustrates schematic drawings of the SCREECH 2 and 3 profiles across the Newfoundland margin and average β values that are calculated at different points along the profiles. Comparing β values between the two seismic lines shows a fairly good correspondence between the stretching values. Both profiles show small β values on the shelf ranging from 1 (no stretching) to around 1.3. The larger β values (1.3) correspond to areas under basins. β values on both profiles are shown to increase rapidly in the area near the slope break. Both profiles show an abrupt change in crustal thickness near the continental shelf break. Under the continental slope and rise the β values increase to ~ 9 on both profiles indicating that the crust has undergone a large amount of stretching and thinning in this region.

In Figure 5.13, extension values calculated by restoring faults along the margin are noted above major basins along SCREECH line 3 (Hall, pers. comm. 2005). These extension values (e) are compared to the β values on various areas of the margin. The Jeanne d'Arc Basin on the shelf shows extension values of 1.15, which corresponds well to the β value calculated under this basin (1.12). This shows that there is a fairly good agreement between both methods on the shelf area of the margin. Across the Bonnition Basin near the slope edge of the margin, extension values of 1.27 are calculated. This value is much lower than the β value that is calculated under the basin (1.8). At the base of the slope and moving to the continental rise, β values increase to 9 and the seaward limit of continental crust, while extension values range from 2.1 near the base of the slope to 1.4 to than to 3.0 further seaward near the interpreted limit of continental crust.

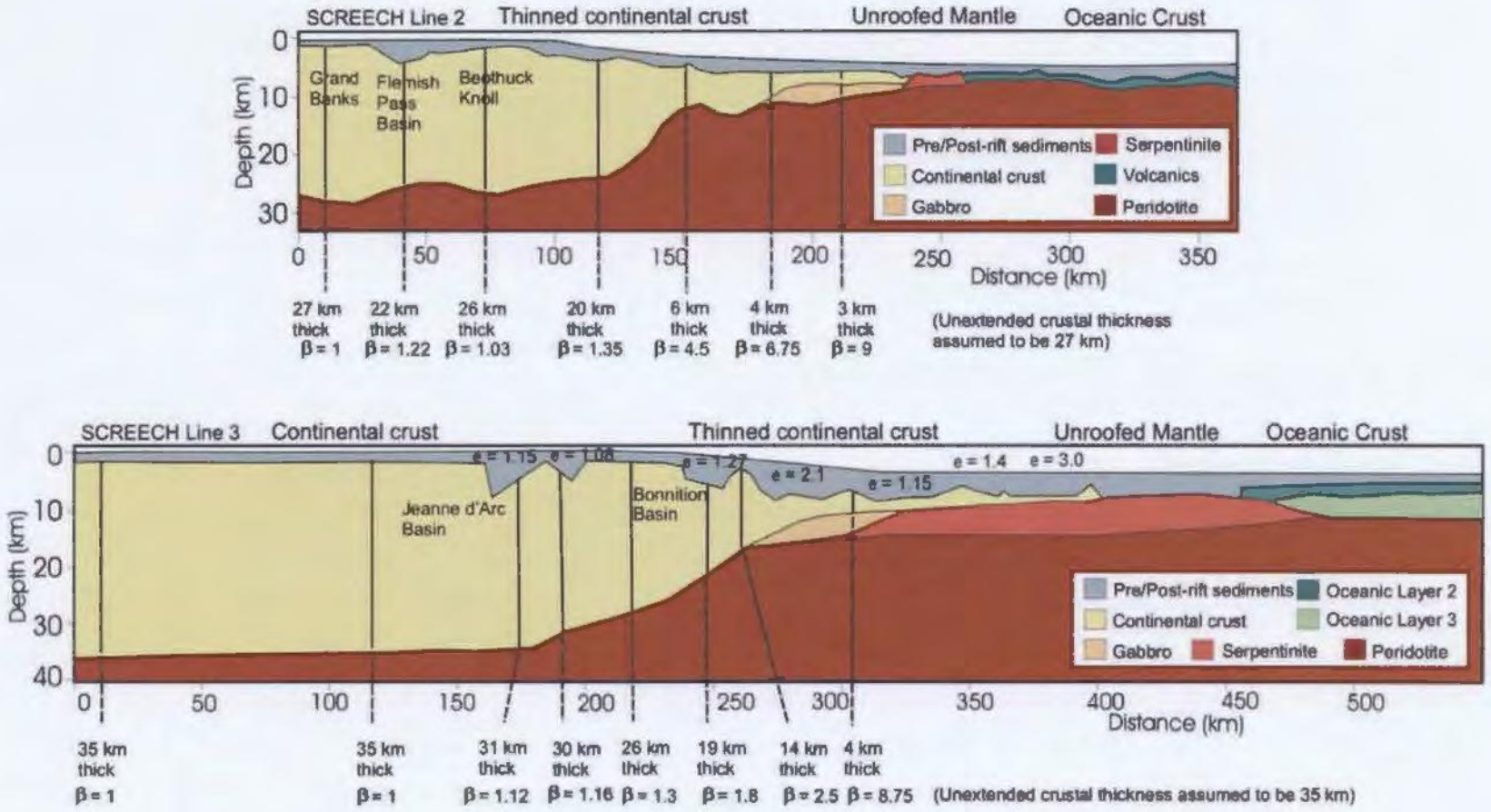

Figure 5.13. Schematic representations of SCREECH 2 and SCREECH 3 profiles on the Newfoundland margin. β values based on changes in crustal thickness are calculated (based on Lau et al. 2005b *in press* and Shillington et al. 2004). These are compared to extension values (e) which were calculated by restoring faults along the margin (Hall, pers.com. 2005).

Comparing the extension values (*e*) estimated from normal fault geometries to those estimated from crustal thinning of the whole crust or estimated from subsidence (β) shows that β tends to be significantly higher than *e*. Many extensional basins show that the horizontal extension measured from faults (*e*) cannot fully account for the crustal thinning (β) measured on passive margins (Pinet et al. 1987). The small extension values, but large crustal thinning values indicate that the crust has thinned much more drastically than what is recorded by extensional faulting.

5.7 Comparison of extension and crustal stretching between Newfoundland and Iberia

A schematic illustration of profiles crossing the Iberian margin is shown in Figure 5.14. This figure illustrates profiles Lusigal 12 and IAM 9 from the Iberian margin. The Lusigal 12 profile is conjugate with the SCREECH 2 profile, while the IAM 9 profile is thought to be just slightly south of the SCREECH 2 profile. The SCREECH 3 profile would then be located further to the south. These 2 profiles on the Iberian margin should offer a good comparison to the SCREECH 2 profile and to some extent to the SCREECH 3 profile in the Newfoundland margin. Extension values (*e*) were calculated across major faults on both profiles on the Iberian margin. Both of the Iberian profiles show similar amounts of extension based on normal faults, with the Lusigal 12 profile showing slightly higher values on average. In Figure 5.14 part A on the Lusigal 12 profile, extension values range from 1.5 near the unextended portion of the margin to around 2.1 out near the edge of the thinned continental crust. Locally, extension values as high as 3.4 were

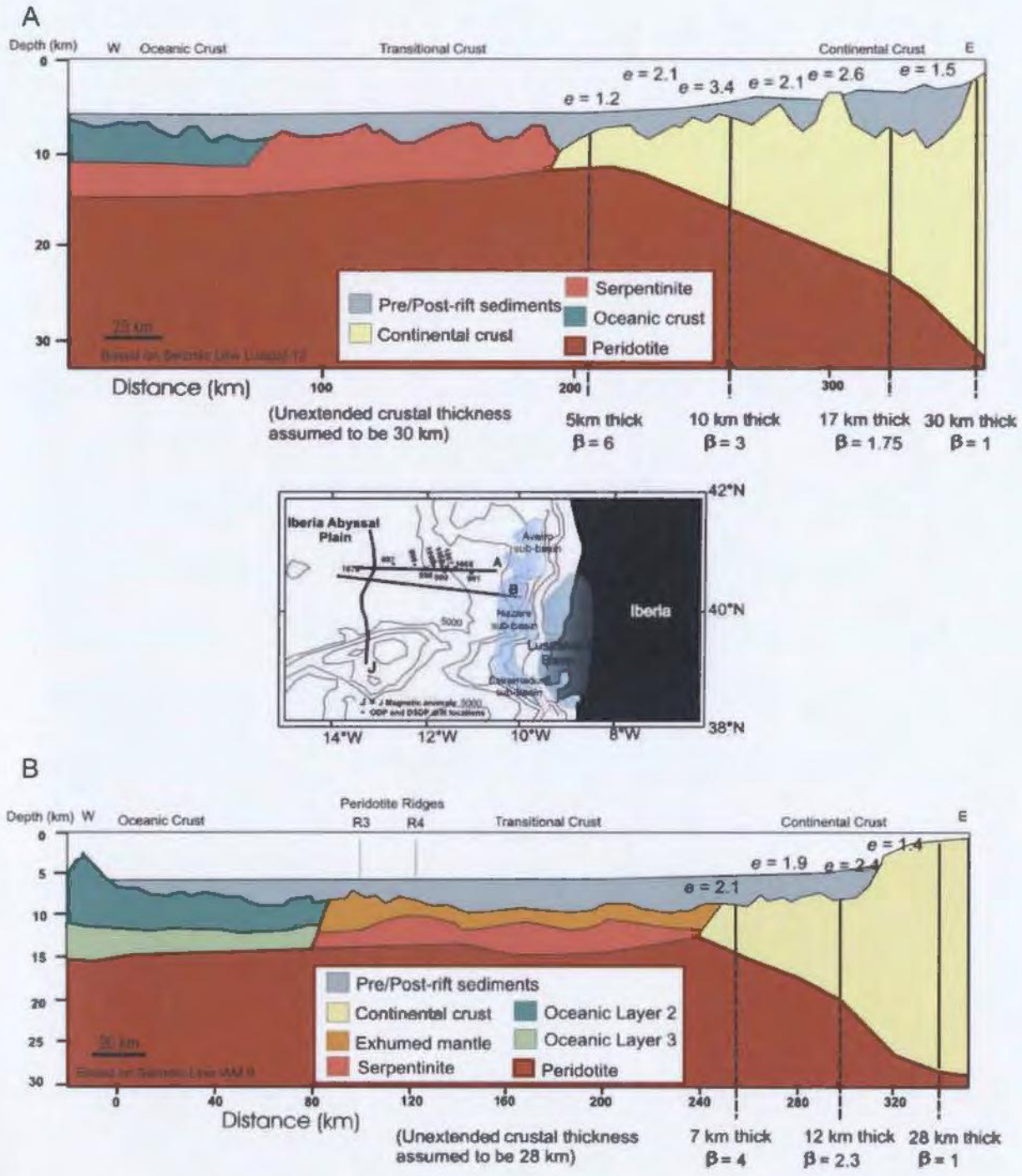

Figure 5.14. Schematic representations of seismic lines Lusigal 12 (A) and IAM 9 (B) on the Iberian margin (based on Dean et al. 2000 and Beslier et al. 1993). β values based on crustal thickness are calculated across the profiles.

calculated. In Figure 5.14 part B, the IAM 9 profile shows extension values ranging from 1.4 near the unextended continental crust out to 2.1 near the edge of the thinned crust, with a high of 2.4 calculated. When these extension values are compared to the Newfoundland margin, it is evident that the Iberian margin tends to illustrate slightly higher extension values.

β values were calculated based on crustal thickness of the continental crust for the two Iberian profiles and are also listed on Figure 5.14. On the Lusigal 12 profile unextended crustal thickness is assumed to be 30 km, while on the IAM 9 profile it is assumed to be 28 km. Both profiles show similar β values along the Iberia margin, ranging to a maximum of around 4 to 6 near the edge of interpreted continental crust. These values are quite different from the values calculated on the Newfoundland margin, which show much larger β values near the edge of continental crust, indicating that the continental crust on the Newfoundland margin has undergone greater thinning and stretching when compared to the Iberia margin.

When the β values on the Iberian margin are compared to *e* values, similar to the Newfoundland margin, Iberia also shows much higher β values than *e* values. When extension values and crustal thinning values are compared across the margin conjugates, they show that the Iberian margin tends to have higher extension values (*e*) than the Newfoundland margin, but has lower β values. Figures 5.13 and 5.14 illustrate a major difference that is noticeable between the margin conjugates. The Newfoundland margin

is shown to contain a large amount of extremely thin continental crust (thickness of 4 km or less) when compared to the Iberian margin, which shows very little.

Four possible explanations for the discrepancy between *e* and β values will be outlined below. The first is the possibility that simple shear stretching is the dominant method of extension in the crust. Simple shear stretching would produce an asymmetric margin with the Newfoundland margin being the "upper plate" and the Iberian margin being the "lower-plate". With this configuration it's possible that continental crust from the Newfoundland margin has ended up on the Iberia margin, which could account for the large discrepancy between *e* and β.

The second possibility is that the crust on the Newfoundland margin was already thin before the first major rifting phase initiated in the Late Triassic. This would mean that the crust near the present day slope was initially thinner than the assumed 35 km for unextended continental crust.

A third possibility is the presence of many small extensional faults that are too small to be mapped seismically. If mapping of these faults was possible, it would serve to increase extension values calculated through normal fault geometries (*e*).

The fourth possibility would be that crustal extension and thinning was not recorded by the early sedimentary record. This would mean that crustal extension and thinning occurred, but little sediment was deposited to record it.

Of these four hypotheses, only the first can be studied in greater detail. It is not possible to determine if the initial crustal thickness was thinner than the estimated 35 km, nor is it possible to map small extensional faults that are not imaged seismically. It would also be difficult to determine if, and how much crustal extension would have occurred without being recorded by the sedimentary record. It is possible to investigate whether simple shear stretching occurred and if the Iberian margin has an abundance of continental crust that cannot be easily explained. This hypothesis will be investigated further in Chapter 6.

CHAPTER 6 Discussion

6.1 Structure of the Iberia margin

Previous chapters have detailed the structure and stratigraphy of the Carson, Bonnition and Salar basins and have restored portions of the southeastern Newfoundland margin. These chapters have shown that the margin appears to be segmented along strike by transfer zones, and has a complex evolutionary history. A discrepancy between extension values calculated through normal fault restoration and those calculated through crustal thinning is also shown to exist. In this chapter a brief outline of the Iberia margin will be given to allow for comparison to the Newfoundland margin. On the Iberia margin, the focus will be directed towards the crustal structure of the margin and the location of transfer zones.

The Iberia margin is divided into 3 distinct sections: the Tagus Abyssal Plain in the south, the Iberia Abyssal Plain in the central area and Galicia Bank towards the north as shown in Figure 6.1. These three distinct sections are structurally different and exhibit many features that are quite different when compared to the Newfoundland margin.

6.1.1 Galicia Margin

The Galicia margin, covered with a thin sedimentary layer, is characterized as a typical sediment-starved margin (Manatschal and Bernoulli, 1999). The margin is composed of 3 major segments; the Interior and Porto basins, the Galicia Bank and the Deep Galicia Margin (Manatschal and Bernoulli, 1999), illustrated in Figure 6.1.

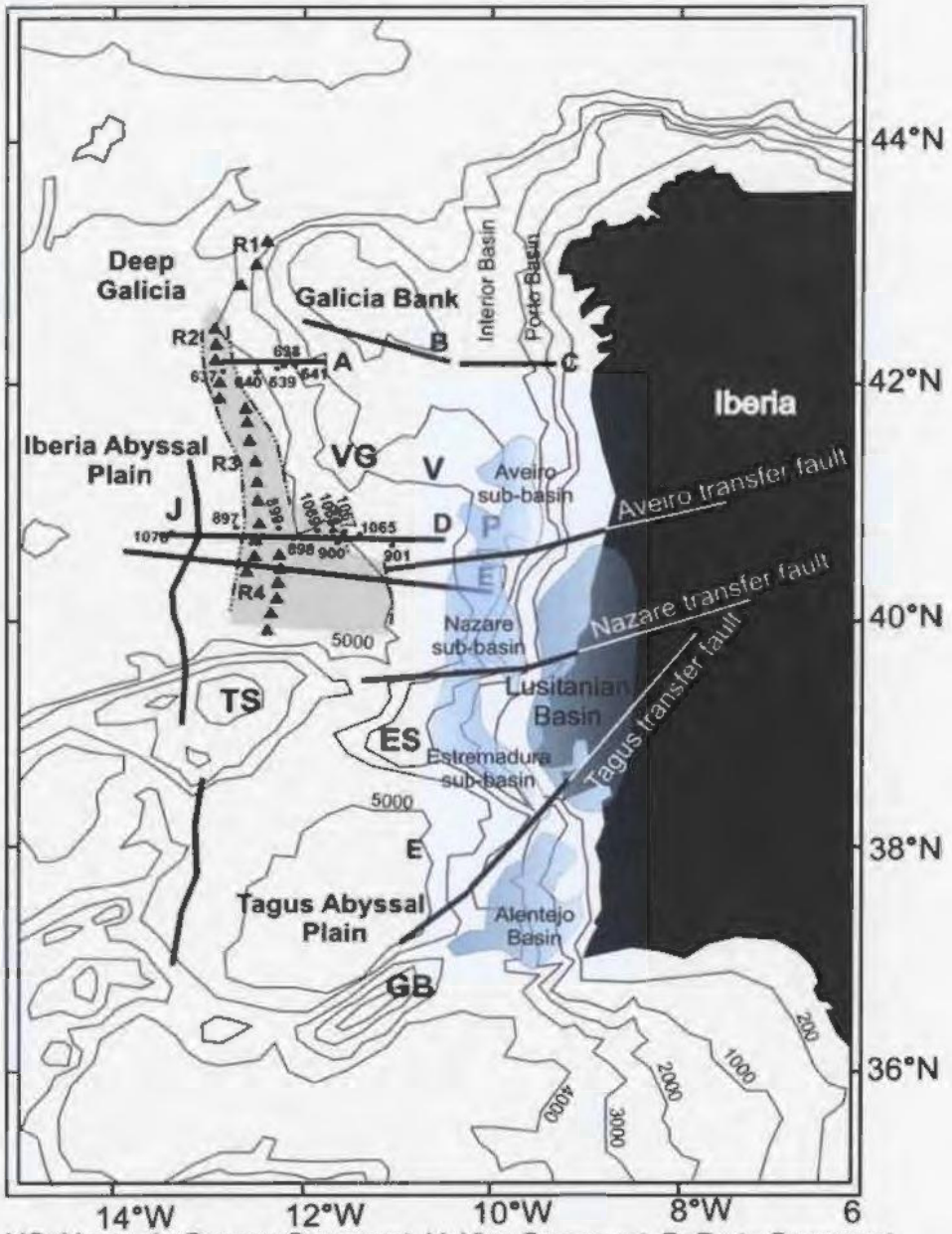

Figure 6.1. Map of the Iberia Margin showing the Vasco da Gamma Seamount (VG), Vigo Seamount (V), Porto Seamount (P), Tore Seamount (TS), Estremadura Spur (ES), Gorringe Bank (GB), J Magnetic Anomaly (J), peridotite ridges (triangles), Seismic Lines (A to E), and ODP drill sites. The grey shaded area represents the transitional crust. *Modified from: Manatschal et al. (2001) and Alves et al. 2003a.*

The eastern portion of the margin (Interior and Porto basins) is considered the northward extension of the Lusitanian Basin. The Interior and Porto basins trend north-south and create symmetric horst and graben structures, bounded by listric faults, with moderately tilted fault blocks. Northeast-southwest trending syn-rift transverse faults (Boillot et al. 1995) that likely resulted from crustal stretching (northeast-southwest direction) in the Early Cretaceous, segment these basins into two distinct sections.

Galicia Bank is an elevated high which separates the Interior Basin from the deep Galicia margin. This high has been interpreted as a horst/ridge that separates two areas of distinctly different tectonic evolution (Manatschal and Bernoulli, 1999).

The Deep Galicia margin is dominated by numerous small fault blocks that tilt towards the continent, dipping west and are spaced about 15 km apart (Reston, 1996 and Whitmarsh et al. 1996) forming a series of half grabens. The fault blocks decrease in size oceanward and appear to detach into the most prominent feature on the margin the "S" reflector. Many interpretations have been made of the "S" reflector (detailed in Reston et al. 1996), with the most common being that it is a west-dipping low angle detachment surface that may mark the crust-mantle boundary (Hopper et al. 2004). This detachment fault appears to either terminate against or is cut by east dipping reflections associated with a peridotite ridge to the west (Reston et al. 1995). The prominent peridotite ridge is exposed at what is considered the ocean-continent transition (OCT) in Galicia, and separates oceanic crust to the west, from transitional crust to the east. The Galicia margin

has a narrow OCT at only ~30km in width. The transverse faults that segment the Interior and Porto basins also offset the peridotite ridge. The northern section of the peridotite ridge is shown to trend in a northeast-southwest manner, while the southern section trends in a north-south manner (Boillot and Winterer et al. 1988). Figure 6.2 parts A, B and C illustrate line drawings of seismic lines and the major features across the Galicia Margin. Part of the peridotite ridge (R2) is illustrated in the far west of the figure and the extent of the stretched continental crust and transitional crust is noted.

Drilling of ODP Leg 103 (Boillot and Winterer, et al. 1987) on the deep Galicia Margin consisted of five sites (637-641). The drilling locations are listed in Figures 6.1 and 6.2 A. Sites 638, 639 and 641 all drilled through syn and possibly pre-rift strata. Site 637, the farthest to the west, recovered upper mantle serpentinized peridotite in an area near what is considered the ocean-continent boundary. The site that was drilled is part of a wide (10 km) and long (60 km) continuous ridge. The peridotite at this site is interpreted to represent sub-continental mantle, with the rocks being emplaced during late rifting of the margin (Boillot, Winterer et al. 1987). Site 640 drilled the top of a ridge in an area composed of thin continental crust and recovered Lower Cretaceous syn-rift sediments that are tilted and slumped. In this area the seismic "S" reflector is present beneath the ridge.

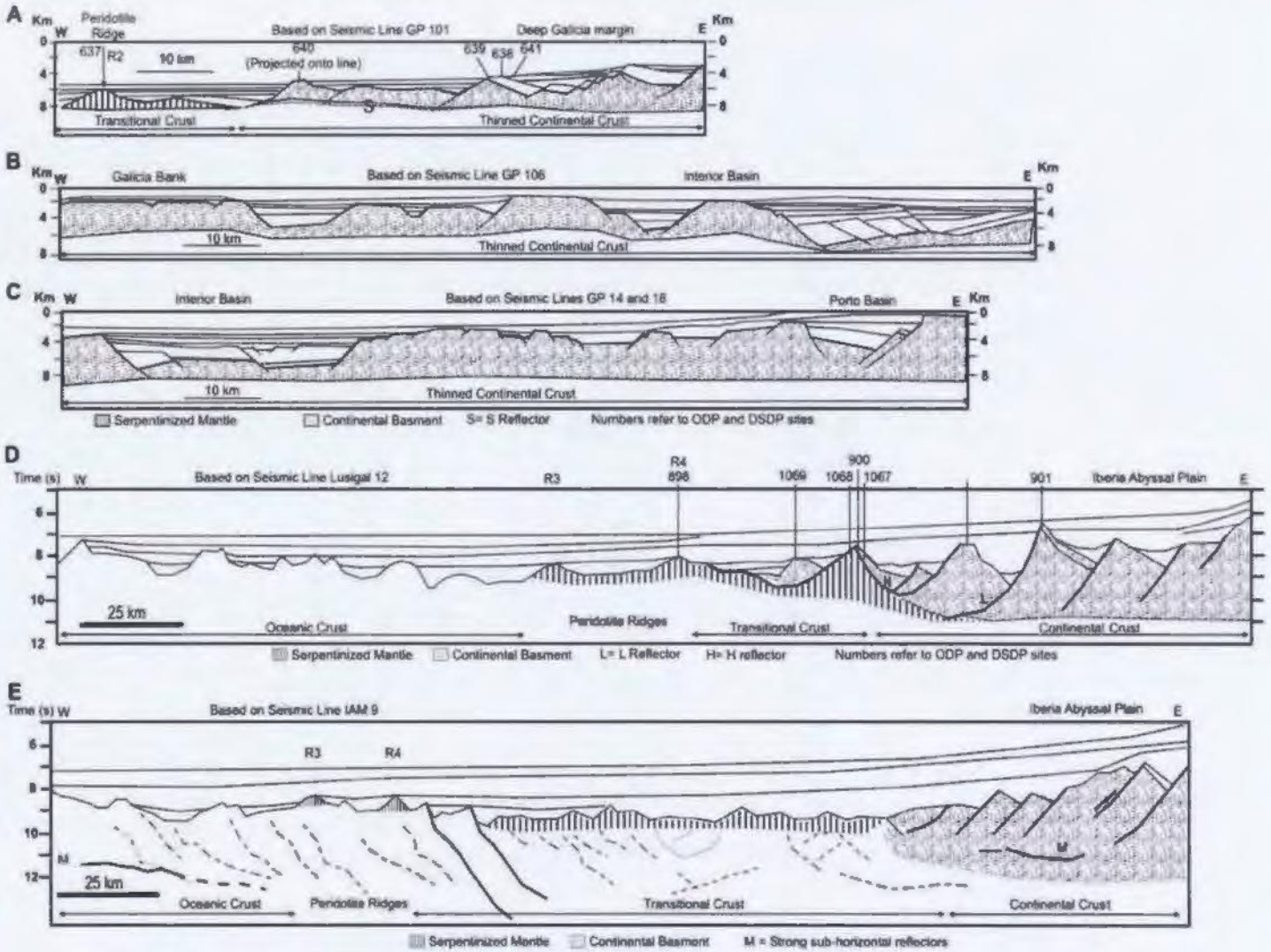

Figure 6.2. Line drawings based on seismic lines over the Iberia margin. A to C represent lines over Galicia Bank. Lines D and E represent lines over the Iberia Abyssal Plain. ODP drill sites are illustrated as are boundaries between extended continental crust, transitional and oceanic crust. *Modified from: Manatschal and Bernoulli (1999), and Pickup et al. (1996).*

6.1.2 Iberia Abyssal Plain

The Iberia Abyssal Plain (IAP) is separated from Galicia Bank (Figure 6.1) by a change in basement depth that occurs south of the Vigo and Porto seamounts (Whitmarsh and Sawyer, 1996). The Iberia Abyssal Plain is characterized by tilted continental fault blocks overlying strong shallow dipping reflectors. The tilted fault blocks are bound by strong, mainly seaward dipping listric fault reflectors (Manatschal et al. 2001). In contrast to the Galicia margin, no obvious reflection similar to "S" is present however the margin does exhibit strong intra-basement reflections. The intrabasement reflections (L, H, and M) from Whitmarsh et al. (2000) are shown to be both landward and seaward dipping (Figure 6.2 D, E). A much wider (130km) ocean-continent transition zone is found on the margin, though this varies significantly along strike with the transition zone being widest in the south and narrowing (30 km) to the north towards Galicia Bank (Pickup et al. 1996). The ocean-continent transition zone is inferred to be a region of exposed mantle that has undergone a variable amount of serpentinization. Study of the transitional zone by Pickup et al. (1996) and Dean et al. (2000) shows that the upper 1.0 to 2.5 km of exposed mantle is non-reflective on seismic images and has velocities ranging from 4.0 to 7.0 km/s. This thin layer is then underlain by a highly reflective zone (7.6 km/s) that then overlies unaltered mantle. Many landward dipping reflectors are present in the transitional crust, extending to depths of 10 to 19 km (Pickup et al. 1996).

The peridotite ridge that is present on the Galicia margin is also found further south on the Iberia Abyssal Plain. In total the peridotite ridge appears to be segmented into four

sections (R1 to R4 as shown in Figures 6.1 and 6.2) and the ridge appears to generally coincide with the eastern-most seafloor spreading anomaly (Dean et al. 2000). Unlike R1 and R2 on the Galicia Margin, R3 and R4 appear to overlap on the Iberia Abyssal Plain.

Drilling of ODP Sites 897 to 901 during Leg 149, and sites 1065 to 1070 during Leg 173, revealed the presence of serpentinized peridotite at multiple outcrops and a surprising absence of basalt. The sites were drilled on basement highs, and sites 897 and 899 drilled serpentinized peridotite, while site 900 drilled metagabbro which through dating indicates it is continental crust. At Site 901, Upper Jurassic sediments were encountered, suggesting that thin continental crust lies below. Site 1070 is drilled over what is presumed to be early oceanic crust. This site encountered serpentinized peridotite intruded with gabbroic veins, however there was no evidence of upper oceanic crust. Sites 1065 to 1069 were drilled in the ocean-continent transition zone (OCT). Sites 1065 and 1069 drilled through continental basement, while site 1067 drilled through mafic rocks, with mid-ocean ridge affinities. Site 1068 encountered breccias with clasts of mafic lithologies, then drilled through serpentinized peridotite, after encountering a shear zone. Examination of the drill results and comparison with the seismic data in the area suggests that the strong seismic reflector (H) shown in Figure 6.2 D (Lusigal 12 seismic line) represents the crust/mantle boundary, separating mafic rocks from the underlying ultramafic rocks. Figure 6.2 E shows the line drawing of IAM 9, south of Lusigal 12. Comparison of parts D and E shows how the width of the transition zone varies from north to south.

6.1.3 Tagus Abyssal Plain

The Tagus Abyssal Plain is at a depth of approximately 5000m and is bounded to the north by the 100 km wide Estremadura Spur and the Tore Seamount (Mauffret et al. 1988). It is bounded to the east by the continental margin of Portugal and to the west by the Madeira-Tore rise (Pinheiro et al. 1992). The southern boundary is composed of the Eurasia/Africa Plate boundary. The transitional crust in this area appears to be similar to the transitional crust found in the Iberia Abyssal Plain. The transitional zone is generally 50 to 80 km wide (Dean et al. 2000) and the crust appears to be thin and overlies mantle with low velocities (7.6-7.9 km/s) (Pinheiro et al. 1992).

6.2 Conjugate Margin Comparisons

6.2.1 Galicia Bank - Flemish Cap conjugate margin pair

Comparisons between the southeast Flemish Cap margin and the Galicia margin show that the conjugate margins have some similarities and differences in their structural characteristics. The southeast Flemish Cap margin has a narrow zone of extended continental crust and a steep continental slope (Hopper et al. 2004), whereas the Galicia margin is shown to have a wider zone of extended continental crust that contains a series of titled fault blocks that gently deepen towards the west (Whitmarsh et al. 1996). The OCT on the Galicia margin is approximately 30km in width and marked by a peridotite ridge. On the Flemish Cap margin, the transition from continental to oceanic crust appears to be abrupt. Thinned continental crust abuts oceanic crust which contains domino-style rotated blocks bounded by seaward dipping normal faults, spaced about 1.5km apart (Hopper et al. 2004). The Flemish Cap margin shows no evidence of

horizontal detachment surfaces similar to the S reflector on the Galicia Bank margin. Crustal thickness varies dramatically across the conjugate pair. In Galicia Bank, the continental crust thins from about 16 km to 3 km thick over a distance of about 100 km. On the Flemish Cap margin, the crust thins from 30 km thick to 5 km over a distance of 70km (Hopper et al. 2004). The oceanic crust on the Flemish Cap margin shows thicknesses of 3 to 4 km, that thin seaward to 1.3 km thick (Hopper et al. 2004). Under thinned continental crust and oceanic crust a 3 to 5 km thick layer with velocities of 7.6-7.9 km/s is present. This layer is interpreted as being serpentinized mantle (Shipboard Scientific Party, 2004a)

6.2.2 Central Grand Banks – West Iberia conjugate margin pair

Comparing profiles between the Central Grand Banks and West Iberia shows an overall asymmetry between the two margins. This portion of the margin is also shown to be quite different from the Galicia Bank - Flemish Cap margin that was described in the previous section. The central Newfoundland margin, shows a zone of extended continental crust and a wide zone of transitional crust visible on both SCREECH lines 2 and 3. The extended continental crust on seismic profile SCREECH 2 thins from 27 km beneath the Flemish Pass to ~6 km underneath the continental slope over a distance of 40 km. SCREECH line 3 shows continental crust thinning from 35 km to approximately 3 km in thickness over a distance of 110 km. Abrupt thinning of the crust occurs under the continental slope thinning from 35 km to 7 km over a distance of 50 km (Lau et al. 2005b *in press*). Both these profiles on the Newfoundland margin show crustal thinning

occurring over a short distance. In contrast, the Iberian margin shows continental crust with an original thickness of ~30 km thinning to 4 to 5 km over a distance ranging from 150 km in the north to 60 km in the south (Dean et al. 2000 and Lau et al. 2005b *in press*). The width of the extended crust zone on the conjugate margins is shown to vary on both sides of the Newfoundland-Iberia rift. On the Newfoundland margin, the zone of extended continental crust is widest in the south and narrows to the north towards the Flemish Cap, while on the Iberia margin the extended crust is widest in the north and narrows to the south (Lau et al. 2005b *in press*).

The nature of the transitional crust on the Newfoundland margin appears to vary along strike and is quite different when compared to the Iberian margin. On the SCREECH 2 profile, the transition zone is ~60 km long, the basement reflection is difficult to identify and intra-crustal reflections are sparse in this area (Shillington et al. 2004). The transitional crust thins from 6km to 2km, and underneath the transitional crust seismic velocities of 8 km/s and higher are found. The SCREECH 3 seismic line shows a transition zone that is ~80 km wide (Lau et al. 2005a *in press*), and the crust is highly faulted showing many rotated fault blocks. Serpentinized exhumed mantle is interpreted to be close to basement based on wide-angle refraction modelling velocities of ~7.5 km/s. These two distinctly different characteristics of the transitional crust on the Newfoundland margin are also seismically different from the transitional crust on the Iberian margin. On the Iberian margin a thin unreflective layer overlies a reflective zone showing landward dipping intracrustal reflections. The width of the transitional crust on

the Iberia margin is also quite variable ranging from 30 km in the north to 130 km towards the south (Dean et al. 2000).

6.3 Rift reconstruction to M0 time

To compare major structures found on the Newfoundland margin to those found on the Iberian margin, the margins are restored back to M0 time and major structural features are superimposed. One of the problems relating to plate reconstruction of the Newfoundland - Iberia margin is restoring Flemish Cap against Galicia Bank. By restoring the margin in this manner, an area to the south hundreds of kilometers wide is left with unusually thin crust. Through modelling of rifting processes it is difficult to produce such a large region of thin crust (Whitmarsh and Sawyer, 1996).

One interpretation of the Flemish Cap area is found in a recent plate reconstruction based on magnetic anomalies. Srivastava et al. (2000) and Sibuet et al. (2005) have proposed that the Flemish Cap area acts as a microplate during rifting. They interpret that the Flemish Cap remained attached to Galicia Bank until ~M3 time (Hauterivian-Barremain time) as seafloor spreading was progressing from south to north. Sea floor spreading in the south would have caused extension in the Flemish Cap area. This would result in the Flemish Cap appearing to rotate in a clockwise direction relative to Newfoundland.

Figure 6.3 represents a schematic of a recent reconstruction to M0 time (from Louden and Lau, 2001, based on Srivastava et al. 2000) showing the conjugate margin positions. Major Mesozoic structural features are superimposed on the figure indicating where major basins and transfer zones on both margins are located.

Similar to the Newfoundland margin, basins on the Iberian margin are segmented along strike (Alves et al. 2003b and Alves et al. 2002). The Lusitanian Basin offshore Portugal is divided into 3 segments by major transfer zones that developed during Mesozoic rifting, mainly in the Jurassic. The Aveiro, Nazare and Tagus transfer faults segment the Lusitanian Basin from north to south and are shown on Figure 6.3. Not only do these transfer faults segment the Lusitanian Basin, but they also segment basins that are under the continental slope. On the Newfoundland margin, transfer zones segment the shelf edge basins (Carson and Bonnition) and the slope basin (Salar).

Figure 6.3 illustrates that the Nazare transfer fault on the Iberia margin may correspond to transfer zone 2 on the Newfoundland margin. These two transfer zones appear to line up close to one another indicating that they may be related, or closely related. The presence of transfer zones on both margins indicates the need for accurate reconstructions based on magnetic data. Conjugate margin pairs need to be accurately reconstructed to ensure that they are being evaluated properly, and that features across major transfer zones are not mistakenly being compared.

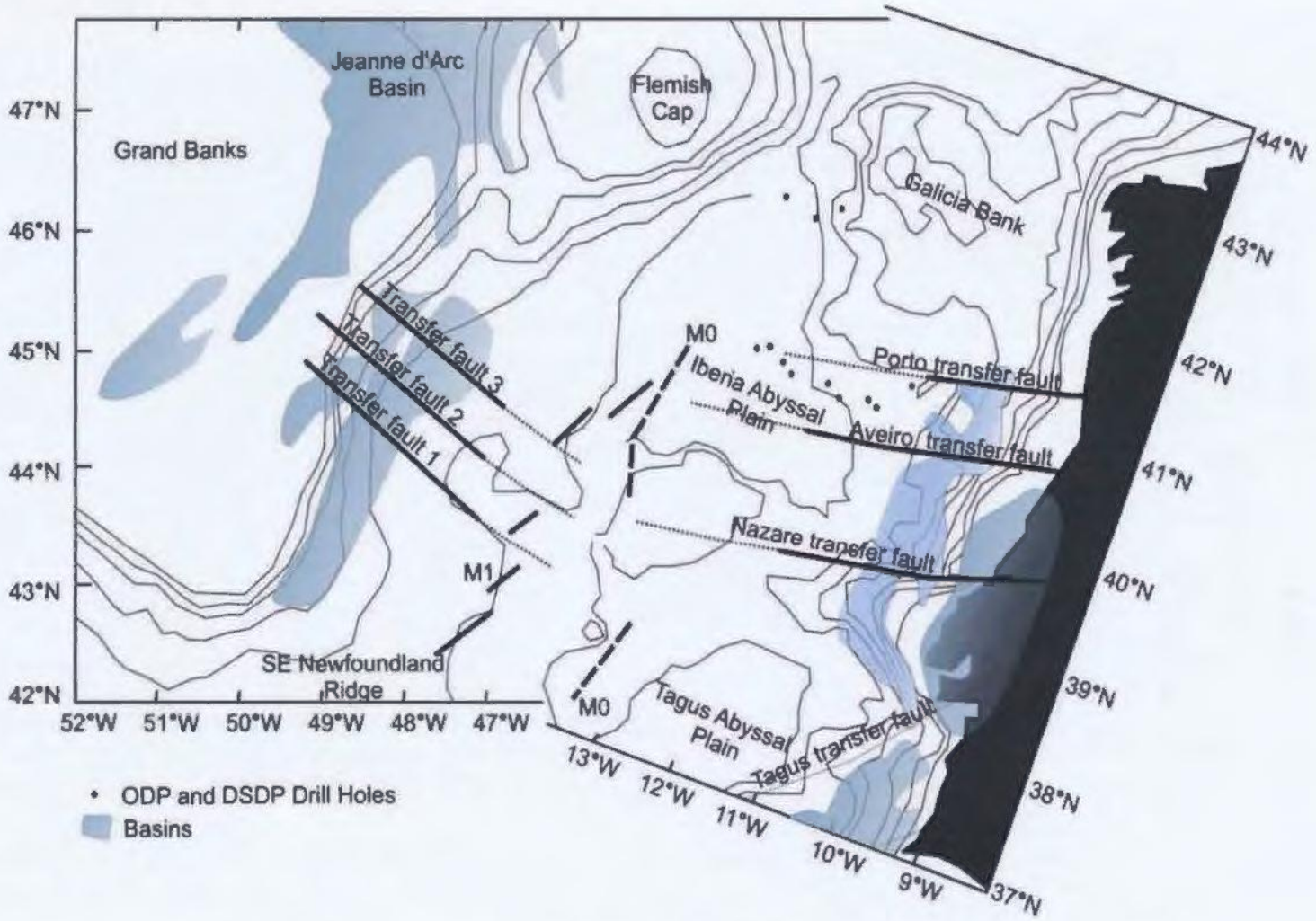

Figure 6.3. Reconstruction back to M0 time of the Newfoundland and Iberia conjugate margins. This figure shows the location of major transfer zones and basins on both margins. *Modified from: Louden and Lau (2001).*

6.4 Analysis of extension between margin conjugates

Both pure and simple shear stretching models have been proposed to characterize the evolution of continental stretching across the Newfoundland and Iberia conjugate margins. As introduced in Chapter 1, pure shear models predict symmetric thinning and geometries between conjugate margin pairs (McKenzie, 1978). Fault geometries and crustal thickness should show strong similarities between margin conjugates if pure shear is the dominate extensional force. Simple shear models predict the formation of asymmetric features on conjugate margins. Extension in simple shear models occurs along detachment faults forming characteristic upper and lower plate margins. Upper plate margins would generally show abrupt thinning and be composed of few extensional features. The lower plate margin would be dominated by numerous rotated fault blocks and possibly expose lower crust and mantle material.

In Chapter 5, one hypothesis for the discrepancy between extension values based on fault restoration (e) and crustal thinning (β) is that simple shear processes dominated during extension. Simple shear extension could cause one margin to end up with an abundance of crust (lower plate margin) while the other side is "missing" crust. It may also be able to account for differences found between e and β values. SCREECH 2 and Lusigal 12 are the 2 profiles that are closest to being conjugate to one another, with IAM 9 and SCREECH 3 being located further to the south. Based on images of the crustal structure from each of the profiles (shown in Figures 5.13, 5.14 and 6.2), it does not appear that either of the margins has an abundance of continental crust. As well there is no evidence

for major detachment surfaces that would indicate simple shear stretching. Therefore simple shear extension does not appear to be dominant on the margin at this location. Both margins show significantly larger β values than *e* values, indicating that on both margins the crust has thinned more than what has been recorded by extensional normal faults.

Although both margins show differences between β and *e* values, the differences tend to be much larger on the Newfoundland margin, where a significant area of thinned continental crust (3 to 4 km thick) exists.

As briefly mentioned in Chapter 5, it is possible that crust thinner than ~35 km was present before rifting initiated or syn-rift sediments were deposited and preserved. Thinner initial crust will produce much lower β values, which would more closely correspond with the measured extension values (*e*). Thinner initial crust would also alleviate the problem of "missing" crust on both the Newfoundland and Iberia margins, since the crust would need to be restored back to a much smaller initial thickness. Small scale extensional faults could also serve to increase the measured *e* value, however it is unlikely that they alone could account for such a large difference between the β and *e* values. It is possible that the sedimentary record did not fully record all the extension that the margin underwent. This however would mean that a large amount of extension is not accounted for. It seems likely that outcomes from all three hypotheses have

contributed to the evolution of the margins to some extent, however having a thinner crust initially is thought to best account for differences between *e* and β.

The Newfoundland-Iberia margin appears to show features that are both symmetric and asymmetric in nature, making it difficult to classify the margin. Presently the favoured interpretation of the conjugate pair is that initial symmetric stretching occurred in a wide rift (>100km) (Lau et al. 2005b *in press*). In wide rift zones break up generally occurs along on edge, which forms a wide/narrow conjugate margin pair (Dunbar and Sawyer, 1989,). In this case, break up is interpreted to have occurred near the Iberia edge, leaving an asymmetric conjugate margin pair, with Newfoundland exhibiting the wide margin characteristics and Iberia exhibiting the narrow margin characteristics.

CHAPTER 7 Conclusions and Recommendations

The objectives of this thesis were seven fold and focused on seismic data that were recorded by the SCREECH project. These deep seismic profiles were supplemented by seismic data from the CNLOPB and data donated by WesternGeco and GSI. These additional profiles along with gravity, magnetic and wide angle seismic data allowed for the slope area of the margin to be interpreted and the crustal structure of the Newfoundland margin to be investigated. This thesis looked at the variation of the Newfoundland margin along strike and compared the results to the Iberian margin when possible. The structure and composition of a major ridge was investigated, as was the lower crust, the Carson, Bonnition and Salar basins, and the Moho. The Newfoundland margin was restored along five profiles, allowing the amount of extension that the margin underwent to be calculated. Comparisons with the Iberia margin were made to infer possible stretching models that could describe the evolution of rifting between the two margins.

7.1 Processing of SCREECH seismic reflection data

The SCREECH lines 401, 402 and 403 were processed with the aim to image basins on the shelf and slope area of the margin, as well as the deep crustal structures. All seismic processing was done with the software package ProMAX by Landmark Graphics. The final processed seismic sections provide good quality images of the shelf and slope areas of the margin and image both basins and deeper crustal structures and the Moho.

7.2 Margin variation along strike

The crustal structure of the southern and central Newfoundland margin exhibits segmentation along strike. Shelf and slope basins on the margin were found to be offset from one another by transfer zones, creating four zones that show different structural characteristics. The first zone to the north on the shelf is dominated by the northern portion of the Bonnition Basin which exhibits complex faulting showing both synthetic and antithetic faulting. In the slope area of the margin north-south trending grabens and half grabens of the Flemish Pass are dominant. Towards the south, the second section on the margin is mainly composed of the southern portion of the Bonnition Basin. The basin formed as a half-graben moving down to the east. Rotated normal fault blocks trending northeast-southwest are found in the slope area of the margin. The third zone further south is composed of a shelf edge basin (Carson Basin) which formed as a half-graben with movement down to the west. The change in polarity of the two shelf edge basins represents a major change in the structure of the margin. The area between the two half grabens represents an accommodation zone, and forms a major transfer zone. The fourth zone segments the Carson Basin into two sections, offsetting the southern section to the south. The southern Carson Basin is shown to shallow to the south.

7.3 Structure and composition of the inter-basin ridge

The major ridge located under the continental slope of the Newfoundland margin was found to be composed of mainly continental material with some salt in localized areas based on gravity modeling. The ridge is a continuous feature running for approximately

170 km along and under the shelf break. The basement ridge is a rotated normal fault block associated with the formation of the Bonnition and Carson basins. The structure of the ridge changes along the strike of the margin appearing wider and higher in elevation in the north, and narrower and lower in elevation in the central area. The ridge is shown to be segmented along strike by transfer zones in at least three places.

7.4 Nature and variation of the Lower Crust and Moho

Unextended crust is found on the landward portion of SCREECH lines 3MCS, 401, and 403 under the continental shelf. Lower crustal reflections are shown to be relatively flat across most of the continental shelf. The Moho is well defined at the base of the horizontal lower crustal reflections. Some westward dipping reflections are present in the lower crust and many appear to cut through the Moho. These dipping reflections are interpreted to represent Neoproterozoic fabrics in the crust. Lower crustal reflection packages are strongest on SCREECH line 403 and show a shallowing of the lower crust and Moho towards the shelf break.

7.5 Extension and evolution of Newfoundland margin

The Newfoundland margin experienced a complex multi-phase rift evolution. The margin was influenced by two major rifting events that caused extension with different orientations. The first rifting event extended the crust in a NW-SE direction, initiating the formation of the major basins on the Grand Banks, while the second was orientated in an E-W direction. Extension values calculated through normal fault restoration are found

to be much lower than crustal stretching values calculated by crustal thinning on the Newfoundland margin. This is also observed on the Iberia margin, indicating that the initial crustal thickness before extension may have been less than the estimated ~ 30 to 35 km to account for the differences. To account for most of the features found on the Newfoundland Iberia conjugate margins, a wide rift model is favoured, with symmetric thinning initially, then break up occurring at one of the ends of the rift.

7.6 Comparison of major structures on other margins

Features found on the Newfoundland margin are comparable to other non-volcanic margins around the world. The segmentation of the Newfoundland margin is a feature that appears to be common occurring on the Iberia, West Africa and the West Australia margins along with others. A change in half graben polarity is noticed between two shelf edge basins on the Newfoundland margin (Carson and Bonnition), and transfer faults are shown to dissect the Newfoundland margin into separate zones of different tectonic regimes. The Iberia margin is also shown to be segmented by transfer zones, and some of these may possibly line up with those on the Newfoundland margin, however this needs to be studied in more detail.

7.7 Petroleum Prospectivity

The southeast Newfoundland margin is shown to have variable petroleum prospectivity in the basins that are present on the shelf and slope. A large portion of the Cretaceous and Upper Jurassic sediments are shown to be eroded in the shelf edge Carson Basin,

limiting the amount of source and reservoir rock that is present. This reduces the prospectivity of the Carson Basin. The Bonnition Basin is more prospective with a wider extent of source and reservoir rock present. The Salar Basin is assumed to have widely distributed source and reservoir rock making this basin prospective, however drilling would have to occur in deeper water.

7.8 Future Work

The Carson, Bonnition and Salar basins are three lesser explored basins on the Newfoundland margin. The complexity of the basins and their variability in structure along strike makes these basins interesting and challenging to study.

The seismic data available on the southeast Newfoundland margin consists of 2D seismic reflection profiles. Most of these seismic lines were acquired before 1984, with the exception of a few recent surveys. Some areas of the margin especially towards the southern Carson Basin have sparse seismic data coverage. In order to image some of the complex faulting and structures in the basins, the acquisition of 3D seismic data could provide a much more detailed and clearer picture of the basin architecture. A 3D seismic data set may also give a clearer image of the slope portion of the margin and provide a more accurate picture of the basement high which appears highly variable in structure along strike.

Processing of the SCREECH multi-channel seismic reflection data revealed areas where more detailed seismic processing may be beneficial, and provide added resolution. In this thesis, all seismic lines were poststack migrated. On some areas of the margin especially near the slope break, the seismic image may be enhanced by performing a prestack migration. SCREECH lines 401 and 403 could benefit from reprocessing of the slope area and performing a prestack migration. As well, the basement high may also benefit from being prestack migrated.

The basins on the southeast Newfoundland margin remain only moderately explored and studied, when compared to the Jeanne d'Arc Basin. Future drilling in the Carson and Bonnition basins would serve to constrain and refine current interpretations, and would give greater insight into the petroleum systems in the basins. Drilling a well similar to the ODP Sites 1276 and 1277 either further north or south along the margin, would also provide invaluable information on the along strike variation in structure along the margin.

The implications of the differences between e and β values should also be studied in greater depth by investigating more transects across both the Newfoundland and Iberia margins and adding geodynamical modelling to define conditions in which crustal thinning might occur without syn-rift deposition. It would also be beneficial to obtain more seismic data to allow for comparison between a greater number of conjugate sections.

Transfer zones are found on both the Newfoundland and Iberia margins and they segment the margins into discrete sections. Future work needs to be done to accurately define and map the positions of the transfer zones and to determine if the transfer zones between the two margins line up with each other. The significance of these transfer zones on crustal stretching models also needs to be considered when studying rifting.

References

Alves, T. M., Gawthorpe, R. L., Hunt, D. W., Monteiro, J. H. 2003a. Cenozoic tectono-sedimentary evolution of the western Iberian margin. Marine Geology, **195**, p. 75-108.

Alves, T. M., Moita, C., Pinheiro, L., Monteiro, J. 2003b. Evolution of deep-margin extensional basins: The continental slope basins offshore west Iberia. AAPG International Conference, Barcelona, Spain.

Alves, T. M., Gawthorpe, R. L., Hunt, D. W., Monteiro, J. H. 2002. Jurassic tectono-sedimentary evolution of the Northern Lusitanian Basin (offshore Portugal). Marine and Petroleum Geology, **19** p. 727-754.

Austin Jr., J. A., Tucholke, B. E., Uchupi, E. 1989. Upper Triassic-Lower Jurassic salt basin southeast of the Grand Banks. Earth and Planetary Science Letters. **92**, p. 357-370.

Beslier, M.O, Ask, M., Boillot, G. 1993. Ocean-continent boundary in the Iberia Abyssal Plain from multichannel seismic data. Tectonophysics, 218. p. 383-393.

Boillot, G., Froitzheim, N. 2001. Non-volcanic rifted margins, continental break-up and the onset of sea-floor spreading: some outstanding questions. ***In:*** *Non-Volcanic Rifting of continental Margins: A comparison of evidence from Land and Sea.* (eds. Wilson, R. C. L., Whitmarsh, R. B., Taylor, B., Froitzheim, N). Geological Society, London, Special Publications, **187**, p. 9-30.

Boillot, G., Beslier, M., Krawczyk, C., Rappin, D., Reston, T. 1995. The formation of passive margins: constraints from the crustal structure and segmentation of the deep Galicia margin, Spain. ***In:*** *The Tectonics, Sedimentation and Palaeoceanography of the North Atlantic Region*, (eds. Scrutton, R., A., Stoker, M. S., Shimmield, G. B., Tudhope, A. W., Geological Society Special Publication, **90**, p. 71-91.

Boillot, G., Winterer, E. L. et al. 1988. 45. Drilling on the Galicia Margin: Retrospect and Prospect. ***In:*** *Proc. ODP, Scientific Results, 103.* College Station, TX.

Boillot, G., Winterer, E. L., et al. 1987. Introduction, Objectives, and Principal Results: Ocean Drilling Program Leg 103, West Galicia Magin, ***In:*** *Proc.ODP, Init. Repts. (Pt. A), 103.* (eds. Boillot, G., Winterer, E. L., Meyer, A. W. et al.). College Station, TX.

Collier, J. S., Watts, A. B. 1997. Seismic-reflection constraints on lithosphere extension: pure versus simple shear. Geophysical Journal International, **129**, p. 737-748.

Dean, S. M., Minshull, T. A., Whitmarsh, R.B. , Louden, K. E. 2000. Deep structure of the ocean-continent transition in the southern Iberia Abyssal Plain from seismic refraction profiles: The IAM-9 transect at 40°20'N. Journal of Geophysical Research, **105**, no. B3, p. 5859-5885, March 10.

Dehler, S. A., Keen, C. E. 1993. Effects of rifting and subsidence on thermal evolution of sediemts in Canada's east coast basins. Canadian Journal of Earth Science. **30**, p. 1782-1798.

Dentith, M. C. and Hall, J. 1990. Application of section balancing techniques to deep seismic reflection data from the offshore eastern Canada: preliminary observations. Can. J. Earth Sci., **27**, p. 494-500.

Deptchuk, M., MacRae, R. A., Shimeld, G., Fensome, R. 2003. Revised Upper Cretaceous and lower Paleogene lithostratigraphy and depositional history of the Jeanne d'Arc Basin, offshore Newfoundland, Canada. AAPG Bulletin, **87**, no. 9, p. 1459-1483.

de Voogd, B., Keen, D. E., Kay, W. A. 1990. Fault reactivation during Mesozoic extension in eastern offshore Canada. Tectonophysics, **173**. p. 567-580.

Driscoll, N., Hogg, J., Christie-Blick, N., Karner, G. 1995. Extensional Tectonics in the Jeanne d'Arc basin, offshore Newfoundland: implications for the timing of break-up between Grand Banks and Iberia. ***In:*** *The tectonics, sedimentation and Palaeocenography of the North Atlantic regions* (eds. Scrutton, R. A., Stoker, M. S., Shimmield, G. B., Tudhope, A. W.). Geological Society Special Publication, **90**, p. 1-28.

Dunbar, J. A., Sawyer, D. S. 1989. Patterns of continental extension along the conjugate margins of he Central and North Atlantic Oceans and Labrador Sea, Tectonics, **8**, 1059-1077.

Einsele, G. 2000. Sedimentary Basins: Evolution, Facies and Sediment Budget. Springer-Verlag Berlin.

Enachescu, M., Fagan, P. 2004. Newfoundland and Labrador Call for Bids NF04-01, Government of Newfoundland and Labrador, Department of Natural Resources, p. 1-35.

Enachescu, M. 1992a. Basement Extension of the Newfoundland Continental Margin (Canadian East Coast). ***In:*** *Basement Tectonics* (ed. Mason, R.). **7**, p. 227-256. Kluwer Academic Publishers.

Enachescu, M. 1992b. Enigmatic basins offshore Newfoundland. Canadian Journal of Exploration Geophysics. **28,** 1, June, p. 44-61.

Enachescu, M. 1988. Extended Basement beneath the intracratonic rifted basins of the Grand Banks of Newfoundland. Canadian Journal of Exploration Geophysics. **24,** 1, June, p. 48-55.

Eustace, G. 2002. Seismolgical imaging of along-strike variation of the Newfoundland-Iberia conjugate margin. Honours dissertation. Department of Earth Sciences, Memorial University of Newfoundland.

Funck, T., Hopper, J. R., Larsen, H.C., Louden, K. E., Tucholke, B. E., Holbrook, S. 2003. Crustal structure of the ocean-continent transition at the Flemish Cap: Seismic Refraction results. Journal of Geophysical research, 108, no. B11, p. 2531.

Gawthorpe, R. L., Leeder, M. R., 2000. Tectono-sedimentary evolution of active extensional basins. ***In:*** *Basin Research*, **12**, p. 195-218.

Gibbs, A. D. 1984. Structural evolution of extensional basin margins. J. geol. Soc. London, **141,** p. 609-620.

Grant, A. C., Jansa, L. F., McAlpine, K. D., Edwards, A. 1988. Mesozoic-Cenozoic Geology of the eastern margin of the Grand Banks and its relation to Galicia Bank. Proceedings of the Ocean Drilling Program, Scientific Results, **103**, p. 787-808.

Hall, 2005. Pers. Comm.

Hopper, J. R., Funck, T., Tucholke, B., Larsen, H. C., Holbrook, S., Louden, K., Shillington, D., Lau, H. 2004. Continental breakup and the onset of ultra-slow seafloor spreading off Flemish Cap on the Newfoundland rifted margin. Geology **32**, p. 93-96.

Hubbard, R. J., Pape, J., Roberts, D. G. 1985. Depositional sequence mapping to illustrate the evolution of a passive continental margin. ***In:*** *Seismic Stratigraphy II.* (eds. Berg, O. R., and Wollverton, D. C.) Memoirs of the American Association of Petroleum Geologists. **39**, p. 93-115.

Huismans, R., Beaumont, C. 2003. Symmetric and asymmetric lithospheric extension: Relative effects of frictional-plastic and viscous strain softening. J. Geophys. Res., **108**, no. B10, 2496, doi:10.1029/2002JB002026, 2003.

Huismans, R., Beaumont, C. 2002. Asymmetric lithosphere extension: The role of frictional plastic strain softening inferred from numerical experiments. Geology, March 2002, **30**, no. 3, p. 211-214.

Jansa, L. F., Bujak, J. P., Willians, G. L. 1980. Upper Triassic salt deposits of the western North Atlantic. Canadian Journal of Earth Sciences, **17**, 5 (May), p. 547-559.

Jarvis, G., McKenzie, D. 1980. Sedimentary basin formation with finite extension rates. Earth and Planetary Science Letters, **48**, no. 1, p. 42-52.

Keen, C. E., Boutilier, R., De Voogd, B., Mudford, B., and Enachescu, M. E. 1987a. Crustal geometry and extensional models for the Grand Banks, Eastern Canada: Constraints from deep seismic reflection data. Canadian Society of Petroleum Geologists, Memoir 12, p 101-115.

Keen, C. E., Dehler, S. A. 1997. Extensional styles and gravity anomalies at rifted continental margins: Some North Atlantic examples. Tectonics, **16**, 5, p. 774-754.

Keen, C. E., Dehler, S. A. 1993. Stretching and Subsidence: Rifting of conjugate margins in the North Atlantic region. Tectonics, **12**, 5, p. 1209 -1229.

Keen, C. E., de Voogd, B. 1988. The continent-ocean boundary at the rifted margin off eastern Canada: New results from deep seismic reflection studies. Tectonics, **7**, 1, p. 107-124.

Keen, C. E., Kay, W. A., Roest, W. R. 1990. Crustal anomaly of a transform continental margin. Tectonophysics, **173**, p. 527-544.

Keen, C. E., Potter, D. P. 1995. Formation and evolution of the Nova Scotian rifted margin: Evidence from deep seismic reflection data. Tectonics, **14**, 4, p. 918-932.

Keen, C. E., Stockmal, G. S., Welsink, H., Quinlan, G., Mudford, B. 1987b. Deep crustal structure and evolution of the rifted margin northeast of Newfoundland: results from LITHOPROBE East. Canadian Journal of Earth Science, **24**, p. 1537-1549.

Larner, K., Chambers, R., Yang, M., Lynn, W., Wai, W. 1983. Coherent noise in marine seismic data. Geophysics. **48**, 7, July, p. 854-886.

Huismans, R., Beaumont, C. 2003. Symmetric and asymmetric lithospheric extension: Relative effects of frictional-plastic and viscous strain softening. J. Geophys. Res., **108**, no. B10, 2496, doi:10.1029/2002JB002026, 2003.

Huismans, R., Beaumont, C. 2002. Asymmetric lithosphere extension: The role of frictional plastic strain softening inferred from numerical experiments. Geology, March 2002, **30**, no. 3, p. 211-214.

Jansa, L. F., Bujak, J. P., Willians, G. L. 1980. Upper Triassic salt deposits of the western North Atlantic. Canadian Journal of Earth Sciences, **17**, 5 (May), p. 547-559.

Jarvis, G., McKenzie, D. 1980. Sedimentary basin formation with finite extension rates. Earth and Planetary Science Letters, **48**, no. 1, p. 42-52.

Keen, C. E., Boutilier, R., De Voogd, B., Mudford, B., and Enachescu, M. E. 1987a. Crustal geometry and extensional models for the Grand Banks, Eastern Canada: Constraints from deep seismic reflection data. Canadian Society of Petroleum Geologists, Memoir 12, p 101-115.

Keen, C. E., Dehler, S. A. 1997. Extensional styles and gravity anomalies at rifted continental margins: Some North Atlantic examples. Tectonics, **16**, 5, p. 774-754.

Keen, C. E., Dehler, S. A. 1993. Stretching and Subsidence: Rifting of conjugate margins in the North Atlantic region. Tectonics, **12**, 5, p. 1209 -1229.

Keen, C. E., de Voogd, B. 1988. The continent-ocean boundary at the rifted margin off eastern Canada: New results from deep seismic reflection studies. Tectonics, **7**, 1, p. 107-124.

Keen, C. E., Kay, W. A., Roest, W. R. 1990. Crustal anomaly of a transform continental margin. Tectonophysics, **173**, p. 527-544.

Keen, C. E., Potter, D. P. 1995. Formation and evolution of the Nova Scotian rifted margin: Evidence from deep seismic reflection data. Tectonics, **14**, 4, p. 918-932.

Keen, C. E., Stockmal, G. S., Welsink, H., Quinlan, G., Mudford, B. 1987b. Deep crustal structure and evolution of the rifted margin northeast of Newfoundland: results from LITHOPROBE East. Canadian Journal of Earth Science, **24**, p. 1537-1549.

Larner, K., Chambers, R., Yang, M., Lynn, W., Wai, W. 1983. Coherent noise in marine seismic data. Geophysics. **48**, 7, July, p. 854-886.

B., Taylor, B., Froitzheim, N). Geological Society, London, Special Publications, **187**, p. 405-428.

Mauffret, A., Mougenot, D., Miles, P. R., Malod, J. A., 1989. Cenozoic deformation and Mesozoic abandoned spreading centre in the Tagus Abyssal Plain (west of Portugal): results of a mutichannel seismic survey. Canadian Journal of Earth Science, **26**, p. 1101-1123.

McApine, K. D. 1990. Mesozoic Stratigraphy, Sedimentary Evolution, and Petroleum Potential of the Jeanne d'Arc Basin, Grand Banks of Newfoundland. Geological Survey of Canada Paper 89-17.

McKenzie, D. 1978. Some Remarks on the Development of Sedimentary Basins. Earth and Planetary Science Letters, **40**, p. 25-32.

McLeod, A., Underhill, J., Davies, S., Dawers, N. 2002. The influence of fault array evolution on synrift sedimentation patterns: Controls on deposition in the Strathspey-Brent-Statfjord half graben, northern North Sea. AAPG Bulletin, **86**, no. 6, p. 1061-1093.

Neugebauer, H. 1987. Models of Lithospheric Thinning. Annual Review of Earth and Planetary Sciences. **15**, p. 421-443.

Newfoundland Energy Branch. 2000. Sedimentary basins and hydrocarbon potential of Newfoundland and Labrador. Government of Newfoundland and Labrador, Dept. of Mines and Energy, Energy Branch, Report 2000-01, p. 1-67.

Oakey, G. N., Delher, S. A. 2004. Atlantic Canada Magnetic Map Series: Grand Banks and surrounds. Geological Survey of Canada, Open File 1816, 1:1 500 000

Parker, R. S. 1999. Ancient Submarine Canyons and Fans of the Carson Basin, Grand Banks, Offshore Newfoundland, Canada. Honours dissertation. Department of Earth Sciences, Dalhousie University.

Peddy, C., Pinet, B., Masson, D., Scrutton, R., Sibuet, J. C., Warner, M. R., Lefort, J. P., Shroeder, I. J. 1989. Crustal structure of the Goban Spur continental margin, Northeast Atlantic, from deep seismic reflection profiling. Journal of the Geological Society, London. **146**, p. 427-437.

Pickup, S. L. B., Whitmarsh, R. B., Fowler, C. M. R., Reston, T. J. 1996. Insight into the nature of the ocean-continent transition off West Iberia from a deep multichannel seismic reflection profile. Geology, **24**, no. 12, p. 1079-1082.

Pinet, B., Montadert, L., Curnelle, R., Cazes, M., Marillier, F., Rolet, J., Tomassino, A., Galdeano, A., Patriat, Ph., Brunet, M. F., Olivet, J. L., Schaming, M., Lefort, J. P., Arrieta, A., Riaza, C. 1987. Crustal thinning on the Aquitaine shelf, Bay of Biscay, from deep seismic data. Nature, **325**, 5 Feb. 1987, p. 513-516

Pinheiro, L. M., Whitmarsh, R. B., Miles, P. R. 1992. The ocean-continent boundary off the western continental margin of Iberia – II. Crustal structure of the Tagus Abyssal Plain. Geophysical Journal International. **109**, p. 106-124.

ProMAX Reference Guide. 1998. A Reference Guide for the ProMAX Geophysical Processing Software, Landmark Graphics Corporation.

Reston, T. J. 1996. The S reflector west of Galicia: the seismic signature of a detachment fault. Geophysics Journal International. **127**, p. 230-244.

Reston, T. J., Krawczyk, Klaeschen, D. 1996. The S Reflector west of Galicia (Spain): Evidence from prestack depth migration for detachment faulting during continental breakup. Journal of Geophysical Research, B, Solid Earth and Planets, **101**, no. 4, p. 8075-8091.

Reston, T. J., Krawczyk, C. M., Hoffmann, H. J. 1995. Detachment tectonics during Atlantic rifting: analysis and interpretation of the S reflection, the west Galicia margin. ***In:*** *The Tectonics, Sedimentation and Palaeoceanography of the North Atlantic Region.* (eds. Scrutton, R. A., Stoker, M. S., Shimmield, G. B., and Tudhope, A. W.) Geological Society Special Publication No. **90**, p. 93-109.

Rosendahl, B. R. 1987. Architecture of Continental Rifts with Special reference to East Africa. Annual Review of Earth and Planetary Sciences, **15**, p. 445-503.

Royden, L. and Keen, C. 1980. Rifting Processes and thermal evolution of the continental margin of eastern Canada determined from subsidence curves. Earth and Planetary Science Letters, **51**, p. 343-361.

Ruppel, C. 1995. Extensional processes in continental lithosphere. Journal of Geophysical Research. **100**, No. B12, p. 24187-24215.

Russell, S. M., Whitmarsh, R. B. 2003. Magmatism at the West Iberia non-volcanic rifted continental margin; evidence from analyses of magnetic anomalies, Geophys. J. Int, **154**, p. 706-730.

Sclater, J. G., and Christie, P. A. F. 1980. Continental Stretching; an explanation of the post-Mid-Cretaceous subsidence on the central North Sea Basin. Journal of Geophysical Research, **85**, no. B7, p. 3711-3739.

Shillington, D. J., Holbrook, W. S., Tucholke, B. E., Hopper, J. R., Louden, K. E., Larsen, H. C., Van Avendonk, H. J. A., Deemer, S., Hall, J. 2004. Data Report: Marine geophysical data on the Newfoundland nonvolcanic rifted margin around SCREECH transect 2. ***In:*** *Proc. ODP, Init. Repts., 210 [Online].* (eds. Tucholke, B. E., Sibuet, J.-C., Klaus, A., et al.). Available from <http://www-odp.tamu.edu/publications/210_IR/chap_05/chap_05.html.

Shipboard Scientific Party, 2003. Leg 210 Preliminary Report. *ODP Prelim. Report.* (Online) Available from: www-odp.tamu.edu/publications/prelim/210-prel/210PREL.PDF (Cited, 2004-01-12).

Shipboard Scientific Party, 2004a. Leg 210 Summary. ***In:*** *Proc. ODP, Init. Repts, 210* (eds. Tucholke, B. E., Sibuet, J.-C., Klaus, A., et al.) p. 1-78. Available from: Ocean Drilling Program, Texas A&M University, College Station TX 77845-9547, USA.

Shipboard Scientific Party, 2004b. Site 1276. ***In:*** *Proc. ODP, Init. Repts, 210* [CD-ROM](eds. Tucholke, B. E., Sibuet, J.-C., Klaus, A., et al.) p. 1-358. Available from: Ocean Drilling Program, Texas A&M University, College Station TX 77845-9547, USA.

Sibuet, J. C., Srivastava, S. P., Enachescu, M. E., Karner, G. 2005. Lower Cretaceous motion of the Flemish Cap in respect with North America: Implication for the formation of Orphan Basin and Flemish Cap/Galicia Bank conjugate margins. 6th Petroleum Geology Conference: North West Europe & Global Perspectives, NSF Intermargins workshop, Pontresina Conference.

Sibuet, J. C. 1992. New constraints on the formation of the non-volcanic continental Galicia-Flemish cap conjugate margins. Journal of the Geological Society, London, **149**, p. 829-840.

Sinclair, I. K. 1995a. Sequence stratigraphic response to Aptian-Albian rifting in conjugate margin basins: a comparison of the Jeanne d'Arc Basin, offshore Newfoundland, and the Porcupine Basin, offshore Ireland. ***In:*** *The Tectonics, Sedimentation and Palaeoceanography of the North Atlantic Region.* (ed. Scrutton, R. A., Stoker, M. S., Shimmield, G. B., and Tudhope, A. W.) Geological Society Special Publication No. **90**, p. 29-49.

Sinclair, I. K. 1995b. Transpressional inversion due to episodic rotation of extensional stresses in Jeanne d'Arc Basin, offshore Newfoundland. ***In:*** *Basin Inversion* (ed. Buchanan, J. G. and Buchanan, P. G.), Geological Society Special Publication. No. **88** p. 249-271.

Srivastava, S. P., Sibuet, J.-C., Cande, S., Roest, W. R., Reid, I. D. 2000. Magnetic evidence for sloe seafloor spreading during the formation of the Newfoundland and Iberian margins. Earth Planet. Sci. Lett., **178**, p. 327-388.

Srivastava, S. P., Verhoef, J. 1992. Evolution of Mesozoic sedimentary basins around the North Central Atlantic: a preliminary plate kinematic solution. ***In:*** *Basins on the Atlantic Seaboard: Petroleum Geology, Sedimentology and Basin Evolution* (ed. Parnell, J.). Geologic Society Special Publication No. **62**, p. 397-420

Tankard, A. J., Welsink, H. J. 1987. Extensional Tectonics and Stratigraphy of Hibernia Oil Field, Grand Banks, Newfoundland. American Association of Petroleum Geologists Bulletin, **71**, 10 (October), p. 1210-1232.

Tankard, A. J., Welsink, H. J., Jenkins, W. A. M. 1989. Chapter 17. Structural Styles and Stratigraphy of the Jeanne d'Arc Basin, Grand Banks of Newfoundland. ***In:*** *Extensional tectonics and stratigraphy of the North Atlantic Margins* (ed. A.J. Tankard and H.R. Balkwill), Mem. **46**, p.265-282.

Tucholke, B. E., Austin Jr.,J. A., Uchupi, E. 1989. Chapter 16. Crustal Structure and Rift-Drift Evolution of the Newfoundland Basin. ***In:*** *Extensional tectonics and stratigraphy of the North Atlantic Margins* (ed. A.J. Tankard and H.R. Balkwill), Mem. **46**, p. 247-263.

Vail, P.R., Hardenbol, J., and Todd, R.G. 1984. Jurassic unconformities, chronostratigraphy, and sea-level changes from seismic stratigraphy and biostratigraphy. ***In:*** *Interregional Unconformities and Hydrocarbon Accumulation* (ed. J. S. Schlee). American Association of Petroleum Geologists Memoir **36**, p. 129-144.

Vail, P., Mitchum, R., M., Jr., Todd, R. G., Widmier, J. M., Thompson, S., III, Sangree, J. B., Bubb, J. N., Hatelid, W., G. 1977. Seismic stratigraphy and global changes of sea level. ***In:*** *Seismic Stratigraphy: Applications to Hydrocarbon Exploration* (ed. Payton, C. E.). Mem. Am. Assoc. Pet. Geol., **26**, p. 49-212.

Wernicke, B. 1985. Uniform-sense normal simple shear of the continental lithosphere. Canadian Journal of Earth Science. **22**, p. 108-125.

Wernicke, B., Burchfiel, B. C. 1982. Modes of extensional tectonics. Journal of Structural Geology. 4, 2, p. 105-115.

Whitmarsh, R. B. Dean, S. M., Minshull, T. A., Tompkins, M. 2000. Tectonic implications of exposure of lower continental crust beneath the Iberia Abyssal Plain, Northeast Atlantic Ocean: geophysical evidence. Tectonics, **19** no. 5, p. 919-942.

Whitmarsh, R. B., Minshull, T. A., Russell, S. M., Dean, S. M., Louden, K. E., Chian, D. 2001. The role of syn-rift magmatism in the rift-to-drift evolution of the West Iberia continental margin: geophysical observations. ***In:*** *Non-Volcanic Rifting of continental Margins: A comparison of evidence from Land and Sea.* (ed. Wilson, R. C. L. , Whitmarsh, R. B., Taylor, B., Froitzheim, N). Geological Society, London, Special Publications, **187**, p. 107-124.

Whitmarsh, R. B., Sawyer, D. S. 1996. The ocean/continent transition beneath the Iberian Abyssal Plain and continental-rifting to seafloor-spreading processes. ***In:*** *Proc. ODP, Sci. Results, Vol. 149* (eds. Whitmarsh, R. B., Sawyer, D. S., Klaus, A., Masson, D. G., Ocean Drilling Program, College Station, TX.). p. 713-736.

Whitmarsh, R B., White, R. S., Horsefield, S. J., Sibuet, J-C., Recq, M., Louvel, V. 1996. The ocean-continent boundary off the western continental margin of Iberia: Crustal structure west of Galicia Bank. Journal of Geophysical Research, **101**, no. B12, p. 28291-28314, December 10.

Williams, H. 1984. Miogeoclines and Suspect Terranes of the Caledonian-Appalachian Orogen: Tectonic Patterns in the North Atlantic Region. Canadian Journal of Earth Sciences, **21**, p. 887-901.

Williamson, M. A. 1992. The subsidence, compaction, thermal and maturation history of the Egret Member source rock, Jeanne d'Arc Basin, offshore Newfoundland. Bulletin of Canadian Petroleum Geology, **40**, no. 2, p.136-150.

Younes, A. I., McClay, K. 2002. Development of accommodation zones in the Gulf of Seuz – Red Sea rift, Egypt. AAPG Bulletin, Vol. **86**, 6, p. 1003-1026.

Appendix 1

Processing Flow for SCREECH Line 401

FLOW – 1.0 SEGYread
Output - line401
SEG-Y Input

FLOW – 2.0 MergingFiles_LoadGeom
Output - Line401_Merged_Geom
Inline Geom Header Load

Water velocity	1480.
Primary header to match database	FFID
Secondary header to match database	None
Match by valid trace number?	No
Drop traces with NULL CDP headers?	Yes
Drop traces with NULL receiver headers?	Yes
Verbose diagnostics?	Yes

FLOW – 3.0 EditShotgathers
Output - shotsmuted
Trace Muting

Re-apply previous mutes	No
Mute time reference	Time 0
TYPE of mute	Bottom
Ending ramp	30.
SELECT mute parameter file	s_1199_bottom

Trace Muting

Re-apply previous mutes	No
Mute time reference	Time 0
TYPE of mute	Bottom
Ending ramp	30.
SELECT mute parameter file	s_1285_bottom

Trace Muting

Re-apply previous mutes	No
Mute time reference	Time 0
TYPE of mute	Bottom
Ending ramp	30.
SELECT mute parameter file	s_1269_bottom

Trace Muting

Re-apply previous mutes	No
Mute time reference	Time 0
TYPE of mute	Bottom
Ending ramp	30.
SELECT mute parameter file	s_1223_bottom

Trace Muting

Re-apply previous mutes	No
Mute time reference	Time 0
TYPE of mute	Bottom
Ending ramp	30.
SELECT mute parameter file	s_1186_bottom

Trace Muting

Re-apply previous mutes	No
Mute time reference	Time 0
TYPE of mute	Bottom
Ending ramp	30.
SELECT mute parameter file	s_1175_bottom

Trace Muting

Re-apply previous mutes	No
Mute time reference	Time 0
TYPE of mute	Bottom
Ending ramp	30.
SELECT mute parameter file	s_1169_bottom

Trace Muting

Re-apply previous mutes	No
Mute time reference	Time 0
TYPE of mute	Bottom
Ending ramp	30.
SELECT mute parameter file	s_1168_bottom

Trace Muting

Re-apply previous mutes	No
Mute time reference	Time 0
TYPE of mute	Bottom
Ending ramp	30.
SELECT mute parameter file	s_1164_bottom

Trace Muting

Re-apply previous mutes	No

Mute time reference	Time 0
TYPE of mute	Bottom
Ending ramp	30.
SELECT mute parameter file	s_1154_bottom

Trace Muting

Re-apply previous mutes	No
Mute time reference	Time 0
TYPE of mute	Bottom
Ending ramp	30.
SELECT mute parameter file	s_1129_bottom

FLOW – 4.0 FK_analysis_shot

Output - 401_FK

Trace Muting

Re-apply previous mutes	No
Mute time reference	Time 0
TYPE of mute	Top
Starting ramp	30.
SELECT mute parameter file	bigmute

Bandpass Filter

TYPE of filter	Time and Space Variant
Type of filter specification	Ormsby bandpass
PHASE of filter	Minimum
Percent additive noise factor	1.
Apply a notch filter?	No
Space-variant filter parameters	
1:7-10-90-110, 7-10-50-60, 5-8-40-50/	
Get time gates from the DATABASE?	No
SELECT Primary time gate header word	Source number
SELECT Secondary time gate header	No trace header
SPECIFY filter time gate parameters	1:0-1500, 3000-6000, 9000-16000

IF Shot 1-4860

True Amplitude Recovery

Basis for spherical spreading	1/(time*vel**2)
Should the velocity be treated as space variable?	No
Specify TAR velocity function	
0-1480, 2000-2500, 5000-4500, 8000-4500, 16000-3500	
APPLY function to data or REMOVE	Apply
Maximum application TIME	0.

ENDIF

IF Shot 4861-5661

True Amplitude Recovery

Basis for spherical spreading	1/(time*vel**2)
Should the velocity be treated as space variable?	No
Specify TAR velocity function	
0-1480, 1000-2500, 5000-3000, 8000-4500, 16000-4800	
APPLY function to data or REMOVE	Apply
Maximum application TIME	0.

ENDIF

Windowed Processing

Apply trace windowing for subsequent process?	Yes
Trace blending mix overlap length	100.
SELECT windowing time gate parameter	Prestack_FK

F-K Filter

Type of F-K filter	ArbitraryPolygon
Test the filter impulse response?	No
Get polygon mute file from the database?	Yes
Select mute parameter file	Shot_Accept
Mode of F-K filter operation	ACCEPT

FLOW - 5.0 NMO_stacking

Output - 401_Shelf_Stack - (only CDPs 429546-466045)

Windowed Processing

Apply trace windowing for subsequent process?	Yes
Trace blending mix overlap length	100.
SELECT windowing time gate parameter file	Prestack_Decon

Predictive Deconvolution

TYPE of deconvolution	Minimum phase predictive
Decon operator length(s)	300
Operator prediction distance(s)	90
Apply prediction filter correction?	No
Operator 'white noise' level(s)	0.1
Time gate reference	Time 0
Get decon gates from the DATABASE?	No
SELECT Primary decon gate header word	CDP bin number
SELECT Secondary decon gate header	RecordingChannel
SPECIFY decon gate parameters	
429546:480:0-5000/ 429546:1:5000-7500	
Output traces or filters	Normal decon
Apply a bandpass filter after decon?	No

Normal Moveout Correction

Direction for NMO application	FORWARD
Stretch mute percentage	0.
Apply any remaining static during NMO?	No
Anisotropy correction parameter eta	0.
Get velocities from the database?	Yes
SELECT Velocity parameter file	NMO_VEL_Repicked

Trace Muting

Re-apply previous mutes	No
Mute time reference	Time 0
TYPE of mute	Top
Starting ramp	30.
SELECT mute parameter file	Nmo_stretchmute

CDP/Ensemble Stack

Sort order of input ensembles	CDP
METHOD for trace summing	Mean
Root power scalar for stack normalization	0.5
Apply final datum statics after stack?	No

FLOW - 6.0 NMO_stackingslope

Output - 401_Slope_Stack (only CDPs 466046-475305)

Normal Moveout Correction

Direction for NMO application	FORWARD
Stretch mute percentage	0.
Apply any remaining static during NMO?	Yes
Anisotropy correction parameter eta	0.
Get velocities from the database?	Yes
SELECT Velocity parameter file	NMO_VEL_Repicked

IF CDP 468546-475305

Windowed Processing

Apply trace windowing for subsequent process?	Yes
Trace blending mix overlap length	100.
SELECT windowing time gate parameter file	slope_radon

Radon Filter

Number of P values	60
Minimum P value (ms)	-100
Maximum P value (ms)	2000
Type of transform to perform	parabolic
Pass modeled data or subtract from input	SUBTRACT

Type of Mute	Top
Get mute file from database	radon_2000

ENDIF

Trace Muting

Re-apply previous mutes	No
Mute time reference	Time 0
TYPE of mute	Bottom
Ending ramp	30.
SELECT mute parameter file	Slope_neartrace

Trace Muting

Re-apply previous mutes	No
Mute time reference	Time 0
TYPE of mute	Top
Starting ramp	30.
SELECT mute parameter file	Nmo_stretchmute

CDP/Ensemble Stack

Sort order of input ensembles	CDP
METHOD for trace summing	Mean
Root power scalar for stack normalization	0.5
Apply final datum statics after stack?	Yes

FLOW - 7.0 Shelf_poststack

Output - 401_Post_Shelf

IF CDP 429546-466046

Windowed Processing

Apply trace windowing for subsequent process?	Yes
Trace blending mix overlap length	100.
SELECT windowing time gate parameter file	401_postshelf_FK

F-K Filter

Type of F-K filter	ArbitraryPolygon
Test the filter impulse response?	No
Get polygon mute file from the database?	Yes
Select mute parameter file	SHELF_CDP
Mode of F-K filter operation	ACCEPT

ENDIF

Inline Sort

Select new PRIMARY sort key	CDP bin number
Select new SECONDARY sort key	No trace header

Maximum traces per output ensemble	1

Trace Header Math

Select mode	Fixed equation
DEFINE trace header equation	
SP = FFID - 59	

Windowed Processing

Apply trace windowing for subsequent process?	Yes
Trace blending mix overlap length	100.
SELECT windowing time gate parameter	Poststack_BP

Bandpass Filter

TYPE of filter	Time and Space Variant
Type of filter specification	Ormsby bandpass
PHASE of filter	Minimum
Percent additive noise factor	1.
Apply a notch filter?	No
Space-variant filter parameters	
429546:7-10-70-90, 7-10-45-60, 5-8-30-45	
Get time gates from the DATABASE?	No
SELECT Primary time gate header word	CDP bin number
SELECT Secondary time gate header	No trace header
SPECIFY filter time gate parameters	
429546:0-1500, 3000-6000, 9000-16000	

FLOW - 8.0 Slope_poststack

Output - 401_Post_Slope

Trace Header Math

Select mode	Fixed equation
DEFINE trace header equation	
SP = FFID - 59	

Time-Variant Scaling

Basis for scaling	USER-VALS
USER TVS Gain Values	
466046:0.5,1.5,1.3,6.0/	
467546:0.5,1.1,1.0,6.0/	
469546:0.5,1.4,0.4,4.0/	
471546:0.5,1.0,0.1,1.5/	
472546:0.5,1.0,0.7,4.0/	
473546:0.5,1.3,0.7,5.0/	
Basis for application	CENTER

Type of output	TRACES
SELECT Time Gate Parameter File	Slope_Scaling

IF CDP 466046 - 469046

Windowed Processing

Apply trace windowing for subsequent process?	Yes
Trace blending mix overlap length	100.
SELECT windowing time gate parameter file	water_multiple

F-K Filter

Type of F-K filter	ArbitraryPolygon
Test the filter impulse response?	No
Get polygon mute file from the database?	Yes
Select mute parameter file	water_multiple
Mode of F-K filter operation	ACCEPT

ENDIF

Inline Sort

Select new PRIMARY sort key	CDP bin number
Select new SECONDARY sort key	No trace header
Maximum traces per output ensemble	1

Windowed Processing

Apply trace windowing for subsequent process?	Yes
Trace blending mix overlap length	100.
SELECT windowing time gate parameter file	PostStack_fk

F-K Filter

Type of F-K filter	ArbitraryPolygon
Test the filter impulse response?	No
Get polygon mute file from the database?	Yes
Select mute parameter file	Slope_CDP
Mode of F-K filter operation	ACCEPT

Windowed Processing

Apply trace windowing for subsequent process?	Yes
Trace blending mix overlap length	100.
SELECT windowing time gate parameter file	Poststack_BP

Bandpass Filter

TYPE of filter	Time and Space Variant
Type of filter specification	Ormsby bandpass
PHASE of filter	Minimum
Percent additive noise factor	1.

Apply a notch filter?	No
Space-variant filter parameters	
466046:7-15-65-80, 7-10-40-50, 5-8-35-45	
470546:7-15-55-65, 7-10-40-50, 5-8-35-45	
Get time gates from the DATABASE?	No
SELECT Primary time gate header word	CDP bin number
SELECT Secondary time gate header word	No trace header
SPECIFY filter time gate parameters	
466046:0-1500, 3000-6000, 9000-16000	
470546:0-3500, 4000-7000, 9000-16000	

Inline Sort

Select new PRIMARY sort key	CDP bin number
Select new SECONDARY sort key	No trace header
Maximum traces per output ensemble	1

FLOW - 9.1 CombineStack

Output - 401_All_PostStack

Automatic Gain Control

Application mode	APPLY
Type of AGC scalar	MEAN
AGC operator length	4000.
BASIS for scalar application	Centered
Robust Scaling?	No

Time-Variant Scaling

Basis for scaling	USER-VALS
USER TVS Gain Values	
429546:1.0,2.6,1.4,1.7,1.0,1.2/	
450546:1.0,2.6,1.3,1.7,1.1,1.2/	
451546:1.0,2.6,1.1,1.7,1.1,1.2/	
454546:1.0,2.4,1.1,1.7,1.1,1.2/	
457046:1.0,2.4,1.3,1.8,1.1,1.2/	
466045:1.0,2.6,1.9,1.8,1.1,1.2/	
466046:1.3,3.2,1.9,1.9,1.3,1.3/	
469046:1.3,2.5,2.4,1.9,1.3,1.2/	
470546:1.3,1.9,1.4,3.9,1.2,1.1/	
472546:1.3,2.9,1.4,3.9,1.2,1.1/	
474046:1.3,2.9,1.4,2.9,1.2,1.1/	
Basis for application	EDGE
Type of output	TRACES
SELECT Time Gate Parameter File	Line_Scaling

Predictive Deconvolution

TYPE of deconvolution	Minimum phase predictive
Decon operator length(s)	300,300
Operator prediction distance(s)	90,90
Apply prediction filter correction?	No
Operator 'white noise' level(s)	0.1,0.1
Time gate reference	Time 0
Get decon gates from the DATABASE?	No
SELECT Primary decon gate header word	CDP bin number
SELECT Secondary decon gate header word	No trace header
SPECIFY decon gate parameters	
429546:0-7000, 5000-16000	
Output traces or filters	Normal decon
Apply a bandpass filter after decon?	No

FLOW - 10.0 Migration

Output – Migration

Kirchhoff Time Migration.

Maximum frequency to migrate (in Hz)	90.
Migration aperture (feet or meters)	17000.
Maximum dip to migrate	45.
Avoid spatial aliasing?	No
Get RMS velocities from database?	Yes
Select RMS vs.time velocity file	Kirchhoff_MigVel
Re-apply trace mutes?	Yes

FLOW - 18.0 Migration_Display

Output – 401_Final

Trace Muting

Re-apply previous mutes	No
Mute time reference	Time 0
TYPE of mute	Bottom
Ending ramp	30.
SELECT mute parameter file	Stacked_seafloor

Windowed Processing

Apply trace windowing for subsequent process?	Yes
Trace blending mix overlap length	100.
SELECT windowing time gate parameter file	Poststack_BP

Bandpass Filter

TYPE of filter	Single Filter
Type of filter specification	Ormsby bandpass
PHASE of filter	Minimum
Percent additive noise factor	1.
Apply a notch filter?	No
Ormsby Filter Frequency Values	5-9-75-100

Automatic Gain Control

Application Mode	APPLY
Type of AGC Scalar	MEAN
AGC operator length	2000.
BASIS for scalar application	Centered
Robust Scaling?	No

F-K Filter

Type of F-K filter	Power Exponent
Power to raise F-K space to:	1.2

Trace Mixing - 9 Trace Mix

1.0,1.0,1.0,1.0,2.0,1.0,1.0,1.0,1.0

Time-Variant Scaling

Basis for scaling: USER-VALS

USER TVS Gain Values

429546:2.3,1.4,1.8,1.6,1.9,1.3,1.1,1.5,1.1/
440546:2.3,1.4,1.5,1.5,1.9,1.3,1.1,1.5,1.1/
449046:2.3,1.4,1.5,1.5,1.9,1.5,1.1,1.5,1.1/
451546:2.3,1.4,1.6,1.7,1.9,1.6,1.1,1.5,1.1/
452546:2.3,1.4,1.9,1.3,1.7,1.5,1.7,1.0,1.1/
454545:2.3,1.4,1.6,1.3,1.7,1.3,1.2,1.0,1.1/
458546:2.3,1.4,1.8,1.7,1.9,1.1,1.2,1.1,1.1/
466045:2.3,1.4,1.8,1.7,1.9,1.1,1.2,1.1,1.1/
469546:1.9,2.4,2.0,1.8,1.0,1.2,1.1,1.1,1.1/
470046:1.9,2.4,3.9,1.6,1.0,1.8,1.1,1.1,1.1/
471546:2.5,1.9,3.9,2.5,1.0,1.5,1.1,1.1,1.1/
472046:2.5,1.9,2.9,2.1,1.0,1.5,1.1,1.1,1.1/
472546:2.2,1.9,1.3,2.5,0.6,1.8,1.1,1.1,1.1/
475305:1.8,1.7,1.4,2.9,0.6,1.9,1.1,1.4,1.1/

Basis for application	EDGE
Type of output	TRACES
SELECT Time Gate Parameter File	Migrated_Scale

Processing Flow for SCREECH Line 403

FLOW - Taperead
Output - Line_403_tape
SEG-Y Input

FLOW - Load_Geom
Output - Geom_2
Inline Geom Header Load

Water velocity	1480.
Primary header to match database	FFID
Secondary header to match database	None
Match by valid trace number?	No
Drop traces with NULL CDP headers?	Yes
Drop traces with NULL receiver headers?	Yes
Verbose diagnostics?	Yes

FLOW - Fk_filter
Output - Fk_Filtered_data
Trace Muting

Re-apply previous mutes	No
Mute time reference	Time 0
TYPE of mute	Top
Starting ramp	30.
SELECT mute parameter file	403_top_mute

Bandpass Filter

TYPE of filter	Time and Space
Type of filter specification	Ormsby bandpass
PHASE of filter	Minimum
Percent additive noise factor	1.
Apply a notch filter?	No
Space-variant filter parameters	
1:7-10-90-110, 7-10-50-60, 5-8-40-50	
Get time gates from the DATABASE?	No
SELECT Primary time gate header word	Source number
SELECT Secondary time gate header	No trace header
SPECIFY filter time gate parameters	
1:0-1500, 3000-6000, 9000-16000	

True Amplitude Recovery

Basis for spherical spreading	1/(time*vel**2)

Should the velocity be treated as space variable?	No
Specify TAR velocity function	
0-1480, 2000-2200, 4000-3200, 8000-4500, 16000-4700	
APPLY function to data or REMOVE	Apply
Maximum application TIME	0.

Windowed Processing

Apply trace windowing for subsequent process?	Yes
Trace blending mix overlap length	100.
SELECT windowing time gate parameter	Prestack_FK

F-K Filter

Type of F-K filter	Arbitrary Polygon
Test the filter impulse response?	No
Get polygon mute file from the database?	Yes
Select mute parameter file	403_fk_shot
Mode of F-K filter operation	ACCEPT

FLOW - NMO_Stacking

Output - 403_nmo_stacked

Trace Length

New trace length	16000.

Trace Muting

Re-apply previous mutes	No
Mute time reference	Time 0
TYPE of mute	Top
Starting ramp	30.
SELECT mute parameter file	403_top_mute

IF CDP = 479106-486006

Trace Muting

Re-apply previous mutes	No
Mute time reference	Time 0
TYPE of mute	Bottom
Ending ramp	30.
SELECT mute parameter file	403_NearTraceMute

ENDIF

IF CDP = 486106-494089

Windowed Processing

Apply trace windowing for subsequent process?	Yes
Trace blending mix overlap length	100.

SELECT windowing time gate parameter file	Prestack_decon_2

Spiking/Predictive Decon

TYPE of deconvolution	Minimum phase predictive
Decon operator length(s)	300
Operator prediction distance(s)	90
Apply prediction filter correction?	No
Operator 'white noise' level(s)	0.1
Time gate reference	Time 0
Get decon gates from the DATABASE?	No
SELECT Primary decon gate header word	CDP bin number
SELECT Secondary decon gate header	Recording channel
SPECIFY decon gate parameters	
486106:480:0-5000/486106:1:5000-8000/	
Output traces or filters	Normal decon
Apply a bandpass filter after decon?	No

ENDIF

Normal Moveout Correction

Direction for NMO application	FORWARD
Stretch mute percentage	0.
Apply any remaining static during NMO?	Yes
Anisotropy correction parameter eta	0.
Get velocities from the database?	Yes
SELECT Velocity parameter file	403_NMO_VEL_2

Trace Muting

Re-apply previous mutes	No
Mute time reference	Time 0
TYPE of mute	Top
Starting ramp	30.
SELECT mute parameter file	403_stretchmute

CDP/Ensemble Stack

Sort order of input ensembles	CDP
METHOD for trace summing	Mean
Root power scalar for stack normalization	0.5
Apply final datum statics after stack?	Yes

FLOW - Post_stack

Output - 403_poststack

Time-Variant Scaling

Basis for scaling	USER-VALS

USER TVS Gain Values	
479106:1.9,2.3,3.0,5.0,5.0,4.0/	
481106:1.6,1.0,3.0,5.0,6.0,5.0/	
482606:1.6,1.0,2.4,5.0,6.0,5.0/	
484606:1.9,1.0,1.5,3.0,4.0,4.0/	
485806:2.9,1.4,1.2,2.0,3.0,6.0/	
486100:2.9,0.6,0.9,3.0,5.3,5.0/	
486300:2.9,1.4,1.3,3.6,4.5,4.5/	
487106:1.6,0.5,1.5,4.9,8.0,8.0/	
487606:1.2,0.7,3.9,4.5,6.0,7.0/	
489606:1.4,3.3,8.0,8.0,8.0,8.0/	
491606:1.4,2.7,4.0,4.0,8.0,8.0/	
493606:1.4,2.7,5.0,8.0,8.0,7.0/	
Basis for application	CENTER
Type of output	TRACES
SELECT Time gate parameter file	403_Scaling

Windowed Processing

Apply trace windowing for subsequent process?	Yes
Trace blending mix overlap length	100.
SELECT windowing time gate parameter file	1_post_FK

F-K Filter

Type of F-K filter	Arbitrary Polygon
Test the filter impulse response?	No
Get polygon mute file from the database?	Yes
Select mute parameter file	1_post_FK
Mode of F-K filter operation	ACCEPT

Inline Sort

Select new PRIMARY sort key	CDP bin number
Select new SECONDARY sort key	No trace header
Maximum traces per output ensemble	1

Windowed Processing

Apply trace windowing for subsequent process?	Yes
Trace blending mix overlap length	100.
SELECT windowing time gate parameter	poststack_decon

Spiking/Predictive Decon

TYPE of deconvolution	Minimum phase predictive
Decon operator length(s)	300,300
Operator prediction distance(s)	90,90
Apply prediction filter correction?	No

Operator 'white noise' level(s)	0.1,0.1
Time gate reference	Time 0
Get decon gates from the DATABASE?	No
SELECT Primary decon gate header word	CDP bin number
SELECT Secondary decon gate header	No trace header
SPECIFY decon gate parameters	
479106:6000-12000, 10000-16000/	
486106:1500-7000, 5000-16000/	
Output traces or filters	Normal decon
Apply a bandpass filter after decon?	No

Windowed Processing

Apply trace windowing for subsequent process?	Yes
Trace blending mix overlap length	100.
SELECT windowing time gate parameter file	Poststack_bp

Bandpass Filter

TYPE of filter	Time and Space
Type of filter specification	Ormsby bandpass
PHASE of filter	Minimum
Percent additive noise factor	1.
Apply a notch filter?	No
Space-variant filter parameters	
479106:8-10-60-80, 5-8-35-50/	
485506:8-15-60-80, 5-8-35-50/	
Get time gates from the DATABASE?	No
SELECT Primary time gate header word	CDP bin number
SELECT Secondary time gate header	No trace header
SPECIFY filter time gate parameters	
479106:6000-10000, 12000-16000/	
485506:2000-8000, 10000-16000/	

Time-Variant Scaling

Basis for scaling	USER-VALS
USER TVS Gain Values	
479106:1.9,2.5,3.0,3.0,3.0,4.0/	
480606:1.7,2.5,3.0,2.5,2.5,3.5/	
481606:1.7,2.5,6.5,6.5,4.0,4.0/	
482606:1.7,1.5,6.3,4.5,3.0,4.0/	
485100:1.7,1.9,5.0,5.0,4.0,5.0/	
485606:1.7,1.5,10.9,10.0,9.0,6.5/	
485956:1.3,1.5,10.4,12.0,8.0,5.5/	
486156:1.9,1.9,7.5,2.0,6.0,8.0/	
486506:1.9,1.5,6.0,8.0,7.0,8.5/	

486806:1.9,3.9,5.0,5.0,7.0,6.0/

Basis for application	CENTER
Type of output	TRACES
SELECT Time gate parameter file	403_Scaling

Automatic Gain Control

Application mode	APPLY
Type of AGC scalar	MEAN
AGC operator length	8000.
BASIS for scalar application	Centered
Robust Scaling?	No

FLOW - Migration

Kirchhoff Time Mig.

Maximum frequency to migrate (in Hz)	80.
Migration aperture (feet or meters)	17000.
Maximum dip to migrate	45.
Avoid spatial aliasing?	Yes
Get RMS velocities from database?	Yes
Select RMS vs.time velocity file	403_MIG_VEL
Re-apply trace mutes?	Yes

FLOW - Plot_CGM

Output - 403_nmo_mig_scaled

Automatic Gain Control

Application mode	APPLY
Type of AGC scalar	MEAN
AGC operator length	4000.
BASIS for scalar application	Centered
Robust Scaling?	No

Windowed Processing

Apply trace windowing for subsequent process?	Yes
Trace blending mix overlap length	100.
SELECT windowing time gate parameter file	403_AGCwindow

Automatic Gain Control

Application mode	APPLY
Type of AGC scalar	MEAN
AGC operator length	500.
BASIS for scalar application	Centered
Robust Scaling?	No

Windowed Processing

Apply trace windowing for subsequent process?	Yes
Trace blending mix overlap length	100.
SELECT windowing time gate parameter	Poststack_bp

Bandpass Filter

Type of filter specification	Ormsby bandpass
PHASE of filter	Minimum
Percent additive noise factor	1.
Apply a notch filter?	No
Ormsby filter frequency values	5-10-70-100

Time-Variant Scaling

Basis for scaling	USER-VALS

USER TVS Gain Values

479106:1.4,1.2,0.8,1.4,1.1,1.2/
482106:1.4,1.3,0.8,1.2,1.1/1.2/
484106:1.4,1.3,0.8,1.4,1.1/1.2/
486106:1.3,1.4,1.0,1.4,1.1,1.2/
487106:1.5,0.8,1.3,1.4,0.9,1.2/
488106:1.5,0.9,1.2,1,3,0.9,1.2/

Basis for application	CENTER

SPECIFY TVS time gates

479106:0-7500,9000-10000,9500-10000,10500-11000,11000-12000,13000-16000
482106:0-5500,6000-6500,6500-7500,8000-10000,10000-12000,13000-16000/
484106:0-6000,6200-7500,7500-9000,8500-10000,10000-12000,12000-16000/
486106:0-5000,5000-6000,6500-8500,8500-9500,9500-10500,10000-16000/
487106:0-2000,2200-5000,5500-7000,7500-9500,10000-11000,10000-16000/
488106:0-2000,2200-3500,4000-75000,8000-10000,10200-12000,10000-16000/

Type of output	TRACES

Trace Mixing -11 trace mix

1.0,1.0,1.0,1.0,1.0,2.0,1.0,1.0,1.0,1.0,1.0

Trace Muting

Re-apply previous mutes	No
Mute time reference	Time 0
TYPE of mute	Top
Starting ramp	30.
SELECT mute parameter file	403_stack_mute

Processing Flow for SCREECH Line 402

FLOW - Taperead
Output - 402_fromtape
SEG-Y Input

FLOW - Load_Geom
Output - 402_Geom_Load
Inline Geom Header Load

Water velocity	1480
Primary header to match database	FFID
Secondary beader to match database	None
Match by valid trace number?	No
Drop traces with NULL CDP headers?	Yes
Drop traces with NULL receiver headers?	Yes
Verbose diagnostics?	Yes

FLOW - Filtering_Shot
Output - 402_FK_Filtered

Bandpass Filter	Time and Space
Type of filter specification	Ormsby bandpass
PHASE of filter	Minimum
Percent additive noise factor	1.
Apply a notch filter?	No
Space-variant filter parameters	
1:7-10-80-100, 7-10-40-60, 5-10-35-45/	
Get time gates from the DATABASE?	No
SELECT Primary time gate header word	Source number
SELECT Secondary time gate header	No trace header
SPECIFY filter time gate parameters	
1:2000-3000, 5000-7000, 9000-16000/	

True Amplitude Recovery

Basis for spherical spreading	1/(time*vel**2)
Should the velocity be treated as space variable?	No
Specify TAR velocity function	
0-1480, 2000-1480, 3000-1900, 8000-2500, 12000-3000	
APPLY function to data or REMOVE	Apply
Maximum application TIME	0.

Windowed Processing

Apply trace windowing for subsequent process?	Yes
Trace blending mix overlap length	100.
SELECT windowing time gate parameter	fk_shot_gates

F-K Filter

Type of F-K filter	Arbitrary Polygon
Test the filter impulse response?	No
Get polygon mute file from	Yes
Select mute parameter file	402_Shot_accept
Mode of F-K filter operation	ACCEPT

FLOW - NMO_stacking

IF SOURCE = 1-51

Trace Muting

Re-apply previous mutes	No
Mute time reference	Time 0
TYPE of mute	Bottom
Ending ramp	30.
SELECT mute parameter file	402_shotbottom

ENDIF

IF SOURCE = 51-91

Trace Muting

Re-apply previous mutes	No
Mute time reference	Time 0
TYPE of mute	Bottom
Ending ramp	30.
SELECT mute parameter file	402_shotmiddle

ENDIF

IF SOURCE = 501-531

Trace Muting

Re-apply previous mutes	No
Mute time reference	Time 0
TYPE of mute	Bottom
Ending ramp	30.
SELECT mute parameter file	402_shotmiddle2

ENDIF

Trace Kill

Trace editing MODE	Kill
SELECT trace Kill parameter file	402_Kill_Noise

Trace Kill

Trace editing MODE	Kill
SELECT trace Kill parameter file	killshot1

Trace Kill

Trace editing MODE	Kill
SELECT trace Kill parameter file	killshot2

Normal Moveout Correction

Direction for NMO application	FORWARD
Stretch mute percentage	30.
Apply any remaining static during NMO?	Yes
Anisotropy correction parameter eta	0.
Get velocities from the database?	Yes
SELECT Velocity parameter file	NMO_Vel

Trace Muting

Re-apply previous mutes	No
Mute time reference	Time 0
TYPE of mute	Bottom
Ending ramp	30.
SELECT mute parameter file	402_NearTraceMute

CDP/Ensemble Stack

Sort order of input ensembles	CDP
METHOD for trace summing	Mean
Root power scalar for stack normalization	0.5
Apply final datum statics after stack?	Yes

FLOW - PostStack

Output - 402_Post_Stack

Windowed Processing

Apply trace windowing for subsequent process?	Yes
Trace blending mix overlap length	100.
SELECT windowing time gate parameter	Poststack_BP
Bandpass Filter - TYPE	Time and Space
Type of filter specification	Ormsby bandpass
PHASE of filter	Minimum
Percent additive noise factor	1.
Apply a notch filter?	No
Space-variant filter parameters	
474858:7-10-65-75, 7-10-35-45, 5-10-35-45	
Get time gates from the DATABASE?	No

SELECT Primary time gate header word	CDP bin number
SELECT Secondary time gate header	No trace header
SPECIFY filter time gate parameters	
474858:3500-5000, 6000-9000, 10000-16000	

Trace Muting

Re-apply previous mutes	No
Mute time reference	Time 0
TYPE of mute	Top
Starting ramp	30.
SELECT mute parameter file	402_stackmute

Time-Variant Scaling

Basis for scaling	USER-VALS
USER TVS Gain Values	474858:3.9,0.3,2.3,1.1,1.3/
Basis for application	CENTER
SPECIFY TVS time gates	
474858: 0-6100, 6200-7200, 7500-8800, 9000-10000, 10100-16000	
Type of output	TRACES

Automatic Gain Control

Application mode	APPLY
Type of AGC scalar	MEAN
AGC operator length	1000.
BASIS for scalar application	Centered
Robust Scaling?	No

Windowed Processing

Apply trace windowing for subsequent process?	Yes
Trace blending mix overlap length	100.
SELECT windowing time gate parameter	fk_poststack_gate

F-K Filter

Type of F-K filter	Arbitrary Polygon
Test the filter impulse response?	No
Get polygon mute file from the database?	Yes
Select mute parameter file	402_poststack
Mode of F-K filter operation	ACCEPT

FLOW - Migration

Output - 402_Migrated

Kirchhoff Time Mig.

Maximum frequency to migrate (in Hz)	90.

Migration aperture (feet or meters)	0.
Maximum dip to migrate	45.
Avoid spatial aliasing?	Yes
Get RMS velocities from database?	Yes
Select RMS vs.time velocity file	402_Mig_vel2
Re-apply trace mutes?	Yes

FLOW - CGM_Plot

Output - 402_Post_Migrated

Windowed Processing

Apply trace windowing	Yes
Trace blending mix overlap length	100.
SELECT windowing time gate parameter	Poststack_BP

Bandpass Filter	Time and Space
Type of filter specification	Ormsby bandpass
PHASE of filter	Minimum
Percent additive noise factor	1.
Apply a notch filter?	No
Space-variant filter parameter	
474858:7-10-65-75, 7-10-35-45, 5-10-40-50	
Get time gates from the DATABASE?	No
SELECT Primary time gate header word	CDP bin number
SPECIFY filter time gate parameters	
474858:3500-5000, 6000-9000, 10000-16000	

Time-Variant Scaling

Basis for scaling	USER-VALS
USER TVS Gain Values	
474858:1.9,1.7,1.0,1.0/	
Basis for application	CENTER
SPECIFY TVS time gates	
474858:2500-5000,6000-7000,8000-11000,12500-16000/	
Type of output	TRACES

Trace Mixing - 9 trace Mix

1.0,1.0,1.0,1.0,2.0,1.0,1.0,1.0,1.0

F-K Filter

Type of F-K filter	Power Exponent
Power to raise F-K space to:	1.18

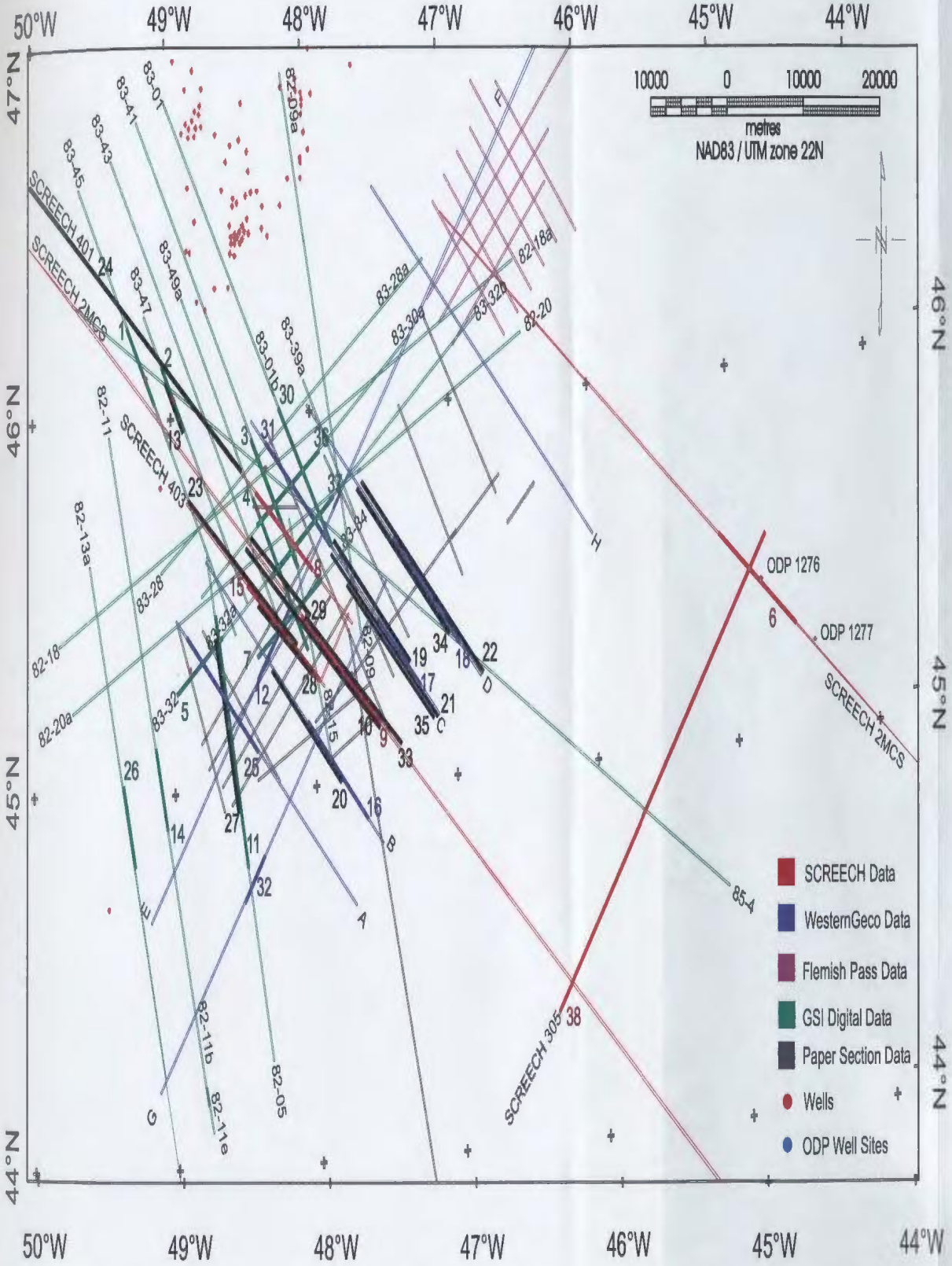

Line and Figure Numbers

1 = Figure 3.7a
2 = Figure 3.7b
3 = Figure 3.8
4 = Figure 3.9, Figure 4.11
5 = Figure 3.10
6 = Figure 3.11
7 = Figure 3.13 a, Figure 3.23
Figure 3.26, Figure 4.9
8 = Figure 3.13 b
9 = Figure 3.14
10 = Figure 3.16
11 = Figure 3.17
12 = Figure 3.19 a
13 = Figure 3.19 b
14 = Figure 3.21
15 = Figure 3.28
16 = Figure 3.35
17 = Figure 3.37 a
18 = Figure 3.37 b
19 = Figure 3.39 a
20 = Figure 3.39 b
21 = Figure 3.41 a
22 = Figure 3.41 b
23 = Figure 3.43
24 = Figure 3.45
25 = Figure 4.6 a
26 = Figure 4.6 b
27 = Figure 4.7
28 = Figure 4.8
29 = Figure 4.10
30 = Figure 4.12 a
31 = Figure 4.12 b
32 = Figure 4.14
33 = Figure 4.15
34 = Figure 4.16
35 = Figure 4.17
36 = Figure 4.19 a
37 = Figure 4.19 b
38 = Figure 4.20

Appendix 2. Location map of seismic lines displayed in figures. Seismic lines A to H are proprietary data provided by WesternGeco.

Appendix 3

Interval Velocity Values for Time-Depth Conversion

File input into Landmark Graphics TDQ Program
#
#FIELDS = Function ID, X, Y, Time, Vint
#FUNCTION_TYPE = TVint
#LINEAR_UNITS = METERS
#DATUM = 0.000000
#

Function1	642240.80	5107426.00	0.0000	1856.8186
Function1	642240.80	5107426.00	59.9031	1856.8186
Function1	642240.80	5107426.00	387.9030	1930.3857
Function1	642240.80	5107426.00	581.9031	2139.1746
Function1	642240.80	5107426.00	805.9031	2584.8206
Function1	642240.80	5107426.00	1467.9031	3027.1907
Function1	642240.80	5107426.00	1959.9025	2853.0830
Function1	642240.80	5107426.00	2077.9031	3510.9146

#

Function2	650141.00	5075688.00	0.0000	1877.5005
Function2	650141.00	5075688.00	54.8475	1877.5005
Function2	650141.00	5075688.00	234.8475	1991.9709
Function2	650141.00	5075688.00	554.8475	2030.1619
Function2	650141.00	5075688.00	714.8475	2095.4998
Function2	650141.00	5075688.00	834.8475	2794.0002
Function2	650141.00	5075688.00	894.8475	4267.3359
Function2	650141.00	5075688.00	980.8475	4465.5806
Function2	650141.00	5075688.00	1054.8475	3707.0249
Function2	650141.00	5075688.00	1154.8475	4267.1963
Function2	650141.00	5075688.00	1280.8474	3870.4795
Function2	650141.00	5075688.00	1384.8475	3399.6138
Function2	650141.00	5075688.00	1454.8475	3657.7253
Function2	650141.00	5075688.00	1594.8470	4354.2949
Function2	650141.00	5075688.00	1662.8475	3801.1594

#

Function3	657352.40	5101156.00	0.0000	1874.9998
Function3	657352.40	5101156.00	60.5057	1874.9998
Function3	657352.40	5101156.00	572.5057	2010.0836
Function3	657352.40	5101156.00	782.5056	2225.5364
Function3	657352.40	5101156.00	1686.5057	2267.4631
Function3	657352.40	5101156.00	1802.5057	3045.4634
Function3	657352.40	5101156.00	2032.5056	2772.9282

#

Function4	666657.00	5022894.00	0.0000	1823.9998
Function4	666657.00	5022894.00	60.7612	1823.9998
Function4	666657.00	5022894.00	362.7612	1841.3516
Function4	666657.00	5022894.00	460.7612	2027.7538

Function4	666657.00	5022894.00	862.7612	2062.3381
Function4	666657.00	5022894.00	960.7608	2282.8618
Function4	666657.00	5022894.00	1362.7611	2746.2180
Function4	666657.00	5022894.00	1460.7611	3048.1589
Function4	666657.00	5022894.00	1862.7601	3709.1611
Function4	666657.00	5022894.00	1960.7611	3663.6562
Function4	666657.00	5022894.00	2262.7612	3754.5007
Function4	666657.00	5022894.00	2276.7612	3875.7493
#				
Function5	690192.50	5009810.55	0.0000	1800.0001
Function5	690192.50	5009810.55	1808.0000	1800.0001
Function5	690192.50	5009810.55	2160.0000	2501.2568
Function5	690192.50	5009810.55	2200.0000	5003.3618
Function5	690192.50	5009810.55	2800.0000	2358.1562
Function5	690192.50	5009810.55	4576.0000	2222.3037
Function5	690192.50	5009810.55	5424.0000	2891.7246
#				
Function6	703534.60	5068984.00	0.0000	1832.7780
Function6	703534.60	5068984.00	113.9891	1832.7780
Function6	703534.60	5068984.00	472.9891	1704.4021
Function6	703534.60	5068984.00	713.9886	1864.4824
Function6	703534.60	5068984.00	736.9887	2072.1858
Function6	703534.60	5068984.00	953.9891	2119.1685
Function6	703534.60	5068984.00	976.9891	2174.7727
Function6	703534.60	5068984.00	1457.9891	2487.3594
Function6	703534.60	5068984.00	1480.9891	2936.5127
Function6	703534.60	5068984.00	2488.9890	3302.1831
Function6	703534.60	5068984.00	2958.9890	3359.2761
Function6	703534.60	5068984.00	2968.9890	3572.0249
Function6	703534.60	5068984.00	2974.9890	3776.7476
#				
Function7	707707.90	5081682.00	0.0000	1824.7466
Function7	707707.90	5081682.00	203.3876	1824.7466
Function7	707707.90	5081682.00	771.3876	1943.2091
Function7	707707.90	5081682.00	835.3873	1905.0149
Function7	707707.90	5081682.00	925.3876	2031.9926
Function7	707707.90	5081682.00	1005.3876	2285.9988
Function7	707707.90	5081682.00	1087.3876	2230.2419
Function7	707707.90	5081682.00	1171.3876	2177.1445
Function7	707707.90	5081682.00	1247.3876	2085.2637
Function7	707707.90	5081682.00	1251.3876	6100.1152
Function7	707707.90	5081682.00	1327.3876	2406.3113
Function7	707707.90	5081682.00	1391.3868	2857.5312
Function7	707707.90	5081682.00	1451.3876	3047.9668
Function7	707707.90	5081682.00	1527.3876	2406.3184
Function7	707707.90	5081682.00	1591.3876	2857.5054
Function7	707707.90	5081682.00	1651.3876	3047.9868
Function7	707707.90	5081682.00	1717.3876	2770.9116

Function7	707707.90	5081682.00	1771.3876	3386.6677
Function7	707707.90	5081682.00	1847.3876	2406.3184
Function7	707707.90	5081682.00	1911.3876	2857.5129
Function7	707707.90	5081682.00	1971.3872	3048.0029
Function7	707707.90	5081682.00	2041.3875	2612.5659
Function7	707707.90	5081682.00	2081.3875	4572.0015
Function7	707707.90	5081682.00	2131.3875	3657.6108
Function7	707707.90	5081682.00	2201.3875	2612.5564
Function7	707707.90	5081682.00	2301.3875	3657.6011
Function7	707707.90	5081682.00	2361.3875	3048.0010
Function7	707707.90	5081682.00	2391.3867	6096.0820
Function7	707707.90	5081682.00	2417.3875	1875.7355
#				
Function8	708689.25	4994508.87	0.0000	1800.0000
Function8	708689.25	4994508.87	2928.0000	1800.0000
Function8	708689.25	4994508.87	3695.9998	2097.1194
Function8	708689.25	4994508.87	4672.0000	2200.0801
Function8	708689.25	4994508.87	5488.0000	2533.9343
Function8	708689.25	4994508.87	6000.0000	3467.0215
Function8	708689.25	4994508.87	6432.0000	3196.5693
#				
Function9	735508.03	5033078.01	0.0000	1800.0001
Function9	735508.03	5033078.01	2048.0000	1800.0001
Function9	735508.03	5033078.01	2959.9990	2052.7002
Function9	735508.03	5033078.01	4192.0000	2015.8281
Function9	735508.03	5033078.01	4384.0000	3976.2590
Function9	735508.03	5033078.01	4900.0000	3112.6958
Function9	735508.03	5033078.01	5168.0000	2437.7029
#				
Function10	736766.25	5002756.03	0.0000	1800.0000
Function10	736766.25	5002756.03	3472.0000	1800.0000
Function10	736766.25	5002756.03	4448.0000	2045.0828
Function10	736766.25	5002756.03	5584.0000	2065.7070
Function10	736766.25	5002756.03	5936.0000	3714.2808
Function10	736766.25	5002756.03	6848.0000	2471.2681
Function10	736766.25	5002756.03	7296.0000	3761.3594
#				
Function11	740700.52	5061489.21	0.0000	1800.0001
Function11	740700.52	5061489.21	1456.0000	1800.0001
Function11	740700.52	5061489.21	1856.0000	2124.4241
Function11	740700.52	5061489.21	1984.0000	2484.5864
Function11	740700.52	5061489.21	2032.0000	5701.5151
Function11	740700.52	5061489.21	2109.0000	4051.0339
Function11	740700.52	5061489.21	2156.0000	4718.3726
#				
Function12	741761.10	5028621.84	0.0000	1800.0001
Function12	741761.10	5028621.84	2320.0000	1800.0001
Function12	741761.10	5028621.84	3380.0000	2004.1777

	Function12	741761.10	5028621.84	4600.0000	2004.3749
	Function12	741761.10	5028621.84	4999.9971	3058.4258
	Function12	741761.10	5028621.84	5300.0000	3323.2019
	Function12	741761.10	5028621.84	6780.0000	2632.8184
#					
	Function13	753711.38	5050904.58	0.0000	1800.0000
	Function13	753711.38	5050904.58	2019.9999	1800.0000
	Function13	753711.38	5050904.58	2800.0000	2042.0880
	Function13	753711.38	5050904.58	4060.0002	1982.5865
	Function13	753711.38	5050904.58	4420.0000	2901.0471
	Function13	753711.38	5050904.58	5540.0000	2561.7729
	Function13	753711.38	5050904.58	6580.0000	2672.2930
#					
	Function14	756210.67	4986636.18	0.0000	1800.0001
	Function14	756210.67	4986636.18	4288.0000	1800.0001
	Function14	756210.67	4986636.18	5200.0000	2134.2893
	Function14	756210.67	4986636.18	6320.0000	2117.4492
	Function14	756210.67	4986636.18	6832.0000	3540.3838
	Function14	756210.67	4986636.18	7615.9980	2160.6562
	Function14	756210.67	4986636.18	8768.0000	2299.3252
#					
	Function15	758764.82	4953028.72	0.0000	1800.0000
	Function15	758764.82	4953028.72	4672.0000	1800.0000
	Function15	758764.82	4953028.72	5632.0000	2317.5852
	Function15	758764.82	4953028.72	6832.0000	1989.7594
	Function15	758764.82	4953028.72	7328.0000	2630.9917
	Function15	758764.82	4953028.72	7904.0000	2438.4185
	Function15	758764.82	4953028.72	8143.9995	3254.8738
#					
	Function16	761823.25	5044226.23	0.0000	1800.9999
	Function16	761823.25	5044226.23	2400.0000	1800.9999
	Function16	761823.25	5044226.23	3291.9988	2131.1553
	Function16	761823.25	5044226.23	4512.0000	2080.6052
	Function16	761823.25	5044226.23	4600.0000	4864.5298
	Function16	761823.25	5044226.23	5504.0000	2646.7031
	Function16	761823.25	5044226.23	6399.9976	2308.6545
#					
	Function17	762651.34	5074771.80	0.0000	1800.0000
	Function17	762651.34	5074771.80	1888.0000	1800.0000
	Function17	762651.34	5074771.80	2448.0000	2060.1355
	Function17	762651.34	5074771.80	3439.9985	2014.2505
	Function17	762651.34	5074771.80	3652.0000	2203.6777
	Function17	762651.34	5074771.80	3751.9993	4204.2529
	Function17	762651.34	5074771.80	3952.0000	2598.6765
#					
	Function18	770809.98	5007726.04	0.0000	1800.0000
	Function18	770809.98	5007726.04	4120.0000	1800.0000
	Function18	770809.98	5007726.04	5340.0000	2065.7258

	Function18	770809.98	5007726.04	5980.0000	2852.1011
	Function18	770809.98	5007726.04	6660.0000	2136.6016
	Function18	770809.98	5007726.04	6899.9961	2887.7969
#					
	Function19	777126.03	5048351.96	0.0000	1800.0000
	Function19	777126.03	5048351.96	2680.0000	1800.0000
	Function19	777126.03	5048351.96	3740.0000	2300.4722
	Function19	777126.03	5048351.96	4959.9990	2167.8835
	Function19	777126.03	5048351.96	5300.0000	2219.6992
	Function19	777126.03	5048351.96	5580.0000	3115.3367
#					
	Function20	783592.60	5057507.61	0.0000	1800.9998
	Function20	783592.60	5057507.61	2768.0000	1800.9998
	Function20	783592.60	5057507.61	4080.0002	1935.8575
	Function20	783592.60	5057507.61	5024.0000	2497.7976
	Function20	783592.60	5057507.61	5344.0000	2281.5203
	Function20	783592.60	5057507.61	6287.9985	2359.9387
	Function20	783592.60	5057507.61	7348.0000	2204.4265
#					
	Function21	784535.25	4997841.58	0.0000	1800.0000
	Function21	784535.25	4997841.58	4432.0000	1800.0000
	Function21	784535.25	4997841.58	5744.0000	2066.7224
	Function21	784535.25	4997841.58	6480.0000	2547.8130
	Function21	784535.25	4997841.58	7040.0000	2210.3362
	Function21	784535.25	4997841.58	7503.9985	2510.0842
	Function21	784535.25	4997841.58	8384.0000	2361.2395
#					
	Function22	786528.41	5023670.25	0.0000	1800.0001
	Function22	786528.41	5023670.25	3840.0000	1800.0001
	Function22	786528.41	5023670.25	5120.0000	2076.9641
	Function22	786528.41	5023670.25	5776.0000	2497.2468
	Function22	786528.41	5023670.25	6272.0000	2770.5542
	Function22	786528.41	5023670.25	7391.9995	2153.2849
	Function22	786528.41	5023670.25	7871.9990	3379.4670
#					
	Function23	803112.61	5010371.30	0.0000	1800.0000
	Function23	803112.61	5010371.30	4192.0000	1800.0000
	Function23	803112.61	5010371.30	5456.0000	2005.4446
	Function23	803112.61	5010371.30	6224.0000	2239.3655
	Function23	803112.61	5010371.30	6848.0000	2913.8665
	Function23	803112.61	5010371.30	8160.0005	2381.4231
	Function23	803112.61	5010371.30	8640.0000	2511.8472
#					
	Function24	822549.88	4970437.25	0.0000	1800.0000
	Function24	822549.88	4970437.25	4880.0000	1800.0000
	Function24	822549.88	4970437.25	6224.0000	1907.3351
	Function24	822549.88	4970437.25	6736.0000	3151.2388
	Function24	822549.88	4970437.25	7247.9976	2835.7488

	Function24	822549.88	4970437.25	7856.0000	2537.5481
	Function24	822549.88	4970437.25	8128.0000	3317.6218
#					
	Function25	822676.30	5025073.15	0.0000	1800.0004
	Function25	822676.30	5025073.15	4177.9980	1800.0004
	Function25	822676.30	5025073.15	5296.0000	2018.5054
	Function25	822676.30	5025073.15	6048.0000	2776.4197
	Function25	822676.30	5025073.15	6528.0000	2444.0774
	Function25	822676.30	5025073.15	7968.0000	2397.0276
	Function25	822676.30	5025073.15	8096.0000	4483.9844
#					
	Function26	908040.43	5094380.99	0.0000	1501.3530
	Function26	908040.43	5094380.99	6045.4800	1501.3530
	Function26	908040.43	5094380.99	6949.4800	1911.2823
	Function26	908040.43	5094380.99	7024.4800	2293.3391
	Function26	908040.43	5094380.99	7149.4800	2400.0000
	Function26	908040.43	5094380.99	7199.4800	1999.9924
	Function26	908040.43	5094380.99	7349.4785	2333.3550
	Function26	908040.43	5094380.99	7519.4800	2685.6724
	Function26	908040.43	5094380.99	7585.4800	6700.8184
#					
	Function27	986152.71	5046901.99	0.0000	1501.3530
	Function27	986152.71	5046901.99	6045.4800	1501.3530
	Function27	986152.71	5046901.99	6949.4800	1911.2823
	Function27	986152.71	5046901.99	7024.4800	2293.3391
	Function27	986152.71	5046901.99	7149.4800	2400.0000
	Function27	986152.71	5046901.99	7199.4800	1999.9924
	Function27	986152.71	5046901.99	7349.4785	2333.3550
	Function27	986152.71	5046901.99	7519.4800	2685.6724
	Function27	986152.71	5046901.99	7585.4800	6700.8184


0
1000
2000